GEOCHEMICAL SIGNALS IN DYNAMIC SEDIMENTARY SYSTEMS ALONG CONTINENTAL MARGINS

EDITED BY: Natascha Riedinger, Laura M. Wehrmann, Susann Henkel and Christian März

PUBLISHED IN: Frontiers in Earth Science

frontiers Research Topics

frontiers

ISSN 1664-8714
ISBN 978-2-88976-098-5
DOI 10.3389/978-2-88976-098-5

About Frontiers

Frontiers is more than just an open-access publisher of scholarly articles: it is a pioneering approach to the world of academia, radically improving the way scholarly research is managed. The grand vision of Frontiers is a world where all people have an equal opportunity to seek, share and generate knowledge. Frontiers provides immediate and permanent online open access to all its publications, but this alone is not enough to realize our grand goals.

Frontiers Journal Series

The Frontiers Journal Series is a multi-tier and interdisciplinary set of open-access, online journals, promising a paradigm shift from the current review, selection and dissemination processes in academic publishing. All Frontiers journals are driven by researchers for researchers; therefore, they constitute a service to the scholarly community. At the same time, the Frontiers Journal Series operates on a revolutionary invention, the tiered publishing system, initially addressing specific communities of scholars, and gradually climbing up to broader public understanding, thus serving the interests of the lay society, too.

Dedication to Quality

Each Frontiers article is a landmark of the highest quality, thanks to genuinely collaborative interactions between authors and review editors, who include some of the world's best academicians. Research must be certified by peers before entering a stream of knowledge that may eventually reach the public - and shape society; therefore, Frontiers only applies the most rigorous and unbiased reviews.
Frontiers revolutionizes research publishing by freely delivering the most outstanding research, evaluated with no bias from both the academic and social point of view. By applying the most advanced information technologies, Frontiers is catapulting scholarly publishing into a new generation.

What are Frontiers Research Topics?

Frontiers Research Topics are very popular trademarks of the Frontiers Journals Series: they are collections of at least ten articles, all centered on a particular subject. With their unique mix of varied contributions from Original Research to Review Articles, Frontiers Research Topics unify the most influential researchers, the latest key findings and historical advances in a hot research area! Find out more on how to host your own Frontiers Research Topic or contribute to one as an author by contacting the Frontiers Editorial Office: frontiersin.org/about/contact

GEOCHEMICAL SIGNALS IN DYNAMIC SEDIMENTARY SYSTEMS ALONG CONTINENTAL MARGINS

Topic Editors:
Natascha Riedinger, Oklahoma State University, United States
Laura M. Wehrmann, Stony Brook University, United States
Susann Henkel, Alfred Wegener Institute Helmholtz Centre for Polar and Marine Research (AWI), Germany
Christian März, University of Leeds, United Kingdom

Citation: Riedinger, N., Wehrmann, L. M., Henkel, S., März, C., eds. (2022). Geochemical Signals in Dynamic Sedimentary Systems Along Continental Margins. Lausanne: Frontiers Media SA. doi: 10.3389/978-2-88976-098-5

Table of Contents

frontiers | Frontiers in Earth Science

EDITORIAL
published: 13 April 2022
doi: 10.3389/feart.2022.876009

Editorial: Geochemical Signals in Dynamic Sedimentary Systems Along Continental Margins

N. Riedinger[1]*, *C. März*[2], *S. Henkel*[3] *and L. M. Wehrmann*[4]

[1]Boone Pickens School of Geology, Oklahoma State University, Stillwater, OK, United States, [2]School of Earth and Environment, University of Leeds, Leeds, United Kingdom, [3]Alfred Wegener Institute, Helmholtz Centre for Polar and Marine Research, Bremerhaven, Germany, [4]School of Marine and Atmospheric Sciences, Stony Brook University, Stony Brook, NY, United States

Keywords: diagenesis, continental margins, non-steady state condition, redox conditions, dynamic depositional settings

Editorial on the Research Topic

Geochemical Signals in Dynamic Sedimentary Systems Along Continental Margins

For decades, the mud depositing at the bottom of our oceans has been used by scientists as an archive of past environmental conditions, informing about the Earth's climate and helping to put current environmental and climate change into a long-term context. One fundamental condition in successful paleo-environmental reconstructions is the accurate "translation" of measurable chemical parameters in the sedimentary record (proxies) into relatable and relevant information about the ocean, which is most straightforward if sediments are accumulating in a regular pattern—a so-called steady state scenario. Of key interest are sedimentary records of when, why, and how the state of the ocean and Earth's climate changed in the past, and often it is this very environmental change that impacts the way marine sediments record environmental signals. Changes in sedimentation rates, the delivery of organic matter to the seafloor, the redox state of the overlying water column and the availability of certain dissolved chemicals in seawater can create a non-steady state situation where the continuity of the seafloor archive is not guaranteed, and diagenetic effects overprint the sedimentary succession (Thomson et al., 1984; Zabel and Schulz, 2001; März et al., 2008; Henkel et al., 2012). Such non-steady state diagenetic conditions are particularly prevalent in marginal marine environments, as these tend to be disproportionately affected by changes in, e.g., sea level, ocean currents, primary productivity, redox conditions, or riverine input (Aller, 2014; Wehrmann and Riedinger, 2016). In this Research Topic, the imprint of early diagenetic processes on sedimentary records on different spatial and temporal scales is illustrated and means of carefully and holistically assessing sedimentary archives to extract useful environmental information are presented.

Starting at the most marginal of marine environments, i.e., the coastline, Zhu et al. test a novel approach to track mm-scale iron and sulfide dynamics in modern salt marshes along the US east coast using two-dimensional sensors—not only showing how inter-annual (seasonal) changes in organic matter input, but also plant roots, can impact the chemistry of the sediments. Moving further offshore into a brackish, semi-enclosed ocean basin, Hardisty et al. study the response of diagenetic processes to changes in redox conditions in the southern Baltic Sea. The authors highlight that periods of restriction and bottom water anoxia impacted diagenetic processes in different parts of the basin in different ways, adding both a wider spatial (i.e., individual sub-basins within the Baltic Sea) and longer temporal (i.e., Holocene) perspective on geochemical proxy reconstructions. Staying with the intimate link between bottom water redox conditions and diagenetic processes at/below the seafloor, Chen et al. investigate how diagenesis in deposits underlying oxygen deficient zones along the eastern Pacific margin impacts the isotopic composition of sedimentary cadmium (Cd). This study shows that generally light Cd isotopes in these sediments could be a result of

OPEN ACCESS

Edited and reviewed by:
Timothy Ian Eglinton,
ETH Zürich, Switzerland

***Correspondence:**
N. Riedinger
natascha.riedinger@okstate.edu

Specialty section:
This article was submitted to Biogeoscience, a section of the journal Frontiers in Earth Science

Received: *14 February 2022*
Accepted: *25 March 2022*
Published: *13 April 2022*

Citation:
Riedinger N, März C, Henkel S and Wehrmann LM (2022) Editorial: Geochemical Signals in Dynamic Sedimentary Systems Along Continental Margins. Front. Earth Sci. 10:876009. doi: 10.3389/feart.2022.876009

biogeochemical processes in the water column, and/or of diagenetic dissolution-precipitation reactions below the seafloor, calling into question the uncritical application of Cd isotopes as paleoenvironmental proxy. Even further offshore and back in time, Giresse et al. make use of glauconite grains in a sediment core from Demerara Rise reaching back ~60,000 years, to postulate that authigenic glauconite records the neodymium (Nd) isotope composition of contemporaneous seawater and thus offers a new archive for water mass distribution that rivals foraminiferal calcite or Fe/Mn (oxyhydr)oxides. The oldest record presented in this Research Topic by Dunn et al. deals with Ordovician (~460 million-year-old) ironstones deposited on an upwelling-affected shelf margin of the now subducted Rheic Ocean. This record appears to reflect not only the impact of variable upwelling and primary productivity on sediment composition (and potentially on biological diversification), but also the occasional reworking by storms—so a non-steady state depositional system forced by interacting physical and chemical drivers.

The generation of biogenic methane in marine sediments is fundamentally controlled by the input of organic matter. There are rather specific diagenetic processes associated with the methanic zone which has an upper boundary that can be found anywhere from a few mm to several tens of meters within the sediment of continental margins (Egger et al., 2018). Studying sediment cores from eutrophic locations off the southern tip of Finland, Jilbert et al. show how the dynamics of diagenetic processes can be shaped by human activity, in this case, commercial forestry: The input of terrestrial organic matter from wood logging and processing activities increased the diagenetic activity, specifically methanogenesis, in the deposits receiving this additional organic carbon loading. The potential issue of sedimentary methane emission to the ocean-atmosphere system is also highlighted by Zhang et al. but in a system offshore Japan where natural methane emissions from both cold seeps and hydrothermal vents are an order of magnitude higher than the global average, illustrating the poorly constrained spatial variability of methane emissions along continental margins worldwide. At locations where methane does not reach the sediment-water interface, this is often due to its anaerobic oxidation by sulfate (at the sulfate-methane transition, SMT), a process studied in detail by Bradbury et al. using sediment cores along a shelf to basin transect on the southwest Iberian margin. Combining chemical analyses with reaction-transport modeling, they propose a revised scheme of how to use the isotopic compositions of pore water sulfate-sulfur and dissolved inorganic carbon in combination to estimate which diagenetic processes (e.g., sulfate reduction, anaerobic methane oxidation, authigenic carbonate formation) are shaping the pore water composition. A similar modeling approach is used by Meister et al. to unravel the contribution of yet another diagenetic process, i.e., the transformation of silicate minerals to quartz and kaolinite (submarine weathering), to the diagenetic dynamics in several hundred meter deep sediments off the Peru margin. Specifically, silicate weathering produces additional alkalinity that can lead to the fixation of formerly organic carbon in the sediment as authigenic carbonates, preventing its recycling to the ocean-atmosphere system. This broad collection of articles enhances our knowledge of the complex interplay of processes at continental margins, which will enable more reliable interpretation of proxy records and diagenetic signals.

AUTHOR CONTRIBUTIONS

All authors listed have made a substantial, direct, and intellectual contribution to the work and approved it for publication.

REFERENCES

Aller, R. C. (2014). "Sedimentary Diagenesis, Depositional Environments, and Benthic Fluxes," in *Treatise on Geochemistry*. Editors H. D. Holland and K. K. Turekian. Second Edition (Oxford: Elsevier), 8, 293–334. doi:10.1016/b978-0-08-095975-7.00611-2

Egger, M., Riedinger, N., Mogollón, J. M., and Jørgensen, B. B. (2018). Global Diffusive Fluxes of Methane in marine Sediments. *Nat. Geosci.* 11 (6), 421–425. doi:10.1038/s41561-018-0122-8

Henkel, S., Schwenk, T., Hanebuth, T. J. J., Strasser, M., Riedinger, N., Formolo, M., et al. (2012). "Pore Water Geochemistry as a Tool for Identifying and Dating Recent Mass-Transport Deposits," in *Submarine Mass Movements and Their Consequences* (Heidelberg: Springer), 31, 87–97. Advances In Natural And Technological Hazards Research Series. doi:10.1007/978-94-007-2162-3_8

März, C., Hoffmann, J., Bleil, U., de Lange, G. J., and Kasten, S. (2008). Diagenetic Changes of Magnetic and Geochemical Signals by Anaerobic Methane Oxidation in Sediments of the Zambezi Deep-Sea Fan (SW Indian Ocean). *Mar. Geol.* 255 (3-4), 118–130. doi:10.1016/j.margeo.2008.05.013

Thomson, J., Wilson, T. R. S., Culkin, F., and Hydes, D. J. (1984). Non-steady State Diagenetic Record in Eastern Equatorial Atlantic Sediments. *Earth Planet. Sci. Lett.* 71 (1), 23–30. doi:10.1016/0012-821x(84)90049-9

Wehrmann, L. M., and Riedinger, N. (2016). "The Sedimentary Deep Subseafloor Biosphere," in *Reference Module in Earth Systems and Environmental Sciences* (Netherlands: Elsevier), 258–274. ISBN 9780124095489. doi:10.1016/B978-0-12-409548-9.09741-4

Zabel, M., and Schulz, H. D. (2001). Importance of Submarine Landslides for Non-steady State Conditions in Pore Water Systems-Lower Zaire (Congo) Deep-Sea Fan. *Mar. Geol.* 176 (1-4), 87–99. doi:10.1016/s0025-3227(01)00164-5

Conflict of Interest: The authors declare that the research was conducted in the absence of any commercial or financial relationships that could be construed as a potential conflict of interest.

frontiers in Earth Science

ORIGINAL RESEARCH
published: 22 September 2020
doi: 10.3389/feart.2020.00333

Distribution and Discharge of Dissolved Methane in the Middle Okinawa Trough, East China Sea

Xianrong Zhang[1,2], Zhilei Sun[1,2], Libo Wang[1,2], Xilin Zhang[1,2], Bin Zhai[1,2], Cuiling Xu[1,2], Wei Geng[1,2], Hong Cao[1,2], Xijie Yin[3] and Nengyou Wu[1,2]**

[1] The Key Laboratory of Gas Hydrate, Ministry of Natural Resources, Qingdao Institute of Marine Geology, Qingdao, China, [2] Key Laboratory of Marine Environmental Geology, Ministry of Natural Resources, Qingdao Institute of Marine Geology, Qingdao, China, [3] Thrid Institute of Oceanography, Ministry of Natural Resources, Xiamen, China

Widespread seepage of methane from seafloor sediments on continental margins are released into seawater, a portion of which may escape to the atmosphere. To assess the water column distribution characteristics of methane and its input to the atmosphere, we investigated methane emissions from the shelf and west slope of the back-arc Okinawa Trough (OT), East China Sea. Our results showed a heterogeneity distribution of methane within the water column. The highest value, which was more than 10 times of the background concentration, occurred near a cold seep in the north of the study area which was discovered by a remotely operated underwater vehicle (ROV). Other sources of methane to the water column of the OT, besides cold seepage input, probably also include *in situ* aerobic methane production, advective transport from the continental shelf, and/or hydrothermal venting. Furthermore, the sea-to-air flux of methane throughout the study area was up to 116 μmol $m^{-2}d^{-1}$, noticeably higher than that in many other continental shelf waters and seep sites globally, indicating that this region is an active CH_4 emission area. Our findings demonstrate that methane discharged from both cold seeps and hydrothermal vents have a significant influence on the methane cycle in the OT, providing a new insight for the methane budget of back-arc basins.

Keywords: methane, distribution, discharge, middle Okinawa trough, cold seepage

OPEN ACCESS

Edited by:
Natascha Riedinger, Oklahoma State University, United States

Reviewed by:
Jiwei Li, Institute of Deep-Sea Science and Engineering (CAS), China
Francois L. L. Muller, National Sun Yat-sen University, Taiwan

***Correspondence:**
Zhilei Sun
zhileisun@yeah.net
Nengyou Wu
wuny@ms.giec.ac.cn

Specialty section:
This article was submitted to Geochemistry, a section of the journal Frontiers in Earth Science

Received: *16 April 2020*
Accepted: *17 July 2020*
Published: *22 September 2020*

Citation:
Zhang X, Sun Z, Wang L, Zhang X, Zhai B, Xu C, Geng W, Cao H, Yin X and Wu N (2020) Distribution and Discharge of Dissolved Methane in the Middle Okinawa Trough, East China Sea. Front. Earth Sci. 8:333. doi: 10.3389/feart.2020.00333

INTRODUCTION

Methane (CH_4), a significant greenhouse gas, has a global warming potential about 20–40 times higher than that of CO_2 on average over a century timescale (St. Louis et al., 2000; IPCC, 2013). Although CH_4 emissions from the oceans account for only a small portion (2%) of the global CH_4 budget (Reeburgh, 2007), it still plays an important role in the atmospheric chemistry, air-sea interaction, and distribution of chemosynthetic communities. Previous studies estimated that marine CH_4 flux to the atmosphere ranges from 0.4 to 1.8 Tg yr^{-1} in the open ocean (Rhee et al., 2009), while it reaches 13 Tg yr^{-1} for continental shelves (Bange et al., 1994). This observation suggested that the continental shelf would be the dominant place for the oceanic CH_4 emissions.

The major sources of dissolved CH_4 in the ocean are terrestrial inputs, sediment emission (including geological sources), and biological metabolism (Fleischer et al., 2001; Jayakumar et al., 2001; Skarke et al., 2014; Mau et al., 2017). Most of this CH_4 gas could be dissolved in seawater

(McGinnis et al., 2006), generating patches of high CH_4 concentration (Leifer et al., 2000), but only a small amount of them can reach the atmosphere (Reeburgh, 2007). In this case, the amount of CH_4 estimated based on sea-air gas flux is markedly lower than that discharged from sediment (Milkov and Sassen, 2003). Nevertheless, due to high variability in hydrochemical properties and release rate of CH_4 from sediment, the oceanic CH_4 budget is poorly documented up to date. Therefore, it is highly essential to carry out more measurements of CH_4 production, dissolution, migration, and emissions from the seabed in order to better understand the oceanic CH_4 budget and potential influence on climate change.

The first studies on the characteristics of dissolved CH_4 in the East China Sea (ECS) have been conducted since the early 1990s (Tsurushima et al., 1996). Previous research demonstrated that terrestrial input and hydrographic circulation systems [Kuroshio, the Taiwan Warm Current Water (TWCW), as well as the East China Sea Coastal Current (ESCC)] were the main controlling factors on CH_4 concentration and distribution patterns (Lee et al., 2000; Rehder and Suess, 2001; Liu et al., 2003; Zhang et al., 2004, 2008). However, given that a variety of mud volcanoes, pockmarks, and cold seeps have been discovered in recent decades in the OT (Yin et al., 2003; Li et al., 2015; Sun et al., 2015; Xu et al., 2018), it is reasonable to infer that they may contribute a substantial amount of CH_4 to seawater. In addition, as a universal extreme system within the OT, modern hydrothermal activity is pervasive and vigorous from north to south, which can also discharge a large amount of CH_4 along with hydrothermal fluids (Sakai et al., 1990; Ishibashi et al., 1995, 2014; Inagaki et al., 2006; Miyazaki et al., 2017). Previous studies found that the distance between the site of the newly discovered cold seeps (Li et al., 2015; Xu et al., 2018) and the hydrothermal vents found in the past (Inagaki et al., 2006; Ishibashi et al., 2014) are less than several tens of kilometers apart. The proximity of the cold seeps to the hydrothermal fluid complicates the material circulation in the OT (Sun et al., 2019). Recently conducted research has confirmed that both hydrothermal and cold seep fluids could contribute a considerable amount of carbon to the seawater (Sun et al., 2019; Zhang et al., 2019). In such situations, due to the complicated supply of methane-rich fluids derived from cold seeps and hydrothermal vents, the aforementioned region has been an important target to explore the characteristics and sources of CH_4 in the OT.

In this study, we measured dissolved CH_4 concentrations and related physical oceanographic parameters from the full-depth water, and then estimated CH_4 fluxes at the sea-air interface in the OT (**Figure 1**). Our study aimed to determine the fate of the discharged methane and evaluated the regional contribution to atmospheric methane, it would shed light on better understanding the methane budget and the biogeochemical carbon cycle in the OT.

GEOLOGICAL SETTING

The OT is an active semi-depth back-arc basin formed behind the Ryukyu arc-trench system in the West Pacific (Sibuet and Olu, 1998; Shinjo et al., 1999). It is approximately 1200 km in length with the average width of approximately 104 km and characterized by active rifting structures and magmatism along the depression. In this trough, a large section of the seawater is deeper than 1000 m, and the maximum depth is about 2300 m. The thickness of sediments in the northern section of the OT is up to 8 km, due to a huge supply of terrigenous matter from the ESC continental shelf (Sibuet et al., 1987). A topographical study showed that the OT has a typical U-shape, and submarine canyons, fans, and turbidite deposits have extensively developed on the western slope. Modern hydrothermal activities are pervasive and vigorous in the middle and southern sections of the OT (Glasby and Notsu, 2003). In addition, seafloor cold seeps have been discovered in the northern and central OT recently (Li et al., 2015; Sun et al., 2015; Xu et al., 2018).

The hydrological and circulation systems in the OT are complex, and are mainly controlled by the force from the Kuroshio Current and coastal current (Yu et al., 2009). Amongst, the Kuroshio Current, carrying oligotrophic waters northward with low concentrations of nutrients and high temperature and salinity, is the most important factor controlling the environment and hydrological characteristics. It flows above the OT as a water mass up to 100 km wide and 800–1,000 m deep and at a velocity ranging from 45 to 150 cm/s (Qin, 1987). It is the only source of heat and ocean material on the shelf of ECS.

MATERIALS AND METHODS

Sampling and Regional Survey

Forty sites of full-depth water column samples were selected in this study from the western slope of the middle OT and continental shelf during the integrated environmental and geological expedition of R/V *Zhang Jian* from June to September 2016 (**Figure 1**). Seawater samples from different sites and depths were collected with cleaned Go-Flo bottles (20-L) mounted on a Seabird 911 plus CTD/rosette. Surface waters were collected at a depth of ∼3 m and near-bottom waters were at ∼50 m above the seafloor. Once on board, water was collected into 40 mL glass serum vials using a silicone tube. The vials were thrice overfilled without introducing any air bubbles in the sample. Then, those were sealed with a butyl rubber stopper and aluminum cap. After that, methane analyses of these samples were conducted in the laboratory immediately. Temperature, salinity, and oxygen data were obtained from the CTD profiles.

A high-quality *in situ* giant clam beds map was obtained by a remotely operated underwater vehicle (ROV) Beaver (Shanghai Jiao Tong University) in the cruise of R/V *Zhang Jian* in 2017 (**Figure 1**). The dive sites were characterized by several acoustically detected flares in the water column, which were first discovered by the Kongsberg EM302 multi-beam echo-sounder on-board.

Dissolved CH_4 Concentration

Headspace gas chromatography was applied for on-board measurements of dissolved gases, as well as high resolution mapping of CH_4 concentrations. Briefly, a 40 mL glass vial with

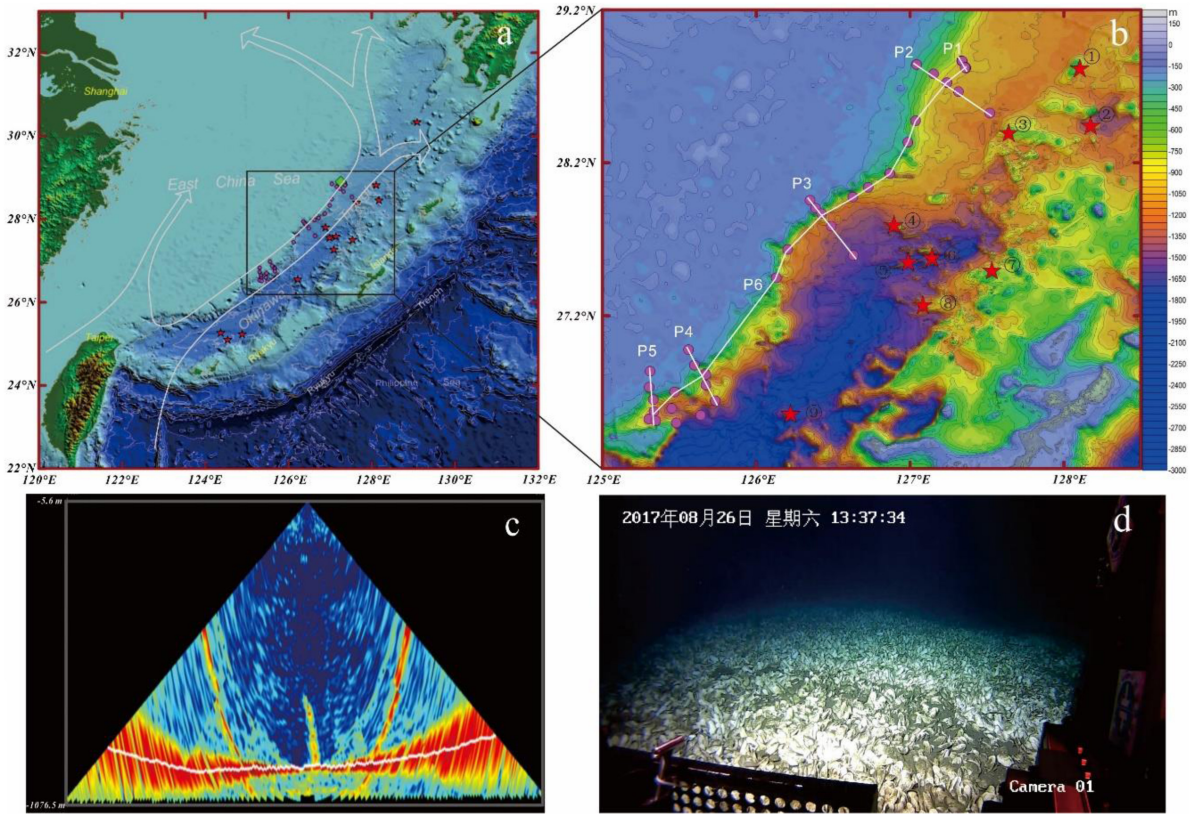

FIGURE 1 | (a) Observational regions and sampling stations in the OT, ECS during the integrated environmental and geological and ROV cruises during 2016 and 2017. The main stream of the Kuroshio Current is shown in solid curves; rose red solid circles represent seawater sampling locations; the green square represents cold seep (Li et al., 2015; Xu et al., 2018); red stars represent hydrothermal vent sites. The identified hydrothermal fields are cited from the InterRidge database (http://interridge.org/) and are listed as follows: (1) Site ES2, (2) Higashi-Ensei, (3) Minami-Ensei Knoll, (4) North Knoll, (5) Iheya Ridge, (6) Natsushima 84-1 Knoll, (7) Yoron Hole, (8) Izena Cauldron, and (9) Higa. **(b)** Location of sampling site with P1–P6, six transects; **(c)** acoustic flare representing seafloor methane bubble plume near the CTD10 site on the west slope of the OT. **(d)** ROV observations of *in situ* Giant clam beds made during the ROV cruises in 2017.

half a sample of seawater was immersed into a 25°C constant temperature water bath to balance the CH_4 distribution between headspace and seawater. After that, 0.5 mL of headspace gas was injected into a gas chromatograph (GC910 produced by Ke Chuang Company, Shanghai) with a flame-ionization detector. High-purity helium (99.999%) was used as the carrier gas at a flow rate of 30 mL/min. The precision of the analytical method was ± 2.5%.

Calculations of Saturation and Sea-Air Flux

Saturation values R, expressed in%, were calculated as the ratio of the concentration of dissolved gas to the expected equilibrium water concentration. The saturation and sea–air CH_4 fluxes (F, $\mu mol \cdot m^{-2} \cdot d^{-1}$) were calculated as follows:

$$R\,(\%) = C_{obs}/C_{eq} \times 100\% \quad (1)$$

$$F\,(\mu mol\ m^{-1}\ d^{-1}) = k \times (C_{obs} - C_{eq}) \quad (2)$$

Where C_{obs} is the observed dissolved CH_4 concentration (mol L^{-1}); C_{eq} is the CH_4 concentration in the seawater equilibrated with air, which can be calculated using *in situ* temperature, salinity, and the solubility equation of Wiesenburg and Guinasso (1979). However, atmospheric CH_4 concentration was not determined in the present study. Therefore, a global mean atmospheric CH_4 mixing ratio of 1831.16 ppb of 2013, taken from the NOAA/ESRL Global Monitoring Division *in situ* program[1], was used for calculations. k (cm h^{-1}) is the gas transfer velocity, which is a function of wind speed and the Schmidt number (Sc). In the current research, the formula presented by Wanninkhof (1992, 2014) was used to calculate the gas transfer coefficient k. The average wind speed during the cruises is 8.3 m s^{-1}.

RESULTS AND DISCUSSION

Horizontal Distribution of CH_4

We collected the methane data from the shelf and west slope of the OT, which ranged from 2.7 to 24.7 nM, with an average of 6.5 nM. The horizontal distributions of CH_4 in water are

[1]http://www.esrl.noaa.gov/gmd

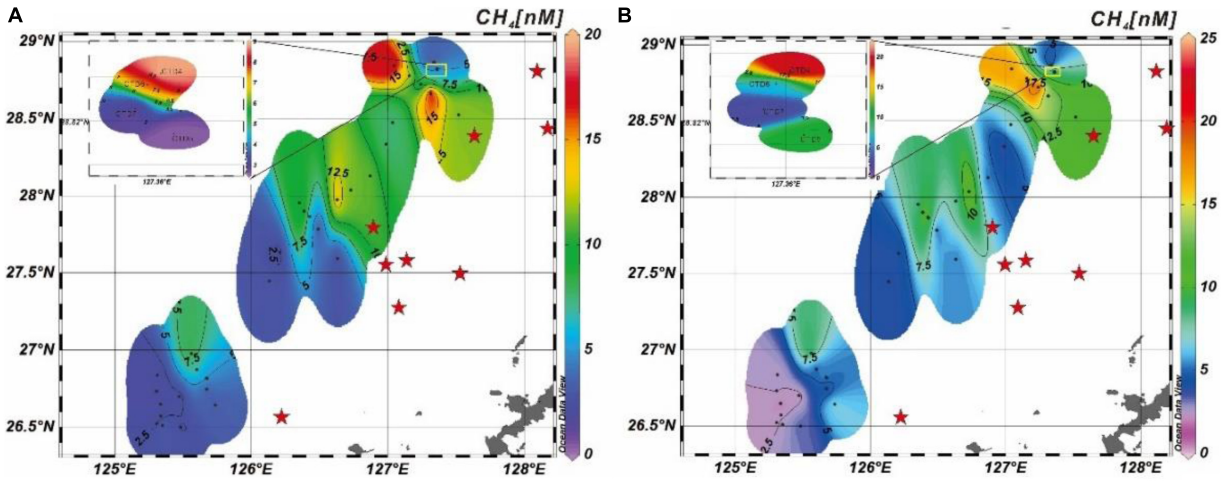

FIGURE 2 | Horizontal distributions of CH_4 in **(A)** surface and **(B)** bottom water of the OT. Red stars represent hydrothermal vent sites in the middle and northern OT, also in **Figure 1**. The plots were generated using Ocean Data View (ODV) Version 5.1.0 (Schlitzer, 2018).

shown in **Figure 2**, presenting a great variation both in the surface and bottom, from 2.0 to 19.9 nM and 2.0 to 24.7 nM, respectively. Careful study found that the CH_4 concentrations in the bottom at about 60% of the sites are approximately 10–270% higher than that in the shallower and surface water (**Figure 2** and **Supplementary Figure S2**). This finding suggests there may be an important benthic CH_4 originating from the underlying sediment, which can be identified through sediment core incubations (Chronopoulou et al., 2017). However, the high CH_4 concentration anomalies are observed on the lower slope of the north study area, with the maximum concentration of 24.7 nM, which is approximately more than 10 times the background concentrations of 2–3 nM in the OT (Tsurushima et al., 1996) and the typical open ocean (Bates et al., 1996; Kock et al., 2008; Tseng et al., 2017). This irregular distribution of CH_4 is possibly pointing to seafloor methane seep from sediment.

Distribution of CH_4 Across the Shelf and Slope

We divided our data into six transects. Transects P1–P5 were conducted across the shelf and slope while P6 followed the contour line of the middle slope (**Figure 1**). Along the P1 transect (**Figure 3**), CH_4 concentrations changed in a wide range, from 2.0 to 20.3 nM. The most conspicuous feature observed in the majority of our sites for the P1 transect was that CH_4 concentrations noticeably elevated from the surface to the bottom water. This was particularly pronounced at CTD4 and CTD5, where CH_4 concentrations decreased from the surface to 600 m, then increased from 600 m to the seabed (**Figure 3**). Finally, they reached the maximum value of 20.3 nM for CTD4 and 10.1 nM for CTD5 at the bottom water, which are far more than that in the typical open ocean (Tilbrook and Karl, 1995; Watanabe et al., 1995).

The CH_4 concentrations of the P2 and P3 transects unveiled a noticeable shelf-to-slope trend, which increased and then decreased with distance from the shelf. On the continental shelf with shallow water depth, all sites were characterized by relatively high CH_4 concentration, with the value > 10 nM, especially in surface waters, which may be influenced by shelf mixed water (Ye et al., 2016; Sun et al., 2018). However, the maximum values in both transects appeared on the slope. In the P3 transect, the highest concentration was 12 times higher than the background value, which appeared at a water depth of approximately 900 m at the site of CTD10. Whereas, the maximum value of P2 appeared at a depth of 1,100 m (near bottom water) at the site of CTD21, with a concentration of 18.4 nM.

Moreover, the characteristics of CH_4 concentration in the P4 and P5 transects showed relatively high value in the shelf area and on the lower slope, while it was relatively low on middle slope. This scene can be observed at the CTD26 site with a water depth of 165 m on the shelf area, where CH_4 concentration in the whole water depth profile was relatively high, with the range from 8.6 to 10.8 nM. That might be associated with the input of high concentration CH_4 from land sources or the production and diffusion from sediment (Ye et al., 2016). However, in the P5 transect located at the canyon in the southern part of the OT, CH_4 concentration was lower than that in other sections and was close to the background value, which may be due to the complex geological structure or hydrography (Nakamura et al., 2013). Previous study showed that the internal waves and tides, combined with the Kuroshio current, enhanced the disturbance and mixing of sea water in submarine canyons (Gao, 1996), that resulted in a rapidly dilution of emitted CH_4 by surrounding waters. Thus, it was one of the important reasons for the relatively low CH_4 concentration in this area.

In the present research, we summarized the distribution characteristic of CH_4 in the P6 transect along the contour line on the west middle slope of the OT. Our results showed that the CH_4 concentration ranged from 1.9 to 24.7 nM, and the maximum and minimum values were at CTD10 in the middle OT and at CTD37 in the southern area (**Figure 3**), respectively. However, at the

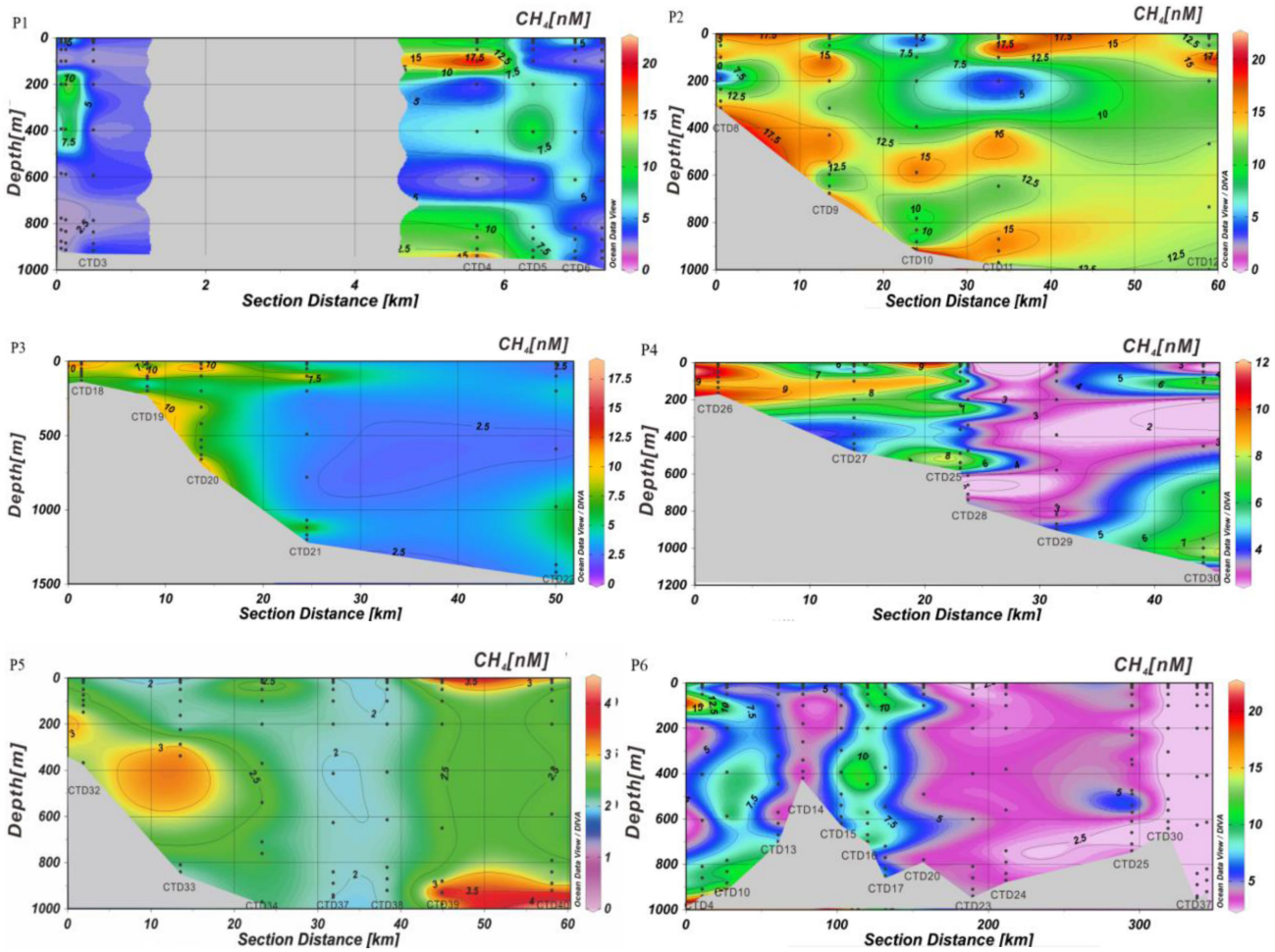

FIGURE 3 | The six transects distribution of CH_4 in the OT. The plots were generated using ODV Version 5.1.0 (Schlitzer, 2018). The "gray spaces" in P1 represent areas where there is too little information for ODV to interpolate.

CTD10 site, a high concentration of CH_4 was noted throughout the water column, which may be attributed to methane seepage and methane bubble plumes (**Figure 1**). Similarly, an abnormally high concentration of CH_4 was found at the depth water of the CTD4 site, with a distance of only 16 km from the CTD10 site. Moreover, the CH_4 concentrations in the near-surface waters of the CTD16 and CTD17 sites were relatively high, with the values of 12.5 and 14.5 nM, respectively.

According to the analysis results of the above-mentioned six transects, it was disclosed that higher CH_4 concentration was observed on the shelf and lower slope area within the depth range of 900–1000 m. In order to identify the CH_4 influence factors of the main water masses and currents, we presented the CTD profile data of all sites in **Figure 4** and **Supplementary Figure S1**. Most data points indicated that the shelf mixed water (SMW) and Kuroshio (salinity > 34‰, with gradual reduction of temperature with depth) played substantial roles in regulating the distribution of CH_4 concentration. The SMW distributed in the shelf edge zone included Changjiang Diluted Water (CDW), TWCW, and Kuroshio Surface Water (KSW) (Zhang et al., 2007; Ye et al., 2016). Previous studies reported that a small number of large rivers in East Asia (Sieburth, 1987) were transporting huge amounts of freshwater along with high concentrations of dissolved CH_4 to the ECS, e.g., about 70.6×10^6 mol yr^{-1} CH_4, were imported from the Changjiang (112–190 nM in the surface water in spring) to the ECS (Tsurushima et al., 1996; Zhang et al., 2004; Ye et al., 2016; Sun et al., 2018). It is noteworthy that dissolved CH_4 in the river water is almost 2 orders of magnitude higher than that found in the continental shelf edge (Sun et al., 2018), and in summer, this river water mass extends further to the continental shelf, which may justify the relatively high CH_4 concentration in this area. However, the main stream of the Kuroshio flowing northeastward along the 200 m isoline (Qin, 1987), is the most important factor that affects the study area (**Figure 4**), with a relatively low CH_4 concentration (Rehder and Suess, 2001; Zhang et al., 2004). This is coupled with our finding in the slope area, and pronounced in the southern area. However, the CH_4 concentration is abnormally high at the sites of the lower slope (e.g., CTD4, 10) even though it is affected by the Kuroshio Intermediate Water (KIW) or Kuroshio Deep Water (KDW)

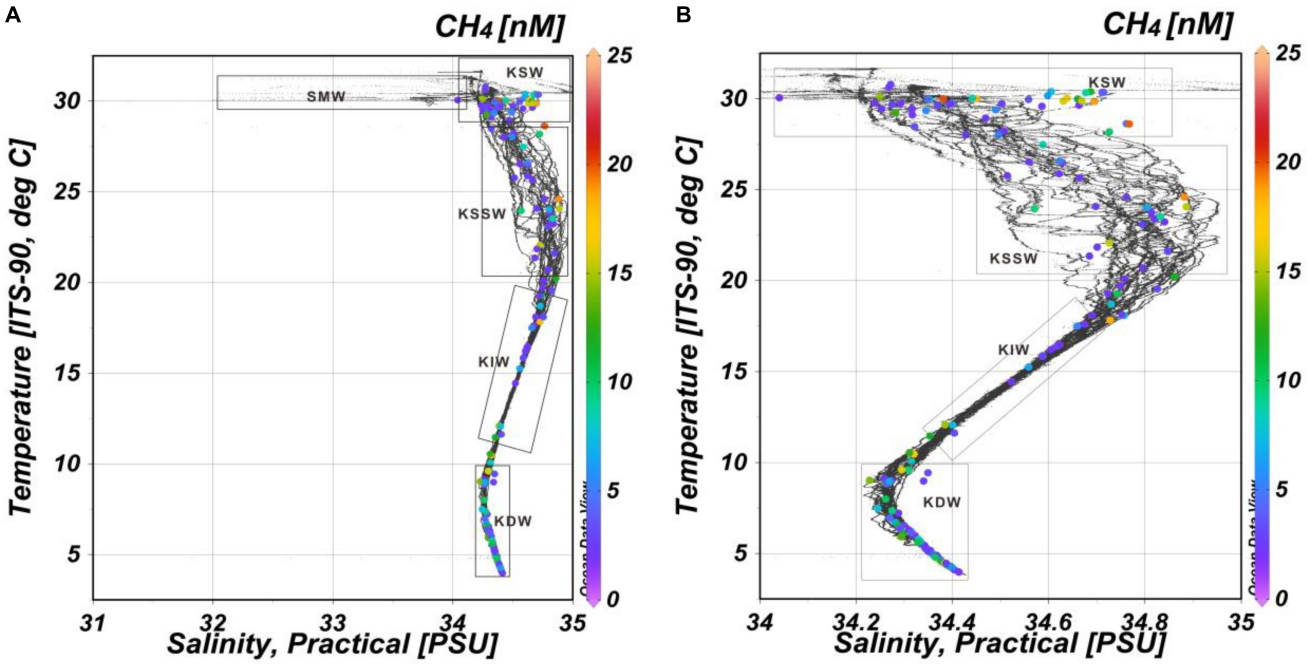

FIGURE 4 | (A) Temperature-salinity diagrams and CH_4 concentrations in the OT. **(B)** A larger version of the Kuroshio Water masses. The dominant water masses are classified according to a previous study (Tang et al., 1997; Li et al., 2012; Qi et al., 2014) and indicated by rectangular outlines. SMW, Shelf Mixed Water; KSW, Kuroshio Surface Water; KSSW, Kuroshio Subsurface Water; KIW, Kuroshio Intermediate Water; KDW, Kuroshio Deep Water. Black dots: non-CH_4 sampling point; Colored dots: CH_4 sampling points, with concentrations indicated by color scale. The plots were generated using ODV Version 5.1.0 (Schlitzer, 2018).

(**Figure 4**). This may be attributed to the observed methane cold seepage (**Figure 1**).

However, CH_4 concentration at the CTD10 and CTD4 sites was found anomalously high in the full depth water column, which was pronounced at a depth of 800–1,100 m near the seafloor. These irregular phenomena are closely related to the cold seepage with methane bubble plumes (**Figure 1**). CH_4 produced in sediments is consumed as it is pushed upward by anaerobic oxidation of methane (AOM) or aerobic CH_4 oxidation (Barnes and Goldberg, 1976). However, if the upward CH_4 is not fully exhausted by these processes, the extra CH_4 is emitted to the ocean, and generates patches of high CH_4 concentration (Leifer et al., 2000; Mau et al., 2017). Furthermore, the presence of gas hydrates is inferred from the bottom-simulating reflections (BSRs) in the OT (Fan and Yang, 2004; Xiwu et al., 2008). Geological models calculated that the water depth of the gas hydrate stability zone of the OT was approximately 500 m (Fan and Yang, 2004). Fittingly, the water depth of the CTD10 and CTD4 sites is about 900 m located in the gas hydrate stability zone. In addition, other evidence of pore-water geochemical anomalies (Li et al., 2015; Xu et al., 2018) and geochemical characteristics of authigenic pyrite associated with AOM (Wang et al., 2015) have been documented with cold seepages activities appearing near our study sites. Although CH_4 concentration is significantly lower than that in the samples collected by a ROV at the cold seepage sites here, previous studies still supported our augment that anomalously high CH_4 concentrations are attributed to the existence of cold seepage. However, the low concentration of CH_4 in our samples compared with that in the samples collected by a ROV was attributed to the greater distance above the seafloor during sampling. After emission from the seafloor, CH_4 concentration may be noticeably reduced due to continuous oxidation, dissolution, diffusion, and dilution of a large amount of seawater (Leifer et al., 2000; McGinnis et al., 2006; Konn et al., 2009; Faure et al., 2010). Not only that, when the CTD seawater was retrieved, CH_4 was partly lost due to a decrease of pressure (Konno et al., 2006). Furthermore, near-surface waters at the CTD16 and CTD17 sites showed high CH_4 concentrations, which were more than six times of the background value of the lower slope area, suggesting that there may be methane seepage. Nevertheless, compared with other areas, e.g., west Spitsbergen (up to 524 nM; Gentz et al., 2014), the Gulf of Mexico (∼600 nM; Solomon et al., 2009), and the Hikurangi Margin of New Zealand (up to 3,500 nM; Faure et al., 2010), it seemed that CH_4 concentration in this study was lower, and the CH_4 seepage was not considerably active in our study area. It is possible that CH_4 seepage is episodic, or the seepage is on a small scale or only very close (decimeters) to the seafloor at active seep sites (in the current study, sampled bottom water depth was about 50 m above seafloor). Therefore, it is difficult to catch the abnormality of methane with CTD sampling. Generally, cold seep in a finer scale is spatially associated with canyons, which incision downward into older strata and landward into the upper slope could physically disrupt gas hydrate or free gas deposits. On the contrary, no abnormal CH_4 concentration in

P5 was detected in the canyon of the study area in spite of the existence of pore water anomalies associated with cold seep (Zhang et al., 2004; Xu et al., 2018). It is also possibly attributed to the episodic characteristic of CH_4 seepage or that emitted CH_4 is diluted swiftly, distributed by surrounding waters, or is actively consumed in oxygenated seawater.

Notably, our sampling site was relatively close to the hydrothermal vents of the OT (**Figures 1**, **2**), thus, the hydrothermal activity may be an influence factor on the CH_4 distribution.

Vertical Distribution of CH_4

The vertical concentration profiles of CH_4 were irregular due to the complex geography and hydrography of the ECS (Zhang et al., 2004; **Figures 3**, **5**). Nonetheless, CH_4 concentrations at nearly half of our study sites exhibited obvious peaks in surface or subsurface water. The largest maximum generally occurred at 50-100 m and coincided with the pycnocline. It was likely the result of *in situ* aerobic CH_4 production caused by microbial biogeochemistry (Reeburgh, 2007). At depths > 200 m, CH_4 peaks were present at some sites; for example, at sites CTD5, 13, and 25 (**Figure 5**), one broad CH_4 peak was present at the depth of ∼400 m, which might be associated with the advection and sinking of shelf water across the shelf break (Patra et al., 1998; Ye et al., 2016). Below the depth of ∼ 400 m, CH_4 concentration in the majority of profiles decreased with increasing depth and with a concurrent decrease in salinity, indicating the influence of the KIW (**Figure 4**). Finally, CH_4 concentrations increased again when approaching the sea bottom (**Figure 5**). For instance, CH_4 concentrations in the water columns of CTD4, 5, 8, 10, 11, 12, 15, 16, 17, 20, 24, and 28 showed a steady increase to the seafloor, with the maximum value of higher than 10 nM. This may be attributed to CH_4 emissions from the underlying sediments discussed above. According to previous studies, biological production of CH_4 is expected to be widespread on the shelf due to a copious supply of terrestrial organic matter (Floodgate and Judd, 1992; Lin et al., 1992; Judd and Hovland, 2009). As this organic matter accumulates faster than the supply rate of oxidizing agents, methanogenesis sets in and causes organic carbon concentrations to be partly oxidized to CO_2 and partly reduced to CH_4 which supports the argument that CH_4 in bottom water is maintained by emission from the underlying organic-rich sediments. The water column increase in CH_4 concentration when approaching the seafloor was particularly pronounced at the CTD4 and CTD10 sites, with the maximum value of higher than 20 nM at the depth of several meters above the seafloor. This can be attributed to CH_4 seepage already reported in this area (Li et al., 2015; Xu et al., 2018).

Contrary to other sites, the CTD9 site showed positive CH_4 anomalies in the entire water column. The CTD10 site showed relatively high CH_4 concentration in the depths ranging from ∼450 to 1,000 m, while at CTD4, elevated CH_4 concentrations were observed in the depth range from ∼ 850 to 1,000 m. This may indicate that the depth range affected by the seabed CH_4 seepage, or the rising height of the methane plume (**Figure 1**). This is also consistent with the observations of the CH_4 bubble plume analyzed through multi-beam data (Sun et al., unpublished data), which revealed that the maximum height of the methane plume can reach 578 m above the seafloor near the CTD10 site where the water depth is about 1,000 m. In general, CH_4 can be transported in the form of dissolved or free gas in water (Faure et al., 2010). Bubble dissolution models tell us that a 9 mm diameter pure CH_4 bubble released into the water column from a depth of 1,000 m will be dissolved completely when it reaches a depth of 495 m, while a bubble of 15 mm will fully dissipate at 366 m (Greinert and McGinnis, 2009; McGinnis et al., 2006). Assuming that methane bubbles from cold seeps rise from 1,000 to 400 m depth and the bubble dissolution model is applicable to our study, we infer that the diameter of the CH_4 bubbles released into the water column must be between 9 and 15 mm.

Methane Lost to the Atmosphere

In this study, we calculated CH_4 saturations in the surface seawater (**Table 1**), which showed obvious spatial variation and was supersaturated throughout the study areas (**Supplementary Figure S3**), ranged from 108 to 1078%, with the high CH_4 saturation mainly noted at lower slope sites surrounding CTD10 and CTD4. This indicated that surface seawater is a net source of atmosphere CH_4. Spatially, CH_4 saturation ranged from 465 to 975% in the shelf edge area, with an average of 676%. Whereas, in the upper slope area (water depth < 800 m), the saturation varied in a comparatively large range, from 110 to 606%. Different from the shelf and upper slope areas, saturation remarkably changed on the lower slope (108–1078%). Spatial variability among different sites was associated with the characteristics of their geological and physical environment, e.g., seep intensity, water depth, and currents.

To quantify the CH_4 lost to the atmosphere in this area, we estimated the sea-air flux. Overall, the sea-air flux of CH_4 throughout the study area presented heterogeneity in space (**Figure 6**), which ranged from 0.74 to 116 $\mu mol\ m^{-2}d^{-1}$, with an average of 26.2 $\mu mol\ m^{-2}d^{-1}$. Compared with the CH_4 sea-air flux reported by Tsurushima et al. (1996) and Sun et al. (2018) in the shelf, our estimation showed a higher value, which may be due to different sampling and detection methods. In this study, we conducted CH_4 analyses immediately after sampling in a laboratory on-board, which made our detection closer to the actual value than measurements taken after months of store time. Furthermore, the range of the sea-air CH_4 flux on the continental shelf is from 34.8 to 104 $\mu mol\ m^{-2}d^{-1}$, with an average of 61.7 $\mu mol\ m^{-2}d^{-1}$, obviously higher than that on the global continental shelf (22–37 μ mol m^{-2} d^{-1}) (Bange et al., 1994). Compared with other continental shelves worldwide, the sea-air flux was also higher than that in other continental shelf areas of the Western Pacific, such as the South China Sea (Tseng et al., 2017). However, an irregular wide range from 0.74 to 116 $\mu mol\ m^{-2}d^{-1}$ on the slope was noted, with the maximum sea-air CH_4 flux value presented around CTD10, which may result from the direct influence of seafloor cold seepage studied previously. Globally, CH_4 spillovers on the lower slope are significantly higher than those in the Gulf of Cádiz (Ferrón et al., 2009), the Beihai (Bange et al., 1994), the Philippine Sea (Tseng et al., 2017),

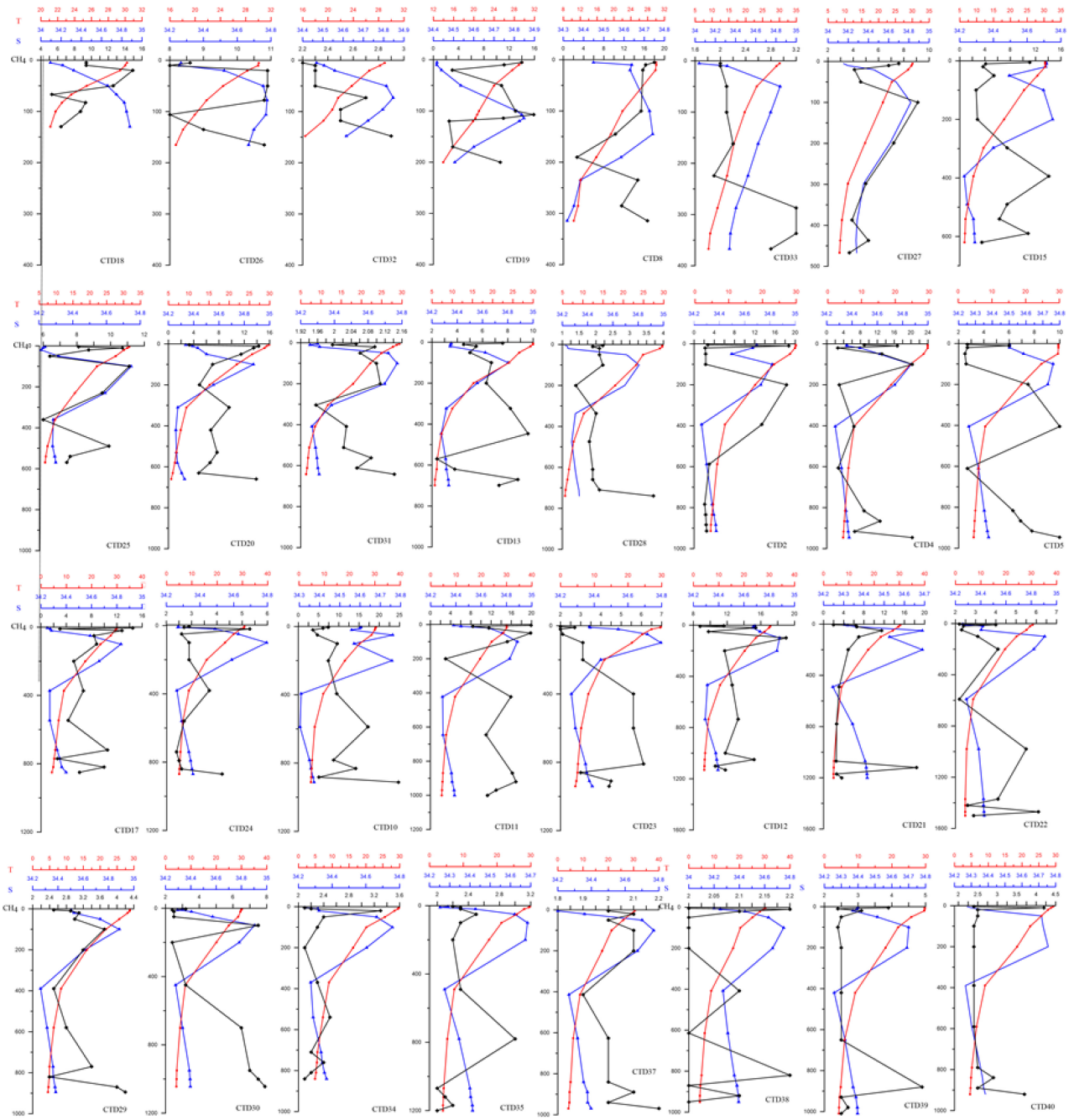

FIGURE 5 | Depth profiles for temperature (°C), salinity (‰), and CH_4 (nM) at representative stations of the OT.

and the Gulf of Mexico (Yvon-Lewis et al., 2011; **Table 1**). In summary, our study area is an active area of CH_4 emissions.

Possible Effects of Hydrothermal Activities

In addition to the contribution from cold seepage to CH_4 in the water of the OT, hydrothermal fluid was noted as an efficient carrier of CH_4. Previous studies demonstrated that approximately more than 20 hydrothermal vents have been discovered since the 1980s in the OT (Halbach et al., 1989; Miyazaki et al., 2017). Significant enrichment of hydrothermal fluids of the OT in gas species is one of the geochemical features compared with those in the typical sediment-starved Mid Ocean Ridge (Sakai et al., 1990; Konno et al., 2006; Kawagucci et al., 2011; Ishibashi et al., 2014). Furthermore, anomalously high CH_4 concentrations were reported in the venting fluid of Iheya North (up to 7.6 mM; Kawagucci et al., 2011) in the

TABLE 1 | Surface concentrations, surface saturations, and sea-to-air fluxes of CH_4 reported in different oceanic areas.

Study area	CH_4(nM)	Surface sat. (%)	Sea to air flux (umol $m^{-2}d^{-1}$)	References
Baltic Sea		113 ± 5	0.0095–14.5[a]	Bange et al., 1994
		395 ± 82	0.101–1200[a]	
North Sea		126 ± 8	2.16 ± 1.99[a]	Bange et al., 1994
North Atlantic (Off Mauritania)	2.1–2.5	96–106		Kock et al., 2008
	2.2–5.5	97–200		
Gulf of Cádiz	1.64–51.1	1 70–1820	4.7 ± 4.6[a] 8.4 ± 7.8[b]	Greinert and McGinnis, 2009
Gulf of Mexico	3.3		0.024[c]	Ferrón et al., 2009
Northern South China Sea	4.5 ± 3.6	230 ± 184	8.6 ± 6.4[d]	Tseng et al., 2017
Upper slope off-shore western Svalbard	5.0	154	20(8–45)	Schmale et al., 2005
East China Sea	24 ± 0.59	141 ± 23.6	1.63 ± 1.67[a]	Zhang et al., 2004
East China Sea			2.77 ± 2.71[b]	
East China Sea	9.49 ± 11.0	487 ± 555	20.9 ± 54.8[a]	Zhang et al., 2004
East China Sea	4.9 ± 3.2	203 ± 126	9.77 ± 16.0[e]	Sun et al., 2018
East China Sea	12.5 ± 3.79	675.86 ± 204.37	68.55 ± 24.24[b] 54.75 ± 19.38[e]	This study (shelf)
East China Sea	6.0 ± 3.23	326.6 ± 177.4	27.15 ± 21.27[b] 21.6 ± 16.90[e]	This study (Slope area < 800 m)
East China Sea	5.33 ± 5.03	280.66 ± 267.8	21.53 ± 31.92[b] 17.18 ± 25.47[e]	This study (Slope area > 800 m)

[a]Kw was estimated by the LM86 equation. [b]Kw was estimated by the W92 equation. [c]Values are calculated according to the results shown in the reference. [d]Kw was estimated by the N2000 equation. [e]Kw was estimated by the W2014 equation.

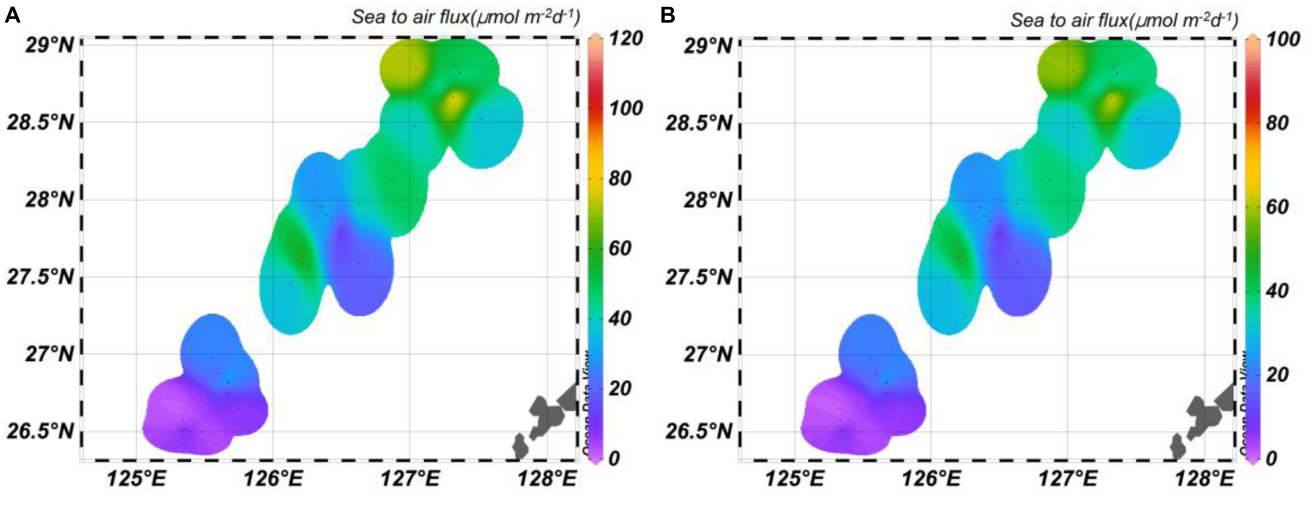

FIGURE 6 | Sea-to-air fluxe of CH_4 [**(A)** Kw was estimated by the W2014 equation; **(B)** Kw was estimated by the W92 equation].

middle OT, and documented CH_4 concentration in hydrothermal fluids of the Minami Ensei nearest to our study sites was approximately 2.1 mM (Kawagucci et al., 2013). These fluids, with CH_4 concentrations generally a thousand times more than the background value, are a significant contributor to the seawater CH_4 (Glasby and Notsu, 2003).

In the current research, CH_4 concentration at different sites was anomalously high in the deep-water of the study area. As shown in **Figures 1**, **2**, distribution of high CH_4 concentrations in the depth water partly appeared near known hydrothermal sites (Inagaki et al., 2006). For instance, in depth of 1050 mbsl (not the bottom water), the data from CTD12 showed a CH_4 concentration of 15.2 nM, and this high concentration may originate from the nearest seep site of CTD10 as discussed earlier. However, it was found to be very close to the Minami Ensei Knoll hydrothermal vent with the high temperature fluid enriched in CH_4. The distance measured between them is approximately only 19 km. Although Cowen et al. (2002) reported that CH_4 in hydrothermal plumes can be dramatically decayed with dispersed distances by the microbial oxidation process along with dilution of the plume with background waters; CH_4 evidence in the hydrothermal plume occurred in a distal station 15 km off the hydrothermal vents of the Juan de Fuca Ridge with a CH_4 concentration of 600 nM. However, CH_4 concentration in the Minami Ensei Knoll (∼2.1 mM) and the velocity of the current in the OT were significantly higher than that in the Juan de Fuca Ridge (Cowen et al., 2002; Nakamura et al., 2008; Kawagucci et al., 2013), thus, CH_4 in the hydrothermal plume could be further

transferred. Therefore, we speculate that the CH_4 concentration in the CTD12 site may be influenced by the Minami Ensei Knoll hydrothermal fluid. In addition, CTD17 showed a high concentration of CH_4 in deep rather than bottom water, with the maximum value of higher than 10 nM, which may be due to the horizontal extra input by non-buoyant plumes (German and Syefried, 2014). Similar to CTD12, a hydrothermal vent was found near the site named Iheya Ridge (**Figure 1**) with an extremely high CH_4 concentration of 7.6 mM (Ishibashi et al., 1995; Kawagucci et al., 2011, 2013). In this case, this might effect the CH_4 concentration of CTD17.

Significance of Methane Seepage for the CH_4 Budget

Methane seepage from seafloor sediments remains poorly quantified, although it is widespread on continental margins (Judd and Hovland, 2009; Boetius and Wenzhöfer, 2013). Most previous studies demonstrated that the contribution of the oceans to the global atmospheric CH_4 budget is minor (Schmale et al., 2005; Yvon-Lewis et al., 2011), with inputs originating from surface seawater, only occurring in regions of supersaturation. In contrast, new sites of seafloor CH_4 seepage are being discovered continually (Skarke et al., 2014), and recent studies on CH_4 fluxes at sites of seepage have been conducted. However, previous results based on traditional indirect sampling techniques and modeling suggested that bubble plumes emitted from cold seepages at depths greater than 200 m do not reach the surface mixed layer due to bubble dissolution and CH_4 oxidation (Valentine et al., 2001). This case is present in deep-water hydrocarbon seepages in offshore Svalbard (Graves et al., 2015) and the northern Gulf of Mexico (Hu et al., 2012), where seafloor makes an insignificant local contribution to the atmosphere due to CH_4 oxidation. Similar to these areas, the sea-air flux that we estimated from the west slope of the OT was relatively small. Based on the mean flux, the preliminarily estimated emission rate of CH_4 from our study area in the ECS was 2.9×10^{-3} Tg yr^{-1}. This indicated that although the study area only accounted for 2.47% of the surface area in the ESC ($\sim 7.7 \times 10^5$ km^2), it accounted for about 4.5% of CH_4 emissions in the ESC (6.4×10^{-2} Tg yr^{-1}) (Ye et al., 2016). Nevertheless, as a unique back-arc basin, the characteristic of CH_4 can be influenced by both the cold seepage and the pervasive hydrothermal fluids as discussed above. Our study area only represented 2.47% of the ESC and was away from the majority of hydrothermal sites; thus, the contribution of emitted CH_4 from sediment to atmosphere in the ESC was remarkably larger than that estimated previously (Ye et al., 2016).

Additionally, these CH_4 emissions from the seafloor extreme systems may have a significant influence on the carbon cycle. Methane seepage allows buried old or deep sourced carbon to be transported to the seafloor (Boetius and Wenzhöfer, 2013), which contributes allochthonous forms of methane carbon to water (Pohlman et al., 2011; Zhang et al., 2019). At the same time, part of the methane carbon is bio-absorbed and then redeposited in carbonate (Sun et al., 2015), which became the methane sink. On the other hand, Zachos et al. (2004) reported that large releases of methane could have contributed to ocean acidification and with that resulting in the dissolution of large amounts of sedimentary carbonate in historic events. In this case, that would speed up the circulation of methane carbon in the ocean.

CONCLUSION

CH_4 concentrations in the seawaters on the west slope of the OT were in the range of 2.7–24.7 nM, with an average of 6.5 nM. The special distributions revealed that CH_4 concentration in the majority of the transections showed a high to low trend from the shelf to the slope. However, CH_4 concentration in the P1 and P2 transections was subjected to high variability, showing high values in the bottom water of the CTD4 and CTD10 sites. The vertical distributions indicated that dissolved CH_4 can be influenced by *in situ* aerobic CH_4 production caused by microbial biogeochemistry or physical advective supply from the shallower depth water of the continental shelf.

CH_4 in the surface water was, in all cases, supersaturated with respect to the atmosphere. Besides, the sea-air flux of CH_4 throughout the study area showed high spatial variations, which ranged from 0.74 to 116 $\mu mol\ m^{-2}d^{-1}$, demonstrating that surface seawater is a net source of CH_4 to the atmosphere. Based on the mean CH_4 flux, the preliminary estimated rate of CH_4 from our study area in the ECS was 2.9×10^{-3} Tg yr^{-1}, which was higher than the value speculated previously. Therefore, the previously estimated CH_4 emission rate in the ESC may be underestimated according to our findings. The coexisted contributions of the cold seepage and hydrothermal vents expand our view of the CH_4 budget of the back-arc basin worldwide.

DATA AVAILABILITY STATEMENT

The raw data supporting the conclusions of this article will be made available by the authors, without undue reservation, to any qualified researcher.

AUTHOR CONTRIBUTIONS

ZS and NW organized and designed sampling strategy. XiaZ, LW, XilZ, and BZ collected the sample. XY analyzed the CH_4 concentrations. XiaZ wrote the manuscript. CX, WG, and HC contributed to the data interpretation and discussion of the manuscript at different stages. All authors contributed to the article and approved the submitted version.

FUNDING

This study was supported by the National Natural Science Foundation of China (Nos. 41606087 and 91858208), the National Key Basic Research and Development Program of China

(Nos. 2018YFC031000303 and 2017YFC0307704), and the Marine Geological Survey Program of China Geological Survey (No. DD20190819).

ACKNOWLEDGMENTS

We thank the captains and crew of *Zhang Jian* for their assistance in recovering the samples during the ECS marine geological Expedition during 2016 and 127 ROV cruises during 2017. We also thank Dr. Meng Wang and his team members from Shanghai Jiao Tong University for their help in exploration and sampling in cold seeping areas by the ROV Beaver.

SUPPLEMENTARY MATERIAL

The Supplementary Material for this article can be found online at: https://www.frontiersin.org/articles/10.3389/feart.2020.00333/full#supplementary-material

REFERENCES

Bange, H. W., Bartell, U., Rapsomanikis, S., and Andreae, M. O. (1994). Methane in the baltic and north seas and a reassessment of the marine emissions of methane. *Global Biogeochem. Cycles* 8, 465–480. doi: 10.1029/94GB02181

Barnes, R., and Goldberg, E. (1976). Methane production and consumption in anoxic marine sediments. *Geology* 4, 297–300. doi: 10.1130/0091-7613(1976)4<297:MPACIA>2.0.CO;2

Bates, T. S., Kelly, K. C., Johnson, J. E., and Gammon, R. H. (1996). A reevaluation of the open ocean source of methane to the atmosphere. *J. Geophys. Res. Atmos.* 101, 6953–6961. doi: 10.1029/95JD03348

Boetius, A., and Wenzhöfer, F. (2013). Seafloor oxygen consumption fuelled by methane from cold seeps. *Nat. Geosci.* 6, 725–734. doi: 10.1038/ngeo1926

Chronopoulou, P.-M., Shelley, F., Pritchard, W. J., Maanoja, S. T., and Trimmer, M. (2017). Origin and fate of methane in the eastern tropical north pacific oxygen minimum zone. *ISME J.* 11, 1386–1399. doi: 10.1038/ismej.2017.6

Cowen, J. P., Wen, X., and Popp, B. N. (2002). Methane in aging hydrothermal plumes. *Geochim. Cosmochim. Acta* 66, 3563–3571. doi: 10.1016/S0016-7037(02)00975-4

Fan, D.-J., and Yang, Z.-S. (2004). Development and distribution of natural gas hydrate in the okinawa trough. *Acta Petrolei Sinica* 25, 11–17.

Faure, K., Greinert, J., von Deimling, J. S., McGinnis, D. F., Kipfer, R., and Linke, P. (2010). Methane seepage along the hikurangi margin of new zealand: geochemical and physical data from the water column, sea surface and atmosphere. *Mar. Geol.* 272, 170–188. doi: 10.1016/j.margeo.2010.01.001

Ferrón, S., Alonso-Pérez, F., Ortega, T., and Forja, J. M. (2009). Benthic respiration on the northeastern shelf of the Gulf of Cádiz (SW Iberian Peninsula). *Mar. Ecol. Prog. Ser.* 392, 69–80. doi: 10.3354/meps08240

Fleischer, P., Orsi, T., Richardson, M., and Anderson, A. (2001). Distribution of free gas in marine sediments: a global overview. *Geo-Mar. Lett.* 21, 103–122. doi: 10.1007/s003670100072

Floodgate, G., and Judd, A. (1992). The origins of shallow gas. *Cont. Shelf Res.* 12, 1145–1156. doi: 10.1016/0278-4343(92)90075-U

Gao, Z. (1996). *Deep Water Traction Current Deposition: Study on Internal Tide, Internal Wave and Isocurrent Deposition*. Beijing: Science Press. (in chinese).

Gentz, T., Damm, E., von Deimling, J. S., Mau, S., McGinnis, D. F., and Schlüter, M. (2014). A water column study of methane around gas flares located at the West Spitsbergen continental margin. *Cont. Shelf Res.* 72, 107–118. doi: 10.1016/j.csr.2013.07.013

German, C. R. Jr., and Syefried, W. E. Jr. (2014). "8.7-hydrothermal processes," in *Treatise Geochem*, 2nd Edn, eds H. D. Holland and K. K. Turekian (Amsterdam: Elsevier), 191–233. doi: 10.1016/B978-0-08-095975-7.00607-0

Glasby, G., and Notsu, K. (2003). Submarine hydrothermal mineralization in the okinawa trough, SW of Japan: an overview. *Ore Geol. Rev.* 23, 299–339. doi: 10.1016/j.oregeorev.2003.07.001

Graves, C. A., Steinle, L., Rehder, G., Niemann, H., Connelly, D. P., Lowry, D., et al. (2015). Fluxes and fate of dissolved methane released at the seafloor at the landward limit of the gas hydrate stability zone offshore western Svalbard. *J. Geophys. Res.: Oceans* 120, 6185–6201. doi: 10.1002/2015JC011084

Greinert, J., and McGinnis, D. F. (2009). Single bubble dissolution model–The graphical user interface SiBu-GUI. *Environ. Model. Softw.* 24, 1012–1013. doi: 10.1016/j.envsoft.2008.12.011

Halbach, P., Nakamura, K.-I., Wahsner, M., Lange, J., Sakai, H., Käselitz, L., et al. (1989). Probable modern analogue of Kuroko-type massive sulphide deposits in the Okinawa Trough back-arc basin. *Nature* 338, 496–499. doi: 10.1038/338496a0

Hu, L., Yvon-Lewis, S. A., Kessler, J. D., and MacDonald, I. R. (2012). Methane fluxes to the atmosphere from deepwater hydrocarbon seeps in the northern Gulf of Mexico. *J. Geophys. Res.* 117, 1–13. doi: 10.1029/2011JC007208

Inagaki, F., Kuypers, M. M., Tsunogai, U., Ishibashi, J.-I., Nakamura, K.-I., Treude, T., et al. (2006). Microbial community in a sediment-hosted CO2 lake of the southern Okinawa Trough hydrothermal system. *Proc. Natl. Acad. Sci. U.S.A.*103, 14164–14169. doi: 10.1073/pnas.0606083103

IPCC (2013). *Climate Change: The Physical Science Basis*. New York, NY: Cambridge University Press.

Ishibashi, J., Sano, Y., Wakita, H., Gamo, T., Tsutsumi, M., and Sakai, H. (1995). Helium and carbon geochemistry of hydrothermal fluids from the mid-okinawa trough back arc basin, southwest of Japan. *Chem. Geol.* 123, 1–15. doi: 10.1016/0009-2541(95)00051-M

Ishibashi, J.-I., Noguchi, T., Toki, T., Miyabe, S., Yamagami, S., Onishi, Y., et al. (2014). Diversity of fluid geochemistry affected by processes during fluid upwelling in active hydrothermal fields in the Izena Hole, the middle Okinawa Trough back-arc basin. *Geochem. J.* 48, 357–369. doi: 10.2343/geochemj.2.0311

Jayakumar, D., Naqvi, S., Narvekar, P., and George, M. (2001). Methane in coastal and offshore waters of the Arabian Sea. *Mar. Chem.* 74, 1–13. doi: 10.1016/S0304-4203(00)00089-X

Judd, A., and Hovland, M. (2009). *Seabed Fluid Flow: the Impact on Geology, Biology and the Marine Environment*. Cambridge: Cambridge University Press.

Kawagucci, S., Chiba, H., Ishibashi, J.-I., Yamanaka, T., Toki, T., Muramatsu, Y., et al. (2011). Hydrothermal fluid geochemistry at the Iheya North field in the mid-okinawa trough: implication for origin of methane in subseafloor fluid circulation systems. *Geochem. J.* 45, 109–124. doi: 10.2343/geochemj.1.0105

Kawagucci, S., Ueno, Y., Takai, K., Toki, T., Ito, M., Inoue, K., et al. (2013). Geochemical origin of hydrothermal fluid methane in sediment-associated fields and its relevance to the geographical distribution of whole hydrothermal circulation. *Chem. Geol.* 339, 213–225. doi: 10.1016/j.chemgeo.2012.05.003

Kock, A., Gebhardt, S., and Bange, H. W. (2008). Methane emissions from the upwelling area off Mauritania (NW Africa). *Biogeosciences* 5, 1119–1125. doi: 10.5194/bg-5-1119-2008

Konn, C., Charlou, J.-L., Donval, J.-P., Holm, N., Dehairs, F., and Bouillon, S. (2009). Hydrocarbons and oxidized organic compounds in hydrothermal fluids from rainbow and lost city ultramafic-hosted vents. *Chem. Geol.* 258, 299–314. doi: 10.1016/j.chemgeo.2008.10.034

Konno, U., Tsunogai, U., Nakagawa, F., Nakaseama, M., Ishibashi, J. I., Nunoura, T., et al. (2006). Liquid CO2 venting on the seafloor: yonaguni knoll IV hydrothermal system, Okinawa Trough. *Geophys. Res. Lett.* 33:L16607. doi: 10.1029/2006GL026115

Lee, H. J., Jung, K. T., Foreman, M., and Chung, J. Y. (2000). A three-dimensional mixed finite-difference Galerkin function model for the oceanic circulation in the Yellow Sea and the East China Sea. *Cont. Shelf Res.* 20, 863–895. doi: 10.1016/S0278-4343(00)00005-4

Leifer, I., Clark, J. F., and Chen, R. F. (2000). Modifications of the local environment by natural marine hydrocarbon seeps. *Geophys. Res. Lett.* 27, 3711–3714. doi: 10.1029/2000GL011619

Li, Q., Cai, F., Liang, J., Shao, H., Dong, G., Wang, F., et al. (2015). Geochemical constraints on the methane seep activity in western slope of the middle Okinawa Trough, the East China Sea. *Sci. China: Earth Sci.* 58, 986–995. doi: 10.1007/s11430-014-5034-x

Li, W., Wang, Y. H., Wang, J. N., and Wei, H. (2012). Distributions of water masses and hydrographic structures in the yellow sea and east china sea in spring and summer 2011. *Oceanol. Limnol. Sin* 43, 615–623. (in Chinese with English Abstract)doi:,

Lin, S., Liu, K., Chen, M., Chen, P., and Chang, F. (1992). Distribution of organic carbon in the KEEP area continental margin sediments. *Terr. Atmos. Ocean Sci.* 3, 365–377. doi: 10.3319/TAO.1992.3.3.365(KEEP)

Liu, K.-K., Peng, T.-H., and Shaw, P.-T. (2003). Circulation and biogeochemical processes in the East China Sea and the vicinity of Taiwan. *Deep Sea Res. II Top. Stud. Oceanogr.* 50, 1055–1064. doi: 10.1016/S0967-0645(03)00009-2

Mau, S., Römer, M., Torres, M. E., Bussmann, I., Pape, T., Damm, E., et al. (2017). Widespread methane seepage along the continental margin off Svalbard-from Bjørnøya to Kongsfjorden. *Sci. Rep.* 7:42997. doi: 10.1038/srep 42997

McGinnis, D. F., Greinert, J., Artemov, Y., Beaubien, S., and Wüest, A. (2006). Fate of rising methane bubbles in stratified waters: How much methane reaches the atmosphere? *J. Geophys. Res.* 111:C09007. doi: 10.1029/2005JC003183

Milkov, A. V., and Sassen, R. (2003). Preliminary assessment of resources and economic potential of individual gas hydrate accumulations in the Gulf of Mexico continental slope. *Mar. Pet. Geol.* 20, 111–128. doi: 10.1016/S0264-8172(03)00024-2

Miyazaki, J., Kawagucci, S., Makabe, A., Takahashi, A., Kitada, K., Torimoto, J., et al. (2017). Deepest and hottest hydrothermal activity in the okinawa trough: the yokosuka site at yaeyama knoll. *R. Soc. Open Sci.* 4:171570. doi: 10.1098/rsos.171570

Nakamura, H., Nishina, A., Ichikawa, H., Nonaka, M., and Sasaki, H. (2008). Deep countercurrent beneath the kuroshio in the okinawa trough. *J. Geophys. Res.* 113:C06030. doi: 10.1029/2007JC004574

Nakamura, H., Nishina, A., Liu, Z., Tanaka, F., Wimbush, M., and Park, J. H. (2013). Intermediate and deep water formation in the Okinawa Trough. *J. Geophys. Res.* 118, 6881–6893. doi: 10.1002/2013JC009326

Patra, P. K., Lal, S., Venkataramani, S., Gauns, M., and Sarma, V. (1998). Seasonal variability in distribution and fluxes of methane in the Arabian Sea. *J. Geophys. Res.* 103, 1167–1176. doi: 10.1029/97JC02590

Pohlman, J. W., Bauer, J. E., Waite, W. F., Osburn, C. L., Chapman, N. R. (2011). Methane hydrate-bearing seeps as a source of aged dissolved organic carbon to the oceans. *Nat. Geosci.* 4, 37–41. doi: 10.1038/ngeo1016

Qi, J., Yin, B., Zhang, Q., Yang, D., and Xu, Z. (2014). Analysis of seasonal variation of water masses in East China Sea. *Chin. J. Oceanol. Limnol.* 32, 958–971. doi: 10.1007/s00343-014-3269-1

Qin, Y. (1987). *Geolygy of the East China Sea*. Beijing: Science Press.

Reeburgh, W. S. (2007). Oceanic methane biogeochemistry. *Chem. Rev.* 107, 486–513. doi: 10.1021/cr050362v

Rehder, G., and Suess, E. (2001). Methane and pCO2 in the Kuroshio and the South China Sea during maximum summer surface temperatures. *Mar. Chem.* 75, 89–108. doi: 10.1016/S0304-4203(01)00026-3

Rhee, T., Kettle, A., and Andreae, M. (2009). Methane and nitrous oxide emissions from the ocean: A reassessment using basin-wide observations in the Atlantic. *J. Geophys. Res. Atmos.* 114:D12304. doi: 10.1029/2008JD011662

Sakai, H., Gamo, T., Kim, E., Tsutsumi, M., Tanaka, T., Ishibashi, J., et al. (1990). Venting of carbon dioxide-rich fluid and hydrate formation in mid-Okinawa trough backarc basin. *Science* 248, 1093–1096. doi: 10.1126/science.248.4959.1093

Schlitzer, R. (2018). *Ocean Data View*. Available online at: https://odv.awi.de (accessed July 8, 2019).

Schmale, O., Greinert, J., and Rehder, G. (2005). Methane emission from high-intensity marine gas seeps in the Black Sea into the atmosphere. *Geophys. Res. Lett.* 32:L07609. doi: 10.1029/2004GL021138

Shinjo, R., Chung, S. L., Kato, Y., and Kimura, M. (1999). Geochemical and Sr-Nd isotopic characteristics of volcanic rocks from the Okinawa Trough and Ryukyu Arc: Implications for the evolution of a young, intracontinental back arc basin. *J. Geophys. Res.: Solid Earth* 104, 10591–10608. doi: 10.1029/1999JB900040

Sibuet, J. C., Letouzey, J., Barbier, F., Charvet, J., Foucher, J. P., Hilde, T. W., et al. (1987). Back arc extension in the Okinawa Trough. *J. Geophys. Res.: Solid Earth* 92, 14041–14063. doi: 10.1029/JB092iB13p14041

Sibuet, M., and Olu, K. (1998). Biogeography, biodiversity and fluid dependence of deep-sea cold-seep communities at active and passive margins. *DSR* 45, 517–567. doi: 10.1016/S0967-0645(97)00074-X

Sieburth, J. M. (1987). "Contrary habitats for redox-specific processes: methanogenesis in oxic waters and oxidation in anoxic waters," in *Microbes in the Sea*, Ed. M. A. Sleigh (Halsted Press: Chichester) 11–38.

Skarke, A., Ruppel, C., Kodis, M., Brothers, D., and Lobecker, E. (2014). Widespread methane leakage from the seafloor on the northern US Atlantic margin. *Nat. Geosci.* 7, 657–661. doi: 10.1038/ngeo2232

Solomon, E. A., Kastner, M., MacDonald, I. R., and Lerfer, I. (2009). Considerable methane fluxes to the atmosphere from hydrocarbon seeps in the gulf of Mexico. *Nat. Geosci.* 2, 561–565. doi: 10.1038/ngeo574

St. Louis, V. L., Kelly, C. A., Duchemin, É, Rudd, J. W., and Rosenberg, D. M. (2000). Reservoir surfaces as sources of greenhouse gases to the atmosphere: a global estimate: reservoirs are sources of greenhouse gases to the atmosphere, and their surface areas have increased to the point where they should be included in global inventories of anthropogenic emissions of greenhouse gases. *Bioscience* 50, 766–775. doi: 10.1641/0006-3568(2000)050[0766:RSASOG]2.0.CO;2

Sun, M.-S., Zhang, G.-L., Ma, X., Cao, X.-P., Mao, X.-Y., Li, J., et al. (2018). Dissolved methane in the East China Sea: Distribution, seasonal variation and emission. *Mar. Chem.* 202, 12–26. doi: 10.1016/j.marchem.2018.03.001

Sun, Z., Wei, H., Zhang, X., Shang, L., Yin, X., Sun, Y., et al. (2015). A unique Fe-rich carbonate chimney associated with cold seeps in the Northern Okinawa Trough, East China Sea. *Deep Sea Res.I Oceanogr. Res Pap.* 95, 37–53. doi: 10.1016/j.dsr.2014.10.005

Sun, Z., Wu, N., Cao, H., Xu, C., Liu, L., Yin, X., et al. (2019). Hydrothermal metal supplies enhance the benthic methane filter in oceans: An example from the Okinawa Trough. *Chem. Geol.* 525, 190–209. doi: 10.1016/j.chemgeo.2019.07.025

Tang, Y. X., Lee, H. J., Cho, C. H., and Lee, J. H. (1997). The hydrographic conditions in the northeastern East China Sea in summer. *J. Oceanogr. Huanghai Bohai Seas* 15, 8–19. (in Chinese with English Abstract)

Tilbrook, B. D., and Karl, D. M. (1995). Methane sources, distributions and sinks from California coastal waters to the oligotrophic North Pacific gyre. *Mar. Chem.* 49, 51–64. doi: 10.1016/0304-4203(94)00058-L

Tseng, H.-C., Chen, C.-T. A., Borges, A. V., DelValls, T. A., and Chang, Y.-C. (2017). Methane in the South China sea and the Western Philippine Sea. *Cont. Shelf Res.* 135, 23–34. doi: 10.1016/j.csr.2017.01.005

Tsurushima, N., Watanabe, S., and Tsunogai, S. (1996). Methane in the East China sea water. *J. Oceanogr.* 52, 221–233. doi: 10.1007/BF02235671

Valentine, D. L., Blanton, D. C., Reeburgh, W. S., and Kastner, M. (2001). Water column methane oxidation adjacent to an area of active hydrate dissociation, Eel River Basin. *Geochim. Cosmochim. Acta* 65, 2633–2640. doi: 10.1016/S0016-7037(01)00625-1

Wang, M., Cai, F., Li, Q., Liang, J., Yan, G., Dong, G., et al. (2015). Characteristics of authigenic pyrite and its sulfur isotopes influenced by methane seep at Core A, Site 79 of the middle Okinawa Trough. *Sci. China Earth Sci.* 58, 2145–2153. doi: 10.1007/s11430-015-5196-1

Wanninkhof, R. (1992). Relationship between wind speed and gas exchange over the ocean. *J. Geophys. Res. Oceans* 97, 7373–7382. doi: 10.1029/92JC00188

Wanninkhof, R. (2014). Relationship between wind speed and gas exchange over the ocean revisited. *Limnol. Oceanogr. Methods* 12, 351–362. doi: 10.4319/lom.2014.12.351

Watanabe, S., Higashitani, N., Tsurushima, N., and Tsunogai, S. (1995). Methane in the western North Pacific. *J. Oceanogr.* 51, 39–60. doi: 10.1007/BF02235935

Wiesenburg, D. A., and Guinasso, N. L. Jr. (1979). Equilibrium solubilities of methane, carbon monoxide, and hydrogen in water and sea water. *J. Chem. Eng. Data* 24, 356–360. doi: 10.1021/je60083a006

Xiwu, L., Wang, K., Hyndman, R., and Willoughby, E. (2008). Bottom simulating reflector and gas seepage in okinawa trough: evidence of gas hydrate in an active back-arc basin. *J. China University of Geosci.* 19, 152–161. doi: 10.1016/S1002-0705(08)60034-5

Xu, C., Wu, N., Sun, Z., Zhang, X., Geng, W., Cao, H., et al. (2018). Methane seepage inferred from pore water geochemistry in shallow sediments in the western slope of the Mid-Okinawa Trough. *Mar. Pet. Geol.* 98, 306–315. doi: 10.1016/j.marpetgeo.2018.08.021

Ye, W., Zhang, G., Zhu, Z., Huang, D., Han, Y., Wang, L., et al. (2016). Methane distribution and sea-to-air flux in the East China Sea during the summer of 2013: impact of hypoxia. *DSR* 124, 74–83. doi: 10.1016/j.dsr2.2015.01.008

Yin, P., Berné, S., Vagner, P., Loubrieu, B., and Liu, Z. (2003). Mud volcanoes at the shelf margin of the East China Sea. *Mar. Geol.* 194, 135–149. doi: 10.1016/S0025-3227(02)00678-3

Yu, H., Liu, Z., Berné, S., Jia, G., Xiong, Y., Dickens, G. R., et al. (2009). Variations in temperature and salinity of the surface water above the middle Okinawa Trough during the past 37 kyr. *Palaeogeogr. Palaeoclimatol. Palaeoecol.* 281, 154–164. doi: 10.1016/j.palaeo.2009.08.002

Yvon-Lewis, S. A., Hu, L., and Kessler, J. (2011). Methane flux to the atmosphere from the Deepwater Horizon oil disaster. *Geophys. Res. Lett.* 38:L01602. doi: 10.1029/2010GL045928

Zachos, J. C., Roehl, U., Schellenberg, S. A., Sluijs, A., Hodell, D. A., Kelly, D. C., et al. (2004). Rapid acidification of the ocean during the paleocene-eocene thermal maximum. *Sci* 308, 1611–1615. doi: 10.1126/science.1109004

Zhang, G., Zhang, J., Kang, Y., and Liu, S. (2004). Distributions and fluxes of methane in the East China Sea and the Yellow Sea in spring. *J. Geophys. Res.* 109:C07011. doi: 10.1029/2004JC002268

Zhang, G., Zhang, J., Ren, J., Li, J., and Liu, S. (2008). Distributions and sea-to-air fluxes of methane and nitrous oxide in the North East China Sea in summer. *Mar. Chem.* 110, 42–55. doi: 10.1016/j.marchem.2008.02.005

Zhang, J., Liu, S., Ren, J., Wu, Y., and Zhang, G. (2007). Nutrient gradients from the eutrophic Changjiang (Yangtze River) Estuary to the oligotrophic Kuroshio waters and re-evaluation of budgets for the East China Sea Shelf. *Prog. Oceanogr.* 74, 449–478. doi: 10.1016/j.pocean.2007.04.019

Zhang, X., Sun, Z., Fan, D., Xu, C., Wang, L., Zhang, X., et al. (2019). Compositional characteristics and sources of DIC and DOC in seawater of the Okinawa Trough, East China Sea. *Cont. Shelf Res.* 174, 108–117. doi: 10.1016/j.csr.2018.12.014

Conflict of Interest: The authors declare that the research was conducted in the absence of any commercial or financial relationships that could be construed as a potential conflict of interest.

frontiers in Earth Science

ORIGINAL RESEARCH
published: 18 March 2021
doi: 10.3389/feart.2021.623720

Isotopically Light Cd in Sediments Underlying Oxygen Deficient Zones

Lena Chen[1,3]*, *Susan H. Little*[2,3], *Katharina Kreissig*[3], *Silke Severmann*[4] and *James McManus*[5]

[1]School of Earth and Environment, University of Leeds, Leeds, United Kingdom, [2]Department of Earth Sciences, University College London, London, United Kingdom, [3]Department of Earth Science and Engineering, Imperial College London, London, United Kingdom, [4]Department of Marine and Coastal Science, Rutgers University, New Brunswick, NJ, United States, [5]Bigelow Laboratory for Ocean Sciences, East Boothbay, ME, United States

Cadmium is a trace metal of interest in the ocean partly because its concentration mimics that of phosphate. However, deviations from the global mean dissolved Cd/PO_4 relationship are present in oxygen deficient zones, where Cd is depleted relative to phosphate. This decoupling has been suggested to result from cadmium sulphide (CdS) precipitation in reducing microenvironments within sinking organic matter. We present Cd concentrations and Cd isotope compositions in organic-rich sediments deposited at several upwelling sites along the northeast Pacific continental margin. These sediments all have enriched Cd concentrations relative to crustal material. We calculate a net accumulation rate of Cd in margin settings of between 2.6 to 12.0 × 10^7 mol/yr, higher than previous estimates, but at the low end of a recently published estimate for the magnitude of the marine sink due to water column CdS precipitation. Cadmium in organic-rich sediments is isotopically light ($\delta^{114/110}Cd_{NIST\text{-}3108}$ = +0.02 ± 0.14‰, n = 26; 2 SD) compared to deep seawater (+0.3 ± 0.1‰). However, isotope fractionation during diagenesis in continental margin settings appears to be small. Therefore, the light Cd isotope composition of organic-rich sediments is likely to reflect an isotopically light source of Cd. Non-quantitative biological uptake of light Cd by phytoplankton is one possible means of supplying light Cd to the sediment, which would imply that Cd isotopes could be used as a tracer of past ocean productivity. However, water column CdS precipitation is also predicted to preferentially sequester light Cd isotopes from the water column, which could obfuscate Cd as a tracer. We also observe notably light Cd isotope compositions associated with elevated solid phase Fe concentrations, suggesting that scavenging of Cd by Fe oxide phases may contribute to the light Cd isotope composition of sediments. These multiple possible sources of isotopically light Cd to sediments, along with evidence for complex particle cycling of Cd in the water column, bring into question the straightforward application of Cd isotopes as a paleoproductivity proxy.

Keywords: CdS precipitation, oxygen deficient zones, continental margin, isotope fractionation, cadmium

OPEN ACCESS

Edited by:
Martyn Tranter,
Aarhus University, Denmark

Reviewed by:
Ruifang Xie,
GEOMAR Helmholtz Center for Ocean Research Kiel, Germany
Claudia Ehlert,
University of Oldenburg, Germany

***Correspondence:**
Lena Chen
eelch@leeds.ac.uk

Specialty section:
This article was submitted to Geochemistry, a section of the journal Frontiers in Earth Science

Received: *30 October 2020*
Accepted: *04 February 2021*
Published: *18 March 2021*

Citation:
Chen L, Little SH, Kreissig K, Severmann S and McManus J (2021) Isotopically Light Cd in Sediments Underlying Oxygen Deficient Zones. Front. Earth Sci. 9:623720. doi: 10.3389/feart.2021.623720

INTRODUCTION

Dissolved cadmium (Cd) displays typical nutrient-type behavior in the oceans (e.g., Bruland et al., 2014), despite its known toxicity (e.g., Brand et al., 1986; Waldron and Robinson, 2009). The reason for its nutrient-type behavior is not fully understood; to date, only one biological function of Cd has been identified, in which it replaces Zn in the enzyme carbonic anhydrase (Price and Morel, 1990; Lane et al., 2005; Xu et al., 2008). Nevertheless, dissolved Cd has a spatial distribution akin to the macronutrient phosphate (PO_4) (e.g., Boyle et al., 1976; Bruland, 1980), and Cd/Ca ratios in calcareous microfossils have been utilized as a proxy for past oceanic P distributions (e.g., Marchitto and Broecker, 2006).

Cadmium isotopes in marine carbonates and organic-rich sediments are emerging as a potential tracer of past ocean productivity (Georgiev et al., 2015; John et al., 2017; Hohl et al., 2017, 2019), contingent on the observation that biological uptake of Cd in the surface ocean is associated with preferential uptake of the light isotope (e.g., Lacan et al., 2006; Ripperger et al., 2007). However, deviations from the global ocean Cd/PO_4 relationship are observed in oxygen deficient zones (ODZ) of the modern ocean (e.g., van Geen et al., 1995; Janssen et al., 2014; Middag et al., 2018), deviations that are in some cases associated with Cd isotope fractionation (e.g., Conway and John 2015a). Thus, further work is required to constrain the cycling of Cd and its isotopes in the ocean.

Stable isotopes are a useful tool to constrain the whole oceanic mass balance of an element. The Cd isotope composition of seawater, denoted here as $\delta^{114/110}Cd_{NIST\ SRM\ 3108}$ (**Eqn. 1**), ranges from 0 to +5‰ at the surface, with a uniform deep water average of about +0.3‰ (Ripperger et al., 2007; Xue et al., 2013; Conway and John, 2015a, 2015b; Xie et al., 2017, 2019a, 2019b; John et al., 2018; Sieber et al., 2019a, 2019b; George et al., 2019; Guinoiseau et al., 2019). The isotopic composition of Cd inputs to the ocean are not well constrained, but two studies find aerosol-borne Cd and dissolved riverine Cd to have an isotopic composition similar to lithogenic material at 0.0‰ and +0.2 ± 0.1‰ respectively (Lambelet et al., 2013; Bridgestock et al., 2017). The deep oceans are isotopically heavier than lithogenic Cd; therefore, mass balance requires an isotopically light sink for Cd in sediments.

To date only Fe-Mn crusts—the chemical signatures of which are often used as a proxy for removal to Fe-Mn oxide phases in oxygenated deep-sea settings—have been analysed for their $\delta^{114}Cd$ values. Fe-Mn crusts have Cd isotope compositions similar to the deep ocean $\delta^{114}Cd$ value, at about +0.3‰ (Schmitt et al., 2009; Horner et al., 2010), and therefore cannot be the isotopically light output flux required to balance the Cd budget.

Organic-rich sedimentary settings along productive continental margins are considered a second important sink for Cd (e.g., van Geen et al., 1995; Morford and Emerson, 1999; Little et al., 2015). Organic matter derived from biological primary productivity in the upper water column is one important source of Cd to margin sediments (Elderfield et al., 1981; Rosenthal et al., 1995). In culture, biological uptake is associated with a preference for isotopically light Cd, consistent with the observed isotopically heavy residual dissolved pool in surface seawater (e.g., Ripperger et al., 2007). Organic matter is thus one isotopically light source of Cd to margin sediments (e.g., Yang et al., 2015, 2018; John et al., 2018; Janssen et al., 2019). A second possible source is the precipitation of CdS, either in reducing microenvironments within sinking organic material (e.g., Janssen et al., 2014; Bianchi et al., 2018; Guinoiseau et al., 2019), or in bottom waters proximal to an anoxic sediment-water interface (Xie et al., 2019b; Plass et al., 2020). Consistent with an isotopically light particulate source of Cd to sediments, Janssen et al. (2019) observed isotopically light particles (size range: 0.8–51 μm), ranging from −0.5 to −0.2‰, at water depths of 200–800 m in the northeast Pacific. They propose that the export and burial of these light particulate phases in organic-rich shelf sediments may balance the oceanic Cd budget (Janssen et al., 2019).

As yet, no Cd isotope compositions from modern organic-rich sediments have been reported. Here, we present data for sediments from the northeast Pacific margin. Our dataset supports the suggestion of an isotopically light sink for Cd in margin settings, and places improved constraints on the Cd mass balance and Cd isotope budget of the oceans. Finally, we consider the implications of our data for the utility of Cd isotopes as a tracer of past ocean productivity.

MATERIALS AND METHODS

Sites and Sampling

Samples were selected from the northeast Pacific margin (**Table 1**; **Figure 1**), specifically, from four of the California Borderland Basins (Santa Barbara, Santa Monica, San Nicolas and Tanner Basin), and three sites along the Mexican margin (Pescadero slope, Soledad Basin and Magdalena margin). Sediment cores were collected using a multicorer, as described by McManus et al. (2006). The sites are situated in regions of elevated productivity resulting from coastal upwelling, with water column oxygen depletion at intermediate depth as a consequence of organic matter remineralization. The seven sites span a range of water column oxygen conditions and resultant sedimentary diagenetic regimes (**Table 1**). They also vary in depositional setting, from restricted basins to open continental margin. The sites and samples have been extensively described previously (see: McManus et al., 2006; Poulson-Brucker et al., 2009; Chong et al., 2012; Little et al., 2016; Little et al., 2017) and are thus only briefly introduced here.

California Borderland Basins

The southern California Borderland Basins are separated from one another by their silled topography, thus they exhibit lower oxygen concentrations at intermediate depth and in bottom waters compared to equivalent depths along the open margin (Emery, 1960). The enhanced upwelling generates an ODZ between the depths of 200 and 1,000 m. The basins are situated at a range of water depths and distances offshore, resulting in a range of low oxygen conditions in the region (**Table 1**).

TABLE 1 | Site descriptions, after Little et al. (2016).

Site	Lat °N	Long °W	Coring Depth (m)	Sill depth (m)	Basin depth (m)	Bottom water O_2 (μM)	Diagenetic regime[a]	Sediment accumulation rate (mg/cm^2/y)	Organic C burial flux (mg/cm^2/y)	References
Santa Barbara Basin	34.3	120.0	493	475	600	0–10	Ferr	92	–	1
Santa Monica Basin	33.7	118.8	905	740	910	2–10	Ferr	16	0.7 ± 0.2	2
San Nicolas Basin	32.8	118.8	1750	1,100	1832	15–35	Mn–ferr	14	–	1
Tanner Basin	33.0	119.7	1,514	1,160	1,550	~30	Mn–ferr	12	0.8 ± 0.1	2
Soledad Basin	25.2	112.7	544	250	545	0	Ferr–sulf	50–90	3.7 ± 0.1	3,4,5
Pescadero slope	24.3	108.2	616	Na	Na	0.4	Ferr	77	–	3
Magdalena margin	23.5	111.6	692	Na	Na	0.9	Ferr–sulf	4–12	–	3

[a]*Ferr—Ferruginous; Mn—Manganese rich; Sulf—Sulphidic.*

Na—Not applicable.

References: 1. Poulson Brucker et al. (2009); 2. McManus et al. (2006); 3. Chong et al. (2012); 4. Silverberg et al. (2004); 5. Bralower and Thierstein (1987).

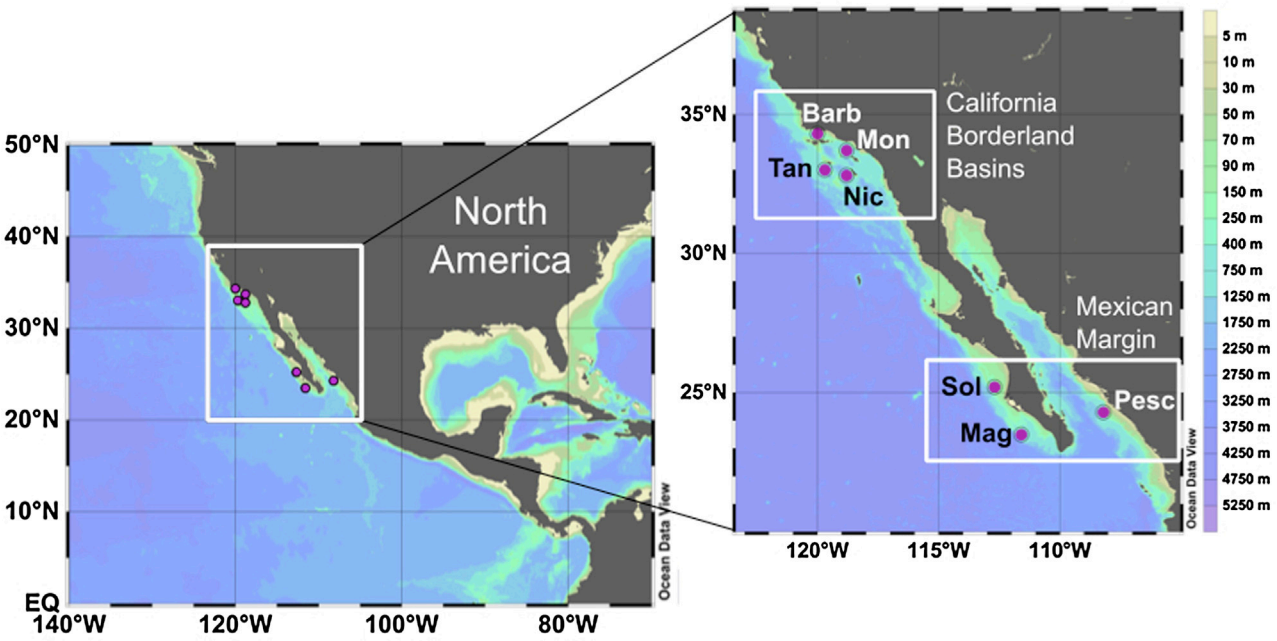

FIGURE 1 | Locations of the sites studied on the northeastern Pacific margin of North America. Enlarged map shows the California Borderland Basins (Barb—Santa Barbara, Mon—Santa Monica, Nic—San Nicolas, Tan—Tanner Basin) and the Mexican Margin sites (Sol - Soledad Basin, Pesc—Pescadero slope, Mag—Magdalena margin). Maps made using Ocean Data View (odv.awi.de; Schlitzer, 2017).

Santa Barbara and Santa Monica are nearshore basins. They are both within the Californian ODZ, thus display low bottom oxygen water conditions of <10 μM, with the Santa Barbara Basin being the most reducing. Both core sites have ferruginous shallow porewaters, which indicate that iron and sulphate reduction are likely to be the dominant electron transfer pathways (McManus et al., 1997; 1998). Santa Barbara has a high sediment accumulation rate (~90 mg/cm^2/yr) compared to the other Borderland Basins (10–20 mg/cm^2/yr), which can be attributed to a higher lithogenic input due to its location close to the continent (Thunell et al., 1995).

By comparison, the offshore basins, San Nicolas and Tanner, provide examples of lower carbon fluxes and higher oxygen concentrations. The San Nicolas and Tanner basins have sill depths below the depth of the ODZ. They have higher bottom water oxygen contents than the nearshore basins, of between 15 and 35 μM, and are diagenetically similar, displaying Mn-Fe rich porewaters, although the Tanner Basin displays lower Fe and Mn than San Nicolas (Shaw et al., 1990; McManus et al., 1997; 1998). At these sites, organic matter is oxidized through a combination of terminal electron acceptors including oxygen, nitrate, Mn, Fe and sulphate.

Mexican Margin

Along the Mexican margin, the sites examined (Pescadero slope, Soledad Basin and Magdalena margin) have considerably lower bottom water oxygen concentrations

(<1 μM) than the Californian Borderland Basins. The ODZ extends more than 1,500 km off the coast of Mexico at depths of 500–1,000 m. The sediment coring depths in this study are all within the ODZ. Therefore, there is likely to be limited bioturbation and excellent preservation of laminated sediments in the cores.

The Pescadero slope is an open margin site on the eastern edge of the mouth of the Gulf of California (**Figure 1**) and receives extensive continental input from the Sierra Madre Occidental Mountains (e.g., Berelson et al., 2005; Chong et al., 2012). The core was collected at a depth of 616 m within the ODZ. The porewaters have high concentrations of dissolved Fe, rapidly increasing from 3 μM at the surface and to a maximum of ~400 μM at a depth of 8 cm (Chong et al., 2012).

Soledad Basin and the Magdalena margin are on the western open ocean margin side of Baja California (**Figure 1**). The core in the Soledad Basin was collected at a water depth of 544 m, close to the deepest point of the basin. This basin is isolated from the open ocean by a sill at approximately 250 m depth (Silverberg et al., 2004). A prior report noted that the sediments are laminated with coccolith laminae (van Geen et al., 2003). By contrast, the Magdalena margin site represents an open, unrestricted continental margin setting. It has a core depth of 692 m and the upper 1–2 cm of sediment is bioturbated. Both locations have dissolved sulphide in the porewaters, increasing from ~10 and 2 μM at the surface to >40 and >20 μM below 8 and 20 cm depth in the Soledad Basin and Magdalena margin respectively (Chong et al., 2012). Unlike the Pescadero slope, these two locations receive very little lithogenic input. Nevertheless, Soledad Basin also has a high sediment accumulation rate of 50–90 mg/cm^2/yr (Silverberg et al., 2004). This high sediment accumulation rate at Soledad Basin indicates elevated productivity, which is supported by a high organic carbon burial flux of 3.7 mg/cm^2/yr at this site (Bralower and Thierstein, 1987).

Analytical Methods

Porewater Analyses

Porewater samples were collected and sampled from sediments as described in prior publications (McManus et al., 1997, 1998, 2006; Severmann et al., 2006; Chong et al., 2012) and porewater Fe and Mn were reported previously for most of the sites discussed here (see references in **Table 1**). However, Santa Barbara and San Nicholas porewater results were not published previously. For these sites porewater Fe and Mn were prepared for analysis by a 20-fold dilution and standard additions of a surface sample from each core. Samples were measured on an Agilent 7500ce quadrupole inductively coupled plasma mass spectrometer (ICP-MS) equipped with a collision cell (using hydrogen gas) at the University of California, Riverside. Analytical precision was ~7% (2 standard deviation) for both Fe and Mn.

Sample Preparation for Cd Isotope Analysis

All sample preparation was conducted in laminar flow hoods (ISO-4). Sediment samples were digested at ETH Zürich (Little et al., 2016). All further sample preparation work for the Cd isotope analysis was conducted in the MAGIC clean room laboratories at Imperial College London. Concentrated HCl, HNO_3 and HF were purified in Teflon DST-1000 Acid Purification Systems from Savillex and diluted to the required concentration with MilliQ water (18.2 MΩ) from a Milli-Q Advantage dispensing system. ~500 mg of each sample were digested, as previously described by Little et al. (2016). In summary, each sample powder was pre-digested with dilute nitric acid at room temperature to dissolve carbonate. The sample and supernatant were then dried down, before complete digestion on a hotplate with a 3:1 mix of concentrated HF and HNO_3. Once digested and dried, samples were treated with concentrated HNO_3 three times to redissolve fluoride salts, before final dissolution in 25 ml 7M HCl. Elemental analysis on an aliquot of these solutions was conducted at ETH Zürich on a Thermo Scientific ELEMENT XR ICP-MS (Little et al., 2016).

An aliquot containing ~100 ng of Cd was then sub-sampled at Imperial College London and spiked with a ^{111}Cd–^{113}Cd double spike to obtain a spike to sample-derived (S/N) Cd ratio of ~1 (Xue et al., 2012). In addition to the samples, two procedural blanks, a column blank, and three aliquots of a USGS basalt reference material (BCR-2) were prepared for Cd isotope analysis. Procedural blanks were ~46 pg Cd, up to a maximum of 0.6% of the Cd content in the smallest sample.

A three-stage column chemistry procedure following Ripperger and Rehkämper (2007) and Xue et al. (2012) was used to separate Cd from the matrix. Briefly, anion-exchange chromatography was performed for the first two stages using AG1-X8 anion-exchange resin. The first two stages differ in column size (2 ml quartz glass columns and 150 μL shrink fit Teflon columns) and resin grain size (100–200 and 200–400 mesh). The last stage of the separation chemistry utilized the same small Teflon columns as during the second-stage procedure, but Biorad Eichrom TRU resin was used to separate Sn and traces of Nb, Zr, Mo in the sample.

Finally, liquid-liquid extraction with *n*-heptane was employed to remove any organic compounds that could be released from the resin (Murphy et al., 2016). The *n*-heptane was pre-cleaned through liquid–liquid extraction with 6M HCl, following the detailed procedure outlined in Murphy et al. (2016). Afterward, the samples were dried twice and re-dissolved with a few drops of concentrated HNO_3 and taken up in 1 ml 2% HNO_3 for mass spectrometry.

Cadmium Isotope Compositions

Cadmium isotope ratio analyses were conducted on the Nu Plasma high resolution multi collector ICP-MS (HR MC-ICP-MS) equipped with a DSN-100 desolvation system and a MicroMist glass nebulizer, with an uptake rate of ~120 μL/min. The ion masses of 114 (Cd), 113 (Cd), 112 (Cd), 111 (Cd) along with 117 (Sn) and 115 (In) were measured simultaneously in low-resolution mode with Faraday cups. The instrumental sensitivity for Cd ranged from 240–310 V/ppm. The S/N ratio and total Cd concentration of the samples matched those of simultaneously measured spiked standard reference

TABLE 2 | Summary of results, including bulk sediment Cd isotope compositions and Cd, Al and Fe concentrations.

Location	Site	Sample	Depth in sediment (cm)	Coring Depth (m)	Cd (μg/g)	Al (wt%)	Fe (wt%)	Org C* (wt%)	δ^{114}Cd (‰)	2σ or 2SD	n[a]
California margin	Santa Barbara Basin	MC17_1	1–1.5	493	0.92	6.6	3.3	3.01	-0.02	0.07	2
		MC17_8	8–8.5		0.8	6.0	3.2	1.50	-0.03	0.06	2
		MC17_40	32–34		0.92	6.3	3.3	2.93	0.04	0.03	2
	Santa Monica Basin	8B3	1–2	905	2.88	5.4	3.2	5.73	0.08	0.05	3
		8B5	3–4		0.81	6.2	4.0	5.23	-0.08	0.03	2
		8B8	6–9		0.98	6.2	3.9	4.19	-0.19	0.05	1
		8B15	18–22		0.99	6.1	3.9	4.50	-0.06	0.04	2
	San Nicolas Basin	MC37 2.5–3	2.5–3	1,750	0.53	4.8	2.7	4.92	-0.04	0.05	1
		MC37 4–4.5	4–4.5		0.65	5.1	2.7	4.85	0.03	0.05	1
		MC37 14–15	14–15		0.65	4.7	2.1	4.25	0.09	0.05	1
		MC37 32–34	32–34		0.92	5.1	3.0	4.41	0.00	0.05	1
	Tanner Basin	12B3	1–2	1,514	1	3.3	1.7	6.69	0.08	0.04	1
		12B5	3–4		0.96	3.3	1.8	6.35	0.11	0.05	1
		12B7	6–9		0.76	3.0	1.5	5.96	0.03	0.04	1
		12B12	12–15		0.67	3.7	1.7	4.31	0.02	0.05	1
Mexican margin	Pescadero slope	Pesc_2	2–3	616	0.69	6.0	2.3	3.55	-0.02	0.05	1
		Pesc_11	11–12		0.70	6.5	2.4	3.45	-0.02	0.06	1
		Pesc_22	22–24		0.74	6.8	2.6	3.07	0.04	0.06	2
		Pesc_30	30–32		0.77	6.4	2.4	3.62	-0.08	0.04	1
	Soledad Basin	Sol2_1	1–2	544	1.88	3.8	1.9	6.47	0.06	0.08	2
		Sol2_11	11–12		1.90	4.1	2.0	6.39	0.04	0.06	1
		Sol2_20	20–22		2.38	3.8	2.0	6.66	0.09	0.02	2
		Sol2_30	30–32		2.15	4.2	2.0	6.23	0.10	0.06	1
	Magdalena margin	MagD_0	0–1	692	1.48	2.3	1.3	10.03	0.09	0.05	1
		MagD_4	4–5		2.75	2.3	1.1	11.71	0.08	0.05	1
		MagD_6	6–7		2.91	2.2	1.0	12.68	0.04	0.05	2

[a]*Number of replicates run through separation chemistry or mass spectrometric analysis, δ^{114}Cd values are presented as means and uncertainties are the 2SD of those values.*
**Organic Carbon data from Little et al. (2016).*

solutions NIST SRM 3108 (NIST) and BAM I012 (BAM) to within ±10%.

Instrumental mass bias was corrected using the double-spike technique described by Xue et al. (2012). Data reduction was carried out offline utilizing the iterative approach of Siebert et al. (2001). The Cd isotope ratios were then reported relative to the bracketing NIST Cd standards in delta notation:

$$\delta^{114/110}\mathrm{Cd} = \delta^{114}\mathrm{Cd} = \left[\frac{(^{114}\mathrm{Cd}/^{110}\mathrm{Cd})_{\mathrm{Sample}}}{(^{114}\mathrm{Cd}/^{110}\mathrm{Cd})_{\mathrm{NIST\ SRM\ 3108}}} - 1\right] \times 1000 \quad (1)$$

Uncertainties reported in **Table 2** are either internal 2σ errors, which represent the within-run uncertainty on each individual Cd isotope analysis, or for duplicate analyses uncertainties are the 2SD of those values. The long-term external reproducibility is calculated based on multiple measurements of the secondary standard BAM (−1.37 ± 0.05‰ 2SD, n = 12) and the BCR-2 reference material (0.02 ± 0.03‰, n = 3).

RESULTS

Sediment Core Data

Cadmium concentrations presented here are normalized to Al in order to account for the presence of Cd from detrital silicates (**Figure 2**). All samples from all sites display elevated Cd/Al ratios compared to the upper continental crust ($\mathrm{Cd/Al_{UCC}} = 0.011 \times 10^{-4}$, Rudnick and Gao, 2003; **Figure 2**), indicating significant bioauthigenic enrichment (see also **section 4.1**). We define 'bioauthigenic' Cd here to include both chemically precipitated and biological Cd sources (i.e., non-lithogenic Cd). Sediment Cd/Al ratios range from 0.1 to 1.3×10^{-4}. The Magdalena margin and Soledad Basin sediment cores are distinctly more enriched in Cd than the cores from the other sites with the average downcore Cd/Al of 1.05×10^{-4} and 0.52×10^{-4} respectively. The Cd/Al ratio of the surface-most sample from Santa Monica is also notably elevated (0.53×10^{-4}) compared to samples deeper in the sediment core (at ~ 0.15×10^{-4}) and other California Borderland Basin sites (≤0.3×10^{-4}). This surface anomaly could reflect a recent anthropogenic source of metals, as previously reported for this site (Finney and Huh, 1989; Bruland et al., 1994).

Sediment Cd isotope compositions range from −0.19 to +0.11‰, with limited δ^{114}Cd variability between sites (**Table 2**; **Figure 2**). This range of values is isotopically lighter than global deep seawater, which has an average δ^{114}Cd value of about +0.3‰ (Ripperger et al., 2007; Xue et al., 2013; Abouchami et al., 2014; Conway and John, 2015a, 2015b; Xie et al., 2017, 2019a, 2019b; John et al., 2018; Sieber et al., 2019a, 2019b; George et al., 2019; Guinoiseau et al., 2019). The most reducing site of the California Borderland Basins, Santa Barbara, has an average δ^{114}Cd of 0.00 ± 0.04‰ (errors reported here are 1 standard

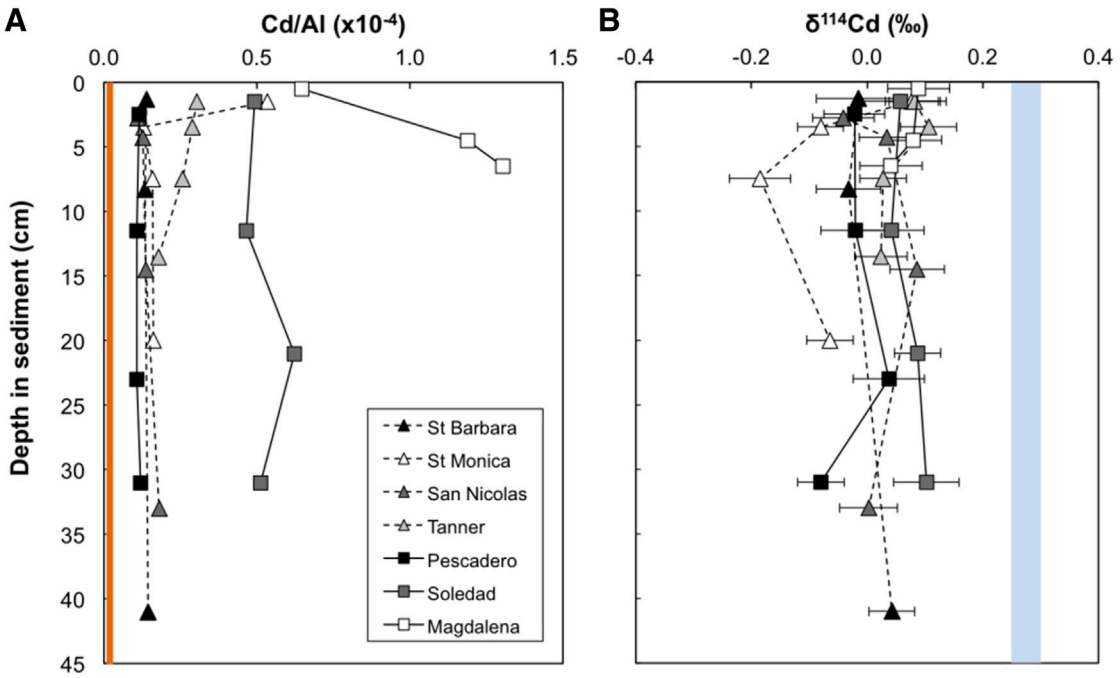

FIGURE 2 | Downcore variability in bulk Cd/Al **(A)** and δ^{114}Cd **(B)** for seven sites from the two continental margin locations (California Borderland Basins—dashed lines, triangles; Mexican Margin—solid lines, squares). The orange bar represents the Cd/Al ratio of the upper continental crust (Rudnick and Gao, 2003). The blue bar represents average deep seawater δ^{114}Cd (+0.25–0.3‰—see text for references). Error bars are the external 2 SD on sample replicates or of a secondary standard (BAM, ± 0.05‰), or the internal 2σ on an individual Cd isotope ratio measurement, whichever is larger.

deviation variation over the entire sediment core), which is similar to the least reducing site, San Nicolas (+0.02 ± 0.05‰), and within analytical uncertainty of the Tanner Basin (+0.06 ± 0.04‰). The isotopic compositions of the Mexican margin sites are similar to the Borderland Basins, with average δ^{114}Cd values of +0.07 ± 0.03‰ at both the Magdalena margin and Soledad Basin, and 0.00 ± 0.06‰ at the Pescadero slope. With the exception of Santa Monica, there are no analytically significant differences or discernible trends in δ^{114}Cd values with sediment depth. Santa Monica has a higher δ^{114}Cd value (+0.08‰) at the surface and lower values, to a minimum of −0.19‰, at depth. Excluding the surface-most sample, Santa Monica has the lowest average downcore $\delta^{114}Cd_{>1.5cm}$ value of −0.11 ± 0.07‰.

Porewater Data

Porewater data and references for previously published sites are presented in **Figure 3** and **Supplementary Table 2**. Data for previously unpublished sites, Santa Barbara and San Nicolas Basin will be briefly described here. Santa Barbara exhibits Fe-rich porewaters at the surface and reaches a peak of 185.2 μM in the top 2 cm of the sediment core. Dissolved Fe concentrations then decrease rapidly reaching ~30 μM at 10 cm depth. Ammonia porewater concentrations steadily increase from 46 to 230 μM with depth, however there is a peak of 220 μM at a depth of 5.5 cm. San Nicolas has Fe–Mn rich porewaters and a porewater profile is presented in **Figure 3C**. Surface dissolved Mn and Fe concentrations increase rapidly from near zero at the surface to a peak of 134.6 and ~12 μM in the top 5 cm. Dissolved ammonia steadily increases from ~0 μM at the surface to a maximum ~70 μM at a depth of 20 cm. Sulphide porewater concentrations were below detection in both cores.

DISCUSSION

Minor Lithogenic Cd in Organic-Rich Sediments

The lithogenic Cd (Cd_{lith}) and bioauthigenic Cd concentrations (Cd_{auth}) can be estimated by using sample Al concentrations (Al_{bulk}) as a proxy for the detrital alumino-silicate fraction, as follows:

$$Cd_{lith} = Cd/Al_{UCC} \times Al_{bulk} \quad (2)$$

$$Cd_{auth} = Cd_{bulk} - Cd_{lith} \quad (3)$$

Assuming a lithogenic endmember similar to upper continental crust (UCC), with $Cd/Al_{UCC} = 0.011 \times 10^{-4}$ (Rudnick and Gao, 2003), lithogenic Cd accounts for a maximum of 10% of the total sample Cd in our samples (**Supplementary Table 1**). We can then correct bulk δ^{114}Cd values ($\delta^{114}Cd_{bulk}$) for this lithogenic contribution by assuming a $\delta^{114}Cd_{lith}$ value of ~0‰ (Schmitt et al., 2009; Lambelet et al., 2013), as follows:

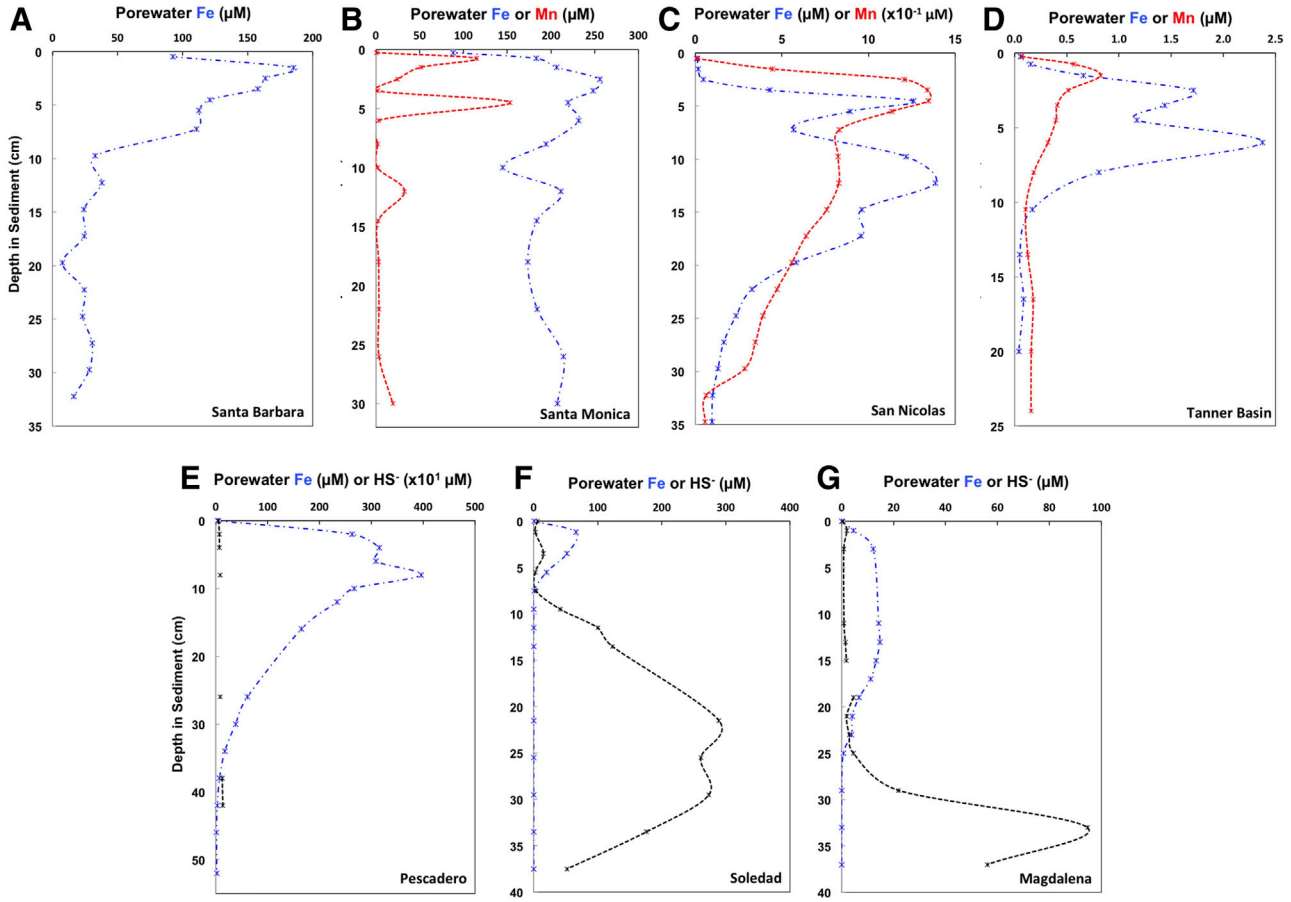

FIGURE 3 | Porewater Fe (blue dash-dot lines), Mn (red dashed lines) and HS^- (black dashed lines) concentrations for seven sites from the two continental margin locations, the California Borderland Basins (**A**–Santa Barbara, **B**–Santa Monica, **C**—San Nicolas, **D**—Tanner Basin) and the Mexican margin (**E**—Soledad Basin, **F**—Pescadero slope, **G**–Magdalena margin). Values and references are shown in **Supplementary Table 2**.

$$\delta^{114}Cd_{auth} = \left(\delta^{114}Cd_{bulk} \times Cd_{bulk} - \delta^{114}Cd_{lith} \times Cd_{Lith}\right)/Cd_{auth} \quad (4)$$

n doing so, all calculated $\delta^{114}Cd_{auth}$ values (i.e., bioauthigenic Cd isotope compositions) are identical to or within analytical uncertainty of $\delta^{114}Cd_{bulk}$ values (**Supplementary Table 1**). Thus, we conclude that the influence of lithogenic Cd on our measured Cd isotope compositions is negligible, and bulk sedimentary $\delta^{114}Cd$ values are considered to represent the bioauthigenic Cd isotope composition (as reported in **Table 2**).

The key finding of this study is that bioauthigenic Cd in organic-rich continental margin sediments has a light isotopic composition, of 0 to +0.1‰, compared to global deep seawater, at about +0.3‰ (**Figure 2**; **Table 2**). Though we lack dissolved phase Cd isotope compositions for the local overlying water column at each site, deep water below the sill depth in the San Pedro Basin, which is an adjacent basin to Santa Monica, has an isotopic composition of +0.3‰, similar to the global deep water average of about +0.3‰ (Conway and John, 2015b); we assume that the deep water Cd isotope composition at our sites is similar.

The observed light Cd isotope composition of organic-rich sediments could reflect either (a) isotope fractionation during diagenesis or (b) an isotopically light particulate source of bioauthigenic Cd.

Limited Cd Isotope Fractionation During Diagenesis in Continental Margin Settings

During oxic diagenesis, it is well-documented that Cd is released to porewaters during remineralization of organic matter (e.g., Klinkhammer et al., 1982; Gobeil et al., 1987; McCorkle and Klinkhammer, 1991; Audry et al., 2006). In suboxic settings, where porewaters contain negligible dissolved oxygen and sulphide, near surface porewater Cd maxima are followed by strong depletion to low Cd concentrations (~0.1 nM) below, reflecting Cd release from organic matter followed by its near quantitative removal to an insoluble authigenic phase (Gobeil et al., 1987; McCorkle and Klinkhammer, 1991). Solid phase authigenic Cd enrichment is subsequently observed at the oxic/suboxic boundary (Rosenthal et al., 1995). Precipitation of authigenic CdS has been invoked to explain the observed Cd

removal in suboxic settings; due to its low sulphide solubility, Cd has a strong tendency to form insoluble sulphides in the presence of trace H_2S (e.g., Elderfield et al., 1981; Westerlund et al., 1986; Jacobs et al., 1987; Rosenthal et al., 1995; Morse and Luther, 1999).

In the anoxic and sulphidic porewaters of Narragansett Bay, Elderfield et al. (1981) found no detectable Cd (<0.5 nM), and also argued for precipitation of CdS (Elderfield, 1981; Elderfield et al., 1981). However, elevated porewater Cd (up to 2 nM) have been observed in strongly sulphidic porewaters of the Peru margin (up to several hundred μM H_2S; Plass et al., 2020). Similarly, porewater Cd concentrations in sediments from the Laurentian Trough decreased to near zero in the suboxic zone, but increased again at depth in the anoxic zone (Gobeil et al., 1987). These observations suggest redissolution of authigenic CdS phases in highly sulphidic environments through the formation of bisulphide or polysulphide complexes (Gobeil et al., 1987; Plass et al., 2020).

In the absence of porewater Cd concentration data, we cannot conclusively evaluate the depth and degree of Cd removal to the solid phase. We note, however, that only one site (Soledad Basin) is strongly sulphidic at depths that overlap those of our sampling (**Figures 2**, **3**), with resultant possible remobilization of CdS as bisulphide or polysulphide complexes. We also observe only muted variations in solid phase δ^{114}Cd and Cd concentrations with depth at all sites, including the Soledad Basin. Further studies coupling porewater and solid phase Cd isotope analysis are required to fully investigate the potential for Cd isotope fractionation during diagenesis. However, our dataset suggests very limited fractionation in reducing continental margin settings, with sedimentary isotopic compositions instead reflecting those of the Cd source(s).

Sources of Isotopically Light Bioauthigenic Cd

In the likely absence of diagenetic isotope fractionation, the relatively light Cd isotope composition of continental margin sediments must reflect an isotopically light water column source (or sources). We consider the following possible sources of bioauthigenic Cd to continental margin sediments: (1) organic matter (Elderfield et al., 1981; Rosenthal et al., 1995; Little et al., 2015), (2) CdS particulates (e.g., Janssen et al., 2014; Conway and John, 2015a; Bianchi et al., 2018; Xie et al., 2019a; Plass et al., 2020), and (3) Fe–oxyhydroxides (Klevenz et al., 2011; Conway and John, 2015a; Lee et al., 2018).

Organic Matter

Phytoplankton take up Cd in culture, and they take up more Cd when it is present at higher concentrations in the media (e.g. Sunda and Huntsman, 1998; Sunda and Huntsman, 2000). Increased uptake of Cd also occurs when stressed by low levels of other bioactive metals like Fe and Zn (Sunda and Huntsman, 2000; Cullen et al., 2003; Xu et al., 2007). Therefore, organic matter is likely to be an important vector transporting Cd to sediments, an assertion that is supported by the positive correlation observed between organic C and Cd/Al ratios in the sediments from this study (**Figure 4A**).

Plass et al. (2020) estimate the proportion of Cd delivered to sediment by organic matter for sites above, within and below the Peruvian ODZ by multiplying organic carbon accumulation rates by the Cd:C ratio in 'average' phytoplankton (i.e., Cd:P ratio of 0.21 mmol/mol, converted to Cd:C assuming a Redfield C:P ratio of 124:1; Ho et al., 2003; Moore et al., 2013). However, cellular Cd quotas vary widely, with Cd:P ratios in bulk particles from open and coastal ocean sites ranging from 0.04 to 2.3 mmol/mol (Martin and Knauer, 1973; Martin et al., 1976; Collier and Edmond, 1984; Kuss and Kremling, 1999; Ohnemus et al., 2016; Bourne et al., 2018; Lee et al., 2018; Black et al., 2019).

Bourne et al. (2018) present the most comprehensive dataset of directly measured particulate Cd:P ratios to date. They find distinct biogeographic and seasonal differences, and higher ratios in HNLC (high nutrient low chlorophyll) zones compared to oligotrophic gyres (Bourne et al., 2018). Although the sites in this study are not open ocean HNLC regions, they are locations of coastal upwelling in the northeast Pacific, and may therefore be expected to exhibit higher than 'average' euphotic zone phytoplankton Cd:P ratios (i.e., 0.21 mmol/mol; Ho et al., 2003). The only water column Cd:P data (dissolved or particulate, to our knowledge) from any one of our study sites supports this prediction: the mean euphotic zone particulate Cd:P ratio from the Santa Barbara Basin is 0.67 mmol/mol (1.13 mmol/mol in the <51 μm size fraction, 0.26 mmol/mol in the >51 μm size fraction; Bourne et al., 2018). Elevated Cd:P at this site is consistent with the high particulate Cd:P measured in the eastern tropical south Pacific (Peru margin) and other HNLC regions (0.49 ± 0.23; Bourne et al., 2018). Therefore, we estimate the proportion of Cd delivered by organic matter to sediments at our sites for a range of Cd:P ratios of 0.21–0.67 mmol/mol (**Table 3**; **Figure 4B**). The lower end of this range (i.e., average phytoplankton; Ho et al., 2003) predicts that organic matter can account for ~50% or more of the Cd at all sites, and for 100% of the Cd in the San Nicolas and Tanner basins, while the upper end of the range allows that all of the Cd at all sites can be delivered by organic matter. In summary, organic matter is likely the primary vector transporting Cd to the sediment in margin settings. But is this Cd isotopically light?

In culture, phytoplankton preferentially take up light Cd, with calculated $\Delta^{114}Cd_{biomass\text{-}medium}$ = −0.3 to −1.3‰ (where $\Delta^{114}Cd_{biomass\text{-}medium} = \delta^{114}Cd_{biomass} - \delta^{114}Cd_{medium}$) (Lacan et al., 2006; Gault-Ringold, 2011; Horner et al., 2013; John and Conway, 2014). Biological uptake of isotopically light Cd is consistent with observations of isotopically heavy surface seawater (e.g., Lacan et al., 2006; Ripperger et al., 2007; Conway and John, 2015a; 2015b) and studies of suspended particulate matter from the surface ocean, which have also found particulate Cd isotope compositions that are generally isotopically lighter than the contemporaneous dissolved phase (Yang et al., 2015, 2018; Janssen et al., 2019). However, particulate δ^{114}Cd ($p\delta^{114}$Cd) values in the surface ocean vary widely in different locations (Yang et al., 2015, 2018; Janssen et al., 2019). The northwest Pacific and the South China Sea exhibit a large range of measured $p\delta^{114}$Cd from −1.5 to +0.5‰ (>0.2 μm size fraction) and −0.9 to +0.7‰ (10 to >150 μm) respectively. Meanwhile, in the Northeast Pacific, small size fraction (0.8–51 μm) particulates from the euphotic zone are more comparable to deep-water dissolved δ^{114}Cd values, in the range +0.34 to +0.54‰ (Jansssen et al., 2019).

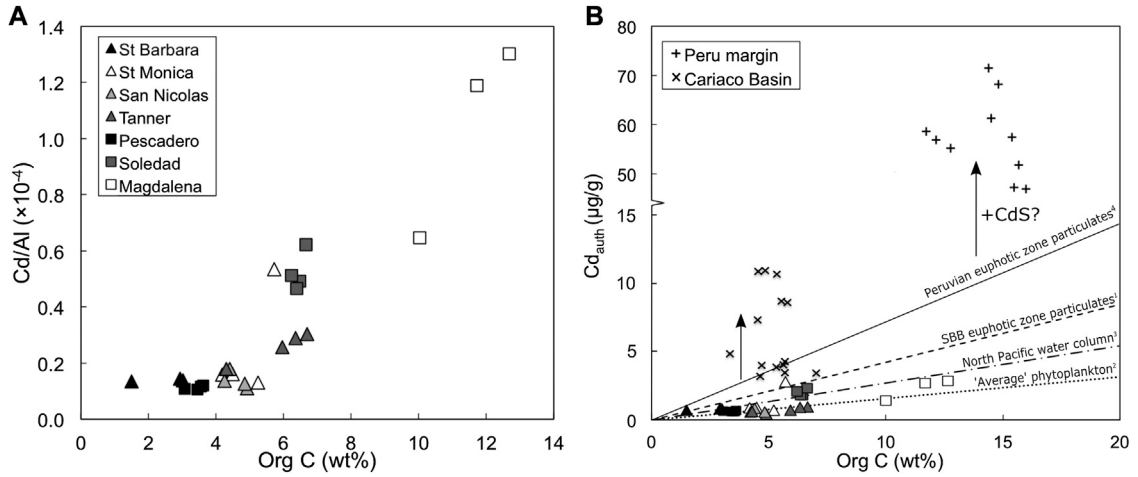

FIGURE 4 | (A) Positive covariation of sedimentary Cd/Al with organic carbon concentrations. **(B)** Bioauthigenic Cd_{auth} concentrations (**Eq. 3**) versus organic carbon concentrations for sediment samples in this study (triangles and squares) to sediments from the Peruvian ODZ (+) and the euxinic Cariaco Basin (x) (data: Little et al., 2015). For comparison, the dashed line gives the average Cd:C ratio from euphotic zone particles in the Santa Barbara Basin (1: Bourne et al., 2018), the dotted line shows Cd:C ratio in 'average' phytoplankton (2: Ho et al., 2003), the dot-dashed line shows the Cd:C ratio estimated for the North Pacific from an analysis of dissolved Cd and P concentration data (3: Quay et al., 2015), and the solid line shows the Cd:C ratio in euphotic zone particles from the Peru margin (4: 7.66×10^{-6}; Bourne et al., 2018). Schematic vertical black arrows represent the proposed impact of CdS precipitation on sedimentary Cd_{auth} concentrations.

TABLE 3 | Calculated authigenic Cd (**Eq. 3**) and organic C mass accumulation rates, and estimated delivery of sedimentary Cd supplied by organic matter.

Site	Cd_{auth} (µg/g)	Cd_{auth} Mass accumulation rate[a] (µmol/m^2/yr)	Organic C accumulation rate[a] (mol/m^2/yr)	Range of Cd from organic matter[b] (µmol/m^2/yr)
Santa Barbara Basin	0.81	6.63	1.9	3.21–10.3
Santa Monica Basin	0.86	1.94	0.65	1.11–3.54
San Nicolas Basin	0.64	0.79	0.54	0.91–2.90
Tanner Basin	0.81	0.87	0.58	0.99–3.15
Pescadero slope	0.66	4.49	2.2	3.71–11.9
Soledad Basin	2.03	12.7	3.8	6.34–20.3
Magdalena margin	2.35	1.67	0.76	1.29–4.13

[a]*Calculated by multiplying mass accumulation rate shown in* ***Table 1*** *by Cd or Organic C concentration (****Table 2****).*
[b]*Calculated by multiplying organic C accumulation rate by molar Cd:C ratio of* 1.69×10^{-6} *(min) and* 5.4×10^{-6} *(max) from Ho et al. (2003) and Bourne et al. (2018).*

Sinking particles (>0.45 mm) from the South China Sea are isotopically heavier than suspended particles, at +0.8 to +2.8‰, and increase with increasing water depth (30–160 m; Yang et al., 2015). However, $p\delta^{114}Cd$ values were not measured at water depths >160 m, and it is uncertain whether these elevated sinking $p\delta^{114}Cd$ values are preserved deeper in the water column. Nevertheless, the authors hypothesize that the processes of microbial degradation/zooplankton repackaging preferentially decompose isotopically light Cd. In contrast, in the northeast Pacific, small size fraction (0.8–51 µm) $p\delta^{114}Cd$ values become more negative with depth (from 150 to 800 m), reaching a minimum of -0.5‰ (Janssen et al., 2019). In this case, the authors attribute the generation of a light signature either to isotope fractionation during remineralization of organic matter (but with the opposite sense to that proposed by Yang et al., 2015, i.e., preferential release of isotopically heavy Cd), or to the presence of multiple particulate Cd phases with variable remineralization labilities (Janssen et al., 2019). It is possible that the light Cd isotope composition of these small size fraction particles is counterbalanced by an isotopically heavy Cd pool in large sinking particles, as observed in the South China Sea (Yang et al., 2015). Large size fraction particles were not analyzed in the northeast Pacific to test this hypothesis. Indeed, though the northeast Pacific small size fraction particles are isotopically lighter than the margin sediments reported herein – suggesting that they may contribute light Cd to the sediment – fast sinking, >50 µm particles are thought to be predominant in terms of mass flux to sediment (e.g., Clegg and Whitfield, 1990).

We conclude that organic matter is certainly a significant source of Cd to margin sediments, and may very well be isotopically light. However, further research is required to (a) better constrain the Cd isotope composition of diverse particulate

phases in the water column and (b) determine the extent to which the Cd isotope composition of organic-rich particles exported from the photic zone is preserved in sediments.

Cadmium Sulphide Precipitation

As discussed above, CdS phases sequester Cd in anoxic and suboxic sediments (e.g., Elderfield et al., 1981; Rosenthal et al., 1995) and precipitate within the water column of euxinic basins (e.g., Jacobs et al., 1985; Tankéré et al., 2001). It has also been hypothesized that CdS precipitation may occur in the open ocean, either in ODZs in reducing microenvironments within decomposing organic matter (Janssen et al., 2014; Conway and John, 2015a; Bianchi et al., 2018) and/or in bottom waters near the sediment-water interface along reducing continental margins (Xie et al., 2019b; Plass et al., 2020). This hitherto unrecognized water column sulphide sink of Cd may be an important flux in the global oceanic Cd budget (e.g., Janssen et al., 2014; Guinoiseau et al., 2019).

Mass balance calculations show evidence for an additional source of particulate Cd to sediments (beyond that supplied by organic matter) for the functionally anoxic Peru margin (Little et al., 2015; Plass et al., 2020) and the modern euxinic Cariaco Basin, where euxinic refers to the presence of free sulphide in the bottom water (Little et al., 2015). Indeed, dissolved Cd is quantitatively removed below the redoxcline in the Cariaco Basin (Jacobs et al., 1987). Authigenic Cd concentrations in Cariaco Basin and Peru margin sediments are significantly elevated above what is likely to be supplied by organic matter (**Figure 4B**). This enrichment is consistent with supply via CdS precipitation, and can be observed as a pseudo-vertical trend in organic C versus Cd_{auth} space (arrows, **Figure 4B**). Of the sites investigated in this study, the Soledad Basin and the Magdalena margin are the most reducing, with sulphidic porewaters (Chong et al., 2012), and these two sites are also the most enriched in Cd (**Figure 4**). Sediment samples from the Soledad Basin also show a near-vertical trend in organic C versus Cd_{auth} space (**Figure 4B**), albeit at much lower levels of overall Cd enrichment than, for example, the Peru margin (**Figure 4B**). It is therefore plausible that a small part of the Cd budget in the Soledad Basin and Magdalena margin sediments was supplied by CdS precipitation, if we assume a Cd:C ratio similar to average phytoplankton (**Table 2**; Ho et al., 2003).

Cadmium isotopes may facilitate the identification of a CdS source, because non-quantitative CdS precipitation is accompanied by light Cd isotope fractionation. In experiments, Guinoiseau et al. (2018) observed an isotope fractionation factor for CdS precipitation of $\Delta^{114}Cd_{CdS\text{-}medium} \approx -0.3‰$ (Guinoiseau et al., 2018), consistent with the light isotope composition of hydrothermal CdS precipitates (Schmitt et al., 2009). Dissolved Cd in the Mauritanian ODZ and the Angola Basin is depleted relative to P and is isotopically heavy (up to 1.3‰; Janssen et al., 2014; Conway and John, 2015a; Guinoiseau et al., 2019), supporting the hypothesized precipitation of CdS within degrading organic matter in ODZs. Furthermore, the complementary particulate Cd pool from the Mauritanian ODZ is enriched relative to phosphate and is isotopically light (−0.01 to +0.35‰; Janssen et al., 2014)

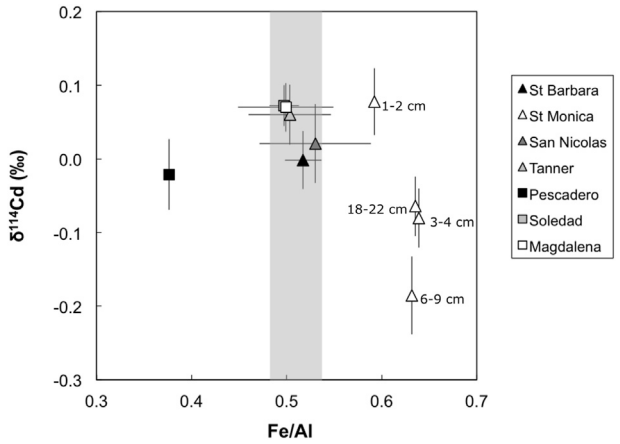

FIGURE 5 | Site-averaged bulk sediment Fe/Al vs. $\delta^{114}Cd$ values, except for Santa Monica where all data points are shown (white triangles). Shaded gray bar represents the Fe/Al ratio of the upper continental crust (UCC; Rudnick and Gao, 2003). Note that Fe/Al ratios are enriched at Santa Monica (and depleted at the Pescadero slope) compared to UCC. Error bars for site average are 1 standard deviation of the entire sediment column and error bars for Santa Monica are external 2 SD on sample replicates or of a secondary standard (BAM, ± 0.05‰), or the internal 2σ on an individual Cd isotope ratio measurement, whichever is larger.

compared to average deep seawater. However, such evidence for CdS precipitation is not observed in all ODZs, including the North Pacific ODZ (Conway and John, 2015b; Janssen et al., 2017) and the open Peru margin ODZ (John et al., 2018; Xie et al., 2019b). The extent to which CdS precipitation occurs in ODZs, and the longevity of these particles as they sink through the water column to the sediment remain topics of ongoing research (Guinoiseau et al., 2019; de Souza et al., in review).

While organic-matter associated CdS precipitation in ODZs and potential burial in sediments remains a topic of contention, CdS precipitation in bottom waters overlying sulphidic continental margin sediments is supported by *in situ* benthic chamber incubations and water column Cd isotope analyses (Xie et al., 2019b; Plass et al., 2020). At sites within the Peruvian ODZ, Plass et al. (2020) report *in-situ* benthic chamber Cd fluxes into the sediment 25–40 times higher than calculated diffusive fluxes of dissolved Cd into the sediments (Plass et al., 2020). The authors suggest that leakage of trace H_2S into bottom waters from sediment porewaters leads to near seafloor CdS precipitation, thus explaining their observed high sedimentary Cd fluxes (Plass et al., 2020). We emphasize that this mechanism is distinct from the organic matter associated-CdS precipitation in the water column (e.g., Janssen et al., 2014; Bianchi et al., 2018). Consistent with near-seafloor CdS precipitation, Xie et al. (2019b) report strong dissolved Cd depletion and Cd isotope fractionation (dissolved $\delta^{114}Cd$ up to +1.30‰) associated with a sulphidic plume that covered much of the Peruvian continental shelf during January 2009 (Schunck et al., 2013). Their data suggest an isotope effect on CdS precipitation of $\Delta^{114}Cd_{CdS\text{-}seawater} = -0.29‰$,

comparable to the experimental estimate of Guinoiseau et al. (2018).

Iron Oxyhydroxides

The Santa Monica Basin samples have variable and generally lower δ^{114}Cd values (+0.08 to –0.19‰) compared to the other sites (**Figure 2**), although only the sample from 6 – 9 cm depth is analytically distinct (–0.19‰). Compared to the other sites Santa Monica Basin sediments have elevated solid phase Fe/Al ratios, which may be linked to the observed low δ^{114}Cd values (**Figure 5**). Iron enrichment in this setting is likely to originate from a form of open-marine Fe 'shuttle' (e.g., Scholz et al., 2014), whereby dissolved Fe (II) is released from reducing shelf sediments and then reprecipitated as Fe (III) oxyhydroxides coupled to microbial nitrate reduction in the ODZ (Scholz et al., 2016; Heller et al., 2017). Though Santa Monica porewaters are strongly ferruginous (McManus et al., 1997; 1998)—a diagenetic regime that would typically be reflected as a *source* of Fe(II) to the water column rather than a sink—solid phase Fe enrichment presumably reflects the basinal geography (e.g., Severmann et al., 2010), which traps Fe supplied to the deep basin via the redox shuttle. Given that there is evidence of deep sulphate reduction in porewaters, the absence of porewater sulphide in the upper sediment package is consistent with its rapid titration by the high concentrations of Fe (McManus et al., 1997; 1998). We note that sediments from the Pescadero slope, which also has strongly ferruginous porewaters (Chong et al., 2012), exhibits solid-phase Fe depletion (**Figure 5**), consistent with a benthic flux of Fe(II) into bottom waters in this unrestricted hydrographic setting.

Scavenging of Cd by Fe oxyhydroxides has been hypothesized previously; for example, it has been suggested that particulate Cd enrichment in the lower Peru margin ODZ is associated with Fe-oxyhydroxide phases (Lee et al., 2018). Such scavenging of Cd by Fe oxyhydroxides may enhance the supply of isotopically light Cd to the Santa Monica Basin.

To our knowledge, there has been no experimental work investigating Cd isotope fractionation during sorption to Fe oxyhydroxides, although it has been suggested that Fe oxyhydroxides may scavenge Cd as a CdS phase (Klevenz et al., 2011; Conway and John, 2015a), which, as discussed, would likely be isotopically light. Experimental sorption of Cd on Mn-oxides initially shows preference for light isotopes, though the magnitude of fractionation ($\Delta^{114}Cd_{MnO2\text{-}aqueous} = \delta^{114}Cd_{MnO2} - \delta^{114}Cd_{aqueous}$) declines from –0.8 to –0.2‰ over time (Wasylenki et al., 2014). In natural settings, Fe-Mn crusts record the Cd isotope composition of ambient seawater without fractionation (Schmitt et al., 2009; Horner et al., 2010). A thorough evaluation of the potential for an Fe redox shuttle influence on the Cd isotope composition of sediments awaits future studies investigating Cd isotope fractionation on sorption to Fe-oxyhydroxide phase, and data from other ferruginous sites like the Santa Monica Basin.

Implications for Cd Oceanic Mass Balance

The sedimentary Cd concentration and δ^{114}Cd data in this study allow us to place new constraints on the outputs of Cd from the ocean and evaluate a recent estimate of the Cd sink driven by water column sulphide formation in the global oceanic Cd budget. Previous estimates of the major input and output fluxes are presented in **Table 4**, along with new estimates from this study.

The main Cd source to the oceans is the dissolved riverine flux, estimated at 0.4–2.7 × 10^7 mol/yr (van Geen et al., 1995; Gaillardet et al., 2003). The best estimate given in **Table 4** is the higher value from Gaillardet et al. (2003), because this study considers a larger compilation of rivers. Estimates of the natural mineral dust flux by van Geen et al. (1995) were made by reducing the total estimated aerosol flux by a factor of 10 to take the increase in anthropogenic emissions into account (Nriagu, 1980). The best estimate for the natural dust flux is thus 0.3 × 10^7 mol/yr (**Table 4**). The best guess isotopic compositions of the mineral dust and dissolved riverine sources of Cd are 0.0‰ and +0.2 ± 0.1‰ respectively (Lambelet et al., 2013; Bridgestock et al., 2017). We note that this riverine isotopic composition is based on a single study reporting the Cd isotope composition of samples spanning the salinity gradient on the Siberian Shelf, and thus represents an average δ^{114}Cd value of the discharge of four Siberian rivers only.

We estimate the flux of Cd to continental margins delivered in association with organic matter by multiplying the estimated global organic carbon deposition on continental margins, of 15.6 × 10^{12} mol/yr (Jahnke, 2010), with a range of estimated Cd:C ratios in phytoplankton (discussed in "**Organic Matter**" section). For Cd:C ratios ranging from 'average phytoplankton', at 1.69 × 10^{-6} (Ho et al., 2003), to that of Peruvian euphotic zone particulates, at 7.66 × 10^{-6} (Bourne et al., 2018), we calculate an organic matter associated Cd flux to continental margin sediments of 2.6–12.0 × 10^7 mol/yr. The minimum end of this range likely underestimates the Cd flux in upwelling regions, while the maximum estimate is probably too high, because such high Cd:C ratios are not observed on a global scale (section "**Organic Matter**"; Quay et al., 2015; Bourne et al., 2018). Instead, we suggest the export-flux-weighted phytoplankton Cd:C ratio (i.e., the average Cd:C ratio of organic matter that is exported from the photic zone globally) is likely to be close to the average upwelling (HNLC) Cd:C ratio of 3.95 × 10^{-6} (or a Cd:P ratio of 0.49 mmol/mol; Bourne et al., 2018). This is because upwelling regions have high sinking particulate fluxes. Hence, we make a best estimate for global organic matter associated Cd flux of 6.2 × 10^7 mol/yr.

We suggest that CdS precipitation is likely a rather minor contributor to sedimentary Cd fluxes globally, albeit locally significant (e.g., in the core of the Peruvian ODZ; Little et al., 2015; Plass et al., 2020). This conclusion contrasts with a recent estimation of the global water column CdS sink, at 0.87–104 × 10^7 mol/yr (Guinoseau et al., 2019), based on the optimized particle cycling model of Bianchi et al. (2018). The large range derived by these authors is due to the uncertainty in the dissolution rate of CdS particles in seawater. The maximum estimate is two orders of magnitude greater than the total known inputs to the ocean, and eight times our maximum estimated continental margin sink (12.0 × 10^7 mol/yr; **Table 4**). Thus, we conclude that the global Cd sink resulting from water-column CdS formation is likely to be

TABLE 4 | Oceanic Mass Balance of Cd from published data and data presented in this study.

	Mass ocean (kg)	**Mass Cd (mol)**			**References**
Global oceans	1.3521×10^{21}	8.36×10^{11}			1
Input fluxes	**Cd flux range ($\times 10^7$ mol/yr)**	**Cd flux best estimate ($\times 10^7$ mol/yr)**	**δ^{114}Cd range (‰)**	**δ^{114}Cd best estimate (‰)**	**References**
Rivers	0.4–2.7	2.7	+0.1 – +0.3	+0.2	2
Dust	0.2–0.4	0.3	−0.2 – +0.2	0.0	2
Hydrothermal	(0.2–2.6)	n			3
Total	0.6–3.8	3.0	+0.0 – +0.3	+0.2	
Output fluxes	**Cd flux range ($\times 10^7$ mol/yr)**	**Cd flux best estimate ($\times 10^7$ mol/yr)**	**δ^{114}Cd range (‰)**	**δ^{114}Cd best estimate (‰)**	**References**
Oxic sediments	n	n	+0.3 – +0.4	+0.3	4
Continental margins[a]	**2.6–12.0**	**6.2**	**−0.2 – +0.1**	**0.0**	**5**
Euxinic	n	n			6
Hydrothermal	(0.2–2.6)				3
Total sink	**2.6–12.0**	**6.2**	**−0.2 – +0.1**	**0.0**	
Residence time (kyrs)	**7–32** 13.5				

Values in parentheses are assumed to be removed quantitatively close to the source and therefore not included in the total mass balance. Values in bold are data presented from this study.
[a]*Continental margins include suboxic and anoxic conditions and basin settings.*
n—negligible.
References: 1. Baumgartner and Reichel (1975); Chester and Jickells (2012) 2. van Geen et al. (1995); Gaillardet et al. (2003); Lambelet et al. (2013); Bridgestock et al. (2017); 3. Von Damm et al., 1985; 4. Schmitt et al. (2009); Horner et al. (2010); 5. van Geen et al. (1995); Morford and Emerson (1999); Little et al. (2015); This study. 6. Little et al. (2015).

at the lower end of the model-based estimate of Guinoseau et al. (2019).

The concentration-weighted average δ^{114}Cd of the organic-rich sediments analyzed in this study is +0.04‰. This value is similar to the estimated Cd isotope compositions of the mineral dust and riverine input fluxes (~0 and ~0.2‰ respectively) (Lambelet et al., 2013; Bridgestock et al., 2017), suggesting that the isotope compositions of the Cd input and output fluxes are approximately balanced. However, our current best estimate of the Cd output flux to sediments is two times larger than the known input fluxes.

To account for this mass imbalance, either the known inputs are underestimated or there remain unrecognized sources of Cd to the ocean. One possible additional input of Cd to the oceans is partial mobilization from riverine particulates in estuaries (as recently suggested for several trace elements: e.g., Jones et al., 2014; Little et al., 2017). Several studies indicate that Cd can behave non-conservatively in estuarine systems (e.g., Elbaz-Poulichet et al., 1987; Comans and Vandijk, 1988; Elbaz-Poulichet et al., 1996; Waeles et al., 2004; Waeles et al., 2005; Lambelet et al., 2013). The mixing of freshwater and saltwater alters the speciation of Cd through the formation of soluble chloro complexes, which can drive the dissolution of particulate Cd (e.g., Elbaz-Poulichet et al., 1987). Particulate riverine Cd fluxes, estimated at 2.05×10^8 mol/yr, are an order of magnitude higher than dissolved fluxes (Gaillardet et al., 2003). Therefore, partial dissolution of riverine particulates, likely with a lithogenic Cd isotope composition (~0‰), could account for the existing flux imbalance.

Conclusion and Outlook for Cd Isotopes as a Proxy

It has been suggested that Cd isotopes may be a useful tracer of past ocean productivity (e.g., Georgiev et al., 2015). Conceptually, an isotopic tracer of productivity (or, more accurately, of nutrient utilization) requires three ingredients:

(1) Isotopic fractionation on biological uptake, which is quantifiable and consistent, e.g., through culturing studies (e.g., Lacan et al., 2006).
(2) Translation of this biological uptake-driven isotope fractionation into observations in the 'real world', i.e., the degree of surface ocean isotopic fractionation should be proportional to the extent of Cd removal into particles (e.g., Ripperger et al., 2007).
(3) Sedimentary archive(s) of either (a) the residual, fractionated surface ocean (e.g., carbonates; Hohl et al., 2017) and/or (b) the cumulative solid phase, i.e., organic matter (e.g., Georgiev et al., 2015). In addition, an archive of the contemporaneous nutrient 'source' (often assumed to be the deep ocean) is required to make quantitative estimates of nutrient utilization (e.g., Fe-Mn crusts; Schmitt et al., 2009; Horner et al., 2010).

In this study, we consider the question: do organic-rich sediments record the isotopic composition of the organic matter exported from the surface ocean? We find that, in sites without the build-up of HS^- in porewaters close to the sediment-water interface, organic matter is the primary source of Cd to margin sediments. In addition, bioauthigenic Cd in organic-rich sediments is isotopically light, consistent with preferential uptake of light isotopes by primary producers. These two first-order findings suggest that Cd isotope compositions in organic-rich sediments do hold promise as a tracer of nutrient utilisation.

However, there are several caveats to this simple interpretation of Cd and Cd isotopes in organic-rich sediments. First, we find that water column CdS precipitation provides a second possible isotopically light source of Cd to sediments, which in the most reducing settings may account for a significant fraction of the Cd budget (e.g., Plass et al., 2020). Scavenging by Fe oxyhydroxides may provide a third isotopically light flux of Cd to sediments. There is no straightforward means to differentiate isotopically light Cd sourced from organic matter and that from water column CdS precipitation (or scavenged by Fe oxyhydroxides).

Second, it is classically assumed that biological uptake in the surface ocean follows a closed-system Rayleigh fractionation model. This model describes Cd isotope systematics quite well in nutrient-rich regions (e.g., Abouchami et al., 2011; Xue et al., 2013; Abouchami et al., 2014; Janssen et al., 2017; Yang et al., 2018), but not in Cd-poor regions, with explanations for non-Rayleigh behavior including open system steady-state, buffering by organic ligands, external Cd sources, or species-specific Cd isotope fractionation factors (Gault-Ringold et al., 2012; Xie et al., 2017; 2019a; Janssen et al., 2017; George et al., 2019; Sieber et al., 2019a; 2019b). This complexity in the dissolved phase is matched by the variable particulate Cd isotope compositions measured to date, which also preclude straightforward interpretation (**Organic matter**; Janssen et al., 2014; 2019; Yang et al., 2015; 2018).

Third, our studied sites have substantially different organic carbon burial rates (**Table 1**) yet similar Cd isotope compositions, suggesting that sedimentary δ^{114}Cd values may not correlate directly with overlying productivity. Only a tiny fraction (<1%) of the organic matter produced in the surface ocean is ultimately preserved in continental margin sediments (e.g., Hedges and Keil, 1995) and the links between export production and sedimentary metal concentrations and isotopic compositions remains an area of active research. Remineralization, for example, is suggested to preferentially release heavy Cd in the modern northeast Pacific, providing another pathway to the generation of isotopically light Cd in sediments (Janssen et al., 2019). We note that the opposite sense of fractionation on remineralization (i.e., preferential release of light Cd) has been proposed based on particulate Cd isotope compositions from the South China Sea (Yang et al., 2015).

To conclude, the degree to which δ^{114}Cd values in underlying organic-rich sediments truly reflect surface ocean nutrient utilization remains uncertain, due to the complex processes that govern Cd isotope fractionation in the water column and the possibility of a water column CdS flux. A recent study of Cd isotope compositions in organic-rich sediments spanning from the Upper Cretaceous (including Oceanic Anoxic Event 2) places similar emphasis on the role of local redox rather than productivity changes in controlling the range of observed sedimentary δ^{114}Cd values (Sweere et al., 2020). In agreement with that study, we recommend that researchers exercise considerable caution if interpreting Cd isotope compositions in ancient organic-rich sediments as solely reflecting changes in past ocean productivity.

DATA AVAILABILITY STATEMENT

The original contributions presented in the study are included in the article/**Supplementary material**, further inquiries can be directed to the corresponding author.

AUTHOR CONTRIBUTIONS

JM and SS collected sediment and porewater samples, and also conducted element porewater analyses. LC, KK and SHL prepared the samples for isotopic analysis and conducted isotopic measurements. LC and SHL wrote the manuscript with inputs from all authors.

FUNDING

SHL acknowledges financial support from the Natural Environment Research Council (NE/P018181/2). JM's contributions were supported by NSF grants OCE-0219651 and OCE-1657832. SS's contributions were supported by NSF grant OC-1657832

ACKNOWLEDGMENTS

We would like to thank two reviewers and the editor Susann Henkel for comments that significantly improved the manuscript. We thank the MAGIC group at Imperial College London for the support and smooth running of the laboratories. We are also grateful for several helpful discussions with Tristan Horner during the project and would also like to thank Gregory de Souza for feedback on an earlier version of the manuscript.

SUPPLEMENTARY MATERIAL

The supplementary Material for this article can be found online at: https://www.frontiersin.org/articles/10.3389/feart.2021.623720/full#supplementary-material.

REFERENCES

Abouchami, W., Galer, S. J. G., de Baar, H. J. W., Alderkamp, A. C., Middag, R., Laan, P., et al. (2011). Modulation of the Southern Ocean cadmium isotope signature by ocean circulation and primary productivity. *Earth Planet. Sci. Lett.* 305, 83–91. doi:10.1016/j.epsl.2011.02.044

Abouchami, W., Galer, S. J. G., de Baar, H. J. W., Middag, R., Vance, D., Zhao, Y., et al. (2014). Biogeochemical cycling of cadmium isotopes in the southern ocean along the zero meridian. *Geochimica et Cosmochimica Acta* 127, 348–367. doi:10.1016/j.gca.2013.10.022

Audry, S., Blanc, G., Schäfer, J., Chaillou, G., and Robert, S. (2006). Early diagenesis of trace metals (Cd, Cu, Co, Ni, U, Mo, and V) in the freshwater reaches of a macrotidal estuary. *Geochimica et Cosmochimica Acta* 70, 2264–2282. doi:10.1016/j.gca.2006.02.001

Baumgartner, A., and Reichel, E (1975). The world water balance. Amsterdam: Elsevier

Berelson, W. M., Prokopenko, M., Sansone, F. J., Graham, A. W., McManus, J., and Bernhard, J. M. (2005). Anaerobic diagenesis of silica and carbon in continental margin sediments: discrete zones of TCO2 production. *Geochimica et Cosmochimica Acta* 69, 4611–4629. doi:10.1016/j.gca.2005.05.011

Bianchi, D., Weber, T. S., Kiko, R., and Deutsch, C. (2018). Global niche of marine anaerobic metabolisms expanded by particle microenvironments. *Nat. Geosci.* 11, 263–268. doi:10.1038/s41561-018-0081-0

Black, E. E., Lam, P. J., Lee, J. M., and Buesseler, K. O. (2019). Insights from the 238 U- 234 Th method into the coupling of biological export and the cycling of cadmium, cobalt, and manganese in the southeast pacific ocean. *Glob. Biogeochem. Cycles* 33, 15–36. doi:10.1029/2018GB005985

Bourne, H. L., Bishop, J. K. B., Lam, P. J., and Ohnemus, D. C. (2018). Global spatial and temporal variation of Cd:P in euphotic zone particulates. *Glob. Biogeochem. Cycles* 32, 1123–1141. doi:10.1029/2017gb005842

Boyle, E. A., Sclater, F., and Edmond, J. M. (1976). On the marine geochemistry of cadmium. *Nature* 263, 42–44. doi:10.1038/263042a0

Bralower, T. J., and Thierstein, H. R. (1987). Organic carbon and metal accumulation rates in Holocene and mid-Cretaceous sediments: palaeoceanographic significance. *Geol. Soc. Lond. Spec. Publications* 26, 345–369. doi:10.1144/gsl.sp.1987.026.01.23

Brand, L. E., Sunda, W. G., and Guillard, R. R. L. (1986). Reduction of marine phytoplankton reproduction rates by copper and cadmium. *J. Exp. Mar. Biol. Ecol.* 96, 225–250. doi:10.1016/0022-0981(86)90205-4

Bridgestock, L., Rehkämper, M., van de Flierdt, T., Murphy, K., Khondoker, R., Baker, A. R., et al. (2017). The Cd isotope composition of atmospheric aerosols from the Tropical Atlantic Ocean. *Geophys. Res. Lett.* 44, 2932–2940. doi:10.1002/2017gl072748

Bruland, K. W., Middag, R., and Lohan, M. C. (2014). Controls of trace metals in SeawaterH.D. Holland, K.K. Turekian (oxford, elsevier). *Treatise Geochem.* 14, 19–51. doi:10.1016/b978-0-08-095975-7.00602-1

Bruland, K. W. (1980). Oceanographic distributions of cadmium, zinc, nickel, and copper in the North Pacific. *Earth Planet. Sci. Lett.* 47, 176–198. doi:10.1016/0012-821x(80)90035-7

Bruland, K. W., Orians, K. J., and Cowen, J. P. (1994). Reactive trace metals in the stratified central North Pacific. *Geochimica et Cosmochimica Acta* 58, 3171–3182. doi:10.1016/0016-7037(94)90044-2

Chester, R., and Jickells, T. (2012). *Marine geochemistry 3rd ed.* London: Willey-Blackwell. doi:10.1002/9781118349083

Chong, L. S., Prokopenko, M. G., Berelson, W. M., Townsend-Small, A., and McManus, J. (2012). Nitrogen cycling within suboxic and anoxic sediments from the continental margin of Western North America. *Mar. Chem.* 128–129, 13–25. doi:10.1016/j.marchem.2011.10.007

Clegg, S. L., and Whitfield, M. (1990). A generalized model for the scavenging of trace metals in the open ocean-I. Particle cycling. *Deep Sea Res. A. Oceanogr. Res. Pap.* 37, 809–832. doi:10.1016/0198-0149(90)90008-j

Collier, R., and Edmond, J. (1984). The trace element geochemistry of marine biogenic particulate matter. *Prog. Oceanogr.* 13, 113–199. doi:10.1016/0079-6611(84)90008-9

Conway, T. M., and John, S. G. (2015a). Biogeochemical cycling of cadmium isotopes along a high-resolution section through the North Atlantic Ocean. *Geochimica et Cosmochimica Acta* 148, 269–283. doi:10.1016/j.gca.2014.09.032

Conway, T. M., and John, S. G. (2015b). The cycling of iron, zinc and cadmium in the North East Pacific Ocean - insights from stable isotopes. *Geochimica et Cosmochimica Acta* 164, 262–283. doi:10.1016/j.gca.2015.05.023

Cullen, J. T., Chase, Z., Coale, K. H., Fitzwater, S. E., and Sherrell, R. M. (2003). Effect of iron limitation on the cadmium to phosphorus ratio of natural phytoplankton assemblages from the Southern Ocean. *Limnol. Oceanogr.* 48, 1079–1087. doi:10.4319/lo.2003.48.3.1079

Cullen, J., and Maldonado, M. (2012). "Biogeochemistry of Cadmium and Its release to the Environment," in *Cadmium: From Toxicity to Essentiality*, Editors A. Sigel, H. Sigel, and R. Sigel (Dordrecht: Springer), 31–62. doi:10.1007/978–94-007–5179-8_2

Elbaz-Poulichet, F., Martin, J. M., Huang, W. W., and Zhu, J. X. (1987). Dissolved Cd behaviour in some selected French and Chinese estuaries. Consequences on Cd supply to the ocean. *Mar. Chem.* 22, 125–136. doi:10.1016/0304-4203(87)90004-1

Elbaz-Poulichet, F. ç., Garnier, J.-M., Guan, D. M., Martin, J.-M., and Thomas, A. J. (1996). The conservative behaviour of trace metals (Cd, Cu, Ni and Pb) and as in the surface plume of stratified estuaries: example of the Rh ône river (France). *Estuarine, Coastal Shelf Sci.* 42, 289–310. doi:10.1006/ecss.1996.0021

Elderfield, H., McCaffrey, R. J., Luedtke, N., Bender, M., and Truesdale, V. W. (1981). Chemical diagenesis in Narragansett Bay sediments. *Am. J. Sci.* 281, 1021–1055. doi:10.2475/ajs.281.8.1021

Elderfield, H. (1981). Metal-organic associations in interstitial waters of Narragansett Bay sediments. *Am. J. Sci.* 281, 1184–1196. doi:10.2475/ajs.281.9.1184

Emery, K. O. (1960). Basin plains and aprons off southern California. *J. Geol.* 68, 464–479. doi:10.1086/626678

Finney, B. P., and Huh, C. A. (1989). History of metal pollution in the Southern California Bight: an update. *Environ. Sci. Technol.* 23, 294–303. doi:10.1021/es00180a005

Gaillardet, J., Viers, J., and Dupré, B. (2003). "Trace elements in river waters," in *Treatise on Geochemistry*. Editors D. H. Heinrich, and Karl, K. T. (Oxford: Elsevier), 225–272. doi:10.1016/b0-08-043751-6/05165-3:

Gault-Ringold, M. (2011). *The marine biogeochemisty of cadmium: studies of cadmium isotopic variations in the southern ocean (thesis, doctor of philosophy)*. Dunedin: University of Otago.

Gault-Ringold, M., Adu, T., Stirling, C. H., Frew, R. D., and Hunter, K. A. (2012). Anomalous biogeochemical behavior of cadmium in subantarctic surface waters: mechanistic constraints from cadmium isotopes. *Earth Planet. Sci. Lett.* 341–344, 94–103. doi:10.1016/j.epsl.2012.06.005

George, E., Stirling, C. H., Gault-Ringold, M., Ellwood, M. J., and Middag, R. (2019). Marine biogeochemical cycling of cadmium and cadmium isotopes in the extreme nutrient-depleted subtropical gyre of the South West Pacific Ocean. *Earth Planet. Sci. Lett.* 514, 84–95. doi:10.1016/j.epsl.2019.02.031

Georgiev, S. V., Horner, T. J., Stein, H. J., Hannah, J. L., Bingen, B., and Rehkämper, M. (2015). Cadmium-isotopic evidence for increasing primary productivity during the Late Permian anoxic event. *Earth Planet. Sci. Lett.* 410, 84–96. doi:10.1016/j.epsl.2014.11.010

Gobeil, C., Silverberg, N., Sundby, B., and Cossa, D. (1987). Cadmium diagenesis in Laurentian Trough sediments. *Geochimica et Cosmochimica Acta* 51, 589–596. doi:10.1016/0016-7037(87)90071-8

Guinoiseau, D., Galer, S. J. G., and Abouchami, W. (2018). Effect of cadmium sulphide precipitation on the partitioning of Cd isotopes: implications for the oceanic Cd cycle. *Earth Planet. Sci. Lett.* 498, 300–308. doi:10.1016/j.epsl.2018.06.039

Guinoiseau, D., Galer, S. J. G., Abouchami, W., Frank, M., Achterberg, E. P., and Haug, G. H. (2019). Importance of cadmium sulfides for biogeochemical cycling of Cd and its isotopes in oxygen deficient zones-A case study of the Angola basin. *Glob. Biogeochem. Cycles* 33, 1746–1763. doi:10.1029/2019gb006323

Hedges, J. I., and Keil, R. G. (1995). Sedimentary organic matter preservation: an assessment and speculative synthesis. *Mar. Chem.* 49, 81–115. doi:10.1016/0304-4203(95)00008-F

Heller, M. I., Lam, P. J., Moffett, J. W., Till, C. P., Lee, J.-M., Toner, B. M., et al. (2017). Accumulation of Fe oxyhydroxides in the Peruvian oxygen deficient zone implies non-oxygen dependent Fe oxidation. *Geochimica et Cosmochimica Acta* 211, 174–193. doi:10.1016/j.gca.2017.05.019

Ho, T. Y., Quigg, A., Finkel, Z. V., Milligan, A. J., Wyman, K., Falkowski, P. G., et al. (2003). The elemental composition of some marine phytoplankton. *J. Phycol.* 39, 1145–1159. doi:10.1111/j.0022-3646.2003.03-090.x

Hohl, S. V., Galer, S. J. G., Gamper, A., and Becker, H. (2017). Cadmium isotope variations in Neoproterozoic carbonates—a tracer of biologic production? *Geochem. Persp. Lett.* 22, 32–44. doi:10.7185/geochemlet.1704

Hohl, S. V., Jiang, S.-Y., Wei, H.-Z., Pi, D.-H., Liu, Q., Viehmann, S., et al. (2019). Cd isotopes trace periodic (bio)geochemical metal cycling at the verge of the Cambrian animal evolution. *Geochimica et Cosmochimica Acta* 263, 195–214. doi:10.1016/j.gca.2019.07.036

Horner, T. J., Schönbächler, M., Rehkämper, M., Nielsen, S. G., Williams, H., Halliday, A. N., et al. (2010). Ferromanganese crusts as archives of deep water Cd isotope compositions. *Geochem. Geophys. Geosyst.* 11, 121. doi:10.1029/2009gc002987

Horner, T., Lee, R., Henderson, G., and Rickaby, R. E. (2013). Nonspecific uptake and homeostasis drive the oceanic cadmium cycle. *Proc. Natl. Acad. Sci. USA.* 110, 2500–2505. doi:10.1073/pnas.1213857110

Jacobs, L., Emerson, S., and Huested, S. S. (1987). Trace metal geochemistry in the Cariaco trench. *Deep Sea Res. Part A. Oceanogr. Res. Pap.* 34, 965–981. doi:10.1016/0198-0149(87)90048-3

Jacobs, L., Emerson, S., and Skei, J. (1985). Partitioning and transport of metals across the interface in a permanently anoxic basin: framvaren Fjord, Norway. *Geochimica et Cosmochimica Acta* 49, 1433–1444. doi:10.1016/0016-7037(85)90293-5

Jahnke, R. (2010). "Global synthesis", in *Carbon and nutrient fluxes in continental margins. Global change—the IGBP series.* Editors K. Liu, L. Atkinson, R. Quiñones, and L. Talaue-McManus (Berlin: Springer), 597–615.

Janssen, D., Conway, T., John, S., Christian, J., Kramer, D., Pedersen, T., et al. (2014). Undocumented water column sink for cadmium in open ocean oxygen-deficient zones. *Proc. Natl. Acad. Sci. USA.* 111, 6888–6893. doi:10.1073/pnas.1402388111

Janssen, D. J., Abouchami, W., Galer, S. J. G., and Cullen, J. T (2017). Fine-scale spatial and interannual cadmium isotope variability in the subarctic northeast Pacific. *Earth and Planetary Science Letters* 472, 241–252. doi:10.1016/j.epsl.2017.04.048

Janssen, D. J., Abouchami, W., Galer, S. J. G., Purdon, K. B., and Cullen, J. T. (2019). Particulate cadmium stable isotopes in the subarctic northeast Pacific reveal dynamic Cd cycling and a new isotopically light Cd sink. *Earth Planet. Sci. Lett.* 515, 67–78. doi:10.1016/j.epsl.2019.03.006

John, S. G., and Conway, T. M. (2014). A role for scavenging in the marine biogeochemical cycling of zinc and zinc isotopes. *Earth Planet. Sci. Lett.* 394, 159–167. doi:10.1016/j.epsl.2014.02.053

John, S. G., Helgoe, J., and Townsend, E. (2018). Biogeochemical cycling of Zn and Cd and their stable isotopes in the eastern tropical south pacific. *Mar. Chem.* 201, 256–262. doi:10.1016/j.marchem.2017.06.001

John, S. G., Kunzmann, M., Townsend, E. J., and Rosenberg, A. D. (2017). Zinc and cadmium stable isotopes in the geological record: a case study from the post-snowball Earth Nuccaleena cap dolostone. *Palaeogeogr. Palaeoclimatol. Palaeoecol.* 466, 202–208. doi:10.1016/j.palaeo.2016.11.003

Jones, M. T., Gislason, S. R., Burton, K. W., Pearce, C. R., Mavromatis, V., Pogge von Strandmann, P. A. E., et al. (2014). Quantifying the impact of riverine particulate dissolution in seawater on ocean chemistry. *Earth Planet. Sci. Lett.* 395, 91–100. doi:10.1016/j.epsl.2014.03.039

Klevenz, V., Bach, W., Schmidt, K., Hentscher, M., Koschinsky, A., and Petersen, S. (2011). Geochemistry of vent fluid particles formed during initial hydrothermal fluid-seawater mixing along the Mid-Atlantic Ridge. *Geochem. Geophys. Geosyst.* 12, 133. doi:10.1029/2011gc003704

Klinkhammer, G., Heggie, D. T., and Graham, D. W. (1982). Metal diagenesis in oxic marine sediments. *Earth Planet. Sci. Lett.* 61, 211–219. doi:10.1016/0012-821X(82)90054-1

Kuss, J., and Kremling, K. (1999). Particulate trace element fluxes in the deep northeast Atlantic Ocean. *Deep Sea Research Part I: Oceanographic Research Papers* 46, 149–169. doi:10.1016/S0967-0637(98)00059-4

Lacan, F., Francois, R., Ji, Y., and Sherrell, R. M. (2006). Cadmium isotopic composition in the ocean. *Geochimica et Cosmochimica Acta* 70, 5104–5118. doi:10.1016/j.gca.2006.07.036

Lambelet, M., Rehkämper, M., van de Flierdt, T., Xue, Z., Kreissig, K., Coles, B., et al. (2013). Isotopic analysis of Cd in the mixing zone of Siberian rivers with the Arctic Ocean-New constraints on marine Cd cycling and the isotope composition of riverine Cd. *Earth Planet. Sci. Lett.* 361, 64–73. doi:10.1016/j.epsl.2012.11.034

Lane, T., Saito, M., George, G., Pickering, I., Prince, R., and Morel, F. M. (2005). A cadmium enzyme from a marine diatom. *Nature* 435, 42.doi:10.1038/435042a

Lee, J.-M., Heller, M. I., and Lam, P. J. (2018). Size distribution of particulate trace elements in the U.S. GEOTRACES eastern pacific zonal transect (GP16). *Mar. Chem.* 201, 108–123. doi:10.1016/j.marchem.2017.09.006

Little, S. H., Vance, D., Lyons, T. W., and McManus, J. (2015). Controls on trace metal authigenic enrichment in reducing sediments: insights from modern oxygen-deficient settings. *Am. J. Sci.* 315, 77–119. doi:10.2475/02.2015.01

Little, S. H., Vance, D., McManus, J., and Severmann, S. (2016). Key role of continental margin sediments in the oceanic mass balance of Zn and Zn isotopes. *Geology* 44, 207–210. doi:10.1130/g37493.1

Little, S. H., Vance, D., McManus, J., Severmann, S., and Lyons, T. W. (2017). Copper isotope signatures in modern marine sediments. *Geochimica et Cosmochimica Acta* 212, 253–273. doi:10.1016/j.gca.2017.06.019

Marchitto, T. M., and Broecker, W. S. (2006). Deep water mass geometry in the glacial Atlantic Ocean: a review of constraints from the paleonutrient proxy Cd/Ca. *Geochem. Geophys. Geosyst.* 7, a. doi:10.1029/2006gc001323

Martin, J. H., Bruland, K. W., and Broenkow, W. W. (1976). "Cadmium transport in the California current," in . Editors H. L. Windom and R. A. Duce (Lexington, MA: D. C. Heath), 159–184.

Martin, J. H., and Knauer, G. A. (1973). The elemental composition of plankton. *Geochimica et Cosmochimica Acta* 37, 1639–1653. doi:10.1016/0016-7037(73)90154-3

McCorkle, D. C., and Klinkhammer, G. P. (1991). Porewater cadmium geochemistry and the porewater cadmium:δ13C relationship. *Geochimica et Cosmochimica Acta* 55, 161–168. doi:10.1016/0016-7037(91)90408-w

McManus, J., Berelson, W. M., Coale, K. H., Johnson, K. S., and Kilgore, T. E. (1997). Phosphorus regeneration in continental margin sediments. *Geochimica et Cosmochimica Acta* 61, 2891–2907. doi:10.1016/s0016-7037(97)00138-5

McManus, J., Berelson, W. M., Klinkhammer, G. P., Johnson, K. S., Coale, K. H., Anderson, R. F., et al. (1998). Geochemistry of barium in marine sediments: implications for its use as a paleoproxy. *Geochimica et Cosmochimica Acta* 62, 3453–3473. doi:10.1016/s0016-7037(98)00248-8

McManus, J., Berelson, W. M., Severmann, S., Poulson, R. L., Hammond, D. E., Klinkhammer, G. P., et al. (2006). Molybdenum and uranium geochemistry in continental margin sediments: paleoproxy potential. *Geochimica et Cosmochimica Acta* 70, 4643–4662. doi:10.1016/j.gca.2006.06.1564

Middag, R., van Heuven, S. M. A. C., Bruland, K. W., and de Baar, H. J. W. (2018). The relationship between cadmium and phosphate in the Atlantic Ocean unravelled. *Earth Planet. Sci. Lett.* 492, 79–88. doi:10.1016/j.epsl.2018.03.046

Moore, C. M., Mills, M. M., Arrigo, K. R., Berman-Frank, I., Bopp, L., and Boyd, P. W. (2013). Processes and patterns of oceanic nutrient limitation. *Nature Geosci.* 6, 701–710. doi:10.1038/ngeo1765

Morford, J. L., and Emerson, S. (1999). The geochemistry of redox sensitive trace metals in sediments. *Geochimica et Cosmochimica Acta* 63, 1735–1750. doi:10.1016/s0016-7037(99)00126-x

Morse, J. W., and Luther, G. W., III (1999). Chemical influences on trace metal-sulfide interactions in anoxic sediments. *Geochimica et Cosmochimica Acta* 63, 3373–3378. doi:10.1016/S0016-7037(99)00258-6

Murphy, K., Rehkämper, M., Kreissig, K., Coles, B., and van de Flierdt, T. (2016). Improvements in Cd stable isotope analysis achieved through use of liquid-liquid extraction to remove organic residues from Cd separates obtained by extraction chromatography. *J. Anal. Spectrom.* 31, 319–327. doi:10.1039/c5ja00115c

Nriagu, J. O. (1980). ""Cadmium in the atmosphere and in precipitation," *Part 1 in Cadmium in the environment. Ecological cycling.* Editor Nriagu, J. O. (New York, NY: John Wiley), 71–114.

Ohnemus, D. C., Rauschenberg, S., Cutter, G. A., Fitzsimmons, J. N., Sherrell, R. M., and Twining, B. S. (2016). Elevated trace metal content of prokaryotic communities associated with marine oxygen deficient zones. *Limnol. Oceanogr.* 62, 3–25. doi:10.1002/lno.10363

Patterson, T. L., and Duce, R. A. (1991). The cycle of atmospheric cadmium over the North Pacific Ocean. *Tellus B: Chem. Phys. Meteorol.* 43, 12–29. doi:10.3402/tellusb.v43i1.15243

Plass, A., Schlosser, C., Sommer, S., Dale, A. W., Achterberg, E. P., and Scholz, F. (2020). The control of hydrogen sulfide on benthic iron and cadmium fluxes in the oxygen minimum zone off Peru. *Biogeosciences* 17, 3685–3704. doi:10.5194/bg-2019-39010.5194/bg-17-3685-2020

Poulson Brucker, R. L., McManus, J., Severmann, S., and Berelson, W. M. (2009). Molybdenum behavior during early diagenesis: insights from Mo isotopes. *Geochem. Geophys. Geosyst.* 10, a. doi:10.1029/2008gc002180

Price, N. M., and Morel, F. M. M. (1990). Cadmium and cobalt substitution for zinc in a marine diatom. *Nature* 344, 658–660. doi:10.1038/344658a0

Quay, P., Cullen, J., Landing, W., and Morton, P. (2015). Processes controlling the distributions of Cd and PO4in the ocean. *Glob. Biogeochem. Cycles* 29, 830–841. doi:10.1002/2014gb004998

Ripperger, S., Rehkämper, M., Porcelli, D., and Halliday, A. N. (2007). Cadmium isotope fractionation in seawater—a signature of biological activity. *Earth Planet. Sci. Lett.* 261, 670–684. doi:10.1016/j.epsl.2007.07.034

Ripperger, S., and Rehkämper, M. (2007). Precise determination of cadmium isotope fractionation in seawater by double spike MC-ICPMS. *Geochimica et Cosmochimica Acta* 71, 631–642. doi:10.1016/j.gca.2006.10.005

Rosenthal, Y., Lam, P., Boyle, E. A., and Thomson, J. (1995). Authigenic cadmium enrichments in suboxic sediments: precipitation and postdepositional mobility. *Earth Planet. Sci. Lett.* 132, 99–111. doi:10.1016/0012-821x(95)00056-i

Rudnick, R. L., and Gao, S. (2003). *Composition of the continental crust 3*. Oxford: Elsevier-Pergamon, 1–64. doi:10.1016/b0-08-043751-6/03016-4

Schlitzer, R. (2017). Ocean data view. odv.awi.de.

Schmitt, A.-D., Galer, S. J. G., and Abouchami, W. (2009). Mass-dependent cadmium isotopic variations in nature with emphasis on the marine environment. *Earth Planet. Sci. Lett.* 277, 262–272. doi:10.1016/j.epsl.2008.10.025

Scholz, F., Löscher, C. R., Fiskal, A., Sommer, S., Hensen, C., Lomnitz, U., et al. (2016). Nitrate-dependent iron oxidation limits iron transport in anoxic ocean regions. *Earth Planet. Sci. Lett.* 454, 272–281. doi:10.1016/j.epsl.2016.09.025

Scholz, F., Severmann, S., McManus, J., and Hensen, C. (2014). Beyond the Black Sea paradigm: the sedimentary fingerprint of an open-marine iron shuttle. *Geochimica et Cosmochimica Acta* 127, 368–380. doi:10.1016/j.gca.2013.11.041

Schunck, H., Lavik, G., Desai, D., Großkopf, T., Kalvelage, T., Löscher, C., et al. (2013). Giant hydrogen sulfide plume in the oxygen minimum zone off Peru supports chemolithoautotrophy. *PLoS ONE* 8, e68661. doi:10.1371/journal.pone.0068661

Severmann, S., Johnson, C. M., Beard, B. L., and McManus, J. (2006). The effect of early diagenesis on the Fe isotope compositions of porewaters and authigenic minerals in continental margin sediments. *Geochimica et Cosmochimica Acta* 70, 2006–2022. doi:10.1016/j.gca.2006.01.007

Severmann, S., McManus, J., Berelson, W. M., and Hammond, D. E. (2010). The continental shelf benthic iron flux and its isotope composition. *Geochimica et Cosmochimica Acta* 74, 3984–4004. doi:10.1016/j.gca.2010.04.022

Shaw, T. J., Gieskes, J. M., and Jahnke, R. A. (1990). Early diagenesis in differing depositional environments: the response of transition metals in pore water. *Geochimica et Cosmochimica Acta* 54, 1233–1246. doi:10.1016/0016-7037(90)90149-f

Sieber, M., Conway, T. M., de Souza, G. F., Hassler, C. S., Ellwood, M. J., and Vance, D. (2019a). High-resolution Cd isotope systematics in multiple zones of the southern ocean from the antarctic circumnavigation expedition. *Earth Planet. Sci. Lett.* 527, 115799. doi:10.1016/j.epsl.2019.115799

Sieber, M., Conway, T. M., de Souza, G. F., Obata, H., Takano, S., Sohrin, Y., et al. (2019b). Physical and biogeochemical controls on the distribution of dissolved cadmium and its isotopes in the Southwest Pacific Ocean. *Chem. Geology.* 511, 494–509. doi:10.1016/j.chemgeo.2018.07.021

Siebert, C., Nägler, T. F., and Kramers, J. D. (2001). Determination of molybdenum isotope fractionation by double-spike multicollector inductively coupled plasma mass spectrometry. *Geochem. Geophys. Geosyst.* 2, 39. doi:10.1029/2000gc000124

Silverberg, N., Martinez, A., Aguíñiga, S., Carriquiry, J. D., Romero, N., Shumilin, E., et al. (2004). Contrasts in sedimentation flux below the southern California Current in late 1996 and during the El Niño event of 1997–1998. *Estuarine, Coastal Shelf Sci.* 59, 575–587. doi:10.1016/j.ecss.2003.11.003

Sunda, W. G., and Huntsman, S. A. (1998). Control of Cd concentrations in a coastal diatom by interactions among free ionic Cd, Zn, and Mn in seawater. *Environ. Sci. Technol.* 32, 2961–2968. doi:10.1021/es980271y

Sunda, W. G., and Huntsman, S. A. (2000). Effect of Zn, Mn, and Fe on Cd accumulation in phytoplankton: implications for oceanic Cd cycling. *Limnol. Oceanogr.* 45, 1501–1516. doi:10.4319/lo.2000.45.7.1501

Sweere, T. C., Dickson, A. J., Jenkyns, H. C., Porcelli, D., Ruhl, M., Murphy, M. J., et al. (2020). Controls on the Cd-isotope composition of upper cretaceous (Cenomanian–Turonian) organic-rich mudrocks from south Texas (eagle ford group). *Geochimica et Cosmochimica Acta* 287, 251. doi:10.1016/j.gca.2020.02.019

Tankéré, S. P. C., Muller, F. L. L., Burton, J. D., Statham, P. J., Guieu, C., and Martin, J.-M. (2001). Trace metal distributions in shelf waters of the northwestern Black Sea. *Continental Shelf Res.* 21, 1501–1532. doi:10.1016/s0278-4343(01)00013-9

Thunell, R. C., Tappa, E., and Anderson, D. M. (1995). Sediment fluxes and varve formation in Santa Barbara Basin, offshore California. *Geology* 23, 1083. doi:10.1130/0091-7613(1995)023<1083:sfavfi>2.3.co;2

van Geen, A., McCorkle, D. C., and Klinkhammer, G. P. (1995). Sensitivity of the phosphate-cadmium-carbon isotope relation in the ocean to cadmium removal by suboxic sediments. *Paleoceanography* 10, 159–169. doi:10.1029/94pa03352

van Geen, A., Zheng, Y., Bernhard, J. M., Cannariato, K. G., Carriquiry, J., Dean, W. E., et al. (2003). On the preservation of laminated sediments along the western margin of North America. *Paleoceanography* 18, 121. doi:10.1029/2003PA000911

Von Damm, K. L., Edmond, J. M., Grant, B., Measures, C. I., Walden, B., and Weiss, R. F. (1985). Chemistry of submarine hydrothermal solutions at 21° N, East Pacific Rise. *Geochimica et Cosmochimica Acta* 49, 2197–2220. doi:10.1016/0016-7037(85)90222-4

Waeles, M., Riso, R. D., and Le Corre, P. (2005). Seasonal variations of cadmium speciation in the Penzé estuary, NW France. *Estuarine, Coastal Shelf Sci.* 65, 143–152. doi:10.1016/j.ecss.2005.06.002

Waeles, M., Riso, R. D., Maguer, J.-F., and Le Corre, P. (2004). Distribution and chemical speciation of dissolved cadmium and copper in the Loire estuary and North Biscay continental shelf, France. *Estuarine, Coastal Shelf Sci.* 59, 49–57. doi:10.1016/j.ecss.2003.07.009

Waldron, K., and Robinson, N. J. (2009). How do bacterial cells ensure that metalloproteins get the correct metal?. *Nat. Rev. Microbiol.* 7, 25–35. doi:10.1038/nrmicro2057

Wasylenki, L. E., Swihart, J. W., and Romaniello, S. J. (2014). Cadmium isotope fractionation during adsorption to Mn oxyhydroxide at low and high ionic strength. *Geochimica et Cosmochimica Acta* 140, 212–226. doi:10.1016/j.gca.2014.05.007

Westerlund, S. F. G., Anderson, L. G., Hall, P. O. J., Iverfeldt, Å., Van Der Loeff, M. M. R., and Sundby, B. (1986). Benthic fluxes of cadmium, copper, nickel, zinc and lead in the coastal environment. *Geochimica et Cosmochimica Acta* 50, 1289–1296. doi:10.1016/0016-7037(86)90412-6

Xie, R. C., Galer, S. J. G., Abouchami, W., and Frank, M. (2019a). Limited impact of eolian and riverine sources on the biogeochemical cycling of Cd in the tropical Atlantic. *Chem. Geol.* 511, 371–379. doi:10.1016/j.chemgeo.2018.10.018

Xie, R. C., Galer, S. J. G., Abouchami, W., Rijkenberg, M. J. A., de Baar, H. J. W., De Jong, J., et al. (2017). Non-Rayleigh control of upper-ocean Cd isotope fractionation in the western South Atlantic. *Earth Planet. Sci. Lett.* 471, 94–103. doi:10.1016/j.epsl.2017.04.024

Xie, R. C., Rehkämper, M., Grasse, P., van de Flierdt, T., Frank, M., and Xue, Z. (2019b). Isotopic evidence for complex biogeochemical cycling of Cd in the eastern tropical South Pacific. *Earth Planet. Sci. Lett.* 512, 134–146. doi:10.1016/j.epsl.2019.02.001

Xu, Y., Feng, L., Jeffrey, P., Shi, Y., and Morel, F. M. (2008). Structure and metal exchange in the cadmium carbonic anhydrase of marine diatoms. *Nature* 452, 56–61. doi:10.1038/nature06636

Xu, Y., Tang, D., Shaked, Y., and Morel, F. M. M. (2007). Zinc, cadmium, and cobalt interreplacement and relative use efficiencies in the coccolithophore Emiliania huxleyi. *Limnol. Oceanogr.* 52, 2294–2305. doi:10.4319/lo.2007.52.5.2294

Xue, Z., Rehkämper, M., Schönbächler, M., Statham, P., and Coles, B. J. (2012). A new methodology for precise cadmium isotope analyses of seawater. *Anal. Bioanal. Chem.* 402, 883–893. doi:10.1007/s00216-011-5487-0

Xue, Z., Rehkämper, M., Horner, T. J., Abouchami, W., Middag, R., van de Flierd, T., et al. (2013). Cadmium isotope variations in the southern ocean. *Earth Planet. Sci. Lett.* 382, 161–172. doi:10.1016/j.epsl.2013.09.014

Yang, S.-C., Lee, D.-C., and Ho, T.-Y. (2015). Cd isotopic composition in the suspended and sinking particles of the surface water of the South China Sea: the effects of biotic activities. *Earth Planet. Sci. Lett.* 428, 63–72. doi:10.1016/j.epsl.2015.07.025

Yang, S.-C., Zhang, J., Sohrin, Y., and Ho, T.-Y. (2018). Cadmium cycling in the water column of the Kuroshio-Oyashio Extension region: insights from dissolved and particulate isotopic composition. *Geochimica et Cosmochimica Acta* 233, 66–80. doi:10.1016/j.gca.2018.05.001

Conflict of Interest: The authors declare that the research was conducted in the absence of any commercial or financial relationships that could be construed as a potential conflict of interest.

frontiers in Earth Science

ORIGINAL RESEARCH
published: 15 April 2021
doi: 10.3389/feart.2021.652501

Neodymium Isotopes in Glauconite for Palaeoceanographic Reconstructions at Continental Margins: A Preliminary Investigation From Demerara Rise

Pierre Giresse[1], Germain Bayon[2]*, Cedric Tallobre[1] and Lies Loncke[1]*

[1] Centre de Formation et de Recherche sur les Environnements Méditerranéens (CEFREM), UMR 5110 CNRS, Université de Perpignan Via Domitia, Perpignan, France, [2] Centre de Bretagne, Institut Français de Recherche pour l'Exploitation de la Mer, Marine Geosciences Unit, Plouzané, France

OPEN ACCESS

Edited by:
Christian März,
University of Leeds, United Kingdom

Reviewed by:
Patrick Blaser,
University of Lausanne, Switzerland
Philipp Böning,
University of Oldenburg, Germany

***Correspondence:**
Pierre Giresse
giresse@univ-perp.fr
Germain Bayon
gbayon@ifremer.fr

Specialty section:
This article was submitted to Geochemistry, a section of the journal Frontiers in Earth Science

Received: 12 January 2021
Accepted: 17 March 2021
Published: 15 April 2021

Citation:
Giresse P, Bayon G, Tallobre C and Loncke L (2021) Neodymium Isotopes in Glauconite for Palaeoceanographic Reconstructions at Continental Margins: A Preliminary Investigation From Demerara Rise. Front. Earth Sci. 9:652501. doi: 10.3389/feart.2021.652501

Contourite sediment accumulations at continental margins are related to strong bottom water circulation, where intense winnowing can result in neoformation of authigenic grains of glauconite at the seafloor. In this study, we investigated whether such glauconite grains could faithfully record ambient bottom-water neodymium (Nd) isotopic compositions, and hence be used as paleoceanographic archives. To this purpose, we measured Nd isotopic compositions (ε_{Nd}) in a series of glauconitic grains, foraminiferal assemblages, leached Fe-Mn oxyhydroxide phases, and detrital clays separated from a contourite sediment record at the Demerara slope off French Guiana (IG-KSF-11; 2370 m water depth), at a location where the present-day ε_{Nd} distribution along the water column is well characterised. We show that the ε_{Nd} composition of core-top glauconite grains (-12.0 ± 0.5) agrees with the expected NADW-like seawater signature at the same location and water depth (-11.6 ± 0.3), while departing from measured ε_{Nd} values for corresponding detrital clays (-11.3 ± 0.2), foraminiferal (-10.9 ± 0.2), and Fe-Mn oxyhydroxide fractions (-9.2 ± 0.2). This finding indicates that glauconitic grains at this particular location are probably best suited for paleoceanographic reconstructions than foraminifera and leached Fe-oxyhydroxide fractions, which appear to be influenced by sediment redistribution and the presence of terrestrial continental Fe-oxides, respectively. Using rare earth elements (REE), we tentatively propose that the acquisition of seawater Nd isotopic signatures by glauconite is controlled by the presence of authigenic REE-bearing phosphate-rich phases intertwined within clay mineral sheets, while confirming previous findings that the process of glauconitisation results in the progressive loss of REE within glauconitic grains. Preliminary paleoceanographic implications suggest strengthened bottom-water circulation of the glacial analogue of NADW at this particular location and water depth, with a ε_{Nd} signature (between -10.8 and -11.5) similar to that of modern NADW.

Keywords: rare earth elements, neodymium isotopes, glauconitisation, Demerara, contourite

INTRODUCTION

Since at least the beginning of the Neogene, the sedimentation at the Guianese margin of the Demerara Plateau has been controlled by large contour currents (Loncke et al., 2016; Tallobre et al., 2016; Fanget et al., 2020). At this location, slope bottom deposits are subject to recurrent winnowing that favours the appearance and mineralogical maturation of green glauconitic grains at the seawater–sediment interface (Tallobre et al., 2019). Each contourite sequence is characterised by high abundance of glauconitic grains (especially in the moat area), but also in a moderately to strongly discontinuous sediment accumulation associated with relatively low sedimentation rates. In contrast with nearby shallower settings along the French Guiana margin that have experienced continuous fine-grained hemipelagic sedimentation during the Late Quaternary (Häggi et al., 2017; Zhang et al., 2017; Crivellari et al., 2018), the Demerara contourite system, as other contourite deposits (e.g., Giresse and Wiewióra, 2001; Giresse, 2008), is characterised by deposition of discontinuous sediment records, which prevents their use for paleoceanographic reconstructions. Additionally, intense bottom current activity at Demerara and other contourite settings at continental margins can also result in substantial sediment redistribution, with potential effect on the reliability of commonly used paleoceanographic archives in marine sediment records.

The purpose of this study is to show the potential interest of using glauconitic grains in such discontinuous sedimentary records for paleoceanographic reconstructions based on radiogenic neodymium isotopes. Neodymium (Nd) isotopic ratios are commonly measured in biogenic material, such as fish teeth or foraminifer shells, or in the associated Fe-Mn oxyhydroxide fractions of the sediment, as tracers of bottom water circulation (e.g., Frank, 2002; Goldstein and Hemming, 2003). In the ocean, each water mass is tagged with a distinctive Nd isotopic composition (typically expressed using the epsilon notation $\varepsilon_{\mathrm{Nd}}$), which reflects, to a large extent, that of the continental masses surrounding their source region (e.g., Tachikawa et al., 2017; Robinson et al., 2021). While Nd isotopes have proven particularly helpful for reconstructing past ocean circulation patterns over various geological timescales, their application to contourite sediment accumulations at ocean margins, such as the Demerara Rise, can be skewed by sedimentary processes related to strong bottom current activity, such as winnowing and reworking.

In oceanic environments, glauconitic grains are the result of transformation and neoformation processes taking place at the water–sediment interface. Various granular supports (mudclasts, faecal pellets, and foraminifera infillings) include inherited 1:1 interstratified clays (or Te-Oc; i.e., clay minerals consisting of one tetrahedral sheet and one octahedral sheet, such as kaolinite) that become gradually replaced by 2:1 clays (Te-Oc-Te) dominated first by smectite, and then glauconite. These processes are accompanied by aluminium and silicium depletion in inherited minerals, together with significant enrichment of iron and potassium in neoformed minerals (e.g., Odin and Matter, 1981). While K in neoformed clays is supplied by ambient seawater, the source of Fe is most likely derived from reactive phases of the terrigenous sediment, such as Fe-oxide and oxyhydroxide phases (Odin and Matter, 1981; Odin and Fullagar, 1988; Giresse and Wiewióra, 2001; Wiewióra et al., 2001; Giresse, 2008; Banerjee et al., 2016). In all cases, these thermodynamic reactions operate at slow kinetic rates, especially regarding the acquisition of seawater-derived K, thereby requiring prolonged residence time at the water–sediment interface, presumably over thousands of years (e.g., Giresse, 1975), and thus reduced sedimentation rates. Earlier studies suggested that such conditions were mostly met at continental platforms, in particular at their outer edges, far from any continental source of terrigenous material. More recently, however, several investigations of contouritic deposits along continental margins revealed important glauconitic accumulations at water depths between ∼2000 and 3000 m (Giresse et al., 1998; Giresse and Wiewióra, 2001; Giresse, 2008; Stow and Faugères, 2008; Faugères and Mulder, 2011). Similar to continental shelf analogues, the occurrence of abundant glauconitic grains in contouritic systems indicates prolonged exposure at the water–sediment interface, reflecting here recurring sediment reworking related to the winnowing action of contouritic currents. Due to Fe incorporation, glauconite grains typically display higher specific gravity (between ∼2.4 and 2.9 g/cm^3; Yadav and Sharma, 1992) than the average surrounding sediment (∼1.7 g/cm^3; Tenzer and Gladkikh, 2014). As a consequence, authigenic grains of glauconite are less likely to be remobilised and dispersed by currents, compared to empty foraminiferal tests. Additionally, because glauconite formation occurs over relatively long timescales at the seawater–sediment interface, unlike other archives of bottom water chemistry (e.g., fish teeth and sedimentary Fe-Mn oxyhydroxide phases), glauconite grains could possibly integrate the signature of bottom water masses over prolonged periods of time (Giresse and Wiewióra, 2001; Giresse, 2008), which, while preventing their use in high-resolution studies, would provide an effective means for yielding reliable average estimates on past ε_{Nd} signatures of bottom water masses. To date, however, this hypothesis has never been tested.

To address this issue, we have investigated the Nd isotopic composition of glauconite grains recovered from contourite sediment deposits at Demerara Rise; at a location where ε_{Nd} signatures of modern water masses are already well characterised (Huang et al., 2014). This ε_{Nd} comparison extends to more conventional paleoceanographic archives (uncleaned foraminifers and leached sedimentary Fe-oxyhydroxide phases), being also complemented by the additional use of rare earth elements (REE) and major element ratios, such as K_2O/Al_2O_3 and Fe_2O/Al_2O_3. Since the different phases of glauconitisation include the transformation and neoformation of phyllosilicate minerals, a careful investigation is also required to assess the degree to which Nd isotopes in glauconite grains may reflect the detrital ε_{Nd} signature of inherited clay minerals within the sediment. Following proxy calibration using core-top sediments, preliminary interpretations will be made of a set of Nd isotopic data for buried glauconitic grains, in the light of the changing paleoceanographic context since the last glacial period.

MODERN AND PAST OCEANOGRAPHIC SETTING

This study focuses on an area of contourite accumulation located at Demerara Rise, along a regional slope failure headscarp, where the bottom current influence is the strongest, with flow velocity up to ∼30 cm/s (Tallobre et al., 2016; **Figure 1**). At this location (∼2400 m water depth), sedimentary dynamics is controlled by uneven accelerations of contour currents that define condensed intervals of deposits, or even lead to significant stratigraphic gaps in the sediment record (Loncke et al., 2016; Tallobre et al., 2016, 2019). Under such conditions, the application of both oxygen isotopes and radiocarbon chronostratigraphic methods has proven generally unreliable (Tallobre et al., 2019), yielding $\delta^{18}O$ depth profiles that cannot be directly tuned to nearby continuous records of hemipelagic sediments (Huang et al., 2014; Häggi et al., 2017).

The present-day distribution of radiogenic Nd isotopes along the water column at Demerara Rise identifies the presence of distinct water masses (**Figure 2**), including the West North Atlantic Central waters (WNACW; $\varepsilon_{Nd} \sim -13$), from surface to ∼500 m water depth, the Antarctic Intermediate Water (AAIW; $\varepsilon_{Nd} \sim -10.5$), between ∼ 500 and 1200 m depth, the North Atlantic Deep Water (NADW; ε_{Nd} from ∼ −12 to −11.5), from

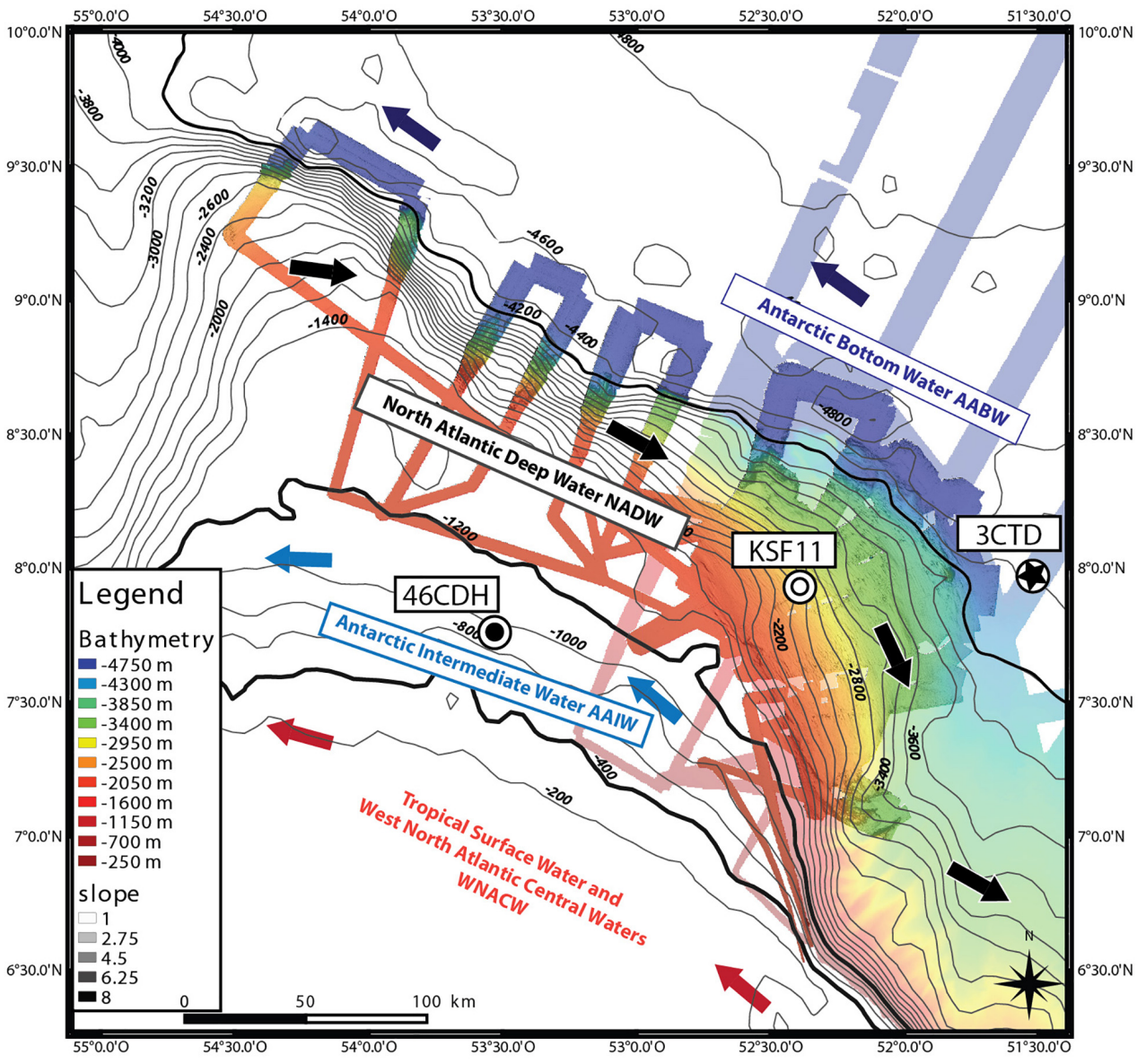

FIGURE 1 | Bathymetric map of the Demerara Plateau and location of studied core IG-KSF-11. The arrows represent surface (red), intermediate (blue), and deep (black) ocean circulation patterns. Also shown for comparison are the location of reference core 46CDH (Huang et al., 2014) and hydrocast station 3CTD (Huang et al., 2014).

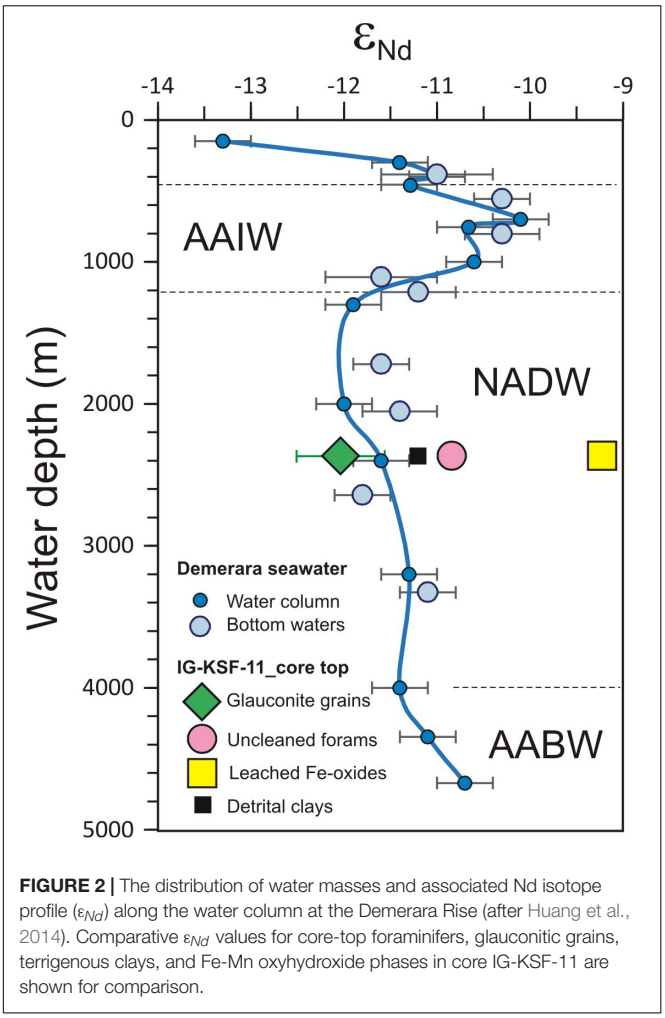

FIGURE 2 | The distribution of water masses and associated Nd isotope profile (ε_{Nd}) along the water column at the Demerara Rise (after Huang et al., 2014). Comparative ε_{Nd} values for core-top foraminifers, glauconitic grains, terrigenous clays, and Fe-Mn oxyhydroxide phases in core IG-KSF-11 are shown for comparison.

$\sim$ 1200 and 4000 m depth, and finally, the Antarctic Bottom Water (AABW; $\varepsilon_{Nd} \sim -10.5$) below 4000 m depth (Huang et al., 2014). In previous investigations, the application of Nd isotope measurements to various paleoceanographic archives retrieved from Demerara Rise (Huang et al., 2014) and other locations in the Atlantic have proven particularly useful to reconstruct past ocean circulation patterns, indicating prominent changes in the Atlantic Meridional Overturning Circulation (AMOC) over glacial–interglacial timescales, with impact on heat transport and carbon storage in the surface and deep ocean, respectively (e.g., Rutberg et al., 2000; Piotrowski et al., 2004, 2005; Pahnke et al., 2008; Böhm et al., 2015; Howe et al., 2016; Lippold et al., 2016; Pöppelmeier et al., 2020). A survey of the spatial distribution of Nd isotopes in the Atlantic during both the recent Holocene and the last glacial periods indicated relatively unradiogenic NADW-like ε_{Nd} values (~ -13) below 1500 m water depth at Demerara Rise (Howe et al., 2016). Further south in the Atlantic Ocean, the Nd isotopic composition of NADW becomes progressively more radiogenic, reflecting gradual dilution of northern-sourced waters with overlying and underlying Antarctic water masses (Howe et al., 2016). As a consequence, the unradiogenic "tongue" of NADW can be traced as the water mass flows southward in the South Atlantic at water depths between $\sim$2000 and 4000 m (e.g., von Blanckenburg, 1999; Howe et al., 2016). During the Last Glacial Maximum (LGM), the deep Atlantic water column displayed a greater influence of southern-sourced waters consistent with a reduced flux of NADW to the Southern Atlantic (Rutberg et al., 2000; Howe et al., 2016; Pöppelmeier et al., 2020). At the Demerara margin, Nd isotopic measurements were previously acquired on uncleaned foraminifera from a nearby sediment core collected at 947 m depth, bathed at present-day by AAIW (Huang et al., 2014; see core 46CDH on **Figure 1**). The obtained ε_{Nd} record for the past 25,000 years indicated similar Nd isotopic compositions during the Holocene and the LGM ($\varepsilon_{Nd} \sim -10$), while revealing pronounced ε_{Nd} excursions towards unradiogenic values (between -11 and -12) during the short-lived North Atlantic cold periods of the Heinrich Stadial 1 (HS1) and the Younger Dryas (YD), interpreted as reflecting strong reduction of the AMOC leading to reduced influence of northward flowing AAIW in the equatorial Atlantic (Huang et al., 2014).

MATERIALS AND METHODS

This study was conducted on sediment core IG-KSF-11 (07°51.85N, 052°29.25W; 2370 m water depth), recovered off French Guiana during the IGUANES cruise (R/V *L'Atalante;* Loncke L., 2013[1]). The sedimentary records retrieved from this dynamic sedimentary environment are characterised by the occurrence of abundant glauconite grains (Tallobre et al., 2019). The sediment is dominated by homogeneous grey-green silty mud with alternation of discrete sand layers (Tallobre et al., 2016, 2019). Core IG-KSF-11 was specifically chosen for this study because foraminifera $\delta^{18}O$ measurements suggest a continuous and coherent stratigraphy for the upper 0–80 cm sediment interval that is considered in this study (**Figure 3A**), which covers approximately the last 60,000 years BP (Tallobre et al., 2019). However, similar to the other sediment records retrieved from the Demerara contourite system, IG-KSF-11 suffers from inherent chronostratigraphic uncertainties due to the presence of recurrent winnowing and other erosional processes, resulting in hiatuses and frequent radiocarbon age inversions in the lower part of the core (from $\sim$2.5 to 6 m depth; Tallobre et al., 2019). As a consequence, in this study, the analysed sediment layers were only assigned a period of deposition (i.e., marine isotope stage 1, MIS 2. . .), rather than a precise stratigraphic age (**Tables 1**, **2**).

For this study, a series of glauconite grains and planktonic foraminifers were collected from six distinct sediment layers (0, 8, 20, 29, 40, and 70 cm) representative of specific time intervals (Holocene, MIS 2, MIS 3) in core IG-KSF-11. Evidence for continuous stratigraphy in this section of core IG-KSF-11 suggests that collected glauconite grains were formed *in situ*. There is no evidence for gravity-induced sediment deposition in this part of the margin. At the Demerara margin, glauconite grains mostly occur as internal fillings of foraminifera. The grains were isolated under the microscope

[1]https://doi.org/10.17600/13010030

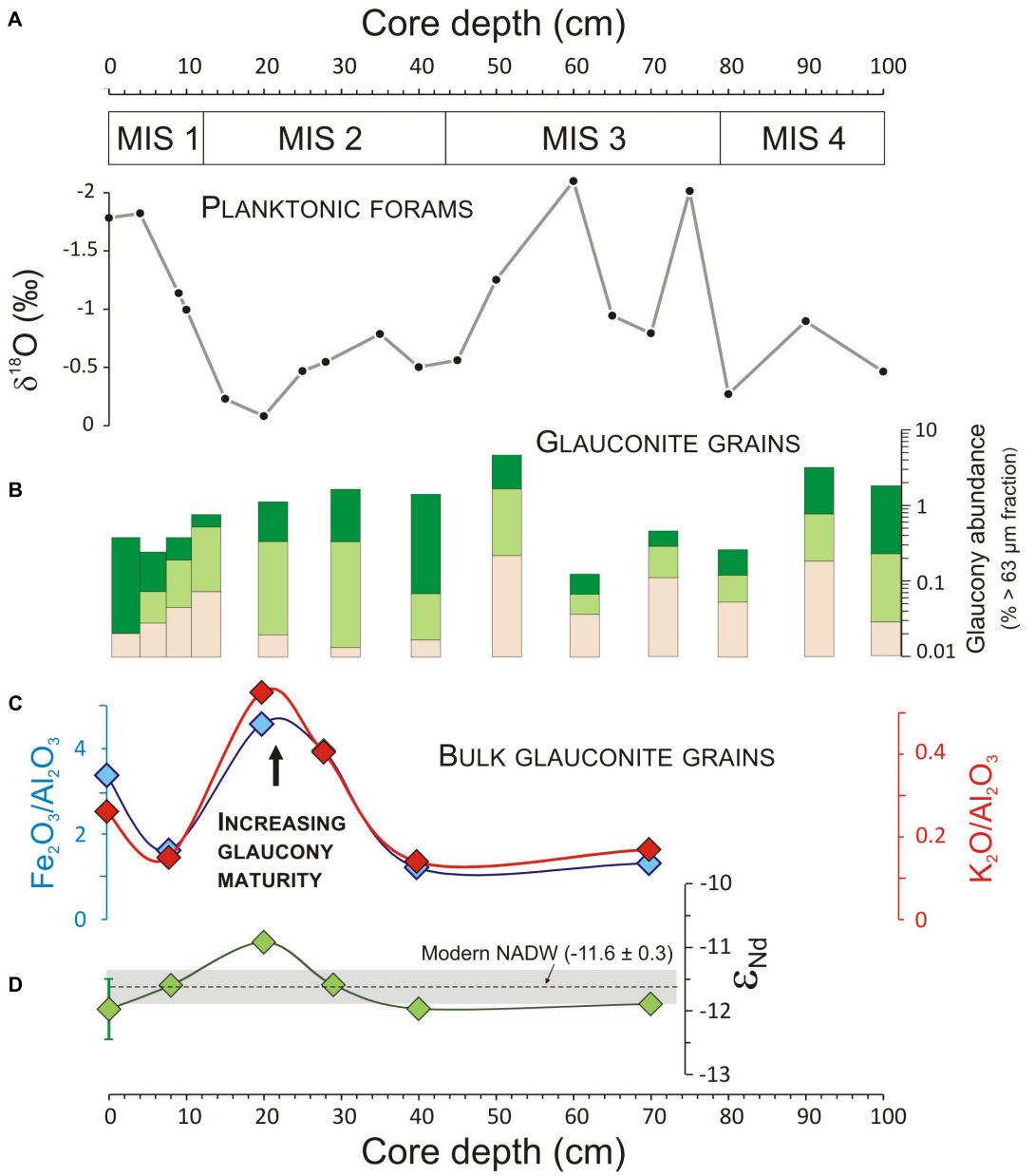

FIGURE 3 | (A) Planktonic foraminifer $\delta^{18}O$ depth profile (Tallobre et al., 2019) and **(B)** relative abundance distribution of glauconitic grains in core IG-KSF-11 (Tallobre et al., 2019). The beige, light green, and dark green boxes correspond to increasing degrees of glauconitic maturity based on visual colour and number of cracks. **(C)** Bulk Fe_2O_3/Al_2O_3 and K_2O/Al_2O_3 ratios of studied glauconite grains (this study), reflecting the degree of glauconitisation. **(D)** Nd isotopic composition (ε_{Nd}) of bulk glauconite grains. The dotted line and associated grey band indicates the present-day ε_{Nd} value of ambient bottom-waters at the same water depth (Huang et al., 2014). Note that the uncertainty on measured ε_{Nd} values (±0.15; 2 SD) is smaller than symbol size, unless reported (sample 0_1 cm).

and were then classified into three main colour categories: (1) beige/grey, (2) light green/green, and (3) dark green (**Figure 4**). Representative samples of each category were selected for SEM observation, using a SEM HITACHI S-4500 (University of Perpignan). Microprobe chemical microanalyses were performed on hemispherical sections obtained after grains were broken. Scanning was performed on both 100 and 2 μm^2 areas in order to obtain representative semi-quantitative analyses of bulk grains and newly formed nano-crystallites.

For geochemical and Nd isotope analyses of glauconite grains, a few grains of ~300–400 µm size were used. Between 30 and 90 mg of powdered sample were digested on hotplate (120°C; 1 day) with distilled 6 M HCl, following a procedure adapted from Yadav and Sharma (1992). This method achieves efficient preferential dissolution of glauconite, yielding almost quantitative recovery of K, while leaving behind more resistant Al- and Si-rich silicate minerals. This implies that major element abundances and ratios (e.g., K_2O/Al_2O_3 and Fe_2O_3/Al_2O_3; see

TABLE 1 | Major (wt %), rare earth elements (μg/g), and Nd isotopic composition of glauconitic grains.

Sample depth	Age	Fe_2O_3	MgO	Al_2O_3	K_2O	CaO	P_2O_5	MnO	Y	La	Ce	Pr	Nd	Sm	Eu	Gd	Tb	Dy	Ho	Er	Yb	Lu	Y/Ho	$^{143}Nd/^{144}Nd$	2 se (10^{-6})	$\varepsilon_{Nd} \pm 2sd$
0–1 cm	MIS 1	23.48	3.38	6.96	1.82	9.09	0.91	0.04	5.06	11.87	11.87	2.74	10.20	1.96	0.42	1.72	0.18	1.03	0.18	0.48	n.d.	0.08	28.8	0.512021	± 24	−12.0 ± 0.5
8–9 cm	MIS 1	18.41	2.62	11.37	1.72	1.91	0.12	0.04	5.04	19.21	33.52	3.87	13.48	2.30	0.41	1.62	0.19	1.05	0.18	0.46	0.42	0.06	27.5	0.512040	± 7	−11.7 ± 0.2
20–21 cm	MIS 2	26.95	3.51	5.89	3.24	3.79	0.15	0.04	3.45	8.33	15.72	1.96	7.29	1.38	0.27	1.09	0.13	0.71	0.13	0.30	0.30	0.04	27.5	0.512075	± 9	−11.0 ± 0.2
29–30 cm	MIS 2	24.99	3.05	6.32	2.57	2.44	0.15	0.03	2.71	8.39	15.12	1.82	6.59	1.21	0.23	0.83	0.10	0.56	0.10	0.26	0.25	0.03	28.2	0.512041	± 8	−11.7 ± 0.2
40–41 cm	MIS 2/3	16.12	2.68	13.23	1.87	1.60	0.13	0.03	5.51	21.80	37.89	4.40	15.08	2.63	0.49	1.89	0.21	1.16	0.20	0.51	0.42	0.06	27.5	0.512021	± 6	−12.0 ± 0.2
70–71 cm	MIS 3	17.28	2.67	13.15	2.24	1.50	0.13	0.03	5.30	22.36	22.36	4.45	15.24	2.62	0.45	1.71	0.19	1.06	0.19	0.48	0.40	0.05	28.0	0.512025	± 7	−12.0 ± 0.2
WRAS[a]		5.71	1.66	13.8	2.26	0.94	0.84	0.03	29.40	37.80	77.69	8.77	32.69	6.15	1.19	5.19	0.82	4.95	1.02	2.97	3.01	0.46	29			

[a]*World River Average Silt (WRAS; Bayon et al., 2015).*

TABLE 2 | Nd isotopic composition of unclean foraminifers, leached Fe-Mn oxyhydroxide phases, and detrital clays.

Sample depth	Age	$^{143}Nd/^{144}Nd$		2 se (10^{-6})	$\varepsilon_{Nd} \pm 2sd$		
Unclean foraminifers							
0–1 cm	MIS 1	0.512079	±	8	−10.9	±	0.2
8–9 cm	MIS 1	0.512087	±	8	−10.7	±	0.2
20–21 cm	MIS 2	0.512116	±	5	−10.2	±	0.2
29–30 cm	MIS 2	0.512103	±	12	−10.4	±	0.2
40–41 cm	MIS 2/3	0.512095	±	9	−10.6	±	0.2
70–71 cm	MIS 3	0.512083	±	8	−10.8	±	0.2
Leached Fe-Mn oxyhydroxides							
4–5 cm	MIS 1	0.512165	±	9	−9.2	±	0.2
9–10 cm	MIS 1	0.512160	±	6	−9.3	±	0.2
20–21 cm	MIS 2	0.512173	±	4	−9.1	±	0.2
28–29 cm	MIS 2	0.512160	±	8	−9.3	±	0.2
40–41 cm	MIS 2/3	0.512168	±	5	−9.2	±	0.2
50–51 cm	MIS 3	0.512173	±	6	−9.1	±	0.2
60–61 cm	MIS 3	0.512163	±	5	−9.3	±	0
70–71 cm	MIS 3	0.512165	±	8	−9.2	±	0
80–81 cm	MIS 4	0.512197	±	8	−8.6	±	0
Detrital clay-rich fractions (<4 μm)							
4–5 cm	MIS 1	0.512060	±	8	−11.3	±	0.2
9–10 cm	MIS 1	0.512046	±	5	−11.6	±	0.2
20–21 cm	MIS 2	0.512051	±	6	−11.5	±	0.2
28–29 cm	MIS 2	0.512050	±	7	−11.5	±	0.2
40–41 cm	MIS 2/3	0.512055	±	6	−11.4	±	0.2
50–51 cm	MIS 3	0.512065	±	5	−11.2	±	0.2
60–61 cm	MIS 3	0.512073	±	7	−11.0	±	0
70–71 cm	MIS 3	0.512043	±	7	−11.6	±	0
80–81 cm	MIS 4	0.512062	±	6	−11.2	±	0

section "Discussion") reported here for glauconitic grains may slightly differ from values that would otherwise be obtained for bulk glauconite digested using HF-based mineralisation methods. For the analyses of foraminiferal tests, about 10–15 mg of mixed planktonic foraminifera assemblages was prepared using the methodology described in Tachikawa et al. (2014), being dissolved using dropwise addition of ultrapure 1 M acetic acid in order to reduce any potential leaching of associated silicate detritus.

In addition, a total of nine bulk sediment samples from the same core interval were processed for isolating Fe-Mn oxyhydroxide phases and detrital clays. Bulk sediments were first treated using a sequential leaching procedure (Bayon et al., 2002) that successively removes biogenic carbonates (with 5% v/v acetic acid), Fe-Mn oxyhydroxide phases (with a mixed 15% acetic acid—0.5 M hydroxylamine hydrochloride solution) and organic matter (with 15% v/v hydrogen peroxide). For Fe-Mn oxyhydroxide phases, the resulting leachates were filtered through 0.45 μm PTFE Nalgene filters, evaporated to dryness, and finally redissolved using ultrapure HNO_3 prior to subsequent elemental analyses. Clay-rich detrital fractions (<4 μm) were separated from the residual detrital material using low-speed centrifugation (Bayon et al., 2015) and further digested by alkaline fusion (Bayon et al., 2009).

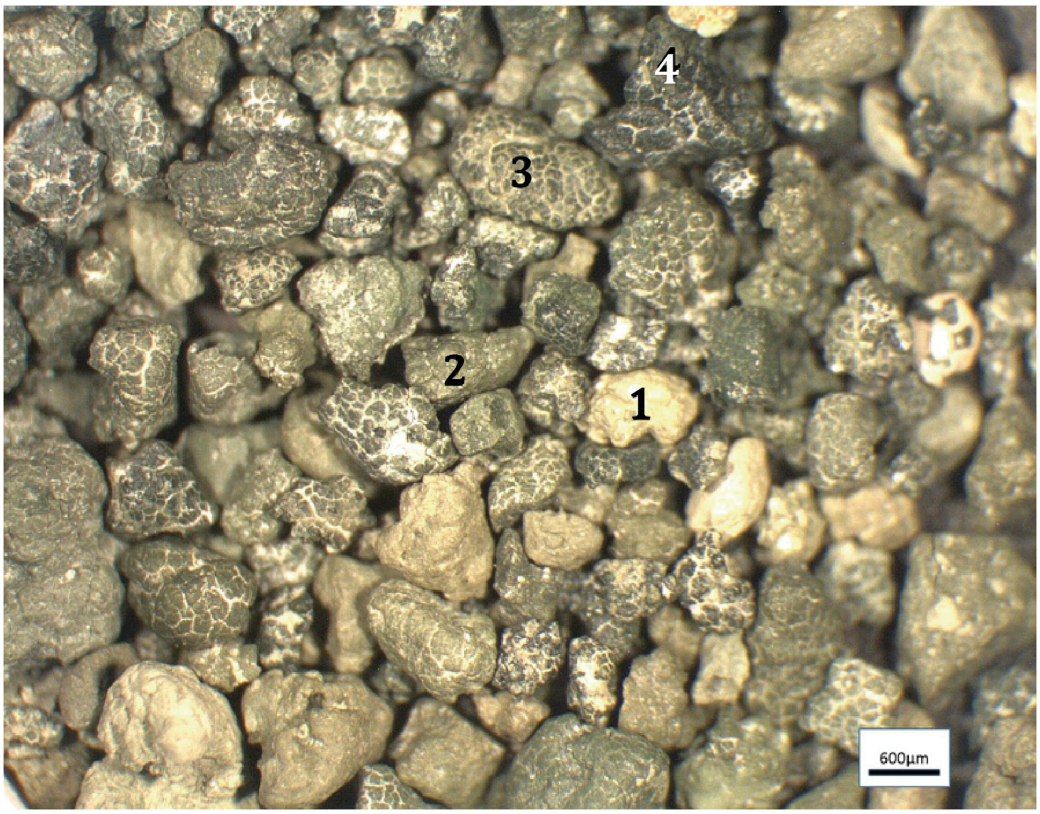

FIGURE 4 | Photograph showing the various degrees of glauconitic maturity inferred from colour and characteristic cracks. (1) Beige grains; (2) light green grains; (3) light green grains with cracks; and (4) dark green grains with cracks.

Major and trace element analyses for 6 M HCl digests of glauconite grains were determined at the Pôle Spectrométrie Océan (PSO, Brest) with a Thermo Scientific Element XR sector field ICP-MS, using the following masses (^{24}Mg, ^{27}Al, ^{31}P, ^{39}K, ^{44}Ca, ^{55}Mn, and ^{57}Fe) acquired in medium mass resolution. Yttrium and REE concentrations were also measured in low resolution mode. Elemental abundances were calculated using the Tm addition method, following the procedures described in Barrat et al. (1996, 2012). The internal precision for all measurements was better than 2%. The precision and accuracy of our data were assessed by analysing a series of silicate rock certified reference materials (CRM) having various chemical compositions (AN-G, AGV-1, BCR-1, DNC-1, DR-N, G-2, and WS-E), digested using conventional HF-HCl-HNO_3 method. The results obtained for these reference materials were in full agreement with reference values from the literature (typically < 8%), with precisions generally better than 10% (RSD; n = 3 for all of the CRMs). Neodymium was isolated using conventional ion chromatography, and isotopic measurements were performed at the PSO-Brest, using a Thermo Scientific Neptune multi-collector ICPMS. Nd isotopic compositions were determined using sample-standard bracketing, by analysing an in-house standard solution (SPEX-Nd) every two samples, yielding a mean value of 0.511687 ± 0.000007 (2 SD, n = 14). Mass bias corrections were made with the exponential law, using ^{146}Nd/^{144}Nd = 0.7219. Analyses of the JNdi-1 standard solution during the course of this study gave ^{143}Nd/^{144}Nd of 0.512114 ± 0.000010 (2 SD, n = 8), in full agreement with the reference value of 0.512115 (Tanaka et al., 2000), and corresponding to an external reproducibility of ∼ ± 0.2 ε (2 SD). Note that epsilon Nd values [$\varepsilon_{Nd} = (^{143}Nd/^{144}Nd_{SAMPLE}/^{143}Nd/^{144}Nd_{CHUR} - 1) \times 10^4$] were calculated using the chondritic (CHUR) ^{143}Nd/^{144}Nd value of 0.512638 (Jacobsen and Wasserburg, 1980).

RESULTS

Microscopic Observations and SEM Microanalyses

As a general rule, the maturity process of glauconitisation is indicated by darker colour and deeper cracks at the grain surface (Giresse and Wiewióra, 2001; Giresse, 2008). Therefore, to a first approximation, both the grain colour and its facies can be used to infer the successive stages of glauconitisation in sedimentary records (**Figure 4**). This descriptive approach was already used by Tallobre et al. (2019), indicating that maximum abundance of mature dark green grains in core IG-KSF-11 generally occurred during MIS 2 (between *ca.* 19–29 kyr BP) and in MIS 4 (∼60–70 kyr BP), in sediment layers also characterised

by high contents of glauconitic grains indicative of enhanced winnowing conditions (**Figure 3B**). Another layer containing relatively high abundance of dark green mature grains is also encountered near the top of the core of Early Holocene age, where the series is extremely condensed (**Figure 3B**). The geochemical results obtained from newly acquired SEM/EDS microanalyses of glauconite grains are listed in **Supplementary Table 1** (Al_2O_3, K_2O, Fe_2O_3, and MgO) and illustrated in **Figures 5**, **6**. These data indicate that at the microscopic scale neoformed microcrystals of dark green grains can yield K_2O and Fe_2O_3 concentrations of up to 8 and 42%, respectively (**Figure 5** and **Supplementary Table 1**). The average Al_2O_3 concentrations in studied glauconitic grains progressively decrease with the degree of maturity of the grains, from 10.1 ± 2.4% (light-coloured grains; n = 17), 6.4 ± 1.6% (green grains; n = 39), and 5.1 ± 2.3% (dark green grains; n = 11). By contrast, both

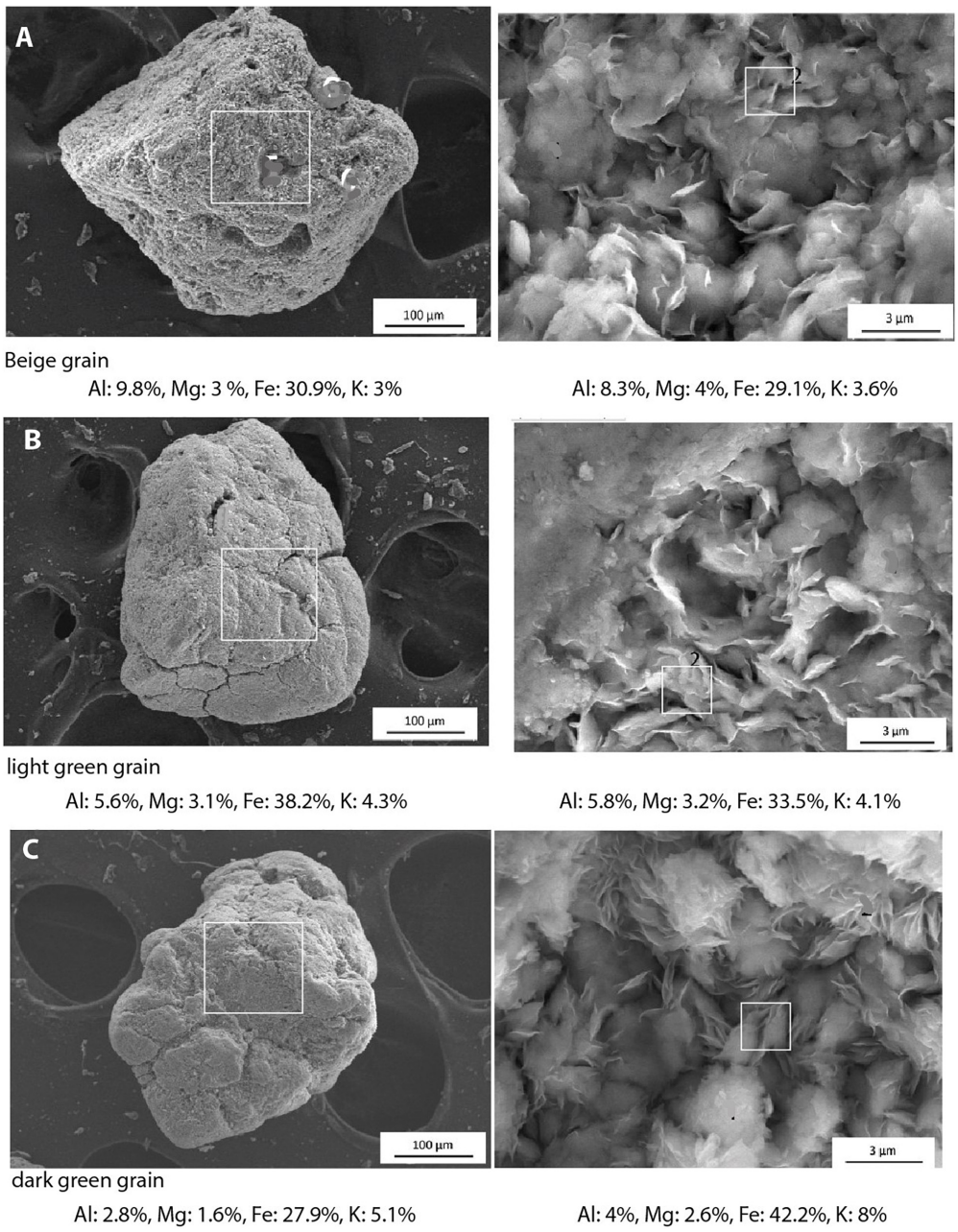

FIGURE 5 | Structural, microstructural, and chemical compositions of the successive glauconitic sequence in core IG-KSF-11. **(A)** Beige grain exhibiting high porosity (left side), showing microstructural evidence of neoformed glauconitic microcrystals (right side). **(B)** Light green grain with minor cracks (left side), exhibiting honeycomb development of newly formed microcrystals (right side). **(C)** Hummocky dark green grain with marked cracks (left side), showing high density of newly formed microcrystals (right side). Note that the white squares indicate microscanned SEM/EDS areas, with corresponding chemical compositions.

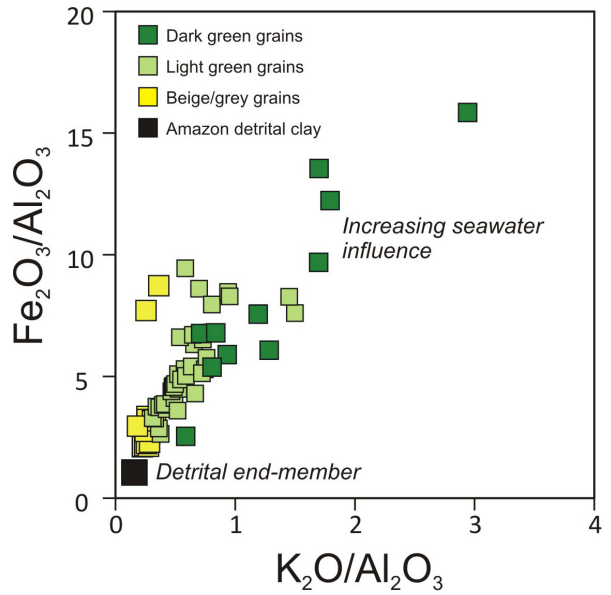

FIGURE 6 | Relationship between Fe_2O_3/Al_2O_3 and K_2O/Al_2O_3 in glauconitic grains of core IG-KSF-11, based on SEM/EDS microanalyses. Values for Amazon detrital clay are from Bayon et al. (2015).

K_2O abundances increase from 2.7 ± 0.7% (light-coloured) to 3.7 ± 0.8% (green) and 5.7 ± 1.1%, similar to Fe_2O_3: 29.1 ± 4.0% (light-coloured) to 32.1 ± 3.7% (green) and 35.9 ± 4.2% (**Supplementary Table 1**). Finally, measured MgO contents remain near constant in beige and light green grains (2.4–4.3%), but decrease in dark green grains (1.1–2.6%; **Supplementary Table 1**) due to progressive replacement of 2:1 (Te-Oc-Te) layers of montmorillonite by glauconite.

Major and Trace Elements and Nd Isotopic Compositions of Glauconitic Grains

The major and trace element concentrations obtained for HCl digests of glauconitic grains are listed in **Table 1**, together with corresponding Nd isotopic compositions. Measured concentrations are reported relative to the initial mass of bulk glauconite grain prior to 6 M HCl digestion. The HCl digests display Fe_2O_3 and Al_2O_3 concentrations ranging from 16.1 to 15.0% and 5.9 to 13.2 wt%, respectively. Potassium (K_2O) concentrations vary from 1.7 to 3.2 wt%, while CaO and P_2O_5 range from 1.5 to 9.1% and 0.1 to 0.9 wt%, respectively. The major element data are also expressed using K_2O/Al_2O_3 and Fe_2O_3/Al_2O_3 ratios (**Figure 3C**). The REE display abundances significantly lower than those for typical detrital sediments, with Nd ranging between ∼6 and 15 μg/g. Measured REE concentrations are also reported as shale-normalised patterns using values for World River Average Silt (WRAS; Bayon et al., 2015), displaying marked light-REE enrichments relative to mid- and heavy-REE (**Figure 7**). The Nd isotopic compositions vary from ε_{Nd} −12.0 (at 0–1 and 40–41 cm depth) to −11.0 (at 20–21 cm) (**Figure 3D**). In comparison, the ε_{Nd} values determined in corresponding uncleaned foraminifers (between −10.9 and −10.2) and leached sedimentary Fe-Mn oxyhydroxide phases (between −9.3 and −8.6) are significantly more radiogenic (**Table 2**). Finally, the Nd isotopic composition of the detrital clay-rich fraction is relatively homogenous along core IG-KSF-11 (between −11.6 and −11.0), with a mean ε_{Nd} signature of −11.4 ± 0.2 (1SD).

DISCUSSION

Glauconitisation at the Demerara Margin

As already shown in Tallobre et al. (2019), the new SEM-EDS data reported in this study indicate that the glauconitic grains formed at site IG-KSF-11 progressively evolve towards darker green shades as they incorporate higher amounts of Fe and K (**Figures 5**, **6**). Successive glauconite neoformation steps are also accompanied by a gradual decrease in Al contents, generally reflecting the gradual disappearance of inherited terrigenous 1:1 minerals, such as kaolinite. By contrast, the corresponding increase in K_2O and Fe_2O_3 is largely independent of the presence of inherited minerals. The source of K in glauconite is directly derived from ambient bottom water, being sequestered between newly formed and/or transformed micaceous sheets. The abundance of K_2O thus directly reflects the process of glauconitogenesis (Odin and Fullagar, 1988; Wiewióra et al., 2001). In the case of core IG-KSF-11, the increase in K_2O contents, and by inference K_2O/Al_2O_3 ratios (**Figure 5**), most likely corresponds to the presence of neoformed sheets of 2:1 clay minerals, such as K-bearing montmorillonite and illite.

In core IG-KSF-11, the abundance of the different types of glauconite grains displays clear correlation with corresponding $\delta^{18}O$ records for both planktonic and benthic foraminifers over the last three isotopic stages (**Figure 3**; Tallobre et al., 2019). The maximum abundance of glauconite grains in the 15–60 and 90–100 cm core intervals of IG-KSF-11 (expressed by the relative weight glauconitic green grains within the sandy fraction; Tallobre et al., 2019) coincides with the glacial periods of MIS 2 and MIS 4, respectively (**Figure 3**). These enriched glauconitic layers were interpreted as reflecting periods characterised by intense winnowing effect, which prevented the burial of the glauconitic grains at that time, favouring their mineralogical evolution at the water–sediment interface. Overall, the occurrence of both higher concentrations of glauconitic grains, higher relative abundances of dark green grains, and higher K_2O/Al_2O_3 and Fe_2O_3/Al_2O_3 ratios (**Figure 3**) collectively point towards a higher dynamics of contouritic currents during MIS 2 and MIS 4, in agreement with what had been proposed by Tallobre et al. (2019).

Core-Top Evidence for a Seawater-Derived Nd Isotopic Signature in Glauconite

A striking feature is the evidence that core-top glauconitic grains at site IG-KSF-11 display a similar Nd isotopic composition

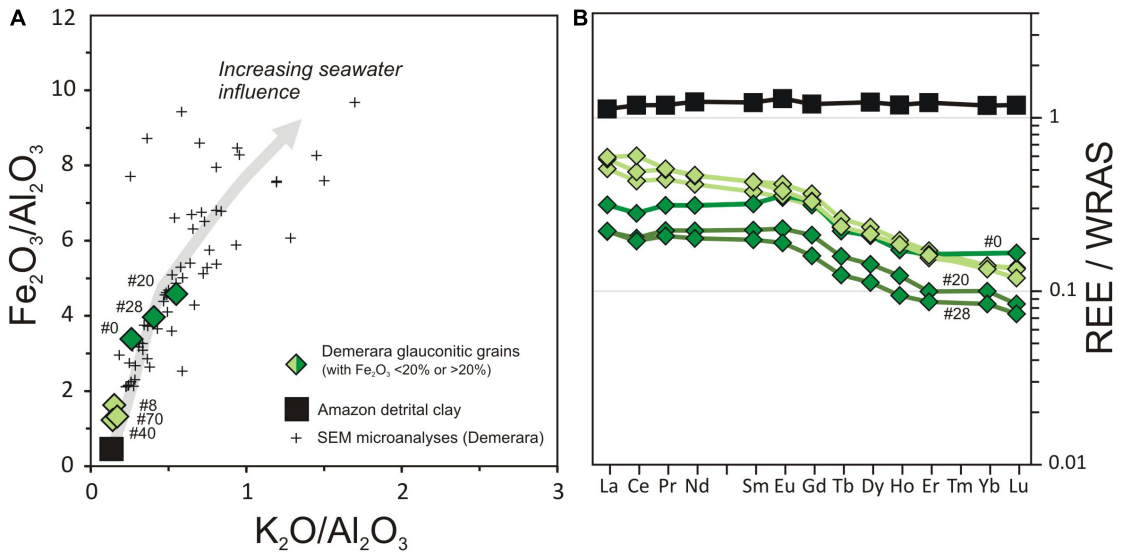

FIGURE 7 | (A) Relationship between Fe_2O_3/Al_2O_3 and K_2O/Al_2O_3 for bulk glauconitic grains from core IG-KSF-11 (diamonds), compared to microscale results obtained by SEM/EDS analyses (crosses). **(B)** Shale-normalised REE patterns of bulk glauconitic grains. WRAS refers to World River Average Silt (Bayon et al., 2015). Note that # refers the sample depth (cm). Values for Amazon detrital clay are from Bayon et al. (2015).

(−12.0 ± 0.5) than that of the corresponding water mass at the Demerara margin (−11.6 ± 0.3; Huang et al., 2014; **Figure 2**). This finding suggests that in highly dynamic depositional environments, characterised by high bottom current velocity, glauconite grains may capture the Nd isotopic composition of ambient bottom water masses. While radiocarbon dating of planktonic foraminifera assemblages suggested possible loss of the surficial sediment layer upon core recovery, the upper 10 cm of core IG-KSF-11 is still assumed to correspond to the Holocene period, hence covering a period of time during which bottom water ε_{Nd} signatures are expected to have remained near present-day values. In marked contrast, both uncleaned foraminifera (−10.9 ± 0.1; 0–1 cm depth) and leached sedimentary Fe-Mn oxyhydroxide (−9.2 ± 0.2; 4–5 cm depth) fractions from the same upper sediment layer depart significantly from the expected NADW-like Holocene seawater signature. Neodymium isotopic measurements on uncleaned foraminifera are usually assumed to reflect the signature of associated Fe-Mn oxyhydroxide coatings that precipitate onto and within the foraminifera tests at the seawater–sediment interface (e.g., Elmore et al., 2011; Tachikawa et al., 2014), hence acquiring the ε_{Nd} composition of ambient bottom waters. The fact that core-top foraminifera at site IG-KSF-11 do not match similar Nd isotopic composition than the overlying water mass suggests that they were initially derived from another depositional environment, before being transported to site IG-KSF-11 by erosion and subsequent bottom current transport. Considering the ε_{Nd} distribution along the water column at the Demerara Rise (Huang et al., 2014; **Figure 2**), we infer that the foraminifera assemblages encountered in the contourite moat at site IG-KSF-11 may be possibly derived from shallower depositional environments, at water depths between 600 m and 800 m bathed by AAIW.

While Fe-Mn oxyhydroxide phases leached from bulk marine sediments are commonly used as paleoceanographic archives (e.g., Rutberg et al., 2000; Piotrowski et al., 2005; Gutjahr et al., 2008), the Fe-oxide fractions extracted from continental margin sediment records can also include pre-formed continental oxides associated with terrigenous material (e.g., Bayon et al., 2004; Kraft et al., 2013; Jang et al., 2020), hence complicating their use for reconstructing past ocean circulation. In this study, the evidence that leached Fe-oxyhydroxide phases significantly depart from NADW-like ε_{Nd} values clearly point towards the presence of such pre-formed continental oxides. In fact, recent investigations have shown that river-borne Fe oxides are almost systematically characterised by more radiogenic Nd isotopic compositions relative to the associated detrital material (Hindshaw et al., 2018; Bayon et al., 2020; Jang et al., 2020). This Nd isotope decoupling between paired Fe oxide and detrital silicate fractions has been attributed to the preferential erosion and/or weathering of sedimentary rocks on continents (e.g., Bayon et al., 2020). For instance, recent sediments deposited near the mouth of the Amazon River display ε_{Nd} values of −8 and −10.7 for leached Fe oxides and detrital fractions, respectively (Bayon et al., 2020). At the Demerara Rise, the main potential sources of sediment include suspended particulate material from the large South American tropical rivers (Amazon, Orinoco, and Maroni) that are subsequently transported by ocean currents. These different sources display pronounced ε_{Nd} compositional variability, which can be used to trace the origin of the lithogenic material deposited on adjacent ocean margins (Rousseau et al., 2019). For instance, over the hydrological year, the Amazon River exhibits particulate ε_{Nd} values ranging from −9.8 to −11.4 (mean −10.6 ± 0.6) while the suspended loads of the Orinoco and the Maroni yield −14.1 ± 0.3 and −23.7 ± 1.2, respectively. By analogy and in agreement with previous studies (Häggi et al., 2017;

Zhang et al., 2017; Crivellari et al., 2018), we infer that measured Nd isotopic compositions for both detrital (-11.4 ± 0.2) and Fe-oxide (-9.1 ± 0.2) fractions in core IG-KSF-11 possibly reflect the dominant presence of Amazon sediments at the studied site.

Taken together, the above findings hence suggest that in highly dynamic environments at continental margins, such as the Demerara Rise, glauconitic grains may be best suited than foraminifera and leached sedimentary Fe-oxides for reconstructing the Nd isotopic composition of ambient bottom water masses.

Mode of Acquisition of Ambient Seawater ε_{Nd} Signatures by Glauconitic Grains

In contrast with Nd isotopes, which suggest a seawater origin for the core-top glauconitic grains at site IG-KSF-11, the distribution of REE in studied grains is far more equivocal, suggesting a complex mode of acquisition of ambient bottom water ε_{Nd} signatures. For instance, Y/Ho, i.e., a proxy for the relative contribution of seawater versus terrestrial signatures in marine sediments (Nozaki et al., 1997) displays values (27.9 ± 0.5; **Table 1**) indistinguishable from detrital river sediments worldwide (WRAS; 28.7 ± 1.3; Bayon et al., 2015), far from the range of seawater values (Y/Ho > ∼40–70; Bau, 1996). To some extent, this finding could indicate that the initial acquisition of REE by glauconitic grains is set by the dissolution of clay minerals, being modified subsequently by sustained isotopic exchange with seawater. Albeit different, such a process would echo with previous investigations that already suggested that fine-grained particles settling in the ocean could interact with seawater through intense dissolved-particle exchange, resulting in no significant Nd enrichment but overall leading to the acquisition of seawater Nd isotopic signatures (e.g., Jeandel et al., 1995; Tachikawa et al., 1997). In marine environments, glauconitisation involves successive dissolutions of dominant 1:1 and subsequent 2:1 clay minerals (smectite), followed by neoformation of other 2:1 micaceous sheets of glauconite. As mentioned above, the process of glauconitisation is accompanied by the loss of several cations (Al and even Si) and the enrichment of other major elements such as Fe and K. Dissolution can also occur when the starting clay phase is mainly composed of 1:1 clay minerals, such as kaolinite. For example, in the case of Fe-bearing montmorillonite green grains from the Ivory Coast-Ghana marginal ridge (ODP Site 359), kaolinite was shown to dissolve slowly with remnants of d (001) and d (060) peaks of kaolinite being still present in the pristine light coloured grains (Wiewióra et al., 2001). At the Demerara Rise, this process can also be illustrated using Fe_2O_3/Al_2O_3 versus K_2O/Al_2O_3 ratios determined in bulk glauconite grains (**Figure 7**), where the observed positive relationship (which perfectly matches with the correlation defined by SEM/EDS data; **Figure 6**) indicates increasing glauconitisation and seawater influence as both Fe_2O_3/Al_2O_3 and K_2O/Al_2O_3 ratios increase. In core IG-KSF-11, the highest Fe and K concentrations are encountered in grains formed during MIS 2 (at 20 and 28 cm depth), in full agreement with the preferential abundance of dark green grains in the corresponding sediment interval, indicative of greater degree of glauconitisation and a longer residence time due to strengthened bottom current activity.

Interestingly, the shale-normalised REE patterns of the green glauconite grains extracted from our Demerara contourite sediments indicate that increasing degrees of glauconitisation is accompanied by a net loss in REE (**Figure 7**). This finding echoes with previous works conducted on glauconitic grains of both Recent (Stille and Clauer, 1994) and Cenozoic (Tóth et al., 2010) ages, which reported similar observations that the REE contents of glauconite grains gradually decrease during glauconitisation. These latter authors proposed that the progressive REE loss during glauconitisation directly resulted from the crystallographic transformation of the phyllosilicate layers, leading to the combined depletion of both Ca and REE (Tóth et al., 2010). Additionally, one striking feature of the studied glauconitic grains from core IG-KSF-11 is that they display apparent LREE enrichment relative to MREE and HREE, resulting in shale-normalised patterns that depart significantly from both the typical seawater and detrital distribution patterns (**Figure 7**). As previously proposed, this particular REE signature could possibly relate to the presence of discrete authigenic REE-rich phosphate phases, such as cryptocrystalline apatite, which are typically found in close association with green glauconite grains in the sedimentary record (Stille and Clauer, 1994; Wigley and Compton, 2007; Tóth et al., 2010; Huggett et al., 2017). Present as inclusions within glauconitic grains, these authigenic REE-rich phosphate phases are thought to play an important role in controlling the REE budget of glauconitic grains (Stille and Clauer, 1994; Tóth et al., 2010). At the Demerara margin, studied grains display no direct correlation between both P_2O_5 and REE contents (**Table 2**), possibly suggesting that the REE composition of accessory phosphate phases may vary substantially amongst glauconitic grains. Nevertheless, based on the above consideration, we propose that the presence of such discrete authigenic phosphate minerals most likely explain why glauconitic grains at the Demerara margin can faithfully record the Nd isotopic composition of ambient bottom waters. In any case, our results suggest that increasing glauconite maturity results in progressive loss of the ε_{Nd} signature of inherited clay minerals, most likely accompanied by a gradual shift towards seawater Nd isotope composition. To some extent, this finding would also be in agreement with the evidence that other authigenic phosphate mineral phases (hydroxyfluorapatite), which control the REE budget of fish teeth following their deposition at seafloor, also act as reliable recorders of the Nd isotopic composition of bottom waters (e.g., Martin and Haley, 2000; Martin and Scher, 2004).

Preliminary Paleoceanographic Implications

As mentioned above, the occurrence of both higher concentrations of glauconitic grains and increasing relative abundances of more evolved dark green grains during MIS 2 has been interpreted as reflecting a strengthening of bottom water circulation along the Demerara margin during glacial times

(Tallobre et al., 2019). Since the studied site is located in the core interval of the modern NADW, at a water depth of ∼2400 m, this finding was taken as evidence for an intensification of the glacial AMOC. This hypothesis was in agreement with recent ε_{Nd}-based paleoceanographic reconstructions, which suggested sustained production of glacial NADW during the last glacial period (Howe et al., 2016; Pöppelmeier et al., 2020). Our newly acquired data also provide additional support for a vigorous flow of the glacial analogue of NADW at the Demerara margin. First, our major element data for bulk glauconite grains further indicate that glauconitisation was enhanced at that time as inferred from significant enrichments in Fe and K in neoformed glauconitic minerals, hence also pointing towards intensifying winnowing during glacial periods (**Figure 3C**). Second, our Nd isotope data for the glauconitic grains formed during MIS 2 (**Figure 3D**) indicate no major change in the ε_{Nd} signature of ambient bottom water masses during glacials (between −11.0 and −11.7) relative to their present-day composition (−11.6 ± 0.3; Huang et al., 2014). The evidence that the glacial NADW flowing along the Demerara margin was slightly more radiogenic compared to the modern NADW ε_{Nd} signature could be explained by the fact that northern-sourced waters may have acquired a distinctive Nd isotopic composition at that time (−10.4 ± 1.0), reflecting the impact of ice sheets on nearby continents on the release of dissolved Nd to the North Atlantic (Zhao et al., 2019). This finding is in agreement with the results obtained by Huang et al. (2014) on uncleaned foraminifera extracted from a nearby shallower sediment core (∼950 m), which also indicated similar ε_{Nd} composition for the overlying AAIW during the Holocene and the LGM. Taken together, these two ε_{Nd} records hence collectively suggest that the structure of the water column at the Demerara margin during glacial times was probably similar to its modern oceanographic configuration.

CONCLUSION AND PERSPECTIVES

Our geochemical investigation of glauconitic grains recovered from a contourite sediment sequence at the Demerara margin suggests that authigenic glauconite can faithfully record the Nd isotopic composition of ambient bottom water masses. The acquisition of ε_{Nd} seawater signatures in glauconitic grains appears to be controlled by the presence of LREE-enriched phases, possibly corresponding to dispersed authigenic phosphate phases intertwined within the neoformed clay mineral sheets. The absence of a strong detrital control on measured Nd isotopic compositions in glauconite grains is further inferred from the evidence for a progressive loss of REE with increasing degrees of glauconitisation; a process that also results in gradual enrichments in Fe and K. Overall, our new results suggest that the application of Nd isotopes to glauconite grains could serve as useful proxies for paleoceanographic reconstructions at continental margins, wherever intense winnowing and/or erosional processes may prevent the use of other more conventional archives of past seawater ε_{Nd} compositions, such as uncleaned foraminifera or leached Fe-Mn oxyhydroxide fractions. In particular, the combined use of Nd isotopes (as tracers of water mass) and various elemental ratios, such as Fe_2O_3/Al_2O_3 and K_2O/Al_2O_3 (as tracers for the degree of glauconitisation), could provide complementary information of both the source and strength of past bottom water circulation. An important requisite prior to establishing Nd isotopes in glauconite grains as robust paleoceanographic archives will be to further demonstrate the preliminary findings reported in this study, by investigating additional sites from the Demerara Rise or from any other contourite systems where bottom water masses and local detrital sediment may display contrasted Nd isotopic compositions.

DATA AVAILABILITY STATEMENT

The original contributions presented in the study are included in the article/**Supplementary Material**. Further inquiries can be directed to the corresponding author/s.

AUTHOR CONTRIBUTIONS

PG and GB contributed to the conception and design of the study and wrote the manuscript with contributions from all authors. CT contributed to the first visual analysis and counting of glauconitic grains in core IKSF11. PG and CT prepared the glauconitic grains and conducted SEM observations and analyses. GB performed all REE and Nd isotopic compositions. LL was the head scientist of the IGUANES cruise allowing the acquisition of IKSF11 core and contributed to the regional understanding of the study area. All authors contributed to the article and approved the submitted version.

FUNDING

The geochemical analyses were performed through internal funding at IFREMER.

ACKNOWLEDGMENTS

We thank the crews of R/V *L'Atalante* and all participants of the IGUANES cruise (2013; Chief scientist: Lies Loncke, https://doi.org/10.17600/13010030) for their assistance at sea. We are most grateful to Alexis De Prunelé for assistance during MC-ICPMS measurements. We also greatly thank two reviewers for providing insightful and constructive comments, together with CM for editorial handling.

SUPPLEMENTARY MATERIAL

The Supplementary Material for this article can be found online at: https://www.frontiersin.org/articles/10.3389/feart.2021.652501/full#supplementary-material

REFERENCES

Banerjee, S., Bansal, U., and Vilas Thorat, A. (2016). A review on palaeogeographic implications and temporal variation in glaucony composition. *J. Palaeogeogr.* 5, 43–71. doi: 10.1016/j.jop.2015.12.001

Barrat, J. A., Keller, F., Amossé, J., Taylor, R. N., Nesbitt, R. W., and Hirata, T. (1996). Determination of rare earth elements in sixteen silicate reference samples by ICP-MS after Tm addition and ion exchange separation. *Geostand. Newslett.* 20, 133–139. doi: 10.1111/j.1751-908x.1996.tb00177.x

Barrat, J. A., Zanda, B., Moynier, F., Bollinger, C., Liorzou, C., and Bayon, G. (2012). Geochemistry of CI chondrites: major and trace elements, and Cu and Zn isotopes. *Geochim. Cosmochim. Acta* 83, 79–92. doi: 10.1016/j.gca.2011.12.011

Bau, M. (1996). Controls on the fractionation of isovalent trace elements in magmatic and aqueous systems: evidence from Y/Ho, Zr/Hf, and lanthanide tetrad effect. *Contrib. Min. Petrol.* 123, 323–333. doi: 10.1007/s004100050159

Bayon, G., Barrat, J. A., Etoubleau, J., Benoit, M., Bollinger, C., and Revillon, S. (2009). Determination of Rare Earth Elements, Sc, Y, Zr, Ba, Hf and Th in Geological Samples by ICP-MS after Tm addition and alkaline fusion. *Geostand. Geoanal. Res.* 33, 51–62. doi: 10.1111/j.1751-908x.2008.00880.x

Bayon, G., German, C. R., Boella, R. M., Milton, J. A., Taylor, R. N., and Nesbitt, R. W. (2002). An improved method for extracting marine sediment fractions and its application to Sr and Nd isotopic analysis. *Chem. Geol.* 187, 179–199. doi: 10.1016/s0009-2541(01)00416-8

Bayon, G., German, C. R., Burton, K. W., Nesbitt, R. W., and Rogers, N. (2004). Sedimentary Fe–Mn oxyhydroxides as paleoceanographic archives and the role of aeolian flux in regulating oceanic dissolved REE. *Earth Planet. Sci. Lett.* 224, 477–492. doi: 10.1016/j.epsl.2004.05.033

Bayon, G., Lambert, T., Vigier, N., De Deckker, P., Freslon, N., Jang, K., et al. (2020). Rare earth element and neodymium isotope tracing of sedimentary rock weathering. *Chem. Geol.* 553:119794. doi: 10.1016/j.chemgeo.2020.119794

Bayon, G., Toucanne, S., Skonieczny, C., André, L., Bermell, S., Cheron, S., et al. (2015). Rare earth elements and neodymium isotopes in world river sediments revisited. *Geochim. Cosmochim. Acta* 170, 17–38. doi: 10.1016/j.gca.2015.08.001

Böhm, E., Lippold, J., Gutjahr, M., Frank, M., Blaser, P., Antz, B., et al. (2015). Strong and deep Atlantic meridional overturning circulation during the last glacial cycle. *Nature* 517, 73–76. doi: 10.1038/nature14059

Crivellari, S., Chiessi, C. M., Kuhnert, H., Häggi, C., da Costa Portilho-Ramos, R., Zeng, J. Y., et al. (2018). Increased Amazon freshwater discharge during late Heinrich Stadial 1. *Quat. Sci. Rev.* 181, 144–155. doi: 10.1016/j.quascirev.2017.12.005

Elmore, A. C., Piotrowski, A. M., Wright, J. D., and Scrivner, A. E. (2011). Testing the extraction of past seawater Nd isotopic composition from North Atlantic deep sea sediments and foraminifera. *Geochem. Geophys. Geosyst.* 12:Q09008. doi: 10.1029/2011GC003741

Fanget, A.-S., Loncke, L., Pattier, F., Marsset, T., Roest, W. R., Tallobre, C., et al. (2020). A synthesis of the sedimentary evolution of the Demerara Plateau (Central Atlantic Ocean) from the late Albian to the Holocene. *Mar. Petrol. Geol.* 114:104195. doi: 10.1016/j.marpetgeo.2019.104195

Faugères, J. C., and Mulder, T. (2011). "Contour currents and contourite drifts," in *Deep Sea Sediments, Developments in Sedimentology*, Vol. 63, eds H. Huüneke and T. Mulder (Amsterdam: Elsevier), 149–205. doi: 10.1016/b978-0-444-53000-4.00003-2

Frank, M. (2002). Radiogenic isotopes: tracers of past ocean circulation and erosional input. *Rev. Geophys.* 40, 1–38.

Giresse, P. (1975). Essai de chronomètrie de la glauconitisation dans le Golfe de Guinée; exemple de vitesse diagénétique au Quaternaire supérieur. *C.R. Somm. Seances Soc. Géol. Fr.* 5, 163–164.

Giresse, P. (2008). "Some aspects of diagenesis in contourites," in *Contourites, Developments in Sedimentology*, Vol. 12, eds M. Rebesco and A. Camerlenghi (Amsterdam: Elsevier), 203–221. doi: 10.1016/s0070-4571(08)10012-7

Giresse, P., Gadel, F., Serve, L., and Barusseau, J.-P. (1998). Indicators of climate – and sediment- source variations at Site 959 : implication for the reconstruction of paleoenvironments in the Gulf of Guinea through Pleistocene times. *Proc. Ocean Drill. Prog. Sci. Results* 159, 585–603.

Giresse, P., and Wiewióra, A. (2001). Stratigraphic condensed deposition and diagenetic evolution of green clay minerals in deep water sediments on the Ivory Coast-Ghana Ridge. *Mar. Geol.* 179, 51–70. doi: 10.1016/s0025-3227(01)00193-1

Goldstein, S. L., and Hemming, S. R. (2003). "Long-lived isotopic tracers in oceanography, paleoceanography, and ice-sheet dynamics," in *Treatise on Geochemistry*, Vol. 6, eds H. Elderfield, H. D. Holland, and K. T. Turekian (Oxford: Elsevier-Pergamon), 453–489. doi: 10.1016/b0-08-043751-6/06179-x

Gutjahr, M., Frank, M., Stirling, C. H., Keigwin, L. D., and Halliday, A. N. (2008). Tracing the Nd isotope evolution of North Atlantic deep and intermediate waters in the Western North Atlantic since the Last Glacial Maximum from Blake Ridge sediments. *Earth Planet. Sci. Lett.* 266, 61–77. doi: 10.1016/j.epsl.2007.10.037

Häggi, C., Chiessi, C. M., Merkel, U., Mulitza, S., Prange, M., Schulz, M., et al. (2017). Response of the Amazon rainforest to late Pleistocene climate variability. *Earth Planet. Sci. Lett.* 479, 50–59. doi: 10.1016/j.epsl.2017.09.013

Hindshaw, R. S., Aciego, S. M., Piotrowski, A. M., and Tipper, E. T. (2018). Decoupling of dissolved and bedrock neodymium isotopes during sedimentary cycling. *Geochem. Perspect. Lett.* 8, 43–46. doi: 10.7185/geochemlet.1828

Howe, J. N., Piotrowski, A. M., Noble, T. L., Mulitza, S., Chiessi, C. M., and Bayon, G. (2016). North Atlantic deep water production during the Last Glacial Maximum. *Nat. Commun.* 7, 1–8. doi: 10.1038/ncomms11765

Huang, K. F., Oppo, D. W., and Curry, W. B. (2014). Decreased influence of Antarctic intermediate water in the tropical Atlantic during North Atlantic cold events. *Earth Planet. Sci. Lett.* 389, 200–208. doi: 10.1016/j.epsl.2013.12.037

Huggett, J., Adetunji, J., Longstaffe, F., and Wray, D. (2017). Mineralogical and geochemical characterisation of warm-water, shallow-marine glaucony from the Tertiary of the London Basin. *Clay Min.* 52, 25–50. doi: 10.1180/claymin.2017.052.1.02

Jacobsen, S. B., and Wasserburg, G. J. (1980). Sm-Nd isotopic evolution of chondrites. *Earth Planet Sci. Lett.* 50, 139–155. doi: 10.1016/0012-821X(80)90125-9

Jang, K., Bayon, G., Han, Y., Joo, Y. J., Kim, J. H., Ryu, J. S., et al. (2020). Neodymium isotope constraints on chemical weathering and past glacial activity in Svalbard. *Earth Planet. Sci. Lett.* 542:116319. doi: 10.1016/j.epsl.2020.116319

Jeandel, C., Bishop, J. K., and Zindler, A. (1995). Exchange of neodymium and its isotopes between seawater and small and large particles in the Sargasso Sea. *Geochim. Cosmochim. Acta* 59, 535–547. doi: 10.1016/0016-7037(94)00367-u

Kraft, S., Frank, M., Hathorne, E. C., and Weldeab, S. (2013). Assessment of seawater Nd isotope signatures extracted from foraminiferal shells and authigenic phases of Gulf of Guinea sediments. *Geochim. Cosmochim. Acta* 121, 414–435. doi: 10.1016/j.gca.2013.07.029

Lippold, J., Gutjahr, M., Blaser, P., Christner, E., de Carvalho Ferreira, M. L., Mulitza, S., et al. (2016). Deep water provenance and dynamics of the (de) glacial Atlantic meridional overturning circulation. *Earth Planet. Sci. Lett.* 445, 68–78. doi: 10.1016/j.epsl.2016.04.013

Loncke, L., Maillard, A., Basile, C., Roest, W. R., Bayon, G., Gaullier, V., et al. (2016). Structure of the Demerara passive-transform margin and associated sedimentary processes. Initial results from the IGUANES cruise. *Geol. Soc. Lond. Spec. Pub.* 431, 179–197. doi: 10.1144/sp431.7

Martin, E. E., and Haley, B. A. (2000). Fossil fish teeth as proxies for seawater Sr and Nd isotopes. *Geochim. Cosmochim. Acta* 64, 835–847. doi: 10.1016/s0016-7037(99)00376-2

Martin, E. E., and Scher, H. D. (2004). Preservation of seawater Sr and Nd isotopes in fossil fish teeth: bad news and good news. *Earth Planet. Sci. Lett.* 220, 25–39. doi: 10.1016/s0012-821x(04)00030-5

Nozaki, Y., Zhang, J., and Amakawa, H. (1997). The fractionation between Y and Ho in the marine environment. *Earth Planet. Sci. Lett.* 148, 329–340. doi: 10.1016/s0012-821x(97)00034-4

Odin, G. S., and Fullagar, P. D. (1988). "Geological significance of the glaucony" in *Green Marine Clays. Oolitic Ironstone Facies, Verdine Facies, Glaucony Facies and Celadonite-Bearing Facies. A Comparative Studyeds*, Vol. 45, ed G.S. Odin (Amsterdam: Elsevier), 295–332. doi: 10.1016/s0070-4571(08)70069-4

Odin, G. S., and Matter, A. (1981). De glauconiarum origine. *Sedimentology* 28, 611–641. doi: 10.1111/j.1365-3091.1981.tb01925.x

Pahnke, K., Goldstein, S. L., and Hemming, S. R. (2008). Abrupt changes in antarctic intermediate water circulation over the past 25,000 years. *Nat. Geosci.* 1, 870–874. doi: 10.1038/ngeo360

Piotrowski, A. M., Goldstein, S. L., Hemming, S. R., and Fairbanks, R. G. (2004). Intensification and variability of ocean thermohaline circulation through the last deglaciation. *Earth Planet. Sci. Lett.* 225, 205–220. doi: 10.1016/j.epsl.2004.06.002

Piotrowski, A. M., Goldstein, S. L., Hemming, S. R., and Fairbanks, R. G. (2005). Temporal relationships of carbon cycling and ocean circulation at glacial boundaries. *Science* 307, 1933–1938. doi: 10.1126/science.1104883

Pöppelmeier, F., Blaser, P., Gutjahr, M., Jaccard, S. L., Frank, M., Max, L., et al. (2020). Northern-sourced water dominated the Atlantic Ocean during the Last Glacial Maximum. *Geology* 48, 826–829. doi: 10.1130/g47628.1

Robinson, S., Ivanovic, R., van de Flierdt, T., Blanchet, C. L., Tachikawa, K., Martin, E. E., et al. (2021). Global continental and marine detrital ε_{Nd}: an updated compilation for use in understanding marine Nd cycling. *Chem. Geol.* 567:120119. doi: 10.1016/j.chemgeo.2021.120119

Rousseau, T. C., Roddaz, M., Moquet, J. S., Delgado, H. H., Calves, G., and Bayon, G. (2019). Controls on the geochemistry of suspended sediments from large tropical South American rivers (Amazon, Orinoco and Maroni). *Chem. Geol.* 522, 38–54.

Rutberg, R. L., Hemming, S. R., and Goldstein, S. L. (2000). Reduced North Atlantic deep water flux to the glacial Southern Ocean inferred from neodymium isotope ratios. *Nature* 405, 935–938. doi: 10.1038/35016049

Stille, P., and Clauer, N. (1994). The process of glauconitization: chemical and isotopic evidence. *Contrib. Min. Petrol.* 117, 253–262. doi: 10.1007/bf00310867

Stow, D. A. V., and Faugères, J. C. (2008). "Contourite facies and the facies model," in *Contourites, Developments in Sedimentology*, Vol. 60, eds M. Rebesco and A. Camerlenghi (Amsterdam: Elsevier), 223–256. doi: 10.1016/s0070-4571(08)10013-9

Tachikawa, K., Arsouze, T., Bayon, G., Bory, A., Colin, C., Dutay, J. C., et al. (2017). The large-scale evolution of neodymium isotopic composition in the global modern and Holocene ocean revealed from seawater and archive data. *Chem. Geol.* 457, 131–148. doi: 10.1016/j.chemgeo.2017.03.018

Tachikawa, K., Handel, C., and Dupré, B. (1997). Distribution of rare earth elements and neodymium isotopes in settling particulate material of the tropical Atlantic Ocean (EUMELI site). *Deep Sea Res.* I 44, 1769–1792. doi: 10.1016/s0967-0637(97)00057-5

Tachikawa, K., Piotrowski, A. M., and Bayon, G. (2014). Neodymium associated with foraminiferal carbonate as a recorder of seawater isotopic signatures. *Quat. Sci. Rev.* 88, 1–13. doi: 10.1016/j.quascirev.2013.12.027

Tallobre, C., Giresse, P., Bassetti, M. A., Loncke, L., Bayon, G., Buscail, R., et al. (2019). Formation and evolution of glauconite in the Demerara Contourite depositional system related to NADW circulation changes during late Quaternary (French Guiana). *J. South Am. Earth Sci.* 92, 167–183. doi: 10.1016/j.jsames.2019.03.011

Tallobre, C., Loncke, L., Bassetti, M. A., Giresse, P., Bayon, G., Buscail, R., et al. (2016). Description of a contourite depositional system on the Demerara Plateau: results from geophysical data and sediment cores. *Mar. Geol.* 378, 56–73. doi: 10.1016/j.margeo.2016.01.003

Tanaka, T., Togashi, S., Kamioka, H., Amakawa, H., Kagami, H., Hamamoto, T., et al. (2000). JNdi-1: a neodymium isotopic reference in consistency with LaJolla neodymium. *Chem. Geol.* 168, 279–281. doi: 10.1016/s0009-2541(00)00198-4

Tenzer, R., and Gladkikh, V. (2014). Assessment of density variations of marine sediments with ocean and sediment depths. *Sci. World J.* 2014:9. doi: 10.1155/2014/823296

Tóth, E., Weiszburg, T. G., Jeffries, T., Williams, C. T., Bartha, A., Bertalan, É, et al. (2010). Submicroscopic accessory minerals overprinting clay mineral REE patterns (celadonite–glauconite group examples). *Chem. Geol* 269, 312–328. doi: 10.1016/j.chemgeo.2009.10.006

von Blanckenburg, F. (1999). Tracing past ocean circulation? *Science* 286, 1862–1863.

Wiewióra, A., Giresse, P., Petit, S., and Wilamowski, A. (2001). A deep-water glauconitization process on the Ivory Coast—Ghana marginal ridge (ODP site 959): determination of Fe 3+-rich montmorillonite in green grains. *Clays Clay Min.* 49, 540–558. doi: 10.1346/ccmn.2001.0490606

Wigley, R., and Compton, J. S. (2007). Oligocene to Holocene glauconite–phosphorite grains from the Head of the Cape Canyon on the western margin of South Africa. *Deep Sea Res. II* 54, 1375–1395. doi: 10.1016/j.dsr2.2007.04.004

Yadav, V. P., and Sharma, T. (1992). Leaching of glauconitic sand stone in acid lixiviants. *Miner. Eng.* 5, 715–720. doi: 10.1016/0892-6875(92)90066-i

Zhang, Y., Chiessi, C. M., Mulitza, S., Sawakuchi, A. O., Häggi, C., Zabel, M., et al. (2017). Different precipitation patterns across tropical South America during Heinrich and Dansgaard-Oeschger stadials. *Quat. Sci. Rev.* 177, 1–9. doi: 10.1016/j.quascirev.2017.10.012

Zhao, N., Oppo, D. W., Huang, K. F., Howe, J. N., Blusztajn, J., and Keigwin, L. D. (2019). Glacial–interglacial Nd isotope variability of North Atlantic Deep Water modulated by North American ice sheet. *Nat. Commun.* 10, 1–10. doi: 10.1038/s41467-019-13707-z

Conflict of Interest: The authors declare that the research was conducted in the absence of any commercial or financial relationships that could be construed as a potential conflict of interest.

frontiers in Earth Science

ORIGINAL RESEARCH
published: 29 April 2021
doi: 10.3389/feart.2021.653698

Small-Scale Geochemical Heterogeneities and Seasonal Variation of Iron and Sulfide in Salt Marshes Revealed by Two-Dimensional Sensors

Qingzhi Zhu[1], J. Kirk Cochran[1]*, Christina Heilbrun[1], Hang Yin[1], Huan Feng[2], Joseph J. Tamborski[3†], Patrick Fitzgerald[1] and Wen Cong[1]*

[1] School of Marine and Atmospheric Sciences, Stony Brook University, Stony Brook, NY, United States, [2] Department of Earth and Environmental Studies, Montclair State University, Montclair, NJ, United States, [3] Department of Geosciences, Stony Brook University, Stony Brook, NY, United States

OPEN ACCESS

Edited by:
Natascha Riedinger, Oklahoma State University, United States

Reviewed by:
Vincent Noel, Stanford University, United States
Sophia LaFond-Hudson, Oak Ridge National Laboratory (DOE), United States

***Correspondence:**
Qingzhi Zhu
qing.zhu@stonybrook.edu
J. Kirk Cochran
kirk.cochran@stonybrook.edu

†Present Address:
Joseph J. Tamborski, Department of Ocean and Earth Sciences, Old Dominion University, Norfolk, VA, United States

Specialty section:
This article was submitted to Biogeoscience, a section of the journal Frontiers in Earth Science

Received: 15 January 2021
Accepted: 06 April 2021
Published: 29 April 2021

Citation:
Zhu Q, Cochran JK, Heilbrun C, Yin H, Feng H, Tamborski JJ, Fitzgerald P and Cong W (2021) Small-Scale Geochemical Heterogeneities and Seasonal Variation of Iron and Sulfide in Salt Marshes Revealed by Two-Dimensional Sensors. Front. Earth Sci. 9:653698. doi: 10.3389/feart.2021.653698

Loss of tidal wetlands is a world-wide phenomenon. Many factors may contribute to such loss, but among them are geochemical stressors such as exposure of the marsh plants to elevated levels on hydrogen sulfide in the pore water of the marsh peat. Here we report the results of a study of the geochemistry of iron and sulfide at different seasons in unrestored (JoCo) and partially restored (Big Egg) salt marshes in Jamaica Bay, a highly urbanized estuary in New York City where the loss of salt marsh area has accelerated in recent years. The spatial and temporal 2-dimensional distribution patterns of dissolved Fe^{2+} and H_2S in salt marshes were *in situ* mapped with high resolution planar sensors for the first time. The vertical profiles of Fe^{2+} and hydrogen sulfide, as well as related solutes and redox potentials in marsh were also evaluated by sampling the pore water at discrete depths. Sediment cores were collected at various seasons and the solid phase Fe, S, N, C, and chromium reducible sulfide in marsh peat at discrete depths were further investigated in order to study Fe and S cycles, and their relationship to the organic matter cycling at different seasons. Our results revealed that the redox sensitive elements Fe^{2+} and S^{2-} showed significantly heterogeneous and complex three dimensional distribution patterns in salt marsh, over mm to cm scales, directly associated with the plant roots due to the oxygen leakage from roots and redox diagenetic reactions. We hypothesize that the oxic layers with low/undetected H_2S and Fe^{2+} formed around roots help marsh plants to survive in the high levels of H_2S by reducing sulfide absorption. The overall concentrations of Fe^{2+} and H_2S and distribution patterns also seasonally varied with temperature change. H_2S level in JoCo sampling site could change from <0.02 mM in spring to >5 mM in fall season, reflecting significantly seasonal variation in the rates of bacterial oxidation of organic matter at this marsh site. Solid phase Fe and S showed that very high fractions of the diagenetically

reactive iron at JoCo and Big Egg were associated with pyrite that can persist for long periods in anoxic sediments. This implies that there is insufficient diagenetically reactive iron to buffer the pore water hydrogen sulfide through formation of iron sulfides at JoCo and Big Egg.

Keywords: salt marsh geochemistry, planar optical sensors, Jamaica Bay, 2-D distributions, Fe^{2+} and H_2S

INTRODUCTION

The worldwide loss of salt marsh wetlands has been linked to many factors, including sea level rise, coastal development, coastal eutrophication and geochemical stressors. Salt marshes need to accrete to keep pace as sea level rises. Marsh accretion is affected by growth of the plants, accumulation of organic matter and lithogenic particles and formation of authigenic phases (e.g., Fe_2S) in marsh peat. Cycling of iron compounds, hydrogen sulfide (H_2S) and nutrients N and P could provide stress on salt marsh plants. Hydrogen sulfide is known as a toxin to marsh plants (Kolker, 2005; Lamers et al., 2013; Alldred et al., 2020), and addition of nutrients and organic matter to marshes may enhance hydrogen sulfide production (Kolker, 2005). The input of iron particles on marsh may increase marsh accretion by reducing dissolved H_2S and forming the mineral pyrite in the marsh. But previous results also imply that the marsh biomass could be degraded if iron in marsh is too high and causes removal of the nutrient phosphorus (Cochran et al., 2018). Therefore, understanding the distribution patterns and seasonal variations of iron and sulfide in salt marshes, as well as possible geochemical constraints on salt marsh loss, is critical for the study of marsh health and resiliency.

Iron (Fe) and sulfur (S) are two important redox-sensitive elements in salt marshes, their distribution patterns with depth reflect multiple biogeochemical reactions and processes in the deposits, for example, organic matter decomposition, sulfate reduction/sulfide oxidation, availability of reactive Fe, and accumulation rate of authigenic pyrite minerals (Berner, 1984; Canfield et al., 1992; Goldhaber, 2003; Jørgensen and Nelson, 2004; Jørgensen and Kasten, 2006; Aller et al., 2010; Luther et al., 2011). All these biogeochemical processes are closely coupled to the environment and ecosystem of salt marshes, including marsh peat degradation, accretion, biomass growth/decline, and species diversities (Luther and Church, 1988; Kostka and Luther, 1995; Sundby et al., 2003; Luo et al., 2017).

Particulate Fe is typically input to coastal marshes through wind-blown dust, river run-off, and tidal flooding. The oxidized Fe-containing mineral particles directly deposit on the marsh surface, and subsequently become involved in early diagenetic reactions in marsh peat. One important pathway for Fe cycling in marsh is microbial iron reduction, a common pathway of Fe^{3+}-oxides reduction to Fe^{2+} by organic matters mediated by Fe^{3+}-reducing microorganisms (Weiss et al., 2005; Luo et al., 2015, 2016, 2017). In sulfidic zones, Fe^{3+}-oxide minerals can also abiotically react with sulfide to produce dissolved Fe^{2+}, which subsequently react with sulfide, generating the authigenic minerals FeS and pyrite (FeS_2) (Berner, 1970; Canfield, 1989; Kostka and Luther, 1995). Hydrogen sulfide in marsh pore water is generally produced from the reduction of sulfate by bacteria as organic matter is oxidized. Because of the large amount of labile organic matter in marshes (e.g., from marsh plants or combined sewer overflows), the active electron acceptors O_2, nitrate/nitrite, Mn/Fe-oxide could be completely consumed by organic matter within a very thin surficial layer of the marsh peat, resulting in an anoxic sulfidic environment in most salt marshes. Under anoxic conditions, sulfate-reducing bacteria use SO_4^{2-} as an electron acceptor for organic matter remineralization, generating H_2S as one of the end products (Goldhaber, 2003; Jørgensen and Nelson, 2004). This anaerobic respiration process often dominates in organic matter-rich salt marshes, resulting in high concentrations of dissolved sulfide at millimolar (mM) levels (Bagarinao, 1992). H_2S, one specie of the total dissolved sulfide ($\Sigma H_2S = [H_2S] + [HS^-] + [S^{2-}]$), is harmful to marsh plants such as *Spartina alterniflora*. Long-term exposures to levels greater than ∼4 mM H_2S in marsh pore water can cause plant die-off, and subsequent peat degradation and subsidence (Kolker, 2005; Cochran et al., 2013; Lamers et al., 2013).

Typically, the intense redox reactions and precipitation/dissolution reactions in the surficial marsh peat generate sharp gradients of Fe^{2+} and H_2S in marsh pore water. The H_2S concentrations can increase from 0 to several mM over depths of millimeters to centimeters, with the concentrations of Fe^{2+} changing by several hundred micromolar (μM). The compositional changes with depth in deposits are usually assumed steady and to occur in an overall average vertical progression. However, the growth of marsh plants and the activities of dwelling fauna can generate significant heterogeneity and complex three dimensional reaction patterns of Fe and S over millimeter to meter scales due to plant rhizosphere development, oxygen transport through roots, burrow construction, and bioirrigation (Aller, 1982, 2001; Sundby et al., 2003; Weiss et al., 2005). The seasonal cycling of Fe and S in salt marsh sediments have been reported (Luther et al., 1986; Kostka and Luther, 1995; Luo et al., 2017), and 2-D distributions of dissolved Fe^{2+} and H_2S in coastal marine sediments have also been discussed elsewhere (Zhu and Aller, 2012, 2013; Yin et al., 2017). However, the small scale 2-D distribution patterns of dissolved Fe^{2+} and H_2S associated with the plant rhizosphere in salt marshes have not been investigated so far. *In situ* measurements of real-time, high-resolution 2-D distributions of H_2S and Fe^{2+} around plant roots may provide insight into the nature of interactions between the oxygen, iron, and sulfur cycles in marsh plant rhizosphere.

Jamaica Bay, New York has suffered considerable loss of salt marsh acreage over the past ∼50 years. A large unrestored marsh island JoCo and a partially restored marsh island Big Egg were selected as study sites in this work. We noted that the H_2S levels at JoCo marsh could be elevated to >6 mM in summer and

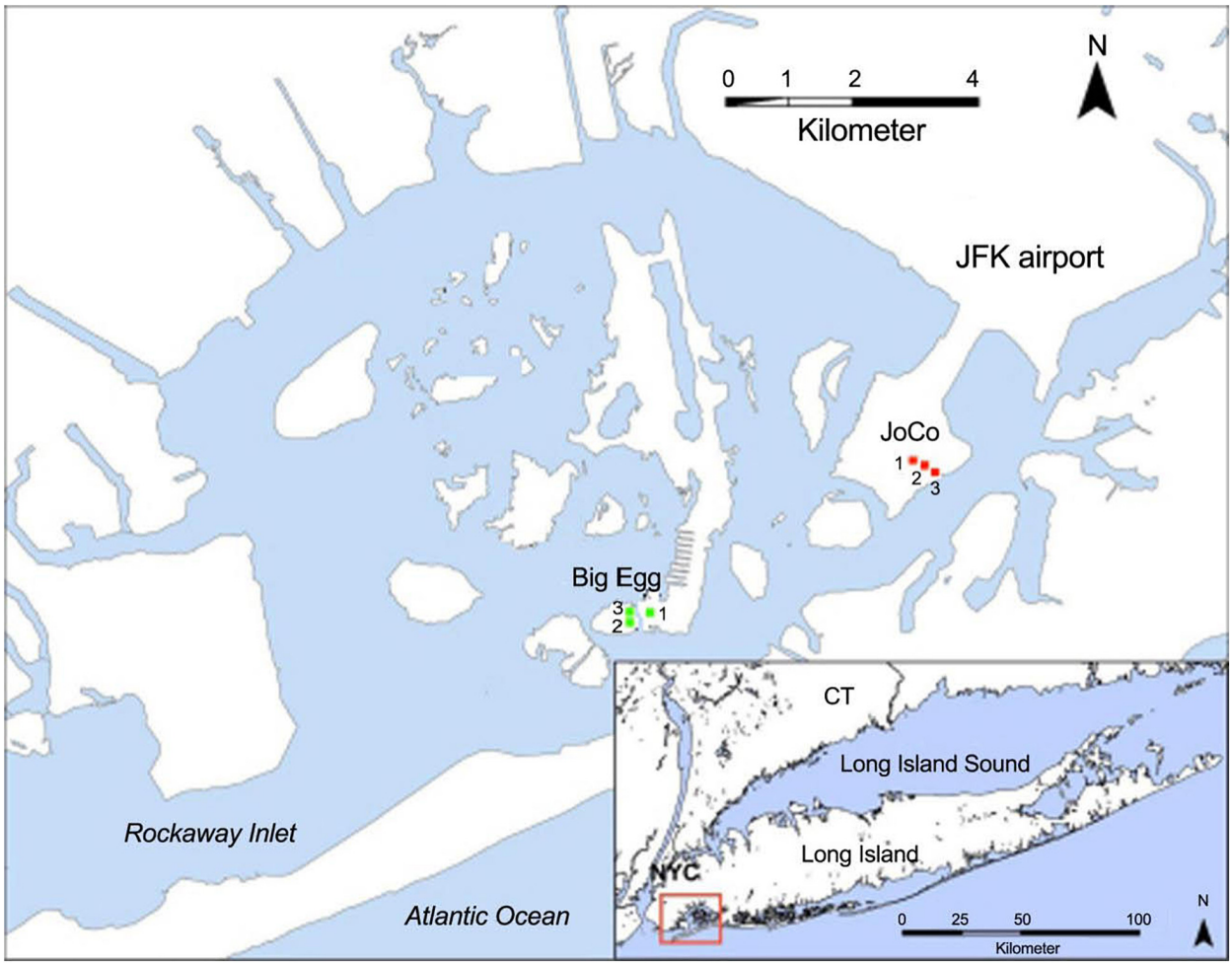

FIGURE 1 | Location of Jamaica Bay and the sampling sites at Big Egg (BE) and JoCo (JC). The GPS coordinates of sampling sites are BE1 (40.59604N, 73.82637W; restored in 2003), BE2 (40.59586N, 40.59586W), BE3 (40.59607N, 73.82812W), JC1 (40.61241N, 73.78779W), JC2 (40.61212N, 73.78724W), and JC3 (40.61173N, 73.78591W), respectively. Modified from Tamborski et al. (2017). Service Layer Credits: Source: Esri, DigitalGlobe, GeoEye, Earthstar Geographics, CNES/Airbus DS, USDA, USGS, AeroGRID, IGN, and the GIS User Community.

fall, but marsh plants grow well and it's still considered as a "healthy" marsh. On the other hand, marsh in the unrestored part of Big Egg seems to be worse, even the H_2S level is lower than JoCo. We hypothesize: (1) a complicated and time-dependent 3-D distribution pattern of low level dissolved H_2S and Fe^{2+} (cold-spots) around individual plant roots can be generated by oxygen transport/leakage from roots, and (2) the cold-spots/oxic layers formed around roots help marsh plants to survive in the high levels of H_2S by reducing sulfide absorption. Accordingly, we collected pore water samples with "sippers"– short tubes that are emplaced to various depths in the peat and through which pore water is drawn into an evacuated syringe, complemented this approach with chemical sensors that provide *in situ* high-resolution mapping linking the structure of marsh peat with spatial and temporal patterns of H_2S and Fe^{2+} concentrations, and collected marsh peat cores to study the distributions of Fe, S, N, C, and chromium reducible sulfur (CRS) in marsh peat solid phase. Our goal is to characterize the significant geochemical heterogeneities of Fe and S in marsh pore water and peat, seasonal variation and the interactions of these solutes in marsh pore water, the characterization of elevated pore water levels of the phytotoxin H_2S, and the effects of the redox cycles of Fe and S on the solid phase reservoirs of these elements.

MATERIALS AND METHODS

Sample Sites

Jamaica Bay is a heavily urbanized estuary (~80 km^2) located primarily between the New York City boroughs of Brooklyn and Queens, with a connection to the Atlantic Ocean through Rockaway Inlet (**Figure 1**). The Bay, consisting of over a dozen isolated marsh islands and a labyrinth of waterways, has been characterized as a eutrophic estuary with water salinity in the range of 20–26 PSU, temperature 1–26°C, and pH 6.8–9, respectively [USFWS (U.S. Fish and Wildlife Service), 1997]. Some of the marsh islands are natural, but many of them have been restored through engineering efforts. The dominant plant

species in the low salt marsh is saltmarsh cordgrass, *S. alterniflora*, and in the high salt marsh is salt meadow cordgrass, *Spartina patens*. These salt marshes provide critical ecological services, including habitat and food sources for wildlife, shoreline erosion control, and water column filtration, as well as serve as a buffer against storm tides and waves (New York City Department of Environmental Protection, 2007a,b; Marsooli et al., 2017). However, Jamaica Bay's salt marsh losses have been severe; about 60% of the Bay's salt marsh has converted into mudflats since 1951, with smaller islands losing up to 78% of their vegetation cover, due to a combination of factors including sediment load reduction, dredging, boat traffic, sea level rise, nutrient enrichment and H_2S concentration increase (Rafferty et al., 2010; Campbell et al., 2017). The nutrient load of the Bay from sewage treatment plant effluent and combined sewer overflows is thought to be an important factor that may contribute to this high rate of marsh loss in recent years (Deegan et al., 2012).

Jamaica Bay has a mean semi-diurnal tidal range of approximately 1.5 m, the investigated marsh sites are all inundated during high tide. Two marsh sites were studied in the present work: one is a natural salt marsh, JoCo (JC), which is considered a "healthy" marsh, and the other is a partially restored salt marsh, Big Egg (BE). Three sampling sites were established in each marsh. One of the three sites at Big Egg (BE1) was previously restored by spraying sandy sediment from the adjacent channel onto the marsh surface as part of a restoration effort in 2003 (Frame et al., 2006), but the remaining two sites (BE2 and BE3) have not yet been restored. The two marshes are dominated by *S. alterniflora*, while JoCo has a mixture of marsh grasses that includes *Spartina patens*, a high marsh species. JoCo experienced a marsh loss of approximately 7% between 1974 and 1999, while losses at Big Egg were up to 38% (NYSDEC, 2006).

Pore water samples, solid marsh cores, and sensor deployment in JoCo were taken on October 10, 2014, May 1, 2015 and September 9, 2015 and April 22, 2016, respectively. In Big Egg sites, they were taken on October 8, 2014, April 13, 2015, September 25, 2015, and April 15, 2016, respectively.

Discrete Pore Water Sampling and Measurements

Discrete pore water samples were taken using pore water "sippers" at depths of 5, 10, 15, and 25 cm in the marsh peat. The sippers are hollow acrylic rods that end in a small opening. Each sipper is connected to Tygon tubing which can be connected to a 50 ml plastic syringe. A valve connected to the Tygon tubing between the syringe and the sipper facilitates purging of the syringe. Pore water samples of ∼50 ml were slowly drawn into the syringe through the sipper, and immediately filtered in the field through 0.45 μm filters. Aliquots for dissolved sulfide, nutrients, and trace elements were collected. The sulfide aliquots were fixed in the field by adding 0.5 ml of 0.05 M $Zn(C_2H_3O_2)_2.2H_2O$ to each sample, the Fe^{2+} aliquots were stabilized by acidification. The concentrations of dissolved sulfide, nutrients (NH_4^+ and HPO_4^{2-}) and dissolved Fe^{2+} in these discrete pore water samples were subsequently measured in lab.

Total dissolved sulfide (as $\Sigma H_2S = [H_2S] + [HS^-] + [S^{2-}]$) and ammonium were measured using techniques described by Kolker (2005) and Cochran et al. (2013). Briefly, total sulfide was measured by spectrometric method (Cline, 1969; Reese et al., 2011) with relative standard deviation (RSD) < 5%. Ammonium and phosphate were measured using a Lachat Nutrient Autoanalyzer with RSD ± 5%, and dissolved Fe^{2+} was determined by spectrometric method described by Stookey (1970). Pore water pH and E_h (ORP; Oxidation-Reduction Potential) were measured in the field with a YSI 1009-1 09C multi-parameter probe that measured pH on the total H^+ scale and used a Pt electrode for E_h. Salinity values were determined in the laboratory through measurement of chloride or with a refractometer.

In situ Measurements of 2-D Pore Water H_2S and Fe^{2+} Using Optical Planar Sensors

2-D distributions of dissolved Fe^{2+} in pore water were measured *in situ* by deploying optical planar Fe^{2+} sensors in salt marsh. The irreversible planar sensor of dissolved Fe^{2+} was fabricated with ferrizone as the optical indicator that was immobilized in polyurethane hydrogel (D4) membrane, modified from our previous publication (Zhu and Aller, 2012). The blank Fe^{2+} sensor film was colorless and transparent, and it rapidly converted to a violet-red color with maximum absorption wavelength at 562 nm after the sensor film was exposed to dissolved Fe^{2+} solution. The sensor response range depends on the sensor deployment time in Fe^{2+} solution, and the sensor showed a good linear response in the range of 0–200 μmol/L of Fe^{2+} with the limit of detection of 5 μmol/L when a 10 min deployment time was applied. A short sensor deployment time was used when Fe^{2+} concentration was higher than 200 μmol/L, and the sensor could respond to dissolved Fe^{2+} as high as 1 mmol/L when it was deployed in the sample for 1 min. In this work, 1–10 min Fe^{2+} sensor deployment time in salt marsh was used, depending on the Fe^{2+} concentration in the marsh pore water.

The sensor film sheet (14 cm × 20 cm) was cut into five sensor film stripes with dimension of 2.8 cm × 20 cm, four strips were used for *in situ* deployment and one for calibration. The sensor film strip was mounted on a 5 cm × 40 cm × 1 cm (width × length × thickness) polycarbonate plastic sheet with a beveled end. *In situ* measurements were performed at low tide by inserting/punching the plastic sheet with attached sensor strip vertically into the salt marsh peat (**Figure 2**) and allowing it to react with dissolved Fe^{2+} in pore water for 1–10 min. After the reaction, the sensor film was pulled out of the marsh and rinsed with seawater. The color-developed Fe^{2+} sensing film was then wrapped with a paper towel and brought back to the laboratory for imaging. *In situ* measurements were duplicated at each marsh sample site. After return to the laboratory, the sensor films were calibrated with identical response time by using Fe^{2+} standards prepared in seawater which was collected from the

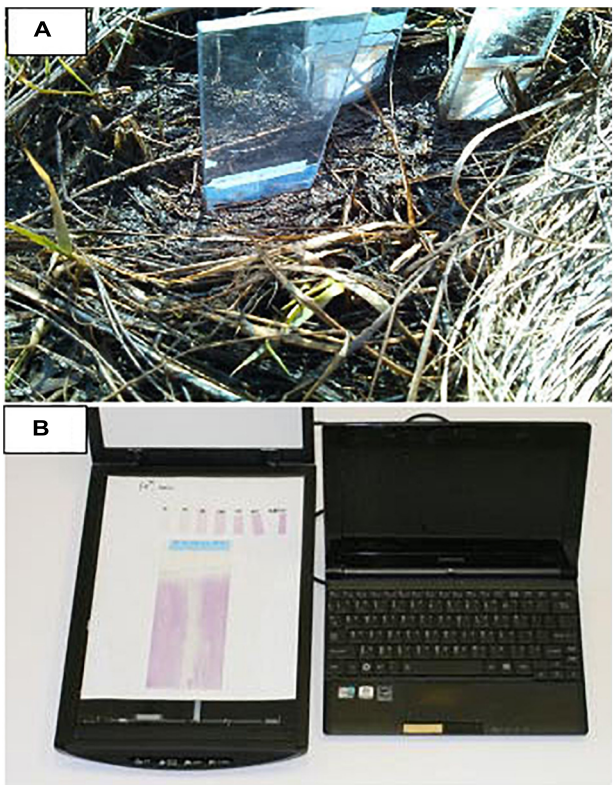

FIGURE 2 | (A) *In situ* deployment of planar optical sensors of Fe^{2+} and H_2S in salt marshes. The sensor sheet strip was mounted on a polycarbonate plastic sheet with a beveled end and inserted into the marsh for a certain time. **(B)** The 2-dimensional sensing image associated with calibration strips was recorded with a flat scanner (Canon). Reprinted from Encyclopedia of Ocean Sciences, 3rd edition, vol. 4. Zhu Q., *In situ* Planar Optical Sensors for Sediment Diagenesis Study, pp. 147–156, Copyright 2019, with permission from Elsevier.

same sample site. The colored Fe^{2+} sensor strips were imaged by a flat scanner (Canon), and all color images were analyzed with Maxim DL image processing software version 2.0X (Diffraction Limited) and Image-Pro plus version 4.1 for Windows (Media Cybernetics). The isolated green bands of the color images were used to calculate the absorbance within individual pixels. *In situ* measurements of 2-D Fe^{2+} distributions in pore water were conducted at October 2014, April 2015, and September 2015.

2-D distributions of dissolved H_2S in salt marshes were measured by two different optical planar H_2S sensors. The 2-D H_2S distributions in the October 2014 samples were measured by a fluorescence planar sensor in box cores which were collected from each site and incubated/re-equilibrated with seawater (collected from the same site) in the laboratory for 24 h at room temperature (22°C) with constant aeration of overlying water. The fluorescence H_2S planar sensor sheet was prepared by non-covalently immobilizing H_2S fluorescence indicator pyronin in an ethyl cellulose polymer membrane on a transparent polyester sheet, and coating with a layer of gas permeable silicone (Zhu and Aller, 2013). The fluorescence sensor responded well to dissolved H_2S in the range of non-detectable to 3.15 mmol/L with detection limit 40 μmol/L dissolved H_2S. The sensor response time was about 60 s, and it was very suitable for H_2S quantification in highly sulfidic salt marshes. However, it was only a moderately reversible fluorescence sensor, losing its response after 5–6 measurement cycles (Zhu and Aller, 2013). The sensor film was cut into the strips of 3 cm × 15 cm for the following 2-D measurement: an H_2S sensor strip was installed on the inside of the front face of the box corer and sensing membrane contacted to the marsh sediment. The bottom of the box core was tightly sealed. After 24 h incubation, the fluorescence image of the H_2S sensor strip was taken at 577 nm (±10 nm) with excitation wavelength at 554 nm by using our home-made imaging system (Zhu and Aller, 2013). Image analysis and data calculations were performed with Maxim DL image processing software version 2.0X (Diffraction Limited) and Image-Pro plus version 4.1 for Windows (Media Cybernetics). Images were split into blue, green and red bands and the red band was used to calculate the intensities of individual pixels.

2-D H_2S distributions in other seasons, April 2015 (spring) and September 2015 (late summer), were obtained by *in situ* deployments using an irreversible H_2S colorimetric planar sensor that was prepared from diphenylcarbazone-Zn^{2+} complex in polyurethane hydrogel (D4) on a transparent polyester sheet, covered by a gas permeable silicone membrane to eliminate possible interfering hydrated ions. The blank sensor film showed a dark purple color with a maximum absorbance at 530 nm, and the sensor absorbance was inversely correlated with dissolved H_2S concentration in the range of 5–4,000 μmol/L (Yin et al., 2017). A 3.5 cm × 20 cm H_2S sensor film was mounted on one side of a 5 cm × 40 cm × 1 cm (width × length × thickness) polycarbonate plastic sheet with a beveled end, and the deployment method was the same as 2-D Fe^{2+} *in situ* measurement as described above. Response time of the H_2S sensor in marsh was 1–10 min (depend on the H_2S concentration in the marsh). After the reaction, the sensor film was pulled out of the sediment and rinsed with seawater. The color-changed sensing film was scanned within 20 min in the field by using a flat scanner (Canon). After return to the lab, the H_2S sensor responses were calibrated for identical response times by using H_2S standard solutions prepared from sodium sulfide in pH < 4 solutions. All color images, including sample sensing images, were analyzed with Maxim DL image processing software version 2.0X (Diffraction Limited) and Image-Pro plus version 4.1 for Windows (Media Cybernetics). The isolated green bands of the color images were used to calculate the absorbance within individual pixels.

Solid Phase Geochemistry

Cores for solid phase geochemistry (sulfur and iron) were taken by carefully inserting an aluminum tube (i.d., 7 cm) into the marsh peat. After the tube was positioned on the marsh surface, vertical cuts were made around the perimeter to minimize compaction as the core was inserted. Immediately after return to the laboratory, the cores were frozen. They were later defrosted only enough to permit the sediment to be extruded and then were sectioned into 1–2 cm intervals. The JoCo sediment cores had more peat and roots whereas the Big Egg sediment cores had fewer large roots and more mud. Small aliquots of sediment were removed from each section for solid phase geochemistry and the

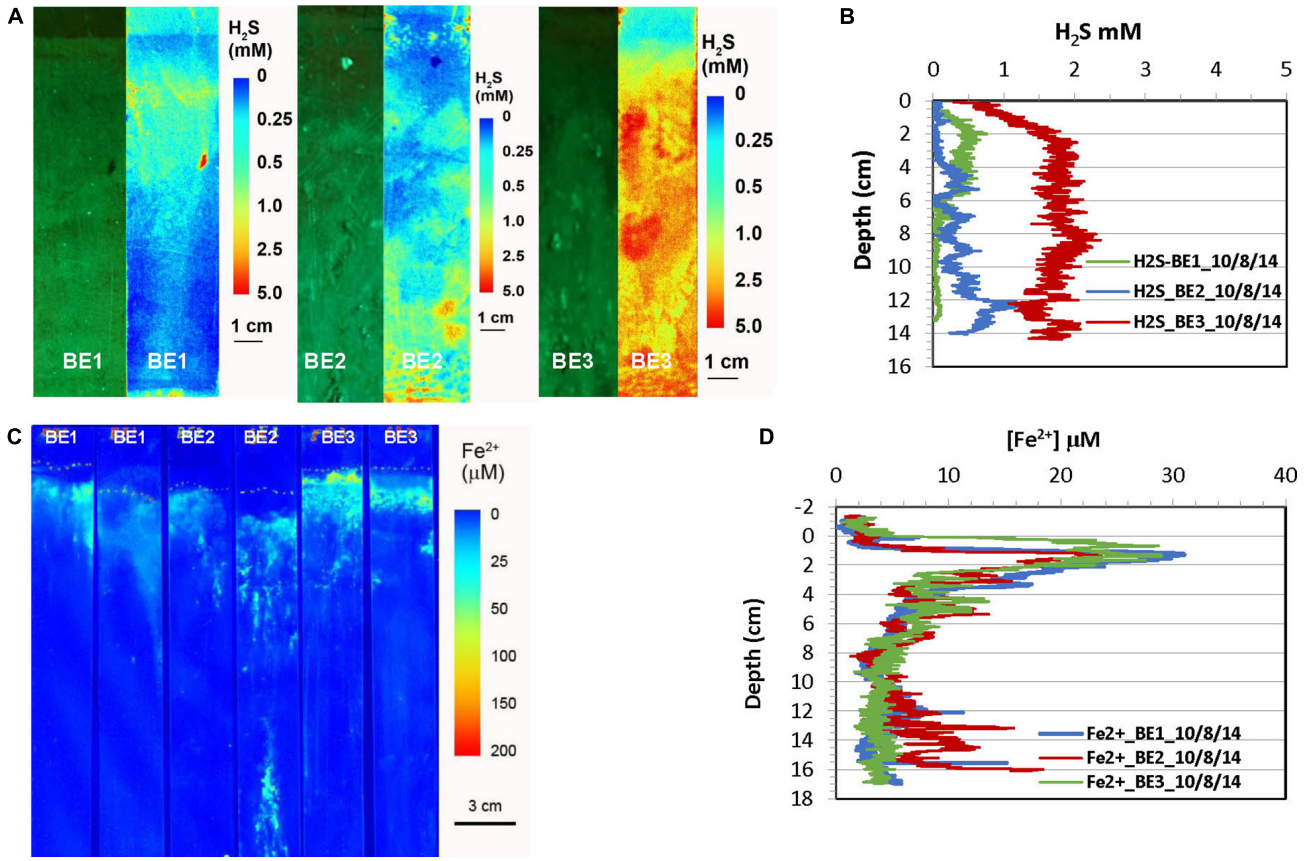

FIGURE 3 | H_2S and dissolved Fe^{2+} distribution patterns in the pore water of Big Egg (BE) marsh peats in fall 2014. **(A)** 2-D H_2S distribution patterns in the sediments, which were incubated 1 day in lab before H_2S imaging. The green panels are physical image of sediments and the color panels (pseudo color) are corresponding 2-D H_2S distributions. **(B)** Vertical H_2S profiles averaged from each 2-D H_2S distribution in panel **(A)**. **(C)** 2-D Fe^{2+} distribution patterns which were obtained by *in situ* deployments; dotted line marks the peat surface. **(D)** Vertical Fe^{2+} profiles averaged from each 2-D Fe^{2+} distributions in panel **(C)**.

remainder was weighed, dried, weighed again to determine water content and then ground to a powder. Solid phase reactive iron was measured by leaching ∼50 mg of dried sediment in 1 N HCl for 24 h at room temperature. Total Fe in the leach solution was measured colorimetrically using the ferrozine method (Stookey, 1970). Sulfur was measured in two pools—chromium reducible sulfides (CRS, dominantly pyrite, and FeS_2) and total sulfur, as described in Kolker (2005) and Cochran et al. (2013).

RESULTS

The high resolution 2-D Fe^{2+} and 2-D H_2S distribution patterns revealed by optical sensors in the six sampling sites in Big Egg (BE) and JoCo (JC) are shown in **Figures 3–8**. Vertical profiles of dissolved H_2S and Fe^{2+} at each site were calculated by averaging the data across each horizontal pixel layer.

The results of H_2S and Fe^{2+} distributions in the early fall sampling (October 2014) obtained by optical sensors are given in **Figures 3**, **4**. The green panels in **Figures 3A**, **4A** are visible images of the side views of marsh cores from Big Egg and JoCo, respectively. The root interweaving patterns can be clearly seen and are directly associated with the 2-D H_2S distribution patterns. The H_2S in all sampling sites showed a gradient in the top 10 cm depth. H_2S level in the surficial sediment of BE1 increased with depth and formed a maximum concentration band from 2 to 5 cm depth, with H_2S 0.5 mM, then sharply decreased to almost 0 below 6 cm. H_2S in BE2 also increased with depth but reached a maximum concentration ∼1 mM H_2S below 12 cm. Higher H_2S concentration was observed in BE3 where H_2S sharply increase from 0 to 2 mM in top 2 cm marsh and then reached maximum H_2S concentration below this depth. The 2-D H_2S distribution patterns in the BE sites showed significant lateral and vertical heterogeneities even though site BE2 was very close to BE3. Many "hot spots" of H_2S in the marsh were also elevated. However, the dissolved Fe^{2+} in the three sites BE1-3 showed a similar distribution pattern (**Figures 3C,D**). Fe^{2+} concentration sharply increased just below the water-sediment interface and reached Fe^{2+} maximum zone at 1–2 cm deep and then quickly dropped to non-detectable level. The maximum Fe^{2+} concretions in all BE sites were between comparable, with values of 20–30 μM Fe^{2+} in pore water (**Figure 3D**).

Figure 4 shows the H_2S and Fe^{2+} distributions in JoCo in the early fall season. Compared with their distributions in Big

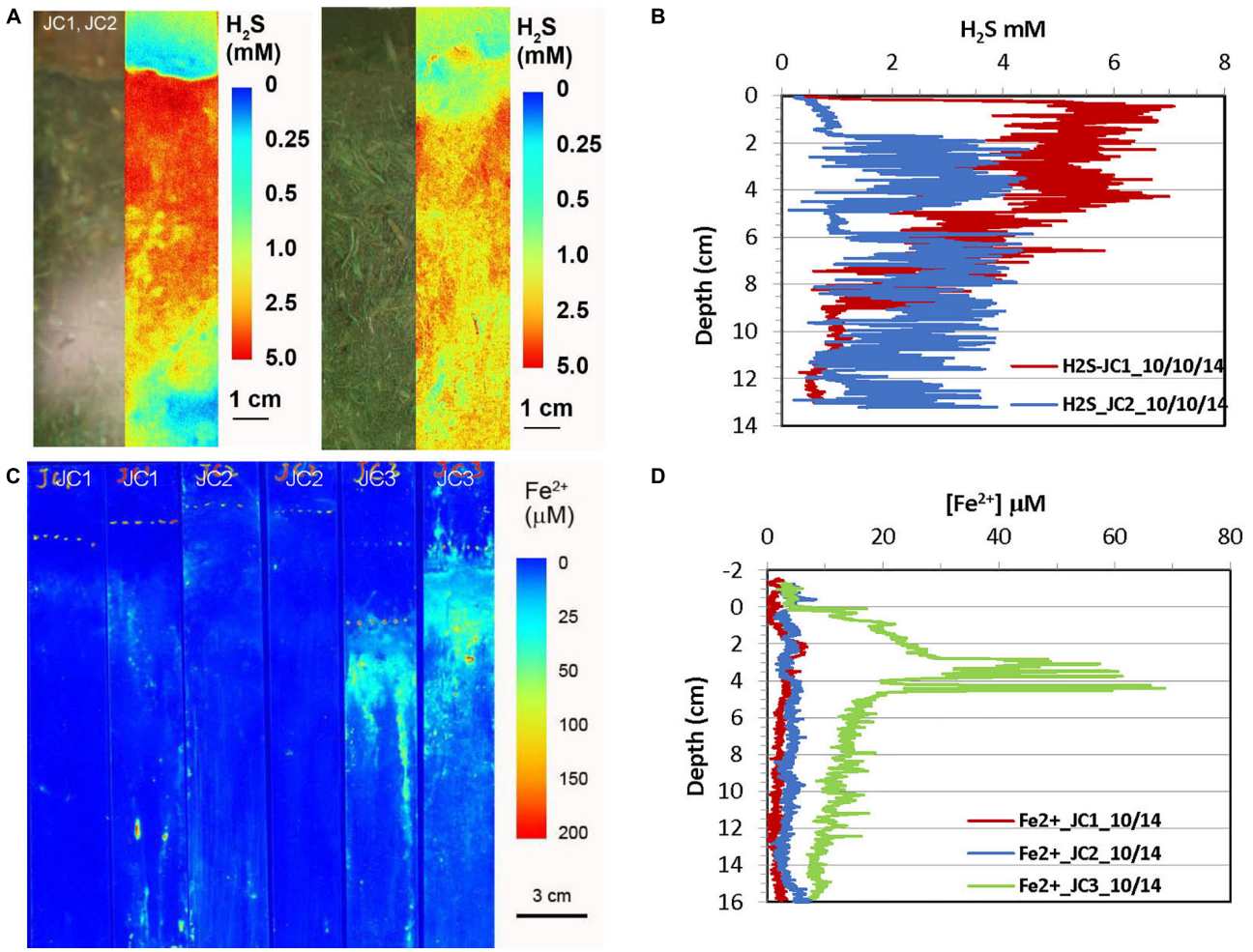

FIGURE 4 | H_2S and dissolved Fe^{2+} distribution patterns in the pore water of JoCo (JC) marsh peats in fall 2014. **(A)** 2-D H_2S distribution patterns in the sediments which were incubated for 24 h in lab before H_2S imaging. The green panels are physical image of sediments and the color panels (pseudo color) are corresponding 2-D H_2S distributions. **(B)** Vertical H_2S profiles averaged from each 2-D H_2S distribution in panel **(A)**. **(C)** *In situ* 2-D Fe^{2+} distribution patterns which were obtained by *in situ* deployments; white line marks the peat surface. **(D)** Vertical Fe^{2+} profiles averaged from each 2-D Fe^{2+} distributions in panel **(C)**.

Egg, H_2S concentrations in JoCo, 3–6 mM, are much higher than those in Big Egg. H_2S concentration in JC1 immediately reached a maximum of 6 mM just below the sediment surface and gradually decreased to 1 mM at 12 cm (**Figures 4A,B**). Accordingly, no Fe^{2+} was found in JC1 and JC2 sites except some Fe^{2+} hot spots due to the high and constant level of H_2S. The 2-D Fe^{2+} distribution pattern in JC3 is similar to that in the BE sites, but reached the maximum zone at 4 cm with Fe^{2+} concentration around 40 μM. It should be emphasized that the 2-D H_2S distributions in the fall 2014 season were measured in the laboratory with a box core incubation for 24 h at room temperature, using a fluorescence H_2S sensor (see section "Materials and Methods," Zhu and Aller, 2013). 2-D H_2S distributions in all other seasons were measured *in situ* with optical sensor sheets, as done for the 2-D Fe^{2+} distribution patterns.

2-D H_2S and Fe^{2+} distributions in the spring season at the site of JoCo and Big Egg were measured *in situ* on 05/01/2015 and 04/13/2015 (**Figures 5**, **6**), respectively. The concentrations of H_2S were generally <20 μM or non-detectable in the top 15 cm of marsh in JoCo (**Figure 5**), however, higher levels of H_2S (1–3 mM) were found at the sites of BE1-3 associated with root distribution patterns (**Figure 6**). Dissolved Fe^{2+} concentrations were non-detectable at JC1 in the top 15 cm, meanwhile dissolved Fe^{2+} was high (20–30 μM) in a very thin 0.5–2 cm layer at JC2, BE2, and BE3. Relatively higher Fe^{2+} levels were observed at JC2 and BE1, particularly at BE1, where dissolved Fe^{2+} was present from the sediment surface to 15 cm deep (Fe^{2+} was not measured deeper than 15 cm in any sampling) with a maximum concentration of 100 μM at 2 cm. The results showed that both dissolved H_2S and Fe^{2+} concentrations in Big Egg site were higher than those at JoCo in the spring season.

2-D distribution patterns of H_2S and Fe^{2+} in marsh pore water were mapped in a late summer sampling in September 2015, and the results from are summarized in **Figures 7**, **8**, respectively. H_2S concentrations were almost non-detectable in

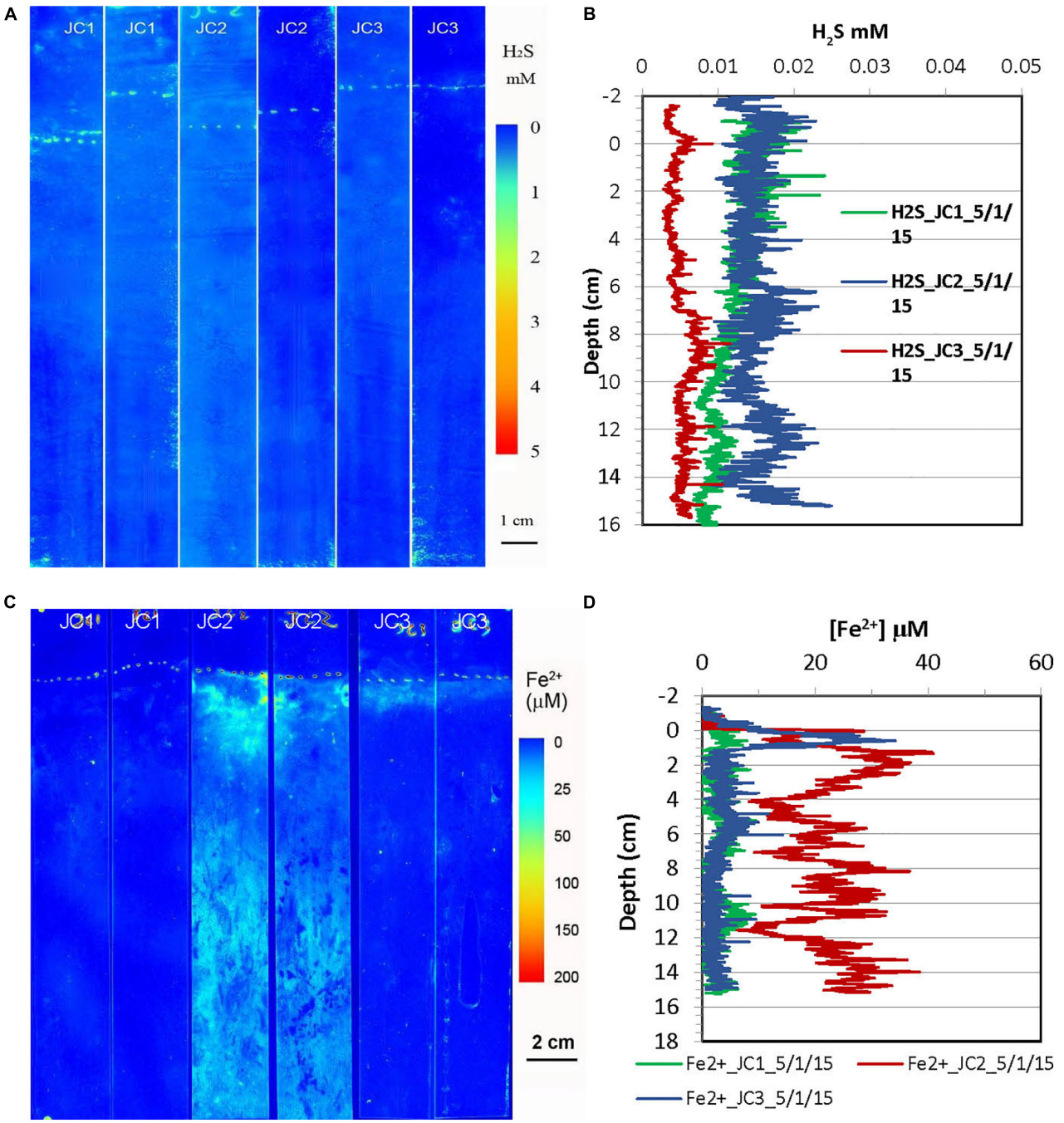

FIGURE 5 | H_2S and dissolved Fe^{2+} distribution patterns in the pore water of JoCo (JC) marsh peats in spring 2015. **(A)** 2-D H_2S distribution patterns (pseudo color) obtained by *in situ* measurements in sediments; white line marks the peat surface. **(B)** Vertical H_2S profiles averaged from each 2-D H_2S distribution in the panel **(A)**. **(C)** 2-D Fe^{2+} distribution patterns obtained by *in situ* deployments; white line marks the peat surface. **(D)** Vertical Fe^{2+} profiles averaged from each 2-D Fe^{2+} distributions in the panel **(C)**.

the top 2 cm of marsh but started to significantly increase below this depth and reached maximum concentrations of 2–3 mM at about 10 cm at the JC1 and JC2 sites. H_2S concentrations at sites of JC3, BE1, and BE2 were in the range of 1–1.5 mM below 8 cm which was smaller than that in JC1 and JC2, and no H_2S was observed in the top 8 cm. At BE3, H_2S was immediately elevated under marsh surface and increased to >2 mM H_2S below 4 cm depth. Similarly to the 2-D H_2S distributions obtained in the lab (**Figures 3A**, **4A**), complicated and heterogeneous H_2S distributions in the marsh can be seen associated with rhizospheres structures (**Figures 7A**, **8A**). 2-D Fe^{2+} vertical distributions in all JoCo sites in summer showed very large

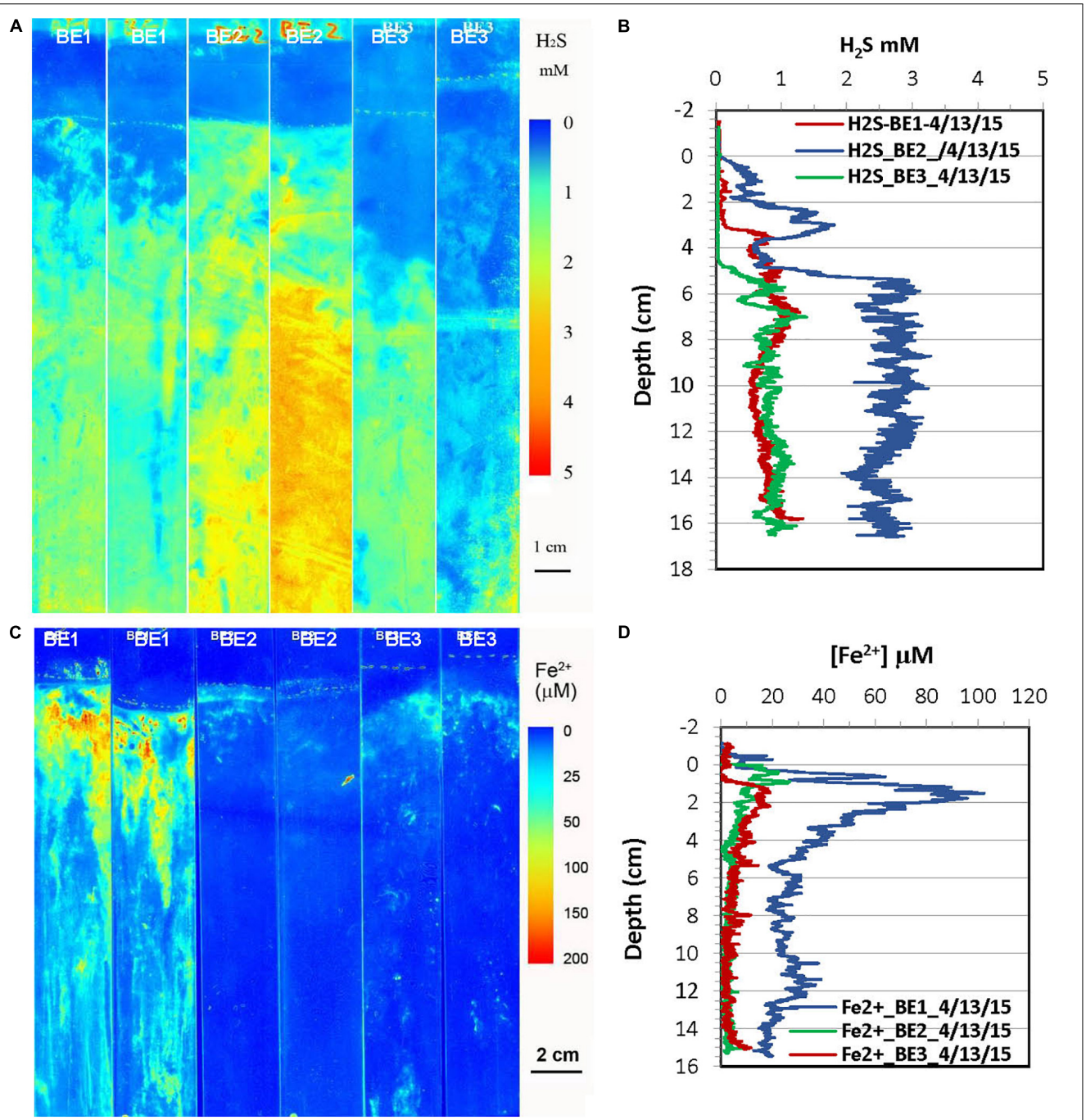

FIGURE 6 | H_2S and dissolved Fe^{2+} distribution patterns in the pore water of Big Egg (BE) marsh peats in spring 2015. **(A)** 2-D H_2S distribution patterns (pseudo color) obtained by *in situ* measurements in sediments; white line marks the peat surface. **(B)** Vertical H_2S profiles averaged from each 2-D H_2S distribution in the panel **(A)**. **(C)** 2-D Fe^{2+} distribution patterns obtained by *in situ* deployments, white line marks the peat surface. **(D)** Vertical Fe^{2+} profiles averaged from each 2-D Fe^{2+} distributions in the panel **(C)**.

variations and many "hot spots" and "cold spots" from the marsh surface down to 14 cm depth. Fe^{2+} concentrations at the hot spots may have reached as high as >200 μM (**Figure 7C**), but may have sharply dropped to non-detectable levels in cold spots. In general, the average Fe^{2+} concentrations in JoCo were smaller than those at the Big Egg sites, where Fe^{2+} showed a maximum zone from 0 to 4 cm, with concentrations of 50–200 μM, and sharp decreases to <50 μM or non-detectable below 4 cm (**Figure 8C**).

The pH, redox potentials (E_h) and salinity of the discrete pore water samples collected at 5, 10, 15, and 25 cm depth at the marsh sites during different seasons are summarized in **Table 1**. The pH

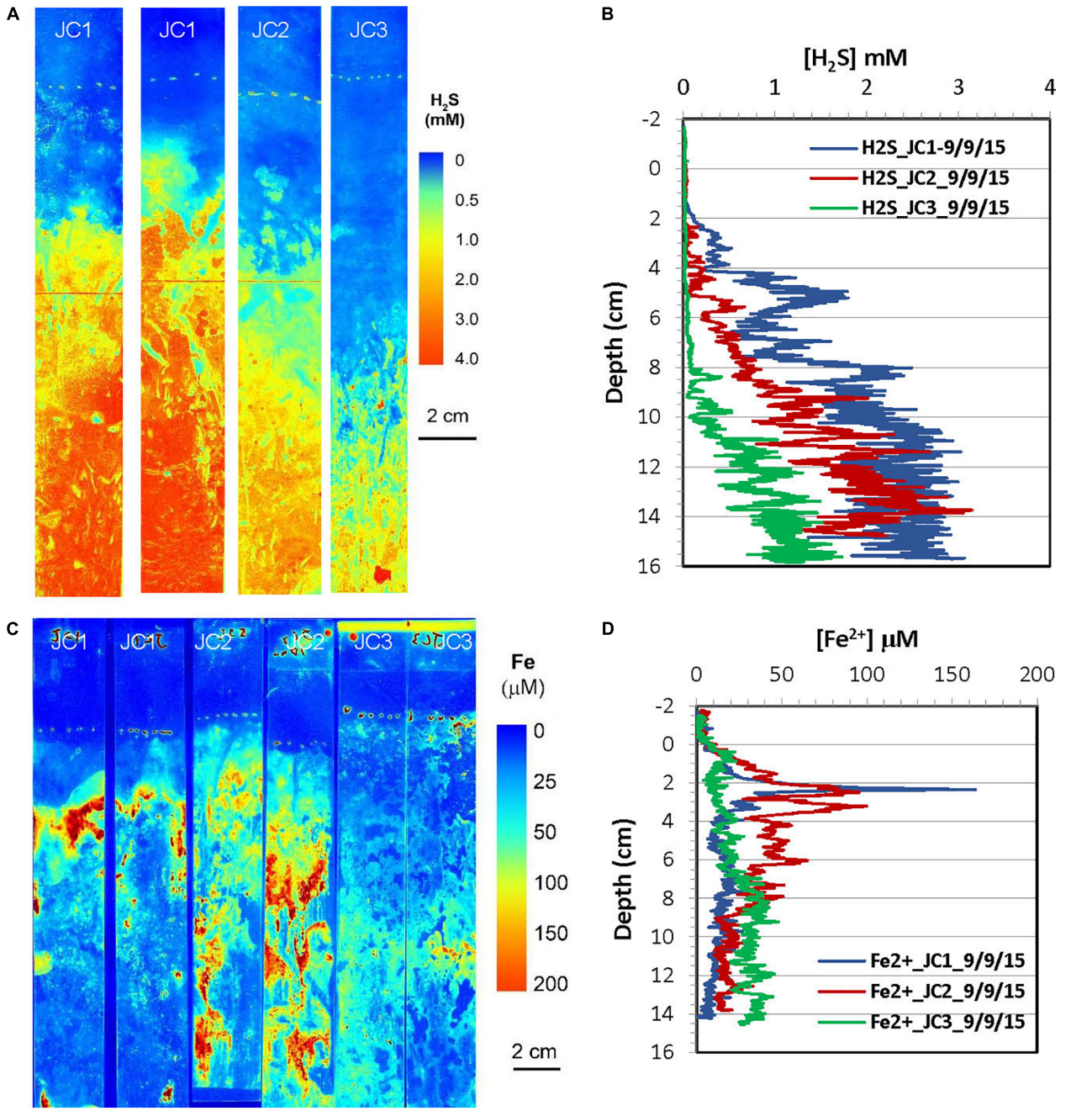

FIGURE 7 | H_2S and dissolved Fe^{2+} distribution patterns in the pore water of JoCo (JC) marsh peats in summer 2015. **(A)** 2-D H_2S distribution patterns (pseudo color) obtained by *in situ* measurements in sediments; white line marks the peat surface. **(B)** Vertical H_2S profiles averaged from each 2-D H_2S distribution in the panel **(A)**. **(C)** 2-D Fe^{2+} distribution patterns obtained by *in situ* deployments; white line marks the peat surface. **(D)** Vertical Fe^{2+} profiles averaged from each 2-D Fe^{2+} distributions in the panel **(C)**.

values of all sites and seasons were mostly <7, and the vertical pH data showed slight increases with depth below 5 cm. No obvious pH seasonal variation was observed at all depths. However, the pH at JoCo was likely lower than pH of Big Egg at the same depth in the same season.

Redox potential (E_h) obtained from each marsh site below 5 cm was negative. It decreased with depth at most sites and also showed a significant seasonal and spatial variation for both Big Egg and JoCo marsh sites. At JoCo, the E_h of summer and fall ranged from ∼ −200 to ∼ −350 mV, and it increased to −40 ∼ −170 mV in spring. The E_h values at Big Egg were in the range of −12 to about −380 mV in summer and fall, but showed high spatial and temporal variance. In the spring season, the E_h values of Big Egg were in the range of −200 ∼ −250 mV at all

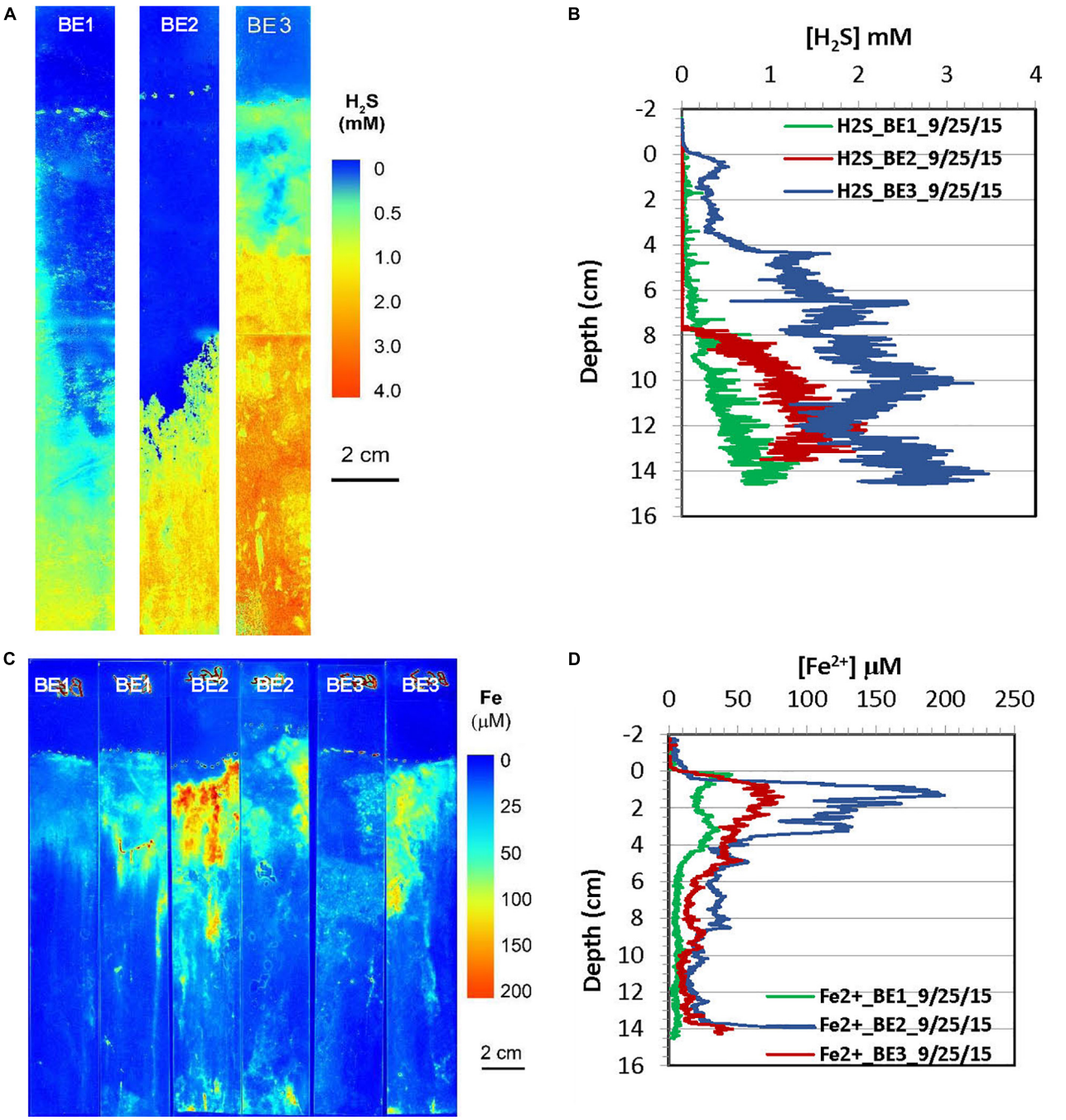

FIGURE 8 | H_2S and dissolved Fe^{2+} distribution patterns in the pore water of Big Egg (BE) marsh peats in summer 2015. **(A)** 2-D H_2S distribution patterns (pseudo color) obtained by *in situ* measurements in sediments; white line marks the peat surface. **(B)** Vertical H_2S profiles averaged from each 2-D H_2S distribution in the panel **(A)**. **(C)** 2-D Fe^{2+} distribution patterns obtained by *in situ* deployments; white line marks the peat surface. **(D)** Vertical Fe^{2+} profiles averaged from each 2-D Fe^{2+} distributions in the panel **(C)**.

depth, but this was consistent with the high H_2S values found in spring in this marsh (**Figures 6A,B**). The salinities of all sampling sites did not show obvious changes either with depth or season, ranging from 27 to 30.

The concentrations of Fe^{2+}, total hydrogen sulfide (ΣH_2S), phosphate and ammonium in pore water were also determined by traditional methods *via* "sipper" sample collection method at discrete depths of 5, 10, 15, and 25 cm. The results are summarized in **Table 2**. Fe^{2+} in pore water of JoCo and Big Egg were generally very low (<10 μM) and no obvious changes with depth except the spring data of JC2 which increased from 77 to 141 μM from 5 to 16 cm. The relative high Fe^{2+} concentration of

TABLE 1 | Pore water pH, redox potential and salinity data obtained *in situ* in Big Egg and JoCo marshes, Jamaica Bay, NY.

		pH			Redox potential E_h(mV)			Salinity (PSU)		
Marsh Site	**Depth (cm)**	**Fall '14**	**Spring '15**	**Summer '15**	**Fall '14**	**Spring '15**	**Summer '15**	**Fall '14**	**Spring '15**	**Summer '15**
JoCo		**10/10/14**	**5/1/15**	**9/9/15**	**10/10/14**	**5/1/15**	**9/9/15**	**10/10/14**	**5/1/15**	**9/9/15**
JC1	5	6.45	4.88	6.2	−230	−41	−325	28	32	ND
	10	6.41	6.08	6.15	−273	−60	−325	29	27	ND
	15	6.50	6.04	6.35	−270	−90	−350	29	28	ND
	25	6.55	6.25	6.23	−290	−210	−350	29	27	ND
JC2	5	6.30	5.40	6.82	−185	−39	−198	28	28	ND
	10	6.55	5.70	6.15	−220	−113	−277	28	26	ND
	15	6.35	5.62	6.13	−230	−98	−307	28	25	ND
	25	6.60	6.30	5.77	−250	−160	−321	28	24	ND
JC3	5	6.13	5.87	6.64	−220	−86	−234	29	35	ND
	10	6.42	6.04	6.06	−270	−106	−247	30	31	ND
	15	6.53	6.67	6.12	−275	−128	−320	32	27	ND
	25	6.64	6.32	5.95	−285	−164	−235	32	28	ND
Big Egg		**10/8/14**	**4/13/15**	**9/25/15**	**10/8/14**	**4/13/15**	**9/25/15**	**10/8/14**	**4/13/15**	**9/25/15**
BE1	5	6.12	7.01	IV	−125	−190	IV	27	28	ND
	10	5.74	7.09	6.79	−75	−233	−345	27	27	ND
	15	6.36	7.12	IV	−190	−186	IV	27	28	ND
	25	6.45	6.84	6.85	−133	−186	−367	27	28	ND
BE2	5	6.70	NS	7.15	−27	NS	−371	28	NS	ND
	10	7.10	7.08	7.02	−12	−217	−374	28	29	ND
	15	IV	6.52	IV	IV	−230	IV	30	29	ND
	25	6.50	6.65	6.67	−240	−195	−383	29	29	ND
BE3	5	6.00	NS	NS	−130	NS	NS	28	NS	NS
	10	6.46	6.88	NS	−200	−250	NS	28	30	NS
	15	6.50	7.26	NS	−150	−187	NS	29	30	NS
	25	6.34	7.09	NS	−230	−186	NS	29	30	NS

ND, not determined; IV, insufficient volume for electrode; NS, no sample.

JC2 in spring was also observed by the optical sensor (**Figure 5C**), but no spatial and seasonal variances of Fe^{2+} concentrations were observed by the traditional lab methods. ΣH_2S measured in the fall and summer seasons was typically higher than in the spring season, and the average ΣH_2S concentrations at the JoCo sites were higher than those at Big Egg. However, the BE sites showed much higher ΣH_2S than JC in the spring season, which was consistent with the dissolved H_2S level obtained by *in situ* sensing (**Figures 5A**, **6A**). Ammonium concentrations also varied with season and location in Jamaica Bay. The NH_4^+ concentrations at sites in BE were as high as 100–900 μM in spring and summer, but decreased to <158 μM in fall. The NH_4^+ concentrations of JC in spring and summer were much lower than those of BE, but they were higher than BE in fall. Similar to ammonium, phosphate also showed relative higher concentrations at the site of BE, and the phosphate concentration sequence at different seasons were summer > spring > fall in both BE and JC sites.

The solid phase organic carbon, total sulfur (S), CRS acid leaching Fe and degree of pyritization (DOP) at different sites and seasons are summarized in **Table 3**. Total sulfur concentrations in JC were slightly higher in fall season, but its distribution at BE2 was different from other sites and higher sulfur was observed in spring at BE2. CRS showed higher concentrations at each depth in the spring than that in summer. It was typically increased with depth but a decreasing pattern was found at site BE2. The distribution patterns of acid-leachable iron in JC and BE were also different– all three JoCo sites showed higher solid phase Fe in summer than in spring, but in contrast, Big Egg marsh had much higher solid phase Fe in spring than summer. CRS and acid leachable Fe in the fall season were not analyzed.

DISCUSSION

Heterogeneities of Fe^{2+} and H_2S Distributions in Salt Marsh Pore Water

Salt marshes are sites of intense biogeochemical reactions involving anoxic organic matter remineralization, which typically result in dramatic changes in the concentration of H^+, Fe^{2+}, H_2S, and other pore water species in the upper layer of marsh sediments (Morse et al., 1987; Canfield et al., 1992; Brendel and Luther, 1995; Bull and Taillefert, 2001; Zhu and Aller, 2013; Yin et al., 2017; Koop-Jakobsen et al., 2018).

TABLE 2 | Pore water solute data obtained from Big Egg and JoCo marshes, Jamaica Bay, NY.

		NH_4^+ (μM)			HPO_4^{3-} (μM)			ΣH_2S (μM)			Fe^{2+} (μM)		
Marsh Site	**Depth (cm)**	**Fall '14**	**Spring '15**	**Summer '15**	**Fall '14**	**Spring '15**	**Summer '15**	**Fall '14**	**Spring '15**	**Summer '15**	**Fall '14**	**Spring '15**	**Summer '15**
JC1	5	2.0	57	4.9	0.2	3.6	14	2,876	4.5	2,314	3	8	5
	10	23	157	41	0.2	7.9	20	6,095	17	4,301	3	3	*NS*
	15	28	193	134	0.2	8.7	20	5,587	43	4,658	7	6	*NS*
	25	77	224	96	0.3	9.2	24	6,697	660	4,275	2	7	*NS*
JC2	5	36	1.6	0.0	0.4	0.0	4.3	846	5.4	*NS*	2	77	15
	10	71	2.6	0.0	0.5	0.0	1.0	1,594	4.5	133	3	96	15
	15	2.6	7.3	0.0	0.3	0.0	1.1	1,973	133	588	3	141	*NS*
	25	198	41	2.0	1.0	7.2	4.7	3,487	343	1,800	4	11	*NS*
JC3	5	10	26	31	0.2	1.1	11	3,470	2.1	282	4	6	15
	10	71	181	35	0.5	4.5	11	5,406	4.9	480	6	4	15
	15	102	291	11	0.1	6.4	22	9,416	24	4,056	4	3	*NS*
	25	170	248	23	0.4	7	22	8,539	390	2,891	20	6	*NS*
BE1	5	14	240	111	0.1	11	90	1,234	272	1,200	5	2	11
	10	4.2	340	207	0.0	40	161	252	882	3,015	5	2	5
	15	59	265	344	0.4	28	44	17	413	1,370	6	4	0
	25	1.0	245	445	0.1	20	91	85	509	5,381	6	3	1
BE2	5	18	882	589	0.2	85	115	17	2,476	2,962	2	3	0
	10	28	336	752	0.2	26	130	9	926	4,022	3	3	2
	15	*NS*	160	522	*NS*	24	111	4,965	2,576	3,178	4	4	5
	25	158	73	637	0.9	11	100	4,436	1,431	5,491	3	2	2
BE3	5	5.8	*NS*	582	0.3	*NS*	164	273	1,846	2,143	4	*NS*	3
	10	4.8	610	759	0.4	72	212	840	226	4,164	4	1	4
	15	6.5	207	NS	2.1	13	*NS*	2,116	368	3,916	3	2	*NS*
	25	14	238	762	1.0	15	85	2,366	*NS*	6,722	3	1	6

NS, no sample.

Compositional changes of $Fe^{2+}$and H_2S with depth in sediment pore water are usually assumed to occur in an overall average vertical progression. Significant heterogeneity and complex three dimensional reaction patterns over mm to cm scales can result, however, from bioturbation activity (Zhu and Aller, 2013; Yin et al., 2017). In salt marshes, the growth of wetland plants and oxygen transport through the aerenchyma lacunae of plants from aboveground sources to rhizosphere can also create a complicated thin layer of aerobic environment around roots through the radial oxygen loss (ROL) from roots (Armstrong, 1979; Howes and Teal, 1994; Colmer, 2003; Han et al., 2016; Koop-Jakobsen et al., 2018). Most of the selected study sites in Jamaica Bay are dominated by saltmarsh cordgrass *S. alterniflora*, in which the roots extensively intergrow into a dense network over at least the top 30 cm of the peat. Thus, it is expected that the 2-D distribution patterns of Fe^{2+} and H_2S in marsh peat are influenced by the plant root growth patterns. We hypothesize that the oxygen transport through plant rhizosphere and the radial oxygen loss can generate a time-dependent 3-D distribution pattern of low level dissolved H_2S and Fe^{2+} (cold-spots) associated with individual plant roots in marsh peat.

In order to test this hypothesis and study Fe^{2+} and H_2S distributions and the associated biogeochemical processes in marsh peat with a high density of living plants, box cores made of clear acrylic plastic were collected from each site in October 2014 and the H_2S sensor deployments were conducted in the laboratory so that the plant root features and sensor foil deployment position can be directly seen from side of the core. The 2-D H_2S distribution measured by a reversible H_2S fluorescence planar sensor was compared to the visible image of peat core (side view). The green color of the visual images (**Figures 3A**, **4A**) was from the visual light source (white is not available in the image system used). The corresponding 2-D H_2S images in **Figures 3A**, **4A** (shown as pseudo-color, reflecting concentrations) revealed that the concentration distribution patterns were directly associated with the plant root structures in marsh peat. The H_2S concentrations around the roots were <1 mM which was five times less than in the surrounding peat. The results in **Figures 3A**, **4A** were measured in the laboratory in incubated box cores with aeration of overlying seawater for 24 h at room temperature without drainage, the changes of environmental conditions could alter oxygen transport and radial oxygen loss in marsh (Howes and Teal, 1994; Colmer, 2003), as well as H_2S and Fe^{2+} distributions around the roots. In order to avoid these possible artifacts, the real-time 2-D H_2S and Fe^{2+} distribution patterns in salt marshes were studied by deploying the irreversible H_2S (Yin et al., 2017) and dissolved Fe^{2+} (Zhu and Aller, 2012) colorimetric planar sensors *in situ* at different seasons. The real-time data in **Figures 5–8A,C** showed that the distribution patterns of H_2S and Fe^{2+} in sulfidic marsh

TABLE 3 | Solid phase organic carbon, total sulfur, chromium reducible sulfide (CRS), acid leachable iron and degree of pyritization (DOP) in the marsh sediments of JoCo and Big Egg, Jamaica Bay, NY.

		C (mmol/g)				S (μmol/g)				CRS (μmol/g)				Fe (μmol/g)				DOP*	
Marsh Site	Depth (cm)	Fall '14	Spring '15	Summer '15	Spring '16	Fall '14	Spring '15	Summer '15	Spring '16	Fall '14	Spring '15	Summer '15	Spring '16	Fall '14	Spring '15	Summer '15	Spring '16	Summer '15	Spring '16
JC1	5	–	26.2	28.4	22.5	–	432	1,040	773	–	–	136	222	–	13.6	12.6	8.0	0.84	0.93
	10	–	24.8	25.8	24.3	–	354	615	907	–	–	121	264	–	9.1	34.1	8.9	0.64	0.94
	15	–	23.8	25.1	27.4	–	344	649	829	–	–	84	154	–	4.8	43.5	5.2	0.49	0.94
	25	–	24.2	20.6	24.7	–	379	715	836	–	–	117	178	–	15.6	43.6	4.4	0.57	0.95
JC2	5	0.36	15.1	23.9	18.2	514	202	660	425	–	–	48	86	–	42.0	126	25.4	0.16	0.63
	10	0.51	17.4	16.0	18.7	496	266	452	694	–	–	127	571	–	24.8	100	10.8	0.39	0.96
	15	0.27	13.6	16.3	11.2	5,412	220	517	464	–	–	194	81	–	33.7	124	44.1	0.44	0.48
	25	1.03	9.8	17.2	15.7	850	209	806	609	–	–	*252*	333	–	39.8	163	31.9	0.44	0.84
JC3	5	0.24	24.1	23.9	22.2	749	365	724	522	–	–	63	20	–	9.5	19.4	7.1	0.62	0.59
	10	0.47	25.1	22.5	26.9	602	318	647	824	–	–	27	179	–	3.3	13.8	6.1	0.49	0.94
	15	0.11	20.7	25.6	21.8	668	330	530	747	–	–	*83*	179	–	5.8	9.6	6.8	0.81	0.93
	25	0.39	25.8	–	22.2	752	377	–	720	–	–	–	109	–	11.5		8.3	–	0.87
BE1	5	–	7.6	0.27	2.48	–	372	31	504	–	–	8	212	–	78.9	13.5	76.7	0.23	0.58
	10	–	–	0.05	3.10	–		15	520	–	–	18	242	–	121.1	5.5	73.6	0.62	0.62
	15	–	5.4	2.3	8.6	–	584	427	711	–	–	166	722	–	156.5	70.7	81.6	0.54	0.82
	25	–	–	5.1	12.1	–		1,029	1,970	–	–	418	590	–	–	71.7	–	–	–
BE2	5	1.70	10.0	3.3	12.3	119	350	170	1,080	–	–	157	343	–	67.6	29.7	98.4	0.73	0.64
	10	5.91	15.8	3.5	8.0	402	853	264	418	–	–	193	160	–	198.6	22.0	60.0	0.81	0.57
	15	*7*	11.0	2.3	6.8	525	668	149	791	–	–	82	461	–	158.4	22.0	93.4	0.65	0.71
	25	–	–	1.1	2.7	–		100	290	–	–	73	85	–	–	19.9	30.0	–	–
BE3	5	8.25	11.0	8.4	7.7	654	436	647	819	–	–	355	383	–	68.3	104	127	0.63	0.60
	10	6.30	6.0	8.4	6.9	728	256	475	894	–	–	244	396	–	49.4	49.5	78.3	0.71	0.72
	15	5.95	6.1	4.4	7.0	620	150	252	831	–	–	192	577	–	45.3	43.9	93.6	0.69	0.76
	25	4.67	4.0	3.2	5.6	560	69	272	693	–	–	150	226	–	21.2	44.6	92.8	0.63	0.55

– Indicates not analyzed.

pore water were significantly complicated by belowground radial oxygen loss from roots into the surrounding marsh peat. The oxygen leaked from the roots formed a thin oxic layer in which the dissolved H_2S and Fe^{2+} were oxidized to sulfate and Fe-oxide (e.g., iron plaque), resulting in a thin zone of low levels of H_2S and Fe^{2+} surrounding the roots in the sulfidic peat. Furthermore, oxygen and/or nitrate, rather than sulfate, served as the electron acceptors for organic matter remineralization in the thin oxic layers. Such an interface of oxic-anoxic sediment around the roots can be seen in both visible peat images and 2-D H_2S images, indicating heterogeneous remineralization patterns. The low and/or undetectable spots/tracks (cold spots) of H_2S and Fe^{2+} associated with root structures in **Figures 3–8A,C** was a direct evidence for our hypothesis, and the cold spots of H_2S and Fe^{2+} surrounding individual roots became more pronounced (**Figures 7**, **8**) when more oxygen transport and high oxygen leakage occurred in the summer season (Colmer, 2003; Soana and Bartoli, 2013).

H_2S is a phytotoxin to marsh plants, with a the threshold that can be harmful to *S. alterniflora* of about 2 mM [see Kolker (2005) and references therein]. Long-term exposure of the marsh plants to high levels of H_2S can cause plant die-off and marsh peat collapse. We noted that the average H_2S levels at JoCo marsh could be >4 mM just below the marsh surface (**Figures 4A,B**) or in deep peat (**Figure 7A**, JC1) in the fall and summer seasons, but JoCo is considered as a "healthy" marsh and plants grow well. We hypothesize that the oxic layers formed around roots of *S. alterniflora* help the plants survive in the high levels of H_2S by reducing sulfide absorption. We tested this hypothesis at the National Synchrotron Light Source-II (Brookhaven National Laboratory; Feng et al., 2018). We used the Hard X-ray Nanoprobe Beamline to obtain nanometer-scale measurements of trace elements in *S. alterniflora* root tissue. The results showed that when iron concentrations in pore water and root epidermis were high, the root epidermis showed lower concentrations of S and P even though sulfide and phosphate in the pore water were high in late summer (Feng et al., 2018). At the same time, pore water Fe was lower than in the spring sampling, but Fe in the root epidermis was high. This pattern is consistent with the roots producing an oxic microenvironment with oxygen transported into the peat through the roots, such that Fe^{2+} in the pore water is oxidized, producing iron "plaque" (i.e. FeOOH) on the root epidermis. This plaque prevents sulfide from entering the root tissue. Phosphate may also be excluded *via* adsorption onto the FeOOH or formation of an iron phosphate phase.

There are also many "hot spots" on the 2-D Fe^{2+} and H_2S images, reflecting the heterogeneous distributions of labile organic matter and the microniches of exoenzymes and microbes on sediment particles (Cao et al., 2013). We also noted that large variation of H_2S and/or Fe^{2+} distributions may occur in same

site in duplicate *in situ* measurements over distances of <1 m between two deployed sensor sheets.

In addition to the microscale heterogeneities of Fe^{2+} and H_2S distributions around plant roots, the 2-D H_2S and Fe^{2+} images also showed clear vertically and laterally heterogeneous distribution patterns. Note that no infaunal burrows were found in the measurements, suggesting that bioturbation is not a factor in these sediments. H_2S concentrations near the surface of the Big Egg sediment were relatively low but sharply increased below the water-sediment interface and reached maxima at ∼2 cm in the fall sampling at BE1 and BE3. The H_2S levels at JoCo marsh were elevated to 4–6 mM just below the marsh surface (**Figures 4A,B**). It should be pointed out that the 2-D H_2S distributions in the fall 2014 season (**Figures 3A**, **4A**) were incubated and measured in laboratory with the box core incubation without water drainage, but in all other sampling seasons, the H_2S measurements were performed *in situ* in the field. The real-time 2-D H_2S distributions (**Figures 5A**, **6A**, **7A**, **8A**) showed that H_2S levels in top 4 cm were low even in the summer season, and gradually increased to higher concentrations at depth. The high H_2S levels elevated just below the water-peat interface in **Figure 3A** (BE3) and **Figure 4A** (JC) were not found in the 2-D *in situ* measurements in the field. This phenomenon is likely caused by the pore water drainage in the marshes. The marshes of Jamaica Bay are periodically (tidally) submerged by seawater. An important pathway by which this water drains from marsh islands such as Big Egg and JoCo is vertically, and the two sites have distinctly different drainage velocities of 7.9 and 25.9 cm/d, respectively, as determined by Ra isotopes (Tamborski et al., 2017). Thus the concentrations of H_2S (and other solutes) in marsh peat pore water result from a balance between the rates of biogeochemical processes that produce or consume them and drainage. In summer and fall seasons, higher H_2S concentrations in JC marsh were produced due to the high sulfate-reduction bacteria activities and the relative high organic carbon concentration in this site (**Table 3**), but the more rapid drainage there produced high flow-through fluxes of H_2S through the marsh peat (Tamborski et al., 2017). As well, the effects of roots on the 2-D H_2S distribution patterns, are especially evident at JC in the summer, a time when marsh plant growth is dense and bacterial activity is high (**Figure 7A**).

2-D Fe^{2+} distributions were measured only by *in situ* sensor deployments, so visible images of the sensing marsh peat were not available. The spatially heterogeneous 2-D Fe^{2+} distributions also showed sharp vertical gradients that were closely correlated to the H_2S vertical distributions, especially in the low drainage BE marsh peats. Fe^{2+} concentration sharply increased just below the water-sediment interface and reached Fe^{2+} maximum zone at 1–2 cm deep. At depths below which the reactive particulate Fe-oxide had been depleted, sulfate reduction dominated the metabolism, producing dissolved sulfide species (H_2S, HS^-, and S^{2-}), and an increase of H_2S with depth in pore water below the Fe^{2+} maximum zone (Bull and Taillefert, 2001; Jørgensen and Kasten, 2006; Johnston, 2011). The free sulfide subsequently scavenged the dissolved Fe^{2+} to form the reactive solid phase FeS, resulting in a Fe^{2+} maximum above the H_2S maximum zone in pore water (Bull and Taillefert, 2001). FeS is unstable and converts to the more stable form pyrite (FeS_2) by a variety of pathways (Howarth, 1979; Berner, 1984).

The *in situ* zonations of 2-D Fe^{2+} and H_2S distributions in **Figures 3–8** clearly showed this sequence: the maximum zones of Fe^{2+} were generally produced at 2–4 cm, and the H_2S levels increased to maxima below 4 cm. The *in situ* heterogeneous 2-D Fe^{2+} and H_2S distributions are useful for determining redox zonation and understanding the dominant biogeochemical processes occurring within the marsh peat. Both dissolved Fe^{2+} and H_2S can be efficiently removed by FeS_2 precipitation from pore water. When millimolar levels of H_2S occurred in marsh pore water, the dissolved Fe^{2+} concentrations were generally <20 μM at the same depths. On the other hand, the high pore water concentrations of Fe^{2+} were linked to low H_2S levels in all seasons. There were some Fe^{2+} "cold spots" co-distributed with low levels of H_2S, as seen in **Figures 7A,C**. As noted above, these cold spots are likely produced in the oxic and suboxic layers around roots and caused by O_2 transport down to the deep sediment through the rhizosphere. Unfortunately, H_2S and Fe^{2+} concentrations could not be simultaneously measured by optical sensor in the present study. Fe^{2+} concentrations at JC and BE were in the range of 10–100 μM, which is typical of coastal marsh pore water. High levels of Fe^{2+} in pore water may be harmful to plants because it may co-precipitate or adsorb the nutrients ammonium and phosphate in the marsh, preventing their uptake by the roots.

Seasonal Variation of H_2S and Fe^{2+} Distributions in Marsh Pore Water

H_2S distributions in marsh pore water at all sites varied seasonally, generally with higher H_2S levels in summer and fall, and lower or undetectable levels in spring (**Table 2** and **Figures 3–8**). At the JoCo marsh sites, dissolved H_2S in pore water was <0.02 mM found by sensors in the spring sensor deployments but it was elevated to as high as 3–6 mM in summer and fall at the same sampling sites. Thus was likely due to loadings of labile organic matter on the marshes produced in the summer in the eutrophic Bay, coupled with the temperature-dependent variation of the rate of microbial decomposition of organic matter. The discrete pore water samples showed the redox potential at JoCo from 5 to 15 cm was in the range of −41 to −200 mV in spring while it was lower, −180 to −350 mV, in summer and fall seasons, indicating less "reducing" environments in the marsh peat in the spring (**Table 1**). Our previous study showed that the exoenzymes and microbes in marine sediments have high activities in the summer and fall, but very low in winter and early spring (Cao et al., 2013). Thus, the temperature dependence of H_2S distributions was a direct reflection of the change in sulfate-reduction microbial activity with temperature. However, data in **Table 1** also showed a clear spatial heterogeneity of the redox potential at different marsh sites in the spring season. Relative lower redox potentials were found at Big Egg marsh sites in the spring compared to fall, the reason for this unusual phenomenon was not clear, but the stronger "reducing" conditions at BE resulted in high H_2S levels in the late spring (April-May) (**Figure 6A**), and as a consequence, likely caused

more plant die-off and marsh loss. H_2S distributions at BE sites in winter and early spring were not measured.

Typically, the high concentration of H_2S (or ΣH_2S) in anaerobic salt marshes comes from the reduction of sulfate during organic matter decomposition, generating a decreasing redox potential with depth (Hambrick III, DeLaune and Patrick, 1980), and a complicated 3-D pattern associated with the roots of plants due to oxygen transport and radial oxygen loss through roots. The redox potential can be used as an indicator of the degree of oxidation of marsh peat. The results in **Table 1** showed that the redox potentials of all sites generally decreased from 5 to 25 cm depth, but exhibited a clear seasonal variation. The redox potential in spring was much higher than that in summer and fall in JC, indicating the lower organic matter oxidation rate by sulfate in spring. The pH values of all sites and depths in summer and fall seasons are in the range of pH 6–7 with vague seasonal variations, implying that the intense oxidation of organic matter by various electron acceptors at warm temperature tend to buffer sediment pore water close to 6–7. Interestingly, the pH values of pore water at JC in spring are in the range of 5–6.5 which are lower than the pH values in other seasons. By integrating other geochemical parameters found at this site in spring, for example the high redox potentials (**Table 1**), extreme low total sulfide (**Table 2**) and non-detectable (<0.02 mM) dissolved H_2S (**Figure 5A**), we conclude that the rate of organic matter decomposition in JC in late spring (April–May) is still high, but oxidants with high redox potentials (such as O_2, nitrate, and Mn/Fe-oxides), rather than sulfate, dominate the redox reactions with organic matter at JC. This might be attributed to the healthy and high-density biomass of *S. alterniflora* and fast pore water drainage velocity in JC. The intertidal nature and fast drainage of the JC salt marsh could result in surface gas exchange playing a more important role in the sediment oxygen transports than in low drainage marshes like BE, resulting in a relatively higher redox potential in JC than BE in the spring season.

Fe^{2+} concentrations in marsh pore water also show seasonal changes (**Table 2** and **Figures 3C–8C**), but the seasonal changes are not very significant compared to the H_2S distribution variations, partially due to the low Fe^{2+} concentrations in the marsh pore water. But, the distribution patterns of Fe^{2+} are closely associated with H_2S distribution patterns in marsh pore water, as discussed above. It seems that Fe^{2+} concentrations in pore water at most sites of JoCo and Big Egg were relatively high in summer than in spring and fall.

The seasonal variation of H_2S and Fe^{2+} in marsh pore water should also be tightly linked to the plant life cycle. The previous studies have shown that the temporal changes in belowground biogeochemical processes, such as oxygen leakages from roots, sulfate reduction, sulfide oxidation, Fe^{2+} oxidation and precipitation etc., were well correlated with the changes in plant physiology (Hines et al., 1989; Soana and Bartoli, 2013; LaFond-Hudson et al., 2018). We did not measure directly the oxygen leakage from roots in this study, but the microscale "cold spots" of H_2S and Fe^{2+} in the 2-D distribution patterns associated with individual roots (**Figures 3–8A,C**) clearly indicated radial oxygen loss from roots. In the spring season, low temperatures decreased oxygen consumption in plant rhizosphere by slowing respiration in roots (Armstrong, 1979), resulting in more "excess" oxygen leakage into surrounding marsh peat and the increase of redox potential in sediment. This could be another possible explanation as to why the redox potential in JC marsh is higher in spring than other seasons (**Table 1**). In the summer season, dissolved organic matter could be released from the roots during active growth of *S. alterniflora* and rapidly enhance the sulfate reduction rate (Hines et al., 1989). We believe that any additional dissolved organic matter released from roots would also fuel the rate of Fe-oxide reduction, resulting in a relative high dissolved Fe^{2+} in marsh pore water (**Figures 7C**, **8C**). As a consequence, more active FeS was formed and accumulated in summer season in JC (**Table 3**).

Interaction of H_2S and Fe^{2+} as Seen in the Solid Phase: Degree of Pyritization

The precipitation of the solid phases FeS and FeS_2 (pyrite) as a result of elevated concentrations of H_2S and Fe^{2+} in the pore water effectively removes H_2S from solution, and is thus a geochemical means of controlling H_2S concentrations (Howarth, 1979; Berner, 1984). The pore water data described in sections "Heterogeneities of Fe^{2+} and H_2S Distributions in Salt Marsh Pore Water" and "Seasonal Variation of H_2S and Fe^{2+} Distributions in Marsh Pore Water" are essentially snapshots of conditions at the time of sampling. The composition of the solid phase can integrate the redox reactions occurring in the sediments over longer periods. We measured fractions of the solid phase S and Fe pools in the peat at all the sites (**Table 3**). For sulfur, the important pools include Acid Volatile Sulfide (AVS), CRS, and Total Sulfur. AVS is a measure of FeS-associated sulfur, CRS of the pyrite-associated sulfur and total S of the AVS, CRS, and all other forms, including organosulfur compounds. For iron, we measured a fraction termed "reactive" Fe, i.e. that obtained by a 1 N HCl cold leach of the dried sediment. This procedure extracts the portion of Fe that is diagenetically mobile and readily able to react with sulfide to produce the iron sulfide phases. Our prior experience in JoCo (Cochran et al., 2013) suggests that AVS < CRS ≤ Total S. The AVS pool is labile and converts to pyrite, which is a longer term sink for Fe and especially S in the marsh peat. In effect, the formation of pyrite removes dissolved sulfide from the pore water and stores it, lowering the exposure of the plants to this phytotoxin. The solid phase measurements enable calculation of a parameter termed the "Degree of Pyritization" (DOP), that is, the degree to which reactive Fe in the solid phase is associated with pyrite and is thus unable to further remove dissolved sulfide from pore water. DOP is defined as:

$$DOP = \frac{Fe_{pyrite}}{Fe_{Pyrite} + Fe_{reactive}} \quad (1)$$

where Fe_{pyrite} is calculated as CRS/2 (i.e. one mole of Fe per two moles of S in FeS_2), and $Fe_{reactive}$ is the acid leachable Fe. **Table 3** gives the solid phase DOP results.

The results in **Table 3** show that the total sulfur at JoCo is generally higher than that at Big Egg, but the CRS-sulfur concentrations are comparable at these two sites and the fraction

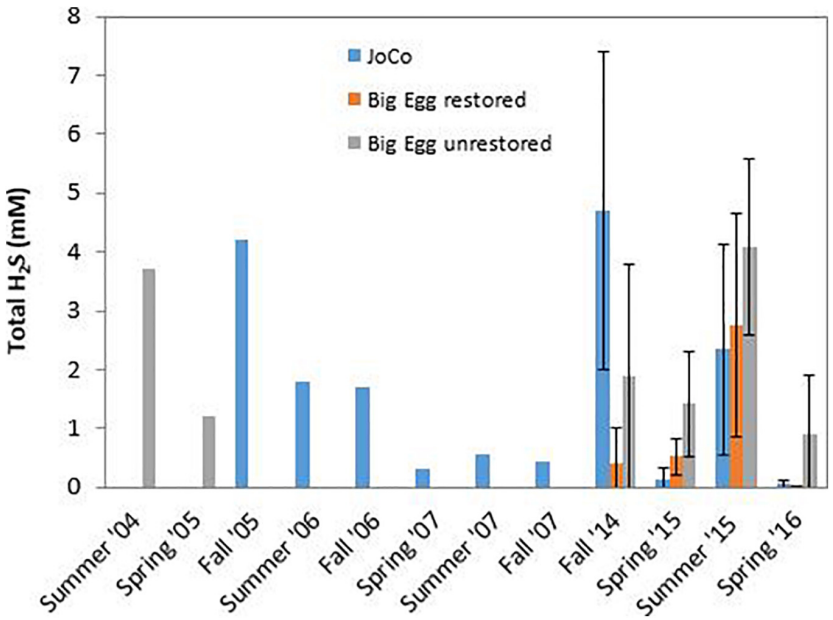

FIGURE 9 | Temporal variation of average total dissolved inorganic sulfide (ΣH_2S) in pore water of JoCo and Big Egg salt marsh at Jamaica Bay. BE1 is the restored marsh, BE2 and BE3 are the unrestored marsh. Data were averaged from ΣH_2S concentrations measured on samples taken at 4–5 discrete depths from 5 to 30 cm. Vertical lines demote 1σ uncertainties of the mean of several sites sampled in each marsh from 2014 to 2016.

of CRS in the total sulfur pool is much smaller in JoCo. To the extent that total sulfur includes diagenetically produced organosulfur compounds and sulfur associated with the marsh plants, this difference can be explainable by the higher organic content of the marsh sediments at JoCo. Both total sulfur and CRS-sulfur show vertical variations at different depths from surface to deep marsh peat, but the pattern at each site is not consistent even in the same season, implying significant heterogeneities of both organosulfur and pyrite-associated sulfur in the solid marsh peat, probably caused by the plant growth. Similar to dissolved H_2S and Fe^{2+} in pore water, the total sulfur, CRS-sulfur and acid leachable Fe in the peat also show seasonal differences between the summer 2015 and spring 2016 samplings. These reflect the redox cycling of the various pools of Fe and S over the year.

The DOP at JoCo is higher than that at Big Egg. Indeed, the DOP values at JoCo can approach 1, indicating that 100% of the reactive iron is associated with pyrite. These high values suggest that the biogeochemical control of pore water H_2S *via* FeS_2 precipitation is close to a limit and that high sulfide but low Fe^{2+} concentrations in the pore water can be expected, as observed.

Time Series of ΣH_2S in JoCo and Big Egg Marshes: 2014–2016

Our group has studied Jamaica Bay marshes since 2004 (Cochran et al., 2013, 2018). In particular, we have pore water ΣH_2S concentrations measured by "sipper" at the two marshes studied here. All samples were taken in the upper 25–30 cm and analyzed for ΣH_2S as described above. Analytical techniques were the same throughout and thus the values are comparable within and between the marshes. However, although sampling sites were in the same general area of each marsh, they were not identical over time. In addition, not all marsh sites were sampled in each year. The record of sampling includes: Big Egg- 2004/05, 2014-2016; JoCo- 2005-2007, 2014-2016. These time series of samples permit us to examine changes in the average concentration of ΣH_2S in pore water of the marsh peat in a depth zone in which root density is high and the plants can be considered susceptible to exposure to elevated levels of his phytotoxin. To do this, we calculated the average ΣH_2S value of the pore water analyses from sippers deployed from ∼5 to 30 cm. Generally, 4–5 sample depths were involved (e.g., 5, 10, 15, and 25 cm). All sites sampled in each marsh at a given time were averaged to produce a single ΣH_2S value, presumed to be representative of that marsh at that time. The results are shown in **Figure 9**, and the patterns in each marsh are as follows:

Big Egg: a portion of this marsh (BE1) was restored in 2003 by spraying sandy sediment from the adjacent subtidal bottom onto the marsh surface (Frame et al., 2006). The unrestored portion of the marsh was sampled in 2004/05 and again in our recent sampling. We also sampled the restored portion of the marsh in the present study (BE1). The effects of the sediment spray are well documented in the ^{210}Pb profile in the core taken in this area of the marsh (Cochran et al., 2018; data not shown). Concentrations of ΣH_2S in the unrestored portion of the marsh are as high as 3.5–4 mM in the summer and are quite similar between 2004/05 and 2014-16, with comparable values in comparable seasons (**Figure 9**). Samples from the restored portion of the marsh appear to have lower ΣH_2S in the pore water, and the offset is especially clear in the fall 2014, and spring 2015 and 2016 samplings.

JoCo: JoCo presents a conundrum in that it is considered a "healthy" marsh in Jamaica Bay, yet over the period 2005–2016, average ΣH_2S levels were >2 mM in summer and fall, 2006 and summer, 2015 and exceeded 4 mM in fall, 2005 and 2014. Offsetting these high concentrations is the fact that levels of ΣH_2S were low (<0.5 mM) at other sampling times, including in the spring, summer and fall, 2007, and were exceptionally low (∼0 mM) in spring, 2015 and 2016. Several factors controlling ΣH_2S are likely in play at JoCo. The large variations in ΣH_2S from sampling to sampling may in part be due to the fact that most of the reactive iron in the JoCo peat is associated with FeS_2 and is thus not able to readily react with H_2S produced *via* sulfate reduction. Secondly, although temperature is a strong control on bacterial activity and hence the production of H_2S, there is no clear relationship between mean air temperature during the month or week of sampling and mean pore water ΣH_2S (data not shown). As noted above, drainage rates in JoCo are the fastest seen of the marshes examined in this study (Tamborski et al., 2017). These rates may vary with time as a function of tides (neap vs. spring) and season (warm vs. cold; variation in precipitation). It is possible that at least the portion of JoCo studied is at or near a "tripping point" for degradation.

CONCLUSION

Pore water H_2S and Fe^{2+} distributions were measured at Big Egg and JoCo marshes in Jamaica Bay using *in situ* optical sensors that produced 2-D images of concentrations. Both H_2S and Fe^{2+} distributions showed significant vertical and horizontal heterogeneities, as well as seasonal variations. The complicated 2-D distribution patterns associated with the effects of roots (e.g., oxygen transport) were also revealed. The sensor measurements were generally in good agreement with the dissolved H_2S values obtained from discrete pore water samples (calculated from ΣH_2S and pH). However, the dissolved Fe^{2+} data obtained from the discrete pore water samples were somewhat less than those from *in situ* sensor measurements. In particular, the traditional discrete method missed the Fe^{2+} maximum zones and spatial resolution of Fe^{2+} in the marsh pore water. The H_2S concentrations measured by *in situ* sensors at JoCo and Big Egg were elevated (2–6 mM) in late summer and early fall, but show a clear seasonal difference. The elevated H_2S levels were higher than the threshold at which adverse effects on marsh plants may occur (∼2 mM). On the other hand, oxic zones formed around roots likely protect the plants from absorbing H_2S in an extreme sulfidic environment. Dissolved Fe^{2+} concentrations in pore water measured with sensors at Big Egg and JoCo are generally low, largely due to the removal by pyrizitation. The data of solid phase S and Fe at Big Egg and JoCo showed that significant amounts (>50%) of diagenetically reactive Fe were associated with the pyrite and thus not readily able to react as pore water H_2S increases. Indeed, at JoCo, virtually all of the reactive Fe was associated with pyrite in the spring, 2016 sampling, suggesting that the negative feedback on pore water H_2S concentrations associated with the coupled Fe and S redox cycles is weak and that the ability of Fe to control pore water sulfide through pyrite formation is limited there.

The present study, together with those conducted by our group since 2004, has permitted us to document the pore water geochemistry of the Big Egg and JoCo. The large change is seen in the significant reduction of the phytotoxin H_2S in the pore water in the restored portion of Big Egg marsh, while the unrestored portions there continue to display high pore water H_2S, especially in summer samplings. At JoCo, sampling in fall, 2005, and summer and fall, 2006 showed high (2–4 mM) average values of H_2S in the pore water. In contrast values in spring, summer and fall, 2007 were <0.5 mM. The recent sampling in 2014-16 shows strong seasonality, with high values in fall, 2014 (>4 mM) and summer, 2015, but low values (<0.2 mM) in the two spring samplings (2015, 2016). Although the marsh plants at JoCo are exposed to occasional high levels of H_2S that might be considered toxic, the marsh is relatively elevated compared with mean sea level, and drainage through the marsh peat is more rapid at JoCo than at Big Egg. This may help explain why JoCo continues to be a "healthy" marsh. Relatively healthy marshes such as JoCo should especially be the subject of continued monitoring, for both geochemical and biological parameters.

DATA AVAILABILITY STATEMENT

The original contributions presented in the study are included in the article/supplementary material, further inquiries can be directed to the corresponding author/s.

AUTHOR CONTRIBUTIONS

QZ and JC: conceived of the project. QZ, JC, CH, HY, HF, JT, PF, and WC: pore water and marsh peat cores sampling in the field. QZ and HY: field and lab sensor deployments and analyses. CH and JC: pore water and sediment analyses in field and lab. QZ, JC, and CH: data interpretation and manuscript preparation. All authors contributed to the article and approved the submitted version.

FUNDING

This work was supported by finding from the National Park Service (Task Agreement P14AC01395, Cooperative Agreement P14AC00888). The sensors were partially support by NSF OCE 1737749 and NSF OCE 1332418.

ACKNOWLEDGMENTS

We would like to thank the Science and Resilience Institute at Jamaica Bay for supporting field work, Robert C. Aller for discussion of results, Yu Qian for assistance in the field. Patricia Rafferty (National Parks Service) Don Riepe, and Elizabeth Manclark (American Littoral Society) provided much appreciated logistical support.

REFERENCES

Alldred, M., Borrelli, J. J., Hoellein, T., Bruesewitz, D., and Zarnoch, C. (2020). Marsh plants enhance coastal marsh resilience by changing sediment oxygen and sulfide concentrations in an urban, eutrophic estuary. *Estuaries Coasts* 43, 801–813. doi: 10.1007/s12237-020-00700-9

Aller, R. C. (1982). "The effects of macrobenthos on chemical properties of marine sediments and overlying water," in *Animal-Sediment Relations*, eds P. L. McCall and M. J. S. Tevesz (New York, NY: Plenum), 53–102. doi: 10.1007/978-1-4757-1317-6_2

Aller, R. C. (2001). "Transport and reactions in the bioirrigated zone," in *The Benthic Boundary Layer*, eds B. P. Boudreau and B. B. Jørgensen (Oxford: Oxford University Press), 269–301.

Aller, R. C., Madrid, V., Chistoserdov, A., Aller, J. Y., and Heilbrun, C. (2010). Unsteady diagenetic processes and sulfur biogeochemistry in tropical deltaic muds: implications for oceanic isotope cycles and the sedimentary record. *Geochim. Cosmochim. Acta* 74, 4671–4692. doi: 10.1016/j.gca.2010.05.008

Armstrong, W. (1979). Aeration in higher plants. *Adv. Bot. Res.* 7, 225–332. doi: 10.1016/s0065-2296(08)60089-0

Bagarinao, T. (1992). Sulfide as an environmental factor and toxicant–tolerance and adaptations in aquatic organisms. *Aquat. Toxicol.* 24, 21–62. doi: 10.1016/0166-445x(92)90015-f

Berner, R. A. (1970). Sedimentary pyrite formation. *Am. J. Sci.* 268, 1–23. doi: 10.2475/ajs.268.1.1

Berner, R. A. (1984). Sedimentary pyrite formation: an update. *Geochim. Cosmochim. Acta* 48, 605–615. doi: 10.1016/0016-7037(84)90089-9

Brendel, P., and Luther, G. W. (1995). Development of a gold amalgam voltammetric microelectrode for the determination of dissolved Fe, Mn, O2 and S(-2) in pore waters of marine and freshwater sediments. *Environ. Sci. Technol.* 29, 751–761. doi: 10.1021/es00003a024

Bull, D. C., and Taillefert, M. (2001). Seasonal and topographic variations in pore waters of a southeastern USA salt marsh as revealed by voltammetric profiling. *Geochem. Trans.* 2, 104. doi: 10.1039/b108493c

Campbell, A., Wang, Y., Christiano, M., and Steverns, S. (2017). Salt Marsh Monitoring in Jamaica Bay, New York from 2003 to 2013: a decade of change from restoration to hurricane sandy. *Remote Sens.* 9:131. doi: 10.3390/rs9020131

Canfield, D. E. (1989). Reactive iron in marine sediments. *Geochim. Cosmochim. Acta* 53, 619–632. doi: 10.1016/0016-7037(89)90005-7

Canfield, D. E., Raiswell, R., and Bottrell, S. (1992). The reactivity of sedimentary iron minerals toward sulfide. *Am. J. Sci.* 292, 659–683. doi: 10.2475/ajs.292.9.659

Cao, Z., Zhu, Q., Aller, R. C., Aller, J. Y., and Waugh, S. (2013). Seasonal, 2-D sedimentary extracellular enzyme activities and controlling processes in Great Peconic Bay. *Long Island. J. Mar. Res.* 71, 399–423. doi: 10.1357/002224013812587573

Cline, J. E. (1969). Spectrophotometric determination of hydrogen sulfide in natural waters. *Limnol. Oceanogr.* 14, 454–458. doi: 10.4319/lo.1969.14.3.0454

Cochran, J. K., Kolker, A. S., Hirschberg, D. J., Renfro, A. A., Goodbred, S. Jr., and Beck, A. J. (2013). *Sulfur Cycling in Salt Marshes of Jamaica Bay, Gateway National Recreation Area: Possible Links to Marsh Loss.* Natural Resource Technical Report NPS/NER/NRTR—2013/730. Fort Collins, CO: National Park Service.

Cochran, J. K., Zhu, Q., Heilbrun, C., Tamborski, J., Yin, H., Fitzgerald, P., et al. (2018). *Health and Resilience of Salt Marshes in Jamaica Bay, NY: Geochemical and Dynamical Perspectives.* Natural Resources Report NPS/NCBN/NRR – 2018/1643. Fort Collins, CO: National Park Service.

Colmer, T. D. (2003). Long-distance transport of gases in plants: a perspective on internal aeration and radial oxygen loss from roots. *Plant Cell Environ.* 26, 17–36. doi: 10.1046/j.1365-3040.2003.00846.x

Deegan, L. A., Johnson, D. S., Warren, R. S., Peterson, B. J., Fleeger, J. W., Fagherazzi, S., et al. (2012). Coastal eutrophication as a driver of salt marsh loss. *Nature* 490, 388–392. doi: 10.1038/nature11533

Feng, H., Qian, Y., Cochran, J. K., Zhu, Q., Heilbrun, C., Li, L., et al. (2018). Seasonal differences in trace element concentrations and distributions in Spartina alterniflora root tissue. *Chemosphere* 204, 359–370. doi: 10.1016/j.chemosphere.2018.04.058

Frame, G. W., Mellander, M. K., and Adamo, D. A. (2006). "Big egg marsh experimental restoration in Jamaica Bay, New York," in *People, Places, and Parks: Proceedings of the 2005 George Wright Society Conference on Parks, Protected Areas, and Cultural Sites*, ed. D. Harmon (Hancock, MI: The George Wright Society), 123–130.

Goldhaber, M. B. (2003). "Sulfur-rich Sediments," in *Treatise on Geochemistry*, Vol. 7, ed. F. T. Mackenzie (Amsterdam: Elsevier), 257–288. doi: 10.1016/b0-08-043751-6/07139-5

Hambrick III, G. A., DeLaune, R. D., and Patrick, W. H. (1980). Effect of estuarine sediment pH and oxidation-reduction potential on microbial hydrocarbon degradation. *Appl. Environ. Microbio.* 40, 365–369. doi: 10.1128/aem.40.2.365-369.1980

Han, C., Ren, J., Tang, H., Xu, D., and Xie, X. (2016). Quantitative imaging of radial oxygen loss from *Valisneria spiralis* roots with a fluorescent planar optode. *Sci. Total Environ.* 569-570, 1232–1240. doi: 10.1016/j.scitotenv.2016.06.198

Hines, M. E., Knollmeyer, S. L., and Tugel, J. B. (1989). Sulfate reduction and other sedimentary biogeochemistry in a northern New England salt marsh. *Limnol. Oceanogr.* 34, 578–590. doi: 10.4319/lo.1989.34.3.0578

Howarth, R. W. (1979). Pyrite: its rapid formation in a salt marsh and its importance in ecosystem metabolism. *Science* 203, 49–51. doi: 10.1126/science.203.4375.49

Howes, B. L., and Teal, J. M. (1994). Oxygen loss from *Spartina alterniflora* and its relationship to salt marsh oxygen balance. *Oecologia* 97, 431–438. doi: 10.1007/bf00325879

Johnston, D. T. (2011). Multiple sulfur isotopes and the evolution of Earth's surface sulfur cycle. *Earth Sci. Rev.* 106, 161–183. doi: 10.1016/j.earscirev.2011.02.003

Jørgensen, B. B., and Kasten, S. (2006). "Sulfur cycling and methane oxidation," in *Marine Geochemistry*, eds H. D. Schulz and M. Zabel (Berlin: Springer), 271–309. doi: 10.1007/3-540-32144-6_8

Jørgensen, B. B., and Nelson, D. C. (2004). "Sufide oxidation in marine sediments: geochemistry meets microbiology," in *Sulfur Biogeochemistry – Past and Present*, Vol. 379, eds J. P. Amend, K. J. Edward, and T. W. Lyons (Boulder, CO: Geological Society of America), 63–81.

Kolker, A. S. (2005). *The Impacts of Climate Variability and Anthropogenic Activities on Salt Marsh Accretion and Loss on Long Island*. Ph.D. Thesis. Stony Brook, NY: Stony Brook University, 260.

Koop-Jakobsen, K., Mueller, P., Meier, R. J., Liebsch, G., and Jensen, K. (2018). Plant-sediment interactions in salt marshes – an optode imaging study of O2, pH, and CO2 gradients in the rhizosphere. *Front. Plant Sci.* 9:541. doi: 10.3389/fpls.2018.00541

Kostka, J. E., and Luther, G. W. (1995). Seasonal cycling of Fe in saltmarsh sediments. *Biogeochemistry* 29, 159–181. doi: 10.1007/bf00000230

LaFond-Hudson, S., Johnson, N. W., Pastor, J., and Dewey, B. (2018). Iron sulfide formation on root surfaces controlled by the life cycle of wild rice (*Zizania palustris*). *Biogeochemistry* 141, 95–106. doi: 10.1007/s10533-018-0491-5

Lamers, L. P. M., Govers, L. L., Jassen, I. C. J. M., Geurts, J. J. M., Van der Welle, M. E. W., and Van Katwijk, M. M. (2013). Sulfide as a soil phytotoxin—a review. *Front. Plant Sci.* 4:268. doi: 10.3389/fpls.2013.00268

Luo, M., Huang, J., Tong, C., Liu, Y., Duan, X., and Hu, Y. (2017). Iron dynamics in a subtropical estuarine tidal marsh: effect of season and vegetation. *Mar. Ecol. Prog. Ser.* 577, 1–15. doi: 10.3354/meps12268

Luo, M., Zeng, C. S., Tong, C., Huang, J. F., Chen, K., and Liu, F. Q. (2016). Iron reduction along an inundation gradient in a tidalsedge (*Cyperus malaccensis*) marsh: the rates, pathways, and contributions to anaerobic organic matter mineralization. *Estuaries Coasts* 39, 1679–1693. doi: 10.1007/s12237-016-0094-0

Luo, M., Zeng, C. S., Tong, C., Huang, J. F., Yu, Q., Guo, Y. B., et al. (2015). Kinetics of chemical and microbial iron reduction along an inundation gradient in a tidal marsh of the Min River Estuary, Southeastern China. *Geomicrobiol. J.* 32, 635–647. doi: 10.1080/01490451.2014.950362

Luther, G. W., and Church, T. M. (1988). Seasonal cycling of sulfur and iron in pore waters of a Delaware salt marsh. *Mar. Chem.* 23, 295–309. doi: 10.1016/0304-4203(88)90100-4

Luther, G. W., Church, T. M., Scudlark, J. R., and Cosman, M. (1986). Inorganic and organic sulfur cycling in salt-marsh pore waters. *Science* 232, 746–749. doi: 10.1126/science.232.4751.746

Luther, G. W., Findlay, A. J., MacDonald, D. J., Owings, S. M., Hanson, T. E., Beinart, R. A., et al. (2011). Thermodynamics and kinetics of sulfide oxidation by oxygen: a look at inorganically controlled reactions and biologically mediated processes in the environment. *Front. Microbiol.* 2:62. doi: 10.3389/fmicb.2011.00062

Marsooli, R., Orton, P. M., and Mellor, G. (2017). Modeling wave attenuation by salt marshes in Jamaica Bay, New York, using a new rapid wave model. *J. Geophys. Res. Oceans* 122, 5689–5707. doi: 10.1002/2016jc012546

Morse, J. W., Millero, F. J., Cornwell, J. C., and Rickard, D. (1987). The chemistry of the hydrogen sulfide and iron sulfide system in natural water. *Earth Sci. Rev.* 24, 1–42. doi: 10.1016/0012-8252(87)90046-8

New York City Department of Environmental Protection (2007a). *Jamaica Bay Watershed Protection Plan*, Vol. I. New York, NY: New York City Department of Environmental Protection.

New York City Department of Environmental Protection (2007b). *Jamaica Bay Watershed Protection Plan*, Vol. II. New York, NY: New York City Department of Environmental Protection.

NYSDEC (2006). *Tidal Wetland Losses in Jamaica Bay*. Queens County, NY: NYSDEC.

Rafferty, P., Castagna, J., and Adamo, D. (2010). *Building Partnerships to Restore an Urban Marsh Ecosystem at Gateway National Recreation Area*. Washington, DC: National Park Service.

Reese, B. K., Finneran, D. W., Mills, H. J., Zhu, M.-X., and Morse, J. W. (2011). Examination and refinement of the determination of aqueous hydrogen sulphide. *Aquat. Geochem.* 17, 567–582. doi: 10.1007/s10498-011-9128-1

Soana, E., and Bartoli, M. (2013). Seasonal variation of radial oxygen loss in *Vallisneria spiralis* L: an adaptive response to sediment redox? *Aqua. Bot.* 104, 228–232. doi: 10.1016/j.aquabot.2012.07.007

Stookey, L. L. (1970). Ferrozine – a new spectrophotometric reagent for iron. *Anal. Chem.* 42, 779–781. doi: 10.1021/ac60289a016

Sundby, B., Vale, C., Caetano, M., and Luther, G. W. (2003). Redox chemistry in the root zone of a salt marsh sediment in the Tagus Estuary, Portugal. *Aquat. Geochem.* 9, 257–271. doi: 10.1023/b:aqua.0000022957.42522.9a

Tamborski, J. J., Cochran, J. K., Heilbrun, C., Rafferty, P., Fitzgerald, P., Zhu, Q., et al. (2017). Investigation of pore water residence times and drainage velocities in salt marshes using short-lived radium isotopes. *Mar. Chem.* 196, 107–115. doi: 10.1016/j.marchem.2017.08.007

USFWS (U.S. Fish & Wildlife Service) (1997). *Significant Habitats and Habitat Complexes of the New York Bight Watershed*. Charlestown, RI: U.S. Fish & Wildlife service.

Weiss, J. V., Emerson, D., and Megonigal, J. P. (2005). Rhizosphere iron (III) deposition and reduction in a *Juncus effusus* L.-dominated wetland. *Soil Sci. Soc. Am. J.* 69, 1861–1870. doi: 10.2136/sssaj2005.0002

Yin, H., Zhu, Q., and Aller, R. C. (2017). An irreversible planar optical sensor for multi-dimensional measurements of sedimentary H2S. *Mar. Chem.* 195, 143–152. doi: 10.1016/j.marchem.2017.03.005

Zhu, Q., and Aller, R. C. (2012). Two-dimensional dissolved ferrous iron distributions in marine sediments as revealed by a novel planar optical sensor. *Mar. Chem.* 136-137, 14–23. doi: 10.1016/j.marchem.2012.04.002

Zhu, Q., and Aller, R. C. (2013). Planar fluorescence sensors for two-dimensional measurements of H2S distributions and dynamics in sedimentary deposits. *Mar. Chem.* 157, 49–58. doi: 10.1016/j.marchem.2013.08.001

Conflict of Interest: The authors declare that the research was conducted in the absence of any commercial or financial relationships that could be construed as a potential conflict of interest.

The handling editor declared a past co-authorship with the authors JC and CH.

frontiers in Earth Science

ORIGINAL RESEARCH
published: 30 April 2021
doi: 10.3389/feart.2021.652960

The Carbon-Sulfur Link in the Remineralization of Organic Carbon in Surface Sediments

Harold J. Bradbury[1], Alexandra V. Turchyn[1], Adam Bateson[1,2], Gilad Antler[3,4], Angus Fotherby[1], Jennifer L. Druhan[5], Mervyn Greaves[1], Duygu S. Sevilgen[6] and David A. Hodell[1]*

[1] Department of Earth Sciences, University of Cambridge, Cambridge, United Kingdom, [2] Department of Meteorology, University of Reading, Reading, United Kingdom, [3] Department of Earth and Environmental Sciences, Ben Gurion University of the Negev, Beersheba, Israel, [4] The Interuniversity Institute for Marine Sciences in Eilat, Eilat, Israel, [5] Department of Geology, University of Illinois at Urbana Champaign, Urbana, IL, United States, [6] Centre Scientifique de Monaco, Monaco, Monaco

OPEN ACCESS

Edited by:
Laura M. Wehrmann, Stony Brook University, United States

Reviewed by:
Huan Cui, Université de Paris, France
Morgan Reed Raven, University of California, Santa Barbara, United States

***Correspondence:**
Harold J. Bradbury
hjb62@cam.ac.uk

Specialty section:
This article was submitted to Biogeoscience, a section of the journal Frontiers in Earth Science

Received: *13 January 2021*
Accepted: *07 April 2021*
Published: *30 April 2021*

Citation:
Bradbury HJ, Turchyn AV, Bateson A, Antler G, Fotherby A, Druhan JL, Greaves M, Sevilgen DS and Hodell DA (2021) The Carbon-Sulfur Link in the Remineralization of Organic Carbon in Surface Sediments. Front. Earth Sci. 9:652960. doi: 10.3389/feart.2021.652960

Here we present the carbon isotopic composition of dissolved inorganic carbon (DIC) and the sulfur isotopic composition of sulfate, along with changes in sulfate concentrations, of the pore fluid collected from a series of sediment cores located along a depth transect on the Iberian Margin. We use these data to explore the coupling of microbial sulfate reduction (MSR) to organic carbon oxidation in the uppermost (up to nine meters) sediment. We argue that the combined use of the carbon and sulfur isotopic composition, of DIC and sulfate respectively, in sedimentary pore fluids, viewed through a $\delta^{13}C_{DIC}$ vs. $\delta^{34}S_{SO4}$ cross plot, reveals significant insight into the nature of carbon-sulfur coupling in marine sedimentary pore fluids on continental margins. Our data show systemic changes in the carbon and sulfur isotopic composition of DIC and sulfate (respectively) where, at all sites, the carbon isotopic composition of the DIC decreases before the sulfur isotopic composition of sulfate increases. We compare our results to global data and show that this behavior persists over a range of sediment types, locations and water depths. We use a reactive-transport model to show how changes in the amount of DIC in seawater, the carbon isotopic composition of organic matter, the amount of organic carbon oxidation by early diagenetic reactions, and the presence and source of methane influence the carbon and sulfur isotopic composition of sedimentary pore fluids and the shape of the $\delta^{13}C_{DIC}$ vs. $\delta^{34}S_{SO4}$ cross plot. The $\delta^{13}C$ of the DIC released during sulfate reduction and sulfate-driven anaerobic oxidation of methane is a major control on the minimum $\delta^{13}C_{DIC}$ value in the $\delta^{13}C_{DIC}$ vs. $\delta^{34}S_{SO4}$ cross plot, with the $\delta^{13}C$ of the organic carbon being important during both MSR and combined sulfate reduction, sulfate-driven AOM and methanogenesis.

Keywords: carbon isotopes, sulfur isotopes, early diagenesis, microbial sulfate reduction, methanotrophy and methanogenesis, reactive transport modeling

INTRODUCTION

Organic carbon oxidation in marine sediments is a key process in the global carbon and oxygen cycles as it mitigates the burial of reduced forms of carbon (Froelich et al., 1979; Berner, 1989; Kump and Arthur, 1999; Diester-Haass et al., 2009; Kump et al., 2011). When oxygen is present, this organic carbon remineralization is dominated by aerobic respiration. However, the depth of penetration of oxygen in marine sediments is limited, particularly on the continental shelf where the delivery of organic carbon is high (Froelich et al., 1979; Tromp et al., 1995; D'Hondt et al., 2015). In the absence of oxygen, anaerobic remineralization of organic carbon continues for many hundreds of meters below the sediment-water interface provided there are suitable alternative electron acceptors present (Froelich et al., 1979; Kasten et al., 2003). This anaerobic remineralization of organic carbon is important because when these electron acceptors are depleted, any remaining organically-derived material may be converted into methane through methanogenesis (Claypool and Kaplan, 1974; Whiticar and Faber, 1986; Whiticar, 1999; Sivan et al., 2007). Thus, exploring the controls on the remineralization of organic carbon is vital to resolving the carbon budget in dynamic sedimentary systems along continental margins.

The study of the subsurface anaerobic oxidation of organic carbon, which in the modern ocean is dominated by microbial sulfate reduction (MSR), is often achieved through the analysis of the chemistry of pore fluids, the fluids trapped between the grains of sediment on the ocean floor (Froelich et al., 1979; Berner, 1980; Kasten et al., 2003). These pore fluids chemically evolve from seawater as a function of the chemical reactions occurring below the seafloor and the rate of transport *via* diffusion of solutes and advection of fluids through the sediments (Berner, 1978; Froelich et al., 1979; Boudreau, 1997). Many studies have attempted to quantify the rate of anaerobic remineralization of organic carbon through numerical modeling of the concentration gradients within pore fluids using the diffusion coefficient of an ion of interest, the sediment porosity and the rate at which the concentration changes with depth (Berner, 1980; Boudreau, 1997; Sivan et al., 2007; Arndt et al., 2009; Wehrmann et al., 2011). One of the challenges of this approach is that the majority of the existing pore fluid data comes from the International Ocean Drilling Programs where the top meter of sediment is disturbed or not sampled. This top meter, sometimes called the sedimentary boundary layer, is often the most dynamic part of the sediment column and is the portion of sediment that is in direct contact with the overlying ocean (Sayles, 1979, 1981; Sun et al., 2016). Far fewer studies have been able to analyze the geochemistry of both the boundary layer and the underlying sediment to understand how processes that are happening in the uppermost sediment may—or may not—link to the better-studied processes occurring deeper within the sediment pile. Previous studies into carbonate recrystallization at ODP Sites, for example, have often failed to capture a significant proportion of the change in the calcium isotope ratio of pore fluids due to the lack of sampling resolution in the uppermost part of the sediment (Fantle and DePaolo, 2007; Fantle, 2015).

An important class of geochemical measurements that offers insight into the subsurface remineralization of organic carbon is the light stable isotope ratios in various dissolved ions in the sediment pore fluid. Organic carbon that reaches the sediment-water interface is enriched in the lighter ^{12}C isotope relative to seawater DIC and when this organic carbon is oxidized, the carbon isotopic composition of the dissolved inorganic carbon (DIC) in the pore fluid is lowered, reflecting the addition of ^{12}C-enriched DIC to the pore fluid (McCorkle et al., 1985; Meister et al., 2019). When organic carbon is converted into methane, the lighter ^{12}C isotope preferentially ends up in the methane, producing methane with a very low $\delta^{13}C$ and leaving the residual DIC enriched in the heavier ^{13}C isotope. In the case of MSR, ^{32}S is preferentially reduced, leaving the ^{34}S behind; therefore, as sulfate concentrations are depleted in sedimentary pore fluids, the sulfur isotopic composition of the remaining sulfate increases (Berner, 1989; Canfield et al., 1993; Kasten and Jørgensen, 2000). Ultimately, the ^{32}S ends up in the product sulfide, and, when iron is present, possibly in the mineralized form, pyrite (Berner, 1989; Algeo et al., 2015). Oxygen isotopes in sulfate are also fractionated in a similar fashion to sulfur isotopes, where the lighter ^{16}O is preferentially reduced leaving the heavy ^{18}O behind (Brunner et al., 2005; Turchyn et al., 2006). Oxygen isotopes in sulfate are affected by an additional isotope equilibrium process with water, which may lead to the oxygen isotopic composition of the sulfate increasing faster than would be predicted for a unidirectional, kinetic isotope effect alone (Wortmann et al., 2007). The relative increase in the sulfur and oxygen isotopic composition of sulfate during MSR has been shown to relate to the rate of MSR (Wortmann et al., 2007; Antler et al., 2013, 2014). In this case, a fast increase in $\delta^{18}O$ of sulfate relative to its $\delta^{34}S$ suggests there is a high rate of back-reaction and equilibration of oxygen isotopes in intermediate-valence-state-sulfur species with water, and thus a slower overall rate of MSR (Antler et al., 2013, 2014). Two other processes impact the sulfur isotope fractionation observed in sediments, the disproportionation of external sulfur intermediates and microbial sulfide oxidation, and the observed sulfur isotopic composition of sulfate may be due to a combination of all three processes (Jørgensen et al., 2019b; Pellerin et al., 2019). It is, in general, not possible to differentiate between sulfate reduction and sulfur disproportionation with only ^{34}S and ^{32}S measurements, although the measurement of other sulfur isotopes (such as ^{33}S) provides greater insight into the oxidative sulfur cycle (Johnston et al., 2005; Bradley et al., 2016; Jørgensen et al., 2019b).

Both the carbon and sulfur isotopic composition of sedimentary pore fluid DIC and sulfate, respectively, have been used, independently, to resolve questions in the deep biosphere and with the sedimentary oxidation or mineralization of carbon. In particular, the carbon isotopic composition of pore fluid DIC has been utilized to investigate the depth distribution of methane production (methanogenesis) and methane oxidation (methanotrophy) in sediments (Sivan et al., 2007; Meister et al., 2019). Similarly, the sulfur isotopic composition of pore fluid sulfate measured in sedimentary pore fluids has been used to explore the depth distribution of MSR and its coupling to

methane oxidation (Jørgensen and Kasten, 2006; Wortmann et al., 2007; Sela-Adler et al., 2017; Jørgensen et al., 2019a). These studies have helped elucidate the redox changes to carbon and sulfur within sedimentary systems, but many questions remain. For example, there is still uncertainty about the proportion of sulfate that is consumed through anaerobic oxidation of methane (AOM) vs. through organic-matter driven MSR when both processes are occurring (Sivan et al., 2007; Egger et al., 2018). Understanding precisely how carbon and sulfur are coupled within marine sediments may be better achieved by directly comparing measurements of $\delta^{13}C_{DIC}$ and $\delta^{34}S_{SO4}$. This would have implications for our understanding of the cycling of carbon, particularly in the uppermost part of the sediment. MSR generates more DIC per mole of electron acceptor reduced than the microbial metal reduction processes such as iron and manganese reduction which should dominate in the uppermost sediment as they are energetically more favorable electron acceptors (Froelich et al., 1979). When MSR does occur in the uppermost sediment, this influences our understanding of the sources and sinks of alkalinity and DIC (Sayles, 1979, 1981).

In 2013, a site survey cruise (JC089) aboard the *RRS James Cook* took a series of surface multicores and longer piston cores along a depth transect on the southwestern Iberian Margin (Hodell et al., 2014). A Megacorer was used to collect multi-cores for pore fluid chemical analyses at each site, with emphasis on high-resolution (cm-scale) pore fluid geochemistry in the upper meter of sediment. Station JC089-06 is at the same location as IODP Site U1385 where deeper cores were recovered to 155.9 mbsf during IODP Leg 339 in December 2011–January 2012.

In this paper we present high resolution pore fluid geochemical and isotopic composition from the cores recovered on Cruise JC089 (**Table 1**). Specifically, we use the sulfur and oxygen isotopic composition of sulfate, along with changes in the concentration of sulfate, and the carbon isotopic composition of DIC to explore the oxidation of organic carbon along the Iberian continental margin, from shallow water depths (628 mbsl) to the abyssal plain (4,672 mbsl). The data are evaluated using a reactive transport model to constrain the underlying processes governing the oxidation of organic carbon and how they manifest as changes in shallow pore fluids. We propose that using $\delta^{13}C_{DIC}$ vs. $\delta^{34}S_{SO4}$ cross plot reveals significant information about the nature of carbon-sulfur coupling in marine sedimentary pore fluids on continental margins.

TABLE 1 | Sampling locations, method of coring and water depth.

Station	Core type	Latitude	Longitude	Water depth (m)
JC089-04	MultiCore (3M)	37° 35.15′	10° 21.89′	3,495
JC089-05	MC (4M) + Piston Core (3P)	37° 36.26′	10° 41.51′	4,672
JC089-06	MultiCore (5M)	37° 33.68′	10° 08.53′	2,645
JC089-09	MC (8M) + Piston Core (6P)	37° 49.83′	09° 49.30′	2,323
JC089-11	MultiCore (10M)	37° 51.51′	09° 20.15′	628

MATERIALS AND METHODS

Analytical Methods

Interstitial waters were extracted from up to three multi-cores at each station, using Rhizon samplers spaced at 1 cm intervals through sealed ports in the multicores. Rhizons and syringes were acid cleaned using 3 M HCl followed by 1.5 M HNO_3 and an overnight soak in high purity deionized water. Pore fluids were extracted from sub-cores of box cores at three sites and from piston cores collected at six sites on board ship. Piston cores were sampled using Rhizon samplers spaced at 20 cm intervals, while the sub-cores of box cores were sampled using Rhizon samplers spaced at 1 cm intervals. *In situ* micro-sensor oxygen concentration measurements were performed shipboard and calibrated using oxygen solubilities at the measured salinities and temperature according to the Unisense Gas tables (Garcia and Gordon, 1992; Skinner et al., 2019). A two-point calibration was performed using oxygen concentrations from the overlying water and in the anoxic part of the sediment. Alkalinity was measured on board (not presented here).

One milliliter aliquots of the pore fluid collected during cruise JC089 were separated from samples taken at five mega core sites (Sites 4, 5, 6, 9, and 11) and two of the piston cores (Sites 5 and 11). To the pore fluid aliquot, 1 mL of barium chloride solution was added to precipitate the aqueous sulfate as barite ($BaSO_4$). This barite was subsequently cleaned with 6 N HCl and three times with deionized water before being dried down to be weighed for isotope analysis. Sulfur isotope ratios in this barite were analyzed through combustion in a Flash Element Analyzer (Flash EA) coupled by continuous flow to a Delta Advantage mass spectrometer at the University of Cambridge in the Godwin Laboratory for Paleoclimate Research. Samples were run in sets of ∼20 bracketed by NBS 127 ($\delta^{34}S$ = 21.1‰) and are reported relative to the international standard VCDT. The 1σ standard deviation of the bracketing standards is used as the standard deviation for the samples in a particular run, although blind duplicates were also run at the end of each column to check the measured $\delta^{34}S$ value. The analytical precision on these runs was 0.2‰.

Oxygen isotope ratios in sulfate were analyzed through pyrolysis in a Temperature Conversion Element Analyzer (TC/EA) coupled by continuous helium flow to a Delta Advantage mass spectrometer. Barite for oxygen isotope analysis was run in triplicate and the average and standard deviation of the triplicate analyses are presented. Samples were bracketed by NBS 127 ($\delta^{18}O_{SO4}$ = 8.6‰) and an internal standard to correct for measurement drift and analytical error. The analytical precision on these runs was usually better than 0.5‰.

Carbon isotope ratios in the DIC were analyzed using a Thermo Scientific GasBench II equipped with a CTC Analytics CombiPAL autosampler coupled to a Thermo Finnigan Delta V Mass Spectrometer. Three or four drops of orthophosphoric acid (100%) were preloaded into a reaction vial, which was capped, sealed and the headspace flushed with Helium gas. Approximately 1.5 ml of sample water was injected into the vial through the butyl rubber septa using a syringe and left to react for

1 h. The sample tubes were transferred to the GasBench and CTC CombiPal Autosampler and the resulting CO_2 in the head space analyzed using a Thermo Delta V Mass Spectrometer. A series of standards and reference samples distributed throughout the run were used to calibrate to the international standard VPDB. Results have a reproducibility of better than $\pm$ 0.1‰.

Sulfate concentrations were measured using ion chromatography on a Thermo Scientific Dionex ICS 5000+ HPIC, with an IonPac AS18 column using potassium hydroxide (31 mM KOH) as the eluent. Samples were diluted 10-fold in ultrapure MilliQ water and calibrated using 2.5–15% IAPSO standard seawater also diluted in ultrapure MilliQ water. Standard calibrations were run at the beginning and end of each measurement run, as well as a smaller subset of standards that were measured every 20 samples to calculate reproducibility and assess any drift in the measured concentrations. The error on repeated measurements of the standard was <2% for all ions.

Modeling Methods

Sulfate Reduction in CrunchTope

To explore the relative changes in pore fluid $\delta^{13}C_{DIC}$ and $\delta^{34}S_{SO4}$, we utilize the multi-component numerical reactive transport software CrunchTope (Druhan et al., 2013, 2014; Steefel et al., 2015). We use CrunchTope to simulate contemporaneous advection, diffusion and chemical reactions over a 10 m pore fluid column with a coexisting solid phase with a seawater Dirichlet upper boundary condition, and a Neumann or dC/dx = 0 lower boundary condition. The porosity is fixed at 0.8, with a constant sediment burial modeled using equal burial and fluid flow rate terms of 11 cm/year, approximately equal to the average burial rate at Site 6—IODP Site U1385 (Hodell et al., 2013). The diffusivity was calculated from a molecular diffusion coefficient of 9.19×10^{-6} cm^2/s and the porosity of the sediment column (Huber et al., 2017) and was the same for all species. The system is run from the initial conditions listed in **Supplementary Table 1** and allowed to run until the fluid concentrations and isotopic composition are no longer changing with time, which is assumed to be steady state. CrunchTope is open-source software, and the input and database files for our model can be found within the **Supplementary Material**, along with the initial conditions (**Supplementary Table 1**) and equilibrium constants used (**Supplementary Table 2**). The goal is to use this isotope-enabled reactive transport model to explore the contemporaneous evolution of $\delta^{13}C_{DIC}$ and $\delta^{34}S_{SO4}$ in surface sediments undergoing MSR.

Microbial sulfate reduction is modeled with formaldehyde (CH_2O) representing the bulk composition of organic matter (Meister, 2013, 2014; Meister et al., 2019):

$$2CH_2O + SO_4^{2-} + 2H^+ \rightarrow 2CO_{2(aq)} + H_2S_{(aq)} + 2H_2O \quad (1)$$

Microbial sulfate reduction is modeled as a catabolic Monod Biomass reaction, using a dual-Monod equation relating the growth rate (r; mol/kg H_2O/year) to the abundance of electron donor/acceptor (Hubbard et al., 2014), which in this case are formaldehyde (CH_2O) and sulfate (SO_4^{2-}):

$$r = \mu \frac{[eDonor]}{[eDonor]\,K_{eDonor}} \frac{[eAcceptor]}{[eAcceptor]K_{eAcceptor}} \quad (2)$$

Where μ (mol/kg H_2O/year) is the maximum specific growth rate of the microorganism, *[eX]* is the concentration of the electron donor/acceptor and K (mol/kg H_2O) is the half-saturation constant of the electron donor/acceptor. In order to track two isotope systems (carbon and sulfur) during sulfate reduction, each isotopologue is written as a separate aqueous kinetic reaction (**Table 2**), with the relative difference in the rate constants (μ) controlling the isotopic fractionation. The sulfur isotope fractionation during sulfate reduction is varied within the different model runs discussed below, while there is assumed to be no partitioning of carbon isotopes during sulfate reduction following experimental work (Londry and Des Marais, 2003).

The modeling of a second isotope system ($\delta^{13}C$) exerts a minor effect on the relative isotope fractionation displayed by the first isotope system ($\delta^{34}S$), as the rate of each of the aqueous reactions is controlled by a Monod biomass equation which is sensitive to the limiting concentrations of both organic carbon and sulfate. This is verified by modeling just the sulfur isotopic composition, without tracking the carbon isotope composition in the pore fluid, then both the sulfur and carbon isotopic composition with the same initial concentrations of organic carbon and sulfate (**Figure 1A**). This shows that by modeling just one isotope system vs. two isotope systems, the impact on the resulting relative isotope fractionation for both carbon and sulfur isotope ratios in the pore fluid is nearly identical. As the rate for each of the individual aqueous reactions is controlled by the concentrations of the isotopologues of organic carbon and sulfate within the pore fluid, the minor-minor isotope reaction (**Table 2**, D) will proceed exceptionally slowly. However, our modeling shows that it is essential this reaction is included (**Figure 1B**) as without the minor-minor reaction the modeled pore fluids differ in their isotopic evolution. Additionally, if the minor-minor reaction were not included two reactions would consume ^{12}C, whereas only one reaction would consume ^{13}C. In order to model no carbon isotope fractionation during sulfate reduction, as detailed above, we must therefore include all of the isotopologue reactions. It is possible that adding a third or fourth isotope system following the same approach would eventually remove the need for tracking the most minor-minor isotope reactions, as their impact on the modeled isotope composition decreases significantly with each additional isotope system.

Aerobic Respiration in CrunchTope

The aerobic respiration of formaldehyde is also modeled using the dual Monod equation described above with the following stoichiometry:

$$CH_2O + O_2 \rightarrow CO_{2(aq)} + H_2O \quad (3)$$

Methanogenesis and Methanotrophy in CrunchTope

In order to investigate the impact that methanogenesis and methanotrophy can have on the cross plot of $\delta^{13}C_{DIC}$ vs.

TABLE 2 | The isotopologue-specific aqueous reactions required to track the carbon and sulfur isotopic composition of DIC and sulfate (respectively) during sulfate reduction.

	Aqueous reaction	Carbon isotope	Sulfur isotope	Rate constant (μ: mol/kg H_2O/year)
A	$2^{12}CH_2O + {}^{32}SO_4^{2-} + 2H^+ \rightarrow 2^{12}CO_{2(aq)} + H_2{}^{32}S_{(aq)} + 2H_2O$	^{12}C	^{32}S	Variable
B	$2^{12}CH_2O + {}^{34}SO_4^{2-} + 2H^+ \rightarrow 2^{12}CO_{2(aq)} + H_2{}^{34}S_{(aq)} + 2H_2O$	^{12}C	^{34}S	$[(^{34}\varepsilon/1{,}000)+1] \times \mu_A$
C	$2^{13}CH_2O + {}^{32}SO_4^{2-} + 2H^+ \rightarrow 2^{13}CO_{2(aq)} + H_2{}^{32}S_{(aq)} + 2H_2O$	^{13}C	^{32}S	μ_A
D	$2^{13}CH_2O + {}^{34}SO_4^{2-} + 2H^+ \rightarrow 2^{13}CO_{2(aq)} + H_2{}^{34}S_{(aq)} + 2H_2O$	^{13}C	^{34}S	$[(^{34}\varepsilon/1{,}000)+1] \times \mu_A$

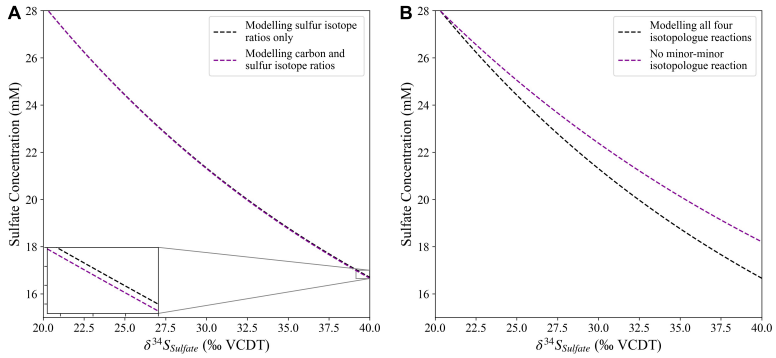

FIGURE 1 | Panel **(A)** shows the minimal impact that simultaneously modeling the carbon and sulfur isotope systems in CrunchTope has on the sulfur isotopic composition of sulfate during microbial sulfate reduction. Panel **(B)** displays the importance of modeling all combinations of the isotope specific aqueous reactions including the minor-minor isotopologue reaction.

$\delta^{34}S_{SO4}$, we add both reactions into the CrunchTope model described above. The controls on the $\delta^{13}C$ of the DIC during methanogenesis and methanotrophy have recently been comprehensively reviewed by Meister et al. (2019). Methane production can be modeled with an initial breakdown of complex organic molecules generating hydrogen (Equation 4), which is then consumed during hydrogenotrophic methanogenesis (Equation 5; Claypool and Kaplan, 1974).

$$2CH_2O + 2H_2O \rightarrow 2CO_{2(aq)} + 4H_{2(aq)} \quad (4)$$

$$2CO_{2(aq)} + 4H_{2(aq)} \rightarrow CH_{4(aq)} + CO_{2(aq)} + 2H_2O \quad (5)$$

Here, the formation of methane enriched in ^{12}C from CO_2 (Equation 5) drives the residual DIC pool to become enriched in ^{13}C. Hydrogenotrophic methanogenesis has been suggested to account for the majority of microbial methanogenesis in marine sediments, with acetoclastic methanogenesis dominating in freshwater environments (Claypool and Kaplan, 1974; Martens and Berner, 1974; Barnes and Goldberg, 1976; Whiticar and Faber, 1986; Whiticar, 1999; Sivan et al., 2007). The two stages of methanogenesis (Equations 4, 5) are also modeled using Monod equations, with the initial stage of methanogenesis requiring a single Monod equation and the final stage of methanogenesis a dual Monod equation.

The carbon isotope fractionation associated with hydrogenotrophic methanogenesis is >55‰ (Whiticar, 1999), and is significantly larger than the carbon isotope fractionation during the initial oxidation of organic matter, which is thought to be relatively insignificant (Meister et al., 2019). As $CO_{2(aq)}$ is found as both a product and a reactant in hydrogenotrophic methanogenesis (Equation 5), it is important to consider the effect that carbon isotope equilibrium during carbonate speciation can have on the carbon isotope composition of the various DIC species (Zhang et al., 1995). Carbon isotope equilibrium among the DIC species has recently been demonstrated in CrunchTope (Druhan et al., 2020) and we take the same modeling approach in this study.

Methanotrophy is modeled as sulfate-driven anaerobic oxidation of methane (AOM; Equation 6):

$$CH_4 + SO_4^{2-} + 2H^+ \rightarrow CO_{2(aq)} + H_2S_{(aq)} + 2H_2O \quad (6)$$

Previous studies have shown that during the anaerobic oxidation of methane there is a substantial carbon isotope fractionation between −38 and −12% (Holler et al., 2009), where the residual methane is enriched in ^{13}C. In the natural environment, this increase in $\delta^{13}C$ of methane during methane oxidation hasn't been readily observed, which has been suggested to be due to carbon isotope exchange between methane and $CO_{2(aq)}$ during AOM (Horita, 2001; Yoshinaga et al., 2014; Meister et al., 2019). This is implemented into CrunchTope as an equilibrium exchange reaction with an equilibrium fractionation factor of α_{eq} = 0.93 (Equation 7; Horita, 2001; Meister et al., 2019).

$$^{12}CO_{2(aq)} + {}^{13}CH_{4(aq)} \leftrightarrow {}^{12}CH_{4(aq)} + {}^{13}CO_{2(aq)} \quad (7)$$

The reaction scheme stoichiometry and rate constants of the model are given in **Table 3**.

TABLE 3 | The isotopologue-specific aqueous reactions required to track the carbon and sulfur isotopic composition of DIC and sulfate (respectively) during AOM and methanogenesis.

	Aqueous reaction	Carbon isotope	Sulfur isotope	Rate constant (μ: mol/kg H_2O/year)
E	$^{12}CH_4 + {}^{32}SO_4^{2-} + 2H^+ \rightarrow {}^{12}CO_{2(aq)} + H_2{}^{32}S_{(aq)} + 2H_2O$	^{12}C	^{32}S	$10 \times \mu_A$
F	$^{12}CH_4 + {}^{34}SO_4^{2-} + 2H^+ \rightarrow {}^{12}CO_{2(aq)} + H_2{}^{34}S_{(aq)} + 2H_2O$	^{12}C	^{34}S	$10 \times \mu_B$
G	$^{13}CH_4 + {}^{32}SO_4^{2-} + 2H^+ \rightarrow {}^{13}CO_{2(aq)} + H_2{}^{32}S_{(aq)} + 2H_2O$	^{13}C	^{32}S	$10 \times \mu_A$
H	$^{13}CH_4 + {}^{34}SO_4^{2-} + 2H^+ \rightarrow {}^{13}CO_{2(aq)} + H_2{}^{34}S_{(aq)} + 2H_2O$	^{13}C	^{34}S	$10 \times \mu_B$
I	$2\,{}^{12}CH_2O + 2H_2O \rightarrow 2\,{}^{12}CO_{2(aq)} + 4H_{2(aq)}$	^{12}C	N/A	$0.5 \times \mu_A$
J	$2\,{}^{13}CH_2O + 2H_2O \rightarrow 2\,{}^{13}CO_{2(aq)} + 4H_{2(aq)}$	^{13}C	N/A	μ_I
K	$2\,{}^{12}CO_{2(aq)} + 4H_{2(aq)} \rightarrow {}^{12}CH_{4(aq)} + {}^{12}CO_{2(aq)} + 2H_2O$	^{12}C	N/A	μ_I
L	$2\,{}^{13}CO_{2(aq)} + 4H_{2(aq)} \rightarrow {}^{13}CH_{4(aq)} + {}^{13}CO_{2(aq)} + 2H_2O$	^{13}C	N/A	$[({}^{13}\varepsilon/1{,}000)+1] \times \mu_I$
M	${}^{12}CO_{2(aq)} + {}^{13}CH_{4(aq)} \leftrightarrow {}^{12}CH_{4(aq)} + {}^{13}CO_{2(aq)}$	$^{12}C/^{13}C$	N/A	1,000

RESULTS

At all five studied sites, the pore fluid sulfate concentrations decrease with depth while the pore fluid sulfate $\delta^{34}S$ and $\delta^{18}O$ values increase with depth (**Figure 2**). We note that pore fluid $\delta^{34}S_{SO4}$ and $\delta^{18}O_{SO4}$ increase fastest with sediment depth at Site 9 (2,323 mbsl) and slowest at the deepest water site, Site 5 (4,672 mbsl). However, the change in the sulfur and oxygen isotopic composition of sulfate as a function of the change in the sulfate concentrations is nearly identical at all sites (**Figure 3**). Over the five sites there is a similar increase in $\delta^{34}S_{SO4}$ vs. $\delta^{18}O_{SO4}$; as mentioned above this slope has been linked to the overall cell-specific rate of MSR, suggesting a similar rate in sediments across the Iberian margin. It appears that the oxygen isotopic composition of sulfate may increase slightly faster than the sulfur isotopic composition of sulfate at Site 11 (**Figure 4A**). At one of the sites with piston core data (Site 9; 2,323 mbsl) we note that the cross plot of $\delta^{34}S_{SO4}$ vs. $\delta^{18}O_{SO4}$ (**Figure 4A**) comes out of the apparent linear phase, where the sulfur and oxygen isotopic compositions covary, and into the equilibration phase, where $\delta^{18}O_{SO4}$ has reset through oxygen isotope equilibrium with water intracellularly and does not change further as the $\delta^{34}S_{SO4}$ values continue to increase (Antler et al., 2014; Antler and Pellerin, 2018; Fotherby et al., 2021).

The carbon isotope composition of the DIC decreases with depth as expected from the oxidation of organic carbon and the return of ^{12}C-rich carbon to the DIC pool (**Figures 2G,H**). It has recently been shown that outgassing of CO_2-enriched pore fluids during Rhizon sampling can have a minor impact on measured $\delta^{13}C_{DIC}$, so measured $\delta^{13}C_{DIC}$ may be slightly enriched in ^{13}C relative to the original pore fluid values (Steiner et al., 2018). We note that when we plot $\delta^{13}C_{DIC}$ vs. $\delta^{34}S_{SO4}$ that $\delta^{13}C_{DIC}$ decreases to −6‰ at all sites before there is an increase in $\delta^{34}S_{SO4}$, and there is a similar trend displayed in $\delta^{13}C_{DIC}$ vs. $\delta^{18}O_{SO4}$ (**Figures 4B,C**).

DISCUSSION

Our data show a systematic correlation between the carbon isotopic composition of DIC and sulfur and oxygen isotopic composition in sulfate (**Figure 4**). We suggest that much of this relationship may be intrinsically linked to pore fluid MSR, as this is the major process which oxidizes organic carbon in modern marine sediment (Jørgensen et al., 2019b). The $\delta^{13}C$ value of organic matter deposited in sediment varies between −20 and −30‰, enriched in the ^{12}C isotope due to carbon isotope fractionation during photosynthesis (Hollander and McKenzie, 1991; Lehmann et al., 2002). During oxidation of organic matter, there is little carbon isotope fractionation (0–2‰; Londry and Des Marais, 2003). Therefore, during organic carbon oxidation $\delta^{13}C_{DIC}$ will decrease toward that of the organic matter independent of the electron acceptor used during the microbial reaction. During MSR as $\delta^{13}C_{DIC}$ trends toward the carbon isotopic composition of organic matter, $\delta^{34}S$ value of the residual sulfate will increase due to the distillation of the ^{32}S into the product sulfide. We initially hypothesize that the initial decrease in $\delta^{13}C_{DIC}$ with a relatively small change in the sulfur isotopic composition of pore fluids sulfate could be due to the oxidation of organic carbon using electron acceptors other than sulfate, before the onset of MSR and the anticipated covariation between $\delta^{13}C_{DIC}$ and $\delta^{34}S_{SO4}$. Although there is a range of depositional conditions across the Iberian Margin, including varying sedimentary organic carbon content, the similarity of the correlation between $\delta^{13}C_{DIC}$ and $\delta^{34}S_{SO4}$ is remarkably consistent apart from at Site 5 (**Figure 4B**), demonstrating that the cross plot of $\delta^{13}C_{DIC}$ vs. $\delta^{34}S_{SO4}$ allows resolution of fundamental processes without much of the added complications of length-scales.

Rayleigh Fractionation Subject to Transport

The two long piston cores, Site 5 and Site 9, have a large difference in the apparent sulfur isotope fractionation as evidenced by the change in $\delta^{34}S_{SO4}$; often when using the change in the isotopic composition of pore fluid to resolve the sulfur isotope fractionation factor during MSR, Rayleigh distillation is used (Rudnicki et al., 2001; Breukelen and Prommer, 2008). When the apparent sulfur isotope fractionation is calculated using this simple closed-system Rayleigh fractionation approach, significantly different sulfur isotope fractionation factors are calculated for Site 5 and Site 9 (**Figure 5A**; Site 5 at −44.5‰ and Site 9 at −32‰). We compare this calculation using Rayleigh distillation with the sulfur isotope fractionation factors calculated using CrunchTope. The modeling approach described above

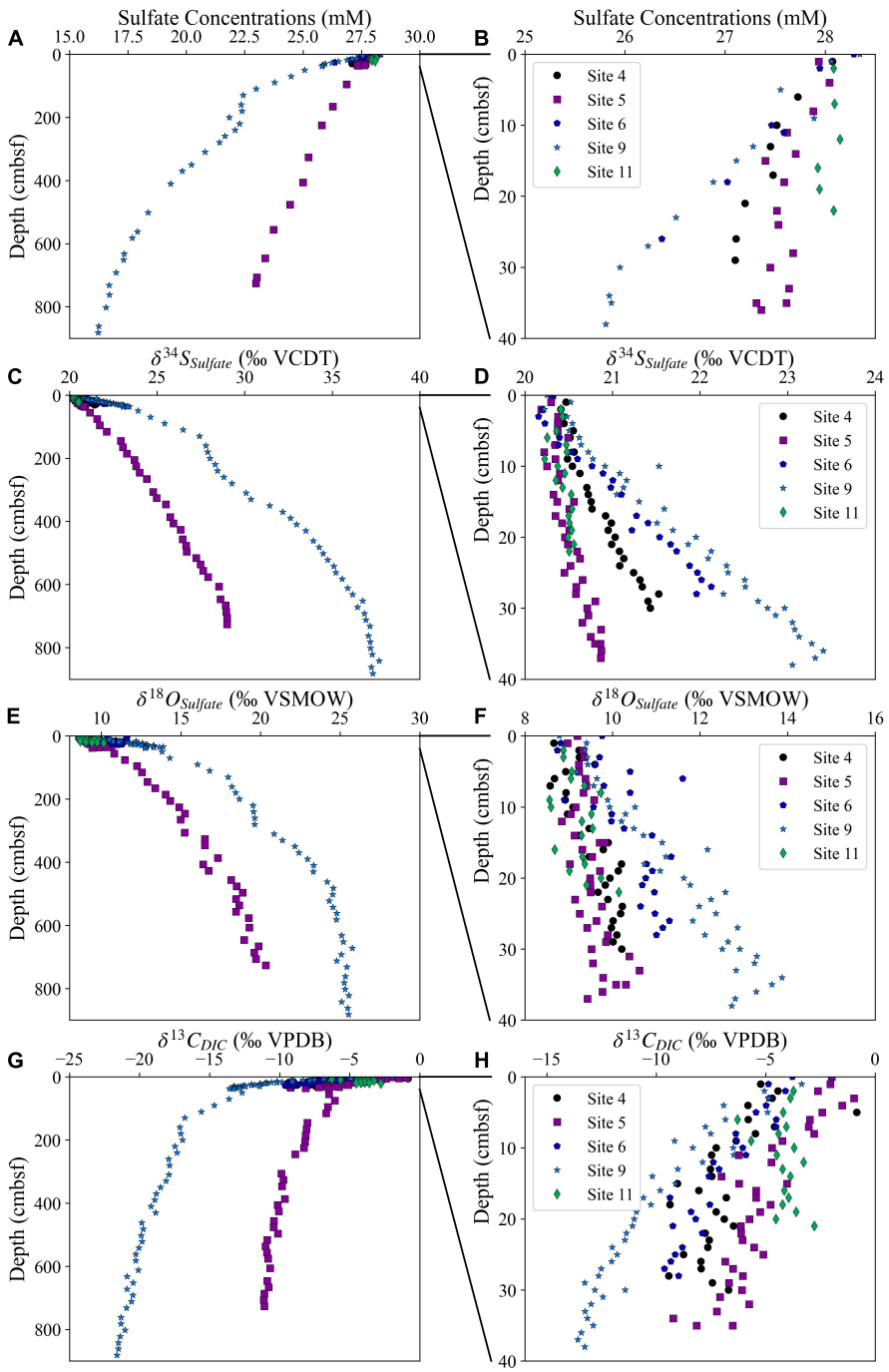

FIGURE 2 | The sulfate concentrations from two piston and three multi cores **(A,B)**, sulfur and oxygen isotopic composition of sulfate **(C–F)** and carbon isotopic composition of the DIC **(G,H)**. Panels **(A,C,E,G)** display measurements over the entire depth range of the piston cores, whereas panels **(B,D,F,H)** display the same measurements over 40 cm below seafloor (cmbsf).

is used, and the forward model of sulfate reduction as well as sediment burial and fluid transport accurately reproduce the measured sulfur isotope variations in both cores when the sulfate reduction rates are matched by controlling the sulfate reduction rate constant (μ_{SR}; mol/mol-CH_2O/year) and all other parameters are held constant. In order to fit the sulfate concentration profiles, the sulfate reduction rate constant (μ_{SR}) is lower at Site 5 (μ_{SR} = 4,200) than at Site 9 (μ_{SR} = 10,200). As Site 5 is located in much deeper water than Site 9 (4,672 mbsl relative to 2,323 mbsl), the difference in sulfate reduction rates is most likely due to the lower flux of organic carbon to the sediment in deeper water. The sulfur isotope fractionation ($^{34}\varepsilon$) is kept consistent

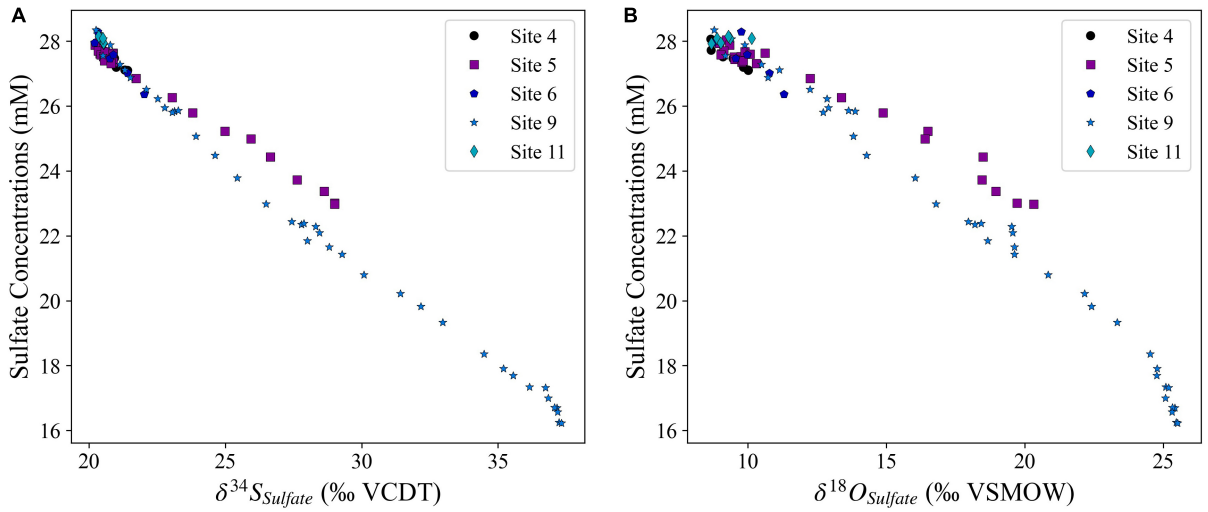

FIGURE 3 | The increase in the sulfur **(A)** and oxygen **(B)** isotopic composition of sulfate as a function of the decrease in pore fluid sulfate concentrations.

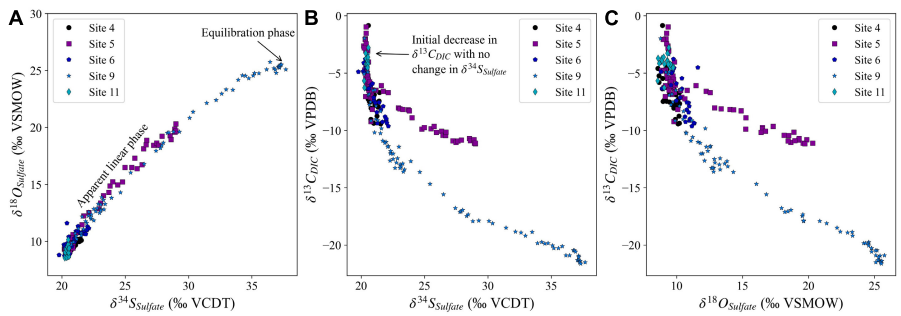

FIGURE 4 | Panel **(A)** displays the relative change in the sulfur and oxygen isotopic composition of pore fluid sulfate at all five sites. The change in the sulfur **(B)** and oxygen **(C)** isotopic composition of sulfate vs. the change in the carbon isotopic composition of dissolved inorganic carbon.

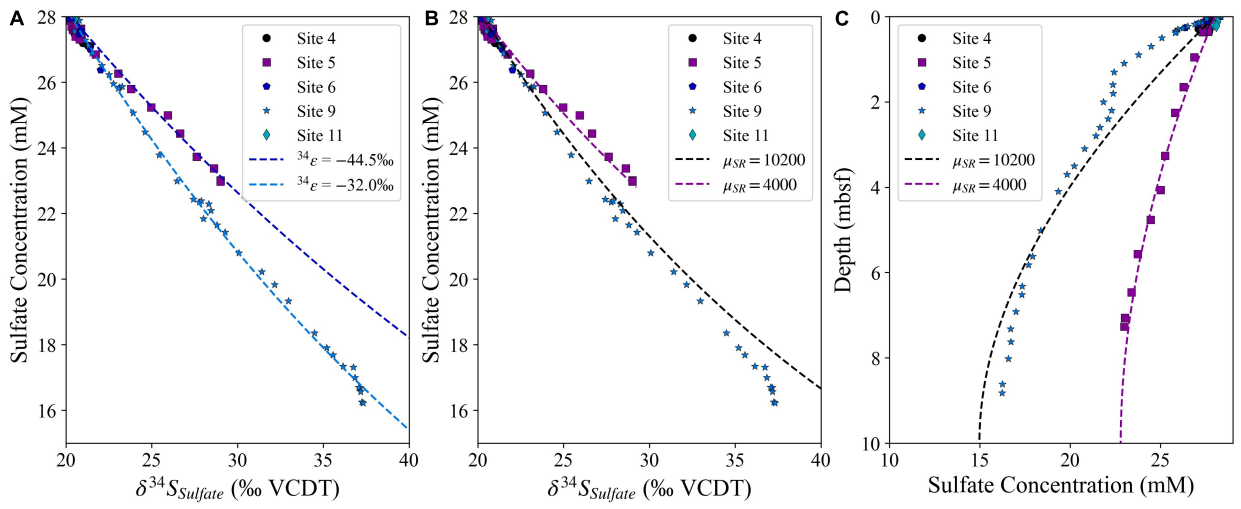

FIGURE 5 | Panel **(A)** displays the change in sulfur isotopic composition of sulfate for modeled Rayleigh fractionation lines for $^{34}\varepsilon$ of –44.5 and –32‰ (dashed lines) compared to the measured data. Panels **(B,C)** display the change in sulfur isotopic composition of sulfate relative to the sulfate concentration and the sulfate concentrations relative to sediment depth, respectively using CrunchTope, with a constant $^{34}\varepsilon$ of –45‰.

for each model run (–45‰). With the higher sulfate reduction rate at Site 9, diffusion of seawater from the top of the column has a more significant impact on the apparent or observed sulfur isotope fractionation, whereas the lower rate of sulfate reduction at Site 5 lowers the impact that diffusion has on the apparent evolution of the sulfur isotopic composition of the pore fluid. Similarly, increasing the diffusion coefficient, or increasing the porosity of the system, will have the same directional impact as decreasing the rate of sulfate reduction, as the slope of the sulfate concentration-sulfur isotope plot is related to the balance of sulfate reduction and diffusion of sulfate within the pore fluid. Isotope-specific diffusion effects are not included for the different isotopologues during sulfate reduction as it has been previously shown that the impact of isotope-specific diffusion coefficients during microbially mediated sulfate reduction is considerably smaller than the error associated with the determination of the fractionation factor (Wortmann and Chernyavsky, 2011). The assumption of a consistent diffusion coefficient for ^{12}C and ^{13}C for both HCO_3^- and CO_3^{2-} has been previously used given the hydration of the molecules by a significant number of water molecules, which means the impact of ^{13}C on the effective size of the molecule is very small (Zeebe et al., 1999).

The key finding is that the same sulfur isotope fractionation factor can explain the pore fluid sulfur isotope data when a full reactive transport model is used (**Figure 5B**). This demonstrates the limitations of modeling pore fluid data assuming closed-system Rayleigh fractionation, and highlights the importance of using reactive transport modeling, especially in the upper part of the sediment column where diffusive exchange with the overlying seawater is critically important. We also note that the sulfate concentration mismatch between the model and the data in the upper part of the sediment column (**Figure 5C**) suggests that the site may not be in steady state, which has previously been observed nearby at Site U1385 (Turchyn et al., 2016). However, when the sulfate concentration and $\delta^{34}S_{SO4}$ profiles are compared in **Figure 5B** it can be seen that the sulfur isotope fractionation is similar throughout the sediment column.

Aerobic Respiration vs. Microbial Sulfate Reduction

Aerobic respiration, the breakdown of organic matter using dissolved oxygen as the electron acceptor, produces the largest free energy change of all of the oxidation reactions (Equation 3; Froelich et al., 1979). Aerobic respiration will persist in the water column and sediment as deep as oxygen can diffuse before it is fully depleted; therefore, in most continental margins, aerobic respiration will continue to, at, and below the sediment-water interface. As aerobic respiration involves release of the ^{12}C-enriched organic carbon, but does not impact $\delta^{34}S_{SO4}$, the relative evolution of the sulfur and carbon cross plot (**Figure 4B**) may be flagging the dynamics of aerobic respiration before the onset of MSR. To evaluate this effect, we compare a model of sulfate reduction (with no aerobic respiration—black line) to a model with both sulfate reduction and aerobic respiration (colored lines—viewed in a cross plot of $\delta^{13}C_{DIC}$ vs. $\delta^{34}S_{SO4}$; **Figure 6**). Our results suggest that the addition of aerobic respiration to a sediment column should cause a small, but noticeable, shift in the carbon isotopic composition of the DIC before the change in $\delta^{34}S_{SO4}$ at the onset of MSR (**Figure 6A**). Changing the rate of aerobic respiration to reproduce the differences in the dissolved oxygen concentration profiles observed at these five sites (**Figure 6B**) has no significant impact on the evolution in the cross plot of $\delta^{13}C_{DIC}$ vs. $\delta^{34}S_{SO4}$, with all five colored lines appearing identical (**Figure 6A**). We note that $\delta^{13}C_{DIC}$ varies before $\delta^{34}S_{SO4}$ even when there is no aerobic respiration, only MSR, due to the low initial concentration of DIC in seawater (~2.5 mM) relative to the initial concentration of sulfate in

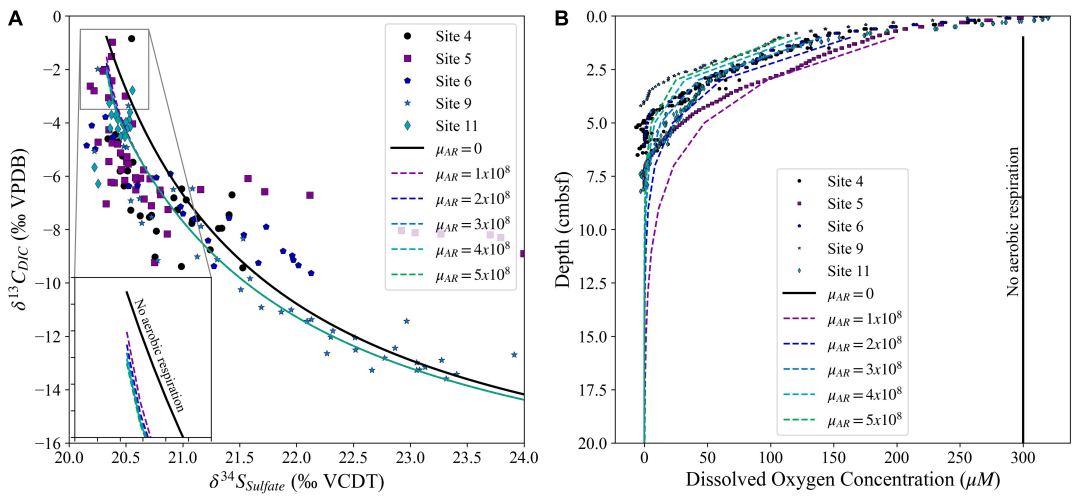

FIGURE 6 | Panel **(A)** displays the change in sulfur isotopic composition of sulfate vs. the change in carbon isotopic composition of the DIC, while panel **(B)** displays the measured dissolved oxygen concentrations over the upper 20 cm of the five sites. In both panels the lines represent model runs for varying rates of aerobic respiration, with a constant rate of sulfate reduction, ranging from no aerobic respiration (black solid line) to aerobic respiration depleting the oxygen in the upper 5 cmbsf (green dashed line).

seawater (28 mM). This means that small additions of DIC with a lower $\delta^{13}C$ value (–20‰ vs. ~0‰ in seawater) have a larger immediate observed geochemical effect than the removal of sulfate through MSR even with the large sulfur isotope fractionation. Furthermore, during MSR there is the release of two mole of DIC during the reduction of one mole of sulfate (Equation 1). The combination of these two factors causes a rapid decrease in $\delta^{13}C_{DIC}$ relative to the slower increase in $\delta^{34}S_{SO4}$, the shape of which can be further augmented by the release of ^{12}C-enriched DIC during aerobic respiration.

In some of the sites studied, however, there is a slightly larger initial decrease in $\delta^{13}C_{DIC}$ relative to the increase in $\delta^{34}S_{SO4}$ than predicted by the model that just includes aerobic respiration and MSR (**Figure 6A**). This hints that the cross plot of $\delta^{13}C_{DIC}$ vs. $\delta^{34}S_{SO4}$ may contain additional information, allowing us to explore other chemical reactions such as iron or manganese reduction that in theory should occur before MSR. We explore the deviation from the model (**Figure 6A**) by performing a sensitivity analysis, varying $\delta^{13}C_{OrgC}$, initial (DIC), and the sulfur isotope fractionation factor to investigate how these variables cause deviations in the cross plot of $\delta^{13}C_{DIC}$ vs. $\delta^{34}S_{SO4}$ in a sedimentary system where aerobic respiration and MSR are occurring (**Figure 7**). Our model suggests that changes in all three variables alter the sulfur/carbon isotope

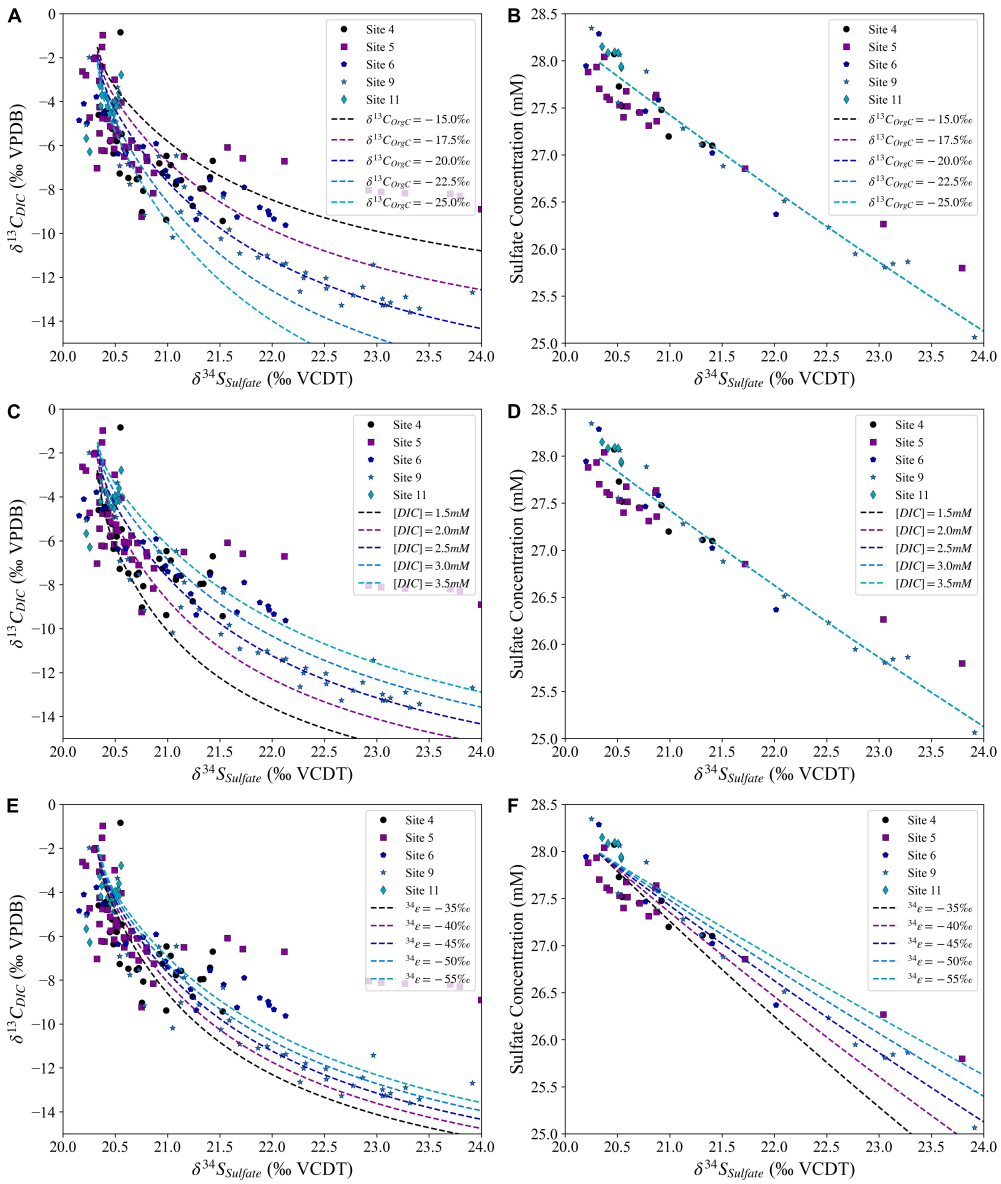

FIGURE 7 | The sulfur and carbon isotopic composition for the model with varying carbon isotope composition of the organic carbon [$\delta^{13}C_{OrgC}$; **(A,B)**], initial dissolved inorganic carbon concentrations [(DIC); **(C,D)**] and sulfur isotope fractionation during sulfate reduction [$^{34}\varepsilon$; **(E,F)**] compared with the measured pore fluid values for the five sites. In panels **(B,D)** all five simulations are plotted; the lines are identical.

cross plot in similar, but slightly different, ways. Increasing the sulfur isotope fractionation factor or the boundary layer concentration of DIC produces a slower change in $\delta^{13}C_{DIC}$ relative to $\delta^{34}S_{SO4}$ (**Figures 7C–F**). However, this does not imply that our data suggest that there are different sulfur isotope fractionation factors among these sites, as a higher or lower sulfur isotope fractionation factor needs to also be consistent with the change in the pore fluid sulfate concentration (**Figure 7F**). We note that a change in the $\delta^{13}C$ value of the organic carbon impacts the minimum carbon isotope composition of the pore fluid DIC as $\delta^{13}C_{DIC}$ approaches the $\delta^{13}C$ value of the organic carbon.

The Impact of Anaerobic Oxidation of Methane and Methanogenesis on the Sulfur/Carbon Cross Plot

We combine data from a wider compilation of sediment cores where both sulfur and carbon isotope compositions for pore fluids have been reported (**Figure 8**; Sivan et al., 2007; Antler et al., 2013, 2014, 2015; Rubin-Blum et al., 2014). Consistent with the sites from JC089, this global compilation shows rapidly decreasing $\delta^{13}C_{DIC}$ before a significant increase in $\delta^{34}S_{SO4}$ is seen. The range in the minimum $\delta^{13}C_{DIC}$ value observed in the cross plot of $\delta^{13}C_{DIC}$ vs. $\delta^{34}S_{SO4}$ can be matched by modeling a range of $\delta^{13}C_{OrgC}$ values from −60 to −5‰. The site with the least-negative minimum in $\delta^{13}C_{DIC}$ is ODP Site 1086, which is located off the coast of South Africa (Diester-Haass et al., 2004). The sediment at ODP Site 1086 is carbonate-rich with low organic carbon content, which causes a very low rate of sulfate reduction, with sulfate concentration reaching zero around 180 mbsf (Bradbury and Turchyn, 2018). The recrystallization of carbonate minerals, which is occurring at this site (Bradbury and Turchyn, 2018), releases carbon from the calcium carbonate

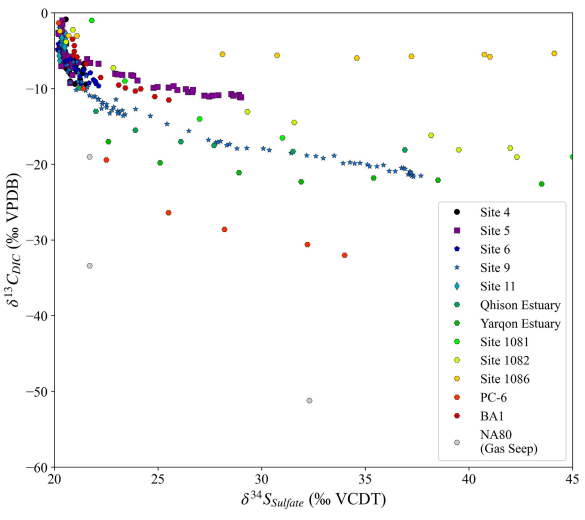

FIGURE 8 | The sulfur and carbon isotopic composition for the sites in this paper with a wider range of sites from the literature (Sivan et al., 2007; Antler et al., 2013, 2014, 2015; Rubin-Blum et al., 2014).

with a $\delta^{13}C$ value of approximately 0‰, which also will raise the minimum $\delta^{13}C_{DIC}$ value. The overprinting of the isotopic signature of the microbial oxidation of organic carbon with carbonate recrystallization is only apparent in locations with very low rates of organic carbon burial and MSR such as ODP Site 1086 and Site 5 from the JC089 cruise.

While the carbon isotope composition of organic carbon may vary between −20‰ and −30‰ depending on the type of organic carbon being respired, it is exceptionally unlikely to become as low as −60‰ as needed to explain some of the lowest data in **Figure 8** (Meyers, 1994; Galimov, 2006). In order to explain the lowest $\delta^{13}C_{DIC}$ values, methane oxidation needs to be invoked. Here we consider the impact on the cross plot of $\delta^{13}C_{DIC}$ vs. $\delta^{34}S_{SO4}$ of the presence of methane at some depth within the sediment column. At several of the sites shown in **Figure 8**, there is methane below the sampled section—for example at IODP Site U1385, which drilled deeper into these sediments at Site 6, there is an upward flux of methane (Turchyn et al., 2016). Below these shallowmost sediments, sulfate concentrations in the pore fluid could be decreasing to a sulfate-methane transition zone, a sharp interval where sulfate concentrations go to zero and methane, supplied by diffusion from sediments below, is oxidized *via* the anaerobic oxidation of methane coupled to MSR (sulfate-driven AOM). Sulfate-driven AOM will have a similar impact on $\delta^{34}S_{SO4}$ as organic-matter driven MSR, but dramatically change $\delta^{13}C_{DIC}$. When methane is oxidized in the sulfate-methane transition zone through sulfate-driven AOM, it returns its ^{12}C-enriched $CO_{2(aq)}$ back to the pore fluid (Whiticar and Faber, 1986; Whiticar, 1999; Sivan et al., 2007; Meister et al., 2019). A pore fluid profile of $\delta^{13}C_{DIC}$ where methanogenesis and methanotrophy are both occurring will contain a rapid decrease from the sediment-water interface to the depth of methanotrophy where $\delta^{13}C_{DIC}$ can be as low as −35‰ (Bradbury and Turchyn, 2019; Meister et al., 2019). Below the zone of methanotrophy, in the zone of methanogenesis, $\delta^{13}C_{DIC}$ increases rapidly and can reach as high as +10 to +20‰ (Bradbury and Turchyn, 2019; Meister et al., 2019).

When MSR, sulfate-driven AOM and methanogenesis are combined, our model shows that the net effect of all three processes causes the minimum $\delta^{13}C_{DIC}$ value to approach $\delta^{13}C_{OrgC}$, similar to previous studies (Meister et al., 2019). When the sulfate-methane transition zone (SMTZ) gets close to the sediment-water interface, however, the minimum $\delta^{13}C_{DIC}$ value is no longer as negative, due to the diffusion of ^{13}C-enriched DIC from the zone of methanogenesis and the overlying seawater and the loss of the ^{12}C-enriched methane into seawater. In order for $\delta^{13}C_{DIC}$ to be significantly lower than $\delta^{13}C_{OrgC}$, the methane must be diffusing from a deeper zone, or a different source, which leads to the release of ^{12}C-enriched DIC into the pore fluid without the local effects of methanogenesis on $\delta^{13}C_{DIC}$. This effect is displayed by creating a simulation with methane being pumped in from the base of the column with a $\delta^{13}C$ value of −75‰. In order to minimize the impact of pumping methane-enriched fluid in at the base of the column on fluid flow during sediment burial, a fluid containing 10 mM of methane was pumped in. Two different rates were tested (3E-6 and 6E-6 kg H_2O/s) and we verified that such low values had

no impact on the velocity profile of fluid flow given sediment burial rates but allowed methane to diffuse up through the column. We can visualize the impact that the flux of methane from the base of the column has compared to higher rates of methanogenesis in **Figure 9**. When there is no methanogenesis and the highest flux of methane, the minimum in $\delta^{13}C_{DIC}$ reaches −55‰, with a corresponding $\delta^{34}S_{SO4}$ of around 42‰. If there is no methanogenesis or methane flux, the $\delta^{34}S_{SO4}$ value increases to the maximum $\delta^{34}S_{SO4}$ possible during sulfate reduction, as the minimum in $\delta^{13}C_{DIC}$ will occur at the base of the sulfate reduction zone. Finally, if there is both methanogenesis and a flux of methane from below, the minimum $\delta^{13}C_{DIC}$ value becomes less negative with an increasing rate of methanogenesis while the corresponding $\delta^{34}S_{SO4}$ value becomes less positive (**Figure 9**).

Summary—How to Interpret a Sulfur/Carbon Isotope Cross Plot

We propose that the cross plot of $\delta^{13}C_{DIC}$ vs. $\delta^{34}S_{SO4}$ holds significant information about the nature of carbon-sulfur coupling in marine sedimentary pore fluids on continental margins. The major controls on the initial decrease in $\delta^{13}C_{DIC}$ relative to $\delta^{34}S$ are related to the early microbial diagenetic reactions as well as to the amount and $\delta^{13}C$ of seawater DIC, which can be visualized in the upper left

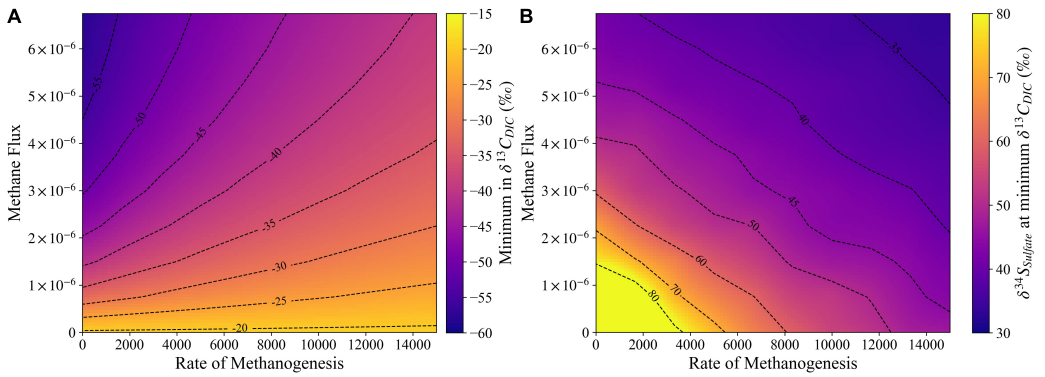

FIGURE 9 | Contour plots displaying the impact of the rate of methanogenesis and methane flux on the minimum $\delta^{13}C$ value **(A)** and the associated $\delta^{34}S$ value **(B)**.

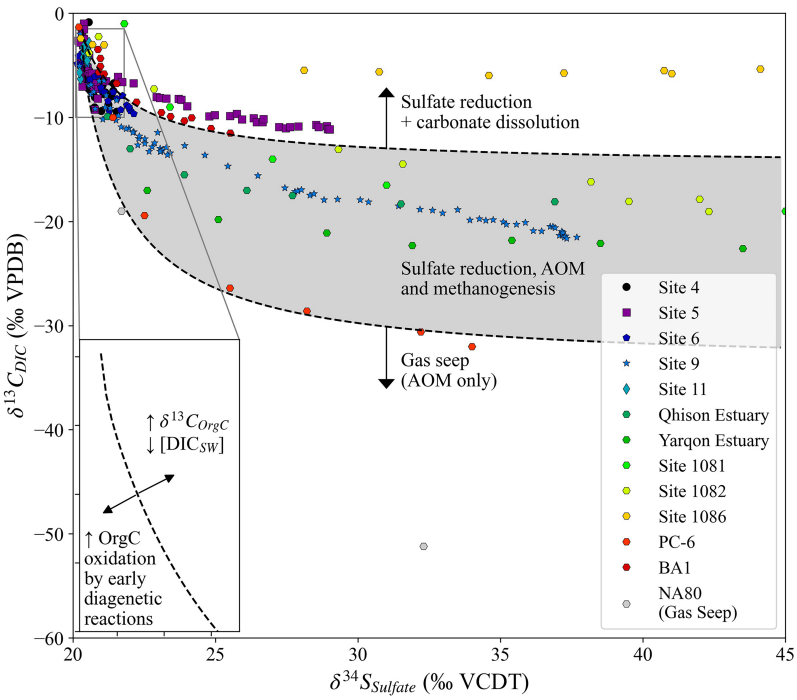

FIGURE 10 | The sulfur and carbon isotopic composition of sulfate and DIC, respectively, for the sites in this paper and a range of literature sites (Sivan et al., 2007; Antler et al., 2013, 2014, 2015; Rubin-Blum et al., 2014). The isotopic compositions of the sites are overlaid by a schematic of the main controls on the sulfur/carbon isotope cross plot and the inset axis contains a schematic for the major controls on the upper left part of the profiles.

of the sulfur/carbon isotope cross plot, with lower DIC and greater intensity or number of early diagenetic reactions causing a larger decrease in $\delta^{13}C_{DIC}$ before $\delta^{34}S_{SO4}$ increases. The carbon isotopic composition of the DIC released from the oxidation of organic matter is a major control on the minimum $\delta^{13}C_{DIC}$ value in the sulfur/carbon isotope cross plot, with $\delta^{13}C$ of the organic carbon being important during both MSR and combined sulfate reduction, sulfate-driven AOM and methanogenesis. When MSR, sulfate-driven AOM and methanogenesis are occurring in the sediment column the minimum $\delta^{13}C_{DIC}$ value is variable, but the overall trend will generally fit within the shaded area in **Figure 10**. In order for the minimum $\delta^{13}C_{DIC}$ value to be below the shaded area, sulfate-driven AOM must occur with a source of methane external to the measured sedimentary pore fluids, with the relative amount of methane coming from *in situ* methanogenesis vs. an external flux of methane (as well as $\delta^{13}C_{CH4}$) controlling the absolute minimum $\delta^{13}C_{DIC}$ value and associated $\delta^{34}S_{SO4}$. Finally, in order for the minimum $\delta^{13}C_{DIC}$ value to be significantly higher than the $\delta^{13}C_{OrgC}$ there must be the release of carbon within the sedimentary system which is not enriched in ^{12}C. We suggest this is occurring at Site 5 and ODP Site 1086, where carbon released during carbonate recrystallization causes the minimum $\delta^{13}C_{DIC}$ value to be around $-5‰$ (**Figure 10**).

DATA AVAILABILITY STATEMENT

The original contributions presented in the study are included in the article/**Supplementary Material**, further inquiries can be directed to the corresponding author/s.

AUTHOR CONTRIBUTIONS

AT, HB, and GA contributed to the conception and design of this study. AB produced the dataset with help from MG, GA, DS, AT, and DH. HB designed and implemented the model in collaboration with AF and JD. HB and AT wrote the manuscript with input from all co-authors.

FUNDING

This work was supported by NERC NE/R013519/1 to HB, ERC 307582 StG (CARBONSINK) to AT and NERC grant NE/J00653X/1 to DH.

ACKNOWLEDGMENTS

We would like to thank all the participants of cruise JC089 on board the R/V James Cook for recovering the Iberian Margin core material and pore fluids used in this study. We would also like to thank the editor LW and the two reviewers whose comments greatly strengthened this manuscript.

SUPPLEMENTARY MATERIAL

The Supplementary Material for this article can be found online at: https://www.frontiersin.org/articles/10.3389/feart.2021.652960/full#supplementary-material

REFERENCES

Algeo, T. J., Luo, G. M., Song, H. Y., Lyons, T. W., and Canfield, D. E. (2015). Reconstruction of secular variation in seawater sulfate concentrations. *Biogeosciences* 12, 2131–2151. doi: 10.5194/bg-12-2131-2015

Antler, G., and Pellerin, A. (2018). A critical look at the combined use of sulfur and oxygen isotopes to study microbial metabolisms in methane-rich environments. *Front. Microbiol.* 9:519. doi: 10.3389/fmicb.2018.00519

Antler, G., Turchyn, A. V., Herut, B., Davies, A., Rennie, V. C. F., and Sivan, O. (2014). Sulfur and oxygen isotope tracing of sulfate driven anaerobic methane oxidation in estuarine sediments. *Estuar. Coastal Shelf Sci.* 142, 4–11. doi: 10.1016/j.ecss.2014.03.001

Antler, G., Turchyn, A. V., Herut, B., and Sivan, O. (2015). A unique isotopic fingerprint of sulfate-driven anaerobic oxidation of methane. *Geology* 43, 619–622. doi: 10.1130/G36688.1

Antler, G., Turchyn, A. V., Rennie, V., Herut, B., and Sivan, O. (2013). Coupled sulfur and oxygen isotope insight into bacterial sulfate reduction in the natural environment. *Geochim. Cosmochim. Acta* 118, 98–117. doi: 10.1016/j.gca.2013.05.005

Arndt, S., Hetzel, A., and Brumsack, H.-J. (2009). Evolution of organic matter degradation in Cretaceous black shales inferred from authigenic barite: a reaction-transport model. *Geochim. Cosmochim. Acta* 73, 2000–2022. doi: 10.1016/j.gca.2009.01.018

Barnes, R. O., and Goldberg, E. D. (1976). Methane production and consumption in anoxic marine sediments. *Geology* 4, 297–300. doi: 10.1130/0091-7613197 64<297:MPACIA<2.0.CO;2

Berner, R. A. (1978). Sulfate reduction and the rate of deposition of marine sediments. *Earth Planet. Sci. Lett.* 37, 492–498. doi: 10.1016/0012-821X(78)90065-1

Berner, R. A. (1980). *Early Diagenesis: A Theoretical Approach*. Princeton, NJ: Princeton University Press.

Berner, R. A. (1989). Biogeochemical cycles of carbon and sulfur and their effect on atmospheric oxygen over phanerozoic time. *Glob. Planet. Change* 1, 97–122. doi: 10.1016/0921-8181(89)90018-0

Boudreau, B. P. (1997). *Diagenetic Models and their Implementation: Modelling Transport and Reactions in Aquatic Sediments*. Berlin: Springer.

Bradbury, H. J., and Turchyn, A. V. (2018). Calcium isotope fractionation in sedimentary pore fluids from ODP Leg 175: resolving carbonate recrystallization. *Geochim. Cosmochim. Acta* 236, 121–139. doi: 10.1016/j.gca.2018.01.040

Bradbury, H. J., and Turchyn, A. V. (2019). Reevaluating the carbon sink due to sedimentary carbonate formation in modern marine sediments. *Earth Planet. Sci. Lett.* 519, 40–49. doi: 10.1016/j.epsl.2019.04.044

Bradley, A. S., Leavitt, W. D., Schmidt, M., Knoll, A. H., Girguis, P. R., and Johnston, D. T. (2016). Patterns of sulfur isotope fractionation during microbial sulfate reduction. *Geobiology* 14, 91–101. doi: 10.1111/gbi.12149

Breukelen, B. M. V., and Prommer, H. (2008). Beyond the rayleigh equation: reactive transport modeling of isotope fractionation effects to improve quantification of biodegradation. *Environ. Sci. Technol.* 42, 2457–2463. doi: 10.1021/es071981j

Brunner, B., Bernasconi, S. M., Kleikemper, J., and Schroth, M. H. (2005). A model for oxygen and sulfur isotope fractionation in sulfate during bacterial sulfate reduction processes. *Geochim. Cosmochim. Acta* 69, 4773–4785. doi: 10.1016/j.gca.2005.04.017

Canfield, D. E., Jørgensen, B. B., Fossing, H., Glud, R., Gundersen, J., Ramsing, N. B., et al. (1993). Pathways of organic carbon oxidation in three continental margin sediments. *Mar. Geol.* 113, 27–40. doi: 10.1016/0025-3227(93)90147-N

Claypool, G. E., and Kaplan, I. R. (1974). "The origin and distribution of methane in marine sediments," in *Natural Gases in Marine Sediments Marine Science*, ed. I. Kaplan (Boston, MA: Springer), 99–139. doi: 10.1007/978-1-4684-2757-8_8

D'Hondt, S., Inagaki, F., Zarikian, C. A., Abrams, L. J., Dubois, N., Engelhardt, T., et al. (2015). Presence of oxygen and aerobic communities from sea floor to basement in deep-sea sediments. *Nat. Geosci.* 8, 299–304. doi: 10.1038/ngeo2387

Diester-Haass, L., Billups, K., Gröcke, D. R., François, L., Lefebvre, V., and Emeis, K. C. (2009). Mid-Mmiocene paleoproductivity in the Atlantic Ocean and implications for the global carbon cycle. *Paleoceanography* 24:A1209. doi: 10.1029/2008PA001605

Diester-Haass, L., Meyers, P. A., and Bickert, T. (2004). Carbonate crash and biogenic bloom in the late miocene: evidence from ODP Sites 1085, 1086, and 1087 in the Cape Basin, southeast Atlantic Ocean. *Paleoceanography* 19:A1007. doi: 10.1029/2003PA000933

Druhan, J. L., Guillon, S., Lincker, M., and Arora, B. (2020). Stable and radioactive carbon isotope partitioning in soils and saturated systems: a reactive transport modeling benchmark study. *Comput. Geosci.* 1–11. doi: 10.1007/s10596-020-09937-6

Druhan, J. L., Steefel, C. I., Conrad, M. E., and DePaolo, D. J. (2014). A large column analog experiment of stable isotope variations during reactive transport: I. A comprehensive model of sulfur cycling and δ34S fractionation. *Geochim. Cosmochim. Acta* 124, 366–393. doi: 10.1016/j.gca.2013.08.037

Druhan, J. L., Steefel, C. I., Williams, K. H., and DePaolo, D. J. (2013). Calcium isotope fractionation in groundwater: molecular scale processes influencing field scale behavior. *Geochim. Cosmochim. Acta* 119, 93–116. doi: 10.1016/j.gca.2013.05.022

Egger, M., Riedinger, N., Mogollón, J. M., and Jørgensen, B. B. (2018). Global diffusive fluxes of methane in marine sediments. *Nat. Geosci.* 11, 421–425. doi: 10.1038/s41561-018-0122-8

Fantle, M. S. (2015). Calcium isotopic evidence for rapid recrystallization of bulk marine carbonates and implications for geochemical proxies. *Geochim. Cosmochim. Acta* 148, 378–401. doi: 10.1016/j.gca.2014.10.005

Fantle, M. S., and DePaolo, D. J. (2007). Ca isotopes in carbonate sediment and pore fluid from ODP Site 807A: the Ca2+(aq)–calcite equilibrium fractionation factor and calcite recrystallization rates in Pleistocene sediments. *Geochim. Cosmochim. Acta* 71, 2524–2546. doi: 10.1016/j.gca.2007.03.006

Fotherby, A., Bradbury, H. J., Antler, G., Sun, X., Druhan, J. L., and Turchyn, A. V. (2021). Modelling the effects of non-steady state transport dynamics on the sulfur and oxygen isotope composition of sulfate in sedimentary pore fluids. *Front. Earth Sci.* 8:587085. doi: 10.3389/feart.2020.587085

Froelich, P. N., Klinkhammer, G. P., Bender, M. L., Luedtke, N. A., Heath, G. R., Cullen, D., et al. (1979). Early oxidation of organic matter in pelagic sediments of the eastern equatorial Atlantic: suboxic diagenesis. *Geochim. Cosmochim. Acta* 43, 1075–1090. doi: 10.1016/0016-7037(79)90095-4

Galimov, E. M. (2006). Isotope organic geochemistry. *Org. Geochem.* 37, 1200–1262. doi: 10.1016/j.orggeochem.2006.04.009

Garcia, H. E., and Gordon, L. I. (1992). Oxygen solubility in seawater: better fitting equations. *Limnol. Oceanogr.* 37, 1307–1312. doi: 10.4319/lo.1992.37.6.1307

Hodell, D. A., Elderfield, H., Greaves, M., McCave, I. N., Skinner, L., Thomas, A., et al. (2014). *The JC089 Scientific Party, JC089 Cruise Report—IODP Site Survey of the Shackleton Sites, SW Iberian Margin*. Liverpool: British ocean data Centre.

Hodell, D. A., Lourens, L., Stow, D. A. V., Hernández-Molina, J., and Alvarez Zarikian, C. A. (2013). The "Shackleton Site" (IODP Site U1385) on the iberian margin. *Sci. Drill.* 16, 13–19. doi: 10.5194/sd-16-13-2013

Hollander, D. J., and McKenzie, J. A. (1991). CO2 control on carbon-isotope fractionation during aqueous photosynthesis: a paleo-pCO2 barometer. *Geology* 19, 929–932. doi: 10.1130/0091-76131991019<0929:CCOCIF<2.3.CO;2

Holler, T., Wegener, G., Knittel, K., Boetius, A., Brunner, B., Kuypers, M. M. M., et al. (2009). Substantial 13C/12C and D/H fractionation during anaerobic oxidation of methane by marine consortia enriched in vitro. *Environ. Microbiol. Rep.* 1, 370–376. doi: 10.1111/j.1758-2229.2009.00074.x

Horita, J. (2001). Carbon isotope exchange in the system CO2-CH4 at elevated temperatures. *Geochim. Cosmochim. Acta* 65, 1907–1919. doi: 10.1016/S0016-7037(01)00570-1

Hubbard, C. G., Cheng, Y., Engelbrekston, A., Druhan, J. L., Li, L., Ajo-Franklin, J. B., et al. (2014). Isotopic insights into microbial sulfur cycling in oil reservoirs. *Front. Microbiol.* 5:480. doi: 10.3389/fmicb.2014.00480

Huber, C., Druhan, J. L., and Fantle, M. S. (2017). Perspectives on geochemical proxies: The impact of model and parameter selection on the quantification of carbonate recrystallization rates. *Geochim. Cosmochim. Acta* 217, 171–192. doi: 10.1016/j.gca.2017.08.023

Johnston, D. T., Farquhar, J., Wing, B. A., Kaufman, A. J., Canfield, D. E., and Habicht, K. S. (2005). Multiple sulfur isotope fractionations in biological systems: a case study with sulfate reducers and sulfur disproportionators. *Am. J. Sci.* 305, 645–660. doi: 10.2475/ajs.305.6-8.645

Jørgensen, B. B., Beulig, F., Egger, M., Petro, C., Scholze, C., and Røy, H. (2019a). Organoclastic sulfate reduction in the sulfate-methane transition of marine sediments. *Geochim. Cosmochim. Acta* 254, 231–245. doi: 10.1016/j.gca.2019.03.016

Jørgensen, B. B., Findlay, A. J., and Pellerin, A. (2019b). The biogeochemical sulfur cycle of marine sediments. *Front. Microbiol.* 10:849. doi: 10.3389/fmicb.2019.00849

Jørgensen, B. B., and Kasten, S. (2006). "Sulfur cycling and methane oxidation," in *Marine Geochemistry*, eds H. D. Schulz and M. Zabel (Berlin: Springer Berlin Heidelberg), 271–309. doi: 10.1007/3-540-32144-6_8

Kasten, S., and Jørgensen, B. B. (2000). "Sulfate reduction in marine sediments," in *Marine Geochemistry*, eds H. D. Schulz and M. Zabel (Berlin: Springer), 263–281. doi: 10.1007/978-3-662-04242-7_8

Kasten, S., Zabel, M., Heuer, V. B., and Hensen, C. (2003). "Processes and signals of non-steady-state diagenesis in deep-sea sediments and their pore waters," in *The South Atlantic in the Late Quaternary: Reconstruction of Material Budgets and Current Systems*, eds G. Wefer, S. Mulitza, and V. Ratmeyer (Berlin: Springer), 431–459. doi: 10.1007/978-3-642-18917-3_20

Kump, L. R., and Arthur, M. A. (1999). Interpreting carbon-isotope excursions: carbonates and organic matter. *Chem. Geol.* 161, 181–198. doi: 10.1016/S0009-2541(99)00086-8

Kump, L. R., Junium, C., Arthur, M. A., Brasier, A., Fallick, A., Melezhik, V., et al. (2011). Isotopic evidence for massive oxidation of organic matter following the great oxidation event. *Science* 334, 1694–1696. doi: 10.1126/science.1213999

Lehmann, M. F., Bernasconi, S. M., Barbieri, A., and McKenzie, J. A. (2002). Preservation of organic matter and alteration of its carbon and nitrogen isotope composition during simulated and in situ early sedimentary diagenesis. *Geochim. Cosmochim. Acta* 66, 3573–3584. doi: 10.1016/S0016-7037(02)00968-7

Londry, K. L., and Des Marais, D. J. (2003). Stable carbon isotope fractionation by sulfate-reducing bacteria. *Appl. Environ. Microbiol.* 69, 2942–2949. doi: 10.1128/AEM.69.5.2942-2949.2003

Martens, C. S., and Berner, R. A. (1974). Methane production in the interstitial waters of sulfate-depleted marine sediments. *Science* 185, 1167–1169. doi: 10.1126/science.185.4157.1167

McCorkle, D. C., Emerson, S. R., and Quay, P. D. (1985). Stable carbon isotopes in marine porewaters. *Earth Planet. Sci. Lett.* 74, 13–26. doi: 10.1016/0012-821X(85)90162-1

Meister, P. (2013). Two opposing effects of sulfate reduction on carbonate precipitation in normal marine, hypersaline, and alkaline environments. *Geology* 41, 499–502. doi: 10.1130/G34185.1

Meister, P. (2014). Two opposing effects of sulfate reduction on carbonate precipitation in normal marine, hypersaline, and alkaline environments: REPLY. *Geology* 42:e315. doi: 10.1130/G35240Y.1

Meister, P., Liu, B., Khalili, A., Böttcher, M. E., and Jørgensen, B. B. (2019). Factors controlling the carbon isotope composition of dissolved inorganic carbon and methane in marine porewater: an evaluation by reaction-transport modelling. *J. Mar. Syst.* 200:103227. doi: 10.1016/j.jmarsys.2019.103227

Meyers, P. A. (1994). Preservation of elemental and isotopic source identification of sedimentary organic matter. *Chem. Geol.* 114, 289–302. doi: 10.1016/0009-2541(94)90059-0

Pellerin, A., Antler, G., Holm, S. A., Findlay, A. J., Crockford, P. W., Turchyn, A. V., et al. (2019). Large sulfur isotope fractionation by bacterial sulfide oxidation. *Sci. Adv.* 5:eaaw1480. doi: 10.1126/sciadv.aaw1480

Rubin-Blum, M., Antler, G., Turchyn, A. V., Tsadok, R., Goodman-Tchernov, B. N., Shemesh, E., et al. (2014). Hydrocarbon-related microbial processes in the deep

sediments of the Eastern Mediterranean Levantine Basin. *FEMS Microbiol. Ecol.* 87, 780–796. doi: 10.1111/1574-6941.12264

Rudnicki, M. D., Elderfield, H., and Spiro, B. (2001). Fractionation of sulfur isotopes during bacterial sulfate reduction in deep ocean sediments at elevated temperatures. *Geochim. Cosmochim. Acta* 65, 777–789. doi: 10.1016/S0016-7037(00)00579-2

Sayles, F. L. (1979). The composition and diagenesis of interstitial solutions—I. Fluxes across the seawater-sediment interface in the Atlantic Ocean. *Geochim. Cosmochim. Acta* 43, 527–545. doi: 10.1016/0016-7037(79)90163-7

Sayles, F. L. (1981). The composition and diagenesis of interstitial solutions—II. Fluxes and diagenesis at the water-sediment interface in the high latitude North and South Atlantic. *Geochim. Cosmochim. Acta* 45, 1061–1086. doi: 10.1016/0016-7037(81)90132-0

Sela-Adler, M., Ronen, Z., Herut, B., Antler, G., Vigderovich, H., Eckert, W., et al. (2017). Co-existence of methanogenesis and sulfate reduction with common substrates in sulfate-rich estuarine sediments. *Front. Microbiol.* 8:766. doi: 10.3389/fmicb.2017.00766

Sivan, O., Schrag, D. P., and Murray, R. W. (2007). Rates of methanogenesis and methanotrophy in deep-sea sediments. *Geobiology* 5, 141–151. doi: 10.1111/j.1472-4669.2007.00098.x

Skinner, L. C., Sadekov, A., Brandon, M., Greaves, M., Plancherel, Y., de la Fuente, M., et al. (2019). Rare earth elements in early-diagenetic foraminifer 'coatings': pore-water controls and potential palaeoceanographic applications. *Geochim. Cosmochim. Acta* 245, 118–132. doi: 10.1016/j.gca.2018.10.027

Steefel, C. I., Appelo, C. A. J., Arora, B., Jacques, D., Kalbacher, T., Kolditz, O., et al. (2015). Reactive transport codes for subsurface environmental simulation. *Comput. Geosci.* 19, 445–478. doi: 10.1007/s10596-014-9443-x

Steiner, Z., Lazar, B., Erez, J., and Turchyn, A. V. (2018). Comparing Rhizon samplers and centrifugation for pore-water separation in studies of the marine carbonate system in sediments. *Limnol. Oceanogr. Methods* 16, 828–839. doi: 10.1002/lom3.10286

Sun, X., Higgins, J., and Turchyn, A. V. (2016). Diffusive cation fluxes in deep-sea sediments and insight into the global geochemical cycles of calcium, magnesium, sodium and potassium. *Mar. Geol.* 373, 64–77. doi: 10.1016/j.margeo.2015.12.011

Tromp, T. K., Van Cappellen, P., and Key, R. M. (1995). A global model for the early diagenesis of organic carbon and organic phosphorus in marine sediments. *Geochim. Cosmochim. Acta* 59, 1259–1284. doi: 10.1016/0016-7037(95)00042-X

Turchyn, A. V., Antler, G., Byrne, D., Miller, M., and Hodell, D. A. (2016). Microbial sulfur metabolism evidenced from pore fluid isotope geochemistry at Site U1385. *Glob. Planet. Change* 141, 82–90. doi: 10.1016/j.gloplacha.2016.03.004

Turchyn, A. V., Sivan, O., and Schrag, D. P. (2006). Oxygen isotopic composition of sulfate in deep sea pore fluid: evidence for rapid sulfur cycling. *Geobiology* 4, 191–201. doi: 10.1111/j.1472-4669.2006.00079.x

Wehrmann, L. M., Risgaard-Petersen, N., Schrum, H. N., Walsh, E. A., Huh, Y., Ikehara, M., et al. (2011). Coupled organic and inorganic carbon cycling in the deep subseafloor sediment of the northeastern Bering Sea Slope (IODP Exp. 323). *Chem. Geol.* 284, 251–261. doi: 10.1016/j.chemgeo.2011.03.002

Whiticar, M. J. (1999). Carbon and hydrogen isotope systematics of bacterial formation and oxidation of methane. *Chem. Geol.* 161, 291–314. doi: 10.1016/S0009-2541(99)00092-3

Whiticar, M. J., and Faber, E. (1986). Methane oxidation in sediment and water column environments—isotope evidence. *Org. Geochem.* 10, 759–768. doi: 10.1016/S0146-6380(86)80013-4

Wortmann, U. G., Chernyavsky, B., Bernasconi, S. M., Brunner, B., Böttcher, M. E., and Swart, P. K. (2007). Oxygen isotope biogeochemistry of pore water sulfate in the deep biosphere: dominance of isotope exchange reactions with ambient water during microbial sulfate reduction (ODP Site 1130). *Geochim. Cosmochim. Acta* 71, 4221–4232. doi: 10.1016/j.gca.2007.06.033

Wortmann, U. G., and Chernyavsky, B. M. (2011). The significance of isotope specific diffusion coefficients for reaction-transport models of sulfate reduction in marine sediments. *Geochim. Cosmochim. Acta* 75, 3046–3056. doi: 10.1016/j.gca.2011.03.007

Yoshinaga, M. Y., Holler, T., Goldhammer, T., Wegener, G., Pohlman, J. W., Brunner, B., et al. (2014). Carbon isotope equilibration during sulphate-limited anaerobic oxidation of methane. *Nat. Geosci.* 7, 190–194. doi: 10.1038/ngeo2069

Zeebe, R. E., Bijma, J., and Wolf-Gladrow, D. A. (1999). A diffusion-reaction model of carbon isotope fractionation in foraminifera. *Mar. Chem.* 64, 199–227. doi: 10.1016/S0304-4203(98)00075-9

Zhang, J., Quay, P. D., and Wilbur, D. O. (1995). Carbon isotope fractionation during gas-water exchange and dissolution of CO2. *Geochim. Cosmochim. Acta* 59, 107–114. doi: 10.1016/0016-7037(95)91550-D

Conflict of Interest: The authors declare that the research was conducted in the absence of any commercial or financial relationships that could be construed as a potential conflict of interest.

The handling editor declared a past co-authorship with one of the authors GA.

frontiers in Earth Science

ORIGINAL RESEARCH
published: 28 May 2021
doi: 10.3389/feart.2021.671401

Holocene Spatiotemporal Redox Variations in the Southern Baltic Sea

Dalton S. Hardisty[1], Natascha Riedinger[2], Noah J. Planavsky[3], Dan Asael[3], Steven M. Bates[4] and Timothy W. Lyons[4]*

[1] Department of Earth and Environmental Sciences, Michigan State University, East Lansing, MI, United States, [2] Boone Pickens School of Geology, Oklahoma State University, Stillwater, OK, United States, [3] Department of Geology and Geophysics, Yale University, New Haven, CT, United States, [4] Department of Earth and Planetary Sciences, University of California, Riverside, Riverside, CA, United States

Low oxygen conditions in the modern Baltic Sea are exacerbated by human activities; however, anoxic conditions also prevailed naturally over the Holocene. Few studies have characterized the specific paleoredox conditions (manganous, ferruginous, euxinic) and their frequency in southern Baltic sub-basins during these ancient events. Here, we apply a suite of isotope systems (Fe, Mo, S) and associated elemental proxies (e.g., Fe speciation, Mn) to specifically define water column redox regimes through the Baltic Holocene in a sill-proximal to sill-distal transect (Lille Belt, Bornholm Basin, Landsort Deep) using samples collected during the Integrated Ocean Drilling Program Expedition 347. At the sill-proximal Lille Belt, there is evidence for anoxic manganous/ferruginous conditions for most of the cored interval following the transition from the Ancylus Lake to Littorina Sea but with no clear excursion to more reducing or euxinic conditions associated with the Holocene Thermal Maximum (HTM) or Medieval Climate Anomaly (MCA) events. At the sill-distal southern sub-basin, Bornholm Basin, a combination of Fe speciation, pore water Fe, and solid phase Mo concentration and isotope data point to manganous/ferruginous conditions during the Ancylus Lake-to-Littorina Sea transition and HTM but with only brief excursions to intermittently or weakly euxinic conditions during this interval. At the western Baltic Proper sub-basin, Landsort Deep, new Fe and S isotope data bolster previous Mo isotope records and Fe speciation evidence for two distinct anoxic periods but also suggest that sulfide accumulation beyond transient levels was largely restricted to the sediment-water interface. Ultimately, the combined data from all three locations indicate that Fe enrichments typically indicative of euxinia may be best explained by Fe deposition as oxides following events likely analogous to the periodic incursions of oxygenated North Sea waters observed today, with subsequent pyrite formation in sulfidic pore waters. Additionally, the Mo isotope data from multiple Baltic Sea southern basins argue against restricted and widespread euxinic conditions, as has been demonstrated in the Baltic Proper and Bothnian Sea during the HTM or MCA. Instead, similar to today, each past Baltic anoxic event is characterized by redox conditions that become progressively more reducing with increasing distance from the sill.

Keywords: Baltic Sea, paleoredox, diagenesis, molybdenum isotopes, iron isotopes, sulfur isotopes, IODP Expedition 347

OPEN ACCESS

Edited by:
Paolo Censi,
University of Palermo, Italy

Reviewed by:
Michael E. Böttcher,
Leibniz Institute for Baltic Sea Research (IOW), Germany
Weiqiang Li,
Nanjing University, China

****Correspondence:***
Dalton S. Hardisty
hardist1@msu.edu

Specialty section:
This article was submitted to Geochemistry, a section of the journal Frontiers in Earth Science

Received: *23 February 2021*
Accepted: *21 April 2021*
Published: *28 May 2021*

Citation:
Hardisty DS, Riedinger N, Planavsky NJ, Asael D, Bates SM and Lyons TW (2021) Holocene Spatiotemporal Redox Variations in the Southern Baltic Sea. Front. Earth Sci. 9:671401. doi: 10.3389/feart.2021.671401

INTRODUCTION

Bottom water oxygen availability in the Baltic Sea is regulated by a combination of warming temperature, eutrophication, salinity stratification, and controls related to basin morphology (Carstensen et al., 2014). Among these, increased nutrient input from land and associated cyanobacterial blooms are most prominently responsible for the tenfold increase in the seafloor area of Baltic low oxygen/anoxic bottom waters observed over the last century, while it has only been over the last 20 years that increased respiration resulting from anthropogenic warming is observable (Carstensen et al., 2014). Importantly, however, even in the absence of anthropogenic factors, salinity gradients and temporal variation from combined natural climate change, unique circulation patterns, and hydrography prime the Baltic Sea for the development of low oxygen bottom waters (Mohrholz et al., 2015). The Baltic Sea is silled at the Danish straits (**Figures 1A,B**), forcing freshwater output from runoff and saline input from the North Sea through the same location. This restriction supports the development of a strong halocline—limiting physical mixing between surface and bottom waters and thus limiting bottom water renewal to lateral advection. Such restricted and stratified conditions are particularly prone to the development of oxygen-depleted bottom waters (**Figures 1C–E** red lines), as is observed in other silled basins including the Black Sea, Cariaco Basin, Framvaren Fjord, and Saanich Inlet. Like these other restricted basins, the modern Baltic water column is reducing enough within some sub-basins to permit the accumulation of hydrogen sulfide—a water column redox state referred to as euxinia (Carstensen et al., 2014; Noordmann et al., 2014). Euxinia precludes the presence of animals and results in strong sequestration of a suite of redox-sensitive metals (for example, Mo and Fe) (Algeo and Lyons, 2006; Lyons and Severmann, 2006; Scott and Lyons, 2012).

The Baltic is unique relative to other modern anoxic settings such as the Black Sea, as the halocline is highly dynamic, with gradients in the spatial ranges, timescales, and depths of salinity fluctuation along transects moving away from the sill (**Figures 1C–E** blue lines). Baltic Sea salinity gradients and short-term oscillations are largely a function of isolated climatic events known as Major Baltic Inflows (MBIs). During these events, saline and oxygen-rich marine waters from the North Sea are introduced into the Baltic beneath the halocline (Carstensen et al., 2014). The MBIs are both barotropic and baroclinic events in which wind and air pressure cause a sea level difference between the Kattegat and Arkona Basin on opposing sides of the sill (**Figure 1**), forcing temporary net inflow of North Sea saline and oxygenated water into the Baltic (Franck et al., 1987; Matthäus, 2006; Mohrholz et al., 2015). Depending on the spatial scale of the MBI and the season of occurrence, most of Baltic Sea can become temporarily oxygenated. This extreme can lead to the oxidation of redox-sensitive chemical species accumulated in the formerly anoxic bottom waters (e.g., Mn(II), Fe(II), H_2S), while simultaneously introducing saline water that maintains the halocline and resulting stratification responsible for the return to and long-term maintenance of anoxic bottom waters (Huckriede and Meischner, 1996; Dellwig et al., 2010, 2018; Scholz et al., 2018; Hermans et al., 2019; Ni et al., 2020; van de Velde et al., 2020). Ultimately, halocline stability and frequency of bottom water renewal act to regulate the maximum reducing potential of bottom waters within individual Baltic sub-basins, resulting in an increased spatial gradient in the occurrence of euxinia and stable anoxic conditions more generally with increasing distance from the sill (**Figures 1C–E** red lines).

The Baltic Basin has undergone a complex evolution since the last glacial maximum, resulting in multiple transitions between freshwater and brackish and naturally occurring ancient anoxic events. Immediately following the last glacial maximum (∼22 ka), melting from the Scandinavian ice sheet formed an ice lake in the Baltic Basin, which eventually underwent a permanent switch to a brackish basin following global sea level rise and resulting connection to the open ocean—the Ancylus Lake-to-Littorina Sea transition—at approximately 8.5 ka (Andrén et al., 2011). Following this transition and associated halocline formation, two major pre-anthropogenic Baltic anoxic periods are known through sedimentary laminations and geochemical signatures (Manheim, 1961; Suess, 1979; Sohlenius, 1996; Sohlenius et al., 1996, 2001; Sternbeck and Sohlenius, 1997; Lepland and Stevens, 1998; Sohlenius and Westman, 1998; Zillén et al., 2008; Mort et al., 2010; Jilbert and Slomp, 2013; Jilbert et al., 2015; Lenz et al., 2015b; Hardisty et al., 2016; Dijkstra et al., 2018a,b; Groeneveld et al., 2018; van Helmond et al., 2018). These events roughly overlap with the Holocene Thermal Maximum (HTM) (8–4 ka) and Medieval Climate Anomaly (MCA) (1.2–0.8 ka) and co-occur with the widespread enhanced deposition of organic matter in many sub-basins (Zillén et al., 2008).

Recent studies of paleoredox conditions for individual sub-basins during these intervals stress that, like today, specific paleoredox regimes have differed among the sub-basins during penecontemporaneous low oxygen events. Further, paleoredox regimes differed among temporally distinct anoxic events within the same sub-basin. For instance, in the currently well-oxygenated Bothnian Sea, paleoredox records provide evidence for relatively stable euxinia during the HTM, while indicating well-oxygenated water column conditions during the MCA (Jilbert et al., 2015; Dijkstra et al., 2018b). In the Landsort Deep, a currently semi-permanently euxinic basin, paleoredox records provide evidence for euxinic conditions during the MCA and HTM (Dijkstra et al., 2016; Hardisty et al., 2016). Paleo-proxy data specific to well-defined paleoredox regimes and anoxic timescales relevant to the modern redox states are relatively sparse from southern Baltic sub-basins, which elevates the importance of this study.

The redox conditions of modern and ancient basins can be quantified by determining the accumulation of reduced products indicative of the main metabolic processes within a specific zone (e.g., Mn, Fe, or S reduction) (Froelich et al., 1979; Canfield and Thamdrup, 2009). Here, we apply Mo, Mn, Fe, and S geochemistry to define the degree to which reduced Mn (manganous) versus Fe (ferruginous) versus S (euxinic) acted as primary redox buffers in the water column—a sequence representing progressively more reducing conditions. We specifically focus on the ancient water columns of southern Baltic sub-basins Lille Belt, Bornholm Basin, and Landsort Deep.

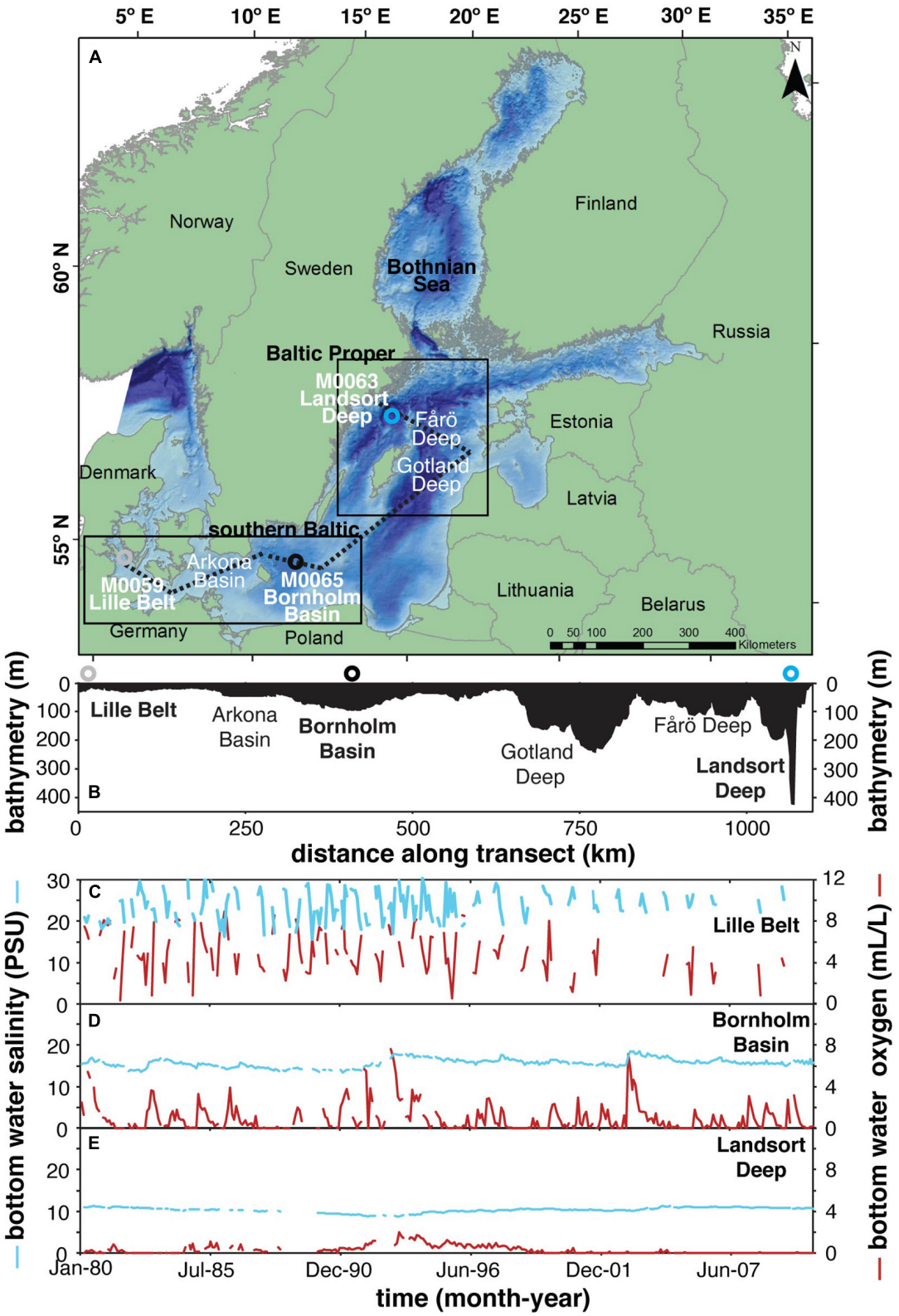

FIGURE 1 | (A) Map showing relevant drilling localities from IODP Expedition 347 and other locations discussed in the text. **(B)** Bathymetry from transect shown in panel **(A)** (dashed line). Panels **(C–E)** represent the mean monthly (1980–2010) bottom water salinity and oxygen concentrations at Lille Belt, Bornholm Basin, Landsort Deep, respectively, from the Baltic Environmental Database of the Baltic Nest Institute, Stockholm University, specifically from stations 450, BY5, and BY31. The red and blue lines represent dissolved oxygen and salinity, respectively.

These sub-basins form a sill-proximal to sill-distal transect (**Figure 1**). We use cores from Integrated Ocean Drilling Program (IODP) Expedition 347 and combined sedimentology; trace element concentrations and Fe speciation; Mo, S, and Fe isotopes; and pore water geochemistry to constrain the specific paleoredox regimes. Our records are combined with previously published data from the Baltic and Bothnian Seas to reconstruct spatiotemporal redox conditions across the Baltic Holocene.

BACKGROUND

Paleoredox Proxy Geochemistry

Ratios of total Fe-to-aluminum (Fe_T/Al) and "highly reactive" Fe-to-total Fe (Fe_{HR}/Fe_T) are related proxies for determining paleo-water column redox, highlighting oxic, ferruginous (Fe-rich), and euxinic conditions (Raiswell et al., 2018). "Highly reactive" Fe represents operationally defined Fe-bearing minerals that are reactive toward hydrogen sulfide on short diagenetic timescales to form Fe sulfides, as well as any Fe sulfides that have formed (Canfield and Berner, 1987; Canfield, 1989; Canfield et al., 1992, 1996; Raiswell and Canfield, 1998; Poulton and Canfield, 2005). Comparisons of Fe_T/Al and Fe_{HR}/Fe_T ratios among sediments from the stable euxinic Black Sea and other similar settings relative to oxic continental margin and deep ocean sediments indicate that "highly reactive" Fe is enriched relative to typical detrital fluxes under anoxic conditions through a process coined the "Fe shuttle" (Canfield et al., 1996; Raiswell and Canfield, 1998; Lyons et al., 2003; Lyons and Severmann, 2006). Detrital values for Fe_{HR}/Fe_T are typically <0.38 in oxic settings (Raiswell and Canfield, 1998). The detrital Fe_T/Al in the Baltic has been specifically calibrated as <0.65 (Fehr et al., 2008). Values clearly above these thresholds represent paleo-anoxic water columns. Pyrite-to-"highly reactive" ratios (Fe_{py}/Fe_{HR}) greater than ∼0.7 in settings with independent indications of anoxia indicate that the majority of the "highly reactive" Fe has formed pyrite, which often results from syngenetic pyrite formation in the water column under euxinic conditions (Canfield et al., 1996; Lyons, 1997; Wijsman et al., 2001b; Lyons and Severmann, 2006; Poulton and Canfield, 2011). Importantly, when Fe_T/Al and Fe_{HR}/Fe_T are not enriched, ratios of Fe_{py}/Fe_{HR} are a proxy for sulfide accumulation in ancient pore waters (Sperling et al., 2015; Hardisty et al., 2018).

Molybdenum cycling can be applied to fingerprint ancient euxinic conditions—but also Fe and Mn cycling. Molybdate is the dominant dissolved Mo species in oxic seawater and is largely sourced from rivers, with a typical concentration near 104 nM in normal oxic marine waters (Miller et al., 2011; Neubert et al., 2011), but with values near ∼20 nM in the brackish Baltic Sea (Noordmann et al., 2014). The largest Mo sink in modern seawater is sorption to Mn and Fe oxides, which deliver molybdate to the sediments until burial and dissolution of the oxides during anoxic diagenesis (Bertine and Turekian, 1973; Krishnaswami, 1976; Kashiwabara et al., 2009). If sulfide is present at appreciable levels, molybdate will convert to tetrathiomolybdate and other polysulfide species (Erickson and Helz, 2000; Dahl et al., 2013; Azrieli-Tal et al., 2014), which are efficiently buried in association with organic matter and sulfides (Erickson and Helz, 2000; Algeo and Lyons, 2006; Dahl et al., 2013, 2017; Azrieli-Tal et al., 2014; Wagner et al., 2017; Vorlicek et al., 2018; Ardakani et al., 2020). This process is favored by relatively high levels of dissolved sulfide. Sediments underlying euxinic waters have elevated Mo concentrations, typically >25 ppm if not much larger (Scott and Lyons, 2012). Lower sedimentary Mo concentrations, but elevated relative to average continental crust of <2 ppm can occur under conditions where sulfide accumulates in pore waters (Taylor and McLennan, 1995; Neubert et al., 2008; Nägler et al., 2011; Scott and Lyons, 2012; Hardisty et al., 2018). Muted enrichments are also a signature of elevated sedimentation rates even under euxinic conditions (Lyons and Kashgarian, 2005; Morford et al., 2009; Hardisty et al., 2018) and in restricted euxinic basins where the sedimentary Mo removal flux outpaces the marine supply (Algeo and Lyons, 2006).

The modern Gotland and Landsort Deep water columns have Mo isotope values of 2.22–2.49‰ (Noordmann et al., 2014), which is similar to that of open ocean seawater (∼2.3‰; Siebert et al., 2003). In stable and restricted euxinic settings with total sulfide concentrations beyond ∼100 μM (e.g., the Black Sea) near-quantitative scavenging of water column Mo in the presence of this ample free sulfide results in sedimentary Mo isotope signatures that mirror that of seawater (Barling et al., 2001; Siebert et al., 2003; Arnold et al., 2004; Neubert et al., 2008; Nägler et al., 2011; Noordmann et al., 2014). Under conditions with unstable euxinia and/or total sulfide concentrations <100 μM, such as the modern Landsort and Gotland Deeps, Mo concentrations are often still elevated relative to oxic settings, but a negative Mo isotope fractionation linked to incomplete conversion of molybdate to tetrathiomolybdate of up to ∼3‰ is captured in the sediments (Tossell, 2005; Neubert et al., 2008; Nägler et al., 2011; Azrieli-Tal et al., 2014; Noordmann et al., 2014). Importantly, however, sorption of Mo to Mn and Fe oxides also exerts negative Mo isotope fractionation relative to seawater as large as 2.9‰ (Barling et al., 2001; Wasylenki et al., 2008) and 2.2‰ (Goldberg et al., 2009), respectively. Smaller negative Mo isotope fractionations near −1.0‰ have also been demonstrated during assimilation and adsorption to organic matter (Zerkle et al., 2011; Kowalski et al., 2013).

MATERIALS AND METHODS

Sample Collection

Coring details, sedimentological, and paleontological descriptions for each site have been summarized previously (Andrén et al., 2015a,b,c). Samples from M0059C,E and M0065C (locations and water depth shown in **Figure 1**) were collected and sealed in N_2-flushed bags onboard the ship immediately following core recovery and stored frozen prior to analysis—minimizing oxidation of redox sensitive Fe minerals important for this study. Cores from M0059A,B,D and M0065A,B were capped and sealed immediately following retrieval and stored at 4°C prior to sample collection, which occurred 4–5 months later at MARUM in Bremen, Germany. Sediments were analyzed at

the University of California, Riverside and Yale University. As described below, we used exclusively fresh material for analysis, scraping and discarding any oxidized sediments.

At M0065, due to potential mustard gas contamination, the upper 2 m of the sediments were not collected and hence the cores from the Bornholm Basin do not clearly capture the MCA. In the absence of age constraints, the broad peak and associated sub-peaks in total organic carbon (TOC) at this site are interpreted to reflect the HTM.

Geochemical Methods

Lille Belt and Bornholm Basin Sediments

Splits of freshly thawed sample were used for the sequential extraction of iron monosulfide phases or acid volatile sulfide (AVS) (mainly iron monosulfides, FeS) (Berner et al., 1979; Chanton and Martens, 1985; Morse and Cornwell, 1987; Lyons, 1997; Hurtgen et al., 1999) and chromium reducible sulfur (CRS) (mainly pyrite, FeS_2) (Canfield and Berner, 1987). The CRS and AVS concentrations were measured via the methylene blue method using a spectrophotometer at wavelength of 660 nm (Cline, 1969). The AVS and CRS fractions were not determined in sequence, thus the pyritic sulfur was determined by subtracting the AVS from CRS, which was then used to calculate the associated Fe concentrations (Fe_{AVS} and Fe_{py}) using the stoichiometries FeS and FeS_2, respectively.

A modified chemical extraction method was applied for characterization of distinctive operationally defined "highly reactive" Fe pools: ascorbate (Fe_{asc}), dithionite (Fe_{dith}), oxalate (Fe_{ox}), and Na-acetate (Fe_{NaAc})—representing labile Fe-oxides, crystalline Fe-oxides, magnetite, and Fe-carbonate, respectively (Kostka and Luther, 1994; Raiswell et al., 1994, 2010; Poulton and Canfield, 2005). Using the same procedure as Hardisty et al. (2016), care was taken during the extractions to prevent artificial inflation of Fe-oxide phases via oxidation of Fe-sulfides or modifications associated with powdering (Raiswell et al., 1994, 2010). Specifically, (1) samples were collected, sealed in bags with N_2 headspace, and immediately frozen onboard IODP 347; (2) only fresh and frozen samples were used for the Fe extractions; (2) samples were not powdered; (3) sample exposure time to the atmosphere was limited to minutes during initial weighing and subsequent reagent additions; (4) all chemical reagents were deoxygenated with N_2 for at least 15 min prior to addition to the sample; (5) the headspace of each centrifuge tube was replaced with N_2 prior to shaking during the extractions. All Fe extracts were quantified via an Agilent 7500ce quadrupole inductively coupled plasma-mass spectrometer (ICP-MS) at UC Riverside following dilution with 0.3 M nitric acid. Separate sub-sample duplicates and triplicates assessed for precision revealed relative whole analysis standard deviations in most cases <0.01 weight % but in a few cases <0.05 weight %; we point out, however, that heterogeneities are expected, as bulk samples were not homogenized prior to taking a sub-sample for the sequential Fe-extraction procedure.

Total carbon and total inorganic carbon (TIC) were determined using an Eltra CS-500 carbon-sulfur analyzer at UC Riverside. TOC was calculated by subtracting TIC from total carbon. The standard reference material (SRM) AR4007 was analyzed routinely, with values within the reported range of 7.32 ± 0.12 wt. %.

Trace metal contents of bulk sediment were determined through a multi-acid digest procedure using dried samples which were powdered and ashed at 450°C for site M0065 and 650°C for site M0059 samples and then digested using trace metal grade HF, HNO_3, and HCl acids, with the residue solubilized as the final step in 0.3 M nitric acid. The ashing temperature was increased for site M0059 samples due to an insoluble residue only observed when ashed at lower temperatures. Each batch of total digests included an SRM for quality control. Total digests were measured for major elements and trace elements via an Agilent 7900 quadrupole ICP-MS at UC Riverside using a multi-element standard solution in a 0.3 M nitric acid matrix. SRMs NIST 2702, USGS SCO-1, and USGS SGR-1 were digested and analyzed in parallel with each batch of samples with all elements analyzed falling within reported ranges.

Molybdenum isotope measurements were performed at the Metal Geochemistry Center at Yale University, New Haven, Connecticut, using the Neptune Thermo Scientific multicollector ICP-MS (Asael et al., 2013, 2018). The 0.3 M nitric acid total digest solution was evaporated and re-constituted in 7 M HCl. An aliquot of the acid split was spiked with a ^{97}Mo–^{100}Mo double spike solution—prepared gravimetrically from Oak Ridge Laboratory metal powders as previously described (Asael et al., 2013, 2018)—according to the Mo concentration determined previously via ICP-MS in order to maintain a constant sample-to-spike ratio. This aliquot was also used for chromatographic separation. A two-stage column procedure was applied for Mo purification: the sample was run through an anion resin (AG-MP-1M) to separate Mo and Fe from the matrix followed by purification through a cation resin (AG50W-X8) to separate Mo from any remaining Fe. Molybdenum isotope compositions are reported using the δ notation, where:

$$\delta^{98}\mathrm{Mo} = \left[\left(^{98}\mathrm{Mo}/^{95}\mathrm{Mo}\right)_{\mathrm{sample}} \Big/ \left(\left(^{98}\mathrm{Mo}/^{95}\mathrm{Mo}\right)_{\mathrm{NIST}} \times 0.99975\right) - 1\right] \times 1000, \quad (1)$$

where $\delta^{98}Mo$ is calculated relative to NIST 3134 (Lot 130418) with a value of −0.25‰ (Nägler et al., 2014). A calibration of the NIST standard relative to Rochester (Lot 862309E) gave:

$$\delta^{98}\mathrm{Mo}_{\mathrm{ROCH}} = \delta^{98}\mathrm{Mo}_{\mathrm{NIST3137}} - 0.32 \pm 0.12‰, \quad (2)$$

Duplicates (n = 6) of reference standard NOD-1 yielded an average $\delta^{98}Mo$ value of −0.63‰ and 1σ of 0.18‰, similar to previously reported values (Asael et al., 2013). Values for Mo isotope measurements and associated error can be found in **Supplementary Tables 1, 2**. Measured errors for individual samples were <0.07‰ but largely <0.04‰.

Landsort Deep Sediments

The Fe extractions, elemental abundances, and Mo isotope compositions from Landsort Deep were previously characterized and reported in Hardisty et al. (2016) according to the same methods described above for Lille Belt and Bornholm Basin. For the current study, we used splits from specific eluents from the Mo isotope chromatographic separation procedure in Hardisty et al. (2016) to measure the Fe isotope composition of bulk sediments. These procedures are described below. In the current study, we also used the TRS and AVS fractions from Hardisty et al. (2016) to determine and report the S isotope composition of reduced sulfides.

Iron isotopes were analyzed for Landsort Deep bulk sediments at the Metal Geochemistry Center at Yale University using the Neptune Thermo Scientific multicollector ICP-MS. Total digests and chromatographic separation for the measurement of Mo isotopes (but not Fe isotopes) were already performed for Hardisty et al. (2016) according to the same procedures described in section "Lille Belt and Bornholm Basin Sediments" for Bornholm Basin and Lille Belt sediments. For the present study, we diluted the Fe fraction—separated during the Mo purification procedure with AG-MP-1M resin during Hardisty et al. (2016)—for measurement of Fe isotopes. Corrections for instrumental mass discrimination were performed using conventional sample-standard bracketing (Busigny et al., 2014), and $^{56}Fe/^{54}Fe$ ratios are expressed in the standard delta notation in per mil (‰) relative to IRMM-014 (Taylor et al., 1992):

$$\delta^{56}\mathrm{Fe} = \left[\left(^{56}\mathrm{Fe}/^{54}\mathrm{Fe}\right)_{\mathrm{sample}} \Big/ \left(^{56}\mathrm{Fe}/^{54}\mathrm{Fe}\right)_{\mathrm{standard}} - 1 \right] \times 1000, \quad (3)$$

We processed a $FeCl_2$ standard alongside the samples, which has a reported value of -0.71 ± 0.18‰ (Teutsch et al., 2009), and report a mean value -0.62 ± 0.12‰ (2SD), which overlaps within error.

Sulfur isotopes of total reduced S (TRS) and AVS fractions from Landsort Deep were measured at the University of California Riverside. TRS and AVS concentrations, but not S isotope compositions, were reported in Hardisty et al. (2016) using the same technique of converting to ZnS described in section "Lille Belt and Bornholm Basin Sediments" for sediments at Lille Belt and Bornholm Basin. For the current study, we used a chromium reduction to convert the ZnS from both AVS and TRS [used for concentration determinations in Hardisty et al. (2016)] to Ag_2S using the same technique described in section "Lille Belt and Bornholm Basin Sediments" for CRS but by replacing the ZnAc trap with $AgNO_3$. The Ag_2S precipitates were then filtered, dried, and homogenized before weighing into tin capsules with excess V_2O_5. The $^{34}S/^{32}S$ ratio for samples were measured using a Thermo Delta V gas-source isotope-ratio mass spectrometer coupled to a Costech 4010 elemental combustion system via a ConFlo III interface for on-line sample combustion and analysis. All sulfur isotope compositions are reported in standard delta notation as permil (‰) deviation relative to Vienna Canyon Diablo Troilite and were corrected using replicate analyses of International Atomic Energy Agency (IAEA) standards IAEA-S1 (−0.3‰), IAEA-S2 (+22.65‰), and IAEA-S3 (−32.5‰). Corrected values for IAEA standards are all within reported ranges with IAEA-S1 of -0.3 ± 0.47‰ ($n = 16$), IAEA-S2 of $+22.7 \pm 0.47$‰ ($n = 15$), and IAEA-S3 of -32.45 ± 0.33‰ ($n = 15$). A total of 21 samples were analyzed in duplicate or replicate for TRS and AVS, with the majority having standard deviations <1.0‰; however, a few samples, particularly those from the upper sapropel, had significantly larger standard deviations. Given the robust observations between replicates generally and the IAEA standards, we recommend that these variations reflect real heterogeneities, as samples for AVS, TRS, and Fe speciation were drawn directly from wet sediment that was not pre-homogenized in order to limit pyrite and AVS oxidation (Hardisty et al., 2016).

RESULTS

At Lille Belt (**Figure 2**), TOC is <1 wt. % from the bottom of the core up to ∼52 mcd, where TOC increases to 3.75 wt. % and gradually increases up the remainder of the core (**Figure 2B**). Superimposed on this increasing TOC trend are two sapropel units at 51.2–44.6 and 7.7–5.9 mcd, with peak values of ∼6.2 and 7.8 wt. %, respectively. Manganese concentrations show a broad peak from 47.5 to 11 mcd, with values oscillating but peaking as high as 1.5 wt. % (**Figure 3C**). "Highly reactive" Fe is reported as the sum of Fe_{AVS}, Fe_{py}, Fe_{asc}, Fe_{dith}, Fe_{ox}, and Fe_{NaAc}. Because of the presence of significant Fe_{AVS} at Lille Belt, we amend the typically reported Fe_{py}/Fe_{HR} to include Fe_{AVS}, thus $(Fe_{py}+Fe_{AVS})/Fe_{HR}$. The Fe_T/Al ratios generally fall around the Baltic detrital baseline of 0.65, and Fe_{HR}/Fe_T ratios are near established thresholds for anoxic conditions but are generally <0.5 (**Figures 3D,E**). The $(Fe_{py}+Fe_{AVS})/Fe_{HR}$ values oscillate but remain <0.7 (**Figure 3F**). The Mo contents are <25 ppm, with the exception of one sample with a concentration of 30.9 ppm (**Figure 3G**). Molybdenum isotope values are between +0.18 to +1.47‰ throughout the sediment column (**Figure 3H**). We note that trends and values in Mo concentration and Fe speciation are similar to those of a previous study of the same core that evaluated a separate sample set (van Helmond et al., 2017). All Lille Belt data are available in **Supplementary Table 1**.

At Bornholm Basin (**Figure 3**), TOC values are below 0.7 wt. % from the bottom of the profile up to 12.75 mcd followed by a steady increase up core throughout the remaining sediment column (**Figure 3B**). There are two peaks between 12.3 and 8.3 mcd and 5.17 and 3.34 mcd to values of ∼4.2 and 6.6 wt. %, respectively. At Bornholm Basin, multiple anoxic indicators fluctuate in association with the two sapropels with elevated TOC (**Figure 4**). Manganese concentrations increase up core exclusively from 9.8 to 6.6 mcd (**Figure 3C**). The Fe_T/Al ratios are generally at or below a baseline of <0.65 other than within the two intervals where TOC peaks (**Figure 3D**). Within these upper and lower sapropels, the Fe_T/Al values increase to 0.69 and 0.90, respectively. Other than within the sapropels, the Fe_{HR}/Fe_T ratio generally stays below 0.38 (**Figure 3E**). Fe_{AVS} was not found to be a significant component (<0.01 wt. %) at Bornholm Basin and was not measured for all samples, but we still maintain the $(Fe_{py}+Fe_{AVS})/Fe_{HR}$ nomenclature

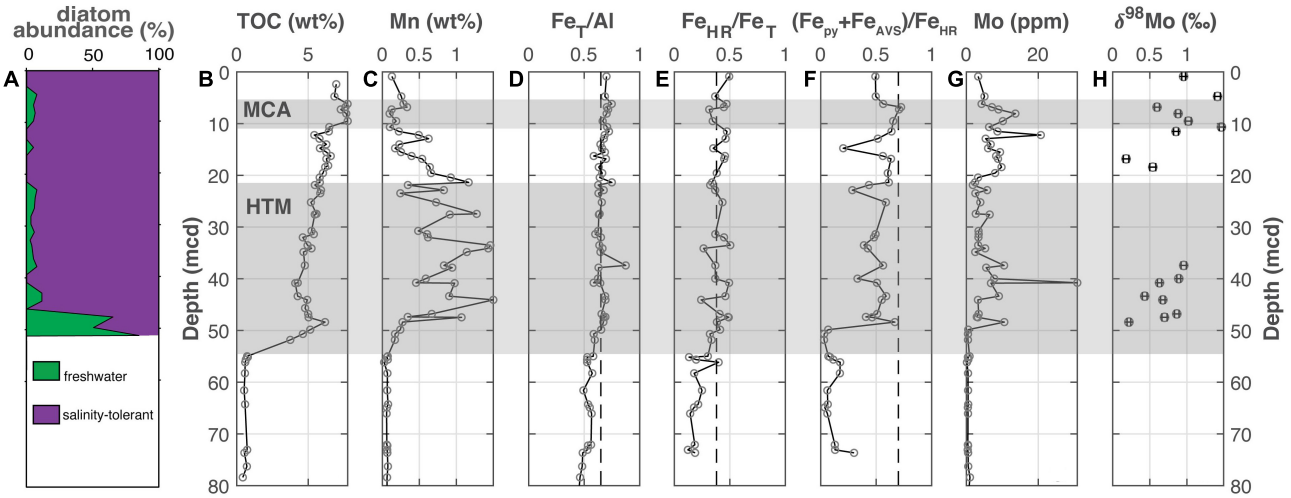

FIGURE 2 | Lille Belt (M0059). **(A)** The abundance of freshwater versus salinity tolerant diatoms [Andrén et al., 2015a; also see Kotthoff et al. (2017) and Warnock et al. (2020) for more detailed reconstructions], **(B)** total organic carbon, **(C)** manganese, **(D)** iron-to-aluminum, **(E,F)** Fe speciation, **(G)** molybdenum concentrations, and **(H)** molybdenum isotopes. The Medieval Climate Anomaly and Holocene Thermal Maximum are highlighted with the horizontal gray bars based on the geochronology from van Helmond et al. (2017) for M0059. Vertical dashed lines for Fe_T/Al, Fe_{HR}/Fe_T, and $(Fe_{py}+Fe_{AVS})/Fe_{HR}$ note thresholds for anoxia, euxinic and ferruginous conditions discussed in the main text.

for simplicity when comparing between the other cores. The Fe_{HR}/Fe_T values increase to 0.62 and 0.43 in the lower and upper sapropel, respectively. Notably, there is a muted Fe_{HR}/Fe_T peak up to 0.43 at 8.1 mcd that is outside of the two main increases in TOC but that overlaps with distinct minima in each $(Fe_{py}+Fe_{AVS})/Fe_{HR}$ and Mo concentration and the main peak in Mn concentrations. Values for $(Fe_{py}+Fe_{AVS})/Fe_{HR}$ are below 0.2 from the bottom of the profile to 10.3 mcd, where values begin to increase to >0.7 for most of the overlying sequence (**Figure 3F**). Molybdenum concentrations are generally <2 ppm from the bottom of the profile to near 9.8 mcd (**Figure 3G**). Above 9.8 mcd, Mo concentrations increase but stay below 27 ppm. Molybdenum isotope values range from −0.29 to +1.04‰ but are distinctly more positive from 6.54 to 3.85 mcd (**Figure 3H**). All Bornholm Basin data are available in **Supplementary Table 2**.

A previously published study from the Landsort Deep includes the Fe speciation and Mo concentration and isotope data shown in **Figures 4A–H** (Hardisty et al., 2016), which are included here for comparison to data discussed in sections "Lille Belt Paleoredox" and "Bornholm Basin Paleoredox" for the southern Baltic sub-basins. The new Fe and S isotope data are shown in **Figures 4I,J**. Iron isotope data from bulk sediments range from −0.12 to +0.46‰ and show distinct negative excursions within the sapropel units, along with corresponding increases in Fe_T/Al, Fe_{HR}/Fe_T, and $(Fe_{py}+Fe_{AVS})/Fe_{HR}$ and other redox-sensitive indicators. The S isotope data from TRS and AVS fractions are displayed together in **Figure 4I** and show overlapping trends. All new Fe and S isotope data from Landsort Deep are available in **Supplementary Tables 3, 4**, respectively.

The pore water dissolved Fe profiles are shown from Lille Belt, Bornholm Basin, and Landsort Deep in **Figure 5**. These data are also reported in the IODP Expedition 347 Reports (Andrén et al., 2015a,b,c) and used as part of detailed diagenetic models in Egger et al. (2017) and Dijkstra et al. (2018a).

DISCUSSION

Our data reveal multiple geochemical transitions in each core consistent with spatiotemporal redox variations associated with increases in organic carbon content. The previous studies discussed and cited in the next section have noted similar changes in organic carbon content at these sites and even in the same IODP cores. In combination with changes in diatom assemblages and other proxies, these past studies provide some context for the relative timing of each of these transitions and hence a more comprehensive reconstruction of spatiotemporal redox variations in the Baltic Sea. These previous studies are discussed below as context for our new results.

Salinity Transitions and Correlations Between Sub-Basins

The combination of carbon and diatom records from this and past studies indicates periods of variable salinity and organic matter preservation, which were already well known from the Baltic. These intervals and horizons are markers that can be used to correlate syndepositional periods and events among the sub-basins. The Lille Belt, Bornholm Basin, and Landsort Deep show a systematic shift in diatom assemblage marking the transition from lacustrine to brackish/marine water column conditions—that is, the Ancylus Lake to Littorina Sea transition (**Figures 2A**, **3A**, **4A**; Sohlenius et al., 2001; van Wirdum et al., 2019; Warnock et al., 2020). The Initial Littorina Stage, the transition period between the lacustrine Ancylus Lake and brackish Littorina Sea, lasted from ∼9.8 to 8.5 ka and is

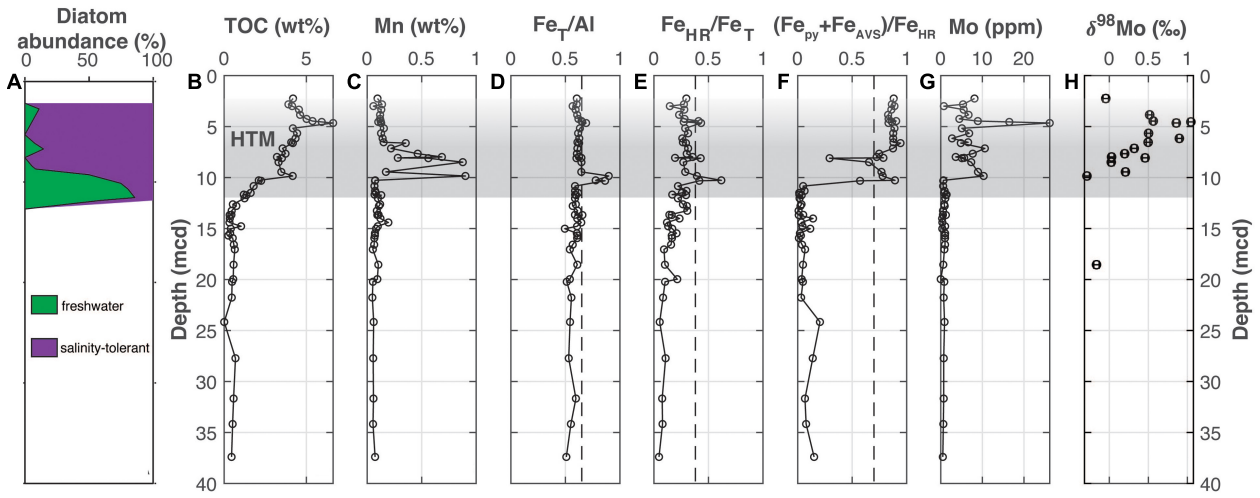

FIGURE 3 | Bornholm Basin (M0065). **(A)** The abundance of freshwater versus salinity tolerant diatoms (Andrén et al., 2015b), **(B)** total organic carbon, **(C)** manganese, **(D)** iron-to-aluminum, **(E,F)** Fe speciation, **(G)** molybdenum concentrations, and **(H)** molybdenum isotopes. The Medieval Climate Anomaly and Holocene Thermal Maximum is highlighted with the horizontal gray bar but is shaded upward to highlight uncertainty in locating the end of the HTM due to a lack of chronological constraints. Vertical dashed lines for Fe_T/Al, Fe_{HR}/Fe_T, and $(Fe_{py}+Fe_{AVS})/Fe_{HR}$ note thresholds for anoxia, euxinic and ferruginous conditions discussed in the main text. Note that the axis label in part F includes Fe_{AVS} in the numerator for simplicity and uniformity when comparing results between sites in the text, but that—as discussed in the results—Fe_{AVS} was negligible in a sample survey from site M0065 and was therefore was not measured in all samples.

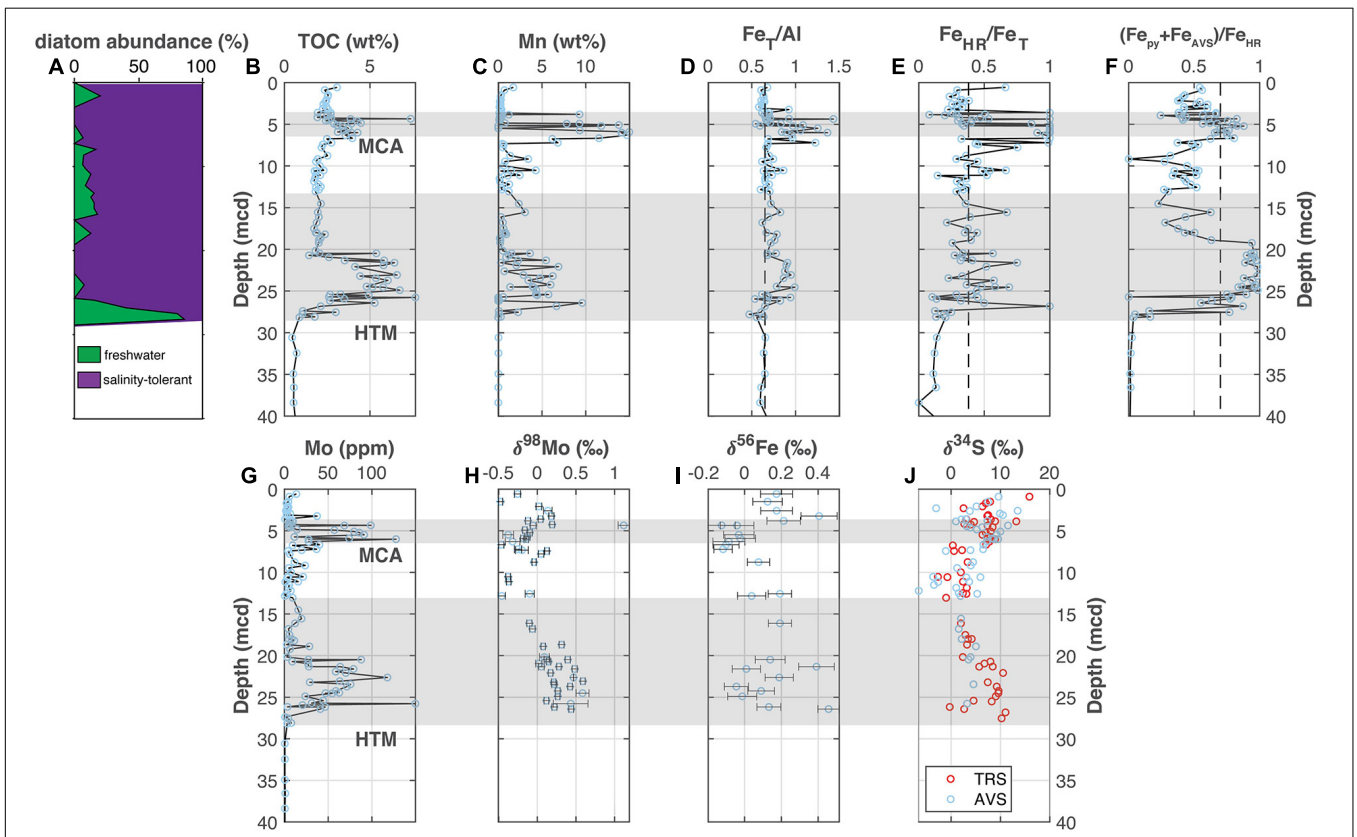

FIGURE 4 | Landsort Deep (M0063). **(A)** The abundance of freshwater versus salinity tolerant diatoms [Andrén et al., 2015c; also see van Wirdum et al. (2019) for more detailed reconstructions], **(B)** total organic carbon, **(C)** manganese, **(D)** iron-to-aluminum, **(E,F)** Fe speciation, **(G)** molybdenum concentrations, **(H)** molybdenum isotopes, **(I)** iron isotopes, and **(J)** sulfur isotopes. The Medieval Climate Anomaly and Holocene Thermal Maximum are highlighted with the horizontal gray bars based on the geochronology from van Wirdum et al. (2019) for M0063. Vertical dashed lines for Fe_T/Al, Fe_{HR}/Fe_T, and $(Fe_{py} + Fe_{AVS})/Fe_{HR}$ note thresholds for anoxia, euxinic and ferruginous conditions discussed in the main text. Geochemical data other than Fe and S isotopes come from Hardisty et al. (2016).

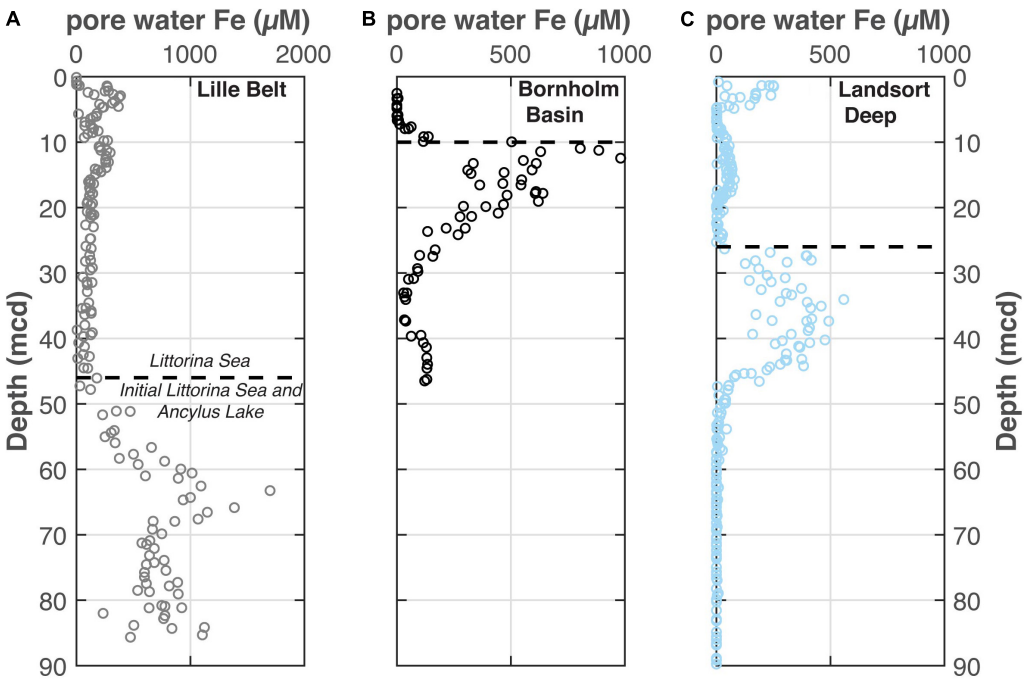

FIGURE 5 | The pore water Fe concentrations from each **(A)** Lille Belt, **(B)** Bornholm Basin, and **(C)** Landsort Deep. Data come from the IODP 347 Expedition Report (Andrén et al., 2015a,b,c; Egger et al., 2017). The dashed line from each site marks the horizon in the profile with the first indications of pore water sulfide accumulation, as constrained from Mo concentrations and $(Fe_{py}+Fe_{AVS})/Fe_{HR}$. In each case this occurs near the transition from the Ancylus Lake (AL) to the Littorina Sea (LS) noted from salinity-tolerant diatoms. Note the variations in the scale of the *x*-axis between these figures.

characterized by pulses of saline waters input into the Baltic Basin (Sohlenius et al., 2001; Björck et al., 2008; Andrén et al., 2011). The shift to sedimentary Mo concentrations >2 ppm (detrital values) alongside the increases in $(Fe_{py}+Fe_{AVS})/Fe_{HR}$ at each site at this transition in phase with the increases in TOC reflects accumulation of sulfide in the pore water (**Figures 2F,G**, **3F,G**, **4F,G**). Sulfide build up, in turn, was related to input of saline water and associated sulfate into the basin during the Initial Littorina Sea. The overlying interval where salinity-tolerant diatoms become relatively more abundant marks the onset of the Littorina Sea and the brackish conditions that still exist today (Sohlenius et al., 2001; van Wirdum et al., 2019; Warnock et al., 2020). This transition occurred 7500-7150 BP at Lille Belt (Kotthoff et al., 2017; Warnock et al., 2020).

Notably, there are peaks in TOC observed in each of the three cores. The lowermost peak can be linked to the HTM (**Figures 2B**, **3B**, **4B**), lasting from 8 to 4 ka (Jilbert and Slomp, 2013; Dijkstra et al., 2016; Hardisty et al., 2016; van Helmond et al., 2017). The HTM was marked by relatively higher temperatures and higher sea level and reduced freshwater input relative to today, likely representing the most saline period in the Baltic Sea since the LGM (Gustafsson and Westman, 2002; van Wirdum et al., 2019; Ni et al., 2020; Warnock et al., 2020). These factors likely contributed to the onset of anoxia observed during this interval (Papadomanolaki et al., 2018). Importantly, the HTM in the Bothnian Sea has been linked to more restricted conditions and widespread euxinia leading to the drawdown of Mo from the water column (Jilbert et al., 2015; Dijkstra et al., 2018b) thus, our Mo isotope data can be used to assess the potential of a syndepositional phenomenon in the southern Baltic sub-basins.

A secondary peak in TOC observed at Lille Belt (**Figure 2B**) and Landsort Deep (**Figure 4B**; Dijkstra et al., 2016, 2018a; Hardisty et al., 2016) is contemporaneous with the MCA (1.2–0.8 ka) and has been observed previously in both Fårö and Gotland Deeps (Jilbert and Slomp, 2013). Enhanced productivity and organic carbon burial during this interval occurred with warmer sea surface temperatures (Kabel et al., 2012; van Wirdum et al., 2019), all of which likely contributed to de-oxygenation during the MCA (Papadomanolaki et al., 2018).

Lille Belt Paleoredox

Individually, the paleoredox proxies at Lille Belt are not particularly diagnostic but together provide support for at least episodically manganous/ferruginous conditions with sulfide likely limited to the pore fluids. For example, intermittent laminations are observed, which are consistent with low oxygen conditions that persisted at least seasonally and largely excluded benthic fauna (Andrén et al., 2015a), a condition similar to that observed today (**Figure 1**). It is possible that low oxygen conditions excluded infaunal habitation outside of the laminated regions, but either seasonal or episodic returns to oxygenated conditions (e.g., MBIs) permitted burrowing and overprinting of laminations in these zones.

Geochemical evidence for at least intermittent anoxia comes from Fe_T/Al and Fe_{HR}/Fe_T values near or at thresholds associated

with anoxia. We note that elevated Fe_T/Al and Fe_{HR}/Fe_T ratios are a robust indicator of anoxic water columns supporting dissolved iron or hydrogen sulfide accumulation. Low water column oxygen levels but lacking sulfide and/or elevated dissolved Fe have not been shown to support increases in Fe proxy values (Hardisty et al., 2018). Our $(Fe_{py}+Fe_{AVS})/Fe_{HR}$ ratios are below the threshold interpreted for euxinia (Raiswell and Canfield, 1998), suggesting ferruginous conditions. Indeed, the persistence of significant non-subsidized "highly reactive" Fe, relatively high Fe_{AVS} (indicating incomplete conversion to pyrite; Berner et al., 1979; Hurtgen et al., 1999), and elevated pore water Fe up to 250 μM throughout the Holocene profile are all consistent with a sulfide-limited system and episodically ferruginous waters. However, while sulfide accumulation in the water column was transient, if present at all, one factor likely contributing to incomplete diagenetic pyrite formation in sediments, even if sulfide was accumulating in pore waters, is the particularly elevated sedimentation rates at Lille Belt (0.66 cm/year; van Helmond et al., 2017). Specifically, elevated sedimentation rates can limit the residence time of "highly reactive" Fe minerals such as magnetite and other Fe-oxides in the sulfidic zone relative to the timescales that these minerals react with sulfide to form pyrite (Boesen and Postma, 1988; Canfield et al., 1992; Hurtgen et al., 1999; Riedinger et al., 2017).

The Mo concentrations and isotope data support the potential for anoxia with sulfide accumulation limited to sedimentary pore fluids. The Mo concentrations are elevated above detrital levels. These concentrations and the Mo isotope range of +0.18 to +1.47‰ are comparable to values observed in low oxygen basins where sulfide is restricted to sedimentary pore fluids. For example, the California Borderland Basins, which exhibit variable degrees of low oxygen conditions, have low Mo enrichments and are characterized by Mo isotope values >0.5‰ but less than seawater (Poulson Brucker et al., 2009). However, the geochemical signature most diagnostic of episodic transitions between oxygenated and likely manganous conditions is the elevated Mn observed throughout the majority of the post-ILS profile. Manganous conditions are documented in the modern Baltic Sea (up to 40 μM Mn in some studies; Dellwig et al., 2018). The water column dissolved Mn is oxidized and returned to sediments during oxygenation events related to seasonal activities or MBIs (Dellwig et al., 2010, 2018; Hermans et al., 2019). The 1.5 wt. % Mn observed in Lille Belt sediments is not as high as concentrations found in some Baltic-proper deeps (e.g., Landsort Deep, **Figure 5**), but Lille Belt Mn levels are elevated relative to sediments without episodic oscillations between manganous and oxygenated conditions (Calvert and Pedersen, 1996).

Importantly, our dataset indicates that conditions more reducing than those present today, specifically euxinia, did not exist throughout the Holocene at Lille Belt, even during the MCA and HTM. Specifically, the Fe speciation and Mo concentration proxies do not show excursions significantly above the thresholds clearly associated with euxinic conditions during any specific intervals. Further, the Mo isotope signatures remain well below that of Baltic seawater and hence provide strong evidence for Fe-Mn oxides as the main source of Mo to the sediments and hence evidence against any widespread and persistent euxinic conditions, which might otherwise have drawn down water column Mo and limited its accumulation in sediments—as has been interpreted in the Bothnian Sea during the HTM (Jilbert et al., 2015; Dijkstra et al., 2018b).

Bornholm Basin Paleoredox

The Fe and Mo sedimentary geochemical records at Bornholm Basin provide evidence for multiple paleoredox shifts associated with the Initial Littorina Sea and HTM. We first propose that the observed Fe and Mo data from the ILS at Bornholm Basin ($Mo < 25$ ppm, $\delta^{98}Mo \sim -0.5$‰, $Fe_T/Al > 0.65$, $Fe_{HR}/Fe_T > 0.38$, and $(Fe_{py}+Fe_{AVS})/Fe_{HR} > 0.7$) reflect anoxia but with hydrogen sulfide largely restricted to pore waters with only transient water column sulfide accumulation (**Figure 3**). The observed negative Mo isotope values and minor sedimentary Mo enrichments are most consistent with either: (1) molybdate to thiomolybdate transformation under conditions with low or intermittent water column sulfide or (2) sedimentary delivery of Mo via Fe and Mn-oxides and sequestration in sulfidic pore fluids—or both. Both processes yield Mo isotope fractionations up to −3‰ (Barling et al., 2001; Wasylenki et al., 2008; Goldberg et al., 2009), which could explain why our values are fractionated by nearly 2.9‰ relative to seawater. Importantly, both euxinic conditions and Fe-oxide deposition could cause enrichments in Fe_{HR}/Fe_T and Fe_T/Al relative to detrital inputs. Although the combination of $(Fe_{py}+Fe_{AVS})/Fe_{HR} > 0.7$ and elevated Fe_{HR}/Fe_T and Fe_T/Al is typically diagnostic of euxinia, the exceptional delivery of "extra" "highly reactive" Fe as Fe-oxides to the sediment could react with pore water sulfide to form pyrite and other Fe sulfides, post-depositionally elevating $(Fe_{py}+Fe_{AVS})/Fe_{HR}$. Such conditions would reflect periodic or episodic oxidation of an Fe-rich water column with delivery of oxides to organic-rich and sulfidic sediments. While post-depositional increases in Fe_T/Al and Fe_{HR}/FeT have not been documented in modern sediments, post-depositional formation of pyrite and associated increases in $(Fe_{py}+Fe_{AVS})/Fe_{HR}$ have been observed in sediments underlying oxic water columns from many localities, including the FOAM site in Long Island Sound (Canfield et al., 1992; Hardisty et al., 2018) and oxic portions of the Black Sea Shelf (Wijsman et al., 2001a), providing precedence for this possibility. While it is difficult to distinguish between these interpretations, anoxic and weakly or intermittently euxinic settings commonly overlap, thus making a single environmental assignment difficult. Indeed, the modern Bornholm Basin water column is characterized by intermittent anoxia and sulfide accumulation (**Figure 1**).

An important additional consideration for the increases in Fe_T/Al and Fe_{HR}/Fe_T specifically at the ILS-Littorina Sea Boundary at Bornholm Basin and other sub-basins is the potential for pore water Fe migration from adjacent sediments layers (Berner, 1969; Boesen and Postma, 1988). The latter is often associated with juxtapositions of organic-lean and organic-rich sediment layers, such as sapropels, and can also reflect sulfate-poor and sulfate-rich pore waters marking a transition from non-marine to marine deposition. Indeed, secondary Fe enrichments may be important at Bornholm Basin (as well as other Baltic sub-basins; e.g., Landsort Deep and Lille Belt), which contains elevated pore water dissolved Fe

concentrations in Ancylus Lake sediments that sharply decrease at the ILS boundary when the basin becomes brackish (**Figure 5**). Specifically, it is possible that the diffusion of underlying Ancylus Lake pore water Fe to the overlying sulfidic Littorina pore waters caused post-depositional Fe enrichments which are independent of water column redox conditions (Boesen and Postma, 1988; Dijkstra et al., 2018a). In order to account for upward Fe diffusing into sulfidic sediments and its potential authigenic Fe contribution to Fe_T/Al, we use Fick's first law of diffusion, as applied to sediments (Berner, 1980), to calculate Fe_{auth} at the AL-ILS transition at Bornholm Basin, Lille Belt, and Landsort Deep (Eqs 4, 5).

$$J = -\varphi D_s \frac{\Delta C}{\Delta Z}, \quad (4)$$

$$Fe_{auth} = \frac{J}{\omega \rho}, \quad (5)$$

where φ is the porosity, D_s is the diffusion coefficient for Fe^{2+} (Li and Gregory, 1974), ΔC is the change in pore water concentration across the sulfide interface, ΔZ is the depth interval from which ΔC is measured (yielding the gradient), ω is the sedimentation rate, and ρ is the sediment density. In our calculation, we model the mass flux (J) of Fe across the redox front from the Ancylus Lake to overlying sulfidic pore fluids, assuming complete precipitation of pore water dissolved Fe as Fe sulfides. The mass flux can then be used, in combination with the sediment density (ρ), porosity (φ), sedimentation rate (ω), and the minimum Al concentration among samples with observed elevated Fe_T/Al (which amplifies our calculated Fe_T/Al to the maximum extent) to estimate a potential range of authigenic Fe_T/Al enrichments. All values are given in **Table 1**.

In all cases considered, calculations suggest that the observed Fe_T/Al cannot be entirely explained by upward Fe migration into sulfidic sediments (**Figure 6**). Specifically, the calculations show the potential for similar post-depositional enrichments in Fe_T/Al at all three basins. Importantly, however, upward Fe migration cannot account for the full observed Fe_T/Al enrichments at the ILS-Littorina Sea Boundary at Bornholm Basin or Landsort Deep. We also highlight that we chose conservative values for variables in our calculations which would most likely overestimate any authigenic contributions to Fe_T/Al. The conservative nature of our estimates is highlighted by the calculated Fe_{auth} flux increases in Fe_T/Al by ~0.11 at Lille Belt, a location where no significant increases in Fe_T/Al are observed through the whole profile. This conclusion ultimately implies that a substantial portion, if not the majority, of the observed Fe_T/Al enrichments at both Bornholm Basin and Landsort Deep in the period following Ancylus Lake deposition likely result from primary water column redox dynamics and the associated Fe shuttle, thus permitting interpretation related to water column redox variations.

Further up in the profile beyond the ILS boundary, a sharp increase in TOC concurrent with an increase in Fe_T/Al, Fe_{HR}/Fe_T, Fe_{py}/Fe_{HR}, and Mo within the sapropel at Bornholm Basin at ~5 mcd (**Figure 3**) indicates a brief interval of likely intermittent euxinic conditions. The Mo concentration approaches the 36 ppm Mo found in modern Bornholm Basin sediments, which underlie an episodically euxinic water column (Mort et al., 2010) and is similar to that of some other localities with episodic euxinia (Scott and Lyons, 2012; Hardisty et al., 2018; Scholz et al., 2018). Lastly, we note that Mo isotope values for this interval—which gradually increase from the ILS within the HTM—are the most positive recorded in the entire profile (approaching +1.6‰; **Figure 3H**). These relationships and heavier Mo isotope signatures are opposite the trend expected for an interval with a prominent oxide-delivered Mo flux to the sediments, as both Mn and Fe oxides fractionate Mo isotopes to more negative values by up to 2.9‰ (Barling et al., 2001; Wasylenki et al., 2008) and 2.2‰ (Goldberg et al., 2009), respectively. A non-oxide origin for the sedimentary Mo from this interval is also supported by a lack of Mn enrichments (**Figure 4C**). Instead, the Mo isotope values are in a range consistent with sulfide concentrations <100 μM and/or sulfide accumulation for only short timescales, both which exert a

TABLE 1 | Values and associated sources for calculations shown in **Figure 6**.

	ΔC (mM)[a]	ρ (g/cm³)[b]	φ[b]	ω (cm/s)	Al_{min} (wt.%)[d]	D (cm²/s)
Lille Belt	1.70	0.75	0.8	0.66[e]	4.9	5.268×10^{-6}
Bornholm Basin	0.98	1.5	0.8	0.21[c]	7.5	5.268×10^{-6}
Landsort Deep	0.56	0.8	0.8	0.12[c]	3.8	5.268×10^{-6}

[a] *Figure 5.*
[b] *Andrén et al., 2015a,b,c.*
[c] *Mort et al., 2010.*
[d] ***Supplementary Tables 1, 2****; Hardisty et al., 2016.*
[e] *van Helmond et al., 2017.*

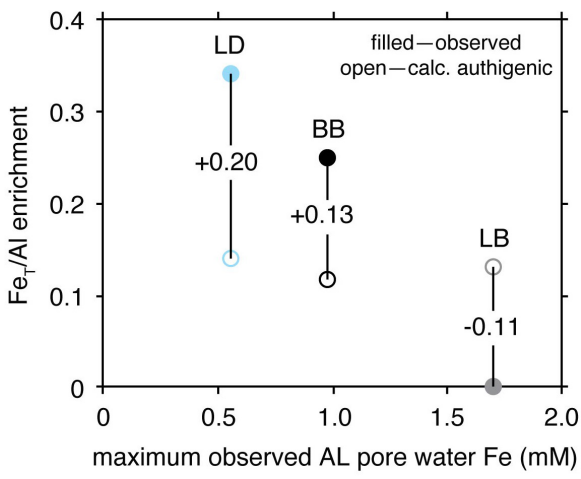

FIGURE 6 | Comparison of observed (filled) and calculated authigenic (open) Fe_T/Al enrichments at Lille Belt (LB), Bornholm Basin (BB), and Landsort Deep (LD). Observed Fe_T/Al enrichments represent the maximum from the interval directly overlying the Ancylus Lake-Littorina Sea transition relative to a detrital baseline of 0.65 (Fehr et al., 2008). Maximum pore water Fe concentrations come from the highest values generally observed in the Ancylus Lake (AL) sediments and represent ΔC in Eq. 5.

fractionation factor during only partial conversion of molybdate to tetrathiomolybdate (Azrieli-Tal et al., 2014), a condition observed in euxinic portions of the Landsort Deep today and in the recent past (Neubert et al., 2008; Noordmann et al., 2014; Hardisty et al., 2016). Alternatively, the Mo isotope values also approach the +1.6‰ that is often observed in continental margin settings with low oxygen bottom waters and sulfidic pore waters (Poulson Brucker et al., 2009). Although these independent elemental and isotopic data sets yield multiple interpretations, the combined proxies point to a system that was at least episodically anoxic with likely intermittent accumulation of water column sulfide at low levels.

Landsort Deep Paleoredox

Previously published Fe and Mo data from Landsort Deep data are distinct from those of Lille Belt and Bornholm Basin and have been interpreted to support variable degrees of euxinic conditions associated with both the HTM and MCA (**Figures 4**, **6**; Dijkstra et al., 2016; Hardisty et al., 2016; Zhou et al., 2017). Similar conditions have also been interpreted for other Baltic Proper sub-basins, albeit in the absence of Mo isotope data (e.g., Gotland Deep and Fårö Deep). Importantly, however, the Landsort Deep Mo isotope signatures are highly fractionated from seawater (**Figure 4H**), indicating some combination of two sources of Mo to the sediments: (1) low or intermittent water column sulfide accumulation inducing large Mo isotope fractionation factors during the formation of thiomolybdate species and (2) sedimentary Mo deposition with Mn- and Fe-oxides. While overlapping isotope fractionations limit our ability to isolate a specific mechanism for Mo deposition, the combined proxies point to cycles of intermittent/weak euxinia interrupted by MBIs driving dissolved Fe-Mn oxidation and oxide deposition, as is observed at Landsort Deep other Baltic-proper deeps today (Dellwig et al., 2018). Our new Fe isotope data from bulk sediment from Landsort Deep support previous indications of anoxic water column conditions as a source for the observed Fe enrichments, while new S isotope data ($\delta^{34}S_{TRS}$) for total reducible S (CRS and AVS) indicate that water column sulfide accumulation beyond transient levels may have been more limited.

The Fe isotope data range from −0.12 to +0.46‰ (**Figure 4I**), with excursions to the most negative values in intervals with elevated Fe_T/Al, Fe_{HR}/Fe_T, $(Fe_{AVS}+Fe_{py})/Fe_{HR}$, and Mo indicative of euxinia during the MCA and HTM (**Figure 4**). A previous study evaluating Fe isotope data from Gotland Deep determined an average value for sediments associated with the Baltic Ice Lake of +0.08 ± 0.13‰, which provides a baseline for the detrital flux (Fehr et al., 2008). Sedimentary Fe enrichments are attributed to shelf-to-basin transport of Fe following repeated cycles of Fe-oxide formation, dissolution in anoxic sediments, benthic fluxes from the shelf, and sequestration in anoxic environments as pyrite—i.e., the Fe shuttle (Lyons and Severmann, 2006; Severmann et al., 2008, 2010; Dellwig et al., 2010; Scholz et al., 2014b,c). The reductive dissolution of Fe oxides favors the light isotopes and results in progressive enrichment of lighter isotope signatures in benthic fluxes along shelf-to-basin transects (Severmann et al., 2010). Under euxinic conditions or events supporting large-scale oxidation of isotopically light reduced Fe (e.g., MBIs), these light Fe isotope signatures are sequestered into the sediments. While our study evaluated bulk rather than mineral-specific iron, the $(Fe_{AVS}+Fe_{py})/Fe_{HR}$ ratios support that pyrite is the largest Fe fraction during sapropel deposition. Consistent with the Fe shuttle model, the most negative Fe isotope values relative to detrital baselines are within the sapropels, which provides support—alongside that of elevated Fe_{HR}/Fe_T and Fe_T/Al—for anoxic conditions at Landsort Deep maintaining elevated Fe fluxes to the sediments. Iron isotope values for Gotland Deep show similar negative excursions during intervals with Fe_T/Al and Mo enrichments typically indicative of euxinia (Fehr et al., 2008, 2010). Importantly, the Fe isotope signatures alone cannot discern the degree to which the Fe flux at Landsort Deep was associated with syngenetic pyrite formation versus pyritization of Fe-oxide fluxes associated with either MBIs or Fe oxidation at the chemocline. Both of these processes could explain the elevated Fe_{HR}/Fe_T, $(Fe_{AVS} + Fe_{py})/Fe_{HR}$, and Mo concentrations and the highly fractionated Mo isotope values during the HTM and MCA.

We note that the most positive Fe isotope values at Landsort Deep near 0.4‰ exceed that of the Baltic detrital baseline presented by Fehr et al. (2008) of 0.08 ± 0.13‰ and are higher than the most positive values found in Littorina Sea sediments from the same study. Importantly, with the exception of one value of 0.39 ± 0.1‰ at 21.3 mcd, the most positive Fe isotope values at Landsort Deep are generally found outside of sapropel deposition. While trapping of isotopically light dissolved Fe as pyrite provides an explanation for the relatively negative Fe isotope values within the sapropels, we note that the downcore trends may be exacerbated by diagenetic trends in Fe-mineral dissolution resulting in more positive values in the intervening intervals. Specifically, the intervals outside of the sapropels have substantial pore water Fe accumulation (up to ∼250 μM; **Figure 5C**) and Fe speciation evidence most consistent with sulfide limitation in the pore waters ($Fe_{py}+Fe_{AVS}/Fe_{HR} < 0.7$; **Figure 4J**). The dissolution of Fe oxides and accumulation of dissolved Fe in sulfide-limited pore waters represents the most likely explanation for these trends. This implies the preferential release of isotopically light Fe to the pore waters, which would have the impact of distilling the remaining sedimentary Fe isotopes, such as that measured in this study, to more positive values. Ultimately, these downcore shifts between higher and lower Fe isotope values may be best explained by the combination of trapping of isotopically light dissolved Fe as sulfides during periods of euxinia or elevated pore water sulfide accumulation which are then juxtaposed against adjacent Fe-dominated intervals favoring release of isotopically light Fe to the pore waters and water column.

The S isotope data support the likelihood that much of the elevated Fe flux to the sediments during anoxic intervals was pyritized in the sediments and not the water column. The $\delta^{34}S_{TRS}$, ranging from −4.3 to +16.7‰, with an excursion to the most positive values during the HTM and MCA (**Figure 4J**), are more negative than that of sulfate in the modern Baltic Sea (+20.5‰; Böttcher and Huckriede, 1997). This relationship is consistent with negative S isotope fractionations during microbial sulfate

reduction to sulfide (Goldhaber and Kaplan, 1974; Habicht and Canfield, 2001); however, the observed $\delta^{34}S_{TRS}$ range is generally more positive than that found in euxinic basins (e.g., Black Sea; Lyons, 1997) and relative to the range observed for total reduced sulfur from a sediment core capturing the Holocene in the shallower (∼250 m), Eastern Landsort Deep (−27 to −40‰; Böttcher and Lepland, 2000). Sulfur isotope fractionations during sulfate reduction in pure cultures typically range up to 46‰ (Chambers and Trudinger, 1979) but can be as high as 70‰ (Rudnicki et al., 2001; Wortmann et al., 2001; Sim et al., 2011). The generally more positive $\delta^{34}S$ values found at Site M0063 compared to other portions of the basin and the excursion to more positive $\delta^{34}S_{TRS}$ values specifically during sapropel deposition point to non-steady steady diagenetic conditions or sulfate limitation in sedimentary pore fluids rather than changes in the $\delta^{34}S$ of Baltic Sea sulfate. This ultimately implies that the elevated $(F_{py}+Fe_{AVS})/Fe_{HR}$ ratios likely reflect processes at or below the sediment-water interface.

An increased flux of syngenetic relative to diagenetic pyrite under euxinic conditions is unlikely to explain the observed heavier pyrite $\delta^{34}S$ values during the HTM and MCA at Landsort Deep. While no sulfur isotope data exist for dissolved sulfide or reduced S fractions in the modern Landsort Deep water column, a large isotope fractionation is expected for pyrite formed in an open system (up to −60‰ in the modern Black Sea; Fry et al., 1991; Lyons, 1997). Relatively positive S isotope values are instead typically observed in diffusion-dominated pore waters where a reservoir effect (Rayleigh fractionation) allows for pore water sulfate S isotope values and associated sulfide and thus pyrite to become enriched in ^{34}S relative to seawater during sulfate reduction as sulfate concentrations become limiting at depth (Hartmann and Nielsen, 2012). Frequently these trends are associated with subsurface peaks in rates of microbial sulfate reduction at sulfate-methane transition zones at depth, with the resulting sulfide from pore water sulfate reduction, and hence pyrite, becoming relatively enriched in ^{34}S (Jørgensen et al., 2004; Borowski et al., 2013; Lin et al., 2016; Riedinger et al., 2017). At M0063, methane was detected in the uppermost sediments sampled (∼1.6 mcd), and sulfate was below detection throughout the Holocene sediments outside of samples with indications of likely seawater contamination during drilling (Egger et al., 2017). Given the shallow sulfate-methane transition zone observed today, this SMT location was likely similar or even shallower during the MCA and HTM when TOC values were as high as 8 wt. %. Under such conditions, depletions in pore water sulfate concentration coupled with increases in the S isotope signature of the sulfate and sulfide may have occurred near or at the sediment-water interface, reacting with high concentrations of "highly reactive" Fe supplied during the MCA and HTM. This would result in elevated Fe_{HR}/Fe_T and post-depositional increases in $(Fe_{py}+Fe_{AVS})/Fe_{HR}$. Alternatively, other unconstrained factors, such as an increase in sedimentation rate or an increase in sulfate reduction rate related to increased organic carbon availability are also known to decrease S isotope fractionations and hence the $\delta^{34}S_{TRS}$ compositions in sediments relative to overlying seawater (Maynard, 1980; Leavitt et al., 2013; Pasquier et al., 2017). However, if applicable, these processes still point to diagenetic origins for the variations in $\delta^{34}S_{TRS}$ in the Holocene sediments. In addition to the previously observed Mo isotope fractionations and Fe-Mn data, these new $\delta^{34}S$ data further indicate that sulfide was mostly restricted to the pore water at or below the sediment-water interface, resulting in diagenetic pyrite formation. This likelihood suggests that the MBIs and resulting oxidation of previously reduced Fe-Mn might have been the main source of Fe, Mn, and perhaps even Mo to the sediments.

Baltic Paleoredox Summary

The occurrence of ancient intervals of anoxia in the Baltic have long been known (Manheim, 1961; Suess, 1979; Sohlenius, 1996; Sohlenius et al., 1996, 2001; Sternbeck and Sohlenius, 1997, Lepland and Stevens, 1998; Sohlenius and Westman, 1998; Zillén et al., 2008), and recent studies have together constructed an increasingly detailed and quantitative understanding of the spatiotemporal variations and drivers of ancient anoxia (Mort et al., 2010; Jilbert and Slomp, 2013; Jilbert et al., 2015; Lenz et al., 2015a,b; Hardisty et al., 2016; Dijkstra et al., 2018a,b; Groeneveld et al., 2018; van Helmond et al., 2018). Our study builds on this established context by providing constraints on the specific paleoredox conditions of individual sub-basins during the Holocene. While each of the investigated sub-basins in this study show already well-known and similar changes from lacustrine to brackish—as indicated by increases in TRS/TOC ratios (Berner and Raiswell, 1984; **Figure 7A**)—and increases in TOC associated with previously established Baltic anoxic events during the HTM and MCA, our new data contribute to growing evidence that redox conditions among the sub-basins as well as between events within a given sub-basin were distinctly different. Specifically, we emphasize that, in contrast to that found in the Baltic Proper and Bothnian Sea, there is little-to-no clear evidence for ancient euxinia beyond transient events in the Lille Belt and Bornholm Basin sub-basins of the southern Baltic. This assertion is supported by comparison of $(Fe_{py}+Fe_{AVS})/Fe_{HR}$ versus Fe_{HR}/Fe_T and Mo versus TOC for these sub-basins relative to Landsort Deep (**Figures 7B,C**), which show a clear contrast.

Additionally, our study provides strong evidence against widespread euxinic conditions with stable sulfide concentrations >100 μM within even the central sub-basin, Landsort Deep—in contrast to the Bothnian Sea during the HTM. Instead, there is specific evidence that euxinia at Landsort Deep was likely isolated and limited to low and intermittent sulfide concentrations: (1) the combined Mo and Fe speciation data indicate the likelihood that water column Mo concentrations did not become depleted due to large-scale transfer to the sediment during intervals where sulfide accumulated in individual sub-basins; (2) the Mo isotope data from the Landsort Deep are all highly fractionated from seawater, which is inconsistent with conditions that were stably euxinic (**Figure 7D**); (3) S isotope evidence that diagenetic pyrite may be an important contribution to the $(Fe_{py}+Fe_{AVS})/Fe_{HR}$ trends at Landsort Deep. We note that minor seawater Mo drawdown is observed in the modern Baltic related to a combination of burial under euxinic conditions and in association with Fe-Mn-oxides (Noordmann et al., 2014), and similar conditions may have occurred previously but cannot be resolved with our proxies.

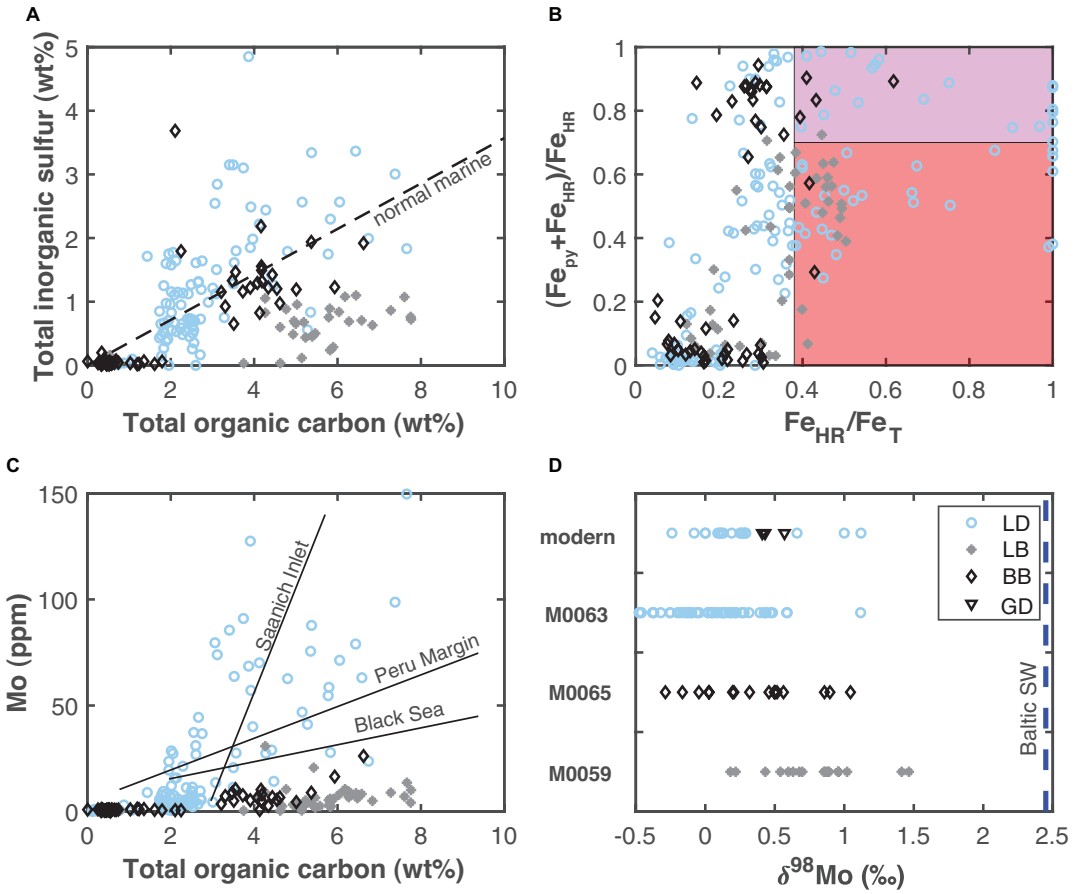

FIGURE 7 | Data comparisons between Lille Belt (LB), Bornholm Basin (BB), and Landsort Deep (LD). **(A)** Comparison of total inorganic sulfur and total organic carbon. The dashed line is the typical ratio found for marine and estuarine systems (Berner and Raiswell, 1984). **(B)** Comparison of Fe speciation. The red and purple shaded field represent that previously established for ferruginous and euxinic conditions (Raiswell et al., 2018). **(C)** Comparison of Mo and total organic carbon, with a comparison of slopes observed at modern localities with known Mo-TOC relationships (Böning et al., 2004; Algeo and Lyons, 2006; Scholz et al., 2014a). **(D)** Comparison of ranges in Mo isotope compositions for each site. The blue vertical line shows the median Mo isotope value for Baltic seawater (Noordmann et al., 2014). The modern Gotland Deep (GD) and Landsort Deep sediment Mo isotope data come from Noordmann et al. (2014) and Neubert et al. (2008).

Still, a recent study used the slope of Mo and TOC correlations from Landsort Deep sediments to suggest Mo drawdown in the Landsort Deep water column during each anoxic event (the modern, MCA, and the HTM event) (van Helmond et al., 2018), and Mo isotope comparisons between the HTM and MCA sediments suggest potentially higher sulfide and a more muted impact of Fe-Mn oxides on Mo deposition during the HTM relative to the MCA (**Figure 4H**; Hardisty et al., 2016). We note that the Mo-TOC slopes at Landsort Deep are similar to those observed in less-restricted euxinic basins (e.g., Saanich Inlet) or the Peru Margin oxygen minimum zone, where Mo deposition to sediments is largely a function of a "particulate shuttle" associated with Fe-oxide deposition as well as diffusion from seawater into underlying sediments, rather than widespread and persistent euxinic conditions (Algeo and Lyons, 2006; Algeo and Tribovillard, 2009; Hancock et al., 2019; Eroglu et al., 2020). This observation is analogous to our multi-proxy indications of Fe-Mn oxides as an important pathway for Mo deposition at Landsort Deep. Given that Mo-TOC relationships used for recognizing Mo reservoir effects are based on comparison of modern localities without major oxide-related Mo contributions to the sediments (Algeo and Lyons, 2006), the Mo-TOC slopes at Landsort Deep may not best fingerprint ancient Mo drawdown associated with euxinia.

A simplified summary of the paleoredox states established for relevant Baltic sub-basins is shown in **Figure 8**. We also note that evidence for low oxygen conditions extends beyond the MCA and HTM at both the Baltic Proper and Southern sub-basins and that redox states also appear to have been dynamic within sapropel units. Specifically, Lille Belt is characterized by anoxia with ferruginous and manganous conditions and sulfide limited to pore waters following the transition to the Littorina Sea, with no clear excursions to more reducing conditions during either the MCA or HTM. Only the HTM was studied for the Bornholm Basin, but evidence for low oxygen conditions for this interval are specific to two distinct periods of anoxia and perhaps transient euxinic conditions during the ILS and again later

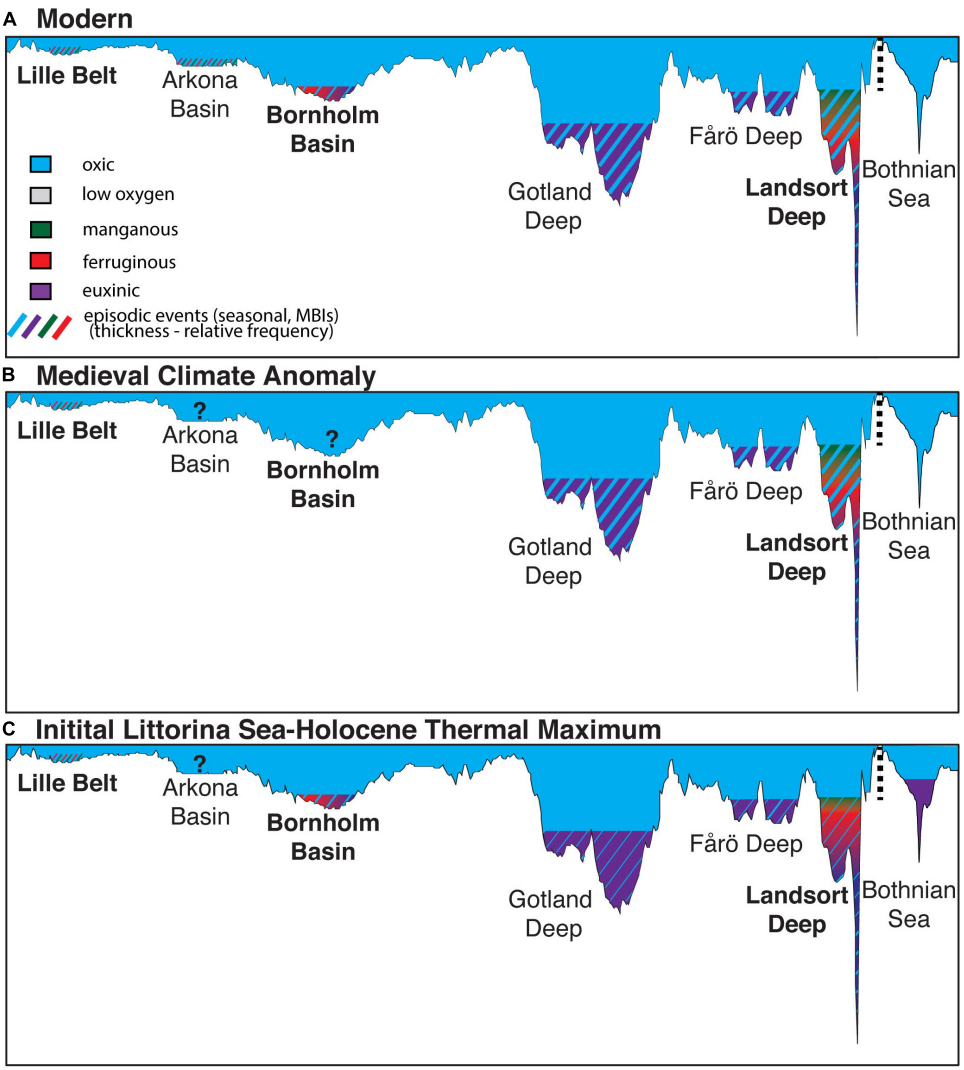

FIGURE 8 | Simplified representations of the generalized water column redox conditions during the **(A)** modern, **(B)** Medieval Climate Anomaly, and **(C)** Initial Littorina Sea and Holocene Thermal Maximum. The illustration includes interpretations from this (bold) and previous studies from Landsort Deep (Dijkstra et al., 2016), Lille Belt (van Helmond et al., 2017), Gotland Deep (van Helmond et al., 2018), Fårö Deep (van Helmond et al., 2018), and the Bothnian Sea (Jilbert et al., 2015; Dijkstra et al., 2018b). Conditions from the modern derived from multiple sources (Dellwig et al., 2012, 2018, 2019; Carstensen et al., 2014; Noordmann et al., 2014). The transect corresponds to the transect in **Figure 1**, but also includes the Bothnian Sea for comparison, with the break in the transect shown by the vertical dashed line. Paleoredox proxies discussed in the text are used to infer the specific paleoredox conditions, including: low oxygen (sediment laminations), manganous (Mn geochemistry), ferruginous (Fe geochemistry), euxinic (Fe, Mo, S geochemistry), and episodic oxygenation events (Mn and Mo geochemistry). Question marks represent basins where low oxygen conditions are recorded today, but bioturbation has been recorded in ancient sediments (Zillén et al., 2008) and insufficient or a lack of geochemical data are available to assess specific paleoredox conditions. The bathymetry matches that of today in each scenario shown, though we acknowledge that both glacio-isostatic rebound of the Baltic seafloor and different sea level would have caused this to vary from today during the ILS-LS transition and HTM.

during the HTM or Littorina Sea stage. These conditions can be further contrasted with Landsort Deep where evidence for low oxygen exists via multiple proxies throughout the Holocene, but there is additional evidence for widespread water column Fe-Mn oxide deposition and euxinia limited to low sulfide levels or transient events during both the HTM and MCA. Molybdenum and Fe_T/Al data similar to those of the Landsort Deep and typical of euxinic conditions have been observed elsewhere in the Baltic Proper (e.g., Fårö Deep and Gotland Deep), but combinations of proxies that specifically track manganous, ferruginous, and euxinic water column conditions and that differentiate pore water redox states have not been applied at those locations. While the paleoredox conditions in each sub-basin are complex, the general interpretations are consistent with the modern relationship of progressively more reducing conditions moving away from the sill and the dynamic redox conditions observed in these basins today (**Figure 1**).

Implications for Proxy Applications to Geologic Record

Our study highlights the need for proxies that constrain a range of pore water and water column redox states (manganous, ferruginous, and euxinic) in dynamic depositional and diagenetic regimes such as the Baltic Sea. This has particular importance for the recognition of diagenetic impacts on Fe speciation and the deposition of Mo, which are both widely used as paleoredox proxies. For example, recognition of diagenetic impacts on Fe speciation may be particularly important for the Precambrian and Paleozoic, when ferruginous conditions were more widespread (Sperling et al., 2015). During such intervals, caution must be taken to assure that Fe speciation indications of euxinia do not reflect ferruginous water columns overlying sediments with sulfidic pore fluids. Specifically, our combined proxies suggest that large Fe, Mn, and Mo enrichments, which today are represented by a combination of sulfides and carbonates, likely originated from deposition as Fe and Mn-oxides, perhaps via events analogous to modern MBIs. Even in Landsort Deep where euxinic conditions are observed today (Dellwig et al., 2010, 2019; Noordmann et al., 2014), we suggest that sedimentary Fe and Mo proxy values typical of euxinia likely indicate a combination of syngenetic and diagenetic origins, with MBIs oxidizing dissolved Fe and Mn that are subsequently deposited as oxides (and associated sorbed Mo). These phases are then converted to sulfides at or near the sediment-water interface. These interpretations from ancient sediments parallel direct modern observations and similar inferences for the oxidation of dissolved Mn and Fe and associated delivery of Mn and Fe-oxides and Mo to the sediments at Gotland Deep (Huckriede and Meischner, 1996; Dellwig et al., 2010, 2018; Scholz et al., 2013; Hermans et al., 2019). This Baltic model clearly differs from the controls on Fe and Mo enrichment in more restricted basins such as the Black Sea but can be distinguished through a combination of Mn enrichments and Mo and S isotope signatures tracking oxide deposition and the relative proportion of syngenetic and diagenetic pyrite formation (e.g., Planavsky et al., 2018).

CONCLUSION

We use a combination of Fe speciation and isotopes, Mo concentration and isotope data, and S isotopes to constrain paleoredox conditions in multiple sub-basins of the Baltic Sea Holocene. The records come from IODP 347 drill cores from Lille Belt, Bornholm Basin, and Landsort Deep, which together form a sill-proximal to sill-distal transect. Our goal was to assess spatiotemporal redox variations in the Baltic. The geochemical proxies provide evidence for redox heterogeneity among the locations during syndepositional events but also temporally at each individual sub-basin. Specifically, proxy evidence at Lille Belt points to sustained manganous/ferruginous conditions since the transition to the brackish Baltic Sea but with no clear excursions to more reducing conditions during the HTM or MCA, which are well-known intervals of enhanced organic carbon burial in the Baltic. Our Bornholm Basin core (which does not include the MCA) provides evidence for episodes of both ferruginous and euxinic conditions during enhanced organic carbon burial associated with HTM, but Mo isotope data limit euxinic conditions to low or transient sulfide concentrations. Lastly, euxinic conditions have already been recognized at Landsort Deep for both the MCA and HTM, but our new S isotope data are most consistent with sulfide beyond low or transient levels having been largely restricted to at or below the sediment-water interface. The Mo isotope data from all three sub-basins are highly fractionated from seawater, suggesting that particulate shuttling via Mn-Fe oxides plays a major role in the delivery of Fe, Mn, and Mo to the sediments. We also provide evidence that pyritization of these Fe-oxide fluxes during early diagenesis may be primarily responsible for increases in pyrite in some anoxic intervals. Together, paleoredox data for syndepositional events indicate more reducing conditions with increasing distance from the sill, as is observed today. Ultimately, the combination of approaches taken gives us a template for identifying specific paleoredox regimes in a highly dynamic sedimentary and diagenetic system and demonstrates the potential to identify large-scale spatial redox heterogeneity among sub-basins within a single silled basinal complex.

DATA AVAILABILITY STATEMENT

The original contributions presented in the study are included in the article/**Supplementary Material**, further inquiries can be directed to the corresponding author/s.

AUTHOR CONTRIBUTIONS

DH, NR, and TL designed the study. DH, SB, DA, and NP contributed to analytical results. DH wrote the manuscript. All authors provided feedback on the manuscript.

FUNDING

DH acknowledges funding from NSF-OCE #1923218 and a Schlanger Ocean Drilling Fellowship. DH and NR acknowledge support by the Consortium for Ocean Leadership–U.S. Science Support Program. TL acknowledges support through NASA Astrobiology Institute under Cooperative Agreement No. NNA15BB03A issued through the Science Mission Directorate.

ACKNOWLEDGMENTS

We thank the captain and crew of the Greatship Manisha and the European Consortium of Ocean Drilling.

SUPPLEMENTARY MATERIAL

The Supplementary Material for this article can be found online at: https://www.frontiersin.org/articles/10.3389/feart.2021.671401/full#supplementary-material

REFERENCES

Algeo, T. J., and Lyons, T. W. (2006). Mo–total organic carbon covariation in modern anoxic marine environments: implications for analysis of paleoredox and paleohydrographic conditions. *Paleoceanography* 21. doi: 10.1029/2004PA001112

Algeo, T. J., and Tribovillard, N. (2009). Environmental analysis of paleoceanographic systems based on molybdenum–uranium covariation. *Chem. Geol.* 268, 211–225. doi: 10.1016/j.chemgeo.2009.09.001

Andrén, T., Björck, S., Andrén, E., Conley, D., Zillén, L., and Anjar, J. (2011). *The Development of the Baltic Sea Basin during the last 130 ka, The Baltic Sea Basin*. Berlin: Springer, 75–97.

Andrén, T., Jørgensen, B. B., Cotterill, C., Green, S., Andrén, E., Ash, J., et al. (2015a). "Site M0059," in *The Expedition 347 Scientists, Proc. IODP*, eds T. Andrén, B. B. Jørgensen, C. Cotterill, and S. Green (College Station, TX: Integrated Ocean Drilling Program).

Andrén, T., Jørgensen, B. B., Cotterill, C., Green, S., Andrén, E., Ash, J., et al. (2015b). "Site M0063," in *The Expedition 347 Scientists, Proc. IODP, 347*, eds T. Andrén, B. B. Jørgensen, C. Cotterill, and S. Green (College Station, TX: Integrated Ocean Drilling Program).

Andrén, T., Jørgensen, B. B., Cotterill, C., Green, S., Andrén, E., Ash, J., et al. (2015c). "Site M0065," in *The Expedition 347 Scientists, Proc. IODP, 347*, eds T. Andrén, B. B. Jørgensen, C. Cotterill, and S. Green (College Station, TX: Integrated Ocean Drilling Program).

Ardakani, O. H., Hlohowskyj, S. R., Chappaz, A., Sanei, H., Liseroudi, M. H., and Wood, J. M. (2020). Molybdenum speciation tracking hydrocarbon migration in fine-grained sedimentary rocks. *Geochim. Cosmochim. Acta* 283, 136–148. doi: 10.1016/j.gca.2020.06.006

Arnold, G. L., Anbar, A., Barling, J., and Lyons, T. (2004). Molybdenum isotope evidence for widespread anoxia in mid-Proterozoic oceans. *Science* 304, 87–90. doi: 10.1126/science.1091785

Asael, D., Rouxel, O., Poulton, S. W., Lyons, T. W., and Bekker, A. (2018). Molybdenum record from black shales indicates oscillating atmospheric oxygen levels in the early Paleoproterozoic. *Am. J. Sci.* 318, 275–299. doi: 10.2475/03.2018.01

Asael, D., Tissot, F. L., Reinhard, C. T., Rouxel, O., Dauphas, N., Lyons, T. W., et al. (2013). Coupled molybdenum, iron and uranium stable isotopes as oceanic paleoredox proxies during the Paleoproterozoic Shunga Event. *Chem. Geol.* 362, 193–210. doi: 10.1016/j.chemgeo.2013.08.003

Azrieli-Tal, I., Matthews, A., Bar-Matthews, M., Almogi-Labin, A., Vance, D., Archer, C., et al. (2014). Evidence from molybdenum and iron isotopes and molybdenum uranium covariation for sulphidic bottom waters during Eastern Mediterranean sapropel S1 formation. *Earth Planet. Sci. Lett.* 393, 231–242. doi: 10.1016/j.epsl.2014.02.054

Barling, J., Arnold, G. L., and Anbar, A. (2001). Natural mass-dependent variations in the isotopic composition of molybdenum. *Earth Planet. Sci. Lett.* 193, 447–457. doi: 10.1016/s0012-821x(01)00514-3

Berner, R. A. (1969). Migration of iron and sulfur within anaerobic sediments during early diagenesis. *Am. J. Sci.* 267, 19–42. doi: 10.2475/ajs.267.1.19

Berner, R. A. (1980). *Early Diagenesis: A Theoretical Approach*. Princeton, NJ: Princeton University Press.

Berner, R. A., Baldwin, T., and Holdren, G. R. Jr. (1979). Authigenic iron sulfides as paleosalinit indicators. *J. Sediment. Res.* 49, 1345–1350.

Berner, R. A., and Raiswell, R. (1984). C/S method for distinguishing freshwater from marine sedimentary rocks. *Geology* 12, 365–368. doi: 10.1130/0091-7613(1984)12<365:cmfdff>2.0.co;2

Bertine, K. K., and Turekian, K. K. (1973). Molybdenum in marine deposits. *Geochim. Cosmochim. Acta* 37, 1415–1434. doi: 10.1016/0016-7037(73)90080-x

Björck, S., Andrén, T., and Jensen, J. B. (2008). An attempt to resolve the partly conflicting data and ideas on the Ancylus-Littorina transition. *Polish Geol. Institute Special Papers* 23, 21–26.

Boesen, C., and Postma, D. (1988). Pyrite formation in anoxic environments of the Baltic. *Am. J. Sci.* 288, 575–603. doi: 10.2475/ajs.288.6.575

Böning, P., Brumsack, H.-J., Böttcher, M. E., Schnetger, B., Kriete, C., Kallmeyer, J., et al. (2004). Geochemistry of Peruvian near-surface sediments. *Geochim. Cosmochim. Acta* 68, 4429–4451. doi: 10.1016/j.gca.2004.04.027

Borowski, W. S., Rodriguez, N. M., Paull, C. K., and Ussler, W. (2013). Are S-34-enriched authigenic sulfide minerals a proxy for elevated methane flux and gas hydrates in the geologic record? *Mar. Petroleum Geol.* 43, 381–395. doi: 10.1016/j.marpetgeo.2012.12.009

Böttcher, M. E., and Huckriede, H. (1997). First occurrence and stable isotope composition of authigenic gamma-MnS in the central Gotland Deep (Baltic Sea). *Mar. Geol.* 137, 201–205. doi: 10.1016/s0025-3227(96)00115-6

Böttcher, M. E., and Lepland, A. (2000). Biogeochemistry of sulfur in a sediment core from the west-central Baltic Sea: evidence from stable isotopes and pyrite textures. *J. Mar. Syst.* 25, 299–312. doi: 10.1016/s0924-7963(00)00023-3

Busigny, V., Planavsky, N. J., Jezequel, D., Crowe, S., Louvat, P., Moureau, J., et al. (2014). Iron isotopes in an Archean ocean analogue. *Geochim. Cosmochim. Acta* 133, 443–462. doi: 10.1016/j.gca.2014.03.004

Calvert, S., and Pedersen, T. (1996). Sedimentary geochemistry of manganese; implications for the environment of formation of manganiferous black shales. *Econ. Geol.* 91, 36–47.

Canfield, D., and Thamdrup, B. (2009). Towards a consistent classification scheme for geochemical environments, or, why we wish the term 'suboxic'would go away. *Geobiology* 7, 385–392. doi: 10.1111/j.1472-4669.2009.00214.x

Canfield, D. E. (1989). Reactive iron in marine sediments. *Geochim. Cosmochim. Acta* 53, 619–632. doi: 10.1016/0016-7037(89)90005-7

Canfield, D. E., and Berner, R. A. (1987). Dissolution and pyritization of magnetite in anoxie marine sediments. *Geochim. Cosmochim. Acta* 51, 645–659. doi: 10.1016/0016-7037(87)90076-7

Canfield, D. E., Lyons, T. W., and Raiswell, R. (1996). A model for iron deposition to euxinic Black Sea sediments. *Am. J. Sci.* 296, 818–834. doi: 10.2475/ajs.296.7.818

Canfield, D. E., Raiswell, R., and Bottrell, S. H. (1992). The reactivity of sedimentary iron minerals toward sulfide. *Am. J. Sci.* 292, 659–683. doi: 10.2475/ajs.292.9.659

Carstensen, J., Andersen, J. H., Gustafsson, B. G., and Conley, D. J. (2014). Deoxygenation of the Baltic Sea during the last century. *Proc. Natl. Acad. Sci. U.S.A.* 111, 5628–5633. doi: 10.1073/pnas.1323156111

Chambers, L. A., and Trudinger, P. A. (1979). Microbiological fractionation of stable sulfur isotopes: a review and critique. *Geomicrobiol. J.* 1, 249–293. doi: 10.1080/01490457909377735

Chanton, J. P., and Martens, C. S. (1985). The effects of heat and stannous chloride addition on the active distillation of acid volatile sulfide from pyrite-rich marine sediment samples. *Biogeochemistry* 1, 375–382. doi: 10.1007/bf02187379

Cline, J. D. (1969). Spectrophotometric determination of hydrogen sulfide in natural waters. *Limnol. Oceanogr.* 14, 454–458. doi: 10.4319/lo.1969.14.3.0454

Dahl, T., Chappaz, A., Hoek, J., McKenzie, C. J., Svane, S., and Canfield, D. (2017). Evidence of molybdenum association with particulate organic matter under sulfidic conditions. *Geobiology* 15, 311–323. doi: 10.1111/gbi.12220

Dahl, T. W., Chappaz, A., Fitts, J. P., and Lyons, T. W. (2013). Molybdenum reduction in a sulfidic lake: evidence from X-ray absorption fine-structure spectroscopy and implications for the Mo paleoproxy. *Geochim. Cosmochim. Acta* 103, 213–231. doi: 10.1016/j.gca.2012.10.058

Dellwig, O., Leipe, T., März, C., Glockzin, M., Pollehne, F., Schnetger, B., et al. (2010). A new particulate Mn–Fe–P-shuttle at the redoxcline of anoxic basins. *Geochim. Cosmochim. Acta* 74, 7100–7115. doi: 10.1016/j.gca.2010.09.017

Dellwig, O., Schnetger, B., Brumsack, H.-J., Grossart, H.-P., and Umlauf, L. (2012). Dissolved reactive manganese at pelagic redoxclines (part II): hydrodynamic conditions for accumulation. *J. Mar. Syst.* 90, 31–41. doi: 10.1016/j.jmarsys.2011.08.007

Dellwig, O., Schnetger, B., Meyer, D., Pollehne, F., Hausler, K., and Arz, H. W. (2018). Impact of the major baltic inflow in 2014 on manganese cycling in the gotland deep (Baltic Sea). *Front. Mar. Sci.* 5:248.

Dellwig, O., Wegwerth, A., Schnetger, B., Schulz, H., and Arz, H. W. (2019). Dissimilar behaviors of the geochemical twins W and Mo in hypoxic-euxinic marine basins. *Earth Sci. Rev.* 193, 1–23. doi: 10.1016/j.earscirev.2019.03.017

Dijkstra, N., Hagens, M., Egger, M., and Slomp, C. P. (2018a). Post-depositional formation of vivianite-type minerals alters sediment phosphorus records. *Biogeosciences* 15, 861–883. doi: 10.5194/bg-15-861-2018

Dijkstra, N., Krupinski, N. B. Q., Yamane, M., Obrochta, S. P., Miyairi, Y., Yokoyama, Y., et al. (2018b). Holocene refreshening and reoxygenation of a bothnian sea estuary led to enhanced phosphorus burial. *Estuaries Coasts* 41, 139–157. doi: 10.1007/s12237-017-0262-x

Dijkstra, N., Slomp, C. P., Behrends, T., and Expedition, S. (2016). Vivianite is a key sink for phosphorus in sediments of the Landsort Deep, an intermittently

anoxic deep basin in the Baltic Sea. *Chem. Geol.* 438, 58–72. doi: 10.1016/j.chemgeo.2016.05.025

Egger, M., Hagens, M., Sapart, C. J., Dijkstra, N., van Helmond, N. A., Mogollón, J. M., et al. (2017). Iron oxide reduction in methane-rich deep Baltic Sea sediments. *Geochim. Cosmochim. Acta* 207, 256–276. doi: 10.1016/j.gca.2017.03.019

Erickson, B. E., and Helz, G. R. (2000). Molybdenum (VI) speciation in sulfidic waters:: stability and lability of thiomolybdates. *Geochim. Cosmochim. Acta* 64, 1149–1158. doi: 10.1016/s0016-7037(99)00423-8

Eroglu, S., Scholz, F., Frank, M., and Siebert, C. (2020). Influence of particulate versus diffusive molybdenum supply mechanisms on the molybdenum isotope composition of continental margin sediments. *Geochim. Cosmochim. Acta* 273, 51–69. doi: 10.1016/j.gca.2020.01.009

Fehr, M. A., Andersson, P. S., Halenius, U., Gustafsson, O., and Mörth, C.-M. (2010). Iron enrichments and Fe isotopic compositions of surface sediments from the Gotland Deep, Baltic Sea. *Chem. Geol.* 277, 310–322. doi: 10.1016/j.chemgeo.2010.08.014

Fehr, M. A., Andersson, P. S., Hålenius, U., and Mörth, C.-M. (2008). Iron isotope variations in Holocene sediments of the Gotland Deep, Baltic Sea. *Geochim. Cosmochim. Acta* 72, 807–826. doi: 10.1016/j.gca.2007.11.033

Franck, H., Matthäus, W., and Sammler, R. (1987). Major inflows of saline water into the Baltic Sea during the present century. *Gerlands Beiträge Geophys.* 96, 517–531.

Froelich, P. N., Klinkhammer, G., Bender, M., Luedtke, N., Heath, G. R., Cullen, D., et al. (1979). Early oxidation of organic matter in pelagic sediments of the eastern equatorial Atlantic: suboxic diagenesis. *Geochim. Cosmochim. Acta* 43, 1075–1090. doi: 10.1016/0016-7037(79)90095-4

Fry, B., Jannasch, H. W., Molyneaux, S. J., Wirsen, C. O., Muramoto, J. A., and King, S. (1991). Stable isotope studies of the carbon, nitrogen and sulfur cycles in the Black Sea and the Cariaco Trench. *Oceanogr. Res. Pap.* 38, S1003–S1019.

Goldberg, T., Archer, C., Vance, D., and Poulton, S. W. (2009). Mo isotope fractionation during adsorption to Fe (oxyhydr) oxides. *Geochim. Cosmochim. Acta* 73, 6502–6516. doi: 10.1016/j.gca.2009.08.004

Goldhaber, M., and Kaplan, I. (1974). "The sulfur cycle," in *The Sea*, Vol. 5, ed. E. D. Goldberg (New York, NY: Wiley-Interscience), 569–655.

Groeneveld, J., Filipsson, H. L., Austin, W. E. N., Darling, K., McCarthy, D., Krupinski, N. B. Q., et al. (2018). Assessing proxy signatures of temperature, salinity, and hypoxia in the Baltic Sea through foraminifera-based geochemistry and faunal assemblages. *J. Micropalaeontol.* 37, 403–429. doi: 10.5194/jm-37-403-2018

Gustafsson, B. G., and Westman, P. (2002). On the causes for salinity variations in the Baltic Sea during the last 8500 years. *Paleoceanography* 17, 12–11. doi: 10.1029/2000pa000572

Habicht, K. S., and Canfield, D. E. (2001). Isotope fractionation by sulfate-reducing natural populations and the isotopic composition of sulfide in marine sediments. *Geology* 29, 555–558. doi: 10.1130/0091-7613(2001)029<0555:ifbsrn>2.0.co;2

Hancock, L. G., Hardisty, D. S., Behl, R. J., and Lyons, T. W. (2019). A multi-basin redox reconstruction for the Miocene Monterey Formation, California, USA. *Palaeogeogr. Palaeoclimatol. Palaeoecol.* 520, 114–127. doi: 10.1016/j.palaeo.2019.01.031

Hardisty, D. S., Lyons, T. W., Riedinger, N., Isson, T. T., Owens, J. D., Aller, R. C., et al. (2018). An evaluatin of sedimentary molybdenum and iron as proxies for pore fluid paleoredox conditions. *Am. J. Sci.* 318, 527–556. doi: 10.2475/05.2018.04

Hardisty, D. S., Riedinger, N., Planavsky, N. J., Asael, D., Andrén, T., Jørgensen, B. B., et al. (2016). A Holocene history of dynamic water column redox conditions in the Landsort Deep, Baltic Sea. *Am. J. Sci.* 316, 713–745. doi: 10.2475/08.2016.01

Hartmann, M., and Nielsen, H. (2012). $\delta^{34}S$ values in recent sea sediments and their significance using several sediment profiles from the western Baltic Sea. *Isotopes Environ. Health Stud.* 48, 7–32. doi: 10.1080/10256016.2012.660528

Hermans, M., Lenstra, W. K., van Helmond, N., Behrends, T., Egger, M., Seguret, M. J. M., et al. (2019). Impact of natural re-oxygenation on the sediment dynamics of manganese, iron and phosphorus in a euxinic Baltic Sea basin. *Geochim. Cosmochim. Acta* 246, 174–196. doi: 10.1016/j.gca.2018.11.033

Huckriede, H., and Meischner, D. (1996). Origin and environment of manganese-rich sediments within black-shale basins. *Geochim. Cosmochim. Acta* 60, 1399–1413. doi: 10.1016/0016-7037(96)00008-7

Hurtgen, M. T., Lyons, T. W., Ingall, E. D., and Cruse, A. M. (1999). Anomalous enrichments of iron monosulfide in euxinic marine sediments and the role of H2S in iron sulfide transformations: examples from Effingham Inlet, Orca Basin, and the Black Sea. *Am. J. Sci.* 299, 556–588. doi: 10.2475/ajs.299.7-9.556

Jilbert, T., Conley, D. J., Gustafsson, B. G., Funkey, C. P., and Slomp, C. P. (2015). Glacio-isostatic control on hypoxia in a high-latitude shelf basin. *Geology* 43, 427–430. doi: 10.1130/g36454.1

Jilbert, T., and Slomp, C. P. (2013). Rapid high-amplitude variability in Baltic Sea hypoxia during the Holocene. *Geology* 41, 1183–1186. doi: 10.1130/g34804.1

Jørgensen, B. B., Böttcher, M. E., Lüschen, H., Neretin, L. N., and Volkov, I. I. (2004). Anaerobic methane oxidation and a deep H2S sink generate isotopically heavy sulfides in Black Sea sediments. *Geochim. Cosmochim. Acta* 68, 2095–2118. doi: 10.1016/j.gca.2003.07.017

Kabel, K., Moros, M., Porsche, C., Neumann, T., Adolphi, F., Andersen, T. J., et al. (2012). Impact of climate change on the Baltic Sea ecosystem over the past 1,000 years. *Nat. Clim. Change* 2, 871–874. doi: 10.1038/nclimate1595

Kashiwabara, T., Takahashi, Y., and Tanimizu, M. (2009). A XAFS study on the mechanism of isotopic fractionation of molybdenum during its adsorption on ferromanganese oxides. *Geochem. J.* 43, e31–e36.

Kostka, J. E., and Luther, G. W. (1994). Partitioning and speciation of solid phase iron in saltmarsh sediments. *Geochim. Cosmochim. Acta* 58, 1701–1710. doi: 10.1016/0016-7037(94)90531-2

Kotthoff, U., Groeneveld, J., Ash, J. L., Fanget, A.-S., Krupinski, N. Q., Peyron, O., et al. (2017). Reconstructing Holocene temperature and salinity variations in the western Baltic Sea region: a multi-proxy comparison from the Little Belt (IODP Expedition 347, Site M0059). *Biogeosciences* 14, 5607–5632. doi: 10.5194/bg-14-5607-2017

Kowalski, N., Dellwig, O., Beck, M., Gräwe, U., Neubert, N., Nägler, T. F., et al. (2013). Pelagic molybdenum concentration anomalies and the impact of sediment resuspension on the molybdenum budget in two tidal systems of the North Sea. *Geochim. Cosmochim. Acta* 119, 198–211. doi: 10.1016/j.gca.2013.05.046

Krishnaswami, S. (1976). Authigenic transition elements in Pacific pelagic clays. *Geochim. Cosmochim. Acta* 40, 425–434. doi: 10.1016/0016-7037(76)90007-7

Leavitt, W. D., Halevy, I., Bradley, A. S., and Johnston, D. T. (2013). Influence of sulfate reduction rates on the Phanerozoic sulfur isotope record. *Proc. Natl. Acad. Sci. U.S.A.* 110, 11244–11249. doi: 10.1073/pnas.1218874110

Lenz, C., Jilbert, T., Conley, D. J., and Slomp, C. P. (2015a). Hypoxia-driven variations in iron and manganese shuttling in the Baltic Sea over the past 8 kyr. *Geochem. Geophys. Geosyst.* 16, 3754–3766. doi: 10.1002/2015gc005960

Lenz, C., Jilbert, T., Conley, D. J., Wolthers, M., and Slomp, C. P. (2015b). Are recent changes in sediment manganese sequestration in the euxinic basins of the Baltic Sea linked to the expansion of hypoxia? *Biogeosciences* 12, 4875–4894. doi: 10.5194/bg-12-4875-2015

Lepland, A., and Stevens, R. L. (1998). Manganese authigenesis in the landsort deep, Baltic Sea. *Mar. Geol.* 151, 1–25. doi: 10.1016/s0025-3227(98)00046-2

Li, Y.-H., and Gregory, S. (1974). Diffusion of ions in sea water and in deep-sea sediments. *Geochim. Cosmochim. Acta* 38, 703–714. doi: 10.1016/0016-7037(74)90145-8

Lin, Z. Y., Sun, X. M., Peckmann, J., Lu, Y., Xu, L., Strauss, H., et al. (2016). How sulfate-driven anaerobic oxidation of methane affects the sulfur isotopic composition of pyrite: a SIMS study from the South China Sea. *Chem. Geol.* 440, 26–41. doi: 10.1016/j.chemgeo.2016.07.007

Lyons, T. W. (1997). Sulfur isotopic trends and pathways of iron sulfide formation in upper Holocene sediments of the anoxic Black Sea. *Geochim. Cosmochim. Acta* 61, 3367–3382. doi: 10.1016/s0016-7037(97)00174-9

Lyons, T. W., and Kashgarian, M. (2005). Paradigm lost, paradigm found. *Oceanography* 18, 86–99. doi: 10.5670/oceanog.2005.44

Lyons, T. W., and Severmann, S. (2006). A critical look at iron paleoredox proxies: new insights from modern euxinic marine basins. *Geochim. Cosmochim. Acta* 70, 5698–5722. doi: 10.1016/j.gca.2006.08.021

Lyons, T. W., Werne, J. P., Hollander, D. J., and Murray, R. (2003). Contrasting sulfur geochemistry and Fe/Al and Mo/Al ratios across the last oxic-to-anoxic transition in the Cariaco Basin, Venezuela. *Chem. Geol.* 195, 131–157. doi: 10.1016/s0009-2541(02)00392-3

Manheim, F. T. (1961). A geochemical profile in the Baltic Sea. *Geochim. Cosmochim. Acta* 25, 52–70. doi: 10.1016/0016-7037(61)90059-x

Matthäus, W. (2006). *The History of Investigation of Salt Water Inflows Into the Baltic Sea: From Early Beginning to Recent Results*. Rostock: Institut für Meereskunde Warnemhunde.

Maynard, J. B. (1980). Sulfur isotopes of iron sulfides in Devonian-Mississippian shales of the Appalachian Basin – control by rate of sedimentation. *Am. J. Sci.* 280, 772–786. doi: 10.2475/ajs.280.8.772

Miller, C. A., Peucker-Ehrenbrink, B., Walker, B. D., and Marcantonio, F. (2011). Re-assessing the surface cycling of molybdenum and rhenium. *Geochim. Cosmochim. Acta* 75, 7146–7179. doi: 10.1016/j.gca.2011.09.005

Mohrholz, V., Naumann, M., Nausch, G., Krüger, S., and Gräwe, U. (2015). Fresh oxygen for the Baltic Sea—an exceptional saline inflow after a decade of stagnation. *J. Mar. Syst.* 148, 152–166. doi: 10.1016/j.jmarsys.2015.03.005

Morford, J. L., Martin, W. R., François, R., and Carney, C. M. (2009). A model for uranium, rhenium, and molybdenum diagenesis in marine sediments based on results from coastal locations. *Geochim. Cosmochim. Acta* 73, 2938–2960. doi: 10.1016/j.gca.2009.02.029

Morse, J. W., and Cornwell, J. C. (1987). Analysis and distribution of iron sulfide minerals in recent anoxic marine sediments. *Mar. Chem.* 22, 55–69. doi: 10.1016/0304-4203(87)90048-x

Mort, H. P., Slomp, C. P., Gustafsson, B. G., and Andersen, T. J. (2010). Phosphorus recycling and burial in Baltic Sea sediments with contrasting redox conditions. *Geochim. Cosmochim. Acta* 74, 1350–1362. doi: 10.1016/j.gca.2009.11.016

Nägler, T., Neubert, N., Böttcher, M., Dellwig, O., and Schnetger, B. (2011). Molybdenum isotope fractionation in pelagic euxinia: evidence from the modern Black and Baltic Seas. *Chem. Geol.* 289, 1–11. doi: 10.1016/j.chemgeo.2011.07.001

Nägler, T. F., Anbar, A. D., Archer, C., Goldberg, T., Gordon, G. W., Greber, N. D., et al. (2014). Proposal for an international molybdenum isotope measurement standard and data representation. *Geostandards Geoanal. Res.* 38, 149–151.

Neubert, N., Heri, A. R., Voegelin, A. R., Nägler, T. F., Schlunegger, F., and Villa, I. M. (2011). The molybdenum isotopic composition in river water: constraints from small catchments. *Earth Planet. Sci. Lett.* 304, 180–190. doi: 10.1016/j.epsl.2011.02.001

Neubert, N., Nägler, T. F., and Böttcher, M. E. (2008). Sulfidity controls molybdenum isotope fractionation into euxinic sediments: evidence from the modern Black Sea. *Geology* 36, 775–778. doi: 10.1130/g24959a.1

Ni, S., Krupinski, N. B. Q., Groeneveld, J., Fanget, A. S., Böttcher, M. E., Liu, B., et al. (2020). Holocene hydrographic variations from the baltic-North Sea transitional area (IODP Site M0059). *Paleoceanogr. Paleoclimatol.* 35, 1–20.

Noordmann, J., Weyer, S., Montoya-Pino, C., Dellwig, O., Neubert, N., Eckert, S., et al. (2014). Uranium and molybdenum isotope systematics in modern euxinic basins: case studies from the central Baltic Sea and the Kyllaren fjord (Norway). *Chem. Geol.* 396, 182–195. doi: 10.1016/j.chemgeo.2014.12.012

Papadomanolaki, N. M., Dijkstra, N., van Helmond, N. A. G. M., Hagens, M., Bauersachs, T., Kotthoff, U., et al. (2018). Controls on the onset and termination of past hypoxia in the Baltic Sea. *Palaeogeogr. Palaeoclimatol. Palaeoecol.* 490, 347–354. doi: 10.1016/j.palaeo.2017.11.012

Pasquier, V., Sansjofre, P., Rabineau, M., Revillon, S., Houghton, J., and Fike, D. A. (2017). Pyrite sulfur isotopes reveal glacial-interglacial environmental changes. *Proc. Natl. Acad. Sci. U.S.A.* 114, 5941–5945. doi: 10.1073/pnas.1618245114

Planavsky, N. J., Slack, J. F., Cannon, W. F., O'Connell, B., Isson, T. T., Asael, D., et al. (2018). Evidence for episodic oxygenation in a weakly redox-buffered deep mid-Proterozoic ocean. *Chem. Geol.* 483, 581–594. doi: 10.1016/j.chemgeo.2018.03.028

Poulson Brucker, R. L., McManus, J., Severmann, S., and Berelson, W. M. (2009). Molybdenum behavior during early diagenesis: insights from Mo isotopes. *Geochem. Geophys. Geosyst.* 10:Q06010.

Poulton, S. W., and Canfield, D. E. (2005). Development of a sequential extraction procedure for iron: implications for iron partitioning in continentally derived particulates. *Chem. Geol.* 214, 209–221. doi: 10.1016/j.chemgeo.2004.09.003

Poulton, S. W., and Canfield, D. E. (2011). Ferruginous conditions: a dominant feature of the ocean through Earth's history. *Elements* 7, 107–112. doi: 10.2113/gselements.7.2.107

Raiswell, R., Canfield, D., and Berner, R. (1994). A comparison of iron extraction methods for the determination of degree of pyritisation and the recognition of iron-limited pyrite formation. *Chem. Geol.* 111, 101–110. doi: 10.1016/0009-2541(94)90084-1

Raiswell, R., and Canfield, D. E. (1998). Sources of iron for pyrite formation in marine sediments. *Am. J. Sci.* 298, 219–245. doi: 10.2475/ajs.298.3.219

Raiswell, R., Hardisty, D., Lyons, T., Canfield, D., Owens, J., Planavsky, N., et al. (2018). The iron paleoredox proxies: a guide to the pitfalls, problems and proper practice. *Am. J. Sci.* 318, 491–526. doi: 10.2475/05.2018.03

Raiswell, R., Vu, H. P., Brinza, L., and Benning, L. G. (2010). The determination of labile Fe in ferrihydrite by ascorbic acid extraction: methodology, dissolution kinetics and loss of solubility with age and de-watering. *Chem. Geol.* 278, 70–79. doi: 10.1016/j.chemgeo.2010.09.002

Riedinger, N., Brunner, B., Krastel, S., Arnold, G. L., Wehrmann, L. M., Formolo, M. J., et al. (2017). Sulfur cycling in an iron oxide-dominated, dynamic marine depositional system: the Argentine continental margin. *Front. Earth Sci.* 5:33. doi: 10.3389/feart.2017.00033

Rudnicki, M. D., Elderfield, H., and Spiro, B. (2001). Fractionation of sulfur isotopes during bacterial sulfate reduction in deep ocean sediments at elevated temperatures. *Geochim. Cosmochim. Acta* 65, 777–789. doi: 10.1016/s0016-7037(00)00579-2

Scholz, F., Baum, M., Siebert, C., Eroglu, S., Dale, A. W., Naumann, M., et al. (2018). Sedimentary molybdenum cycling in the aftermath of seawater inflow to the intermittently euxinic Gotland Deep, Central Baltic Sea. *Chem. Geol.* 491, 27–38. doi: 10.1016/j.chemgeo.2018.04.031

Scholz, F., McManus, J., Mix, A. C., Hensen, C., and Schneider, R. R. (2014a). The impact of ocean deoxygenation on iron release from continental margin sediments. *Nat. Geosci.* 7, 433–437. doi: 10.1038/ngeo2162

Scholz, F., McManus, J., and Sommer, S. (2013). The manganese and iron shuttle in a modern euxinic basin and implications for molybdenum cycling at euxinic ocean margins. *Chem. Geol.* 355, 56–68. doi: 10.1016/j.chemgeo.2013.07.006

Scholz, F., Severmann, S., McManus, J., and Hensen, C. (2014b). Beyond the Black Sea paradigm: the sedimentary fingerprint of an open-marine iron shuttle. *Geochim. Cosmochim. Acta* 127, 368–380. doi: 10.1016/j.gca.2013.11.041

Scholz, F., Severmann, S., McManus, J., Noffke, A., Lomnitz, U., and Hensen, C. (2014c). On the isotope composition of reactive iron in marine sediments: redox shuttle versus early diagenesis. *Chem. Geol.* 389, 48–59. doi: 10.1016/j.chemgeo.2014.09.009

Scott, C., and Lyons, T. W. (2012). Contrasting molybdenum cycling and isotopic properties in euxinic versus non-euxinic sediments and sedimentary rocks: refining the paleoproxies. *Chem. Geol.* 324, 19–27. doi: 10.1016/j.chemgeo.2012.05.012

Severmann, S., Lyons, T. W., Anbar, A., McManus, J., and Gordon, G. (2008). Modern iron isotope perspective on the benthic iron shuttle and the redox evolution of ancient oceans. *Geology* 36, 487–490. doi: 10.1130/g24670a.1

Severmann, S., McManus, J., Berelson, W. M., and Hammond, D. E. (2010). The continental shelf benthic iron flux and its isotope composition. *Geochim. Cosmochim. Acta* 74, 3984–4004. doi: 10.1016/j.gca.2010.04.022

Siebert, C., Nägler, T. F., von Blanckenburg, F., and Kramers, J. D. (2003). Molybdenum isotope records as a potential new proxy for paleoceanography. *Earth Planet. Sci. Lett.* 211, 159–171. doi: 10.1016/s0012-821x(03)00189-4

Sim, M. S., Bosak, T., and Ono, S. (2011). Large sulfur isotope fractionation does not require disproportionation. *Science* 333, 74–77. doi: 10.1126/science.1205103

Sohlenius, G. (1996). Mineral magnetic properties of Late Weichselian—Holocene sediments from the northwestern Baltic Proper. *Boreas* 25, 79–88. doi: 10.1111/j.1502-3885.1996.tb00837.x

Sohlenius, G., Emeis, K.-C., Andrén, E., Andrén, T., and Kohly, A. (2001). Development of anoxia during the Holocene fresh–brackish water transition in the Baltic Sea. *Mar. Geol.* 177, 221–242. doi: 10.1016/s0025-3227(01)00174-8

Sohlenius, G., Sternbeck, J., Andrén, E., and Westman, P. (1996). Holocene history of the Baltic Sea as recorded in a sediment core from the Gotland Deep. *Mar. Geol.* 134, 183–201. doi: 10.1016/0025-3227(96)00047-3

Sohlenius, G., and Westman, P. (1998). Salinity and redox alternations in the northwestern Baltic proper during the late Holocene. *Boreas* 27, 101–114. doi: 10.1111/j.1502-3885.1998.tb00871.x

Sperling, E. A., Wolock, C. J., Morgan, A. S., Gill, B. C., Kunzmann, M., Halverson, G. P., et al. (2015). Statistical analysis of iron geochemical data suggests limited late Proterozoic oxygenation. *Nature* 523, 451–454. doi: 10.1038/nature14589

Sternbeck, J., and Sohlenius, G. (1997). Authigenic sulfide and carbonate mineral formation in Holocene sediments of the Baltic Sea. *Chem. Geol.* 135, 55–73. doi: 10.1016/s0009-2541(96)00104-0

Suess, E. (1979). Mineral phases formed in anoxic sediments by microbial decomposition of organic matter. *Geochim. Cosmochim. Acta* 43, 339–352. doi: 10.1016/0016-7037(79)90199-6

Taylor, P. D. P., Maeck, R., and Debievre, P. (1992). Determination of the absolute isotopic composition and atomic-weight of a reference sample of natural iron. *Int. J. Mass Spectr. Ion Processes* 121, 111–125. doi: 10.1016/0168-1176(92)80075-c

Taylor, S. R., and McLennan, S. M. (1995). The geochemical evolution of the continental crust. *Rev. Geophys.* 33, 241–265. doi: 10.1029/95rg00262

Teutsch, N., Schmid, M., Muller, B., Halliday, A. N., Burgmann, H., and Wehrli, B. (2009). Large iron isotope fractionation at the oxic-anoxic boundary in Lake Nyos. *Earth Planet. Sci. Lett.* 285, 52–60. doi: 10.1016/j.epsl.2009.05.044

Tossell, J. (2005). Calculating the partitioning of the isotopes of Mo between oxidic and sulfidic species in aqueous solution. *Geochim. Cosmochim. Acta* 69, 2981–2993. doi: 10.1016/j.gca.2005.01.016

van de Velde, S. J., Hylen, A., Kononets, M., Marzocchi, U., Leermakers, M., Choumiline, K., et al. (2020). Elevated sedimentary removal of Fe, Mn, and trace elements following a transient oxygenation event in the Eastern Gotland Basin, central Baltic Sea. *Geochim. Cosmochim. Acta* 271, 16–32. doi: 10.1016/j.gca.2019.11.034

van Helmond, N., Jilbert, T., and Slomp, C. P. (2018). Hypoxia in the Holocene Baltic Sea: comparing modern versus past intervals using sedimentary trace metals. *Chem. Geol.* 493, 478–490. doi: 10.1016/j.chemgeo.2018.06.028

van Helmond, N., Krupinski, N. B. Q., Lougheed, B. C., Obrochta, S. P., Andren, T., and Slomp, C. P. (2017). Seasonal hypoxia was a natural feature of the coastal zone in the Little Belt, Denmark, during the past 8 ka. *Mar. Geol.* 387, 45–57. doi: 10.1016/j.margeo.2017.03.008

van Wirdum, F., Andren, E., Wienholz, D., Koffhoff, U., Moros, M., Fanget, A.-S., et al. (2019). Middle to late holocene variations in salinity and primary productivity in the Central Baltic Sea: a multiproxy study from the landsort deep. *Front. Mar. Sci.* 6:51. doi: 10.3389/fmars.2019.00051

Vorlicek, T. P., Helz, G. R., Chappaz, A., Vue, P., Vezina, A., and Hunter, W. (2018). Molybdenum burial mechanism in sulfidic sediments: iron-sulfide pathway. *Acs Earth Space Chem.* 2, 565–576. doi: 10.1021/acsearthspacechem.8b00016

Wagner, M., Chappaz, A., and Lyons, T. W. (2017). Molybdenum speciation and burial pathway in weakly sulfidic environments: insights from XAFS. *Geochim. Cosmochim. Acta* 206, 18–29. doi: 10.1016/j.gca.2017.02.018

Warnock, J., Andren, E., Juggins, S., Lewis, J., Ryves, D. B., Andren, T., et al. (2020). A high-resolution diatom-based Middle and Late Holocene environmental history of the Little Belt region, Baltic Sea. *Boreas* 49, 1–16. doi: 10.1111/bor.12419

Wasylenki, L. E., Rolfe, B. A., Weeks, C. L., Spiro, T. G., and Anbar, A. D. (2008). Experimental investigation of the effects of temperature and ionic strength on Mo isotope fractionation during adsorption to manganese oxides. *Geochim. Cosmochim. Acta* 72, 5997–6005. doi: 10.1016/j.gca.2008.08.027

Wijsman, J. W., Middelburg, J. J., and Heip, C. H. (2001a). Reactive iron in Black Sea sediments: implications for iron cycling. *Mar. Geol.* 172, 167–180. doi: 10.1016/s0025-3227(00)00122-5

Wijsman, J. W., Middelburg, J. J., Herman, P. M., Böttcher, M. E., and Heip, C. H. (2001b). Sulfur and iron speciation in surface sediments along the northwestern margin of the Black Sea. *Mar. Chem.* 74, 261–278. doi: 10.1016/s0304-4203(01)00019-6

Wortmann, U. G., Bernasconi, S. M., and Böttcher, M. E. (2001). Hypersulfidic deep biosphere indicates extreme sulfur isotope fractionation during single-step microbial sulfate reduction. *Geology* 29, 647–650. doi: 10.1130/0091-7613(2001)029<0647:hdbies>2.0.co;2

Zerkle, A. L., Scheiderich, K., Maresca, J. A., Liermann, L. J., and Brantley, S. L. (2011). Molybdenum isotope fractionation by cyanobacterial assimilation during nitrate utilization and N_2 fixation. *Geobiology* 9, 94–106. doi: 10.1111/j.1472-4669.2010.00262.x

Zhou, X., Jenkyns, H. C., Lu, W., Hardisty, D. S., Owens, J. D., Lyons, T. W., et al. (2017). Organically bound iodine as a bottom-water redox proxy: preliminary validation and application. *Chem. Geol.* 457, 95–106. doi: 10.1016/j.chemgeo.2017.03.016

Zillén, L., Conley, D. J., Andrén, T., Andrén, E., and Björck, S. (2008). Past occurrences of hypoxia in the Baltic Sea and the role of climate variability, environmental change and human impact. *Earth Sci. Rev.* 91, 77–92. doi: 10.1016/j.earscirev.2008.10.001

Conflict of Interest: The authors declare that the research was conducted in the absence of any commercial or financial relationships that could be construed as a potential conflict of interest.

frontiers in Earth Science

ORIGINAL RESEARCH
published: 18 August 2021
doi: 10.3389/feart.2021.669476

Middle Ordovician Upwelling-Related Ironstone of North Wales: Coated Grains, Ocean Chemistry, and Biological Evolution

Sarah K. Dunn[1], *Peir K. Pufahl*[2,1]*, *J. Brendan Murphy*[3] *and Stephen W. Lokier*[4]

[1]*Department of Earth and Environmental Science, Acadia University, Wolfville, Nova Scotia,* [2]*Department of Geological Sciences and Geological Engineering, Queen's University, Kingston, ON, Canada,* [3]*Department of Earth Sciences, St. Francis Xavier University, Antigonish, Nova Scotia,* [4]*School of Ocean Sciences, Bangor University, Bangor, United Kingdom*

Middle Ordovician phosphatic ironstone of the Welsh Basin provides new insight into the paleoenvironmental significance of ironstone and Ordovician ocean chemistry. Deposition occurred in a back-arc basin along the southern margin of Avalonia as the Rheic Ocean opened to the south. Ironstone is interpreted to have accumulated as part of an aggradational parasequence on a storm-dominated shelf with coastal upwelling. This parasequence has a laminated pyritic mudstone base that grades upward into variably bioturbated mudstone and coated grain-rich, intraclastic ironstone, which is overlain in turn by cross-stratified grainstone composed entirely of coated Fe grains. A coarser clastic parasequence composed of more proximal lithofacies rests conformably above and suggests the contact between the two parasequences is a maximum flooding surface marking the onset of highstand conditions. Lithofacies associations suggest that sustained coastal upwelling created a wedge of nutrient-rich, ferruginous seawater on the middle shelf that stimulated high surface ocean productivities. Large, coated Fe grains (granule size) composed of discontinuous and concentric carbonate fluorapatite, hematite, and chamosite cortical layers record fluctuations in pore water E_h that are interpreted to have been related to changes in upwelling intensity and intermittent storm reworking of the seafloor. Results support an emerging model for Ordovician ironstone underpinned by the development of ferruginous bottom water that was periodically tapped by coastal upwelling. Expanding, semi-restricted seaways such as the Rheic Ocean were ideal locations for the ponding of this anoxic, hydrothermally enriched seawater, especially during the early Paleozoic when the deep ocean was variably and inconsistently oxygenated. The coincidence of ironstone depositional episodes with graptolite diversification events suggests that, in addition to Fe, the sustained supply of upwelling-related P may have driven the radiation of some planktonic ecosystems during the Great Ordovician Biodiversification Event. Concomitant minor extinctions of benthic trilobites occurred as these ferruginous waters impinged on the shelf.

Keywords: ironstone, Wales, sedimentology, geochemistry, upwelling, ferruginous seawater, coated grains, biologic evolution

OPEN ACCESS

Edited by:
Natascha Riedinger, Oklahoma State University, United States

Reviewed by:
Maxwell Lechte, McGill University, Canada
Michelle Abshire, Valley City State University, United States

***Correspondence:**
Peir K. Pufahl
peir.pufahl@queensu.ca

Specialty section:
This article was submitted to Biogeoscience, a section of the journal Frontiers in Earth Science

Received: *18 February 2021*
Accepted: *03 August 2021*
Published: *18 August 2021*

Citation:
Dunn SK, Pufahl PK, Murphy J B and Lokier SW (2021) Middle Ordovician Upwelling-Related Ironstone of North Wales: Coated Grains, Ocean Chemistry, and Biological Evolution. Front. Earth Sci. 9:669476. doi: 10.3389/feart.2021.669476

INTRODUCTION

Ironstone is a Phanerozoic marine biochemical sedimentary rock type with an Fe content of greater than 15 wt% (Van Houten and Bhattacharyya, 1982; Van Houten and Arthur, 1989; Young et al., 1989; Pufahl, 2010). Most ironstone is aluminous, phosphate-rich, and contemporaneous with major intervals of phosphorite accumulation (Young, 1992). Phosphorite, an important fertilizer ore, is also a marine biochemical sedimentary rock containing at least 18 wt% P_2O_5 (Filippelli, 2008; Pufahl, 2010). The two most prominent episodes of coincident ironstone-phosphorite deposition occurred in the Ordovician and the Jurassic (Van Houten and Arthur, 1989; Young, 1992). Both periods generally correspond to intervals of increased tectonic activity, elevated hydrothermal input, globally warm climate, and biologic radiation in the marine realm (**Figure 1**; Van Houten and Bhattacharyya, 1982; Van Houten and Arthur, 1989; Sturesson et al., 2000; Servais et al., 2010).

The interplay of these processes ultimately controls the delivery, cycling, and sedimentation of Fe and P in the ocean (Pufahl, 2010; Föllmi, 2016). Although the deposition of phosphatic sediment is generally well understood (e.g., Föllmi, 1996; Pufahl and Groat, 2017), processes governing ironstone accumulation remain poorly constrained. Phosphatic ironstone of the Welsh Basin (ca. 467 Ma) provides a unique opportunity to investigate these processes and their potential relationship to the Great Ordovician Biodiversification Event (GOBE; ca. 480–445 Ma), which is the largest sustained marine radiation in Earth history (Servais et al., 2009, 2010; Edwards, 2019). A distinguishing characteristic of this ironstone is the occurrence of large coated Fe grains. The size and variable mineralogy of coated grains provide an unparalleled window into water column and seafloor processes that facilitated ironstone precipitation.

The oceanography and depositional environments of phosphatic ironstone in the Welsh Basin are herein constrained by documenting their sedimentology and sequence stratigraphy. The diagenesis and paragenesis of lithofacies are interpreted in this framework to place these ironstones in their paleoenvironmental context, providing the basis for

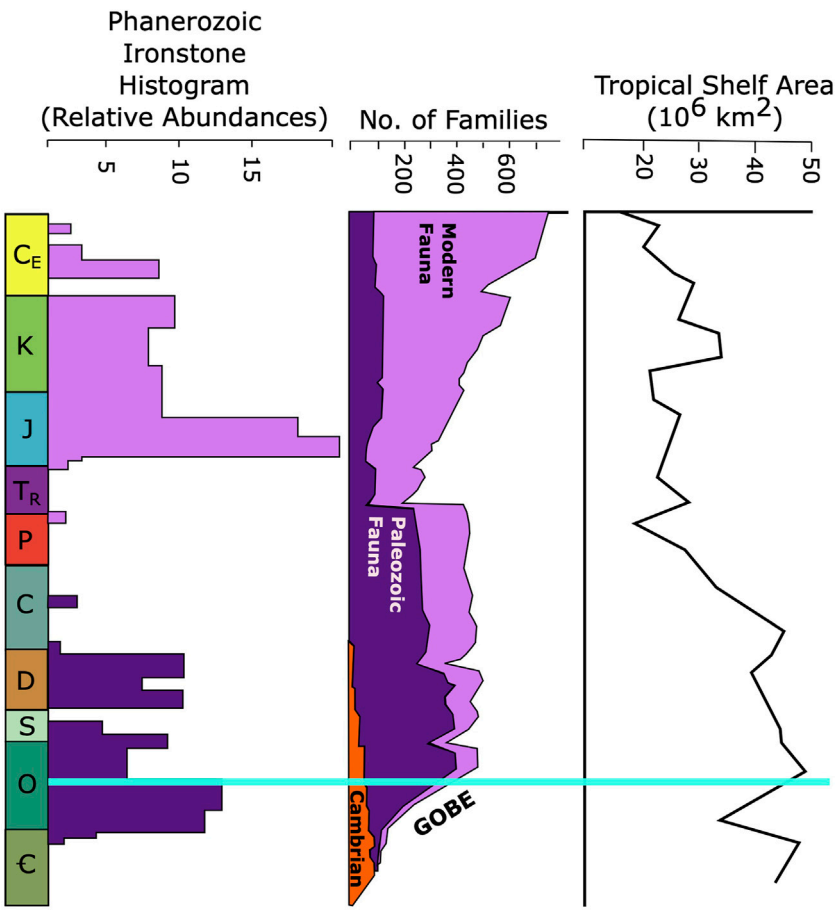

FIGURE 1 | Ironstone deposition and related biological and climatic events. Ironstone histogram (Van Houten and Bhattacharyya, 1982), "Sepkoski" marine invertebrate diversity curve (Servais et al., 2009), tropical shelf area (Walker et al., 2002) and global climate (James and Jones, 2016). Teal line indicates temporal occurrence of Welsh Basin ironstone from this study. GOBE = Great Ordovician Biodiversification Event. Shades of purple highlight the correlation between the Paleozoic (dark purple) and Mesozoic-Cenozoic (light purple) pulses of ironstone deposition with faunal diversification.

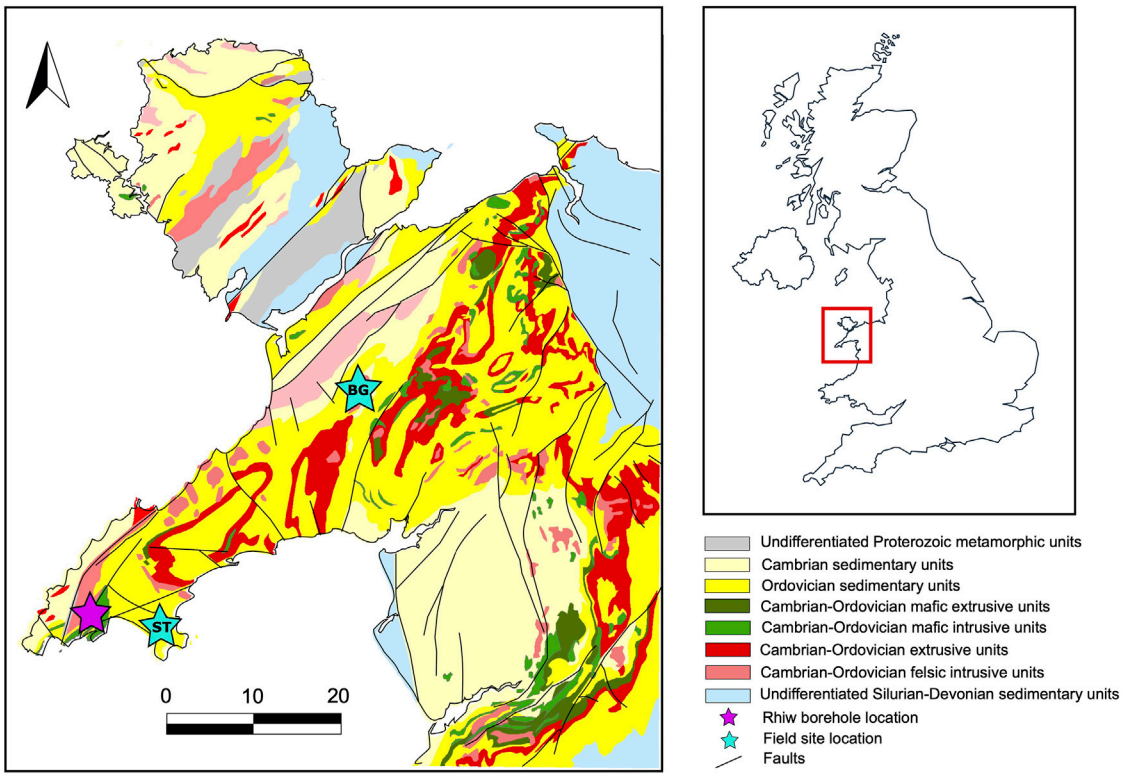

FIGURE 2 | Simplified geological map of North Wales, United Kingdom. BG = Betws Garmon; ST = St. Tudwal's Peninsula; R = Rhiw. From British Geological Survey materials © UKRI [2018].

understanding how changes in the benthic cycling of Fe and P produced coated Fe grains. Collectively, these data assist with understanding the relationship between changes in seawater chemistry, Ordovician tectonic events, and the GOBE.

GENERAL GEOLOGY AND STRATIGRAPHY

The Welsh Basin records major tectonic events in the early Paleozoic evolution of Avalonia (**Figure 2**). Sedimentation began in the Cambrian along a passive margin. By the Floian, the Welsh Basin had evolved into a back-arc basin with the onset of subduction along the southern flank of the Iapetus Ocean (Prigmore et al., 1997; Rushton and Howells. 1998; Brenchley et al., 2006; Howells, 2007; Murphy et al., 2008; van Staal et al., 2012). Such subduction caused rifting of Avalonia from Gondwana and the opening of the Rheic Ocean as a back-arc basin. As Avalonia drifted northward, the widening Rheic Ocean experienced increasing faunal endemism (Cocks and Torsvik, 2002; Fortey and Cocks, 2003; Linnemann et al., 2012; Pothier et al., 2015; Henderson et al., 2016). Arc-related volcanism in the Welsh Basin ceased when Baltica and Avalonia collided during the late Sandbian to earliest Katian (van Staal et al., 1998; Torsvik and Rehnström, 2003; Murphy et al., 2004; Henderson et al., 2016).

In the Welsh Basin, Ordovician strata consist of the ironstone-bearing Ogwen Group (Woodcock, 1990), which is bounded by major, basin-wide unconformities. Its basal unconformity records uplift associated with the onset of Iapetan subduction whereas the upper unconformity developed during collision with Baltica (Woodcock, 1990; Rushton and Fortey, 2000; Brenchley et al., 2006; Howells, 2007). The Ogwen Group ranges in thickness from 1 to 2 km and preserves a continuous record of early Floian to middle Katian (Arenig to Caradoc in the United Kingdom) marine sedimentation (Rushton and Howells, 1998; Rushton and Fortey, 2000; Brenchley et al., 2006; Howells, 2007). From base to top, the Ogwen Group consists of the Wig Bach Formation, Llanengan Mudstone Formation, Tygarn Formation, unsubdivided Nant Ffrancon Subgroup, Ty'r Gawen Mudstone Formation, Cwm Eigiau Formation, and Nod Glas Formation (**Figure 3**; Rushton and Fortey, 2000). Collectively, these units define a fining upward and deepening succession from fan delta and shoreface deposits to deep-water, pyrite-rich, graptolitic mudstone (Howells and Smith, 1997; Rushton and Fortey, 2000; Young et al., 2002). Paleocurrent directions from cross-bedded and rippled sandstones indicate a predominance of east-northeast directed shelf currents on a south-easterly dipping paleoslope (Beckly, 1988; Young et al., 2002; Howells, 2007).

Phosphatic granular ironstone occurs as discrete decimeter-thick horizons in the Wig Bach, Tygarn and Ty'r Gawen Mudstone formations. These horizons are penecontemporaneous with other ironstone beds in eastern

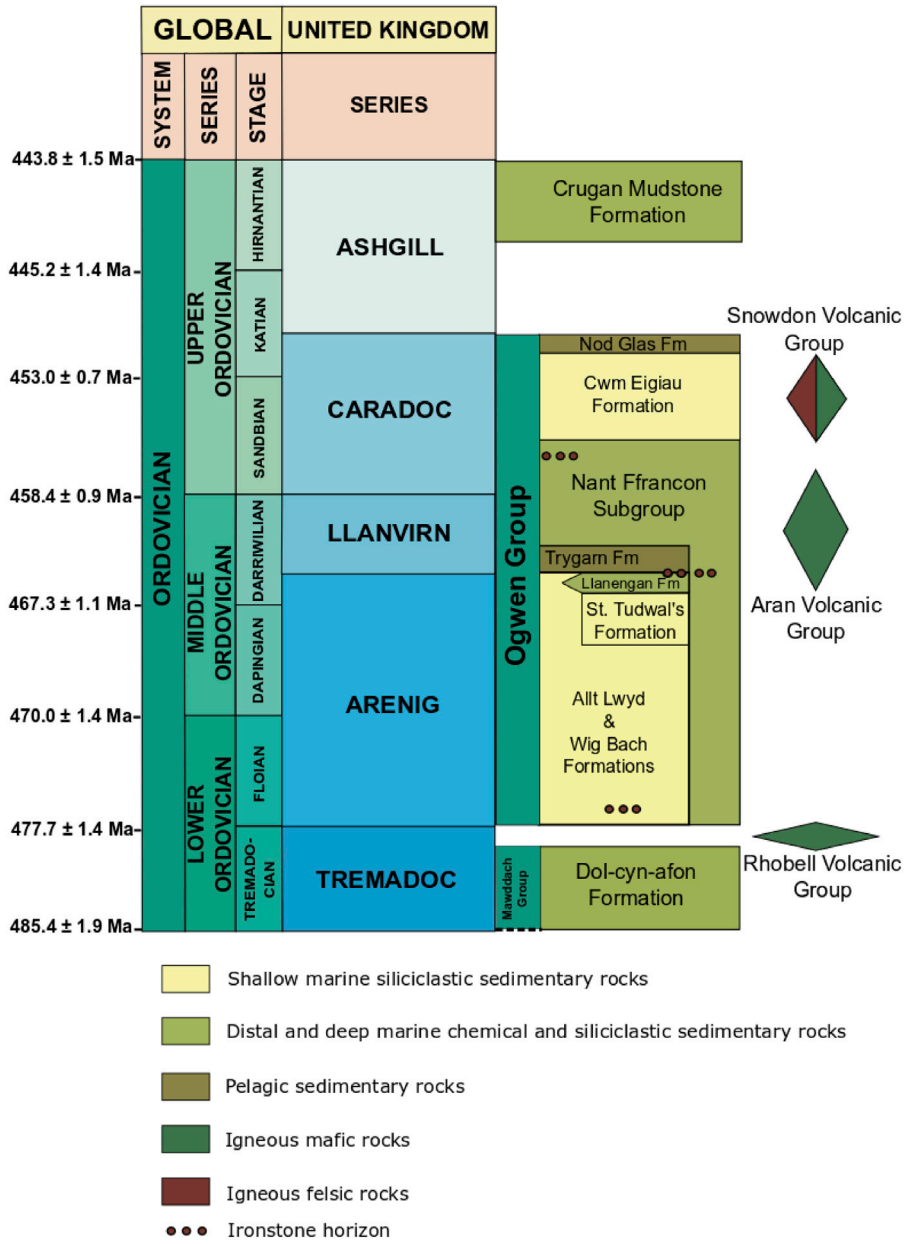

FIGURE 3 | General stratigraphy of Ordovician sedimentary rocks, North Wales (modified from Rushton and Fortey, 2000). Only the ironstone of the Arenig/Llanvirn boundary was investigated in this study. Global (Cohen et al., 2019) and local series names (Cooper et al., 2012) are shown for comparison.

North America, southwestern Europe and North Africa (Young, 1989; Young et al., 1989; Woodcock, 1990; Young, 1992; Young et al., 2002; Todd et al., 2019), which also accumulated along the margins of the Rheic Ocean. Research herein focuses on the Darrwilian Hen-dy-Capel Ironstone Member of the Tygarn Formation (**Figure 3**; Trythall et al., 1987; Young et al., 2002) because it provides the clearest window into ironstone depositional processes. Unlike other ironstone horizons in Wales, the Hen-dy-Capel Ironstone Member is well-exposed in old mining adits and quarries.

METHODS

Three field sites and two drill cores were examined to investigate the lateral and vertical facies variation of the Hen-dy-Capel Ironstone Member (**Figure 2**). At Betws Garmon eight adits, mined during the 19th century and through World War 1 for steel production (Strahan et al., 1920), allowed lateral correlation of lithofacies along 1 km of depositional strike. Two field sites on St. Tudwal's Peninsula in small, abandoned open pit mines yielded information on the regional variability of ironstone and associated

facies. Drill cores from near the town of Rhiw (Brown and Evans, 1989) provided further insight into the stacking relationships of lithofacies. Stratigraphic sections were described on a bed-by-bed basis to develop a lithofacies nomenclature, define important sequence stratigraphic surfaces, and interpret paleoenvironments of deposition through time. The Folk classification (Folk, 1980) was used to define terrigenous clastic facies, whereas a modified Dunham classification scheme (Dunham, 1962) was employed to characterize ironstone because these chemical sedimentary rocks share similar textural attributes to limestone (Young, 1989; Pufahl, 2010). Bioturbation was categorized using the Droser and Bottjer (1986) ichnofabric index from 1 (no activity) to 6 (complete homogenization by bioturbation).

Seventy-four polished thin sections were examined using a Nikon Optiphot-POL transmitted and reflected light microscope. Modal compositions of minerals and fossils were estimated using a visual percentage chart (Terry and Chilingar, 1955) with an abundance index of rare (<10%), uncommon (11–40%), common (41–70%), and abundant (>70%). Minerals were identified in thin section by their petrographic characteristics and through profile-fitting of X-ray powder diffractograms. Plagioclase compositions were determined under transmitted light using the Michel-Lévy method (Sørensen, 2013).

Twelve whole rock powders were analyzed on a Malvern-Panalytical Empyrean Series 2 X-ray diffractometer with a programmable PIXcel3D area detector across scattering angles from 4° to 80° using a copper X-ray target source. Although a Cu source causes fluorescence of Fe-rich minerals, programming the peak height discrimination setting on the detector to 54% improved peak-to-background ratios on diffractograms for mineral identification in ironstone lithofacies. Mineralogy was interpreted from X-ray powder diffractograms using Malvern-Panalytical's HighScore Plus software package.

Important paragenetic relationships were further analyzed using a JEOL JSM6400 scanning electron microscope (SEM) equipped with a Genesis Energy Dispersive X-ray Analyzer at the Microscopy and Microanalysis Facility at the University of New Brunswick—Fredericton. Backscattered electron images and energy dispersive X-ray spectra were generated using an accelerating voltage of 15 kV and a working distance of 27 mm. Carbonate-rich samples were also investigated using a Nikon Eclipse E400-POL microscope equipped with a Reliotron III cathodoluminescence system to understand paragenetic relationships not visible under transmitted and reflected light microscopy and SEM imaging.

Whole rock geochemical analysis of 60 samples provides major, minor, and trace element data to further constrain ironstone depositional processes. Analyses were performed at AGAT Laboratories, Mississauga, using a combination of Li borate fusion with an X-ray fluorescence finish and Na peroxide fusion with an inductively coupled plasma optical emission spectrometry (ICP-OES)/inductively coupled plasma mass spectrometry (ICP-MS) finish. Total organic C (TOC) was analyzed using LECO combustion infrared spectroscopy. Replicate analyses indicate a reproducibility for major elemental concentrations using Li borate fusion and an XRF finish of ± 2%. REE + Y and other trace element concentrations determined using a Na peroxide fusion and an ICP-OES/ICP-MS finish have a reproducibility of ±10%. The reproducibility of TOC concentrations using LECO combustion is ±1%. Organic-matter-rich lithofacies contain >0.5 wt% TOC (Trabucho-Alexandre, 2015). The geostandards SY-4 (diorite gneiss), 692 (iron ore), GBM998-10 (multi-metal nickel ore), and Till-2 (till) were used as matrix matching standards for various facies. Whole-rock geochemical data were plotted using GCDkit 5.0 in R 3.4.3 (Janoušek et al., 2016).

Rare earth elements and yttrium (REE + Y) concentrations are normalized with respect to the Post Archean Australian Shale standard (PAAS; McLennan, 1989) to understand redox controlled processes of Fe and P precipitation. Ce and Eu anomalies are calculated as shale normalized (subscript SN) Ce_{SN}/Ce_{SN}^* and Eu_{SN}/Eu_{SN}^*, respectively (Bau et al., 2014), where:

$$Ce_{SN}^* = 0.5La_{SN} + 0.5Pr_{SN}$$
$$Eu_{SN}^* = 0.5Sm_{SN} + 0.5Gd_{SN}$$

Geochemical data are interpreted in paragenetic and sequence stratigraphic context to elucidate the source of Fe to the Welsh Basin and to create an oceanographic model for ironstone accumulation.

LITHOFACIES AND PALEOENVIRONMENT

Three terrigenous and four ironstone lithofacies are recognized in the Ogwen Group. Facies 1, 2, and 3 are siliciclastic and Facies 4, 5, 6, and 7 are authigenic and related to ironstone deposition. Lithofacies associations suggest deposition on an unrestricted, storm-dominated shelf.

Facies 1—Wavy Laminated Sandy Siltstone

Facies (F1) is composed of intercalated light and dark grey, wavy laminae that are 1–4 mm thick (**Figures 4A,B**). Light grey laminae are normally graded and composed of subrounded, very fine-grained and silt-sized quartz grains with rare detrital muscovite in a clay matrix. Dark grey laminae contain organic matter with disseminated silt-sized quartz grains and are locally bioturbated with an ichnofabric index of 2.

Light grey, sandy laminae are interpreted as distal tempestites that formed near storm wave base because storm-induced combined flow was too weak to produce hummocky cross-stratification (Plint, 2010; Smit et al., 2012). Dark grey laminae reflect suspension rain of sedimentary organic matter and silt-sized quartz grains during fairweather conditions (Parrish, 1982; Ghadeer and Macquaker, 2011). The bioturbated nature of some laminae indicates the seafloor was at times sufficiently oxygenated to permit infaunal colonization between storms (Droser and Bottjer, 1986; Schieber, 2003).

Facies 2—Parallel Laminated Micaceous Shale

Facies 2 (F2) is a densely cleaved, thinly laminated, organic matter-bearing shale (**Figures 4C,D**) with silt-sized detrital muscovite and quartz grains. The strong cleavage precludes the identification of burrows and other sedimentary structures that exist in some mudstone (Schieber, 2003; Ghadeer and Macquaker, 2011).

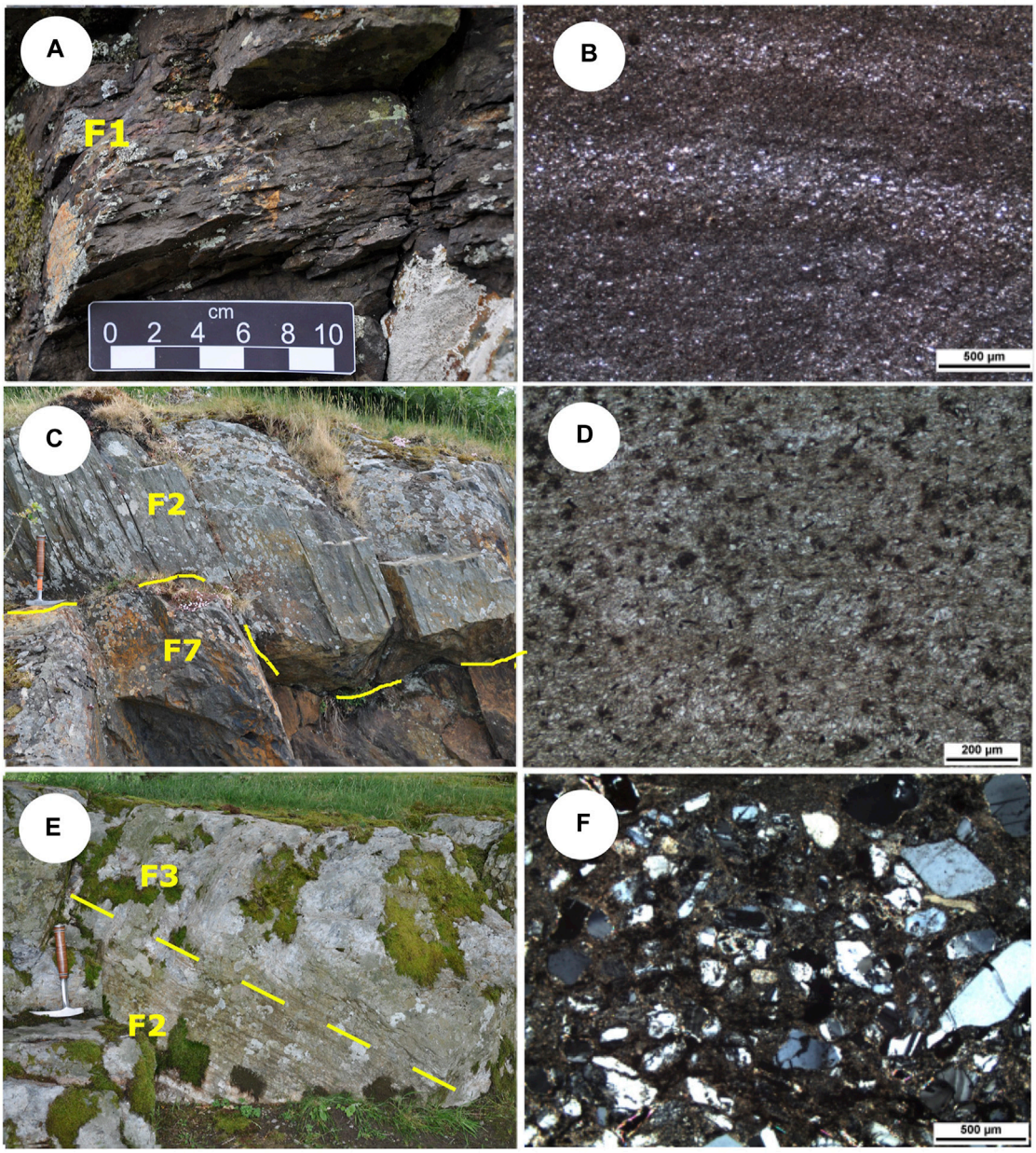

FIGURE 4 | (A) F1 wavy laminated sandy siltstone outcrop at Betws Garmon. **(B)** Photomicrograph of F1 silt and very fine grained sand laminae of quartz and Fe-silicate (PPL). Sample HC-18-15 **(C)** F2 sharply overlying Fe-grainstone (F7) at Betws Garmon. Note near-vertical cleavage of the F2 slate. Hammer for scale is 30 cm in length; **(D)** F2 photomicrograph of low grade metamorphically altered shale (phyllite; PPL). Sample BG-18-01 **(E)** F3 outcrop separated by yellow line above laminated F2. Hammer for scale 30 cm **(F)** Photomicrograph of F3 Lithic and feldspar-rich grains. Note undulose and uniform extinction in quartz grains (XPL). Sample BG-18-17.

The microbial respiration of organic matter accumulating beneath a productive surface ocean is interpreted to have increased the biological oxygen demand at the sediment-water interface and limited the establishment of an infaunal community (Parrish, 1982; Droser and Bottjer, 1986; Dunbar and Barrett, 2005). Although not observed because of the cleavage, cryptoburrows, organo-mineralic aggregates, subtle erosion features, and floc-ripples that likely formed as mud accumulated near storm wave base through a combination of suspension settling, density flow, and traction currents (Schieber, 2003; Ghadeer and Macquaker, 2011).

Facies 3—Hummocky Cross-Stratified Sublitharenite

Facies 3 (F3) is a light grey, hummocky cross-stratified (HCS) sublitharenite (**Figures 4E,F**). Bedsets are sometimes difficult

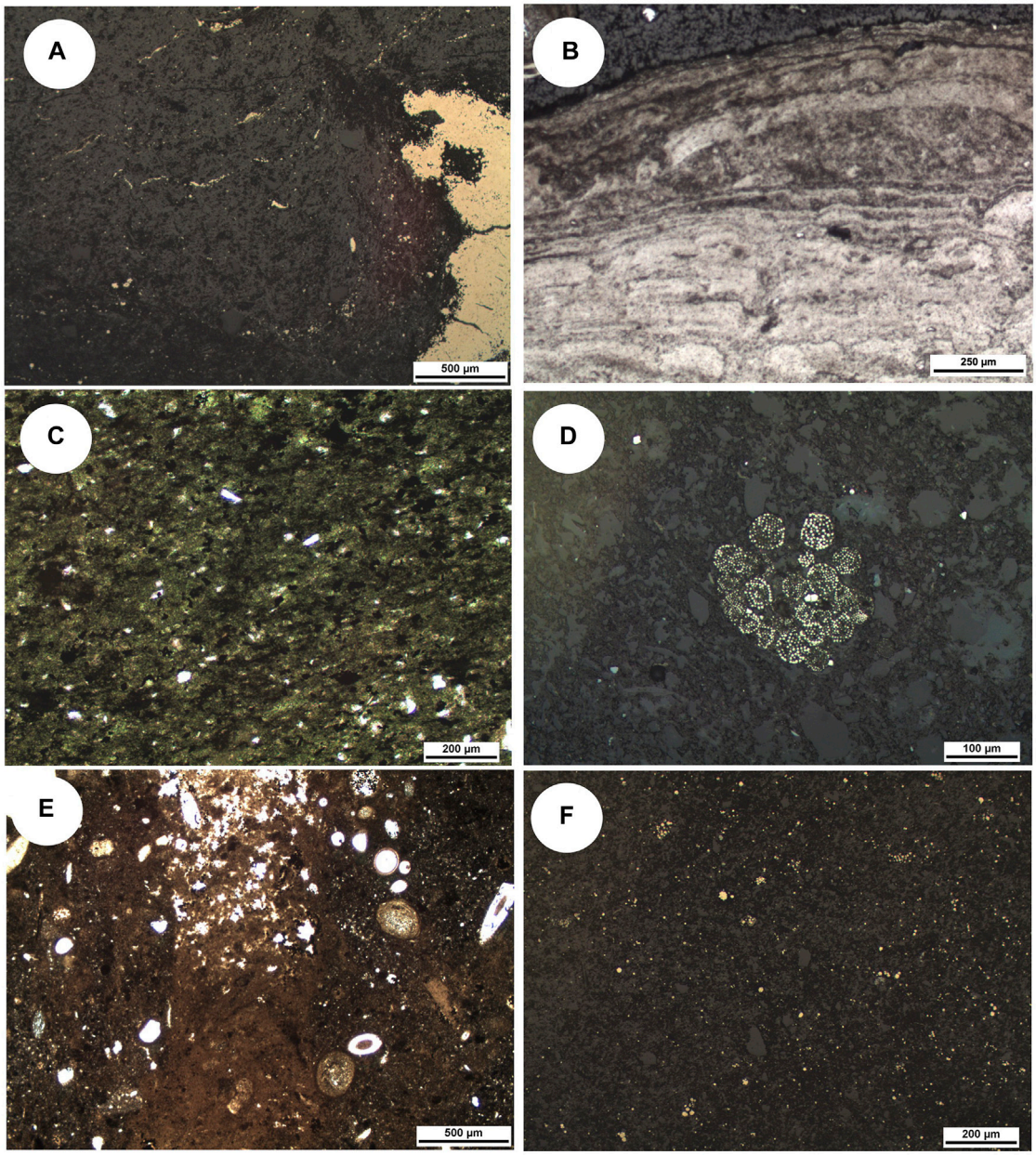

FIGURE 5 | (A) Reflected light (RL) photomicrograph of F4 laminated pyritic mudstone displaying rare pyrite nodule to right of frame. Sample HC-18-08 **(B)** Bacteriogenic precipitate of CFA (photomicrograph in PPL). Sample HC-18-09 **(C)** Photomicrograph of F5 massive chamosite mudstone with very fine quartz silt and organics (PPL). Sample BG-18-34B **(D)** Framboidal pyrite preserved in F5, only occurs as local clusters 100–200 µm diameter (RL photomicrograph). Sample HC-18-04 **(E)** Transmitted light photomicrograph of burrow preserved in a phosphate intraclast with passive infilling by terrigenous grains in F6. **(F)** Reflected light photomicrograph showing abundant disseminated framboidal pyrite (bright specs) in organic rich F6. Sample HC-18-16.

to discern because of intense localized bioturbation (ichnofabric index 6). Silt and fine sand-sized quartz, plagioclase (An_{35} - andesine), K-feldspar, and lithic clasts are subrounded and moderately well-sorted in a detrital clay matrix.

This facies is interpreted to have accumulated between fair-weather and storm wave-bases through combined flow (Dott and Bourgeois, 1982; Dumas and Arnott, 2006; Boyd, 2010; Quin, 2011; Mulhern et al., 2019). The intense bioturbation reflects accumulation on a well oxygenated seafloor. The immaturity of grains and occurrence of andesine probably records the delivery of clastic material derived from a proximal igneous source of intermediate to felsic composition (Anthony et al., 2001; Nesse, 2015).

Facies 4—Laminated Black Pyritic Mudstone

Facies 4 (F4) is a blue-black, organic matter-rich mudstone with an ichnofabric index of 1 (**Figures 5A,B**). Laminae are 1–3 mm thick and, in addition to abundant organic matter, contain common framboidal pyrite ($Fe^{2+}S_2$) and rare coated Fe grains. The most organic matter-rich laminae may also contain granule-sized, *in situ* carbonate fluorapatite (CFA; Ca10-a-bNaaMgb(PO4)6-x(CO3)x-y-z(CO3·F)x-y-z(SO4)zF2) peloids.

The abundance of organic matter in this facies implies deposition beneath a highly productive surface ocean (Froelich et al., 1979; Challands et al., 2009; Piper and Calvert, 2009; Pufahl and Groat, 2017). The thinly laminated character of the facies suggests deposition below storm wave base. The lack of bioturbation and presence of framboidal pyrite are interpreted to record anoxic bottom and pore waters (Glenn and Arthur, 1988; Taylor and Macquaker, 2000; Schieber, 2003. The co-occurrence of framboidal pyrite and *in situ* authigenic CFA peloids indicate that as sedimentary organic matter was respired by a consortium of microbes, bacterial sulfate reduction not only produced H_2S for pyrite precipitation, but also released phosphate to pore water for phosphogenesis (Schieber, 2002; Arning et al., 2009; Taylor and Konhauser, 2011; Hiatt et al., 2015).

Facies 5—Bioturbated Chamositic Mudstone

Facies 5 (F5) is a dark blue-black chamositic mudstone (**Figures 5C,D**). Bioturbation has destroyed bedding (ichnofabric index of 4–5) to create diffuse layers containing varying proportions of silt-sized quartz grains and rare, granule-to pebble-sized coated Fe grains. Coated grain mineralogy is dependent on whether cortical layers completely or partially envelop the nucleus. Continuous cortical layers are composed primarily of chamosite ($Fe_3^{2+}Mg_{1.5}AlFe_{0.5}^{3+}Si_3AlO_{12}(OH)_6$) intercalated with CFA and chert (SiO_2). Discontinuous cortical layers are typically dominated by goethite ($Fe^{3+}O(OH)$) or hematite ($Fe_2^{3+}O_3$). More organic-rich areas of this facies also contain rare framboidal pyrite and rare pebble-sized CFA nodules (1–3 cm in diameter).

Pervasive bioturbation and the occurrence of chamosite are characteristic of a well oxygenated seafloor and suboxic sediment pile where precipitation near the Fe-redox boundary produced coated grains (Droser and Bottjer, 1986; Glenn and Arthur, 1988; Pufahl and Grimm, 2003). Suboxic in this sense refers to a relative measure of oxygen levels in the sediment and does not refer to specific oxygen concentrations (cf. Canfield and Thamdrup, 2009).

Chamosite characteristically contains both Fe^{2+} and Fe^{3+} and thus, is interpreted to have precipitated during suboxic authigenesis in conditions that straddled the Fe-redox boundary (Harder, 1980; Glenn and Arthur, 1988; Pufahl and Grimm, 2003). Fe-redox pumping probably sustained precipitation by maintaining high levels of Fe beneath the seafloor. Fe-redox pumping is a cyclic mechanism that concentrates mobile Fe^{2+} in pore water through the dissolution of Fe-(oxyhydr)oxide buried below the Fe redox interface (Heggie et al., 1990). Dissolution and liberation of Fe^{2+} is aided by the microbial reduction of Fe (Konhauser et al., 2011). The escape of Fe out of the sediment is prevented by reprecipitation of Fe-(oxyhydr)oxide above this boundary.

As in coated phosphate grains, intercalated CFA and chert cortical layers in coated chamosite grains are interpreted to record minor fluctuations in the vertical position of the Fe-redox boundary in sediment and changes in the concentrations of pore water phosphate and silica. Phosphate was probably released to pore water through a combination of Fe-redox pumping, which also concentrates pore water P, and microbial degradation of sedimentary organic matter (Heggie et al., 1990; Jarvis et al., 1994; Arning et al., 2009; Hiatt et al., 2015; Pufahl and Groat, 2017). Silicon required for chamosite precipitation was probably derived from silica remobilized through the dissolution of sponge spicules in the sediment.

Coated grains composed of discontinuous hematite and goethite cortical layers preserve micro-unconformities and indicate that F5 is a condensed facies (Todd et al., 2019). These internal cortical erosion surfaces record multiple episodes of precipitation, exhumation, and erosion, followed by reburial and further precipitation near the Fe redox boundary (Pufahl and Grimm, 2003). Such stratigraphic condensation is interpreted to have stabilized this zone of precipitation beneath the seafloor long enough to create pebble-sized coated grains (Pufahl and Grimm, 2003; Raiswell and Canfield, 2012; Föllmi, 2016).

The growth of pebble-sized CFA nodules also reflects the importance of low sedimentation rates on maintaining high pore water phosphate levels (Jarvis et al., 1994; Föllmi, 2016; Pufahl and Groat, 2017). As in F4, the co-occurrence of framboidal pyrite indicates bacterial sulfate reduction was an important source of this phosphate.

Facies 6: Structureless Coated Fe Grain Packstone

Facies 6 (F6) is generally a blue-black, structureless, chamositic packstone composed of coarse-grained to granule-sized coated Fe grains, mudstone intraclasts, and pebble-sized CFA nodules (**Figures 5E,F**). Locally, HCS and scouring occur where the grainsize is finer. Matrix material is a chamosite-rich siltstone containing sponge spicules and framboidal pyrite. Although bioturbation appears negligible (ichnofabric index of 2), the grain size and dark colour make it difficult to assess.

Large coated Fe grains (ca. 15 mm in diameter) are the most conspicuous characteristic of this facies (**Figures 6A,B**). Grain cortices are formed of concentric and discontinuous layers of CFA, hematite, and chamosite. Cortical layers nucleated on chamositic mudstone clasts, sponge spicules, and benthic foraminifera.

The authigenic processes that produced coated grains, CFA nodules, and framboidal pyrite are similar to those that produced coated grains in F5. The occurrence of coated grains and intraclasts reinforce the interpretation that F6 is also a condensed facies (Pufahl and Grimm, 2003; Föllmi, 2016; Todd et al., 2019), but the HCS and scouring suggests

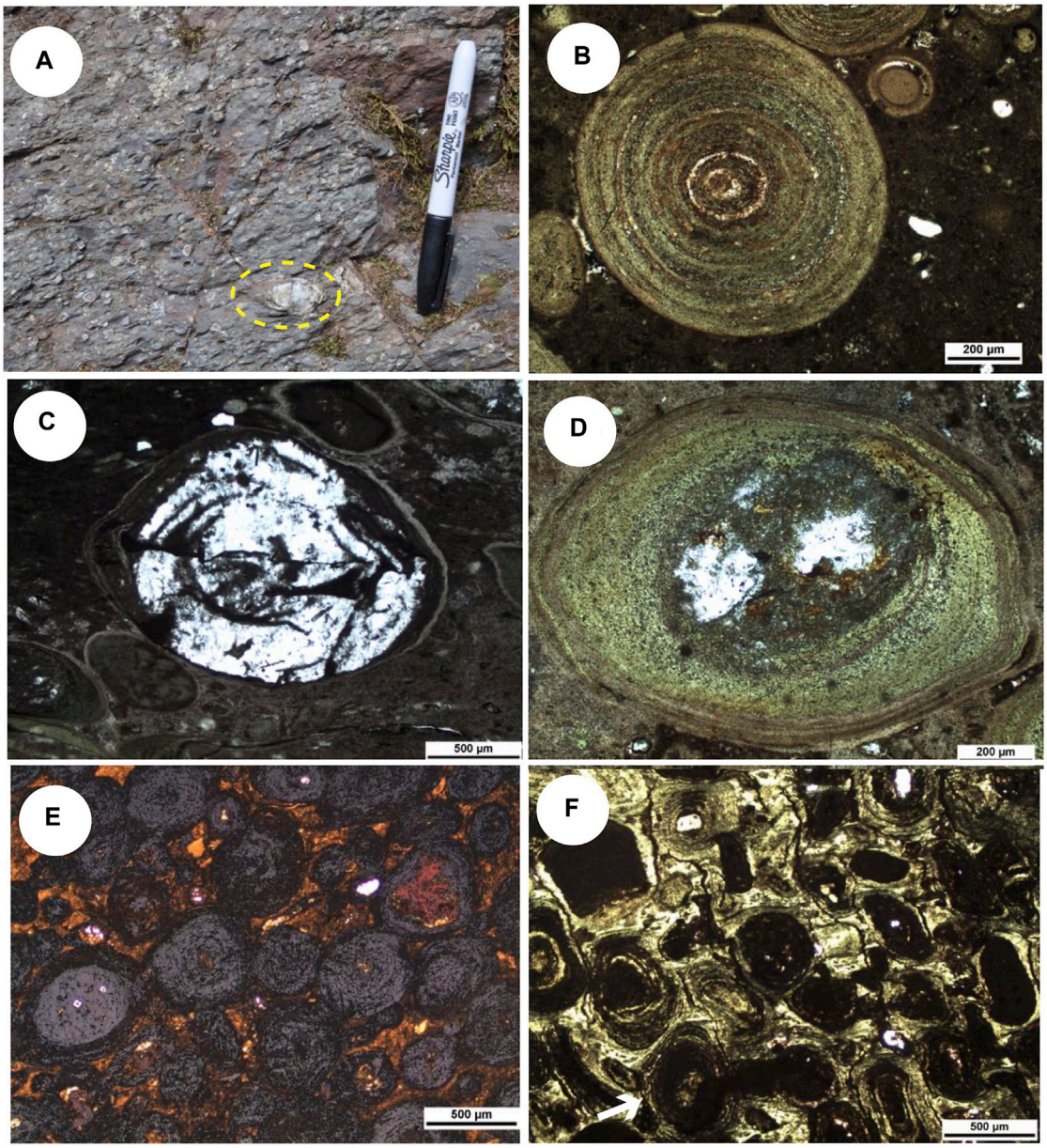

FIGURE 6 | (A) F6 Field photograph displaying the coarsest coated grains (ca. 15 mm) observed in the Welsh ironstone, Betws Garmon. Yellow dashed ellipse highlights pebble-sized phosphtaic nodule. 15 cm marker for scale. **(B)** F6 Thin section photomicrograph of a, Fe-silicate rich coated grain preserved within a CFA nodule. Mineralogical variation of laminae is apparent. Sample HC-18-07. **(C,D)** F6 transmitted light photomicrographs of silicified benthic foraminifera subsequently coated in CFA and chamosite laminae. **(E)** F7 transmitted and reflected light photomicrograph of magnetitic grainstone with cement oxidizing to goethite (orange). Sample BG -18-06. **(F)** F7 transmitted light photomicrograph of magnetitic grainstone with chamosite cement (light green). Spastolithic deformation with later compaction fractures from burial pressure after cementation. White arrow indicates spalled cortical layers in coated grain. Sample BG-18-26.

reworking by waves above storm wave base (Dott and Bourgeois, 1982; Dumas and Arnott, 2006; Quin, 2011). The abundance of sponge spicules implies a productive and well-oxygenated middle shelf capable of supporting filter feeders (Botting and Muir, 2013; Kidder and Tomescu, 2016). The nucleation of CFA on spicules indicates authigenic precipitation was rapid, occurring before the spicules dissolved and silica was remobilized through pore water (Behl and Garrison, 1994).

Facies 7—Trough Cross-Stratified Coated Fe Grain Grainstone

Facies 7 (F7) is a blue-black trough cross-stratified grainstone. Trough cross-stratified beds are ca. 10–50 cm thick and composed of well-sorted, fine-grained coated Fe grains (**Figures 6C–F**). Intraclast lags of reworked and broken CFA nodules occur at the base of some beds. In some beds, intense bioturbation (ichnofabric index of 6) has destroyed foresets and

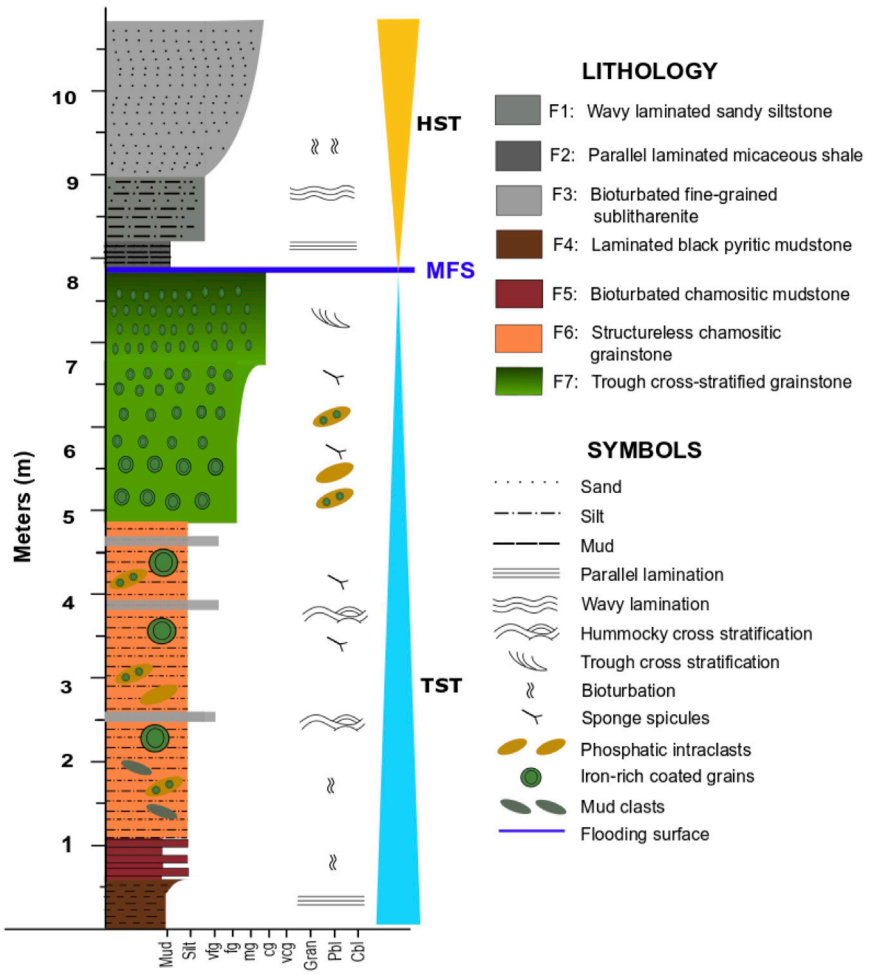

FIGURE 7 | Composite stratigraphic column showing stacking patterns of Welsh Basin ironstone. A shallowing-upward parasequence of abundant chemical sediments is sharply overlain by coarsening upward siliciclastic facies representing fundamentally different depositional regimes, of the transgressive and highstand system tracks (TST and HST), respectively. Grains size mud = mud, silt = silt, vfg = very fine grained, fg = fine-grained, mg = medium grained, vcg = very coarse grained, gran = granule, pbl = pebble, cbl = cobble.

homogenized bedding contacts. Pore spaces are filled with chamosite and goethite (**Figure 6E**). Coated grains have a detrital quartz nucleus with discontinuous cortical layers composed primarily of chamosite and rare hematite. Where metamorphosed, grain cortices are altered to magnetite ($Fe^{2+}Fe_2^{3+}O_4$). Spastolithic deformation indicates grains were soft during early burial, and fracturing occurred after cementation during compaction from burial pressure (**Figure 6F**).

Small-scale trough cross-stratification generally reflects traction current deposition near fair weather wave base (Shanmugam et al., 1993; Dumas and Arnott, 2006; Plint, 2010). Fair weather waves and unidirectional currents are interpreted to have exhumed coated grains actively precipitating beneath the seafloor, reworking them into subaqueous dunes. Frequent reworking of the seafloor and exhumation of sediment in this proximal environment produced smaller coated grains with numerous cortical erosion surfaces (Todd et al., 2019). Chamosite cementing grains is interpreted to have precipitated where coated grains were buried deep enough to stop their exhumation. Although such reworking was a prerequisite for the genesis of coated grains in this facies, it prevented the authigenic cementation of grains until they were immobilized through burial (Pufahl and Grimm, 2003). Goethite between grains is probably a by-product of the oxidative chemical weathering of chamosite (Masuda et al., 2012; Galmed et al., 2021).

SEQUENCE STRATIGRAPHY

A parasequence is a relatively conformable succession of genetically related beds bounded at the bottom and top by flooding surfaces (Van Wagoner et al., 1988). Parasequences are the primary components of systems tracts, which define a stratigraphic sequence recording deposition through a complete

TABLE 1 | Major element and total organic carbon (TOC) concentrations in lithofacies of the Hen-dy-Capel Ironstone Member, Tygarn Formation.

Sample	Facies	Al_2O_3	Fe_2O_3	K_2O	P_2O_5	SiO_2	TiO_2	TOC
		wt%	wt%	wt%	wt%	wt%	wt%	wt%
BG-18-04	1	15.30	27.40	0.86	0.50	44.80	0.80	0.49
HC-18-15	1	17.60	31.40	0.36	0.43	38.20	0.85	0.27
BG-18-20	2	12.50	27.00	0.08	1.10	48.80	0.64	0.39
BG-18-27	2	13.40	32.40	—	0.53	44.00	0.67	0.38
HC-18-19	2	21.00	13.70	3.65	0.23	50.80	0.97	0.25
BG-18-30	4	13.60	14.20	2.18	0.41	60.90	0.67	0.32
HC-18-18	4	20.00	20.30	2.49	0.16	44.80	1.02	0.97
BG-18-43	4	6.39	55.60	0.01	1.67	13.80	0.24	4.63
BG-18-13	5	3.84	69.40	0.01	3.38	6.37	0.13	0.23
BG-18-24	5	13.20	39.20	—	0.42	37.80	0.70	0.55
BG-18-25	5	12.40	36.20	—	0.90	41.30	0.62	0.37
BG-18-29	5	12.30	32.30	—	0.57	43.40	0.56	0.34
BG-18-38	5	13.00	31.00	0.01	1.56	43.20	0.67	0.31
BG-18-39	5	14.20	35.10	—	0.50	39.90	0.76	0.30
BG-18-40	5	10.70	35.70	—	1.62	40.10	0.58	0.36
BG-18-45	5	13.50	37.40	—	1.14	35.30	0.71	0.60
HC-18-08	5	15.90	35.50	0.01	0.13	38.50	0.86	0.55
PYG-18-07	5	14.80	31.50	0.34	0.39	42.50	0.86	0.54
BG-18-01-A	6	6.53	53.90	0.06	1.96	24.30	0.29	1.07
BG-18-14	6	12.10	31.00	0.05	1.93	39.90	0.70	0.66
BG-18-15	6	8.08	45.00	0.03	2.14	30.20	0.36	0.37
BG-18-23	6	9.09	34.00	0.01	4.99	33.40	0.42	0.41
BG-18-28	6	9.47	44.30	0.03	0.64	31.20	0.46	0.59
BG-18-31	6	14.60	35.00	0.01	3.14	33.20	0.64	0.44
BG-18-34b	6	12.20	40.50	0.02	0.52	37.20	0.68	0.27
BG-18-37	6	5.51	49.00	0.02	8.91	17.50	0.22	0.27
BG-18-46	6	11.30	37.30	0.01	2.29	32.70	0.54	0.44
BG-18-47	6	13.20	32.60		4.26	34.10	0.55	0.45
HC-18-01	6	12.00	27.40	0.02	2.57	45.30	0.46	0.72
HC-18-03	6	6.56	49.00	0.01	2.75	19.70	0.28	3.33
HC-18-04	6	15.10	8.27	2.65	1.57	62.70	0.75	0.45
HC-18-07	6	6.38	41.20	0.01	7.06	16.70	0.27	4.43
HC-18-09	6	11.40	27.10	—	3.93	43.30	0.53	0.67
HC-18-12	6	14.10	29.60	0.02	2.22	41.20	0.68	0.56
HC-18-16	6	15.70	30.60	0.10	0.33	40.20	0.96	1.00
PYG-18-01	6	14.40	22.10	1.14	1.40	49.70	0.68	0.46
PYG-18-02	6	12.00	22.70	0.56	2.04	48.20	0.44	1.19
PYG-18-03	6	14.30	27.80	0.86	0.75	44.90	0.72	0.65
PYG-18-06	6	11.00	37.70	0.03	1.33	37.50	0.54	0.57
101,524	7	12.50	23.90	0.22	0.81	51.30	0.72	0.10
101569	7	11.60	38.00	0.02	2.22	34.10	0.47	0.18
101570	7	8.02	47.30	0.07	1.54	29.20	0.45	0.57
101571	7	10.00	56.00	0.12	1.15	19.40	0.49	0.30
101572	7	5.91	69.30	0.03	1.99	12.90	0.42	0.17
101573	7	5.91	65.50	0.10	1.72	17.10	0.40	0.08
101574	7	8.58	56.00	0.05	1.68	18.50	0.62	0.08
101575	7	5.69	55.90	0.06	1.90	24.90	0.40	0.09
101576	7	8.57	57.40	0.06	1.35	19.70	0.53	0.10
BG-18-05	7	8.81	50.50	0.03	6.02	16.80	0.37	0.35
BG-18-06	7	7.59	63.50	0.09	0.95	17.40	0.33	0.21
BG-18-07	7	8.33	54.40	0.03	4.45	17.80	0.33	0.19
BG-18-11	7	6.92	68.00	0.03	0.88	15.90	0.29	0.47
BG-18-12	7	5.56	70.60	0.01	2.59	11.60	0.19	0.30
BG-18-16	7	5.23	71.00	—	2.68	12.40	0.21	0.30
BG-18-22	7	7.00	62.00	—	1.05	17.30	0.30	2.20
BG-18-26	7	7.99	50.30	0.01	3.35	21.40	0.30	0.88
BG-18-32	7	6.71	48.50	0.06	7.29	20.00	0.29	0.32
BG-18-35	7	6.14	62.90	0.03	5.29	12.50	0.25	0.28
BG-18-41	7	6.70	65.70	—	1.14	14.30	0.27	0.14
HC-18-17	7	10.50	33.50	0.06	2.06	36.80	0.51	1.00

sea level cycle (Catuneanu et al., 2011; Couneanu, 2019). Thus, parasequences record smaller scale fluctuations in relative sea level superimposed on longer wavelengths of sea level oscillation.

Outcrop exposures and lithofacies stacking patterns indicate that two laterally correlative parasequences are preserved in the study area (**Figure 7**). At Betws Garmon, vertical and lateral facies trends are consistent between mine adits along 0.8 km of depositional strike. With minor variations in facies thickness, these trends are persistent between Betws Garmon, St. Tudwal's Peninsula and Rhiw.

Parasequence 1 is an aggradational ironstone succession that is at least 8 m thick. This parasequence is interpreted to record a gradual change from distal through middle shelf sedimentation to deposition near fair weather wave base. Basal laminated, organic-rich mudstone (F4) accumulated below storm wave base and grades stratigraphically upward into a bioturbated mudstone (F5) that was the locus of intense authigenesis. These mudstones are rich in chamosite and are, in turn, overlain by an intraclastic, Fe coated grain packstone with locally developed HCS (F6), which records shallowing to just above storm wave base. The top of Parasequence 1 is a trough cross stratified grainstone (F7) reflecting continued aggradation and increased reworking of coated grains near fair weather wave base. Such intense reworking, winnowing, and authigenesis in this chemical sedimentary succession is consistent with stratigraphic condensation in a late transgressive systems tract, suggesting its upper contact is the maximum flooding surface (MFS; Catuneanu et al., 2011; Föllmi, 2016; Catuneanu, 2019).

Parasequence 2 rests sharply on Parasequence 1 and is interpreted to record progradation of clastic middle shelf deposits during early highstand conditions. Unlike Parasequence 1, Parasequence 2 lacks an authigenic overprint and is purely clastic in nature. Parasequence 2 coarsens upward from micaceous shale (F2) and interbedded siltstone (F1), reflecting accumulation below storm wave base, to an HCS sublitharenite (F3) recording deposition between storm and fair weather wave bases. The top of Parasequence 2 is the modern erosion surface.

The link between ironstone deposition and maximum flooding is observed in other Paleozoic ironstones (Young, 1992; Todd et al., 2019; Pufahl et al., 2020). The MFS marks the deepest water facies in a sequence and the change from retrogradational to progradational parasequence stacking (Catuneanu et al., 2011; Catuneanu, 2019). Because the MFS represents the time at which the accommodation is greatest, siliciclastics are trapped in nearshore environments to favour stratigraphic condensation and authigenesis on the distal shelf (Glenn et al., 1994; Taylor and Macquaker, 2000; Pufahl and Groat, 2017). Such low rates of clastic sedimentation stabilize the zone of authigenesis beneath the seafloor (cf. Föllmi, 2016) and permit waves to rework precipitating authigenic muds and coated Fe grains into granular deposits (Todd et al., 2019; Pufahl et al., 2020; Matheson and Frank, 2021).

GEOCHEMISTRY

Authigenic lithofacies (F5, F6, F7) composing Parasequence 1 contains $Fe_2O_{3\ total}$, SiO_2, and Al_2O_3 concentrations that total >80 wt% (**Table 1**), reflecting the abundance of goethite, hematite, chamosite, metamorphic magnetite, and chert. TOC concentrations are highest at the base of Parasequence 1 (F4) with a maximum value of 4.6 wt% (**Table 1**). P_2O_5 concentrations are greatest in the middle of Parasequence 1 (F2) with values that range between 0.6 and 8.9 wt% (**Table 1**). TiO_2 and K_2O concentrations are low and <1 wt% through the thickness of this parasequence (**Table 1**). In siliciclastic facies (F1, F2, F3) of Parasequence 2, TiO_2 and K_2O concentrations are higher than in Parasequence 1 with maximum values of 1.02 wt% and wt. 3.65%, respectively (**Table 1**).

Total REE + Y concentrations in all lithofacies vary between 178 and 560 ppm **Table 2**). Authigenic facies (F5, F6, F7) of Parasequence 1 are enriched in middle rare earth elements (MREE) and heavy rare earth elements (HREE). Ce/Ce* and Eu/Eu* values in both parasequences range from 0.801 to 1.25 and 0.606 to 1.13, respectively. True negative Ce anomalies characterize the base of Parasequence 1 (**Figure 8**; Bau and Dulski, 1994; Bau et al., 1996; Planavsky et al., 2010). Ce/Ce* and Pr/Pr* values in bioturbated chamositic mudstone at the base (F5) range between 0.85 and 0.93 and between 1.06 and 1.13, respectively. Negative Eu anomalies occur in terrigenous clastic (F1, F2) lithofacies and samples of authigenic facies (F5, F6) with a significant detrital component. In samples of authigenic facies (F5, F6) devoid of siliciclastics and containing ≥1 wt% of synsedimentary CFA, minor positive Eu anomalies are common (**Figure 9**).

Average concentrations of the redox elements V, Cr, and Zn in authigenic facies are 393 ppm, 163 ppm, and 156 ppm, respectively, which are significantly higher than shale composite values of 130 ppm, 125 ppm, and 100 pm (**Table 3**; Morgan et al., 1978; Gromet et al., 1984; Condie, 1993). Other Eh sensitive elements such as Mo, Ni, U are near shale composite values, whereas Pb, Co, and Cu are lower (**Figure 10**; Morgan et al., 1978; Gromet et al., 1984; Condie 1993).

Seawater Redox Conditions and Fe Source

The REE + Y composition of authigenic facies provide important insights into the presence of oxygen gradients in the Welsh Basin during ironstone accumulation. Because these elements are thought to be relatively immobile during hydrothermal and metamorphic alteration, they are interpreted as a proxy for seawater Eh at the time of deposition (Elderfield and Greaves, 1982; Bau, 1991). The concentration of REE + Y in pore water can mimic that of seawater just beneath the seafloor but changes systematically with decreasing Eh as the pore water system becomes progressively more isolated beneath the sediment-water interface during burial (Haley et al., 2004). MREE-HREE enrichment and a trend towards negative Ce anomalies through the thickness of Parasequence 1 (F4, F5, F6, F7; **Figure 8**) support sedimentologic data indicating siliciclastic sediment was trapped in the nearshore, resulting in increased authigenesis in progressively deeper and increasingly anoxic environments away from the coast (Piper et al., 1988; Dubinin, 2004; Bau et al., 2014).

TABLE 2 | REE + Y concentrations in lithofacies of the Hen-dy-Capel Ironstone Member, Tygarn Formation.

Sample	Facies	La	Ce	Pr	Nd	Sm	Eu	Gd	Tb	Y	Dy	Ho	Er	Tm	Yb	Lu
		ppm	ppm	ppm	ppm	ppm	ppm	ppm	ppm	ppm	ppm	ppm	ppm	ppm	ppm	ppm
BG-18-04	1	28.1	59.8	6.72	23.4	3.9	0.98	3.28	0.48	14.7	2.64	0.52	1.77	0.30	2.2	0.35
HC-18-15	1	53.5	114.0	12.40	46.2	7.8	1.42	7.16	1.08	34.4	5.99	1.22	3.61	0.49	3.4	0.51
BG-18-20	2	47.8	104.0	12.20	48.9	10.2	2.25	10.10	1.54	51.1	8.47	1.69	4.84	0.67	4.4	0.68
BG-18-27	2	56.9	141.0	14.40	56.8	11.0	2.16	10.70	1.63	46.4	8.61	1.68	4.75	0.66	4.4	0.62
HC-18-19	2	50.2	106.0	11.10	41.0	6.9	1.16	5.58	0.88	27.4	4.96	1.01	2.91	0.41	2.9	0.42
BG-18-30	4	57.4	135.0	14.10	57.0	11.5	2.74	11.30	1.71	52.2	9.12	1.77	4.91	0.63	4.2	0.57
HC-18-18	4	61.7	124.0	14.30	55.7	9.6	1.51	7.98	1.19	41.9	6.87	1.44	4.24	0.58	4.0	0.59
BG-18-43	4	46.6	107.0	12.80	52.0	12.2	2.56	14.70	2.38	75.9	13.80	2.73	7.41	0.99	6.4	0.90
BG-18-13	5	33.8	75.1	9.03	39.3	10.0	2.75	13.50	2.18	82.9	12.80	2.56	7.09	0.93	5.8	0.88
BG-18-24	5	39.7	82.7	9.73	38.2	7.7	1.37	7.24	1.11	37.7	6.24	1.30	3.75	0.50	3.5	0.52
BG-18-25	5	62.2	138.0	16.00	63.9	13.6	2.61	13.70	2.20	61.8	11.80	2.29	6.11	0.79	5.2	0.71
BG-18-29	5	50.4	129.0	12.40	50.7	10.1	1.75	9.69	1.40	45.2	7.52	1.45	4.05	0.55	3.6	0.55
BG-18-38	5	53.0	102.0	12.80	50.2	10.4	1.97	11.20	1.76	61.8	10.10	2.01	5.79	0.79	5.0	0.74
BG-18-39	5	40.4	86.0	9.81	37.7	6.4	1.03	5.61	0.84	29.5	4.84	1.02	3.21	0.45	3.0	0.46
BG-18-40	5	45.4	92.0	11.00	44.4	9.2	2.04	9.98	1.53	51.7	8.66	1.72	4.82	0.65	4.1	0.61
BG-18-45	5	58.6	126.0	15.00	59.8	12.3	2.20	12.70	2.04	63.2	10.90	2.23	6.08	0.81	5.4	0.76
HC-18-08	5	41.9	85.5	9.72	35.8	4.9	0.53	3.31	0.57	22.6	3.65	0.79	2.64	0.39	2.9	0.46
PYG-18-07	5	51.5	115.0	12.30	46.4	7.3	1.27	6.69	1.09	39.5	6.70	1.38	4.46	0.66	4.8	0.73
BG-18-01-A	6	45.9	125.0	11.60	48.6	11.0	2.59	12.40	2.07	74.6	11.70	2.39	6.94	0.92	5.8	0.86
BG-18-14	6	47.2	98.8	11.60	45.4	9.5	2.03	10.20	1.61	54.3	8.79	1.79	4.87	0.67	4.4	0.62
BG-18-15	6	41.8	86.9	9.99	42.6	9.7	2.52	11.30	1.73	58.3	9.49	1.86	5.20	0.67	4.2	0.60
BG-18-23	6	55.6	113.0	14.40	60.4	14.1	3.36	16.50	2.73	98.4	15.50	3.13	8.37	1.12	6.8	0.93
BG-18-28	6	42.7	112.0	11.00	44.7	9.0	1.68	9.54	1.53	46.4	8.83	1.75	4.86	0.66	4.7	0.66
BG-18-31	6	75.7	154.0	19.70	81.0	18.5	3.56	20.80	3.34	116.0	18.80	3.70	9.95	1.30	7.8	1.08
BG-18-34b	6	41.9	87.1	10.20	39.5	7.7	1.40	7.52	1.18	37.8	6.58	1.26	3.75	0.50	3.4	0.53
BG-18-37	6	44.0	93.5	11.80	50.0	12.5	3.36	15.60	2.55	108.0	15.10	3.13	8.76	1.16	7.1	1.01
BG-18-46	6	65.3	136.0	16.50	66.2	14.0	2.98	15.40	2.49	83.7	14.10	2.84	7.74	1.08	6.8	0.96
BG-18-47	6	63.7	132.0	17.30	72.4	17.5	3.60	19.60	3.09	104.0	17.50	3.38	9.27	1.24	7.4	0.99
HC-18-01	6	57.0	117.0	14.00	56.5	13.0	3.36	15.90	2.52	84.7	13.50	2.76	7.54	0.99	6.0	0.86
HC-18-03	6	42.6	76.0	10.10	40.4	9.0	2.38	11.40	1.89	68.1	10.50	2.16	5.85	0.77	4.7	0.66
HC-18-04	6	53.0	129.0	13.50	57.1	13.9	3.27	16.40	2.51	73.0	12.90	2.48	6.54	0.84	5.4	0.77
HC-18-07	6	48.4	84.1	12.10	56.4	14.1	3.67	16.80	2.53	97.6	14.00	2.76	7.32	0.88	5.5	0.75
HC-18-09	6	45.7	98.2	11.70	51.2	12.4	3.11	13.90	2.13	65.2	11.50	2.15	5.62	0.72	4.7	0.67
HC-18-12	6	66.2	143.0	16.20	61.9	12.6	2.71	14.50	2.38	77.0	13.50	2.69	7.38	0.99	6.4	0.92
HC-18-16	6	60.3	120.0	13.90	50.2	6.5	1.10	5.15	0.82	35.2	5.18	1.18	3.93	0.60	4.2	0.64
PYG-18-01	6	51.0	124.0	12.90	52.9	12.2	2.81	12.70	2.01	63.1	11.40	2.25	6.15	0.84	5.3	0.83
PYG-18-02	6	39.1	94.0	10.80	48.2	14.2	3.27	16.60	2.53	76.1	13.90	2.70	7.38	0.98	6.4	0.94
PYG-18-03	6	43.1	94.4	10.00	38.0	7.2	1.60	7.51	1.22	39.8	7.04	1.43	4.21	0.60	4.1	0.63
PYG-18-06	6	43.0	96.7	10.60	41.4	8.9	1.93	9.57	1.62	52.2	9.09	1.88	5.20	0.76	4.8	0.72
101524	7	56.6	134.0	15.40	64.2	14.6	3.47	15.30	2.55	74.7	14.40	2.90	8.28	1.21	7.9	1.15
101569	7	29.7	69.0	8.32	33.7	7.7	1.61	7.77	1.30	41.1	7.80	1.53	4.28	0.65	4.4	0.62
101570	7	48.1	104.0	13.40	56.4	13.3	2.84	15.10	2.55	85.5	14.80	2.92	8.23	1.11	7.3	1.07
101571	7	37.2	96.1	11.00	47.1	12.2	2.79	13.90	2.50	75.7	15.30	3.06	8.79	1.27	8.6	1.23
101572	7	42.2	101.0	11.30	46.9	11.3	2.53	12.30	2.08	60.3	12.40	2.47	7.01	1.01	6.7	0.97
101573	7	45.2	117.0	13.40	57.6	14.2	3.22	16.40	2.78	80.8	16.60	3.35	9.83	1.40	9.5	1.36
101574	7	35.8	92.6	11.00	47.2	11.7	2.77	13.80	2.42	74.5	14.50	2.95	8.66	1.25	8.4	1.19
101575	7	56.0	134.0	15.20	62.3	14.1	3.25	15.50	2.53	74.3	14.70	2.89	8.51	1.22	8.3	1.17
101576	7	43.9	112.0	12.80	55.4	13.5	2.91	15.50	2.66	80.9	15.80	3.18	9.29	1.36	9.1	1.34
BG-18-05	7	75.6	161.0	20.30	84.5	20.9	4.89	25.70	4.24	147.0	23.80	4.82	13.00	1.75	10.6	1.51
BG-18-06	7	31.9	78.7	9.25	37.9	8.5	1.85	9.53	1.55	49.0	8.91	1.79	4.94	0.65	4.4	0.62
BG-18-07	7	97.6	220.0	26.40	109.0	22.9	4.49	25.20	4.00	126.0	22.00	4.32	11.80	1.56	9.8	1.40
BG-18-11	7	46.8	110.0	12.60	52.2	11.6	2.55	13.30	2.22	66.0	12.10	2.37	6.41	0.85	5.4	0.75
BG-18-12	7	41.2	94.3	11.10	45.9	11.1	2.34	13.40	2.34	83.5	13.50	2.77	8.02	1.09	7.1	0.98
BG-18-16	7	39.1	91.5	10.80	45.3	11.4	2.35	13.20	2.26	81.7	13.00	2.69	7.43	1.03	6.5	0.93
BG-18-22	7	46.9	99.2	12.20	48.2	10.7	2.44	12.00	1.88	57.1	10.60	1.99	5.46	0.74	4.7	0.66
BG-18-26	7	70.4	157.0	19.10	81.5	19.5	4.24	22.90	3.77	129.0	21.50	4.31	12.00	1.54	9.7	1.36
BG-18-32	7	57.6	124.0	15.40	66.5	17.0	4.30	20.70	3.41	131.0	19.80	3.91	11.00	1.43	8.9	1.26
BG-18-35	7	56.9	126.0	15.40	65.5	16.3	3.80	20.60	3.44	137.0	20.40	4.17	11.60	1.57	9.6	1.37
BG-18-41	7	39.6	88.6	10.50	41.6	9.0	2.15	10.10	1.62	53.2	9.19	1.83	4.94	0.68	4.4	0.63
HC-18-17	7	53.8	111.0	13.30	52.1	10.9	2.36	12.20	1.93	64.1	10.80	2.09	6.01	0.78	5.0	0.73

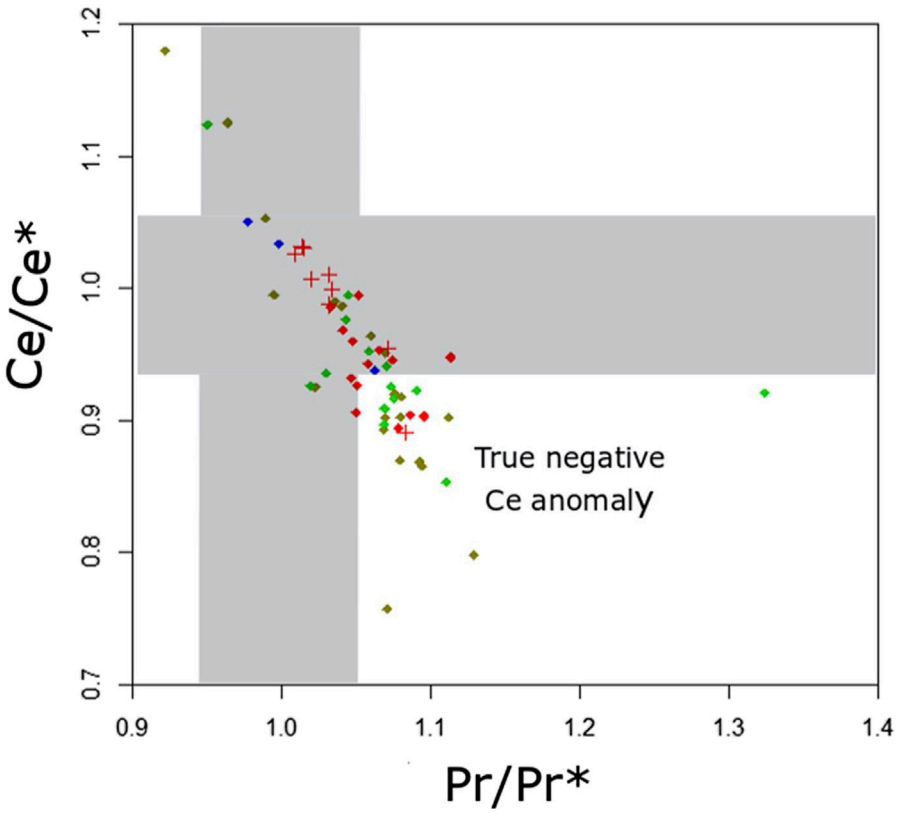

FIGURE 8 | Plot of Ce and Pr anomalies. Grey areas indicate no true anomaly (Bau and Dulski, 1994; Planavsky et al., 2010). Colours reflect facies: blue = clastic rich F1 and F3, green = F5, brown = F6, red = F7, red crosses = F7 from drill core. 'True' Ce anomalies are defined by Ce versus Pr values above and below unity, discriminating between positive La and true negative Ce anomalies as described by Bau and Dulski (1994).

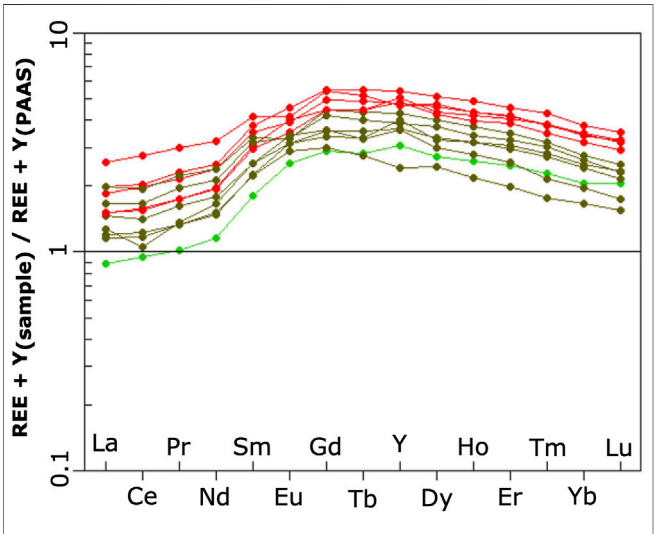

FIGURE 9 | PAAS-normalized REE distribution of P-rich samples (>3 wt %) from Welsh Basin ironstone (**Table 2**). Colours reflect facies: blue = clastic rich F1 and F3, green = F5, brown = F6, red = F7, red crosses = F7 from drill core.

On the middle shelf, oxidative scavenging by synsedimentary Fe-(oxyhydr)oxides removed Ce from seawater producing a negative Ce anomaly in CFA-rich facies (F6, F7; Elderfield and Greaves, 1982; Bau, 1991; Ohta and Kawabe, 2001). Authigenic CFA readily incorporates REEs during precipitation, passively recording the contemporary seawater signature to chemical sediments accumulating away from the direct influence of terrigenous clastic input (Jarvis et al., 1994; Watkins et al., 1995). The enrichment of MREEs and HREEs in CFA-rich facies probably reflects the preferential removal of the other light rare earth elements (LREE), which are scavenged compared to the heavier REEs due to their lower stability in seawater Ce (Jarvis et al., 1994).

Minor positive Eu anomalies in chamosite- and phosphate-rich authigenic facies (F5, F6) suggest ironstone deposition was fueled by the delivery of anoxic seawater enriched in hydrothermally derived Fe (McLennan, 1989; Derry and Jacobsen, 1990; Danielson et al., 1992; Erel and Stolper, 1993; Klein, 2005; Hannigan et al., 2010). At mid-ocean ridges, Eu is reduced during the alteration of basalt resulting in decreased sorption of Eu^{2+} compared to Eu^{3+}, producing discharging fluids enriched in total Eu (Danielson

TABLE 3 | Trace metal concentrations + Fe in lithofacies of the Hen-dy-Capel Ironstone Member, Tygarn Formation.

Sample	Facies	Fe	Cr	V	Zn	Mo	Ni	U	Pb	Co	Cu
		%	ppm	ppm	ppm	ppm	ppm	ppm	ppm	ppm	ppm
BG-18-04	1	40.00	150	336	109	5	46	2.43	18	5.2	44
HC-18-15	1	17.00	200	378	124	7	34	3.98	7	19.9	11
BG-18-20	2	26.30	190	371	146	5	35	2.70	10	8.9	16
BG-18-27	2	33.10	190	481	110	7	46	2.62	8	19.9	5
HC-18-19	2	38.30	100	347	140	3	39	2.56	6	18.5	13
BG-18-30	4	49.00	180	470	52	7	40	2.36	8	17.2	46
HC-18-18	4	44.40	120	361	60	4	35	2.07	7	5.0	9
BG-18-43	4	25.30	250	358	169	10	60	2.61	55	8.0	8
BG-18-13	5	40.40	140	352	104	5	55	2.39	—	30.0	156
BG-18-24	5	38.50	160	389	121	5	34	2.32	9	14.1	—
BG-18-25	5	37.40	120	353	114	2	45	2.70	—	4.7	5
BG-18-29	5	19.80	150	208	194	3	64	2.17	9	32.3	23
BG-18-38	5	34.80	210	677	188	—	51	4.40	13	5.3	21
BG-18-39	5	44.20	270	550	194	10	59	1.85	13	6.7	6
BG-18-40	5	36.50	160	437	206	4	76	3.80	8	11.5	30
BG-18-45	5	46.40	210	736	145	5	64	1.77	5	7.1	11
HC-18-08	5	>50	230	707	256	5	45	3.61	6	29.3	9
PYG-18-07	5	46.00	100	273	731	5	96	9.52	22	24.7	16
BG-18-01-A	6	21.90	180	411	105	16	25	2.65	10	15.0	28
BG-18-14	6	30.60	200	258	463	13	39	2.61	15	6.6	47
BG-18-15	6	47.00	180	568	70	2	27	2.73	6	19.9	118
BG-18-23	6	19.30	290	334	221	11	43	3.09	—	6.0	40
BG-18-28	6	42.90	200	661	106	3	27	2.32	—	9.5	18
BG-18-31	6	23.00	160	425	90	5	27	3.37	—	8.0	8
BG-18-34b	6	26.90	120	270	130	6	74	2.37	—	16.6	23
BG-18-37	6	26.10	130	404	100	—	36	2.71	—	4.5	16
BG-18-46	6	34.30	210	946	74	—	34	5.31	—	9.0	100
BG-18-47	6	22.90	140	343	142	—	53	2.86	7	3.6	38
HC-18-01	6	30.70	170	518	126	—	29	2.29	—	9.3	210
HC-18-03	6	22.80	120	184	158	—	73	3.98	—	11.0	10
HC-18-04	6	10.10	170	215	88	6	40	3.00	51	42.3	74
HC-18-07	6	25.00	170	322	160	—	46	2.98	—	5.2	13
HC-18-09	6	34.30	160	568	188	2	33	4.47	13	12.5	8
HC-18-12	6	27.50	120	297	121	3	45	1.96	6	10.6	8
HC-18-16	6	42.60	190	678	88	3	28	4.48	13	15.2	21
PYG-18-01	6	35.90	230	343	70	10	23	5.78	15	9.5	33
PYG-18-02	6	21.60	130	314	220	—	35	3.29	8	4.8	42
PYG-18-03	6	25.50	130	284	164	3	59	2.34	—	15.4	31
PYG-18-06	6	25.00	140	342	273	2	44	2.34	5	15.1	32
101524	7	45.60	150	542	224	4	34	1.83	—	19.9	—
101569	7	38.20	230	738	87	4	38	2.04	—	19.2	36
101570	7	25.30	140	462	159	—	35	2.72	6	14.3	25
101571	7	26.30	180	598	205	3	29	3.97	11	33.5	—
101572	7	23.50	140	332	165	—	20	3.33	19	32.6	—
101573	7	20.50	170	352	169	3	46	2.62	52	20.2	—
101574	7	33.80	100	287	101	—	32	1.96	21	22.3	—
101575	7	5.82	140	171	114	4	63	3.78	206	25.6	—
101576	7	30.30	100	175	94	3	25	3.88	25	18.7	13
BG-18-05	7	24.80	100	240	146	3	53	3.76	16	8.2	35
BG-18-06	7	18.90	120	248	114	3	43	2.92	98	14.9	27
BG-18-07	7	21.20	180	416	124	6	57	3.08	22	16.9	51
BG-18-11	7	21.70	120	300	200	3	77	2.51	65	13.4	32
BG-18-12	7	22.30	150	393	166	—	58	3.55	71	6.2	43
BG-18-16	7	24.20	160	391	136	—	42	2.67	41	5.0	6
BG-18-22	7	14.40	140	181	104	98	51	3.35	152	6.5	8
BG-18-26	7	9.75	120	136	119	4	58	2.43	6	11.2	35
BG-18-32	7	15.40	140	215	132	4	54	3.18	52	7.4	18
BG-18-35	7	15.70	250	362	149	7	37	2.52	68	5.6	—
BG-18-41	7	19.40	150	264	156	5	62	2.95	60	7.4	17
HC-18-17	7	21.70	120	294	191	2	67	3.75	21	13.8	32

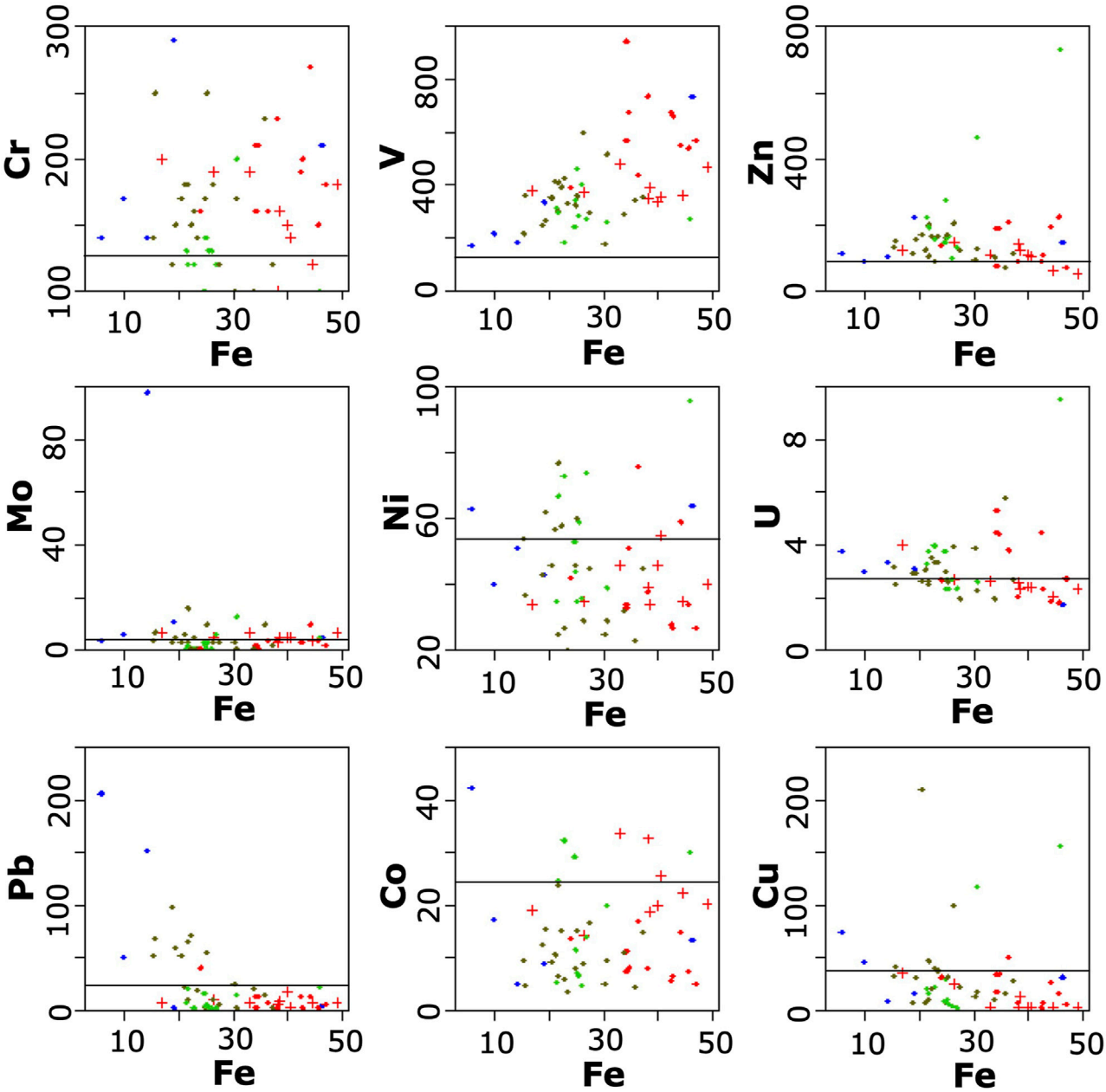

FIGURE 10 | Redox sensitive trace metals (ppm) versus Fe concentrations (%; **Table 3**). Black line denotes shale composite concentrations: Cr = 125 ppm, V = 130 ppm, Zn = 100 ppm, U = 2.7 ppm, Ni = 58 ppm, Cu = 35 ppm, Pb = 20ppm, Mo = 2 ppm; Co = 25 ppm (Composite values from Morgan et al., 1978; Gromet et al., 1984; Condie 1993). Colours reflect facies: blue = clastic rich F1 and F3, green = F5, brown = F6, red = F7, red crosses = F7 from drill core.

et al., 1992; Klein, 2005). In oxidizing environments away from the vent, Eu is scavenged by precipitating Fe-(oxyhydr)oxide to produce a positive Eu anomaly in accumulating authigenic Fe deposits. Because Eu anomalies are not produced by other REE + Y sources they are considered a robust indicator of hydrothermal input (Derry and Jacobsen, 1990; Olivarez and Owen, 1991; Danielson et al., 1992; Bau and Dulski, 1999; Bayon et al., 2015). The opening Rheic Ocean was ideal for the production and ponding of hydrothermally derived ferruginous seawater (**Figure 11**; Todd et al., 2019; Pufahl et al., 2020). Mid-ocean ridges discharged hydrothermal Fe as Avalonia rifted from Gondwana. Areas of early back-arc extension in the Welsh Basin may have locally increased this supply of hydrothermal Fe (Kokelaar et al., 1984; Woodcock, 1990; Brenchley et al., 2006; Howells, 2007). Sluggish seawater exchange in this narrow seaway is thought to have allowed anoxic bottom water to develop and transport Fe away from areas of active spreading.

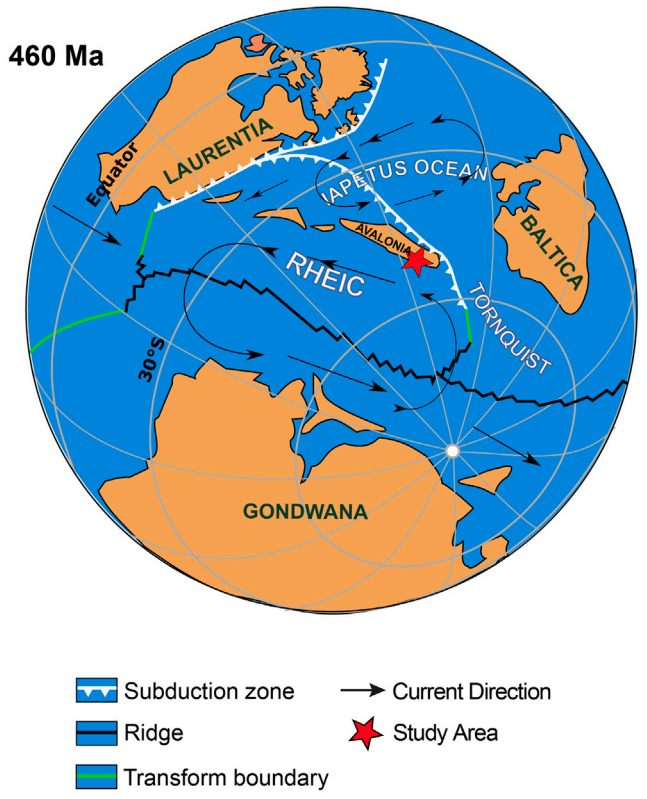

FIGURE 11 | Paleogeography of the Middle Ordovician. Global dispersal of continents and major oceans with paleo surface currents (modified from Torsvik and Cocks, 2013; Pohl et al., 2016).

The delivery of ferruginous seawater to continental shelves via coastal upwelling is analogous to the Precambrian when widespread anoxia allowed hydrothermal Fe to concentrate in the global ocean (Pufahl et al., 2020; Matheson and Pufahl, 2021). In the Neoarchean and Paleoproterozoic, the combination of a large Fe reservoir that was periodically tapped by upwelling along favourably positioned continents produced aerially extensive iron formations (Gross, 1983; Bekker et al., 2010; Pufahl, 2010; Pufahl et al., 2020). These continental margin iron formations are the largest iron deposits on Earth. More pronounced positive Eu anomalies in continental margin iron formations are generally attributed to the lack of contamination by siliciclastics (Danielson et al., 1992), which is common in less voluminous, Phanerozoic ironstones (Van Houten and Bhattacharyya, 1982; Van Houten and Arthur, 1989; Pufahl, 2010). Fe-redox pumping in sediment (Heggie et al., 1990; Jarvis et al., 1994) may have further muted Eu anomalies. With enough time, the cyclic scavenging and release of REEs adsorbed onto Fe-(oxyhydr) oxides restores pore water REE ratios to near shale values (Derry and Jacobsen, 1990; Planavsky et al., 2010).

Paleozoic Plume-Related Magmatism and Hydrothermal Fe

Geodynamic models predict that plume-related magmatism should preferentially occur along the margins of Gondwana in the aftermath of Late Neoproterozoic Pan-African continental collisions that resulted in its amalgamation (Murphy et al., 2021; Wang et al., 2021). Although Rheic oceanic lithosphere has been largely destroyed by subduction, there are several examples in which independent studies identify plume-related magmatism in Cambrian-Ordovician successions on both flanks of this ocean. Along its northern flank, these examples include mid-to-late Cambrian alkalic basalts (Greenough and Papezik, 1985; Murphy et al., 1985) in Avalonian rocks of Atlantic Canada. Such magmatism may have heralded the onset of rifting that led to Rheic Ocean development and input of hydrothermal Fe in this

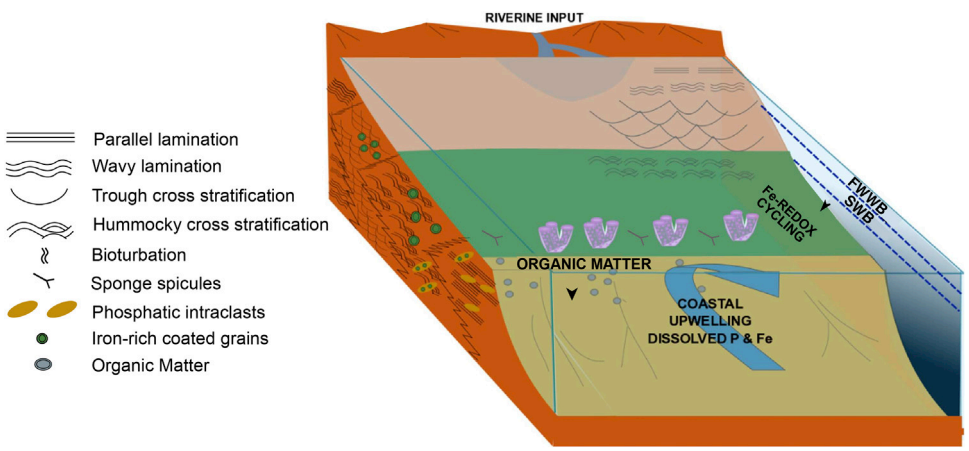

FIGURE 12 | Depositional model for Welsh Basin ironstone. Coastal upwelling provides micronutrients Fe and P to the shelf stimulating primary productivity and the food source of filter feeding sponges on the shelf. Fe-redox cycling on the shelf concentrates the nutrients in the sediment, with redox conditions and hydrodynamics as the primary control of facies distributions. A riverine source for terrigenous clastics is inferred. FWWB, fair-weather wave base; SWB, storm wave base. Modified from Todd et al. (2019).

narrow seaway (**Figure 11**; e.g., Nance et al., 2010). Along its southern flank, examples include late Cambrian–early Ordovician alkalic mafic magmatism in the Ossa Morena Zone of Iberia (Sánchez-García et al., 2003, 2008) and the 495–470 Ma voluminous magmatism of the Ollo de Sapo "formation". The Ollo de Sapo "formation" is recognized in every major Variscan massif, and palinspastic reconstructions suggest it extended for as much as 2,000 km along the north African margin (Montero et al., 2009; Talavera et al., 2015; Gutiérrez-Alonso et al., 2016; Casas and Murphy 2018; García-Arias et al., 2018). The ca. 530 Ma Blovice complex of the Bohemian Massif is interpreted as a collage of oceanic arcs, with a mantle plume located beneath a spreading ridge in a back-arc basin (Ackerman et al., 2019).

DEPOSITIONAL MODEL

Lithofacies associations in the Hen-dy-Capel Ironstone Member are interpreted to record ironstone accumulation along the northern margin of the Rheic Ocean on a storm-dominated shelf with active coastal upwelling (**Figure 12**). Organic-rich mudstone, phosphatic nodules, and biogenic silica (F4, F5, F6, F7) are diagnostic of upwelling environments and a productive surface ocean (Jahnke et al., 1983; Behl and Garrison, 1994; Glenn et al., 1994; Sharp, 2007; Föllmi, 1996; Pufahl and Groat, 2017). Modern upwelling systems such as the Humboldt and Benguela current regions along the coasts of Peru and southern Africa, respectively, are characterized by this triad of sedimentary deposits (Suess and Von Huene, 1990; Wefer et al., 2002). Modelling of surface currents in the Rheic Ocean suggest upwelling in this narrow seaway was driven by east-blowing winds and Ekman transport along the southern margin of Avalonia, which formed the northern side of a cyclonic gyre (**Figure 11**; Pohl et al., 2016; Todd et al., 2019; Pufahl et al., 2020).

The REE + Y composition of ironstone lithofacies (F4, F5, F6, F7) corroborates sedimentologic data suggesting upwelling delivered a sustained supply of anoxic bottom water enriched in hydrothermal Fe to an otherwise oxygenated shelf. Near the upwelling front, where primary production and deposition of sedimentary organic matter were highest (Beckly, 1988 Woodcock, 1990; Brenchley et al., 2006; Howells, 2007), intense bacterial sulfate reduction in the sediment is interpreted to have produced a pyritiferous black shale (F4; **Figure 12**). Inboard, diminished primary production, advection of ferruginous waters away from the upwelling front, and the cyclic, benthic redox recycling of Fe (Raiswell, 2011) into shallower oxygenated environments are interpreted to have stimulated widespread authigenesis and ironstone accumulation (F5, F6, F7; Petránek, 1991; Todd et al., 2019; Pufahl et al., 2020; Matheson and Pufahl, 2021). The presence of HCS constrains the deposition of ironstone to water depths no deeper than ca. 50 m (**Figure 12**; Dumas and Arnott, 2006).

Such an interpretation is consistent with other upwelling-related ironstones that accumulated along the margins of the Rheic and Iapetus oceans (Petránek, 1991; Todd et al., 2019; Pufahl et al., 2020; Matheson and Pufahl, 2021). What is different about ironstone from the Welsh Basin is the ubiquity of large, coated Fe grains. An upwelled source of Fe contrasts the more traditional view of ironstone deposition that relies on a greenhouse climate and increased chemical weathering for the delivery of continentally derived Fe to the shelf (Van Houten and Bhattacharyya, 1982; Young, 1989, 1992; Van Houten, 2000; Yilmaz et al., 2015).

Coated Fe Grains

Polymineralic coated grains are the granular equivalent of condensed beds, preserving a high-fidelity record of changing bottom- and pore-water chemistry (Pufahl and Grimm, 2003; Wigley and Compton, 2013; Föllmi, 2016; Diaz and Eberli, 2018). These changes are commonly associated with variations in surface ocean productivity and the export of organic carbon to the seafloor, which, in turn, drives fluctuations in the biological oxygen, pore water Eh, and the precipitation of authigenic minerals forming coated grains (Pufahl and Grimm, 2003). In some environments, bioturbation can periodically flush the sediment with oxygenated seawater to influence pore-water redox potential and authigenesis (Aller, 1982, 1994; Brasier and Callow, 2007). The zone of authigenic precipitation is maintained near the sediment-water interface by intense and prolonged reworking of the seafloor.

Two types of coated grains are the result of the interplay of these processes. Unconformity-bounded grains range in diameter from 200 to 600 μm and contain internal erosion surfaces attributed to multiple episodes of reworking, exhumation, and reburial into the zone of authigenic precipitation (Pufahl and Grimm, 2003; Wigley and Compton, 2013). Redox aggraded grains are larger, up to ca. 15 mm in diameter, and composed of concordant, concentric cortical layers recording minute changes in pore water Eh without wholesale exhumation of grains (Pufahl and Grimm, 2003). Although both grain types occur in the Hen-dy-Capel Ironstone Member (F5, F6, F7), unconformity-bounded grains increase in abundance through Parasequence 1, reflecting aggradation and intensified reworking as the seafloor shallowed to fair weather wave base. Unconformity-bounded grains at the top of Parasequence 1 (F7) are smaller than coated grains near its base (F5; **Figure 7**) because they are interpreted to have spent less time in the zone of precipitation and there was an abundance of detrital nuclei for cortical layers to form around. Thus, grain type is a sensitive and independent indicator of shelf hydrodynamics through time. With an understanding of cortex mineralogy, oceanographic processes can be related to oxygen gradients in the sediment and across the Welsh Basin.

Redox aggraded grains formed of chamosite and CFA at the base of Parasequence 1 precipitated in sediment (F5) that was accumulating just inboard of the upwelling front. Chamositic cortical laminae record authigenic precipitation in suboxic pores (Glenn and Arthur, 1988; Pufahl and Grimm, 2003). Bioturbation indicates that the irrigation of sediment with oxygenated bottom water was important for maintaining suboxic conditions and focusing the Fe-redox boundary in sediment. Minor productivity-driven changes in pore water Eh are recorded by intercalated CFA cortical layers. Increased deposition and microbial degradation of sedimentary organic matter on the seafloor is interpreted to have

sufficiently lowered pore water Eh to periodically stop chamosite precipitation and promote the formation of CFA. Although phosphogenesis is a redox independent process, contingent only on the concentration of dissolved phosphate (Glenn and Arthur, 1988; Pufahl, 2010), intensified organic matter degradation is interpreted to have saturated pore water with phosphate. Precipitation of cortical layers was rapid, preserving sponge spicules that usually dissolve quickly in silica-undersaturated pore water (Won and Below, 1999; Kidder and Tomescu, 2016).

Comparison of this high-fidelity record of distal suboxic authigenesis to the redox conditions that formed hematitic unconformity bounded grains in proximal environments (F7) is consistent with an increase in the ichnofabric index that also indicates oxygen levels rose towards the shore. Hematite is interpreted to have formed during diagenesis from an original authigenic Fe-(oxyhydr)oxide precursor. This precursor was likely ferrihydrite ($Fe_2^{3+}O_3.0.5(H_2O)$, which reflects precipitation under higher Eh conditions than chamosite (Taylor and Konhauser, 2011; Taylor and Macquaker, 2011). Cortical layers were produced where ferrous Fe supplied through benthic redox cycling combined with well-oxygenated pore water. Constant wave reworking of the seafloor and intense bioturbation were undoubtedly important for oxygenating pore water.

PALEOZOIC IRONSTONE, OCEAN CHEMISTRY, AND EVOLUTION

Ventilation of the deep ocean began during the Neoproterozoic Oxygenation Event (800–500 Ma; Och and Shields-Zhou, 2012; Scott & Lyons, 2012; Shields, 2017), but mounting evidence suggests that a persistently oxygenated deep ocean did not develop until the Permian (Elrick et al., 2011; Kah et al., 2016; Edwards et al., 2017; Lu et al., 2018; Edwards, 2019; Todd et al., 2019; Pufahl et al., 2020; Matheson and Pufahl, 2021). Modelling demonstrates that oxygen concentrations in the ocean-atmosphere system were probably lowest in the Middle Ordovician (Edwards et al., 2017). Occurrences of upwelling-related granular ironstone provide critical insights into this history because they capture nuances of ocean redox structure at the interface between shallow- and deep-water masses. Thus, these occurrences link shelf and abyssal processes to further illuminate the relationship between ocean circulation, seawater chemistry, nutrient availability, and biological evolution.

The ubiquity of upwelling-related ironstone in the Paleozoic suggests that bottom-water anoxia and input of hydrothermal Fe were common in many restricted seaways (Pufahl et al., 2020; Matheson and Pufahl, 2021). Pronounced episodes of ironstone accumulation in the Ordovician and Devonian (Van Houten and Arthur, 1989; Young, 1992) likely correspond to periods of plate reorganization and increased hydrothermal activity during mantle plume events (Murphy et al., 2009; Yang et al., 2012; Algeo et al., 2016). During these tectonic episodes, the input of volcanogenic CO_2 is thought to have acidified the global ocean (Veron, 2008; Kiessling and Simpson, 2011; Torsvik and Cocks, 2017; McKenzie and Jiang, 2019) and greenhouse warming decreased the solubility of O_2 in seawater (Veron, 2008; McKenzie and Jiang, 2019).

Ocean acidification is deleterious to calcareous organisms, causing brittle shells and partial dissolution (Kiessling and Simpson, 2011; Hönisch et al., 2012). In contrast, acidic seawater has a neutral to positive effect on the development of siliceous organisms (Webby, 2002; Kidder and Tomescu, 2016). In upwelling-related ironstone, the absence of a diverse assemblage of carbonate-producing organisms and abundance of sponges with siliceous spicules is consistent with this relationship. In the Welsh Basin, sponges, phosphatic brachiopods, and trilobites (Trythall et al., 1987) apparently flourished in waters too acidic to support a healthy carbonate community. The absence of carbonate skeletons in nutrient-rich environments may also reflect a dysoxic seafloor and dissolution associated with the microbial respiration of accumulating organic matter (James et al., 2005). CFA nodules and cortical layers composed of coated Fe grains record this bacterial process, which also liberates P from degrading organic matter (Jarvis et al., 1994; Pufahl and Groat, 2017). Sponges thrive under such low Eh and Ph conditions and therefore can dominate productive middle and distal shelf environments (Mills et al., 2014; Leys and Kahn, 2018; Matheson and Frank, 2020; Chen et al., 2021).

Under a greenhouse climate and diminished capacity for warmer seawater to retain oxygen, anoxic conditions were probably readily established in the narrow, restricted seaways of the Paleozoic. Such anoxia was a pre-requisite for the concentration of hydrothermal Fe and deposition of ironstone in these volcanically active basins. In addition to Fe, upwelling of these ferruginous waters would have delivered a sustained supply of deleterious trace elements to the shelf (Cd, Cu, As, Zn, Co, Ni, Se, Cr, Ba, Ge, As, Pd, Te, and REEs; Wilde et al., 1990), some of which are elevated in the Hen-dy-Capel Ironstone Member. In conjunction with the impingement of anoxic seawater on the shelf, the availability of these toxic trace elements is interpreted to have triggered regional extinctions that punctuate major biological diversification events such as the GOBE (Vandenbroucke et al., 2015; Pufahl et al., 2020; Matheson and Pufahl, 2021). The accumulation of upwelling-related ironstone in periods of post-extinction recovery suggests that over time ironstone accumulation was also an important sink that lowered the metal toxicity of seawater (Pufahl et al., 2020). The cyclic changes in pore water redox potential required to sequester these trace elements through repeated episodes of scavenging and absorption at the seafloor are preserved in the cortical mineralogy of coated Fe grains. This "kill and cure" mechanism (Pufahl et al., 2020) is interpreted to have contributed to pulses of graptolite diversification in the Welsh Basin (Kokelaar et al., 1985; Brenchley et al., 2006; Howells, 2007) by providing upwelling derived nutrients (Young et al., 2002; Pohl et al., 2016) and lowering metal toxicity (Matheson and Pufahl, 2021). This negative feedback process is thought to have contributed to other post-extinction faunal recoveries that assisted with increasing marine biodiversity through the GOBE (Pufahl et al., 2020). A similar feedback may have also been important in the Devonian when biological turnover was also linked to environmental volatility and periods of shelf anoxia

(Bond and Wignall, 2008; Brett et al., 2020). Application of this upwelling model to even younger ironstones and contemporaneous trace element enriched black shales may also provide important new constraints regarding the redox structure and oxygenation history of the Mesozoic oceans.

CONCLUSION

1) Ironstone of the Hen-dy-Capel Ironstone Member of the Tygarn Formation, Ogwen Group, constitutes a single shallowing upward parasequence (Parasequence 1) recording stratigraphic condensation during maximum transgression. Overlying terrigenous clastic facies form a second parasequence (Parasequence 2) interpreted to record the onset of progradation during highstand conditions.
2) Lithofacies associations in Parasequence 1 are consistent with ironstone accumulation on a storm-dominated shelf with active coastal upwelling. Conspicuous coated Fe grains augment this understanding by linking shelf and abyssal processes to capture nuances in ocean chemistry and seawater redox structure.
3) For the first time, the REE + Y and the trace metal composition of Phanerozoic ironstone is used to corroborate sedimentologic data suggesting upwelling delivered a sustained supply of anoxic bottom water enriched in hydrothermal Fe to an otherwise oxygenated shelf. Such an interpretation is consistent with other upwelling-related ironstones that accumulated along the margins of the Rheic and Iapetus oceans. This style of Fe delivery harks back to the Precambrian when upwelling produced giant continental margin iron formations.
4) In addition to Fe, upwelling of this hydrothermally enriched seawater would have delivered a sustained supply of toxic trace elements to the shelf, triggering regional extinctions that punctuate major biological diversification events such as the GOBE. The accumulation of upwelling-related ironstone during periods of post-extinction recovery suggests that with time the accumulation of ironstone titrated these metals and lowered seawater toxicity. This "kill and cure" mechanism is a chemical-ecological feedback process that may have contributed to biological turnover until the deep ocean became fully oxygenated in the late Paleozoic.

DATA AVAILABILITY STATEMENT

The original contributions presented in the study are included in the article, further inquiries can be directed to the corresponding author.

AUTHOR CONTRIBUTIONS

The manuscript is based on the MSc thesis research of SD. As SD's supervisor, PP assisted in the field, data collection, data interpretation, and manuscript preparation. JM and BM also assisted in the field, broad-scale conceptual ideas critical to the science, and manuscript review.

FUNDING

Natural Sciences and Engineering Research Council of Canada (NSERC) Discovery Grants to PP and BM. Acadia Graduate Awards and a NSERC Canada Graduate Scholarship to SD.

ACKNOWLEDGMENTS

Reviews by Guest Editor Riedinger and three reviewers improved this manuscript. P. Frail prepared polished thin sections. C. Koebernick reviewed previous iterations of the text. J. Malone assisted with fieldwork. AGAT Laboratories are gratefully acknowledged for geochemical analyses.

REFERENCES

Ackerman, L., HajnáZák, J. J., Žák, J., Erban, V., Sláma, J., Polák, L., et al. (2019). Architecture and Composition of Ocean Floor Subducted beneath Northern Gondwana during Neoproterozoic to Cambrian: a Palinspastic Reconstruction Based on Ocean Plate Stratigraphy (OPS). *Gondwana Res.* 76, 77–97. doi:10.1016/j.gr.2019.07.001

Algeo, T. J., Marenco, P. J., and Saltzman, M. R. (2016). Co-evolution of Oceans, Climate, and the Biosphere during the 'Ordovician Revolution': A Review. *Palaeogeogr. Palaeoclimatol. Palaeoecol.* 458, 1–11. doi:10.1016/j.palaeo.2016.05.015

Aller, R. C. (1994). Bioturbation and Remineralization of Sedimentary Organic Matter: Effects of Redox Oscillation. *Chem. Geology.* 114, 331–345. doi:10.1016/0009-2541(94)90062-0

Aller, R. C. (1982). "The Effects of Macrobenthos on Chemical Properties of marine Sediment and Overlying Water," in *In Animal-Sediment Relations - Topics in Geobiology 100*. Editors P.L. McCall and M.J.S. Tevesz (Boston: Springer), 53–102. doi:10.1007/978-1-4757-1317-6_2

Anthony, J. W., Bideaux, R. A., Bladh, K. W., and Nichols, M. C. (2001). "Silica, Silicates," in *Handbook of Mineralogy*. Editors J.W. Anthony, R.A. Bideaux, K.W. Bladh, and M.C. Nichols (Chantilly, VA, USA): Mineralogical Society of America), 458.

Arning, E. T., Birgel, D., Brunner, B., and Peckmann, J. (2009). Bacterial Formation of Phosphatic Laminites off Peru. *Geobiology* 7, 295–307. doi:10.1111/j.1472-4669.2009.00197.x

Bau, M., and Dulski, P. (1999). Comparing Yttrium and Rare Earths in Hydrothermal Fluids from the Mid-Atlantic Ridge: Implications for Y and REE Behaviour during Near-Vent Mixing and for the Y/Ho Ratio of Proterozoic Seawater. *Chem. Geology.* 155, 77–90. doi:10.1016/S0009-2541(98)00142-9

Bau, M., and Dulski, P. (1994). Evolution of the Yttrium-Holmium Systematics of Seawater through Time. *Mineralogical Mag.* 58A, 61–62. doi:10.1180/minmag.1994.58A.1.35

Bau, M., Koschinsky, A., Dulski, P., and Hein, J. R. (1996). Comparison of the Partitioning Behaviours of Yttrium, Rare Earth Elements, and Titanium between Hydrogenetic marine Ferromanganese Crusts and Seawater. *Geochimica et Cosmochimica Acta* 60, 1709–1725. doi:10.1016/0016-7037(96)00063-4

Bau, M. (1991). Rare-earth Element Mobility during Hydrothermal and Metamorphic Fluid-Rock Interaction and the Significance of the Oxidation State of Europium. *Chem. Geology.* 93, 219–230. doi:10.1016/0009-2541(91)90115-8

Bau, M., Schmidt, K., Koschinsky, A., Hein, J., Kuhn, T., and Usui, A. (2014). Discriminating between Different Genetic Types of marine Ferro-Manganese Crusts and Nodules Based on Rare Earth Elements and Yttrium. *Chem. Geology.* 381, 1–9. doi:10.1016/j.chemgeo.2014.05.004

Bayon, G., Toucanne, S., Skonieczny, C., André, L., Bermell, S., Cheron, S., et al. (2015). Rare Earth Elements and Neodymium Isotopes in World River Sediments Revisited. *Geochimica et Cosmochimica Acta* 170, 17–38. doi:10.1016/j.gca.2015.08.001

Beckly, A. J. (1988). The Stratigraphy of the Arenig Series in the Aberdaron to Sarn Area, Western Llŷcn, North Wales. *Geol. J.* 23, 321–337. doi:10.1002/gj.3350230404

Behl, R., and Garrison, R. E. (1994). The Origin of Chert in the Monterey Formation of California (USA). *Proc. 29th Int. Geol. Congress*, 101–132.

Bekker, A., Slack, J. F., Planavsky, N., Krapež, B., Hofmann, A., Konhauser, K. O., et al. (2010). Iron Formation: The Sedimentary Product of a Complex Interplay Among Mantle, Tectonic, Oceanic, and Biospheric Processes. *Econ. Geology.* 105, 467–508. doi:10.2113/gsecongeo.105.3.467

Bond, D. P. G., and Wignall, P. B. (2008). The Role of Sea-Level Change and marine Anoxia in the Frasnian-Famennian (Late Devonian) Mass Extinction. *Palaeogeogr. Palaeoclimatol. Palaeoecol.* 263, 107–118. doi:10.1016/j.palaeo.2008.02.015

Botting, J. P., and Muir, L. A. (2013). Spicule Structure and Affinities of the Late Ordovician Hexactinellid-like Sponge Cyathophycus Loydelli from the Llanfawr Mudstones Lagerstätte, Wales. *Lethaia* 46, 454–469. doi:10.1111/let.12022

Boyd, R. (2010). "Trangressive Wave-Dominated Coasts," in *In Facies Models 4*. Editors N. P. James and R. W. Dalrymple (St. John's, Canada: Geological Association of Canada)), 265–294.

Brasier, M. D., and Callow, R. H. T. (2007). Changes in the Patterns of Phosphatic Preservation across the Proterozoic-Cambrian Transition. *Mem. Assoc. Australas. Palaeontologists* 34, 377–389.

Brenchley, P. J., Rushton, A. W. A., Howells, M. F., and Cave, R. (2006). "Cambrian and Ordovician: the Early Palaeozoic Tectonostratigraphic Evolution of the Welsh Basin, Midland and Monian Terranes of Eastern Avalonia," in *The Geology of England and Wales*. Editors P. J. Brenchley and P. F. Rawson (Bath, UK: Geological Society of London), 25–74.

Brett, C. E., Zambito, J. J., McLaughlin, P. I., and Emsbo, P. (2020). Revised Perspectives on Devonian Biozonation and Environmental Volatility in the Wake of Recent Time-Scale Revisions. *Palaeogeogr. Palaeoclimatol. Palaeoecol.* 549, 108843–108910. doi:10.1016/j.palaeo.2018.06.037

Brown, M. J., and Evans, A. D. (1989). 89/14. Keyworth, UK: British Geological Survey Technical Report WF/, 84.Geophysical and Geochemical Investigations of the Manganese Deposits of Rhiw, Western Llyn, North Wales

Canfield, D. E., and Thamdrup, B. (2009). Towards a Consistent Classification Scheme for Geochemical Environments, or, Why We Wish the Term 'suboxic' Would Go Away. *Geobiology* 7, 385–392. doi:10.1111/j.1472-4669.2009.00214.x

Casas, J. M., and Brendan Murphy, J. (2018). Unfolding the Arc: the Use of Pre-orogenic Constraints to Assess the Evolution of the Variscan belt in Western Europe. *Tectonophysics* 736, 47–61. doi:10.1016/j.tecto.2018.04.012

Catuneanu, O., Galloway, W. E., Kendall, C. G. S. t. C., Miall, A. D., Posamentier, H. W., Strasser, A., et al. (2011). Sequence Stratigraphy: Methodology and Nomenclature. *nos* 44, 173–245. doi:10.1127/0078-0421/2011/0011

Catuneanu, O. (2019). Scale in Sequence Stratigraphy. *Mar. Pet. Geology.* 106, 128–159. doi:10.1016/j.marpetgeo.2019.04.026

Challands, T. J., Armstrong, H. A., Maloney, D. P., Davies, J. R., Wilson, D., and Owen, A. W. (2009). Organic-carbon Deposition and Coastal Upwelling at Mid-latitude during the Upper Ordovician (Late Katian): A Case Study from the Welsh Basin, UK. *Palaeogeogr. Palaeoclimatol. Palaeoecol.* 273, 395–410. doi:10.1016/j.palaeo.2008.10.004

Chen, F., Pufahl, P. K., Wang, Q., Matheson, E. J., Shabaga, B. M., Zhang, Q., et al. (2021). A New Model for the Genesis of Carboniferous Mn Ores, Longtou deposit, South China Block. *Econ. Geology*. doi:10.5382/econgeo.4855

Cocks, L. R. M., and Torsvik, T. H. (2002). Earth Geography from 500 to 400 Million Years Ago: a Faunal and Palaeomagnetic Review. *J. Geol. Soc.* 159, 631–644. doi:10.1144/0016-764901-118

Cohen, K. M., Finney, S. C., Gibbard, P. L., and Fan, J. (2019). The ICS International Chronostratigraphic Chart. *Episodes* 36, 199–204. doi:10.18814/epiiugs/2013/v36i3/002

Condie, K. C. (1993). Chemical Composition and Evolution of the Upper continental Crust: Contrasting Results from Surface Samples and Shales. *Chem. Geology.* 104, 1–37. doi:10.1016/0009-2541(93)90140-E

Cooper, R. A., Sadler, P. M., Hammer, O., and Gradstein, F. M. (2012). "The Ordovician Period," in *"Chapter 20 - the Ordovician Period," in the Geologic Time Scale*. Editors F. M. Gradstein, J. G. Ogg, M. D. Schmitz, and G. M. Ogg (Boston: Elsevier), 489–523. doi:10.1016/B978-0-444-59425-9.00020-2

Danielson, A., Möller, P., and Dulski, P. (1992). The Europium Anomalies in Banded Iron Formations and the thermal History of the Oceanic Crust. *Chem. Geology.* 97, 89–100. doi:10.1016/0009-2541(92)90137-T

Derry, L. A., and Jacobsen, S. B. (1990). The Chemical Evolution of Precambrian Seawater: Evidence from REEs in Banded Iron Formations. *Geochimica et Cosmochimica Acta* 54, 2965–2977. doi:10.1016/0016-7037(90)90114-Z

Diaz, M. R., and Eberli, G. P. (2019). Decoding the Mechanism of Formation in marine Ooids: A Review. *Earth-Science Rev.* 190, 536–556. doi:10.1016/j.earscirev.2018.12.016

Dott, R. H., and Bourgeois, J. (1982). Hummocky Stratification: Significance of its Variable Bedding Sequences. *Geol. Soc. America Bull.* 93, 663–680. doi:10.1130/0016-7606(1982)93<663:HSSOIV>2.0.CO;2

Droser, M. L., and Bottjer, D. J. (1986). A Semiquantitative Field Classification of Ichnofabric. *J. Sediment. Res.* 56, 558–559. doi:10.1306/212F89C2-2B24-11D7-8648000102C1865D

Dubinin, A. V. (2004). Geochemistry of Rare Earth Elements in the Ocean. *Lithology Mineral. Resour.* 39, 289–307. doi:10.1023/b:limi.0000033816.14825.a2

Dumas, S., and Arnott, R. W. C. (2006). Origin of Hummocky and Swaley Cross-Stratification- the Controlling Influence of Unidirectional Current Strength and Aggradation Rate. *Geol* 34, 1073. doi:10.1130/G22930A.1

Dunham, R. J. (1962). "Classification of Carbonate Rocks According to Depositional Texture," in *In Classification of Carbonate Rocks*. Editor W.E. Ham (Tulsa, OK: AAPG)), 108–121.

Edwards, C. T. (2019). Links between Early Paleozoic Oxygenation and the Great Ordovician Biodiversification Event (GOBE): A Review. *Palaeoworld* 28, 37–50. doi:10.1016/j.palwor.2018.08.006

Edwards, C. T., Saltzman, M. R., Royer, D. L. D., and Fike, D. A. D. (2017). Oxygenation as a Driver of the Great Ordovician Biodiversification Event. *Nat. Geosci* 10, 925–929. doi:10.1038/s41561-017-0006-3

Elderfield, H., and Greaves, M. J. (1982). The Rare Earth Elements in Seawater. *Nature* 296, 214–219. doi:10.1038/296214a0

Elrick, M., Rieboldt, S., Saltzman, M., and McKay, R. M. (2011). Oxygen-isotope Trends and Seawater Temperature Changes across the Late Cambrian Steptoean Positive Carbon-Isotope Excursion (SPICE Event). *Geology* 39, 987–990. doi:10.1130/g32109.1

Filippelli, G. M. (2008). The Global Phosphorus Cycle: Past, Present, and Future. *Elements* 4, 89–95. doi:10.2113/gselements.4.2.89

Folk, R. L. (1980). *Petrology of Sedimentary Rocks*. Austin: Hemphill Publishing), 184. p.

Föllmi, K. B. (2016). Sedimentary Condensation. *Earth-Science Rev.* 152, 143–180. doi:10.1016/j.earscirev.2015.11.016

Föllmi, K. (1996). The Phosphorus Cycle, Phosphogenesis and marine Phosphate-Rich Deposits. *Earth-Science Rev.* 40, 55–124. doi:10.1016/0012-8252(95)00049-6

Fortey, R. A., and Cocks, L. R. M. (2003). Palaeontological Evidence Bearing on Global Ordovician-Silurian continental Reconstructions. *Earth-Science Rev.* 61, 245–307. doi:10.1016/S0012-8252(02)00115-0

Froelich, P. N., Klinkhammer, G. P., Bender, M. L., Luedtke, N. A., Heath, G. R., Cullen, D., et al. (1979). Early Oxidation of Organic Matter in Pelagic Sediments of the Eastern Equatorial Atlantic: Suboxic Diagenesis. *Geochimica et Cosmochimica Acta* 43, 1075–1090. doi:10.1016/0016-7037(79)90095-4

García-Arias, M., Díez-Montes, A., Villaseca, C., and Blanco-Quintero, I. F. (2018). The Cambro-Ordovician Ollo de Sapo magmatism in the Iberian Massif and its Variscan evolution: A review. *Earth-Science Rev.* 176, 345–372. doi:10.1016/j.earscirev.2017.11.004

Ghadeer, S. G., and Macquaker, J. H. S. (2011). 168. London, 1121–1132. doi:10.1144/0016-76492010-016Sediment Transport Processes in an Ancient

Mud-Dominated Succession: a Comparison of Processes Operating in marine Offshore Settings and Anoxic Basinal Environments*J. Geol. Soc.*

Glenn, C., Föllmi, K., Riggs, S., Baturin, G., Grimm, K., Trappe, J., et al. (1994). Phosphorus and Phosphorites: Sedimentology and Environments of Formation. *Eclogae Geologicae Helvetica* 87, 747–788.

Glenn, C. R., and Arthur, M. A. (1988). Petrology and Major Element Geochemistry of Peru Margin Phosphorites and Associated Diagenetic Minerals: Authigenesis in Modern Organic-Rich Sediments. *Mar. Geology.* 80, 231–267. doi:10.1016/0025-3227(88)90092-8

Greenough, J. D., and Papezik, V. S. (). Petrology and Geochemistry of Cambrian Volcanic Rocks from the Avalon Peninsula, Newfoundland. *Can. J. Earth Sci.* 22, l594–l60l. doi:10.1139/e85-168

Gromet, L. P., Haskin, L. A., Korotev, R. L., and Dymek, R. F. (1984). The "North American Shale Composite": Its Compilation, Major and Trace Element Characteristics. *Geochimica et Cosmochimica Acta* 48, 2469–2482. doi:10.1016/0016-7037(84)90298-9

Gross, G. A. (1983). Tectonic Systems and the Deposition of Iron-Formation. *Precambrian Res.* 20, 171–187. doi:10.1016/0301-9268(83)90072-4

Gutiérrez-Alonso, G., Gutiérrez-Marco, J. C., Fernández-Suárez, J., Bernárdez, E., and Corfu, F. (2016). Was There a Super-eruption on the Gondwanan Coast 477 Ma Ago? *Tectonophysics* 681, 85–94. doi:10.1016/j.tecto.2015.12.012

Haley, B. A., Klinkhammer, G. P., and McManus, J. (2004). Rare Earth Elements in Pore Waters of marine Sediments. *Geochimica et Cosmochimica Acta* 68, 1265–1279. doi:10.1016/j.gca.2003.09.012

Harder, H. (1980). Syntheses of Glauconite at Surface Temperatures. *Clays and Clay Minerals* 28, 217–222. doi:10.1346/ccmn.1980.0280308

Heggie, D. T., Skyring, G. W., O'Brien, G. W., Reimers, C., Herczeg, A., Moriarty, D. J. W., et al. (1990). Organic Carbon Cycling and Modern Phosphorite Formation on the East Australian continental Margin: an Overview. *Geol. Soc. Lond. Spec. Publications* 52, 87–117. doi:10.1144/gsl.sp.1990.052.01.07

Henderson, B. J., Collins, W. J., Murphy, J. B., Gutierrez-Alonso, G., and Hand, M. (2016). Gondwanan Basement Terranes of the Variscan-Appalachian Orogen: Baltican, Saharan and West African Hafnium Isotopic Fingerprints in Avalonia, Iberia and the Armorican Terranes. *Tectonophysics* 681, 278–304. doi:10.1016/j.tecto.2015.11.020

Hiatt, E. E., Pufahl, P. K., and Edwards, C. T. (2015). Sedimentary Phosphate and Associated Fossil Bacteria in a Paleoproterozoic Tidal Flat in the 1.85Ga Michigamme Formation, Michigan, USA. *Sediment. Geology.* 319, 24–39. doi:10.1016/j.sedgeo.2015.01.006

Hönisch, B., Ridgwell, A., Schmidt, D. N., Thomas, E., Gibbs, S. J., Sluijs, A., et al. (2012). The Geological Record of Ocean Acidification. *Science* 335, 1058–1063. doi:10.1126/science.1208277

Howells, M. F. (2007). "Ordovician," in *British Regional Geology: Wales*. Editor M. F. Howells (Keyworth, Nottingham: British Geological Survey)), 36–71.

Howells, M. F., and Smith, M. (1997). *Geology of the Country Around Snowdon*. London: Memoir of the British Geological Survey, Sheet 119 (England and Wales).

Jahnke, R. A., Emerson, S. R., Roe, K. K., and Burnett, W. C. (1983). The Present Day Formation of Apatite in Mexican continental Margin Sediments. *Geochimica et Cosmochimica Acta* 47, 259–266. doi:10.1016/0016-7037(83)90138-2

James, N. P., Bone, Y., and Kyser, T. K. (2005). Where Has All the Aragonite Gone? Mineralogy of Holocene Neritic Cool-Water Carbonates, Southern Australia. *J. Sediment. Res.* 75, 454–463. doi:10.2110/jsr.2005.035

James, N. P., and Jones, B. (2016). "The Time Machine," in *Origin of Carbonate Sedimentary Rocks*. Editors N. P. James and B. Jones (West Sussex, United Kingdom: John Wiley & Sons), 261–272.

Janoušek, V., Moyen, J.-F., Martin, H., Erban, V., and Farrow, C. (2016). *Geochemical Modelling of Igneous Processes – Principles and Recipes in R Language: Bringing the Power of R to a Geochemical Community*. Berlin Heidelberg: Springer-Verlag.

Jarvis, I., Burnett, W. C., Nathan, Y., Almbaydin, F. S. M., Attia, A. K. M., and Castrol, L. N. (1994). Phosphorite Geochemistry: State of the Art and Environmental Concerns. *Eclogae Geol. Helv.* 87, 643–700.

Kah, L. C., Thompson, C. K., Henderson, M. A., and Zhan, R. (2016). Behavior of marine Sulfur in the Ordovician. *Palaeogeogr. Palaeoclimatol. Palaeoecol.* 458, 133–153. doi:10.1016/j.palaeo.2015.12.028

Kidder, D. L., and Tomescu, I. (2016). Biogenic Chert and the Ordovician Silica Cycle. *Palaeogeogr. Palaeoclimatol. Palaeoecol.* 458, 29–38. doi:10.1016/j.palaeo.2015.10.013

Kiessling, W., and Simpson, C. (2011). On the Potential for Ocean Acidification to Be a General Cause of Ancient Reef Crises. *Glob. Change Biol.* 17, 56–67. doi:10.1111/j.1365-2486.2010.02204.x

Klein, C. (2005). Some Precambrian Banded Iron-Formations (BIFs) from Around the World: Their Age, Geologic Setting, Mineralogy, Metamorphism, Geochemistry, and Origins. *Am. Mineral.* 90, 1473–1499. doi:10.2138/am.2005.1871

Kokelaar, B. P., Bevins, R. E., and Roach, R. A. (1985). Submarine Silicic Volcanism and Associated Sedimentary and Tectonic Processes, Ramsey Island, SW Wales. *J. Geol. Soc.* 142, 591–613. doi:10.1144/gsjgs.142.4.0591

Kokelaar, B. P., Howells, M. F., Bevins, R. E., Roach, R. A., and Dunkley, P. N. (1984). The Ordovician Marginal basin of Wales. *Geol. Soc. Lond. Spec. Publications* 16, 245–269. doi:10.1144/GSL.SP.1984.016.01.19

Leys, S. P., and Kahn, A. S. (2018). Oxygen and the Energetic Requirements of the First Multicellular Animals. *Integr. Comp. Biol.* 58, 666–676. doi:10.1093/icb/icy051

Linnemann, U., Herbosch, A., Liégeois, J.-P., Pin, C., Gärtner, A., and Hofmann, M. (2012). The Cambrian to Devonian Odyssey of the Brabant Massif within Avalonia: A Review with New Zircon Ages, Geochemistry, Sm-Nd Isotopes, Stratigraphy and Palaeogeography. *Earth-Science Rev.* 112, 126–154. doi:10.1016/j.earscirev.2012.02.007

Lu, W., Ridgwell, A., Thomas, E., Hardisty, D. S., Luo, G., Algeo, T. J., et al. (2018). Late Inception of a Resiliently Oxygenated Upper Ocean. *Science* 361, 174–177. doi:10.1126/science.aar5372

Matheson, E. J., and Frank, T. D. (2020). Phosphorites, Glass Ramps and Carbonate Factories: the Evolution of an Epicontinental Sea and a Late Palaeozoic Upwelling System (Phosphoria Rock Complex). *Sedimentology*. doi:10.1111/sed.12731

Matheson, E. J., and Pufahl, P. K. (2021). Clinton Ironstone Revisited and Implications for Silurian Earth System Evolution. *Earth-Science Rev.* 215, 103527–103535. doi:10.1016/j.earscirev.2021.103527

McKenzie, N. R., and Jiang, H. (2019). Earth's Outgassing and Climatic Transitions: The Slow Burn towards Environmental "Catastrophes"? *Elements* 15, 325–330. doi:10.2138/gselements.15.5.325

McLennan, S. M. (1989). Chapter 7. RARE EARTH ELEMENTS IN SEDIMENTARY ROCKS: INFLUENCE of PROVENANCE and SEDIMENTARY PROCESSES. *Rev. Mineralogy* 21, 169–200. doi:10.1515/9781501509032-010

Montero, P., Talavera, C., Bea, F., Lodeiro, F. G., and Whitehouse, M. J. (2009). Zircon Geochronology of the Ollo de Sapo Formation and the Age of the Cambro-Ordovician Rifting in Iberia. *J. Geology.* 117, 174–191. doi:10.1086/595017

Morgan, J. W., Higuchi, H., Takahashi, H., and Hertogen, J. (1978). A "Chondritic" Eucrite Parent Body: Inference from Trace Elements. *Geochimica et Cosmochimica Acta* 42, 27–38. doi:10.1016/0016-7037(78)90213-2

Mulhern, J. S., Johnson, C. L., and Martin, J. M. (2019). Modern to Ancient Barrier Island Dimensional Comparisons: Implications for Analog Selection and Paleomorphodynamics. *Front. Earth Sci.* 7. doi:10.3389/feart.2019.00109

Murphy, J. B., Cameron, K., Dostal, J., Keppie, J. D., and Hynes, A. J. (1985). Cambrian Volcanism in Nova Scotia, Canada. *Can. J. Earth Sci.* 22, 599–606. doi:10.1139/e85-059

Murphy, J. B., Dostal, J., and Keppie, J. D. (2008). Neoproterozoic-Early Devonian Magmatism in the Antigonish Highlands, Avalon Terrane, Nova Scotia: Tracking the Evolution of the Mantle and Crustal Sources during the Evolution of the Rheic Ocean. *Tectonophysics* 461, 181–201. doi:10.1016/j.tecto.2008.02.003

Murphy, J. B., Fernández-Suárez, J., and Jeffries, T. E. (2004). Lithogeochemical and Sm-Nd and U-Pb Isotope Data from the Silurian-Lower Devonian Arisaig Group Clastic Rocks, Avalon Terrane, Nova Scotia: A Record of Terrane Accretion in the Appalachian-Caledonide Orogen. *Geol. Soc. America Bull.* 116, 1183–1201. doi:10.1130/B25423.1

Murphy, J. B., Nance, R. D., Cawood, P. A., Collins, W. J., Dan, W., Doucet, L., et al. (2021). "Pannotia: In Defence of its Existence and Geodynamic Significance," in *Pannotia to Pangea: Neoproterozoic and Paleozoic Orogenic Cycles in the Circum-North Atlantic Region*. Editors J. B. Murphy, R. A. Strachan, and C. Quesada (Bath, UK: Geological Society, London, Special Publication), 503, 13–39. doi:10.1144/sp503

Murphy, J. B., Nance, R. D., and Cawood, P. A. (2009). Contrasting Modes of Supercontinent Formation and the Conundrum of Pangea. *Gondwana Res.* 15, 408–420. doi:10.1016/j.gr.2008.09.005

Nance, R. D., Gutiérrez-Alonso, G., Keppie, J. D., Linnemann, U., Murphy, J. B., Quesada, C., et al. (2010). Evolution of the Rheic Ocean. *Gondwana Res.* 17, 194–222. doi:10.1016/j.gr.2009.08.001

Nesse, W. (2015). *"Silicates," in Introduction to Mineralogy*. Oxford, United Kingdom: Oxford University Press, 183–200.

Och, L. M., and Shields-Zhou, G. A. (2012). The Neoproterozoic Oxygenation Event: Environmental Perturbations and Biogeochemical Cycling. *Earth-Science Rev.* 110, 26–57. doi:10.1016/j.earscirev.2011.09.004

Ohta, A., and Kawabe, I. (2001). REE(III) Adsorption onto Mn Dioxide (δ-MnO2) and Fe Oxyhydroxide: Ce(III) Oxidation by δ-MnO2. *Geochimica et Cosmochimica Acta* 65, 695–703. doi:10.1016/S0016-7037(00)00578-0

Olivarez, A. M., and Owen, R. M. (1991). The Europium Anomaly of Seawater: Implications for Fluvial versus Hydrothermal REE Inputs to the Oceans. *Chem. Geology.* 92, 317–328. doi:10.1016/0009-2541(91)90076-4

Parrish, J. T. (1982). Upwelling and Petroleum Source Beds, with Reference to Paleozoic. *Am. Assoc. Pet. Geol. Bull* 66, 750–774. doi:10.1306/03B5A30E-16D1-11D7-8645000102C1865D

Petránek, J. (1991). Ordovician Oolitic Ironstones and Their Source of Iron. *Věst. Ústř. Úst. geol.(Praha)* 66, 321–327.

Piper, D. Z., Baedecker, P. A., Crock, J. G., Burnett, W. C., and Loebner, B. J. (1988). Rare Earth Elements in the Phosphatic-Enriched Sediment of the Peru Shelf. *Mar. Geology.* 80, 269–285. doi:10.1016/0025-3227(88)90093-x

Piper, D. Z., and Calvert, S. E. (2009). A marine Biogeochemical Perspective on Black Shale Deposition. *Earth-Science Rev.* 95, 63–96. doi:10.1016/j.earscirev.2009.03.001

Planavsky, N., Bekker, A., Rouxel, O. J., Kamber, B., Hofmann, A., Knudsen, A., et al. (2010). Rare Earth Element and Yttrium Compositions of Archean and Paleoproterozoic Fe Formations Revisited: New Perspectives on the Significance and Mechanisms of Deposition. *Geochimica et Cosmochimica Acta* 74, 6387–6405. doi:10.1016/j.gca.2010.07.021

Plint, A. G. (2010). "Wave- and Storm-Dominated Shallow marine Systems," in *In Facies Models 4*. Editors N. P. James and R. W. Dalrymple (St. John's, Canada: Geological Association of Canada)), 167–199.

Pohl, A., Nardin, E., Vandenbroucke, T. R. A., and Donnadieu, Y. (2016). High Dependence of Ordovician Ocean Surface Circulation on Atmospheric CO2 Levels. *Palaeogeogr. Palaeoclimatol. Palaeoecol.* 458, 39–51. doi:10.1016/j.palaeo.2015.09.036

Pothier, H. D., Waldron, J. W. F., Schofield, D. I., and DuFrane, S. A. (2015). Peri-Gondwanan Terrane Interactions Recorded in the Cambrian-Ordovician Detrital Zircon Geochronology of North Wales. *Gondwana Res.* 28, 987–1001. doi:10.1016/j.gr.2014.08.009

Prigmore, J. K., Butler, A. J., and Woodcock, N. H. (1997). Rifting during Separation of Eastern Avalonia from Gondwana: Evidence from Subsidence Analysis. *Geol* 25, 203–206. doi:10.1130/0091-7613(1997)025<0203:rdsoea>2.3.co;2

Pufahl, P. K. (2010). in *"Bioelemental Sediments," in Facies Models 4*. Editors N. P. James and R. W. Dalrymple (St. John's, Canada: Geological Association of Canada)), 477–504.

Pufahl, P. K., and Grimm, K. A. (2003). Coated Phosphate Grains: Proxy for Physical, Chemical, and Ecological Changes in Seawater. *Geol* 31, 801–804. doi:10.1130/G19658.1

Pufahl, P. K., and Groat, L. A. (2017). Sedimentary and Igneous Phosphate Deposits: Formation and Exploration: An Invited Paper. *Econ. Geology.* 112, 483–516. doi:10.2113/econgeo.112.3.483

Pufahl, P. K., Squires, A. D., Murphy, J. B., Quesada, C., Lokier, S. W., Álvaro, J. J., et al. (2020). Ordovician Ironstone of the Iberian Margin: Coastal Upwelling, Ocean Anoxia and Palaeozoic Biodiversity. *Depositional Rec.* 6, 581–604. doi:10.1002/dep2.113

Quin, J. G. (2011). Is Most Hummocky Cross-Stratification Formed by Large-Scale Ripples? *Sedimentology* 58, 1414–1433. doi:10.1111/j.1365-3091.2010.01219.x

Raiswell, R., and Canfield, D. E. (2012). The Iron Biogeochemical Cycle Past and Present. *GeochemPersp* 1, 1–220. doi:10.7185/geochempersp.1.1

Raiswell, R. (2011). Iron Transport from the Continents to the Open Ocean: The Aging-Rejuvenation Cycle. *Elements* 7, 101–106. doi:10.2113/gselements.7.2.101

Rushton, A. W. A., and Fortey, R. A. (2000). "North Wales," in *A Revised Correlation Ordovician Rocks*. R. A. Fortey, D. A. T. Harper, J. K. Ingham, A. W. Owen, M. A. Parkes, A. W. A. Rushton, et al. (Bath, UK: Geological Society of London), 18–24. doi:10.1144/SR24.5

Rushton, A. W. A., and Howells, M. F. (1998). *Stratigraphical Framework for the Ordovician of Snowdonia and the Lleyn Peninsula: A Discussion of the Tremadoc to Caradoc Rocks Lying between the Menai Straits and the Llanderfel Syncline, and Including an Appendix on Cambrian Rocks*. Keyworth: British Geological Survey). Report No. RR/98/001.

Sánchez-García, T., Bellido, F., and Quesada, C. (2003). Geodynamic Setting and Geochemical Signatures of Cambrian–Ordovician Rift-Related Igneous Rocks (Ossa-Morena Zone, SW, Iberia). *Tectonophysics* 365, 233–255. doi:10.1016/s0040-1951(03)00024-6

Sánchez-García, T., Quesada, C., Bellido, F., Dunning, G. R., and González del Tánago, J. (2008). Two-step Magma Flooding of the Upper Crust during Rifting: The Early Paleozoic of the Ossa Morena Zone (SW Iberia). *Tectonophysics* 461, 72–90. doi:10.1016/j.tecto.2008.03.006

Schieber, J. (2002). Sedimentary Pyrite: A Window into the Microbial Past. *Geology*, 30, 2. doi:10.1130/0091-7613(2002)030<0531:spawit>2.0.co;2

Schieber, J. (2003). Simple Gifts and Buried Treasures-Implications of Finding Bioturbation and Erosion Surfaces in Black Shales. *Sed Rec.* 1, 4–8. doi:10.2110/sedred.2003.2.4

Scott, C., and Lyons, T. W. (2012). Contrasting Molybdenum Cycling and Isotopic Properties in Euxinic versus Non-euxinic Sediments and Sedimentary Rocks: Refining the Paleoproxies. *Chem. Geology.* 324-325 (325), 19–27. doi:10.1016/j.chemgeo.2012.05.012

Servais, T., Harper, D. A. T., Munnecke, A., Owen, A. W., and Sheehan, P. M. (2009). Understanding the Great Ordovician Biodiversification Event (GOBE): Influences of Paleogeography, Paleoclimate, or Paleoecology. *GSA Today* 19, 4–10. doi:10.1130/gsatg37a.1

Servais, T., Owen, A. W., Harper, D. A. T., Kröger, B., and Munnecke, A. (2010). The Great Ordovician Biodiversification Event (GOBE): The Palaeoecological Dimension. *Palaeogeogr. Palaeoclimatol. Palaeoecol.* 294, 99–119. doi:10.1016/j.palaeo.2010.05.031

Shanmugam, G., Spalding, T. D., and Rofheart, D. H. (1993). Traction Structures in deep-marine, Bottom-Current-Reworked Sands in the Pliocene and Pleistocene, Gulf of Mexico. *Geology* 21, 929–932. doi:10.1130/0091-7613(1993)021<0929:TSIDMB>2.3.CO;2

Shields, G. A. (2017). "Earth System Transition during the Tonian-Cambrian Interval of Biological Innovation: Nutrients, Climate, Oxygen and the marine Organic Carbon Capacitor," in *In Earth System Evolution and Early Life: A Celebration of the Work of Martin Brasier*. Editors A. T. Brasier, D. McIlroy, and N. McLoughlin (London): Geological Society), 448, 161–177. doi:10.1144/sp448.17*Geol. Soc. Lond. Spec. Publications*

Smit, J., Laffra, C., Meulenaars, K., and Montanari, A. (2012). Probable Late Messinian Tsunamiites Near Monte Dei Corvi, Italy, and the Nijar Basin, Spain: Expected Architecture of Offshore Tsunami Deposits. *Nat. Hazards* 63, 241–266. doi:10.1007/s11069-011-9947-9

Sørensen, B. E. (2013). A Revised Michel-Lévy Interference Colour Chart Based on First-Principles Calculations. *ejm* 25, 5–10. doi:10.1127/0935-1221/2013/0025-2252

Strahan, A., Gibson, W., Cantrill, T. C., Sherlock, R. L., and Dewey, H. (1920). *Iron Ores (contd.) Pre-carboniferous and Carboniferous Bedded Ores of England and Wales*, Vol. XIII. London): The Lords Commissioner of His Majesty's Treasury, 131.

Sturesson, U., Heikoop, J. M., and Risk, M. J. (2000). Modern and Palaeozoic Iron Ooids-A Similar Volcanic Origin. *Sediment. Geology.* 136, 137–146. doi:10.1016/S0037-0738(00)00091-9

Suess, E., Von Huene, R., et al. (1990). *Proceedings of the Ocean Drilling Program, Scientific Results, 112*, College Station: Ocean Drilling Program.

Talavera, C., Martínez Poyatos, D., and González Lodeiro, F. (2015). SHRIMP U-Pb Geochronological Constraints on the Timing of the Intra-alcudian (Cadomian) Angular Unconformity in the Central Iberian Zone (Iberian Massif, Spain). *Int. J. Earth Sci. (Geol Rundsch)* 104, 1739–1757. doi:10.1007/s00531-015-1171-5

Taylor, K. G., and Konhauser, K. O. (2011). Iron in Earth Surface Systems: A Major Player in Chemical and Biological Processes. *Elements* 7, 83–88. doi:10.2113/gselements.7.2.83

Taylor, K. G., and Macquaker, J. H. S. (2000). Early Diagenetic Pyrite Morphology in a Mudstone-Dominated Succession: the Lower Jurassic Cleveland Ironstone Formation, Eastern England. *Sediment. Geology.* 131, 77–86. doi:10.1016/S0037-0738(00)00002-6

Taylor, K. G., and Macquaker, J. H. S. (2011). Iron Minerals in Marine Sediments Record Chemical Environments. *Elements* 7, 113–118. doi:10.2113/gselements.7.2.113

Terry, R. D., and Chilingar, G. V. (1955). Summary of "Concerning Some Additional Aids in Studying Sedimentary Formations," by M. S. Shvetsov. *J. Sediment. Res.* 25, 229–234. doi:10.1306/74d70466-2b21-11d7-8648000102c1865d

Todd, S. E., Pufahl, P. K., Murphy, J. B., and Taylor, K. G. (2019). Sedimentology and Oceanography of Early Ordovician Ironstone, Bell Island, Newfoundland: Ferruginous Seawater and Upwelling in the Rheic Ocean. *Sediment. Geology.* 379, 1–15. doi:10.1016/j.sedgeo.2018.10.007

Torsvik, T. H., and Cocks, L. R. M. (2013). Chapter 2 New Global Palaeogeographical Reconstructions for the Early Palaeozoic and Their Generation. *Geol. Soc. Lond. Mem.* 38, 5–24. doi:10.1144/M38.2

Torsvik, T. H., and Cocks, L. R. M. (2017). "Climates Past and Present," in *In Earth History and Palaeogeography*. Editors T. H. Torsvik and L. R. M. Cocks (Cambridge: Cambridge University Press), 271–287.

Torsvik, T. H., and Rehnström, E. F. (2003). The Tornquist Sea and Baltica-Avalonia Docking. *Tectonophysics* 362, 67–82. doi:10.1016/S0040-1951(02)00631-5

Trabucho-Alexandre, J. (2015). "Organic Matter-Rich Shale Depositional Environments," in *In Fundamentals of Gas Shale Reservoirs*. Editor R. Rezaee (Hoboken: Wiley), 21–45. doi:10.1002/9781119039228.ch2

Trythall, R. J. B., Eccles, C., Molyneux, S. G., and Taylor, W. E. G. (1987). Age and Controls of Ironstone Deposition (Ordovician) North Wales. *Geol. J.* 22, 31–43. doi:10.1002/gj.3350220505

Van Houten, F. B., and Arthur, M. A. (1989). Temporal Patterns Among Phanerozoic Oolitic Ironstones and Oceanic Anoxia. *Geol. Soc. Lond. Spec. Publications* 46, 33–49. doi:10.1144/GSL.SP.1989.046.01.06

Van Houten, F. B., and Bhattacharyya, D. P. (1982). Phanerozoic Oolitic Ironstones--Geologic Record and Facies Model. *Annu. Rev. Earth Planet. Sci.* 10, 441–457. doi:10.1146/annurev.ea.10.050182.002301

Van Houten, F. B. (2000). "Ooidal Ironstones and Phosphorites-A Comparison from a Stratigrapher's View," in *Marine Authigenesis from Global to Microbial SEPM Special Publication*. Editors C. R. Glenn, L. Prévôt-Lucas, and J. Lucas (Oklahoma: Society for Sedimentary Geology)), 127–132. doi:10.2110/pec.00.66.0127

van Staal, C. R., Barr, S. M., and Murphy, J. B. (2012). Provenance and Tectonic Evolution of Ganderia: Constraints on the Evolution of the Iapetus and Rheic Oceans. *Geology* 40, 987–990. doi:10.1130/g33302.1

van Staal, C. R., Dewey, J. F., Niocaill, C. M., and McKerrow, W. S. (1998). "The Cambrian-Silurian Tectonic Evolution of the Northern Appalachians and British Caledonides: History of a Complex, West and Southwest Pacific-type Segment of Iapetus," in *In Lyell: The Past Is the Key to the Present*. Editors D. J. Blundell and A. C. Scott (London: Geological Society Special PublicationThe Geological Society)), 143, 197–242. doi:10.1144/gsl.sp.1998.143.01.17

Vandenbroucke, T. R. A., Emsbo, P., Munnecke, A., Nuns, N., Duponchel, L., Lepot, K., et al. (2015). Metal-induced Malformations in Early Palaeozoic Plankton Are Harbingers of Mass Extinction. *Nat. Commun.* 6, 7966, 2015 . https://www.nature.com/artic les/ncomm s8966. doi:10.1038/ncomms8966

Veron, J. E. N. (2008). Mass Extinctions and Ocean Acidification: Biological Constraints on Geological Dilemmas. *Coral Reefs* 27, 459–472. doi:10.1007/s00338-008-0381-8

Von Wagoner, J. C., Posamentier, H. W., Mitchum, R. M., Vail, P. R., Sarg, J. F., Loutit, T. S., et al. (1988). "An Overview of Sequence Stratigraphy and Key Definitions," in *Sea Level Changes – an Integrated Approach, SEPM 42*. Editors C.K. Wilgus, B.S. Hastings, C.G.S.C. Kendall, H.W. Posamentier, C.A. Ross, and J.C. Van Wagoner, 39–45.

Walker, L. J., Wilkinson, B. H., and Ivany, L. C. (2002). Continental Drift and Phanerozoic Carbonate Accumulation in Shallow-Shelf and Deep-Marine Settings. *J. Geology.* 110, 75–87. doi:10.1086/324318

Wang, C., Mitchell, R. N., Murphy, J. B., Peng, P., and Spencer, C. J. (2021). The Role of Megacontinents in the Supercontinent Cycle. *Geology* 49, 402–406. doi:10.1130/G47988.1

Watkins, R. T., Ridley, M. K., Pougnet, M. A. B., and Willis, J. P. (1995). Determination of Rare-Earth Elements in Coal Using Microwave Digestion and Gradient Ion Chromatography. *Chem. Geology.* 121, 273–283. doi:10.1016/0009-2541(94)00119-S

Webby, B. (2002). "Patterns of Ordovician Reef Development," in *In Phanerozoic Reef Patterns SEPM Special Publication*. Editors W. Kiessling, E. Flügel, and G. Golonka. doi:10.2110/pec.02.72.0129

Wefer, G., BergerRichter, C., et al. (2002). *Proceedings of the Ocean Drilling Program, Scientific Results, 175*, College Station: Ocean Drilling Program.

Wigley, R. A., and Compton, J. S. (2013). Microstratigraphy of a Miocene Layered Phosphatic Pebble from the Western Margin of South Africa. *Sedimentology* 60, 666–678. doi:10.1111/j.1365-3091.2012.01355.x

Wilde, P., Quinby-Hunt, M. S., and Berry, W. B. N. (1990). "Vertical Advection from Oxic or Anoxic Water from the Main Pycnocline as a Cause of Rapid Extinction or Rapid Radiations," in *In Extinction Events in Earth History*. Editors E.G. Kauffman and O.H. Walliser (Berlin, Heidelberg: Springer-Verlag), 85–98.

Won, M.-Z., and Below, R. (1999). Cambrian Radiolaria from the Georgina Basin, Queensland, Australia. *Micropaleontology* 45, 325–363. doi:10.2307/1486119

Woodcock, N. H. (1990). Sequence Stratigraphy of the Palaeozoic Welsh Basin. *J. Geol. Soc.* 147, 537–547. doi:10.1144/gsjgs.147.3.0537

Yang, G., Li, Y., Santosh, M., Yang, B., Yan, J., Zhang, B., et al. (2012). Geochronology and Geochemistry of Basaltic Rocks from the Sartuohai Ophiolitic Mélange, NW China: Implications for a Devonian Mantle Plume within the Junggar Ocean. *J. Asian Earth Sci.* 59, 141–155. doi:10.1016/j.jseaes.2012.07.020

Yilmaz, İ. Ö., Göncüoğlu, M. C., Demiray, D. G., and Gedik, İ. (2015). An Approach to Paleoclimatic Conditions for Devonian (Upper Lochkovian and Middle Givetian) Ironstone Formation, NW Anatolian Carbonate Platform. *Turkish J. Earth Sci.* 24, 21–38. doi:10.3906/yer-1406-7

Young, T. P. (1989). "Eustatically Controlled Ooidal Ironstone Deposition: Facies Relationships of the Ordovician Open-Shelf Ironstones of Western Europe," in *In Phanerozoic Ironstones Geological Society Special Publication No. 46*. Editors T. P. Young and W. E. G. Taylor (London: Geological Society)), 46, 51–63. doi:10.1144/gsl.sp.1989.046.01.07*Geol. Soc. Lond. Spec. Publications*

Young, T. P., Gibbons, W., and McCarroll, D. (2002). *Geology of the Country Around Pwllheli*. England and WalesLondon: Memoir of the British Geological Survey. Sheet 134.,

Young, T. P. (1992). Ooidal Ironstones from Ordovician Gondwana: a Review. *Palaeogeogr. Palaeoclimatol. Palaeoecol.* 99, 321–347. doi:10.1016/0031-0182(92)90021-V

Young, T. P., Young, T. P., and Taylor, W. E. G. (1989). "Phanerozoic Ironstones: an Introduction and Review," in *Phanerozoic Ironstones Geological Society Special Publications No 46* (London: Geological Society)), ix–xxv. doi:10.1144/gsl.sp.1989.046.01.02

Conflict of Interest: The authors declare that the research was conducted in the absence of any commercial or financial relationships that could be construed as a potential conflict of interest.

Publisher's Note: All claims expressed in this article are solely those of the authors and do not necessarily represent those of their affiliated organizations, or those of the publisher, the editors and the reviewers. Any product that may be evaluated in this article, or claim that may be made by its manufacturer, is not guaranteed or endorsed by the publisher.

frontiers in Earth Science

ORIGINAL RESEARCH
published: 28 October 2021
doi: 10.3389/feart.2021.716416

Anthropogenic Inputs of Terrestrial Organic Matter Influence Carbon Loading and Methanogenesis in Coastal Baltic Sea Sediments

Tom Jilbert[1,2,3], Greg Cowie[4], Luukas Lintumäki[3], Sami Jokinen[1,5], Eero Asmala[1,2], Xiaole Sun[6], Carl-Magnus Mörth[6], Alf Norkko[2,6] and Christoph Humborg[2,6]*

[1]Aquatic Biogeochemistry Research Unit, Ecosystems and Environment Research Program, Faculty of Biological and Environmental Sciences, University of Helsinki, Helsinki, Finland, [2]Tvärminne Zoological Station, University of Helsinki, Hanko, Finland, [3]Department of Geosciences and Geography, Faculty of Science, University of Helsinki, Helsinki, Finland, [4]Marine Geosciences Group, School of Geosciences, Edinburgh University, Edinburgh, United Kingdom, [5]Marine Geology, Geological Survey of Finland (GTK), Espoo, Finland, [6]Baltic Sea Centre, Stockholm University, Stockholm, Sweden

OPEN ACCESS

Edited by:
Christian März,
University of Leeds, United Kingdom

Reviewed by:
Tobias Goldhammer,
Leibniz-Institute of Freshwater Ecology and Inland Fisheries (IGB), Germany
Laura Lapham,
University of Maryland Center for Environmental Science (UMCES), United States

***Correspondence:**
Tom Jilbert
tom.jilbert@helsinki.fi

Specialty section:
This article was submitted to Biogeoscience, a section of the journal Frontiers in Earth Science

Received: 28 May 2021
Accepted: 08 October 2021
Published: 28 October 2021

Citation:
Jilbert T, Cowie G, Lintumäki L, Jokinen S, Asmala E, Sun X, Mörth C-M, Norkko A and Humborg C (2021) Anthropogenic Inputs of Terrestrial Organic Matter Influence Carbon Loading and Methanogenesis in Coastal Baltic Sea Sediments. Front. Earth Sci. 9:716416. doi: 10.3389/feart.2021.716416

Coastal regions globally have experienced widespread anthropogenic eutrophication in recent decades. Loading of autochthonous carbon to coastal sediments enhances the demand for electron acceptors for microbial remineralization, often leading to rearrangement of the sediment diagenetic zonation and potentially enhancing fluxes of methane and hydrogen sulfide from the seafloor. However, the role of anthropogenic inputs of terrestrial organic matter ($OM_{terr.}$) in modulating diagenesis in coastal sediments is often overlooked, despite being of potential importance in regions of land-use and industrial change. Here we present a dated 4-m sediment and porewater geochemistry record from a eutrophic coastal location in the northern Baltic Sea, to investigate sources of recent carbon loading and their impact on modern diagenetic processes. Based on an end-member mixing model of sediment N/C ratios, we observe that a significant fraction of the late-20th century carbon loading at this location was contributed by $OM_{terr.}$. Furthermore, analysis of lignin in this material shows depleted ratios of syringyl/vanillyl (S/V) and cinnamyl/vanillyl (C/V) phenols, indicative of enhanced inputs of woody gymnosperm tissue likely from forest industries. The rapid loading of organic matter from combined terrestrial and autochthonous sources during the late 20th century has stimulated methanogenesis in the sediment column, and shoaled the sulfate-methane transition zone (SMTZ) to a depth of 5–20 cm. Optical parameters of colored dissolved organic matter confirm that $OM_{terr.}$ is actively degrading in the methanogenic layer, implying a role for this material in diagenetic processes. Porewater CH_4, SO_4^{2-} δ^{13}C-DIC, and $\sum S^{2-}$ data suggest that the modern SMTZ is a broad zone in which organoclastic sulfate reduction, methanogenesis and anaerobic oxidation of methane (AOM) co-occur. However, fluxes of CH_4 and SO_4^{2-} show that rates of these processes are similar to other marine locations with a comparably shallow SMTZ. We suggest that the shallow depth of the modern SMTZ is the principal reason for high observed diffusive and ebullitive methane fluxes from sediments in this area. Our results highlight that anthropogenic activities lead to multiple pathways of carbon loading to coastal

sediments, and that forest industry impacts on sedimentation in the northern Baltic Sea may be more widespread than previously acknowledged.

Keywords: terrestrial organic matter, forestry, lignin, diagenesis, methane, blue carbon, baltic sea

INTRODUCTION

Anthropogenic impacts on coastal environments have accelerated in parallel with industrialization during the late 20th century (Diaz and Rosenberg, 2008). Among the most widespread and important impacts is eutrophication, defined as an increased supply of organic matter to a coastal ecosystem (Nixon, 1995), and often primarily driven by enhancement of autochthonous productivity due to loading of nutrients such as nitrogen and phosphorus (Bonsdorff et al., 1997; Anderson et al., 2002). Eutrophication increases the amount of fixed organic carbon in coastal ecosystems and alters the primary producer community structure (Heisler et al., 2008), consequently raising the oxygen demand of microbial remineralization of organic matter (OM) (Middelburg and Levin, 2009; Breitburg et al., 2018). In turn, consumption of oxygen leads to further ecosystem impacts associated with benthic hypoxia (Carstensen et al., 2014; Rabalais et al., 2014). Because a significant fraction of OM remineralization in shallow coastal systems takes place in the underlying sediments, eutrophication can severely impact rates of microbial processes in the sediment column. Ultimately, these processes dictate the rate of organic carbon turnover and burial (Arndt et al., 2013) and hence play a critical role in the global carbon cycle.

One of the key consequences of eutrophication for coastal sediment microbial processes is to enhance rates of anaerobic remineralization after the exhaustion of oxygen (Middelburg and Levin, 2009). Organoclastic sulfate reduction is the dominant pathway of anaerobic remineralization in marine sediments (Jorgensen, 1982; Canfield, 1991; Bowles et al., 2014), but in settings with low salinity and high flux of sedimenting OM, sulfate may become completely exhausted within the upper sediment column (e.g., Slomp et al., 2013; Thang et al., 2013). In such cases, a significant fraction of OM remineralization occurs through methanogenesis (Rooze et al., 2016), creating the potential for emissions of this potent greenhouse gas to the water column and ultimately the atmosphere (Bange et al., 1994; Gelesh et al., 2016; Humborg et al., 2019; Myllykangas et al., 2020a). Many studies have demonstrated the presence of methane within the uppermost meter of the sediment column in low-salinity coastal settings (e.g., Albert et al., 1998; Martens et al., 1998; Mogollon et al., 2011; Egger et al., 2015), and human-impacted estuaries are considered hotspots for methane emissions (Borges and Abril, 2011). Because such emissions may offset the climate benefits of carbon burial (Dean et al., 2018), it is essential to understand the controls on methanogenesis in human-impacted coastal sediments.

Associated to changes in vertical zonation of primary anaerobic remineralization pathways, eutrophication can also strongly modify the network of secondary microbial processes in the sediment column. For example, a key consequence of enhanced methanogenesis in human-impacted systems is enhanced rates of anaerobic oxidation of methane (AOM). This process proceeds mainly through coupling to sulfate reduction at the so-called sulfate methane transition zone (SMTZ) (Knittel and Boetius, 2009), but can also be coupled to reduction of nitrate (Ettwig et al., 2010) or metal oxides (Beal et al., 2009; Sivan et al., 2011; Egger et al., 2015). Crucially, AOM strongly reduces the fluxes of methane from the sediments to the water column relative to the amount of methane produced during sedimentary methanogenesis, thus acting as a filter for methane emissions (Dean et al., 2018).

In addition to inputs of autochthonous OM, coastal sediments also receive carbon loading from terrestrial organic matter ($OM_{terr.}$) (Blair and Aller, 2012). Up to 200 Tg particulate organic carbon (POC) are delivered by rivers to coastal environments annually (Schlunz and Schneider, 2000), while a similar flux has been calculated for dissolved organic carbon (DOC) (Dai et al., 2012). The DOC contribution typically dominates $OM_{terr.}$ inputs in boreal systems (e.g. Mattsson et al., 2005). The importance of DOC inputs for coastal sediment carbon loading in the Baltic Sea is not well constrained, but several studies have suggested that salt-mediated flocculation may transfer carbon from the dissolved to particulate phase at the land-sea transition (Sholkovitz et al., 1978; Asmala et al., 2014; Jilbert et al., 2018). Typically, the reactivity of $OM_{terr.}$ in microbial remineralization is considered lower than that of autochthonous material (Hedges et al., 2000). This is due to a combination of its refractory molecular composition, being dominated by lignin, cellulose and cutin (de Leeuw and Largeau, 1993) and physical association to protective minerogenic material prior to deposition (Mayer, 1994; Hedges and Keil, 1995). However, riverine fluxes, molecular composition and biological reactivity of OM_{terr} have been shown to be sensitive to anthropogenic activities such as deforestation, ditching, agriculture and industry (e.g., Lambert et al., 2017; Asmala et al., 2019; Deininger and Frigstad, 2019; Landsman-Gerjoi et al., 2020). Rapid inputs of such "anthropogenic" $OM_{terr.}$ to coastal sediments may be expected to confer higher reactivity to $OM_{terr.}$ in the sediment column. Yet, few studies have explicitly investigated the impacts of anthropogenic $OM_{terr.}$ inputs on coastal sediment biogeochemistry.

In boreal regions, a key driver of anthropogenic $OM_{terr.}$ inputs to the marine environment over the last century is forestry and the associated paper and pulp industry. Forest industry processes, including debarking, pulping, bleaching and washing (Ali and Sreekrishnan, 2001), have introduced large point-source emissions of raw and processed $OM_{terr.}$ to aquatic systems, in many cases proximal to the coastal environment (Pocklington and McGregor, 1973; Louchouarn et al., 1999; Brandenberger et al., 2011). The molecular composition of solid forest industry

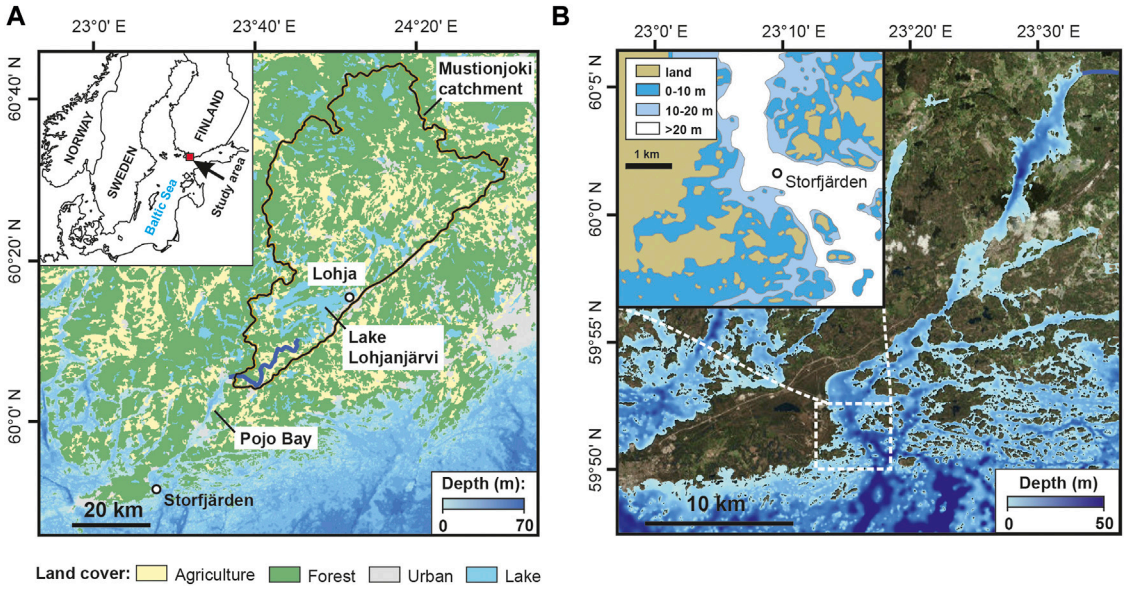

FIGURE 1 | Location of the study. **(A)** (inset) Study area in the northern Baltic Sea. (main) Catchment of the Mustionjoki river (black) showing the location of the city of Lohja and adjacent Lake Lohjanjärvi. Blue line shows the Mustionjoki river itself, connecting the catchment to the Pojo Bay estuarine system draining into Storfjärden. **(B)** (main) location of Storfjärden at the southern end of the estuary. (inset) zoom of the coring location in Storfjärden.

wastes in sediments includes the major wood polymers cellulose and lignin (Louchouarn et al., 1997; Dahlberg et al., 2020), together with a wide array of additional compounds from the raw material and its treatment processes, including tannins, resin acids, and polychlorinated biphenyls (PCBs) (Lacorte et al., 2003). Sedimentary contents of such materials have been shown to vary with distance from industrial sources, with the most concentrated deposits (e.g., cellulose-rich *fiberbanks*) consisting of nearly pure organic material (Dahlberg et al., 2020; Dahlberg et al., 2021).

To date, several studies have used organic biomarkers such as lignin phenols and persistent organic pollutants (POPs) to identify the presence of forest industry-derived anthropogenic $OM_{terr.}$ in boreal coastal sediments, and to quantify its local contribution to total $OM_{terr.}$ or total sedimentary organic matter (e.g., Louchouaran et al., 1997; 1999; Dahlberg et al., 2020). However, few studies have combined these analyses with a porewater biogeochemistry approach to determine the potential role of such inputs on sediment diagenetic processes, including methanogenesis. This is an important gap in knowledge, since $OM_{terr.}$ has been shown to promote methanogenesis in lakes (Tittel el al., 2019) and fiberbank material in particular shows strong methanogenic potential (Kokko et al., 2018). Here, we employ a comprehensive analysis of sediment bulk inorganic and organic chemical parameters, including lignin phenol analysis, coupled to detailed porewater chemical profiling, to determine the impacts of recent anthropogenic $OM_{terr.}$ inputs on diagenesis at a site in the northern Baltic Sea. The site is located tens of kilometers from the nearest forest industry point source, allowing investigation of larger spatial-scale impacts of anthropogenic $OM_{terr.}$ than previous studies focused on fiberbanks close to industrial point sources.

SITE DESCRIPTION

The Baltic Sea is a landlocked brackish marine system in northern Europe with a N-S salinity gradient of 3–15 (Leppäranta and Myrberg, 2009). The whole Baltic Sea was strongly eutrophied by nutrient loading during the 20th century (Gustafsson et al., 2012), leading to the development of widespread deep water hypoxia and anoxia in the central basins (Conley et al., 2009). Many coastal areas have shown localized trends towards oxygen depletion during recent decades, as a consequence of direct nutrient inputs from adjacent land areas leading to coastal eutrophication (Conley et al., 2011). The contribution of $OM_{terr.}$ to Baltic Sea sediments as a whole is estimated as ≤30% of total OM, with a N-S compositional gradient from gymnosperm-to angiosperm-dominated material (Miltner and Emeis, 2001). A recent study demonstrated clearly higher $OM_{terr.}$ contributions to sedimentary carbon in northern areas such as the Gulf of Bothnia and Gulf of Finland (Nilsson et al., 2021).

This study focuses on the Storfjärden site on the Finnish coast of the Gulf of Finland in the northern Baltic Sea (**Figure 1**). Storfjärden is a shallow coastal basin forming part of the Tvärminne archipelago system at the mouth of the Pojo Bay estuary, draining the Mustionjoki river catchment in southern Finland. Since the most recent deglaciation at 12250 cal year BP, Storfjärden has been successively covered by late- and post-glacial lacustrine clays and most recently by brackish-water muds (Virtasalo et al., 2014; Virtasalo., 2019). The Gulf of Finland

TABLE 1 | Sediment cores on which geochemical analyses of porewaters and sediments were performed, along with depth intervals presented in this study. For GEMAX cores from 2015, sediment parameters derive from the April core, while porewater parameters derive from the June core.

	Porewater parameters							Sediment parameters			
	NH_4^+	Alk	δ^{13}C-DIC	S (ICP-OES)	$\sum S^{2-}$	CH_4	DOM (peak C, HIX)	Pb_{tot}, $^{206/207}Pb$	C, N	Lignin phenols	Fe, Mn, S (ICP-OES)
GEMAX April/June 2015 0–40 cm	●				●[a]			●	●	●	●[a]
GEMAX Sept. 2018 0–60 cm		●	●	●		●					
GEMAX June 2020 0–60 cm							●				
Piston Sept. 2017 40–400 cm	●							●	●	●	●
Piston Sept. 2018 60–550 cm		●	●	●		●	●				

[a]*Data reproduced from Jilbert et al. (2018).*

coastal areas were affected by eutrophication during the 20th century (Weckström, 2006), and the majority of the OM in the modern sediments is derived from autochthonous production (Jilbert et al., 2018). However, Jokinen et al. (2020) measured elevated contents of $OM_{terr.}$ in nearby sediments during the depositional interval corresponding to the late 20th century, suggesting an anthropogenic influence on $OM_{terr.}$ fluxes from the Mustionjoki catchment during this period. The city of Lohja in the southern part of the catchment has been a major center of the Finnish pulp and paper industry since the early 20th century (Katko et al., 2005).

MATERIALS AND METHODS

Sediment Coring

Sediments were collected from the Storfjärden site (33 m water depth, **Figure 1**) during various sampling campaigns from 2015 to 2020, onboard the vessels R/V Saduria, R/V Electra and R/V Augusta (**Table 1**). A twin-barrel GEMAX coring device was used to recover the intact sediment surface and approximately the uppermost half meter of the sediment column. A piston corer onboard R/V Electra was used to recover longer sediment cores (max. length 4.5 m in September 2017; 5.5 m in September 2018). Seasonal changes in sediment and porewater chemistry on the decimeter scale are known to be minimal at this site (Myllykangas et al., 2020a), hence the figures in this paper present combined data from multiple sampling campaigns.

Porewater Sampling and Treatment

Porewater samples for most parameters were collected with Rhizons™ (pore size 0.15 µm). For each core, a vertical series of holes (diameter 4 mm) was pre-drilled into the liner and taped prior to sampling (resolution 2 cm for GEMAX cores, 10 cm for piston cores). After core recovery, the tape was penetrated and Rhizons™ inserted. Porewater was collected under vacuum in an attached plastic syringe and transferred to vials for subsampling. After transfer from the syringes, subsampling and treatment were performed immediately to minimize oxidation artefacts. Subsamples for analysis of dissolved sulfur (S) by ICP-OES were acidified with 10–20 µl 65% HNO_3 per ml. Subsamples for analysis of ammonium were frozen. Subsamples for analysis of δ^{13}C-DIC were injected into helium-flushed glass vials (Labco 12 ml Exetainer, model 738W) pre-loaded with 0.1 ml H_3PO_4 per ml. Finally, subsamples for analysis of total alkalinity (Alk_T), and of optical characteristics of colored and fluorescent dissolved organic matter (CDOM and FDOM), were stored at 4°C. For determination of total dissolved sulfide ($\sum S^{2-}$) in the GEMAX core of June 2015, a series of syringes were pre-loaded with 1 ml 10% w/v zinc acetate solution prior to sampling with Rhizons™. Samples were stored at room temperature after precipitation of zinc sulfide (ZnS).

Porewater samples for dissolved methane were collected as described in Egger et al. (2015) and Myllykangas et al. (2020a). Briefly, core liners were pre-drilled with a series of holes (diameter 30 mm) and taped prior to sampling (resolution 2.5 cm for GEMAX cores, 10 cm for piston cores). A 10 ml sample of wet sediment was extracted using a cut-off plastic syringe and transferred directly into a 65-ml glass bottle containing supersaturated NaCl solution. The bottles were closed with a butyl rubber stopper and screw cap. A headspace of 10 ml N_2 gas (purity 5.0) was injected through the stopper within 24 h of sampling and bottles were stored inverted until analysis.

Porewater Analyses

Dissolved S was determined by ICP-OES after dilution (Thermo iCAP 6000 at University of Helsinki), and is assumed to predominantly represent SO_4^{2-}. Hydrogen sulfide (H_2S) is lost during acidification hence does not contribute to dissolved S in the ICP-OES subsample (Jilbert and Slomp, 2013). We acknowledge that at low SO_4^{2-} concentrations, such as in deeper layers of the sediments, non-zero dissolved S values may indicate the presence of dissolved organic sulfur (Jilbert et al., 2020). However, the present study focuses on S gradients in the near-surface sediments, where this fraction is considered negligible, hence we assume dissolved S ≈ SO_4^{2-}. Reproducibility of the ICP-OES analyses is <5% RSD. Dissolved ammonium (NH_4^+) was determined by the indophenol method (Koroleff, 1976) using an autoanalyzer (Lachat QuikChem 8000, reproducibility <5% RSD). Analysis of δ^{13}C-DIC in headspace gas from the H_3PO_4-acidified vials was performed on a Thermo Gasbench II coupled to a MAT 253 mass spectrometer at Stockholm University and is reported in conventional delta notation relative to Vienna PeeDee Belemnite (VPDB). Standard deviation was less than 0.1‰.

Total alkalinity (Alk_T) was determined by HCl titration with a Metrohm Titrando 809 (reproducibility <2% RSD).

Total dissolved sulfide ($\sum S^{2-}$) concentrations in the Zn acetate-treated samples from June 2015 were determined by spectrophotometry (670 nm) after direct addition of an acidic solution of $FeCl_3$ and n,n-dimethyl-p-phenylenediamine (Cline, 1969; Reese et al., 2011) to the sample vials. The procedure dissolves the ZnS precipitate and immediately complexes S as methylene blue for spectrophotometric analysis. Total dissolved sulfide concentrations were calibrated against a series of standard solutions of $Na_2S{\cdot}3H_2O$, fixed in Zn acetate in the same manner as the samples. The exact concentration of S in the $Na_2S{\cdot}3H_2O$ stock solution was determined by iodometric titration (Burton et al., 2008).

Dissolved methane (CH_4) concentrations were determined by gas chromatography. Subsamples of 1 ml were taken from the headspace of each 65 ml glass bottle with a gas-tight glass syringe and transferred to evacuated 12-ml glass tubes with a butyl rubber septum (LabCo Exetainer™ model 839W). Exetainers were then pressurized with 20 ml N_2 (purity 5.0). The mole fraction of methane in headspace of the samples was analyzed with a FID-equipped gas chromatograph (Agilent Technologies 7890B, University of Helsinki) against a standard series of known CH_4 concentrations. Porewater concentrations were calculated assuming quantitative evolution of methane into the headspace from the original 10 ml wet sediment sample, using the measured porosity profile from sediment sample processing. Due to use of unpressurized coring apparatus and sampling on deck, partial degassing of CH_4 from the cores after recovery cannot be avoided (e.g. Thang et al., 2013; Egger et al., 2016). The saturation concentration range of CH_4 at *in situ* salinity, 1 atm pressure and range of temperatures experienced on deck is therefore given in the plots of dissolved CH_4 concentrations to assess the potential impact of degassing.

Absorbance of CDOM was determined using a Shimadzu 2401PC spectrophotometer with 5-cm quartz cuvette (spectral range from 200 to 800 nm with 1 nm resolution). Excitation–emission matrices (EEMs) of FDOM were determined with a Varian Cary Eclipse spectrofluorometer (Agilent). Ultrapure water was used as the blank for all samples, and EEMs were corrected and optical proxies extracted as in Asmala et al. (2018).

Porewater Data Processing

GEMAX and piston core profiles were spliced on the basis of overlaps in the NH_4^+ and Alk_T data. For the purposes of this study, we apply the simplification outlined in Miller et al. (2017) to utilize the Alk_T data directly to investigate gradients in dissolved inorganic carbon (DIC) as represented by the bicarbonate ion HCO_3^-:

$$A1K_T \approx [HCO_3^-] + [HS^-] \quad (1)$$

In practice, our maximum detected value of HS^- (determined from $\sum S^{2-}$ analyses) contributed less than 2% of the Alk_T value at the equivalent depth, which is similar to the precision of the titration method. Therefore, we assume $Alk_T \approx [HCO_3\text{-}] \approx [DIC]$.

Values of $\Delta[DIC]$ and $\Delta[SO_4^{2-}]$, i.e. *change* in concentration between water column and a given depth in the sediments, are often used to investigate diagenetic process at the SMTZ (e.g. Chatterjee et al., 2011). We estimated these values relative to typical local bottom water [DIC] and $[SO_4^{2-}]$ of 2.0 mmol/L and 6.0 mmol/L, respectively. Gradients of [DIC], $[CH_4]$ and $[SO_4^{2-}]$ in the vicinity of the SMTZ (all sampled during the September 2018 campaign) were estimated from linear regression lines through a subset of data points from the profiles of each parameter. Fick's First Law was applied to calculate diffusive fluxes of each species, using the measured porosity profile and assuming a constant temperature of 7.5°C (determined from bottom water during sampling):

$$J = \frac{D \cdot \varphi}{\theta^2} \frac{dC}{dz} \quad (2a)$$

$$\theta^2 = 1 - ln(\varphi)^2 \quad (2b)$$

in which J = flux (initially calculated in $\mu mol\ cm^{-2}\ s^{-1}$; here negative values indicate downwards fluxes towards the SMTZ, and vice versa), D = ion-specific diffusion coefficient, corrected for temperature, taken from Boudreau (1997), φ = porosity and θ =tortuosity, defined as per Boudreau (1997), and $\frac{dC}{dz}$ is the concentration gradient as given by the linear regression line.

Although fluctuation in temperature in the core profile is expected with depth in the sediments due to propagation of seasonal changes in bottom water temperature (e.g., Mogollon et al., 2011; Mueller et al., 2016), the potential error in calculated fluxes is expected to be <20% for absolute values of each species (based on the climatological range of bottom water temperature at the site (Merkouriadi and Leppäranta, 2015) and <3% for the flux ratios, due to the parallel effects of temperature on all species.

For assessing the optical fingerprint of porewater DOM, the magnitude of the C-fluorescence peak (Coble, 1996) and humification index (HIX; Zsolnay et al., 1999) were calculated from the measured and corrected EEMs. Absorbance spectra and EEMs were processed using the cdom and eemR packages for R software (Massicotte and Markager 2016; Massicotte 2019, respectively).

Sediment Sampling, Processing and Analysis

Sediment cores were sliced on deck (GEMAX) or in the laboratory (piston) at intervals of 1 cm (uppermost 10 cm) or 2 cm (>10 cm depth) into plastic bags. Samples were stored frozen until further processing, then freeze-dried and homogenized in an agate mortar. Volumetric porosity was estimated from weight loss on freeze drying, assuming a sediment density of 2.5 g cm^{-3}. Dried subsamples were analyzed for total carbon and nitrogen contents by thermal combustion elemental analysis (LECO TruSpec Micro, University of Helsinki, analytical precision and accuracy <10% RSD). A subsample of 3–4 mg dried sediment was weighed into tin cups and loaded into an autosampler rosette. Inorganic carbon and nitrogen forms are considered negligible in this setting, hence measured total carbon and nitrogen concentrations are

TABLE 2 | Lignin phenol oxidation products analyzed in this study. Codes indicate provenance as described by Hedges and Ertel (1982). G = gymnosperms, woody tissue; g = gymnosperms, non-woody tissue; A = angiosperms, woody tissue; a = angiosperms, non-woody tissue.

Vanillyl phenols (V)		Syringyl phenols (S)		Cinnamyl phenols (C)	
GgAa	Vanillin	Aa	Syringaldehyde	ga	Coumaric acid
GgAa	Acetovanillone	Aa	Acetosyringone	ga	Ferulic acid
GgAa	Vanillic acid	Aa	Syringic acid		

considered equivalent to the concentrations of the organic forms (C_{org}, N_{org}).

Dried subsamples were prepared for further bulk elemental analysis by a triple-acid digestion procedure. From 0.1–0.2 g of sediment was extracted over night with 5 ml HF (45%) and 5 ml of mixed $HClO_4$ (70%)/HNO_3 (65%) (volumetric ratio 3:2) at 90°C in closed teflon vials. The acids were then evaporated at 160°C until samples displayed a gel-like consistency, and 15 ml 1 M HNO_3 was added to re-dissolve the material. Where necessary, further dilution was applied prior to analysis. Extracts were analyzed by ICP-OES (Thermo iCAP 6000, Helsinki, analytical precision <5% RSD) for total iron (Fe_{tot}), managanese (Mn_{tot}) and sulfur (S_{tot}), and by ICP-MS (Thermo Element 2, Utrecht University) for total lead (Pb_{tot}) and stable isotopic ratios of Pb ($^{206}Pb/^{207}Pb$, analytical precision <5% RSD). Reproducibility of the total extraction procedure determined by replicates was <15% RSD. Absolute accuracy of the entire sample preparation, digestion, and analysis, as determined by comparison with standard reference material ISE-921 (Van der Veer, 2006), was <15% for Fe, Mn and S and <25% for Pb.

Dried subsamples from selected depths were subjected to alkaline CuO oxidation in closed vessels in a furnace for the extraction of lignin phenols (slight modification to Hedges and Ertel, 1982). Briefly, 0.5 g sediment was added to the vessel with 1 g purified CuO and 100 mg $Fe(NH_4)_2(SO_4)_2.6H_2O$ (to scavenge O_2), 7.0 ml of 8% (wt/wt) aqueous NaOH, and a small stainless steel bar agitator. The oxidation procedure was carried out for 3 h at 155°C, after which the mixture was acidified to pH 1 with HCl. Organic oxidation products were then extracted with purified ethyl acetate and then concentrated, first by rotoevaporation and then to near dryness with a flow of N_2 over the final ~1-ml volume, in the presence of anhydrous $NaSO_4$ to remove moisture. The concentrated extract was re-dissolved in pyridine with trans-cinnamic acid as internal standard and N,O-bis(trimethylsilyl) trifluoroacetamide (BSTFA) as derivitizing agent. Samples were analyzed for concentrations of 8 vanillyl, syringyl and cinnamyl lignin phenols (**Table 2**) by GC-MS at the University of Edinburgh.

Sediment Data Processing

A simple two end-member mixing model was used to investigate bulk OM sources. The calculation uses only the molar N/C ratio of organic matter, and end-member values, N/C_{EM}, based on the studies of Goñi et al. (2003) and Jilbert et al. (2018):

$$\%\,OC_{phyt} = \frac{\left(N/C_{sample} - N/C_{EM-terr}\right)}{\left(N/C_{EM-phyt} - N/C_{EM-terr}\right)} \times 100 \quad (3)$$

$$\%\,OC_{terr} = 100 - \%\,OC_{phyt} \quad (4)$$

where $\%OC_{phyt.}$ and $\%OC_{terr.}$ are the respective contributions of phytoplankton and terrestrial material to total sedimentary organic carbon (OC), with $N/C_{EM\text{-}terr} = 0.04$, and $N/C_{EM\text{-}phyt} = 0.13$. The mixing model assumes that terrestrial plant matter and phytoplankton are the only sources of organic material, that their N/C values are spatially and temporally fixed at the end-member values, and that these values do not alter significantly during sedimentation and burial of organic matter.

Absolute and relative concentrations of lignin phenol oxidation products were computed according to standard notations. These include: $\sum_8$ = sum of 8 measured phenols reported as $\mu g\,g^{-1}$ sediment; Λ_8 = sum of 8 phenols reported as mg/100g C; Λ_V = sum of 3 vannilyl phenols reported as mg/100g C (Bianchi and Canuel, 2011). Phenol compositions are expressed through ratios of the summed cinnamyl and syringyl phenols to the summed vannilyl phenols (C/V and S/V, respectively) (**Table 2**).

Age vs Depth Model

An age vs depth model for the Storfjärden site was produced from the sediment Pb_{tot} data, combining samples from the GEMAX core of June 2015 with the piston core of September 2017 (**Figure 2**). We used seven tie-points in the combined Pb_{tot} profile, identified as per Brännvall et al. (1999), Zillen et al. (2012) and Jokinen et al. (2018), and assumed to represent known temporal changes in the deposition of anthropogenic Pb over the last two millennia. Age uncertainty of pre-20th century tie-points was set at 25 years, while that of the 1970 tie-point was set at 10 years. Depth uncertainties were set at 4–8 cm. The model was produced from the tie-points using the *Undatable* software of Lougheed and Obrochta (2019), applying 10^5 simulations with an xfactor of 0.1 and 15% bootstrapping. Of these, the xfactor dictates the maximum allowable variation in sediment accumulation rate between all pairs of age-depth constraints, while the bootstrapping percentage determines the number of tie-points that are randomly excluded from the simulations. The approach takes into account uncertainty in both age and depth, with uncertainty allowed to increase with distance from tie-points, and uses a Bayesian approach to estimate a probability-density cloud for the upper 310 cm of the sediment. A subset of tie-points in the Pb_{tot} profile were checked by comparison with $^{206}Pb/^{207}Pb$ data, but the latter were not used in the construction of the model due to the observed low signal-to-noise ratio in the profile. Linear sedimentation rate (LSR) and mass accumulation rate (MAR) were estimated for each segment between tie-points using the measured porosity profile. Accumulation rate of $OC_{terr.}$ was estimated for each sampled interval from the estimated content of OC_{terr} (**Eq. 4**) and MAR of the corresponding segment.

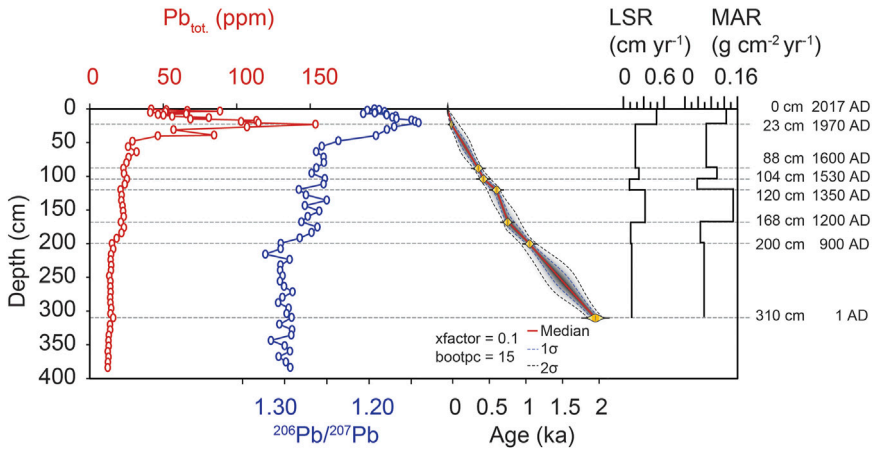

FIGURE 2 | Construction of the age vs depth model for the Storfjärden site. Note that Age 0 ka = AD 1950. The figure combines data from the GEMAX core of April 2015 (0–40 cm) and the piston core of September 2017 (40–400 cm). Seven tie-points in the Pb_{tot} profile (red), in addition to the sediment-water interface, were used to constrain the chronology based on temporal changes in anthropogenic Pb deposition (Brännvall et al., 1999; Jokinen et al., 2018). The *Undatable* software generates a probability-density cloud (grey shaded region, note 1σ and 2σ windows) between the tie-points. Age and depth uncertainty of the tie-points themselves is indicated by the yellow symbols. The ^{206}Pb/^{207}Pb profile is shown for comparison. Note that these data were not used to constrain tie-points due to observed low signal-to-noise ratio.

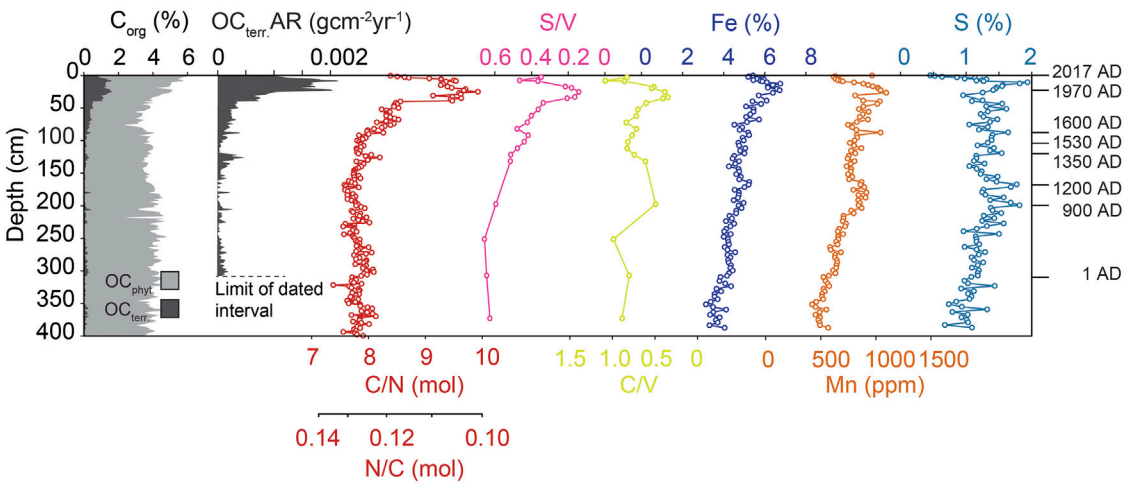

FIGURE 3 | Solid-phase components of the sediments at the Storfjärden site. The figure combines data from the GEMAX core of April 2015 (0–40 cm) and the piston core of September 2017 (40–400 cm). Fractions of C_{org} derived from phytoplankton ($OC_{phyt.}$) and terrestrial organic matter ($OC_{terr.}$) were calculated from N/C data using **Eq. 3** and **Eq. 4**. Dates on the right-hand margin correspond to tie-points in the Pb_{tot}-based age vs depth model (**Figure 2**).

RESULTS

Sedimentation Rate and Mass Accumulation Rate

The age vs depth model shows that the 4-m studied interval covers at least the last two millennia (**Figure 2**), with the earliest dating tie-point identified as 1 AD (as per Zillen et al., 2012). Both LSR and MAR have varied over the studied interval, showing ranges of 0.1–0.5 cm/yr and 0.04–0.15 g/cm^2/yr, respectively. The most recently deposited interval (1970–present) is characterized by relatively high values compared to the preceding 500 years (LSR = 0.49 cm/yr, MAR = 0.13 g/cm^2/yr), indicating enhanced inputs of sediment at this site in the recent past. One earlier interval of comparably high LSR and MAR values is observed deeper in the sediment column, corresponding to 1200–1350 AD.

Solid-Phase Profiles

Major changes occurred in bulk composition during the deposition of the uppermost meter of the sediments, corresponding to the interval since AD 1600 (**Figure 3**). Most importantly, this interval is characterized by an increase in organic matter content, as evidenced by elevated C_{org} values

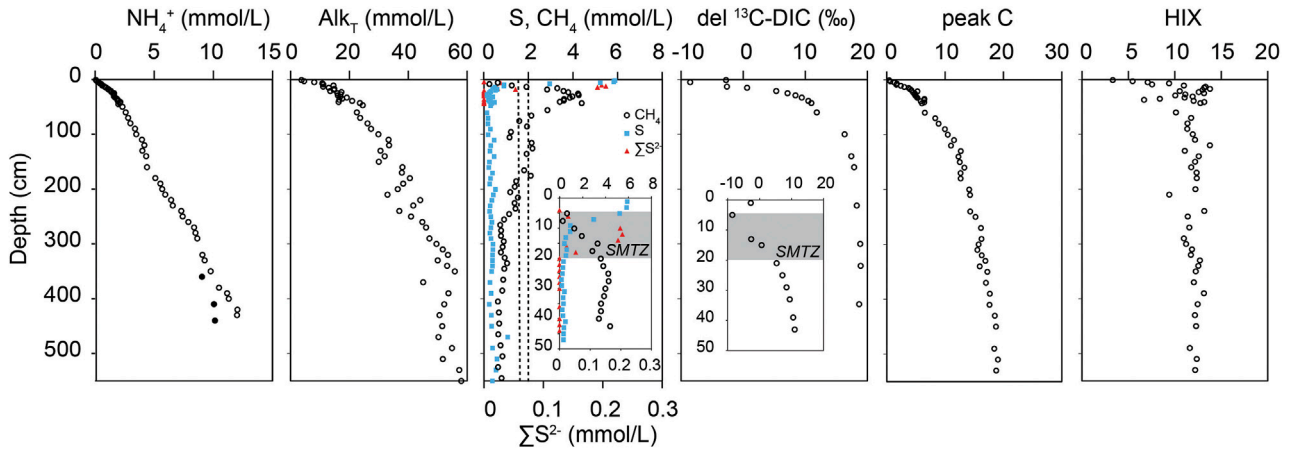

FIGURE 4 | Porewater profiles from the Storfjärden site. The figure combines data from multiple GEMAX and piston cores as described in **Table 1**. In all cases, the uppermost 40–60 cm derive from GEMAX cores preserving the sediment-water interface. Inserts show expanded profiles through the SMTZ. Note that sulfur (S) is considered to represent SO_4^{2-} (see text). Vertical dashed lines indicate saturation range of CH_4 at 1 atm pressure and 7.5–15ºC (bottom water temperature and air temperature on deck). Peak C = humic-like DOM fluorescence; HIX = DOM humification index.

up to 4–6% by weight (relative to <4% deeper in the sediments). Changes in the inputs of both terrestrial and phytoplankton-derived OM are responsible for this general increase, although the evolution of the two components since AD 1600 differs markedly (**Supplementary Figure S1**). While $OC_{phyt.}$ shows fairly stable contents until ~AD 1900 and a steady rise thereafter, $OC_{terr.}$ shows a steady rise from AD 1600 to ~AD 1850, followed by two abrupt increases between the mid-19th century and mid-20th century. Here we note that the absolute ages of events within the interval between the tie-points of AD 1600 and AD 1970 are subject to uncertainty as defined by the age vs depth model (**Figure 2**). In particular, it is plausible that sedimentation rate began to increase in parallel with changes in sediment composition, whereas the age model assumes linear sedimentation between the two tie-points. This would have the effect of making the estimated dates too old in the interval of most rapid compositional changes.

When the contributions of $OC_{phyt.}$ and $OC_{terr.}$ are combined, we observe that a significant fraction of total C_{org} in the late 20th century sediments (up to 30% according to **Eq. 3** and **Eq. 4**) is provided by terrestrial material (**Figure 3**). This fraction is far higher than in the deeper sediments, indicating a relative increase in $OC_{terr.}$ input over time. Furthermore, the absolute accumulation rate of $OM_{terr.}$ during this interval (up to 0.002 $gcm^{-2}yr^{-1}$) is unprecedented in the record (**Figure 3**). The accumulation rate of $OM_{terr.}$ has declined since the late 20th century maximum but the surface-sediment C/N ratio, and thus the calculated contribution of $OM_{terr.}$, remains elevated with respect to the deeper sediments.

Similar profiles to that of $OC_{terr.}$ are observed in the ratios of syringyl to vanillyl (S/V) and cinnamyl to vanillyl (C/V) phenols. Both the S/V and C/V phenol ratios show pronounced minima during the interval of maximum accumulation rate of $OM_{terr.}$ (**Figure 3**). However, the absolute ranges of S/V (0.1–0.6) and C/V (0.3–1.0) are similar to those observed in previous studies of lignin phenols in Baltic Sea sediments (Miltner and Emeis, 2001). Iron (Fe) and manganese (Mn) contents show a parallel evolution throughout the sediment record. Both elements' contents show a general increase from the core base upwards, towards maximum values of 6.7% (Fe) and 0.1% (Mn) within the interval of maximum $OM_{terr.}$ accumulation. Contents of Fe and Mn decline from this layer towards the sediment surface but the uppermost sample shows elevated values for both elements. Sulfur (S) displays a distinctly different profile, with higher variability throughout the record, and a pronounced maximum at 11 cm depth, clearly shallower than the maxima in $OM_{terr.}$, Fe and Mn.

Porewater Profiles

Porewater NH_4^+ and Alk_T show increasing concentrations with increasing depth in the sediment column, towards values of approximately 10 mmol/L and 50 mmol/L, respectively at 400 cm depth (**Figure 4**). The degree of curvature in both profiles is greatest in the uppermost 50 cm of the sediments, while the gradients below this depth are quite linear. Porewater CH_4 concentrations show a distinct maximum of >4 mmol/L at approximately 25 cm depth, very close to the 1970 horizon at the center of the layer of enhanced $OM_{terr.}$ deposition (**Figure 3**). A steep upwards gradient in CH_4 concentrations is observed between this layer and the SMTZ, defined as the interval of detectable porewater $\sum S^{2-}$ concentrations and encompassing the depth of equal concentrations of CH_4 and S (assumed equivalent to SO_4^{2-}). Below the porewater CH_4 maximum, a reverse gradient is observed towards background concentrations of ~1 mmol/L below 3 m depth. We cannot rule out that this gradient is an artefact of degassing effects due to the use of non-pressurized coring apparatus, and that true porewater CH_4 concentrations at depth are much higher as described in e.g. Egger et al. (2016). The increasing NH_4^+ and Alk_T concentrations below this horizon would support such a hypothesis, since all three species are

produced during methanogensis. However, it is also possible that the profile is genuine, and that the linear NH_4^+ and Alk_T gradients reflect upwards diffusion of these species from a deep source. We note that measured CH_4 concentrations decline to values well below the saturation concentration range during sampling on deck (1.6–2.0 mmol/L, **Figure 3**), whereas degassing typically leads to a plateau of values close to this range (Egger et al., 2016). This observation would support the hypothesis of a genuine reverse gradient in porewater CH_4. Above the SMTZ, concentrations of dissolved S (assumed equivalent to SO_4^{2-}) rise steeply towards the bottom water concentration of approximately 6 mmol/L.

Porewater δ^{13}C-DIC values show a minimum of −8.5‰ close to the SMTZ, while the uppermost measured sample at 1 cm depth has a value of −2.8‰. Below the SMTZ, δ^{13}C-DIC values show an asymptotic increase towards a stable value of +18–+19‰ in the deeper sediments. In terms of the CDOM optical properties of the porewaters, the peak C (considered to approximate the concentration of humic-like DOM; Coble, 1996) shows a generally concave profile similar to those of NH_4^+ and Alk_T. In contrast, the humification index (HIX; representing the extent of humification of the CDOM pool, Zsolnay et al., 1999) shows elevated values of up to 14 in the interval of enhanced $OM_{terr.}$ accumulation, superimposed on a trend from lower values at the surface (<6) to a consistent background of 10–12 at depth.

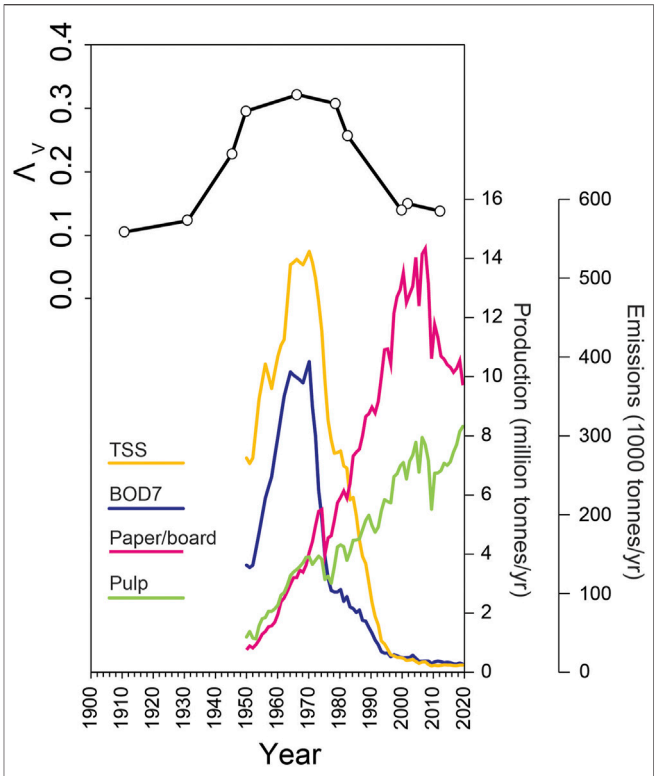

FIGURE 5 | Time series of production and emissions from forest industries in Finland since 1950 (https://www.forestindustries.fi/statistics/environment/), compared with the dated sediment record of total vanillyl phenols, reported as mg/100 g C (Λ_V). TSS = total suspended solids, BOD_7 = 7th day biological oxygen demand.

DISCUSSION

Terrestrial Organic Matter Loading to the Sediments During the 20th Century

Many coastal areas of the Baltic Sea show evidence for anthropogenic eutrophication (Conley et al., 2011) which often leads to enhanced carbon loading to sediments (Jokinen et al., 2018; Helmond et al., 2020). At Storfjärden, we observe a steady rise in OC_{phyt} contents in the period since ~AD 1900 (**Supplementary Figure S1**), consistent with eutrophication. However, a novel observation of this study is that a significant proportion of the additional recent carbon at this site is derived from terrestrial sources. The coincident minima in C/V and S/V phenol ratios during the period of maximum $OM_{terr.}$ accumulation rates indicate a shift towards more gymnosperm-dominated material (lower S/V phenol ratio) simultaneously with a shift towards more woody material (lower C/V phenol ratio, see **Table 2**), implying inputs of material originally derived from the Finnish forests.

Recent changes in C/V and S/V phenol ratios in estuarine settings have previously been interpreted as evidence for inputs of lignin-rich waste products from pulp and paper industries in North America (Louchouarn et al., 1999; Brandenberger et al., 2011). Such an interpretation appears plausible also for Storfjärden. Pulp production at Lohja, in the catchment of the River Mustionjoki (**Figure 1**), began in 1907 while paper production began in 1938 Heikkinen (2000). By 1957, the site was operating two paper machines with a combined potential output of 70 kt/y. Considering the uncertainty of the age vs depth model in this interval, the abrupt increases in $OC_{terr.}$ observed in **Supplementary Figure S1** could well relate to these major changes in industrial activity in the catchment. We also note that sedimentary contents of $OC_{terr.}$ were already increasing for several centuries prior to this time, indicating additional inputs potentially from land use change prior to the onset of industrial activity (e.g. Yang et al., 2021).

Emissions of waste products from forest industries are expected to be a function of the scale of operations, as well as the degree of waste water treatment, both of which may change over time (Katko et al., 2005). Data from the website of Finnish Forest Industries (https://www.forestindustries.fi/statistics/environment/) show that national estimates of total suspended solids (TSS) and 7th-day biological oxygen demand (BOD_7; a proxy for organic matter) emissions from forest industries to Finnish aquatic systems peaked in the period 1950–1980 (**Figure 5**). The decline in emissions since this period is primarily due to the introduction of on-site water recycling, sedimentation ponds and activated sludge treatment (Luonsi et al., 1988; Saunamäki, 1997; Katko et al., 2005). Such improvements were also enacted at the industrial sites in Lohja, reducing emissions significantly despite ongoing high levels of production until closure of operations in 2015.

A comparison of the time series of TSS and BOD_7 with the sedimentary content of vanillyl phenol oxidation products (Λ_V) at Storfjärden clearly shows the coincidence of maximum late

TABLE 3 | Estimate of carbon stored in fiber banks and fiber-rich sediments of 29 mapped locations in the Swedish coastal zone (Norrlin and Josefsson, 2017).

	Fiberbanks	Fiber-rich sediments	Total
Volume of wet sediment in 29 mapped locations, km^{3a}	0.007	0.011	
Volume of solid material, km^{3b}	0.0007	0.0011	
Mass of solid material (kilotonnes)[c]	1400	2750	
Mass of carbon (kilotonnes)[d]	210	129	339

[a]*Data provided in* ***Table 1*** *of Norrlin and Josefsson (2017).*
[b]*Estimated assuming volumetric porosity of 0.9 for both fiberbanks and fiber-rich sediments.*
[c]*Estimated assuming solid-phase density of 2.0 g* cm^{-3} *(fiberbanks) and 2.5 g* cm^{-3} *(fiber-rich sediments).*
[d]*Estimated from geometric mean* $\%C_{org}$ *of sediments from the Väja site (fiberbanks = 15%,* n = *4; fiber-rich sediments = 4.7%,* n = *4).*

20th century lignin accumulation with maximum emissions from forest industries in Finland (**Figure 5**, note that age vs depth uncertainties are lower in this interval due to the tie-point at 1970). Furthermore, Heikkinen (2000) reported high contents of sedimentary resin acids during the same period in the southern part of Lake Lohjanjärvi, adjacent to the industrial site (**Figure 1**), while high contents of $OM_{terr.}$ in sediments close to Storfjärden were reported by Jokinen et al. (2020). Combined, these studies strongly support the interpretation that emissions from industries in Lohja were the main reason for the high inputs of $OM_{terr.}$ to Storfjärden during the late 20th century. This observation is remarkable, as it implies that significant amounts of waterborne waste materials were transported through Lake Lohjanjärvi, the Mustionjoki river and Pojo Bay as far as the archipelago area where the study site is situated, a linear distance of over 60 km (**Figure 1**).

An ongoing mapping exercise in the Swedish coastal zone has identified 29 locations of fiberbank deposits close to point source industrial sites (Norrlin and Josefsson, 2017). In terms of surface area at any given location, true fiberbanks (sediments dominated by coarse waste material fibers) typically occupy up to 10 hectares, while fiber-rich sediments (sediments with visible fibers) may extend over up to 1 square kilometer. Our data raises the possibility that the true spatial extent of anthropogenic $OM_{terr.}$ inputs to sediments of the northern Baltic Sea may be larger, due to the transport of finer particulate and dissolved material away from point sources. Using the Swedish coastal area as an example due to the good data coverage, we performed a speculative mass balance calculation to investigate the scale of carbon accumulation in mapped fiberbank locations in relation to total inputs from forest industry sources (**Table 3**). From the reported sediment carbon concentrations in Dahlberg et al. (2020), we estimate that 0.34 million tonnes of carbon currently reside in the fiberbanks and fiber-rich sediments at the 29 mapped locations of Norrlin and Josefsson (2017). We subsequently derived a first-order estimate for the magnitude of forest industry carbon inputs to the Baltic Sea from Sweden. This estimate is based on an assumed Gaussian distribution of total COD emissions from Swedish forest industries over the period 1930–2000, fitted to the existing data from the Swedish Forest Industries Federation (**Supplementary Figure S2**) and corrected downwards assuming that only 5–15% of Swedish forest industry point source emissions enter the Baltic Sea, based on the locations of point sources in the maps of Norrlin and Josefsson (2017). The conversion from COD to total organic carbon (TOC) is based on the regression for high-latitude systems presented by Jiao et al. (2021). This exercise yields a total carbon input of 3.2–9.5 million tonnes, up to an order of magnitude greater than the estimated carbon stock in the 29 mapped locations (**Table 4**). Approximately half of the expected Swedish coastal point sources to the Baltic Sea have been mapped, thus its seems likely that the total fiberbank and fiber-rich sediment carbon stock in the Swedish coastal zone, once known, will be significantly less than the total input of carbon from anthropogenic $OM_{terr.}$ during 1930–2000. In this context, a diffuse contribution of anthropogenic $OM_{terr.}$ to a larger coastal sediment area is plausible, although part of the difference may be explained by mineralization and other transformations in the coastal environment.

Additionally, we estimated the quantitative significance of anthropogenic $OM_{terr.}$ inputs in the context of total terrestrial carbon loading to the Baltic Sea from Finland and Sweden. During the period 1993–2012, when standardized TOC analysis protocols were routinely used and therefore data are most reliable (Asmala et al., 2019), annual TOC loading to the Baltic Sea from the two countries combined varied from approximately 1.0–2.5 million tonnes per year (**Table 4**). Using the same Gaussian approach described above to provide a first-order estimate of the historical point source anthropogenic $OM_{terr.}$ inputs from Finland (**Supplementary Figure S2**) we calculate a total loading during the period 1930–2000 of approximately 4–13 million tonnes of TOC for the two countries combined. During the loading maximum of the mid-1960s, we estimate approximately 0.18–0.53 million tonnes TOC per year. In conclusion, during the period of maximum emissions, carbon inputs from industrial sources may have been a significant component (up to >10%) of total annual carbon loading from Finland and Sweden, although the contribution likely declined steeply during the last decades of the 20th century.

Overall Impact of Carbon Loading on Sediment Diagenesis

The additional carbon loading from both aquatic primary production and terrestrial sources has contributed to higher LSR and MAR at Storfjärden in the recent past, and driven high rates of remineralization in the upper sediments, as

TABLE 4 | Estimate of total carbon emissions to the Baltic Sea from forest industry point sources in Finland and Sweden during 1930–2000.

	Finland	Sweden	Total
Forest industry emissions 1930–2000			
Modeled integrated BOD[a] or COD[b] 1930–2000 (kilotonnes)	9496	69973	
Modeled integrated TOC[c] 1930–2000 (kilotonnes)	24350	63612	
Modeled integrated TOC to Baltic Sea 1930–2000 (kilotonnes, 5%)[d]	1217	3181	4398
Modeled integrated TOC to Baltic Sea 1930-2000 (kilotonnes, 15%)[e]	3652	9542	13194
Modeled max. annual TOC to Baltic Sea 1965 (kilotonnes, 5%)	49	127	176
Modeled max. annual TOC to Baltic Sea 1965 (kilotonnes, 15%)	146	380	527
Total riverine carbon inputs to Baltic Sea			
TOC to Baltic Sea 1993–2012 (kilotonnes/yr)[f,g]			
High	1148	1399	2547
Low	404	547	961

[a]*Total emissions in Finland, modeled using data for BOD_7 from Finnish Forest Industries from 1950 to 2000 (**Figure 5**) with hindcasting to 1930 assuming a Gaussian distribution (**Supplementary Figure S2**).*
[b]*Total emissions in Sweden, modeled using data for COD from Swedish Forest Industries Federation from 1978 to 2000 and hindcasted to 1930 assuming a parallel Gaussian distribution to that observed in Finland (**Supplementary Figure S2**).*
[c]*Estimated using the regressions for BOD and COD vs DOC in high-latitude systems presented in Jiao et al. (2021), assuming DOC = TOC.*
[d]*5% of modeled integrated TOC emissions 1930–2000.*
[e]*15% of modeled integrated TOC emissions 1930–2000.*
[f]*Data from Asmala et al. (2019)*
[g]*Data from Baltic Environmental Database.*

shown by the curvature of the NH_4^+ and Alk_T profiles in the upper 50 cm. The porewater data suggest that enhanced demand for electron acceptors has driven a rearrangement of the diagenetic zones in the upper sediment column (e.g., Middelburg and Levin, 2009). Most notably, carbon loading has enhanced methanogenesis and consequently shoaled both the interval of organoclastic sulfate reduction and the SMTZ. This sequence of eutrophication-driven changes in diagenetic zonation in the northern Baltic Sea has been described in several previous studies (e.g., Slomp et al., 2013; Egger et al., 2015; Rooze et al., 2016; Jilbert et al., 2018). A key piece of evidence for non-steady state conditions – the solid-phase S maximum indicating enhanced formation of sulfide minerals in the modern SMTZ – is observed in our profiles at 11 cm depth (**Figure 3**). Our data suggests that the methanogenic horizon is focused in the recently deposited sediments, with a gradient towards lower CH_4 concentrations observed in deeper layers. Even in the case of degassing impacting on the methane profile, the strong curvature of the NH_4^+ and Alk_T profiles in the upper 50 cm supports the theory that this interval is characterized by enhanced rates of methanogenesis relative to the rest of the sediment column. This confirms that enhanced methane production, and associated effluxes to the water column, are truly a legacy effect of recent carbon loading as postulated by Myllykangas et al. (2020a) from short-core data. Indeed, promotion of methanogenesis through rapid accumulation of organic material in sediments has been described previously in both freshwater and estuarine systems (e.g., Egger et al., 2016; Steinsberger et al., 2017). In the northern Baltic Sea, naturally low sulfate concentrations and modern high sedimentation rates allow degradable organic material to pass through the zone of sulfate reduction within the uppermost decimeters of the sediment column, thereby facilitating high rates of methanogenesis (e.g., Thang et al., 2013; Sawicka and Bruechert, 2017).

Methanogenesis, Organoclastic Sulfate Reduction and Anaerobic Oxidation of Methane

The shoaling of the diagenetic zones has triggered a cascade of secondary redox reactions in the sediment column at Storfjärden. Most importantly, the presence of methane in the shallow porewaters has likely led to the initiation of anaerobic oxidation of methane (AOM). Elevated rates of methane oxidation in the SMTZ at this site have been previously suggested from porewater data (Jilbert et al., 2018) and later confirmed by $^{14}CH_4$ incubations (Myllykangas et al., 2020b). The present study shows the enrichment of $\sum S^{2-}$ at the SMTZ reported in Jilbert et al. (2018) in the context of the wider porewater data (**Figure 4**). The enrichment is considered to indicate sulfide production via sulfate-mediated AOM (S-AOM):

$$CH_{4(aq)} + SO_{4(aq)}^{2-} + CO_{2(aq)} \rightarrow H_2S_{(aq)} + 2HCO_{3(aq)}^{-} + H_2O_{(l)} \quad (5)$$

To further investigate the dynamics of methanogenesis, organoclastic sulfate reduction and S-AOM at Storfjärden, we determined the δ^{13}C-DIC of porewaters throughout the core profile. Porewater δ^{13}C-DIC is influenced by each of these processes as described by Whiticar (1999) and Meister and Reyes (2019). Namely, organoclastic sulfate reduction depletes δ^{13}C-DIC from the bottom water value of ~0‰ towards the value of decaying organic matter (~−20‰). If S-AOM is active at the SMTZ, this process further depletes δ^{13}C-DIC due to consumption of isotopically light methane. In the underlying methanogenic zone, in contrast, δ^{13}C-DIC becomes enriched due to preferential consumption of

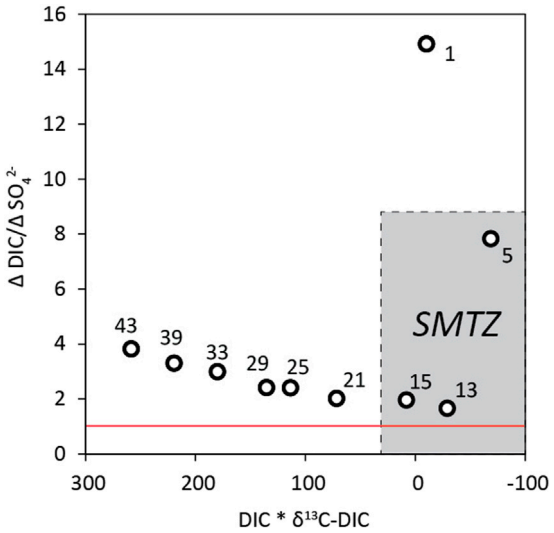

FIGURE 6 | Crossplot of $\Delta[DIC]/\Delta[SO_4^{2-}]$ vs. [DIC] * δ^{13}C-DIC for the upper sediment column, after Miller et al. (2017). Delta notation refers to change in concentration with respect to bottom water values. Numbers adjacent to data points indicate depth in cm. Horizontal red line shows the 1:1 ratio predicted for systems dominated by sulfate-mediated AOM (**Eq. 5**).

isotopically light DIC during hydrogenotrophic methanogenesis. The overall shape of the δ^{13}C-DIC profile at Storfjärden is consistent with those reported in other systems, with minimum values at or close to the SMTZ (e.g., Torres and Rugh, 2006; Chatterjee et al., 2011; Wehrmann et al., 2011; Yoshinaga et al., 2014). However we observe minimum δ^{13}C-DIC values of just −8.5‰ at 5 cm depth (**Figure 4**). Although low sampling resolution may have aliased the magnitude and precise depth of this minimum, the value is strongly enriched relative to those reported in the aforementioned studies. Below the SMTZ, δ^{13}C-DIC increases towards a stable background value of +18–+19‰. We interpret the generally enriched profile to indicate the presence of methanogenesis throughout the SMTZ (e.g., Thang et al., 2013) which dilutes the depletion of δ^{13}C-DIC expected from S-AOM and organoclastic sulfate reduction.

Previous studies have used variations on a crossplot of Δ[DIC] vs $\Delta[SO_4^{2-}]$ (the change in DIC and SO_4^{2-} concentrations relative to bottom water values) to attempt to quantify the relative importance of S-AOM and organoclastic sulfate reduction at the SMTZ (e.g., Kastner et al., 2008; Hu et al., 2015). The approach is based on the theory that AOM produces DIC and consumes SO_4^{2-} in a 1:1 ratio (**Eq. 5**) whereas for dissimilatory reduction the ratio is 2:1. Hence, the closer the value of $\Delta[DIC]/\Delta[SO_4^{2-}]$ is to 1, the greater the contribution of AOM. We chose to adopt the variation of Miller et al. (2017) to integrate δ^{13}C-DIC values into this analysis, in order to reduce the uncertainty introduced by unconstrained fluxes of DIC from deeper sediment layers (Chatterjee et al., 2011). Thus we plot $\Delta[DIC]/\Delta[SO_4^{2-}]$ against [DIC] * δ^{13}C-DIC (**Figure 6**, note that significant down-core changes in $[Ca^{2+}]$ are not observed in this system hence corrections to Δ[DIC] to account for carbonate mineral precipitation are neglected).

The relationship between $\Delta[DIC]/\Delta[SO_4^{2-}]$ and [DIC] * δ^{13}C-DIC strongly varies with depth in the upper sediment column (**Figure 6**). Samples from the SMTZ plot in the lower-right corner of the diagram, with $\Delta[DIC]/\Delta[SO_4^{2-}]$ values <2 coincident with negative [DIC] * δ^{13}C-DIC. Although the [DIC] * δ^{13}C-DIC values are less negative than observed in Miller et al. (2017) due to the diluting effect of methanogenesis in this system, the progression towards $\Delta[DIC]/\Delta[SO_4^{2-}]$ values <2 supports the hypothesis that sulfate-AOM occurs in the SMTZ. However, the minimum detected value for $\Delta[DIC]/\Delta[SO_4^{2-}]$ at 13 cm depth is 1.65, still significantly elevated with respect to the 1:1 value predicted from sulfate-AOM alone. This result suggests that an important fraction of total sulfate consumption is in the SMTZ is likely contributed by organoclastic sulfate reduction (e.g., Jorgensen et al., 2019). This is further supported by the relative diffusive fluxes of SO_4^{2-} and CH_4 into the SMTZ, which show a ratio of 2.66 (**Table 5**), clearly in excess of the 1:1 requirement of the reactants of sulfate-AOM (**Eq. 5**). Combined, the results imply that the SMTZ at our study site should be considered as a broad zone of overlapping diagenetic processes, in which methanogenesis, organoclastic sulfate reduction and S-AOM are all active simultaneously.

Consequences of the Shallow Sulfate-Methane Transition Zone at Storfjärden

The SMTZ at Storfjärden, similarly to much of the northern Baltic Sea today, is among the shallowest in the marine realm. Due to the strong correlation observed globally between SMTZ depth and associated diffusive fluxes of SO_4^{2-} and CH_4 (Egger et al., 2018), the values of these fluxes at Storfjärden are also high in global terms. Our calculated values for JCH_4 and JSO_4^{2-}, as well as the flux ratio of 2.66, fall within the ranges of compiled data for 40 marine coring sites with SMTZ depth <1 m (**Table 5**), suggesting that rates of methane-related processes at this site are typical for similar coastal locations of high carbon loading in the modern ocean.

While consumption of upwards-diffusing methane by AOM in marine sediments is considered near-quantitative on a global scale (Reeburgh, 2007; Saunois et al., 2016), sites with a shallow SMTZ often show inefficient AOM and significant fluxes of CH_4 to the water column and hence potentially to the atmosphere (e.g. Thang et al., 2013; Egger et al., 2016). Indeed, the Storfjärden area today is characterized by active fluxes of methane from sediments through both diffusion (Myllykangas et al., 2020a) and ebullition (Humborg et al., 2019). Our data confirms that the ultimate source of these emissions is the methanogenic layer in the late 20th century sediments, and hence that these emissions are a direct consequence of anthropogenic carbon loading through both eutrophication and inputs of OM_{terr}.

TABLE 5 | Comparison of fluxes of methane (JCH_4) and sulfate (JSO_4^{2-}) into the SMTZ at Storfjärden with 40 other locations in the marine realm with SMTZ depth < 1 m (data from Egger et al. (2018). Only sites with data for all parameters were used in the analysis.

	SMTZ depth (m)	JCH_4 (mmol/m^2/d)	JSO_4^{2-} (mmol/m^2/d)	JSO_4^{2-}:JCH_4
Storfjärden, Baltic Sea (this study)	0.12	1.73	4.59	2.66
40 sites of SMTZ < 1 m depth Egger et al. (2018)				
mean	0.44	1.81	1.31	1.38
min	0.04	0.07	0.06	0.60
max	1.00	15.93	13.07	3.69

Specific Impacts of $OM_{terr.}$ Inputs on Diagenetic Processes

Our data show indications that the additional loading of $OM_{terr.}$ during the 20th century has had specific impacts on diagenetic processes at Storfjärden. Terrestrial OM is traditionally considered to be relatively inert to remineralization in sediments (Hedges et al., 2000; Arndt et al., 2013) due to its refractory macromolecular composition (de Leeuw and Largeau, 1993) as well as protective associations formed with other materials prior to sedimentation (e.g., Hedges and Keil, 1995; Huguet et al., 2009). Indeed, lignin in sediments has been studied extensively as a biomarker for $OM_{terr.}$ largely due to its high preservation potential (Bianchi et al., 2018). However, several studies have reported that sites influenced by large direct inputs from forest industry display evidence for relatively high reactivity of this material in the sediment column. For example, high potential rates of methanogenesis were recently observed in wood fiber-rich sediments from the Finnish Lake Nasijärvi (Kokko et al., 2018). Similarly, fiber-rich sediments in Swedish coastal areas of the Baltic Sea support diffusive fluxes of organic contaminants to overlying waters, implying release from the solid-phase during diagenesis (Dahlberg et al., 2021).

At Storfjärden, we observe a maximum in the humification index (HIX) of porewater CDOM (values up to 14) coincident with the layer of enhanced $OM_{terr.}$ accumulation (**Figure 4**). This maximum is superimposed onto a trend from lower values at the surface (<6) to a consistent background of 10–12 at depth in the profile. Previous studies of HIX in sediment porewaters have typically interpreted this index as a proxy for CDOM sources in the degrading sedimentary OM, with low values (e.g. <3) indicative of autochthonous or microbial material and high values (e.g >6) indicative of terrestrial humic matter (Chen et al., 2016; Li et al., 2021). Our values are generally higher than those reported in these studies, implying an overall more humic composition of the source material. Furthermore, maximum values are observed in the layer of maximum $OM_{terr.}$ accumulation, suggesting solubilization of lignin and other terrestrial macromolecules, which are important components of humic-like CDOM (Del Vecchio & Blough, 2004). The underlying trend in HIX is also of interest. The observation of low-HIX CDOM in the shallowest layers and a stable background of high-HIX CDOM at depth implies a diagenetic shift in CDOM composition after sedimentation of degrading OM. Specifically, low-HIX CDOM produced during degradation in the shallowest layers appears to be consumed after release into the porewaters, leaving a residual accumulation of high-HIX CDOM at depth. We suggest that such consumption may occur through utilization of low-HIX DOM, which is considered more labile, by the microbial community. We note that the HIX profile contrasts with that of peak C, which shows a concave-down profile throughout the sediment column (**Figure 4**). This suggests that overall production of humic-like CDOM occurs similarly to that of inorganic degradation products such as NH_4^+ and Alk_T.

The additional flux of $OM_{terr.}$ to the coring location during the 20th century was likely accompanied by other terrestrial materials transported in association with organic matter. As described by Jokinen et al. (2020), metals such as Fe, Mn, Co, Cd, Pb, Sn and Zn are all enriched in the same depth interval as $OM_{terr.}$ in sediment cores from the Storfjärden area. Our long core data confirm that contents of Fe and Mn are higher in this layer than at any other depth in the sediment column (**Figure 3**). These metals derive from the terrestrial environment (including from anthropogenic sources), and are sedimented both as oxide minerals physically associated with organic matter, and as metal-OM complexes that undergo flocculation and aggregation at the estuarine salinity gradient (Widerlund and Ingri, 1996; Jilbert et al., 2018). Temporal changes in the inputs of oxides and metal-OM complexes may impact on diagenetic processes in several ways. For example, higher inputs of oxides may affect rates of oxide-mediated AOM (Lenstra et al., 2018) and thus the potential for phosphorus retention through vivianite formation (Slomp et al., 2013). Furthermore, complexation between OM and Fe in sediments has been shown to generally protect OM from remineralization and thus promote long-term carbon burial (Lalonde et al., 2012; Shields et al., 2016). Hence, not only the direct $OM_{terr.}$ inputs from forest industry themselves, but also the associated materials, may have altered diagenetic processes at Storfjärden during the 20th century.

CONCLUSION

This study shows that recent carbon loading to coastal sediments of the northern Baltic Sea has occurred not only as a consequence of increased aquatic primary production due to increased nutrient loading, but also of enhanced inputs of terrestrial organic matter from forest industry activities. This additional material has contributed to high sedimentation rates and demand for electron acceptors for organic matter remineralization, leading to a shoaling of the diagenetic zones in the sediment column. At the Storfjärden site, a distinct layer of elevated $OM_{terr.}$ contents in the late 20th century sediments are characterized by lignin phenol signatures typical of woody gymnosperm material, implying inputs from forest industries in the catchment. This layer coincides with high porewater methane concentrations and

high curvature in the profiles of NH_4^+ and Alk_T, indicating that the carbon loading has enhanced methanogenesis in the recently deposited sediments. Moreover, optical characteristics of porewater CDOM indicate active degradation of OM_{terr}. in the same layer. The SMTZ is observed directly above the methanogenic layer, and is characterized by sulfate-mediated AOM occurring alongside organoclastic sulfate reduction and methanogenesis. Fluxes of methane and sulfate into the SMTZ are high, but typical for similar eutrophic systems throughout the coastal oceans.

The broader spatial impact of anthropogenic OM_{terr}. inputs on coastal sediment biogeochemistry in the northern Baltic Sea remains to be established. Our data from Storfjärden shows that the signatures of such inputs may be identifiable several tens of kilometers from the industrial sources, confirming previous observations from the St. Lawrence estuary (Louchouarn et al., 1999). Moreover, our estimates of carbon storage in fiberbank locations in the Baltic Sea show that these proximal deposits are unlikely to account for the entire carbon loading from forest industry sources to the Baltic Sea during the 20th century. Determining the wider extent of anthropogenic OM_{terr}.-rich deposits in boreal coastal zones is essential for constraining carbon budgets in these areas, both in terms of carbon burial and greenhouse gas emissions.

DATA AVAILABILITY STATEMENT

All new data presented in the paper are accessible via Zenodo from 1 December 2021 (10.5281/zenodo.5570261) or directly from the corresponding author without undue reservation.

AUTHOR CONTRIBUTIONS

TJ devised the study, led the field and lab work and wrote the manuscript. GC and LL performed lignin phenol analyses and contributed to the interpretations and writing. SJ produced the age vs depth model and contributed to the interpretations and writing. EA performed the porewater CDOM analyses and contributed to the interpretations and writing. XS and CM performed the porewater $\delta^{13}C$ and Alkalinity analyses and contributed to the interpretations and writing. CH and AN co-ordinated the field campaigns with R/V Electra and contributed to the interpretations and writing.

FUNDING

This work was supported by Academy of Finland grants 317684 and 319956 and a University of Helsinki Tenure Track starting package to TJ. Support for a student exchange visit (LL) from Helsinki to Edinburgh was provided by University of Helsinki Department of Geosciences and Geography. The data in this study are contribution #5 from the Environmental and Mineralogical Laboratories (Hellabs) of the Department of Geosciences and Geography, University of Helsinki.

ACKNOWLEDGMENTS

This work forms part of the Baltic Bridge strategic partnership between the Stockholm University and the University of Helsinki. We thank the crew and captain of R/V Electra and technical staff at Tvärminne Zoological Station for support during field campaigns. We also thank all laboratory personnel who assisted with sample preparation and analytical work, especially Juhani Virkanen (University of Helsinki) and Steve Mowbray (University of Edinburgh).

SUPPLEMENTARY MATERIAL

The Supplementary Material for this article can be found online at: https://www.frontiersin.org/articles/10.3389/feart.2021.716416/full#supplementary-material

REFERENCES

Albert, D. B., Martens, C. S., and Alperin, M. J. (1998). Biogeochemical Processes Controlling Methane in Gassy Coastal Sediments-Part 2: Groundwater Flow Control of Acoustic Turbidity in Eckernförde Bay Sediments. *Continental Shelf Res.* 18, 1771–1793. doi:10.1016/S0278-4343(98)00057-0

Ali, M., and Sreekrishnan, T. R. (2001). Aquatic Toxicity from Pulp and Paper Mill Effluents: a Review. *Adv. Environ. Res.* 5, 175–196. doi:10.1016/S1093-0191(00)00055-1

Anderson, D. M., Glibert, P. M., and Burkholder, J. M. (2002). Harmful Algal Blooms and Eutrophication: Nutrient Sources, Composition, and Consequences. *Estuaries* 25, 704–726. doi:10.1007/BF02804901

Arndt, S., Jørgensen, B. B., LaRowe, D. E., Middelburg, J. J., Pancost, R. D., and Regnier, P. (2013). Quantifying the Degradation of Organic Matter in marine Sediments: A Review and Synthesis. *Earth-Science Rev.* 123, 53–86. doi:10.1016/j.earscirev.2013.02.008

Asmala, E., Bowers, D. G., Autio, R., Kaartokallio, H., and Thomas, D. N. (2014). Qualitative Changes of Riverine Dissolved Organic Matter at Low Salinities Due to Flocculation. *J. Geophys. Res. Biogeosci.* 119, 1919–1933. doi:10.1002/2014JG002722

Asmala, E., Carstensen, J., and Räike, A. (2019). Multiple Anthropogenic Drivers behind Upward Trends in Organic Carbon Concentrations in Boreal Rivers. *Environ. Res. Lett.* 14, 124018. doi:10.1088/1748-9326/ab4fa9

Asmala, E., Haraguchi, L., Markager, S., Massicotte, P., Riemann, B., Staehr, P. A., et al. (2018). Eutrophication Leads to Accumulation of Recalcitrant Autochthonous Organic Matter in Coastal Environment. *Glob. Biogeochem. Cycles* 32, 1673–1687. doi:10.1029/2017GB005848

Bange, H. W., Bartell, U. H., Rapsomanikis, S., and Andreae, M. O. (1994). Methane in the Baltic and North Seas and a Reassessment of the marine Emissions of Methane. *Glob. Biogeochem. Cycles* 8, 465–480. doi:10.1029/94GB02181

Beal, E. J., House, C. H., and Orphan, V. J. (2009). Manganese- and Iron-dependent marine Methane Oxidation. *Science* 325, 184–187. doi:10.1126/science.1169984

Berg, P., Risgaard-Petersen, N., and Rysgaard, S. (1998). Interpretation of Measured Concentration Profiles in Sediment Pore Water. *Limnol. Oceanogr.* 43, 1500–1510. doi:10.4319/lo.1998.43.7.1500

Bianchi, T. S., and Canuel, E. A. (2011). *Chemical Biomarkers in Aquatic Ecosystems*. Princeton, NJ: Princeton University Press.

Bianchi, T. S., Cui, X., Blair, N. E., Burdige, D. J., Eglinton, T. I., and Galy, V. (2018). Centers of Organic Carbon Burial and Oxidation at the Land-Ocean Interface. *Org. Geochem.* 115, 138–155. doi:10.1016/j.orggeochem.2017.09.008

Blair, N. E., and Aller, R. C. (2012). The Fate of Terrestrial Organic Carbon in the marine Environment. *Annu. Rev. Mar. Sci.* 4, 401–423. doi:10.1146/annurev-marine-120709-142717

Bonsdorff, E., Blomqvist, E. M., Mattila, J., and Norkko, A. (1997). Coastal Eutrophication: Causes, Consequences and Perspectives in the Archipelago Areas of the Northern Baltic Sea. *Estuarine, Coastal Shelf Sci.* 44, 63–72. doi:10.1016/S0272-7714(97)80008-X

Borges, A. V., and Abril, G. (2011). *Carbon Dioxide and Methane Dynamics in Estuaries*. San Diego; 525 B Street, Suite 1900 San Diego, CA 92101-4495 USA: Elsevier Academic Press Inc.

Boudreau, B. P. (1997). *Diagenetic Models and Their Implementation: Modelling Transport and Reactions in Aquatic Sediments*. Berlin-Heidelberg, Germany: Springer-Verlag.

Bowles, M. W., Mogollon, J. M., Kasten, S., Zabel, M., and Hinrichs, K.-U. (2014). Global Rates of marine Sulfate Reduction and Implications for Sub-sea-floor Metabolic Activities. *Science* 344, 889–891. doi:10.1126/science.1249213

Brandenberger, J. M., Louchouarn, P., and Crecelius, E. A. (2011). Natural and post-urbanization Signatures of Hypoxia in Two Basins of Puget Sound: Historical Reconstruction of Redox Sensitive Metals and Organic Matter Inputs. *Aquat. Geochem.* 17, 645–670. doi:10.1007/s10498-011-9129-0

Brännvall, M.-L., Bindler, R., Renberg, I., Emteryd, O., Bartnicki, J., and Billström, K. (1999). The Medieval Metal Industry Was the Cradle of Modern Large-Scale Atmospheric Lead Pollution in Northern Europe. *Environ. Sci. Technol.* 33, 4391–4395. doi:10.1021/es990279n

Breitburg, D., Levin, L. A., Oschlies, A., Grégoire, M., Chavez, F. P., Conley, D. J., et al. (2018). Declining Oxygen in the Global Ocean and Coastal Waters. *Science* 359, eaam7240. doi:10.1126/science.aam7240

Burton, E. D., Sullivan, L. A., Bush, R. T., Johnston, S. G., and Keene, A. F. (2008). A Simple and Inexpensive Chromium-Reducible Sulfur Method for Acid-Sulfate Soils. *Appl. Geochem.* 23, 2759–2766. doi:10.1016/j.apgeochem.2008.07.007

Canfield, D. E. (1991). Sulfate Reduction in Deep-Sea Sediments. *Am. J. Sci.* 291, 177–188. doi:10.2475/ajs.291.2.177

Carstensen, J., Conley, D. J., Bonsdorff, E., Gustafsson, B. G., Hietanen, S., Janas, U., et al. (2014). Hypoxia in the Baltic Sea: Biogeochemical Cycles, Benthic Fauna, and Management. *Ambio* 43, 26–36. doi:10.1007/s13280-013-0474-7

Chatterjee, S., Dickens, G. R., Bhatnagar, G., Chapman, W. G., Dugan, B., Snyder, G. T., et al. (2011). Pore Water Sulfate, Alkalinity, and Carbon Isotope Profiles in Shallow Sediment above marine Gas Hydrate Systems: A Numerical Modeling Perspective. *J. Geophys. Res.* 116, B09103. doi:10.1029/2011JB008290

Chen, M., Kim, J.-H., Nam, S.-I., Niessen, F., HongKang, W.-L. M.-H., Kang, M.-H., et al. (2016). Production of Fluorescent Dissolved Organic Matter in Arctic Ocean Sediments. *Sci. Rep.* 6, 39213. doi:10.1038/srep39213

Cline, J. (1969). Spectrophotometric Determination of Hydrogen Sulfide in Natural Waters. *Limnol. Oceanogr.* 14, 454–458. doi:10.4319/lo.1969.14.3.0454

Coble, P. G. (1996). Characterization of marine and Terrestrial DOM in Seawater Using Excitation-Emission Matrix Spectroscopy. *Mar. Chem.* 51, 325–346. doi:10.1016/0304-4203(95)00062-3

Conley, D. J., Björck, S., Bonsdorff, E., Carstensen, J., Destouni, G., Gustafsson, B. G., et al. (2009). Hypoxia-Related Processes in the Baltic Sea. *Environ. Sci. Technol.* 43, 3412–3420. doi:10.1021/es802762a

Conley, D. J., Carstensen, J., Aigars, J., Axe, P., Bonsdorff, E., Eremina, T., et al. (2011). Hypoxia Is Increasing in the Coastal Zone of the Baltic Sea. *Environ. Sci. Technol.* 45, 6777–6783. doi:10.1021/es201212r

Dahlberg, A.-K., Apler, A., Frogner-Kockum, P., Göransson, G., Snowball, I., Wiberg, K., et al. (2021). Dispersal of Persistent Organic Pollutants from Fiber-Contaminated Sediments: Biotic and Abiotic Pathways. *J. Soils Sediments* 21, 1852–1865. doi:10.1007/s11368-020-02871-1

Dahlberg, A.-K., Apler, A., Vogel, L., Wiberg, K., and Josefsson, S. (2020). Persistent Organic Pollutants in wood Fiber-Contaminated Sediments from the Baltic Sea. *J. Soils Sediments* 20, 2471–2483. doi:10.1007/s11368-020-02610-6

Dai, M., Yin, Z., Meng, F., Liu, Q., and Cai, W.-J. (2012). Spatial Distribution of Riverine DOC Inputs to the Ocean: an Updated Global Synthesis. *Curr. Opin. Environ. Sustainability* 4, 170–178. doi:10.1016/j.cosust.2012.03.003

de Leeuw, J. W., and Largeau, C. (1993). "A Review of Macromolecular Organic Compounds that Comprise Living Organisms and Their Role in Kerogen, Coal, and Petroleum Formation," in *Organic Geochemistry, Principles and Applications*. Editors M. H. Engel and S. A. Macko (New York: Plenum Press), 23–72. doi:10.1007/978-1-4615-2890-6_2

Dean, J. F., Middelburg, J. J., Röckmann, T., Aerts, R., Blauw, L. G., Egger, M., et al. (2018). Methane Feedbacks to the Global Climate System in a Warmer World. *Rev. Geophys.* 56, 207–250. doi:10.1002/2017RG000559

Deininger, A., and Frigstad, H. (2019). Reevaluating the Role of Organic Matter Sources for Coastal Eutrophication, Oligotrophication, and Ecosystem Health. *Front. Mar. Sci.* 6, 210. doi:10.3389/fmars.2019.00210

Del Vecchio, R., and Blough, N. V. (2004). On the Origin of the Optical Properties of Humic Substances. *Environ. Sci. Technol.* 38, 3885–3891. doi:10.1021/es049912h

Diaz, R. J., and Rosenberg, R. (2008). Spreading Dead Zones and Consequences for marine Ecosystems. *Science* 321, 926–929. doi:10.1126/science.1156401

Egger, M., Lenstra, W., Jong, D., Meysman, F. J. R., Sapart, C. J., van der Veen, C., et al. (2016). Rapid Sediment Accumulation Results in High Methane Effluxes from Coastal Sediments. *Plos One* 11, e0161609. doi:10.1371/journal.pone.0161609

Egger, M., Rasigraf, O., Sapart, C. J., Jilbert, T., Jetten, M. S. M., Röckmann, T., et al. (2015). Iron-mediated Anaerobic Oxidation of Methane in Brackish Coastal Sediments. *Environ. Sci. Technol.* 49, 277–283. doi:10.1021/es503663z

Egger, M., Riedinger, N., Mogollón, J. M., and Jørgensen, B. B. (2018). Global Diffusive Fluxes of Methane in marine Sediments. *Nat. Geosci* 11, 421–425. doi:10.1038/s41561-018-0122-8

Ettwig, K. F., Butler, M. K., Le Paslier, D., Pelletier, E., Mangenot, S., Kuypers, M. M. M., et al. (2010). Nitrite-driven Anaerobic Methane Oxidation by Oxygenic Bacteria. *Nature* 464, 543–548. doi:10.1038/nature08883

Gelesh, L. Marshall, K., Boicourt, W., and Lapham, L. (2016). Methane Concentrations Increase in Bottom Waters during Summertime Anoxia in the Highly Eutrophic Estuary, Chesapeake Bay, U.S.A. *Limnol. Oceanogr.* 61, S253–S266. doi:10.1002/lno.10272

Goñi, M. A., Teixeira, M. J., and Perkey, D. W. (2003). Sources and Distribution of Organic Matter in a River-Dominated Estuary (Winyah Bay, SC, USA). *Estuarine, Coastal Shelf Sci.* 57, 1023–1048. doi:10.1016/S0272-7714(03)00008-8

Gustafsson, B. G., Schenk, F., Blenckner, T., Eilola, K., Meier, H. E. M., Müller-Karulis, B., et al. (2012). Reconstructing the Development of Baltic Sea Eutrophication 1850-2006. *Ambio* 41, 534–548. doi:10.1007/s13280-012-0318-x

Hedges, J. I., and Ertel, J. R. (1982). Characterization of Lignin by Gas Capillary Chromatography of Cupric Oxide Oxidation Products. *Anal. Chem.* 54, 174–178. doi:10.1021/ac00239a007

Hedges, J. I., and Keil, R. G. (1995). Sedimentary Organic Matter Preservation: an Assessment and Speculative Synthesis. *Mar. Chem.* 49, 81–115. doi:10.1016/0304-4203(95)00008-F

Hedges, J. I., Mayorga, E., Tsamakis, E., McClain, M. E., Aufdenkampe, A., Quay, P., et al. (2000). Organic Matter in Bolivian Tributaries of the Amazon River: A Comparison to the Lower Mainstream. *Limnol. Oceanogr* 45, 1449–1466. doi:10.4319/lo.2000.45.7.1449

Heikkinen, P. (2000). *Paperitehtaan Jätevesikuormituksen Ympäristövaikutukset –sedimenttitutkimus Lohjanjärven Osuniemenlahdelta Ja Sen Lähiympäristöstä*. Turku: University of Turku, 1–143.

Heisler, J., Glibert, P. M., Burkholder, J. M., Anderson, D. M., Cochlan, W., Dennison, W. C., et al. (2008). Eutrophication and Harmful Algal Blooms: A Scientific Consensus. *Harmful Algae* 8, 3–13. doi:10.1016/j.hal.2008.08.006

Helmond, N. A. G. M., Lougheed, B. C., Vollebregt, A., Peterse, F., Fontorbe, G., Conley, D. J., et al. (2020). Recovery from Multi-millennial Natural Coastal Hypoxia in the Stockholm Archipelago, Baltic Sea, Terminated by Modern Human Activity. *Limnol. Oceanogr.* 65, 3085–3097. doi:10.1002/lno.11575

Holler, T., Wegener, G., Knittel, K., Boetius, A., Brunner, B., Kuypers, M. M. M., et al. (2009). Substantial13C/12C and D/H Fractionation during Anaerobic Oxidation of Methane by marine Consortia Enrichedin Vitro. *Environ. Microbiol. Rep.* 1, 370–376. doi:10.1111/j.1758-2229.2009.00074.x

Hu, Y., Feng, D., Liang, Q., Xia, Z., Chen, L., and Chen, D. (2015). Impact of Anaerobic Oxidation of Methane on the Geochemical Cycle of Redox-Sensitive Elements at Cold-Seep Sites of the Northern South China Sea. *Deep Sea Res. Part Topical Stud. Oceanography* 122, 84–94. doi:10.1016/j.dsr2.2015.06.012

Huguet, A., Vacher, L., Relexans, S., Saubusse, S., Froidefond, J. M., and Parlanti, E. (2009). Properties of Fluorescent Dissolved Organic Matter in the Gironde Estuary. *Org. Geochem.* 40, 706–719. doi:10.1016/j.orggeochem.2009.03.002

Humborg, C., Geibel, M. C., Sun, X., McCrackin, M., Mörth, C.-M., Stranne, C., et al. (2019). High Emissions of Carbon Dioxide and Methane from the Coastal Baltic Sea at the End of a Summer Heat Wave. *Front. Mar. Sci.* 6, 493. doi:10.3389/fmars.2019.00493

Jiao, N., Liu, J., Edwards, B., Lv, Z., Cai, R., Liu, Y., et al. (2021). Correcting a Major Error in Assessing Organic Carbon Pollution in Natural Waters. *Sci. Adv.* 7, eabc7318. doi:10.1126/sciadv.abc7318

Jilbert, T., Asmala, E., Schröder, C., Tiihonen, R., Myllykangas, J.-P., Virtasalo, J. J., et al. (2018). Impacts of Flocculation on the Distribution and Diagenesis of Iron in Boreal Estuarine Sediments. *Biogeosciences* 15, 1243–1271. doi:10.5194/bg-15-1243-2018

Jilbert, T., Jokinen, S., Saarinen, T., Mattus-Kumpunen, U., Simojoki, A., Saarni, S., et al. (2020). Impacts of a Deep Reactive Layer on Sedimentary Phosphorus Dynamics in a Boreal lake Recovering from Eutrophication. *Hydrobiologia* 847, 4401–4423. doi:10.1007/s10750-020-04289-9

Jilbert, T., and Slomp, C. P. (2013). Iron and Manganese Shuttles Control the Formation of Authigenic Phosphorus Minerals in the Euxinic Basins of the Baltic Sea. *Geochimica et Cosmochimica Acta* 107, 155–169. doi:10.1016/j.gca.2013.01.005

Jokinen, S. A., Jilbert, T., Tiihonen-Filppula, R., and Koho, K. (2020). Terrestrial Organic Matter Input Drives Sedimentary Trace Metal Sequestration in a Human-Impacted Boreal Estuary. *Sci. Total Environ.* 717, 137047. doi:10.1016/j.scitotenv.2020.137047

Jokinen, S. A., Virtasalo, J. J., Jilbert, T., Kaiser, J., Dellwig, O., Arz, H. W., et al. (2018). A 1500-year Multiproxy Record of Coastal Hypoxia from the Northern Baltic Sea Indicates Unprecedented Deoxygenation over the 20th century. *Biogeosciences* 15, 3975–4001. doi:10.5194/bg-15-3975-2018

Jørgensen, B. B., Beulig, F., Egger, M., Petro, C., Scholze, C., and Røy, H. (2019). Organoclastic Sulfate Reduction in the Sulfate-Methane Transition of marine Sediments. *Geochimica et Cosmochimica Acta* 254, 231–245. doi:10.1016/j.gca.2019.03.016

Jørgensen, B. B. (1982). Mineralization of Organic Matter in the Sea Bed-The Role of Sulphate Reduction. *Nature* 296, 643–645. doi:10.1038/296643a0

Kastner, M., Claypool, G., and Robertson, G. (2008). Geochemical Constraints on the Origin of the Pore Fluids and Gas Hydrate Distribution at Atwater Valley and Keathley Canyon, Northern Gulf of Mexico. *Mar. Pet. Geology.* 25, 860–872. doi:10.1016/j.marpetgeo.2008.01.022

Katko, T., Luonsi, A., and Juuti, P. (2005). Water Pollution Control and Strategies in Finnish Pulp and Paper Industries in the 20th century. *Ijep* 23, 368–387. doi:10.1504/IJEP.2005.007600

Knittel, K., and Boetius, A. (2009). Anaerobic Oxidation of Methane: Progress with an Unknown Process. *Annu. Rev. Microbiol.* 63, 311–334. doi:10.1146/annurev.micro.61.080706.093130

Kokko, M., Koskue, V., and Rintala, J. (2018). Anaerobic Digestion of 30–100-Year-Old Boreal lake Sedimented Fibre from the Pulp Industry: Extrapolating Methane Production Potential to a Practical Scale. *Water Res.* 133, 218–226. doi:10.1016/j.watres.2018.01.041

Koroleff, F. (1976). "Determination of Nutrients," in *Methods of Seawater Analysis*. Editors E. Grasshof, E. Kremling, and E. Weinhein (New York: Verlag Chemie).

Lacorte, S., Latorre, A., Barcelo, D., Rigol, A., Malmiqvist, A., and Welander, T. (2003). Organic Compounds in Paper-Mill Process Waters and Effluents. *Trac Trends Anal. Chem.* 22, 725–737. doi:10.1016/S0165-9936(03)01009-4

Lalonde, K., Mucci, A., Ouellet, A., and Gélinas, Y. (2012). Preservation of Organic Matter in Sediments Promoted by Iron. *Nature* 483, 198–200. doi:10.1038/nature10855

Lambert, T., Bouillon, S., Darchambeau, F., Morana, C., Roland, F. A. E., Descy, J.-P., et al. (2017). Effects of Human Land Use on the Terrestrial and Aquatic Sources of Fluvial Organic Matter in a Temperate River basin (The Meuse River, Belgium). *Biogeochemistry* 136, 191–211. doi:10.1007/s10533-017-0387-9

Landsman-Gerjoi, M., Perdrial, J. N., Lancellotti, B., Seybold, E., Schroth, A. W., Adair, C., et al. (2020). Measuring the Influence of Environmental Conditions on Dissolved Organic Matter Biodegradability and Optical Properties: a Combined Field and Laboratory Study. *Biogeochemistry* 149, 37–52. doi:10.1007/s10533-020-00664-9

Lenstra, W. K., Egger, M., van Helmond, N. A. G. M., Kritzberg, E., Conley, D. J., and Slomp, C. P. (2018). Large Variations in Iron Input to an Oligotrophic Baltic Sea Estuary: Impact on Sedimentary Phosphorus Burial. *Biogeosciences* 15, 6979–6996. doi:10.5194/bg-15-6979-2018

Leppäranta, M., and Myrberg, K. (2009). *Physical Oceanography of the Baltic Sea*. Heidelberg, Germany: Springer-Praxis.

Li, S., Lu, L., Wu, Y., Zhao, Z., Huang, C., Huang, T., et al. (2021). Investigation on Depth-dependent Properties and Benthic Effluxes of Dissolved Organic Matter (DOM) in Pore Water from Plateau lake Sediments. *Ecol. Indicators* 125, 107500. doi:10.1016/j.ecolind.2021.107500

Louchouarn, P., Lucotte, M., Canuel, R., Gagné, J.-P., and Richard, L.-F. (1997). Sources and Early Diagenesis of Lignin and Bulk Organic Matter in the Sediments of the Lower St. Lawrence Estuary and the Saguenay Fjord. *Mar. Chem.* 58, 3–26. doi:10.1016/S0304-4203(97)00022-4

Louchouarn, P., Lucotte, M., and Farella, N. (1999). Historical and Geographical Variations of Sources and Transport of Terrigenous Organic Matter Within a Large-Scale Coastal Environment. *Org. Geochem* 30, 675–699. doi:10.1016/S0146-6380(99)00019-4

Lougheed, B. C., and Obrochta, S. P. (2019). A Rapid, Deterministic Age-Depth Modeling Routine for Geological Sequences with Inherent Depth Uncertainty. *Paleoceanography and Paleoclimatology* 34, 122–133. doi:10.1029/2018PA003457

Luonsi, A., Junna, J., and Nevalainen, I. (1988). The Development of Waste Water Treatment in the Finnish Pulp and Paper Industry. *Water Sci. Technol.* 20, 25–36. doi:10.2166/wst.1988.0005

Martens, C. S., Albert, D. B., and Alperin, M. J. (1998). Biogeochemical Processes Controlling Methane in Gassy Coastal Sediments-Part 1. A Model Coupling Organic Matter Flux to Gas Production, Oxidation and Transport. *Continental Shelf Res.* 18, 1741–1770. doi:10.1016/S0278-4343(98)00056-9

Massicotte, P. (2019). eemR: Tools for Pre-processing Emission-Excitation Matrix (EEM) Fluorescence Data. R Package Version 1.0.1.

Massicotte, P., and Markager, S. (2016). Using a Gaussian Decomposition Approach to Model Absorption Spectra of Chromophoric Dissolved Organic Matter. *Mar. Chem.* 180, 24–32. doi:10.1016/j.marchem.2016.01.008

Mattsson, T., Kortelainen, P., and Räike, A. (2005). Export of DOM from Boreal Catchments: Impacts of Land Use Cover and Climate. *Biogeochemistry* 76, 373–394. doi:10.1007/s10533-005-6897-x

Mayer, L. M. (1994). Relationships between mineral Surfaces and Organic Carbon Concentrations in Soils and Sediments. *Chem. Geology.* 114, 347–363. doi:10.1016/0009-2541(94)90063-9

Meister, P., and Reyes, C. (2019). The Carbon-Isotope Record of the Sub-seafloor Biosphere. *Geosciences* 9, 507. doi:10.3390/geosciences9120507

Merkouriadi, I., and Leppäranta, M. (2015). Influence of Sea Ice on the Seasonal Variability of Hydrography and Heat Content in Tvärminne, Gulf of Finland. *Ann. Glaciol.* 56, 274–284. doi:10.3189/2015AoG69A003

Middelburg, J. J., and Levin, L. A. (2009). Coastal Hypoxia and Sediment Biogeochemistry. *Biogeosciences* 6, 1273–1293. doi:10.5194/bg-6-1273-2009

Miller, C. M., Dickens, G. R., Jakobsson, M., Johansson, C., Koshurnikov, A., O'Regan, M., et al. (2017). Pore Water Geochemistry along continental Slopes north of the East Siberian Sea: Inference of Low Methane Concentrations. *Biogeosciences* 14, 2929–2953. doi:10.5194/bg-14-2929-2017

Miltner, A., and Emeis, K. C. (2001). Terrestrial Organic Matter in Surface Sediments of the Baltic Sea, Northwest Europe, as Determined by CuO Oxidation. *Geochimica et Cosmochimica Acta* 65, 1285–1299. doi:10.1016/S0016-7037(00)00603-7

Mogollón, J. M., Dale, A. W., L'Heureux, I., and Regnier, P. (2011). Impact of Seasonal Temperature and Pressure Changes on Methane Gas Production, Dissolution, and Transport in Unfractured Sediments. *J. Geophys. Res.* 116, G03031. doi:10.1029/2010JG001592

Müller, C., Usbeck, R., and Miesner, F. (2016). Temperatures in Shallow marine Sediments: Influence of thermal Properties, Seasonal Forcing, and Man-Made Heat Sources. *Appl. Therm. Eng.* 108, 20–29. doi:10.1016/j.applthermaleng.2016.07.105

Myllykangas, J.-P., Hietanen, S., and Jilbert, T. (2020a). Legacy Effects of Eutrophication on Modern Methane Dynamics in a Boreal Estuary. *Estuaries and Coasts* 43, 189–206. doi:10.1007/s12237-019-00677-0

Myllykangas, J.-P., Rissanen, A. J., Hietanen, S., and Jilbert, T. (2020b). Influence of Electron Acceptor Availability and Microbial Community Structure on Sedimentary Methane Oxidation in a Boreal Estuary. *Biogeochemistry* 148, 291–309. doi:10.1007/s10533-020-00660-z

Nilsson, M. M., Hylén, A., Ekeroth, N., Kononets, M. Y., Viktorsson, L., Almroth-Rosell, E., et al. (2021). Particle Shuttling and Oxidation Capacity of Sedimentary Organic Carbon on the Baltic Sea System Scale. *Mar. Chem.* 232, 103963. doi:10.1016/j.marchem.2021.103963

Nixon, S. W. (1995). Coastal marine Eutrophication: A Definition, Social Causes, and Future Concerns. *Ophelia* 41, 199–219. doi:10.1080/00785236.1995.10422044

Norrlin, J., and Josefsson, S. (2017). Förorenade Fibersediment I Svenska Hav Och Sjöar. SGU Report 2017:07. Uppsala, Sweden: Geological Survey of Sweden. Available at: http://resource.sgu.se/produkter/sgurapp/s1707-rapport.pdf (Accessed October 14, 2021)

Pocklington, R., and Macgregor, C. D. (1973). The Determination of Lignin in Marine Sediments and Particulate Form in Seawater. *Int. J. Environ. Anal. Chem.* 3, 81–93. doi:10.1080/03067317308071070

Rabalais, N., Cai, W.-J., Carstensen, J., Conley, D., Fry, B., Hu, X., et al. (2014). Eutrophication-Driven Deoxygenation in the Coastal Ocean. *oceanog* 27, 172–183. doi:10.5670/oceanog.2014.21

Reeburgh, W. S. (2007). Oceanic Methane Biogeochemistry. *Chem. Rev.* 107, 486–513. doi:10.1021/cr050362v

Reed, D. C., Slomp, C. P., and Gustafsson, B. G. (2011). Sedimentary Phosphorus Dynamics and the Evolution of Bottom-Water Hypoxia: A Coupled Benthic-Pelagic Model of a Coastal System. *Limnol. Oceanogr.* 56, 1075–1092. doi:10.4319/lo.2011.56.3.1075

Reese, B. K., Finneran, D. W., Mills, H. J., Zhu, M.-X., and Morse, J. W. (2011). Examination and Refinement of the Determination of Aqueous Hydrogen Sulfide by the Methylene Blue Method. *Aquat. Geochem.* 17, 567–582. doi:10.1007/s10498-011-9128-1

Rooze, J., Egger, M., Tsandev, I., and Slomp, C. P. (2016). Iron-dependent Anaerobic Oxidation of Methane in Coastal Surface Sediments: Potential Controls and Impact. *Limnol. Oceanogr.* 61, S267–S282. doi:10.1002/lno.10275

Saunamäki, R. (1997). Activated Sludge Plants in Finland. *Sci. Technol.* 35, 235–243. doi:10.1016/S0273-1223(96)00936-510.2166/wst.1997.0527

Saunois, M., Bousquet, P., Poulter, B., Peregon, A., Ciais, P., Canadell, J. G., et al. (2016). The Global Methane Budget 2000-2012. *Earth Syst. Sci. Data* 8, 697–751. doi:10.5194/essd-8-697-2016

Sawicka, J. E., and Brüchert, V. (2017). Annual Variability and Regulation of Methane and Sulfate Fluxes in Baltic Sea Estuarine Sediments. *Biogeosciences* 14, 325–339. doi:10.5194/bg-14-325-2017

Schlünz, B., and Schneider, R. R. (2000). Transport of Terrestrial Organic Carbon to the Oceans by Rivers: Re-estimating Flux- and Burial Rates. *Int. J. Earth Sci.* 88, 599–606. doi:10.1007/s005310050290

Shields, M. R., Bianchi, T. S., Gélinas, Y., Allison, M. A., and Twilley, R. R. (2016). Enhanced Terrestrial Carbon Preservation Promoted by Reactive Iron in Deltaic Sediments. *Geophys. Res. Lett.* 43, 1149–1157. doi:10.1002/2015GL067388

Sholkovitz, E., Boyle, E., and Price, N. (1978). The Removal of Dissolved Humic Acids and Iron during Estuarine Mixing. *Earth Planet. Sci. Lett.* 40, 130–136. doi:10.1016/0012-821X(78)90082-1

Sivan, O., Adler, M., Pearson, A., Gelman, F., Bar-Or, I., John, S. G., et al. (2011). Geochemical Evidence for Iron-Mediated Anaerobic Oxidation of Methane. *Limnol. Oceanogr.* 56, 1536–1544. doi:10.4319/lo.2011.56.4.1536

Slomp, C. P., Mort, H. P., Jilbert, T., Reed, D. C., Gustafsson, B. G., and Wolthers, M. (2013). Coupled Dynamics of Iron and Phosphorus in Sediments of an Oligotrophic Coastal basin and the Impact of Anaerobic Oxidation of Methane. *Plos One* 8, e62386. doi:10.1371/journal.pone.0062386

Steinsberger, T., Schmid, M., Wüest, A., Schwefel, R., Wehrli, B., and Müller, B. (2017). Organic Carbon Mass Accumulation Rate Regulates the Flux of Reduced Substances from the Sediments of Deep Lakes. *Biogeosciences* 14, 3275–3285. doi:10.5194/bg-14-3275-2017

Thang, N. M., Brüchert, V., Formolo, M., Wegener, G., Ginters, L., Jørgensen, B. B., et al. (2013). The Impact of Sediment and Carbon Fluxes on the Biogeochemistry of Methane and Sulfur in Littoral Baltic Sea Sediments (Himmerfjärden, Sweden). *Estuaries and Coasts* 36, 98–115. doi:10.1007/s12237-012-9557-0

Tittel, J., Hüls, M., and Koschorreck, M. (2019). Terrestrial Vegetation Drives Methane Production in the Sediments of Two German Reservoirs. *Sci. Rep.* 9, 15944. doi:10.1038/s41598-019-52288-1

Torres, M. E., and Rugh, W. D. (2006). "Data Report: Isotopic Characterization of Dissolved Inorganic Carbon in Pore Waters Leg 204,". *Proc. ODP. Sci. Results. 204*. Editors A. M. Tréhu, G. Bohrmann, M. E. Torres, and F. S. Colwell. College Station,TX: Ocean Drilling Program, 1–16. doi:10.2973/odp.proc.sr.204.117.200

van der Veer, G. (2006). Geochemical Soil Survey of The Netherlands. Atlas of Major and Trace Elements in Topsoil and Parent Material; Assessment of Natural and Anthropogenic Enrichment Factors. *Neth. Geogr. Stud.* 347, 1–245. Available at: http://igitur-archive.library.uu.nl/dissertations/2006-1011-200742/full.pdf.

Virtasalo, J. J., Hämäläinen, J., and Kotilainen, A. T. (2014). Toward a Standard Stratigraphical Classification Practice for the Baltic Sea Sediments: the CUAL Approach. *Boreas* 43, 924–938. doi:10.1111/bor.12076

Virtasalo, J. J., Schröder, J. F., Luoma, S., Majaniemi, J., Mursu, J., and Scholten, J. (2019). Submarine Groundwater Discharge Site in the First Salpausselkä Ice-Marginal Formation, South Finland. *Solid Earth* 10, 405–423. doi:10.5194/se-10-405-2019

Weckström, K. (2006). Assessing Recent Eutrophication in Coastal Waters of the Gulf of Finland (Baltic Sea) Using Subfossil Diatoms. *J. Paleolimnol.* 35, 571–592. doi:10.1007/s10933-005-5264-1

Wehrmann, L. M., Risgaard-Petersen, N., Schrum, H. N., Walsh, E. A., Huh, Y., Ikehara, M., et al. (2011). Coupled Organic and Inorganic Carbon Cycling in the Deep Subseafloor Sediment of the Northeastern Bering Sea Slope (IODP Exp. 323). *Chem. Geology.* 284 (3-4), 251–261. doi:10.1016/j.chemgeo.2011.03.002

Whiticar, M. J. (1999). Carbon and Hydrogen Isotope Systematics of Bacterial Formation and Oxidation of Methane. *Chem. Geology.* 161, 291–314. doi:10.1016/S0009-2541(99)00092-3

Widerlund, A., and Ingri, J. (1996). Redox Cycling of Iron and Manganese in Sediments of the Kalix River Estuary, Northern Sweden. *Aquat. Geochem.* 2, 185–201. doi:10.1007/BF00121631

Yang, B., Ljung, K., Nielsen, A. B., Fahlgren, E., and Hammarlund, D. (2021). Impacts of Long-Term Land Use on Terrestrial Organic Matter Input to Lakes Based on Lignin Phenols in Sediment Records from a Swedish forest lake. *Sci. Total Environ.* 774, 145517. doi:10.1016/j.scitotenv.2021.145517

Yoshinaga, M. Y., Holler, T., Goldhammer, T., Wegener, G., Pohlman, J. W., Brunner, B., et al. (2014). Carbon Isotope Equilibration during Sulphate-Limited Anaerobic Oxidation of Methane. *Nat. Geosci* 7, 190–194. doi:10.1038/NGEO2069

Zillén, L., Lenz, C., and Jilbert, T. (2012). Stable lead (Pb) Isotopes and Concentrations - A Useful Independent Dating Tool for Baltic Sea Sediments. *Quat. Geochronol.* 8, 41–45. doi:10.1016/j.quageo.2011.11.001

Zsolnay, A., Baigar, E., Jimenez, M., Steinweg, B., and Saccomandi, F. (1999). Differentiating with Fluorescence Spectroscopy the Sources of Dissolved Organic Matter in Soils Subjected to Drying. *Chemosphere* 38, 45–50. doi:10.1016/S0045-6535(98)00166-0

Conflict of Interest: The authors declare that the research was conducted in the absence of any commercial or financial relationships that could be construed as a potential conflict of interest.

Publisher's Note: All claims expressed in this article are solely those of the authors and do not necessarily represent those of their affiliated organizations, or those of the publisher, the editors and the reviewers. Any product that may be evaluated in this article, or claim that may be made by its manufacturer, is not guaranteed or endorsed by the publisher.

frontiers in Earth Science

ORIGINAL RESEARCH
published: 17 January 2022
doi: 10.3389/feart.2021.756591

Microbial Alkalinity Production and Silicate Alteration in Methane Charged Marine Sediments: Implications for Porewater Chemistry and Diagenetic Carbonate Formation

Patrick Meister[1]*, *Gerhard Herda*[1], *Elena Petrishcheva*[2], *Susanne Gier*[1]*, *Gerald R. Dickens*[3], *Christian Bauer*[4] *and Bo Liu*[5]

[1]Department of Geology, University of Vienna, Vienna, Austria, [2]Department of Lithospheric Research, University of Vienna, Vienna, Austria, [3]Department of Geology, Trinity College Dublin, Dublin, Ireland, [4]Institute of Mechanics and Mechatronics, Vienna University of Technology, Vienna, Austria, [5]Alfred-Wegener Institute Helmholtz Centre for Polar and Marine Research, Bremerhaven, Germany

OPEN ACCESS

Edited by:
Laura M. Wehrmann, Stony Brook University, United States

Reviewed by:
Xiaole Sun, Stockholm University, Sweden
William Patrick Gilhooly, Indiana University—Purdue University Indianapolis, United States

***Correspondence:**
Patrick Meister
patrick.meister@univie.ac.at
Susanne Gier
susanne.gier@univie.ac.at

Specialty section:
This article was submitted to Biogeoscience, a section of the journal Frontiers in Earth Science

Received: *10 August 2021*
Accepted: *24 November 2021*
Published: *17 January 2022*

Citation:
Meister P, Herda G, Petrishcheva E, Gier S, Dickens GR, Bauer C and Liu B (2022) Microbial Alkalinity Production and Silicate Alteration in Methane Charged Marine Sediments: Implications for Porewater Chemistry and Diagenetic Carbonate Formation. Front. Earth Sci. 9:756591. doi: 10.3389/feart.2021.756591

A numerical reaction-transport model was developed to simulate the effects of microbial activity and mineral reactions on the composition of porewater in a 230-m-thick Pleistocene interval drilled in the Peru-Chile Trench (Ocean Drilling Program, Site 1230). This site has porewater profiles similar to those along many continental margins, where intense methanogenesis occurs and alkalinity surpasses 100 mmol/L. Simulations show that microbial sulphate reduction, anaerobic oxidation of methane, and ammonium release from organic matter degradation only account for parts of total alkalinity, and excess CO_2 produced during methanogenesis leads to acidification of porewater. Additional alkalinity is produced by slow alteration of primary aluminosilicate minerals to kaolinite and SiO_2. Overall, alkalinity production in the methanogenic zone is sufficient to prevent dissolution of carbonate minerals; indeed, it contributes to the formation of cemented carbonate layers at a supersaturation front near the sulphate-methane transition zone. Within the methanogenic zone, carbonate formation is largely inhibited by cation diffusion but occurs rapidly if cations are transported into the zone *via* fluid conduits, such as faults. The simulation presented here provides fundamental insight into the diagenetic effects of the deep biosphere and may also be applicable for the long-term prediction of the stability and safety of deep CO_2 storage reservoirs.

Keywords: alkalinity, microbial activity, methanogenesis, silicate alteration, clay minerals, diagenetic carbonate, Peru margin

INTRODUCTION

Microbial activity below the seafloor (in the deep biosphere) affects global cycling of carbon. In sediments on many continental margins, microbes convert buried organic matter through a series of reactions to methane (CH_4) and dissolved inorganic carbon (DIC), both of which can return back to the water column through advection or diffusion (e.g., Dickens, 2003; Krumins et al., 2013). In some areas, high rates of organic carbon decomposition lead to oversaturation of porewater with respect to different carbonate minerals (e.g., Baker and Burns, 1985; Moore et al., 2004; Meister et al., 2006;

Meister et al., 2007; Meister, 2015; Wehrmann et al., 2016). Precipitation of diagenetic carbonates can even occur within carbonate-free ocean margin sediment sequences (e.g., Pisciotto and Mahoney, 1981; Kelts and McKenzie, 1984; Baker and Burns, 1985). Importantly, these carbonates add to the total worldwide carbon burial flux, and variations in their accumulation over time may have contributed to past changes in global carbon cycling, such as during times of widespread anoxia (Schrag et al., 2013; Sun and Turchyn, 2014). Nevertheless, gaps remain in the understanding of organic carbon decomposition and diagenetic carbonate formation, particularly in sediment sequences characterized by strong methanogenesis.

While production of DIC drives diagenetic carbonate precipitation, a simultaneous increase in the pH buffering capacity and total alkalinity must happen to increase the activity of dissolved CO_3^{2-} and, hence, the saturation state with respect to various carbonate phases. The total alkalinity (titration alkalinity) has been defined as "excess of proton acceptors over donors with respect to carbonic acid": $TA = [HCO_3^-] + 2\,[CO_3^{2-}] + [OH^-] + [B(OH)_4^-] + [HPO_4^{2-}] + 2\,[PO_4^{3-}] + [H_3SiO_4^-] + [NH_3] + [HS^-] + 2\,[S^{2-}] - [H^+] - [HF] - [HSO_4^-] - [H_3PO_4]$ (Dickson, 1981; Middelburg et al., 2020). Several microbially mediated reactions increase alkalinity, including iron-reduction (Raiswell and Fisher, 2000; Wehrmann et al., 2009), organoclastic sulphate reduction (OSR), and anaerobic oxidation of methane (AOM; Moore et al., 2004; Ussler and Paull, 2008; Meister, 2013). In general, these processes progress with depth below the seafloor, according to their redox potential and free energy yield (e.g., Froelich et al., 1979). They also affect alkalinity differently. Notably, OSR produces two moles of DIC and two moles of alkalinity per mole of sulphate consumed, with a 1:1 ratio of TA:DIC (**Eq. 1**):

$$SO_4^{2-} + 2\,[CH_2O] \rightarrow HS^- + 2\,HCO_3^- + H^+ \quad (1)$$

By contrast, AOM generates more alkalinity relative to DIC (TA: DIC = 2:1; **Eq. 2**):

$$SO_4^{2-} + CH_4 \rightarrow HS^- + HCO_3^- + H_2O \quad (2)$$

In the absence of any terminal electron acceptor, subseafloor fermentation of organic matter can still occur, releasing CH_4, organic acids, and CO_2 to porewater. A dominant overall process is "methanogenesis", which proceeds mainly through autotrophic reduction of CO_2 with H_2 as an electron donor (Conrad, 1999; Meister and Reyes, 2019):

$$2\,[CH_2O] \xrightarrow{+2H_2O} 2\,CO_2 + 4\,H_2 \xrightarrow{-2H_2O} CO_2 + CH_4 \quad (3)$$

Crucially, the overall pathway results in excess CO_2, but without producing further alkalinity.

A current problem in our collective knowledge of the deep biosphere and the role of methanogenesis for subseafloor biogeochemical processes revolves around the fate of CO_2 and extreme porewater alkalinity. Production of CO_2 (**Eq. 3**) should lead to acidification and undersaturation of porewater with respect to carbonate minerals. This is because CO_2 dissolves in water and generates protons, but does not change alkalinity (**Eq. 4**):

$$CO_2 + H_2O \rightarrow HCO_3^- + H^+ \quad (4)$$

However, porewaters along continental margins and within zones of significant methanogenesis consistently exhibit very high alkalinity, often exceeding 50 mmol/L (**Figure 1**) and sometimes surpassing 160 mmol/L (Wefer et al., 1998). Furthermore, the high alkalinity mostly reflects dissolved HCO_3^- concentrations (except near depths of HS^- production), the pH usually exceeds 7, and early diagenetic carbonate (dolomite) often has positive $\delta^{13}C$ values, indicative of precipitation under methanogenenic conditions (Claypool and Kaplan, 1974; Kelts and McKenzie, 1984). As side-stepped in various works (e.g., Chatterjee et al., 2011; Meister et al., 2011), there is a "lost proton problem". How can sufficient alkalinity, as HCO_3^-, occur in such sub-seafloor environments to the point of driving significant amounts of carbonate precipitation?

Several additional sources of alkalinity in marine sediments have been discussed in previous studies (e.g., Chatterjee et al., 2011; Meister et al., 2011). Given a nominal C/N ratio >7:1, organic matter degradation generally produces ammonia in most continental margin sediments (e.g., Arndt et al., 2013). Due to uptake of a proton, each mole of NH_4^+ (from NH_3) also produces one mole of alkalinity:

$$NH_3 + H^+ \rightarrow NH_4^+ \quad (5)$$

While NH_4^+ accumulates in the porewater, it may adsorb to clay mineral surfaces, in exchange for Ca^{2+} and Mg^{2+}, which are readily released into the porewater (Von Breymann et al., 1990; Ockert et al., 2014; Mavromatis et al., 2015). Dissolved organic species, which almost certainly form in methanogenic systems, also need consideration (Smith, 2005).

Several authors (e.g., Aloisi et al., 2004; Wallmann et al., 2008; Meister et al., 2011; Archer et al., 2012; Solomon et al., 2014) have suggested that alteration of silicate minerals, particularly clay minerals, occurs within methanogenic zones and may produce sufficient alkalinity to drive diagenetic carbonate precipitation. At low pH and low temperatures, silicates may alter to secondary minerals by loss of oxides of alkali and earth alkali metals, which react to hydroxides upon protonation, thereby buffering acidification of dissolved CO_2 (Amiotte Suchet et al., 2003; Colbourn et al., 2015; **Eq. 6**):

$$MgO + 2\,H^+ \rightarrow Mg^{2+} + H_2O \quad (6)$$

Often silicate alteration reactions also show a loss of SiO_2, which upon water uptake reacts to H_4SiO_4 and which, hence, does not contribute to total alkalinity production. As a consequence of **Eq. 6**, alkalinity also can be expressed by the balance of conservative ions. This has been shown by Wolf-Gladrow et al. (2007), who derived an explicit conservative expression of total alkalinity: $TA_{ec} = [Na^+] + 2\,[Mg^{2+}] + 2\,[Ca^{2+}] + [K^+] - [Cl^-] - [TNH_3] - 2\,[TSO_4]$ (here only including the components relevant for the considered system). The advantage of this expression is that all parameters are conservative and can be directly measured. TA_{ec} also provides a clearer understanding of how mineral reactions affect the porewater alkalinity.

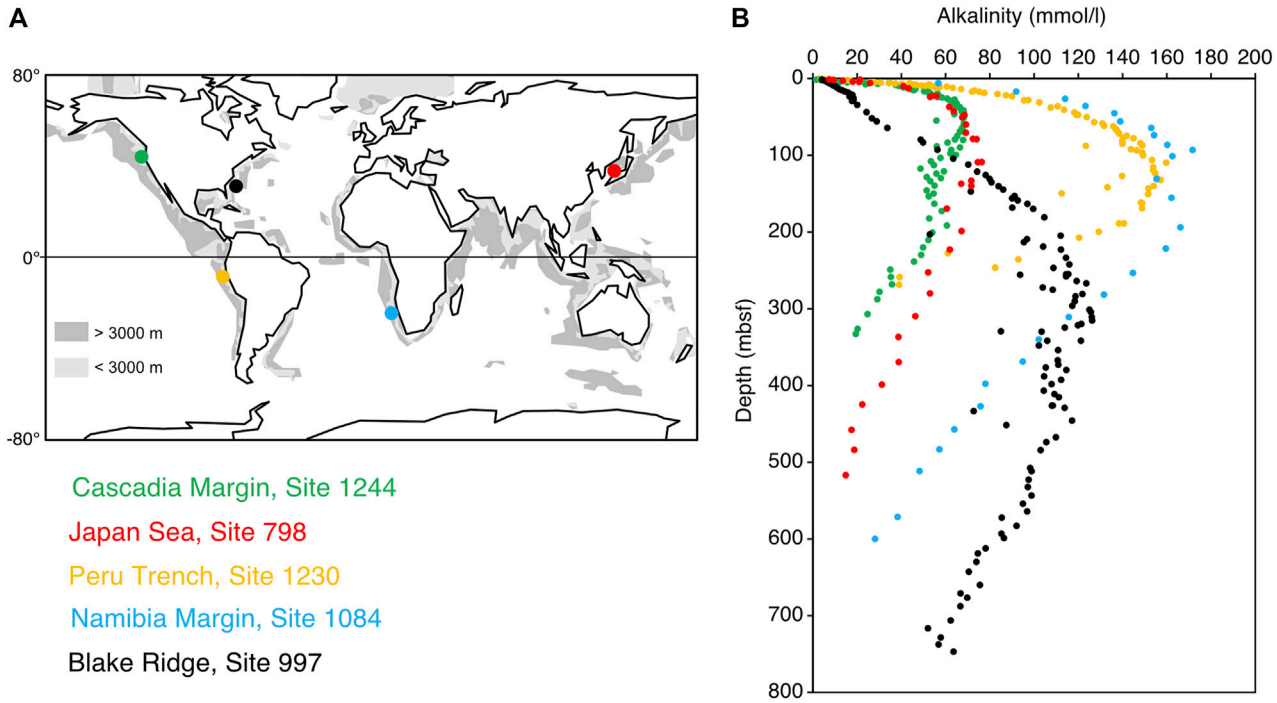

FIGURE 1 | Global map showing representative ODP sites along continental margins with thick methanogenic zones **(A)** and compilation of their porewater alkalinity profiles with respect to metres below seafloor (mbsf), highlighting greatly elevated alkalinity in the upper few hundreds of metres of sediment **(B)**. Data are from Ingle et al. (1990; Japan Sea, Site 798), Paull et al. (1996; Blake Ridge, Site 997), Wefer et al. (1998; Namibia Margin, Site 1084), D'Hondt et al. (2003; Peru Margin, Site 1230), and Tréhu et al. (2003; Hydrate Ridge, Site 1244).

Both ion exchange with NH_4^+ and silicate mineral alteration may enrich porewaters in dissolved Mg^{2+}, Na^+, and K^+ (Von Breymann et al., 1990; Wallmann et al., 2008), while Ca^{2+} typically becomes depleted due to carbonate precipitation. But which scenario is correct, and why and how extremely high alkalinity arises in zones of high microbial activity, remains unclear. Understanding the production of alkalinity and its effect on carbonate equilibrium is not only essential for understanding diagenetic carbonate formation and the natural carbon cycle, but also links to long-term storage of CO_2 in geological rock reservoirs (Bickle et al., 2007; Kasina et al., 2014).

In this study, we examine data from Ocean Drilling Program (ODP) Site 1230 on the Peru Margin (D'Hondt et al., 2003; Donohue et al., 2006). This site was drilled to examine microbiological and porewater expressions in an exemplary modern-day methanogenic system. Although Site 1230 has one of the most complete porewater datasets in ocean drilling history, the available information has yet to be placed into context. We developed a numerical reaction-transport model to simulate alkalinity production and its effect on the carbonate equilibrium as a result of microbial activity and mineral reactions in natural methanogenic zones over millions of years. Rates of microbial metabolic reactions (OSR and methanogenesis) are linked to an overall organic matter degradation rate. The rate of organic matter degradation (R_{TOC}; TOC = total organic carbon) was determined using a presumed decay function and determining the decay parameters by fitting the simulated porewater profiles to the measured porewater data. Also rates of ion exchange on clay mineral surfaces and rates of dissolution/precipitation of the minerals detected by X-ray diffraction analysis were determined in this way. We then assessed how the different processes affect total alkalinity and carbonate saturation. This simulation aims at clarifying the longstanding enigma of how diagenetic carbonates form in deep methanogenic zones below the seafloor.

STUDY SITE AND MEASURED POREWATER PROFILES

Intense coastal upwelling and high primary productivity characterize surface waters along the Peruvian continental margin. In 2002, ODP Leg 201 drilled and cored Site 1230 on the lower slope of the Peru margin (9° 6.7525′ S / 80° 35.0100′ W; **Supplementary Figure S1A**) at 5,086 m water depth, and within 100 m from ODP Site 685. The site comprises five holes (A-E), from which cores collected sediment to 278 m below seafloor (mbsf). Except for a few short pressure cores to collect gas, sediment recovery over the upper 216 m was accomplished using an advanced hydraulic piston core (APC) tool while recovery below this depth was accomplished mostly using an extended core barrel (XCB) tool.

The overall sequence has two main lithological units, which match those recovered at Site 685 (**Supplementary Figure S1B**;

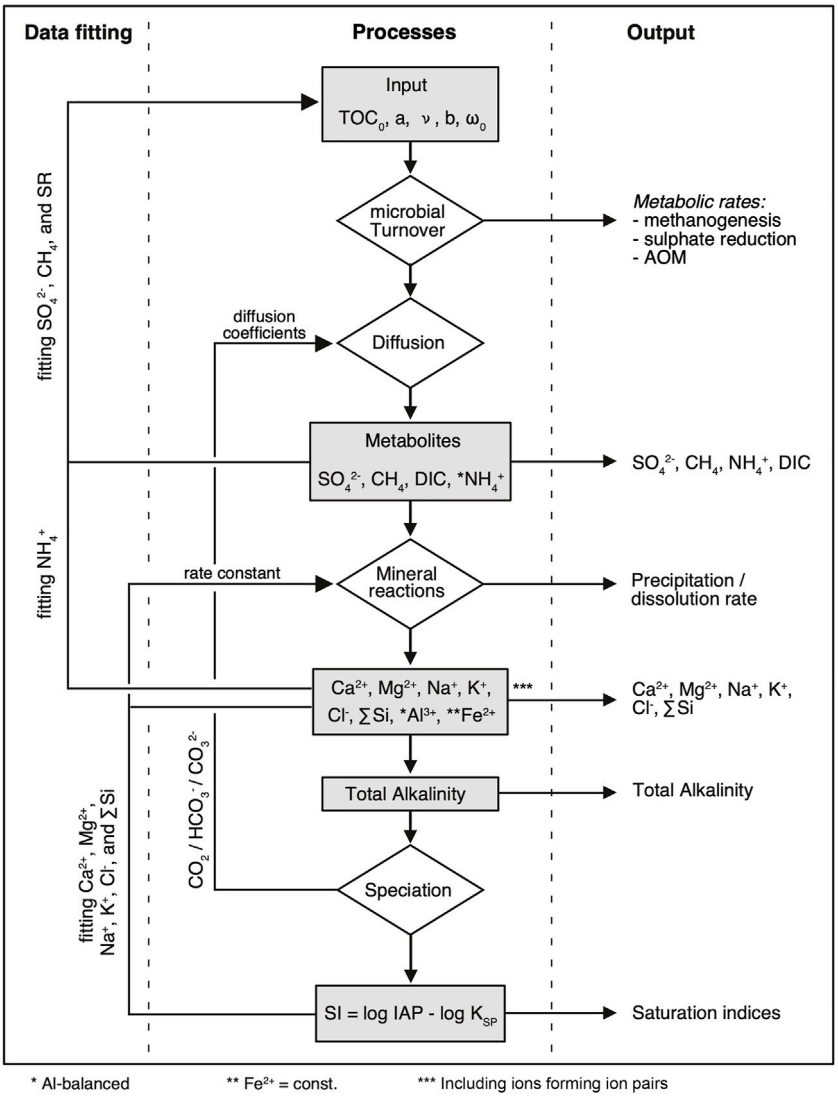

FIGURE 2 | Flow chart representation of the basic reaction-transport and precipitation model, including feedbacks, data fitting, and output. TOC_0 is the initial total organic carbon content (wt%) at the time of sediment deposition. The parameters a and ν describe the function of organic matter degradation according to Boudreau and Ruddick (1991), ω is the sedimentation rate after compaction, and b defines the compaction with depth. AOM = anaerobic oxidation of methane.

D'Hondt et al., 2003). The upper 230 m (Unit I) consist of Pleistocene-Holocene diatom ooze with variable mud content, traces of biogenic carbonate (nannofossils and foraminifera) and commonly pyrite. Total organic carbon content ranges between 2 and 3.5 wt%, with a nearly constant C/N ratio of about 9 (Prokopenko et al., 2006). By contrast, total inorganic carbon (TIC) content of bulk sediment mostly lies below 0.2 wt%, but reaches up to 1 wt% in the middle part of the unit (Meister et al., 2005). A 10-m-scale cyclicity in chromaticity (D'Hondt et al., 2003) spans the upper 118 m and reflects alternating domains enriched in diatom-ooze or dark-green clay, presumably linked to glacial and interglacial intervals. A change in chromaticity coincides with an interval of lower diatom content between 118 and 148 mbsf. The clay-rich diatom ooze shows signs of increasing consolidation and fissility towards the base of Unit I (D'Hondt et al., 2003).

A sharp boundary at 216 mbsf delineates Unit I and Unit II, and marks a downward shift to strongly consolidated Miocene sediments. The boundary likely represents a décollement surface within the accretionary prism (D'Hondt et al., 2003; Matmon and Bekins, 2006), as it is characterized by a 20-cm-thick fault breccia cemented by syntectonic dolomite (Meister et al., 2011) and a ~4 Ma gap in age (Suess 1988).

Porewater profiles show major changes in fluid composition with depth, including a steep and near linear negative sulphate gradient with a thin sulphate-methane transition zone (SMT) at approximately 9 mbsf. Sulphide reaches ca. 10 mmol/L at the SMT and decreases to zero at 20 mbsf. Below the SMT, a methanogenic zone prevails throughout the sequence. Extremely high concentrations of up to 300 mmol/L methane were reconstructed by Spivack et al. (2006), and gas hydrates were

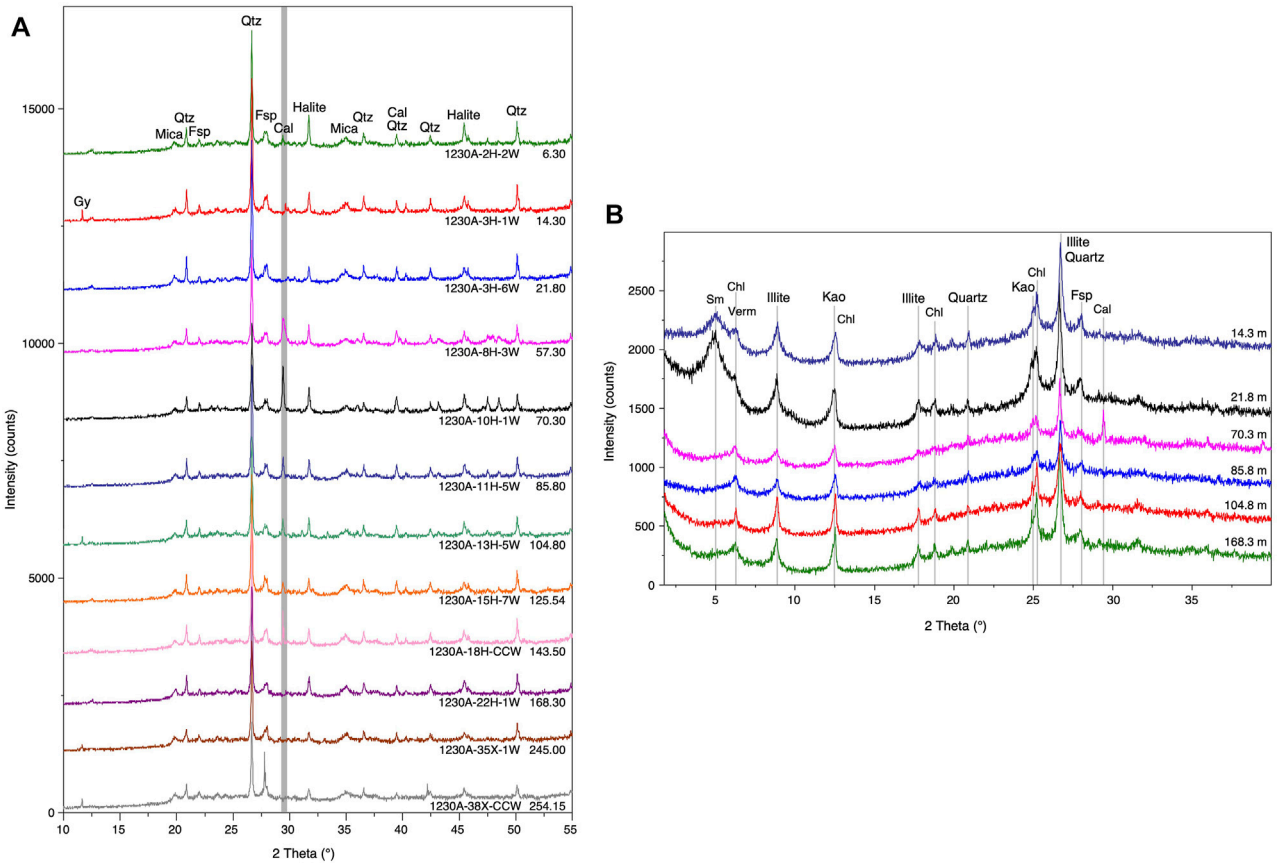

FIGURE 3 | X-ray pattern of analysed sediment samples from ODP Site 1230. **(A)** Bulk sediment showing quartz (Qtz), feldspar (Fsp), mica, and calcite (Cal). The spectra are arranged in the sequence as they occur through the drilled core. Halite and gypsum (Gy) usually form due to evaporation during sample storage. **(B)** X-ray patterns of Mg-glycerol saturated clay fractions, arranged in the same sequence as they occur through the drilled core. The spectra were interpreted to indicate smectite (Sm), vermiculite (Verm), chlorite (Chl), kaolinite (Kao), and illite, based on comparison of spectra from the fractions treated with Mg-ions, K-saturated fractions treated with ethylene glycol, and fractions heated to 550°C (shown for sample 21.8 mbsf; **Supplementary Material**).

detected at 82 and 148 mbsf (D'Hondt et al., 2003). Measured DIC and alkalinity both reach concentrations of more than 150 mmol/L near 150 mbsf (D'Hondt et al., 2003). Below 150 mbsf, alkalinity, ammonia, and Mg^{2+} concentrations decrease downwards towards the Unit I-II boundary (D'Hondt et al., 2003; Donohue et al., 2006). A sudden change in porewater chemistry occurs at this depth (D'Hondt et al., 2003), as indicated by more radiogenic Sr isotope values; likely this is due to fluid transported along the fault (Kastner et al., 1990; Meister et al., 2011).

MATERIAL AND METHODS

Mineral Analysis

Sediment samples from ODP Site 1230 were selected from undisturbed core sections recovered from 6 to 254 mbsf. For bulk mineralogical analysis, powdered sediment samples were analysed by X-ray diffraction (XRD) using a Panalytical X'Pert PRO diffractometer (Cu-Kα radiation, 40 kV, 40 mA, step size 0.0167, 5 s per step).

For clay mineral separations, six sediment samples were slightly crushed by hand to pieces of approximately 3 mm. Organic matter was removed by oxidation with diluted H_2O_2, and the samples were further disaggregated with a 400 W ultrasonic probe for 3 min. The <2 µm grain-size fraction was separated from bulk sediment by sedimentation in an Atterberg-cylinder for 24 h and 33 min (Engelhardt et al., 1974; Gaucher et al., 2004) and dried at 50°C. The homogenized samples were then saturated with K^+ and Mg^{2+} ions and oriented samples were prepared by dispersing 10 mg of clay in 1 ml of water, pipetting the suspensions onto glass slides, and drying at room temperature. The oriented, K- and Mg-saturated samples were analysed in air-dried state and after vapour solvation with either ethylene glycol (K-samples) or glycerol (Mg-samples) at 60°C for 24 h to identify expandable clay minerals like smectite and vermiculite. Additional K-saturated samples were heated to 550°C to destroy kaolinite and expandable clay minerals (Eslinger and Pevear, 1988; Jasmund and Lagaly, 1993; Moore and Reynolds, 1997).

Reaction Transport Model

Concentrations of dissolved species were simulated with a one-dimensional reaction-transport model (**Figure 2**) according to Fick's second law of diffusion in the form given by Boudreau (1997):

$$\frac{\partial \phi C}{\partial t} = -\frac{\partial \phi \omega C}{\partial z} + \frac{\partial}{\partial z}\left(\frac{\phi D}{\tau^2}\cdot\frac{\partial C}{\partial z}\right) \pm \sum \phi R \quad (7)$$

where C is the concentration of a solute (mmol/L), z is the depth in metres below seafloor (mbsf), dt is the time interval (years), and ϕ is porosity. The first term on the righthand side is a downward advection term, simulating burial with the sedimentation rate ω, whereby a steady-state compaction ($d\phi/dt = 0$; $\phi\cdot\omega$ is constant) was assumed. The downward decreasing porosity was calculated as:

$$\phi(z) = \phi_\infty + (\phi_0 - \phi_\infty)e^{-z/b} \quad (8)$$

where ϕ_0 and ϕ_∞ are constant porosities at sediment depth z = 0 and ∞, respectively, and b is the porosity e-folding distance (the distance over which $(\phi_0-\phi_\infty)$ decreases by a factor of e).

The second term on the righthand side of **Eq. 7** accounts for diffusion, where D is the diffusion constant (m^2/s; see below). The tortuosity τ was calculated from porosity according to Boudreau (1997):

$$\tau^2 = 1 - \ln\phi^2 \quad (9)$$

The third term on the righthand side of **Eq. 7** represents any source or sink (or combination thereof), where R is the rate of production or consumption of the solute (mmol L^{-1} a^{-1}). For dissimilatory metabolic reactions (sulphate reduction and methanogenesis, according to **Eqs 1**, **3**), the source and sink terms are stoichiometrically related to the degradation rate of TOC. The degradation of TOC was calculated using the reactive continuum (RC) model of Boudreau and Ruddick (1991):

$$TOC(t) = TOC_0\left[\frac{a_{RC}}{(a_{RC}+t)}\right]^\nu \quad (10)$$

where TOC(t) is the TOC at sediment age t, TOC_0 is the initial TOC upon sedimentation, and a_{RC} and ν are fitting parameters in the reactive continuum model. The source/sink s_{TOC} was calculated from the derivative of organic matter decay after time:

$$s_{TOC} = \partial\left(\frac{TOC\,\rho_s\,(1-\phi)}{100\,M_C\,\phi}\right)/\partial t \quad (11)$$

where ρ_s is the density of the dry sediment and M_C is the molecular weight of carbon. Also, TOC degradation is linked stoichiometrically to the release of ammonium via a prescribed C/N ratio.

For sulphate reduction and AOM, a Monod kinetic term was applied (Treude et al., 2003; Arndt et al., 2006; Arndt et al., 2009; Knab et al., 2008):

$$s_{AOM} = k_{AOM}[CH_4]\frac{[SO_4^{2-}]}{K_{S,AOM} + [SO_4^{2-}]} \quad (12)$$

where K_s and K_{AOM} are the half saturation constants for sulphate reduction and AOM, respectively, and k_{AOM} is the first-order rate constant for methane. Most sulphide produced by sulphate reduction is consumed by Fe-sulphide formation at the sulphide-iron front below the SMT. To calculate the sink of sulphide, FeS-precipitation was stoichiometrically coupled with reductive dissolution of Fe, with a Monod-term to limit reaction at very small sulphide concentrations. The rate constant was varied to fit the measured sulphide profile.

Due to the high pressure and low temperature at >5,000 m water depth, free gas phase should not reside within the porewater over the upper few hundred metres below the seafloor. However, dissolved CH_4 concentrations can surpass those for gas hydrate saturation. The saturation conditions were calculated according to an approach given by Tishchenko et al. (2005), based on Duan et al. (1992). Gas hydrate formation and dissociation was included in the transport model as a source/sink-term, with a rate depending on the oversaturation of dissolved CH_4. Burial of the solid phase (given in mmol equivalents per litre of porewater) was calculated using the sedimentation rate.

Cation Exchange on Mineral Surfaces

For the calculation of cation exchange on clay minerals, we assumed that adsorbed ions are in equilibrium with surrounding pore fluids. This is justified, because radiotracer experiments (Ockert et al., 2014) show that Ca^{2+}-NH_4^+ exchange occurs very rapidly, over a few hours. The conditional exchange coefficients (K_{Ex}) were found by solving a partition function with respect to ammonium for each cation (here exemplary for Ca^{2+}):

$$K_{NH4-Ca} = \frac{X_{NH4}^2}{X_{Ca}}\cdot\frac{[Ca]}{[NH_4]^2} \quad (13)$$

and by assuming the sum of all mole fractions (X) equals to one (Boatman and Murray, 1982). The cation concentrations were fitted to the porewater concentrations by varying the exchange coefficients. Rates of adsorption and desorption were calculated from the depth gradients of each adsorbed ion times the burial velocity and were included as source/sink terms in the reaction-transport function.

Speciation and Mineral Reactions

Measured concentrations of dissolved ions in porewater of marine sediment generally do not account for speciation. For example, Mg concentrations determined via inductively coupled plasma atomic emission spectrometry, such as done on ODP Leg 201, inextricably include those from Mg^{2+}, $MgCl^+$, and $MgSO_4^{(0)}$ (e.g., Katz and Ben-Yaakov, 1980). For the aqueous speciation and calculation of mineral saturation states the program Phreeqc (Version 3.5.0; Parkhurst and Appelo, 2013) was used. The reaction-transport model was linked to the PhreeqRM module (Parkhurst and Wissmeier, 2015). From the initial ion concentrations (here assumed as seawater concentrations), an initial (hypothetical) solution containing up to 90 species was calculated (**Figure 2**). The speciation was then renewed at each time step. Charge balance during transport was maintained, using the correction factor for Coulombic effects (Boudreau et al., 2004) and leaving chloride concentration variable. Charge balance also

TABLE 1 | List of parameters and values used for the reaction transport model.

Parameter	Symbol	Value	Unit	Reference
Domain and physical constraints				
Water depth	Zw	5086	m	D'Hondt et al. (2003)
Domain size	Z_D	230	m	Pleistocene; D'Hondt et al (2003)
Depth interval	dz	1	m	—
Time step	dt	100	a	—
Total duration	T	$2.3*10^6$	a	To reach steady state
Salinity	S	35	‰	Sea water
T-gradient	T_{grad}	0.0343	°C/m	D'Hondt et al. (2003)
Bottom seawater temperature	BST	2	°C	D'Hondt et al. (2003)
Density	D_{sw}	1029	kg/m^3	Sea water
Initial porosity	Φ_0	0.78	—	Fitted to data; D'Hondt et al. (2003)
Porosity at infinity	Φ	0.63	—	Fitted to data; D'Hondt et al. (2003)
Porosity decay constant	b	60	—	Fitted to data; D'Hondt et al. (2003)
Sedimentation rate at infinity	ω	0.1	m/ka	Min. for TOC Degradation
TOC degradation				
Initial TOC (during sedimentation)	TOC_0	3.5	wt%	Based on data fitting
Grain density of sediment	ρ_s	$2.45*10^3$	kg/L	Average based on data D'Hondt et al. (2003)
Initial age of organic matter	a_{RC}	25000	a	Boudreau and Ruddick (1991)
RC-parameter	ν	0.33	a	Boudreau and Ruddick (1991)
C/N-ratio	r	9.85	—	Fitted to data; Prokopenko et al. (2006)
Kinetic constants for metamolic and mineral reactions				
Half saturation constant for sulphate reduction	K_s	1	mM	Amdt et al. (2006)
For high-affinity sulphate reduction	K_s'	$2.6*10^{-3}$	mM	Tarpgaard et al. (2011)
For AOM	$K_{s,\ AOM}$	1	mM	Nauhaus et al. (1995)
First order rate constant for AOM	k_{AOM}	$8*10^{-3}$	a^{-1}	Fitted to porewater date
Cation exchange capacity	CEC	100	(meq/100 g)	typical for smectite; Ockert et al. (2014)
Weight fraction of exchange in solid phase	EX	0.2	—	Estimate from XRD
Rate constant for calcite precipitation	k_{cal}	0	mmol/(L*a)	Based on diagenetic dolomite
Rate constant for dolomite precipitation	k_{dol}	0.0005	mmol/(L*a)	Based on diagenetic dolomite precipitation above SI = 1
Rate constant for chlorite precipitation	k_{chl}	0	mmol/(L*a)	Fitted to pore water chemistry only disolution above 100 mbsf
Rate constant for K-vermiculite precipitation	k_{verm}	0.00005	mmol/(L*a)	Fitted to pore water chemistry only disolution above 100 mbsf
Rate constant for smectite, illite, K-feldspar and albite were assumed as zero as these minerals are near to saturated				
Rate constant for kaolinite precipitation	k_{kao}	Linked to Al	mmol/(L*a)	Where supersaturated only precipitation
Rate constant for cristobalite precipitation	k_{op}	0.01	mmol/(L*a)	Fitted to pore water chemistry disolution and Precipitation
Boundary Conditions				
*Upper BC**				
Alkalinity	Conc.	2.3	mmol/L	Sea water concentration
C(4)	Conc.	2.4	mmol/L	Sea water concentration
C(–4)	Conc.	0	mmol/L	Sea water concentration
N(–3)	Conc.	1	mmol/L	Sea water concentration
Ca	Conc.	10.3	mmol/L	Sea water concentration
Mg	Conc.	52	mmol/L	Sea water concentration
Na	Conc.	470	mmol/L	Sea water concentration
K	Conc.	10.2	mmol/L	Sea water concentration
Cl	Conc.	550	mmol/L	Sea water concentration
S(6)	Conc.	28	mmol/L	Sea water concentration
S(–2)	Conc.	0.0001	mmol/L	Sea water concentration
Si	Conc.	0.1	mmol/L	Sea water concentration
Al	Conc.	0.0000005	mmol/L	Sea water concentration
*also used as initial conditions				
Lower BC				
Alkalinity	Conc.	100	mmol/L	Fitted to porewater data
C(4)	Conc.	180	mmol/L	Fitted to porewater data
C(–4)	Conc.	Ghsol	mmol/L	Gas hydrated solubility
N(–3)	Conc.	3.2	mmol/L	Fitted to porewater data
Ca	Conc.	10.3	mmol/L	Fitted to porewater data
Mg	Conc.	44	mmol/L	Fitted to porewater data
Na	Conc.	450	mmol/L	Fitted to porewater data
K	Conc.	14	mmol/L	Fitted to porewater data
Cl	Conc.	520	mmol/L	Fitted to porewater data

(Continued on following page)

TABLE 1 | (*Continued*) List of parameters and values used for the reaction transport model.

Parameter	Symbol	Value	Unit	Reference
S(6)	Conc.	0	mmol/L	Fitted to porewater data
S(–2)	Conc.	0.0001	mmol/L	Fitted to porewater data
Si	Conc.	0.95	mmol/L	Saturation concentration at P/T conditions
Al	Conc.	0.0000005	mmol/L	Conc. to keep kaolinite supersaturated

was maintained for reactions. The program determines ion activity product (IAP) and the solubility product (K_{SP}).

The saturation indices (SI = log IAP – log K_{SP}) of calcite, dolomite, and all silicate phases detected by XRD were calculated for *in-situ* temperature and pressure conditions. Rates of mineral precipitation or dissolution were calculated as k·SI (cf. Lasaga, 1998; Morse et al., 2007), whereby the rate constants k were assumed to exponentially decrease with depth, and the decay parameters were found by fitting the porewater profiles to measured data (**Supplementary Material**). Sources and sinks of ions were calculated in stoichiometric proportion to the amounts of mineral dissolved or precipitated. Since Al in porewater is extremely depleted, it was not possible with the present model to simulate reaction rates with respect to Al species using a reasonable time step. For this reason, Al was kept constant at a meaningful concentration, i.e., at an intermediate concentration at which kaolinite remains always supersaturated while other silicate minerals remain undersaturated. Mineral dissolution and precipitation were then stoichiometrically coupled so that no Al was added to or removed from the solution.

Activity correction was calculated according to the Brønsted-Guggenheim-Satchard model (also known as specific ion interaction theory, SIT; Brønsted, 1921; Guggenheim and Turgeon, 1955), using the formalism presented by Grenthe and Plyasunov (1997; **Eq. 14**).

$$\log\gamma_i = -\frac{0.51 \cdot z_i^2 \sqrt{I}}{1 + 1.5\, r_i \sqrt{I}} + \sum_k \epsilon_{i,k}\, c_k \qquad (14)$$

In **Eq. 14** the activity coefficient γ_i is calculated for ion "i" as a function of ionic charge z, the ion radius r, the ionic strength I of the solution, and the sum of interactions with each ion k in the solution, with the interaction coefficient ϵ between ions "i" and "k" and the molar concentration c_k.

Parameterization and Boundary Conditions

The reaction-transport equation was solved using the finite differences method with an explicit-implicit scheme. The non-linear terms, including different source and sink terms, were solved explicitly. The simulations were run until a steady state was reached. All parameters, their symbols, values (or ranges), units, and references are listed in **Table 1**. The porewater concentration data used for fitting the model are mostly ODP Leg 201 shipboard data (D'Hondt et al., 2003; 2004) supplemented with shore-based measurements of Ca, K, Mg, and Na by Donohue et al. (2006). For the initial solution, major ion concentrations of seawater (**Table 1**) were used, and the calculated solution was also set at the seafloor as an upper domain boundary condition. Elevated DIC concentrations may occur in deep-sea bottom water due to accumulation of CO_2 from aerobic respiratory production (Zeebe, 2007), which accordingly affects the pH of the boundary condition. The lower domain boundary was defined at 230 mbsf, where the concentrations are assumed as constant. This stipulation is necessary because diverse species show a gradient across the lower boundary due to the influence of fluid advection along the fault at 230 mbsf.

TABLE 2 | List of minerals and their stoichiometric compositions selected from the sit.dat database.

Mineral name (in database)	Stoichiometry
Albite-low	$Na\ Al\ Si_3\ O_8$
Calcite	$Ca\ CO_3$
Clinochlore	$Mg_5\ Al_2\ Si_3\ O_{10}\ (OH)_8$
Cristobalite	$Si\ O_2$
Dolomite	$Ca\ Mg\ (CO_3)_2$
Illite-Mg	$K_{0.85}\ Mg_{0.25}\ Al_{2.35}\ Si_{3.4}\ O_{10}\ (OH)_2$
Kaolinite	$Al_2\ (Si_2\ O_5)\ (OH)_4$
Microcline	$K\ Al\ Si_3\ O_8$
Montmorillonite-BCMg	$Mg_{0.17}\ Mg_{0.34}\ Al_{1.66}\ Si_4\ O_{10}\ (OH)_2$
Vermiculite-K	$K_{0.86}\ Mg_3\ Si_{3.14}\ Al_{0.86}\ O_{10}\ (OH)_2$
Vermiculite-Mg	$Mg_{0.43}\ Mg_3\ Si_{3.14}\ Al_{0.86}\ O_{10}\ (OH)_2$

A minimal long-term sedimentation rate of 0.1 m/ka was assumed based on the thickness of the Pleistocene-Holocene interval of 230 m according to the Leg 112 age model (Suess, 1988). The porosity function was fitted to the measured porosity data. Diffusion coefficients were calculated for P, T, and salinity at each depth, using the functions and constants given in Boudreau (1997). No temperature and pressure derivatives of the diffusion coefficients were considered, since these effects were determined to be negligible.

We used the rate constants of AOM given in Arndt et al. (2006) and references therein and the half-saturation constant for organoclastic sulphate reduction as reported by Tarpgaard et al. (2017). Initial TOC content and parameters *a* and ν were found by fitting the concentration profiles of metabolites, such as sulphate and ammonium to the measured data and by fitting the SMT to 9 mbsf (**Supplementary Material**). In particular, varying *a* and ν also affects the curvature of the sulphate profile (Meister et al., 2013). Production of NH_4^+ was stoichiometrically linked to the rate of TOC-degradation, assuming a C/N ratio of 9 (Prokopenko et al., 2006; also consistent with ratios given in; Burdige and Komada, 2013).

Cation concentrations were fitted to the measured porewater data by varying the adsorption constants, using a CEC of 100 meq/100 g based on Ockert et al. (2014). The conditional

exchange coefficients only control the relative proportions in which the ions are adsorbed or desorbed, and they were adjusted to fit the data. Downward decreasing dissolution rate constants for individual clay minerals were found by fitting the data (**Supplementary Material**), while the precipitation of kaolinite was linked via the transfer of aluminium (see discussion for details).

For speciation and calculation of saturation states we used the parameters in the database for the specific ion interaction theory, given in the Phreeqc package (sit.dat database). The minerals were selected from the database according to the mineral assemblage detected by XRD and according to their stoichiometric composition commonly observed in marine sediments (e.g., Marinoni et al., 2008; Park et al., 2019; **Table 2**). For thermodynamic calculations *in-situ* pressure and temperature at each depth were used, with a linear temperature gradient between the mudline-temperature of 1.7 and 11.2°C at 278 mbsf at Site 1230 (D'Hondt et al., 2003).

ANALYTICAL RESULTS

Bulk Mineralogy

Bulk XRD-analyses (**Figure 3A**) show quartz (peak at 3.34 Å; 26.67° 2θ) as the most abundant phase. The second most abundant phase is feldspar, whereby albite/anorthite (3.19 Å; 27.92° 2θ) is more abundant than K-feldspar (3.24 Å, 27.53° 2θ) in all samples. Small amounts of mica or illite (peak-positions at 10 Å, 8.83° 2θ) are present in all samples. Calcite is detected in the samples from 6 mbsf and 57 to 144 mbsf. Two separate carbonate phases, a low-Mg calcite at 3.03 Å (29.4° 2θ) and a Mg calcite at 3.02 Å (29.5° 2θ), occur. A halite (NaCl) peak at 2.82 Å (31.7° 2θ) is usually present as the samples were not washed before analysis.

Clay Mineral Analysis

All analysed samples contain different amounts of smectite, vermiculite, chlorite, kaolinite, and illite (**Figure 3B**). Additionally, the clay fractions contain small amounts of quartz, feldspar, and calcite (only in one sample at 70.3 mbsf). Here, the identification of the clay minerals is explained for the sample from 21.8 mbsf (**Supplementary Figure S2**). Smectite was identified by a broad peak at 14.1 Å (6.3° 2θ) with Mg saturation which shifted to 11.8 Å (7.5° 2θ) with K saturation and collapsed to 9.9 Å (8.9° 2θ) after heating to 550°C. Saturation of the K-sample with ethylene glycol expanded smectite again to 16.8 Å (5.3° 2θ), the Mg-sample with glycerol to 18 Å (4.9° 2θ). Chlorite was identified by the peaks at 14.1, 7.07, 4.7 and 3.53 Å (6.3°, 12.5°, 18.8°, and 25.1° 2θ), which did not change position during treatments. Illite peaks at 9.9, 4.97 Å, and 3.33 Å (8.9°, 17.8°, and 26.7° 2θ) also kept their positions. Kaolinite peaks at 7.13 Å and 3.57 Å (12.4° and 24.9° 2θ) disappeared after heating to 550°C. Mg-saturated vermiculite was recognized based on a strong peak at 14 Å (6.3° 2θ), which shifted to 10 Å (8.83° 2θ) with K saturation, while saturation with Mg and glycerol (MgGly) did not change the 14 Å peak position (only present in traces in the sample from 21.8 mbsf, but more abundant in the other samples).

Looking at a depth plot of the Mg + glycerol saturated clay fractions (**Figure 3B**), it is obvious that only the uppermost two samples contain large amounts of smectite (18 Å, 4.9° 2θ). The deeper samples show only small smectite peaks, but additionally contain another expandable clay mineral, vermiculite (14 Å, 6.3° 2θ). Illite, chlorite, and kaolinite are present in samples of all depths.

MODEL RESULTS AND DISCUSSION

Biogeochemical Reactions and Effects on Alkalinity

The basic parameters used for the geochemical simulation, temperature, pressure, sedimentation rate, porosity, TOC content, and C/N ratio were fitted as good as possible to the measured data (**Figures 4A–D**; **Supplementary Figure S3**). Modelled porewater profiles, shown in **Figure 5**, reach a steady state after <1 Ma, even though 2.3 Ma are needed for burial of the gas hydrates below 230 m at a sedimentation rate of 0.1 m/ka. Therefore, the time needed to reach a steady state is well within the time frame of deposition of the Pleistocene interval, throughout which the sediment composition does not fundamentally change. The geochemistry within the underlying Miocene interval is decoupled by fluid flow along the décollement, essentially setting the boundary conditions for the Pleistocene evolution of the porewater profiles.

The measured sulphate profile is well reproduced by the model (**Figure 5A**), with an SMT at 9 mbsf. However, the rather linear gradient of the measured sulphate profile is difficult to reconcile with sulphate reduction rates of more than 1,000 pmol/cm^{3}d typically measured near the surface using radiotracer experiments (e.g., Parkes et al., 2005), which are about three orders of magnitude higher than the ones used in the present simulation (cf. also several magnitudes lower values modelled by Wang et al., 2008). Such high rates of organoclastic sulphate reduction should result in a more curved sulphate profile (Meister et al., 2013) and a lower contribution of methanogenic activity. Our simulation clearly shows that, assuming a C/N ratio of 9.85 and a TOC_0 of 3.5 wt% and the organic carbon degradation parameters a = 25,000 a and ν = 0.33, not only the solid phase parameters, but also the distribution of sulphate and methane could be well reproduced (**Supplementary Figure S3**). Methane falls within the range of concentrations determined with the argon method (Spivack et al., 2006) down to a depth of 60 mbsf (**Figure 5A**), where gas hydrate saturation is reached. Below this depth, a large scatter in the methane data probably reflects a heterogeneous distribution of gas hydrates, which contrasts with the simulation showing gas hydrate contents increasing continuously with burial and microbial production of methane. Besides sulphate and methane, ammonium concentration provides a reliable indicator for dissimilatory microbial activity (Heini et al., 2015), and the ammonium profile is well reproduced by the model in consistency with the measured C/N ratios (**Figure 5B**). It is important to notice

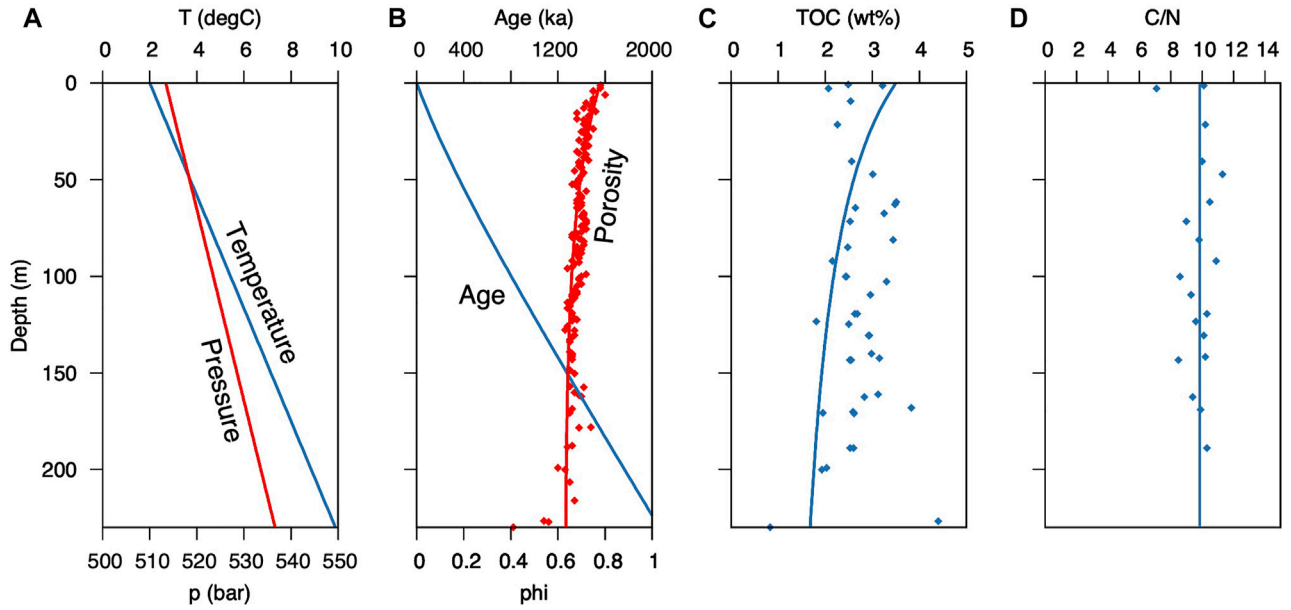

FIGURE 4 | Sediment properties and organic matter content vs. depth at ODP Site 1230: **(A)** porewater temperature and hydrostatic pressure; **(B)** sediment age and porosity (data from D'Hondt et al., 2003); **(C)** total organic carbon content (data from Meister et al., 2005); **(D)** measured C/N ratios from Site 1230 (Prokopenko et al., 2006). The solid lines indicate the values assumed for the model.

that the ammonium curve strongly depends on the parameters used for the organic carbon degradation function. Generally, a more reactive organic matter pool, with a smaller value for "a", leads to a steeper increase of ammonium in the upper part and a lower increase in the lower part of the profile. Hence, ammonium distribution can be used as a further constraint to fine-tune the organic matter degradation function.

As a result of the constrained metabolic activity, bicarbonate shows a steep increase above the SMT, while dissolved CO_2 reaches its highest concentrations only below 100 mbsf (**Figure 5C**). The high CO_2 concentrations relate to the pH drop to about 6 in the methanogenic zone (short-dashed line in **Figure 5D**). The simulated DIC increases with depth to more than 250 mmol/L around 150 mbsf (**Figure 5E**), which is considerably larger than measured data, which reach only ca. 150 mmol/L. This is expected, since a significant portion of DIC was probably lost during core recovery. *In-situ* loss of CO_2 (e.g., Paull et al., 1996) due to partitioning of CO_2 into escaping methane gas bubbles can be excluded, as no gas phase is present at the high pressure at 5,000 m water depth. Sampling loss of CO_2 would also explain the offset of the simulated pH from the measured pH. Indeed, the measured pH could be largely restored by re-equilibrating the simulated porewater solutions with 2 L of headspace per litre of porewater at atmospheric pressure (dashed lines in **Figures 5D,E**). This means that CO_2 escape would have mainly occurred by equilibration with a closed headspace during core recovery or sample storage (in the core liner or in a sample container), whereas an equilibration with the open atmosphere did not occur.

The top 10 mbsf are characterized by a strong increase in porewater alkalinity, which is largely the result of sulphate reduction and AOM. However, below the SMT (~9 mbsf) methanogenesis would only cause a small increase in alkalinity, due to the release of ammonium. Phosphate concentrations only reach up to 0.5 mmol/L (D'Hondt et al., 2003), so that the effect on alkalinity would be small. Assuming microbial activity alone, alkalinity only reaches ~100 mmol/L between 100 and 150 mbsf (**Figure 5E**, dotted line), which is lower than in the measured profile. Thus, the model scenario that includes microbial activity without ion exchange or mineral reactions reproduces the concentration profiles of the main metabolites relatively well, but it cannot explain the concentrations of some of the cations (mainly Mg^{2+} and K^{+}) and the full extent of alkalinity in the porewater.

Mineral Reactions and Their Effect on Porewater Chemistry

In the microbial activity scenario discussed above several conservative ions that count towards total alkalinity are not reproduced correctly (**Figures 5F,G**; dotted lines). Most prominently, the increase in Mg^{2+} significantly contributes to total alkalinity (TA_{ec}). The increase in Mg^{2+} may be a result of release in exchange for NH_4^{+} (Von Breymann et al., 1990). It is well known that especially smectites have a high ion exchange capacity due to their large surface area and also due to their ability to expand (e.g., Boatman and Murray, 1982). Therefore, we tested the effect of ion exchange, assuming a relatively high CEC of 100 meq/100 mg, which is typical for smectites (Ockert et al., 2014), and an extremely high content of exchanger of 50% in the sediment (approx. 10% smectite occurs in the uppermost two samples), however this did not show any significant effect on

major cations Ca^{2+}, Mg^{2+}, Na^+, K^+, and NH_4^+ in the porewater. This may seem surprising, because such a high content of an exchanger provides an ion exchange capacity on the order of hundreds of meq per liter of porewater solution. However, the minimal effect can be explained by the low sedimentation rate of 0.1 m/ka resulting in a very slow exchange of ions. Therefore, another explanation must be found for the discrepancy in simulated and measured alkalinity and conservative ion concentrations.

The alternative effect that could modify the ion content of the porewater would be recrystallization (Wallmann et al., 2008, and further references above). Unlike during ion exchange, the minerals are structurally decomposed and/or modified during this process, as commonly observed during the degradation of sheet silicates by weathering. Under diffusion-limited conditions in sediments and with a high rock/water ratio, concentrations would increase upon dissolution of some minerals until equilibrium is reached. If several different mineral phases are present, as in the modelled case, some minerals dissolve, others precipitate, allowing for larger mass transfer to occur (e.g., Michalopoulos and Aller, 1995). Effectively, the water acts as a medium, and mineral reactions are driven by the thermodynamic stabilities of the minerals under prevailing P/T conditions.

Analysed samples contain various amounts of vermiculite, chlorite, illite, smectite, and kaolinite, but there is no significant change in the peak pattern with depth indicative of ongoing phyllosilicate alteration. Also, the depletion of smectite below 70 mbsf must result from changing sedimentation, because smectite remains supersaturated and would rather form than dissolve throughout the profile. The coexistence of more phases than allowed by the Gibbs phase rule is indicated by the results from XRD (**Figures 3A,B**), so that equilibrium of the solution with all mineral phases cannot be reached. Instead, they are probably limited by reaction kinetics.

The model results show that increasing acidification leads to a minor decrease in the saturation indices of the silicate phases k-feldspar, albite, smectite, and illite, (**Figures 6A,B**), while they remain supersaturated at the SMT. In contrast, vermiculite and chlorite are strongly undersaturated below the SMT (**Figure 6C**). Porewater (**Figure 6D**) is most supersaturated with respect to kaolinite throughout the section and only slightly undersaturated at the sediment-water interface. Even if the simulated saturation indices are somewhat arbitrary, because the Al concentrations in porewater are assumed, the response to pH and ionic compositions seems reasonable. In particular, the suggested dissolution and precipitation reactions based on the saturation states correspond to known mineral alteration reactions: vermiculite and chlorite commonly weather to illite, and illite weathers to smectite (Chamley, 1989). According to the classical Goldich series, silicate-rich minerals are more resistant to chemical weathering at low temperature (Goldich, 1938; Kowalewski and Rimstidt, 2003). Most insoluble are Al_2O_3 octahedra, and accordingly the solubility decreases with increasing Al-content (Chamley, 1989). Saturation states in **Figure 6** are consistent with this rule, showing Al-poor minerals chlorite and vermiculite to be more undersaturated and more susceptible to acidification of porewater. In contrast, Al-rich minerals, feldspar and kaolinite are supersaturated. Kaolinite precipitation is then limited by Al available from the dissolving clay minerals. As a result of alteration of Al-poor to Al-rich minerals, alkali and Earth alkali metal ions are preferentially released to the solution, along with some silica. During dissolution and precipitation, charge balance is maintained as the cations dissolve from the silicates in oxide form and the oxide is readily protonated upon dissolution, yielding free ions and H_2O (**Eq. 6**), hence, contributing to the excess of conservative cations and increasing TA_{ec}.

By allowing the undersaturated silicates to dissolve and supersaturated silicates to precipitate, while adjusting the kinetic constants of different mineral phases, it was possible to improve the fit of porewater profiles to the measured data, in particular the increase of Mg^{2+} and K^+ (**Figures 5F,G**; solid lines). It was found that the simulated porewater profiles best fit to the measured data if the reaction rate decreases exponentially with depth (**Supplementary Figure S4**). The dissolution of minerals other than chlorite and vermiculite had no significant effect on porewater chemistry, as their departure from equilibrium was minimal (**Supplementary Figure S5**). While the dissolution of chlorite only delivers Mg^{2+}, K-vermiculite also provides sufficient K^+ to reproduce the K^+ profile. Also, a minor amount of Na^+ may originate from mineral reactions, although albite, the Na-endmember of plagioclase, is not undersaturated and is, thus, unlikely a significant source of Na. After inclusion of additional conservative cations released from silicate alteration, the simulated alkalinity almost entirely matches the measured alkalinity (**Figure 5E**, solid line).

Alternatively, also volcanic glass may react with porewater and provide in particular K^+ and Na^+. Volcanic glass in ash layers is fairly reactive and may undergo the generalized reaction (Scholz et al., 2013):

$$\left[(K,Na)_2O;MgO;CaO;\cdot Al_2O_3;\cdot SiO_2\right] + H_4SiO_4 + 6CO_2 + 3H_2O \rightarrow Al_2Si_2O_5(OH)_4 + K^+ + Na^+ + Mg^{2+} + Ca^{2+} + 6HCO_3^- \quad (15)$$

Although this has been suggested as a source of alkalinity for diagenetic carbonate formation elsewhere (e.g., Wehrmann et al., 2016), no major ash layers were reported from the sedimentary record at Site 1230. Interlayers of expandable smectites could furnish a further source of Na^+. For example, a strong increase in Na^+ with depth, which is decoupled from the chlorinity, occurs at Namibia margin Site 1084 and was interpreted as being derived from clay-rich sediment with up to 30% smectite in the clay fraction (Kastanja et al., 2006). However, as discussed above, ion exchange alone did not significantly affect the porewater chemistry.

Below 150 mbsf, full speciation using the measured concentrations and alkalinity would result in a charge imbalance. Since the model conserves charges, it cannot be forced to adopt this unbalance. Chloride was arbitrarily chosen to compensate the excess of negative charges, so that charge balance is maintained, which results in a decrease in Cl^- concentration. Despite this uncertainty near the bottom of

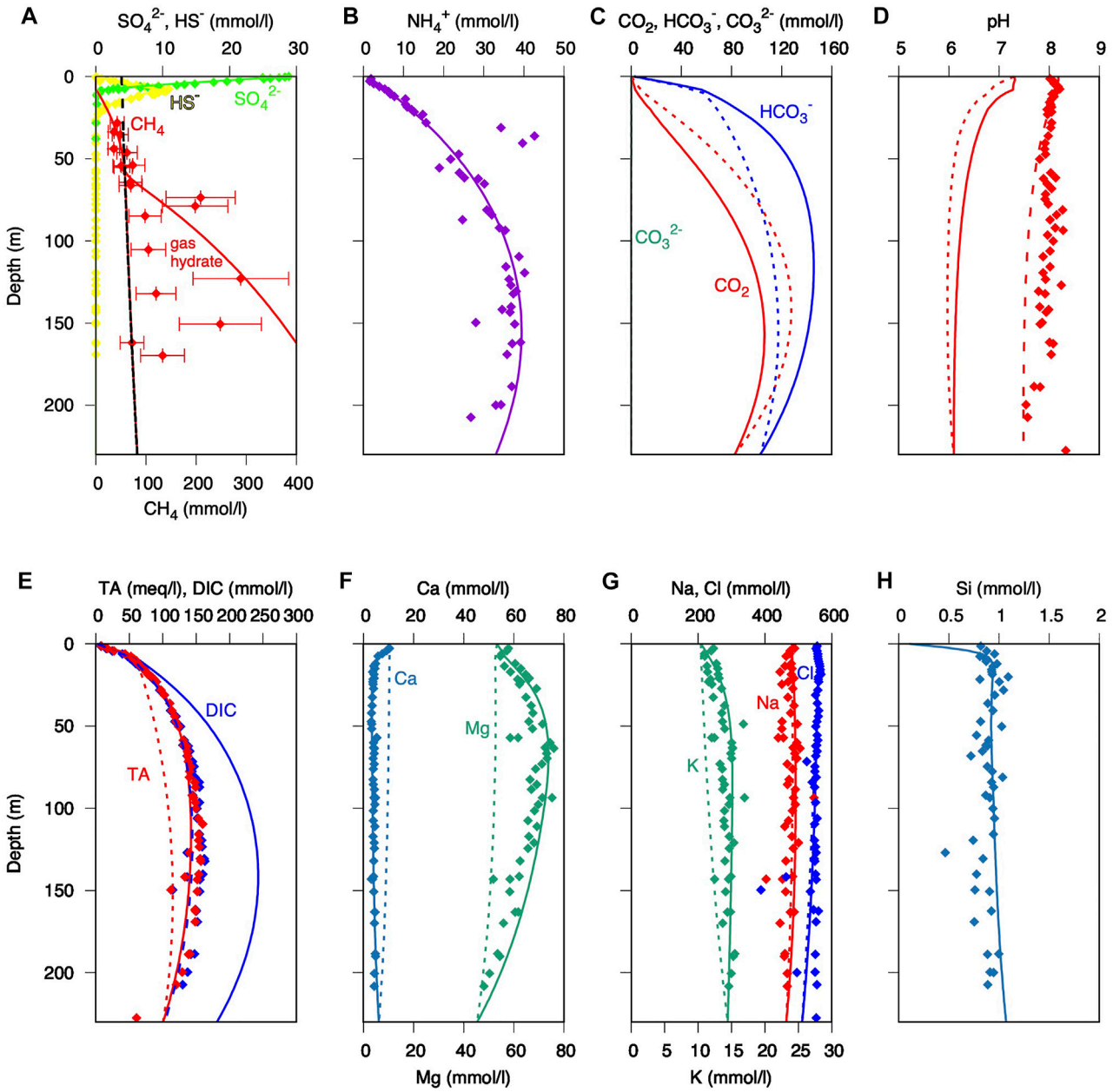

FIGURE 5 | Measured (solid symbols) and simulated porewater concentration profiles (lines) vs. depth: **(A)** sulphate and methane; **(B)** ammonium; **(C)** inorganic carbon species; **(D)** pH (dashed line: after equilibration with headspace); **(E)** dissolved inorganic carbon and total alkalinity; **(F)** Ca and Mg; **(G)** K, Na, and Cl; and **(H)** total Si. All concentrations are reported in mmol/L. Dotted lines: simulation including microbial reactions; solid lines: simulation including microbial and mineral reactions. Measured data are from D'Hondt et al. (2003) and Donohue et al. (2006).

the domain, the high alkalinity between 50 and 200 mbsf is real and can only be reached by including silicate alteration.

In addition to these mineral reactions, opal needs discussion as the sediment contains abundant diatoms (D'Hondt et al., 2003), as also indicated by an elevated baseline in the XRD-patterns. The measured concentrations of dissolved silica are clearly below the saturation of opal-A, but the simulations follow the data fairly well with opal-C/T as an equilibrium phase (**Figures 5H**, **6D**). Indeed, it is surprising that the dissolution of opal-A, which is available in large amounts, does not dominate silica concentrations in the porewater. But it is known that opal-A dissolution can be inhibited, as diatoms are covered by organic matter (Van Cappellen, 1996). Opal-C/T as the thermodynamically more stable phase then should form, according to Ostwald's step rule (e.g., Meister et al., 2014). The curve in the silica concentration profile near the seafloor is due to the fact that silica is strongly undersaturated in seawater. The slight

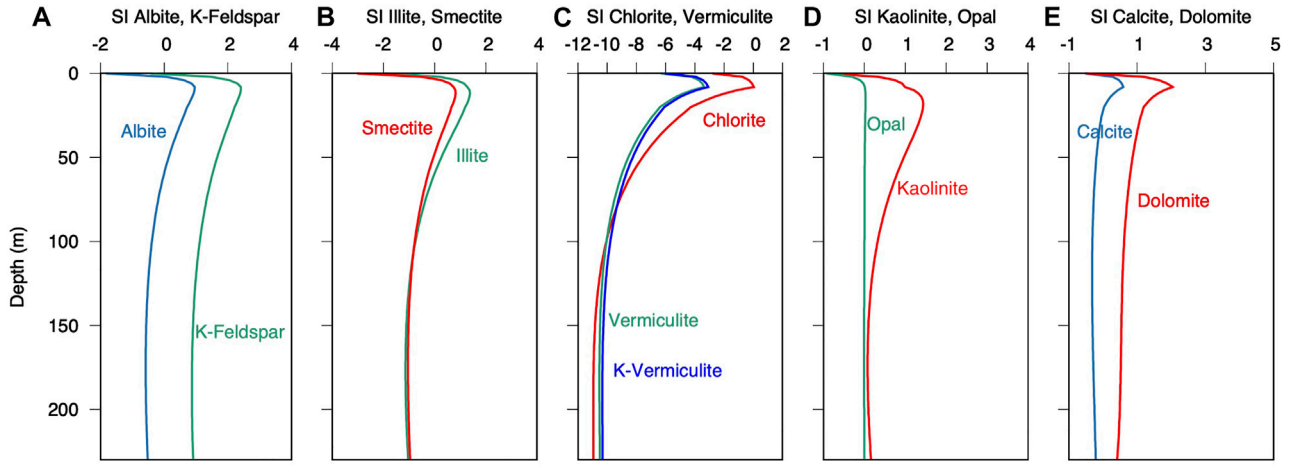

FIGURE 6 | Saturation indices (SI) of silicate minerals **(A)** albite and K-feldspar, **(B)** illite and smectite, **(C)** vermiculite and chlorite, **(D)** kaolinite and cristobalite, and **(E)** calcite and dolomite.

increase with depth is explained by the increasing solubility with temperature.

Overall, alteration of silicate minerals contributes to the very high total alkalinity (~150 mmol/L) measured at ODP Site 1230. This additional alkalinity effect significantly buffers acidification of the porewater by the production of CO_2 during microbial methanogenesis. In contrast, the production of alkalinity by anaerobic metabolisms (organoclastic sulphate reduction and AOM) and the dissimilatory release of ammonium alone would not be sufficient to explain the measured alkalinity. High (>80 mmol/L) alkalinity concentrations characterize porewaters recovered from within the uppermost few hundred metres below the seafloor at many drill sites along continental margins of the world. Away from the Peru Margin, examples include DSDP Site 262 (Timor Sea, Indian Ocean; Cook, 1974), ODP Sites 994, 995, and 997 (Blake Ridge, Atlantic Ocean; Paull et al., 1996), Site 1019 (California Margin, Pacific; Lyle et al., 1997), Site 1082 (Namibian Margin, Atlantic; Murray and Wigley, 1998) and IODP Sites U1426 and U1427 (Sea of Japan, west Pacific; Tada et al., 2015; see also the examples in **Figure 1**). All these sites have several commonalities: high accumulation rates of clay and organic carbon, a shallow SMT, and within underlying porewaters, high methane, elevated NH_4^+ and K^+, and low Ca^{2+} concentrations. However, unlike Site 1230, some of them have low Mg^{2+} concentrations in porewater and lack gas hydrate. We suspect that microbial methane production and consequent mineral reactions are ubiquitous processes on continental margins around the world, but the rates and details vary depending on parameters embedded in our modelling. These would include pressure and temperature, but also the rate and composition of sedimentary inputs, from organic carbon to aluminosilicates. Not all minerals react equally. In particular, the Mg-rich clay minerals, vermiculite and chlorite dominating in areas of physical weathering under cold and temperate conditions (Chamley, 1989), and to some extent probably also volcanic ash, provide a strong capacity to buffer the pH by increasing alkalinity in the porewater. Future modelling efforts at other sites should lead to further testing and refinement of ideas presented here.

Factors Controlling Carbonate Precipitation

Having established the effects of biogeochemical activity and silicate alteration on the alkalinity and DIC content, we can now assess the factors controlling the saturation state of carbonates (**Figure 6E**). Calcite and dolomite are only slightly supersaturated or undersaturated in the bottom water, which is partially due to high amounts of CO_2 produced by aerobic respiration in the water column, below the oxygen minimum zone at a water depth of 5,000 m (e.g., Zeebe, 2007). In the top few metres of the sediment, pH generally converges to values near 7 as a result of sulphate reduction (Soetaert et al., 2007; Meister, 2013; Meister, 2014), whereby additional alkalinity from AOM results in a sharp terrace at the SMT at 9 mbsf (solid line in **Figure 5D**), and saturation indices of calcite and dolomite reach maxima (**Figure 6E**). Ca^{2+} concentration decreases from the surface to the SMT and also Mg^{2+} shows a kink at this depth, suggesting recent or ongoing precipitation of calcite and dolomite. The kinks can be largely reproduced by the model if dolomite precipitation is included. Indeed, a hard-lithified dolomite from 6.5 mbsf shows $\delta^{13}C$ values more negative than −30‰, which is a clear indication of an AOM-induced dolomite (Meister et al., 2007; Meister et al., 2011; Meister et al., 2019a).

In the methanogenic zone below 9 mbsf, DIC increase to 250 mmol/L would cause a pH decrease to <6, but taking into account alkalinity production from mineral reactions more moderate pH values above 6 are reached (**Figure 5D**). The saturation indices of carbonates remain near saturation, which is due to the buffering effect of the alkalinity reaching 150 mmol/L near 100 mbsf. Hence, alkalinity production due to NH_4^+ release and silicate alteration largely prevents the dissolution of carbonates in the methanogenic zone, as it would be expected based on CO_2 production alone. Carbonates may even become slightly

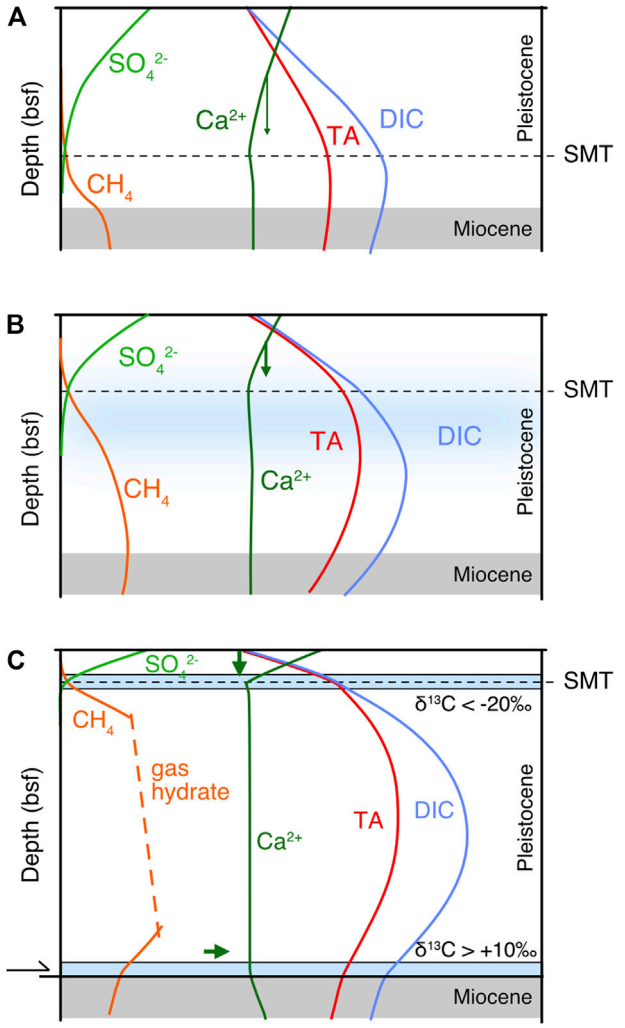

FIGURE 7 | Conceptual model to explain the formation of diagenetic carbonates in relation to the evolution of the methanogenic zone: **(A)** During Pleistocene sedimentation over the Miocene, dissimilatory reactions lead to the onset of a methanogenic zone. **(B)** Within the expanding methanogenic zone alkalinity builds up, but insignificant carbonates (disseminated calcite or dolomite; blue shaded area) are precipitated as the diffusion distance for Ca^{2+} and Mg^{2+} are too long. **(C)** The methanogenic zone has now further expanded and a gas hydrate zone has established. The gradients near the surface are steep, with a shallow SMT driving carbonate precipitation (lithified dolomites; blue bars). Also at depth, fluid flow along the décollement provides Ca^{2+}, inducing carbonate precipitation. The two types of dolomite show contrasting $\delta^{13}C$ values, derived from dissimilatory sulphate reduction and methanogenesis, respectively.

supersaturated due to this effect, but their precipitation would be hampered by the slow supply of Ca^{2+} due to the long diffusion distances from the seafloor.

Calcite was detected by XRD in the bulk sediments in the top 150 mbsf, with higher amounts between 50 and 150 mbsf (**Figure 3A**). This carbonate is clearly part of the sediment, whereas an *ex-situ* precipitation due to degassing during core recovery can be excluded, as from porewater with 4 mmol/L Ca^{2+} only ca. 1 g $CaCO_3$ per kg sediment could precipitate, which would be far below the detection limit of the XRD analysis. Besides low-Mg calcite also traces of Mg-calcite were detected. While the calcite may be diagenetic, precipitation of significant amounts of carbonate is probably not possible at present core depth, due to lack of Ca supply. Thus, the disseminated calcite detected between 50 and 150 mbsf formed most likely in the past, when the according sediment was located sufficiently near to the sediment surface to allow for a sufficient supply of Ca^{2+} from seawater, but not as shallow as during the formation of the lithified layer of dolomite at 6.5 mbsf.

The formation of hard lithified diagenetic carbonates vs. fine disseminated carbonate is a longstanding problem (cf. Garrison et al., 1984). At Site 1230 no dolomite layers occur between 6.5 and 220 mbsf throughout the zone of abundant methane production. Having demonstrated that porewaters are not carbonate-undersaturated in the methanogenic zone, it cannot be argued that past dolomite layers have been dissolved in the methanogenic zone. Apparently, they have never formed, despite the intense methane production that should have maintained a pronounced SMT. However, a possible explanation for the lack of dolomite layers could be that initially methane was not available for intense AOM at the SMT (scenario in **Figure 7A**). Due to the great water depth, a gas hydrate zone established and expanded as the Pleistocene interval increased in thickness. At this stage, disseminated calcite or dolomite could have formed (**Figure 7B**). Only when the thickness of the methanogenic zone became sufficiently large to induce an SMT at shallow depth, a dolomite layer could have formed at 6.5 mbsf (**Figure 7C**). The SMT may have migrated a few metres upward and downward, possibly due to variation of bottom water temperature or variation of TOC and sedimentation rate, which are not resolved by the simulation.

While carbonate formation in relation with AOM has been discussed, it is still not clear how carbonates (in particular dolomite) with a strongly positive carbon isotope signature may form. A 20-cm-thick, hard-lithified dolomite breccia was recovered from 230 mbsf at Site 1230, exhibiting a $\delta^{13}C$ of up to 15‰ (Meister et al., 2011). Inorganic carbon in methanogenic zones typically shows positive $\delta^{13}C$ values, as DIC becomes enriched and CH_4 depleted in ^{13}C as a result of fractionation within the methanogenic pathways (see Meister and Reyes, 2019 for details). At Site 1230, Meister et al. (2011) showed the influence of fluid with more radiogenic $^{87}Sr/^{86}Sr$ ratios transported along an active fault zone at 230 mbsf, providing Ca^{2+} and inducing precipitation of a dolomitic fault breccia. As Ca^{2+} was delivered into the midst of a zone with high alkalinity, large amounts of dolomite could have precipitated (**Figure 7C**). The formation of a dolomite breccia showing a syntectonic cement structure with compromise boundaries (Meister et al., 2011) also suggests a rapid precipitation. However, these conditions are specific to the tectonic situation in an accretionary prism, where fluid is driven upwards, but they still do not explain how hard lithified dolomite layers form in methanogenic zones elsewhere.

More extensive dolomite layers showing a methanogenic $\delta^{13}C$ signature are found, for example, in the Miocene Monterey Fm. of

California (e.g., Murata et al., 1969; Burns and Baker, 1987; Mozley and Burns, 1993; Loyd et al., 2012) and in many organic carbon rich marine sediments drilled by ODP (e.g., Kelts and McKenzie, 1984; Thornburg and Suess, 1992; Rodriguez et al., 2000). As these sites are partially located on the shelf, they may often be affected by CH_4 loss under dynamic conditions (Arning et al., 2012; Contreras et al., 2013), and gas escape must be taken into account, whereby partitioning of CO_2 in methane bubbles could lead to escape of CO_2 and thereby inducing carbonate formation via pH increase (Meister and Reyes, 2019; Meister et al., 2019b). However, none of these effects would be expected in the deep sea, where free gas is not present at low temperatures. In order to simulate carbonate diagenesis on the shelf, gas transport will have to be included in future modelling studies.

CONCLUSION

The Neogene sediment sequence at ODP Site 1230 in the Peru-Chile Trench contains porewaters with extreme alkalinity, reaching ~150 mmol/L at ca. 100 mbsf. Full-speciation reaction-transport modelling shows that these concentrations result from several reactions. Much of the alkalinity is produced by organoclastic sulphate reduction and AOM in the upper part of the profile but also through release of ammonium from organic matter degradation throughout the sequence. The alteration of silicate minerals, in particular vermiculite and chlorite to kaolinite and opal-C/T, contributes substantial amounts of Mg^{2+} and K^+ and further increases alkalinity in the methanogenic zone. In combination, microbial processes and clay mineral alteration produce sufficient alkalinity within the methanogenic zone to buffer acidification caused by increased DIC (up to 250 mmol/L) from dissimilation of organic matter and, thus, to prevent undersaturation and dissolution of carbonates. Within the methanogenic zone, diagenetic carbonate formation is largely calcium-limited, due to the long diffusion distances, but dolomite beds readily form if Ca^{2+} is supplied, such as at the SMT or along a fault zone. The SMT dolomites generally show a negative $\delta^{13}C$ signature, whereas dolomites forming within the methanogenic zone show a positive $\delta^{13}C$ signature, but in the absence of a gas phase, a shift of the dolomitization front due to CO_2 degassing does not occur within the gas hydrate stability zone.

While our simulation provides insight into carbonate diagenesis in deep methanogenic zones, it also would be applicable to human-made CO_2 storage reservoirs. Our study shows that reservoirs rich in specific clay minerals, vermiculite and chlorite, would have an extremely high capacity to trap CO_2 as bicarbonate, although the kinetics of these reactions are rather slow. In any case, having a quantitative model at hand that can realistically simulate carbonate diagenesis in marine sediments will be essential to understand the role of sub-surface fluid-microbe-mineral interactions in the global carbon cycle.

DATA AVAILABILITY STATEMENT

The original contributions presented in the study are included in the article/**Supplementary Material**, further inquiries can be directed to the corresponding authors.

AUTHOR CONTRIBUTIONS

PM: Design of the study, supervision, developing the model, interpretion, writing the manuscript; GH: Modelling with Phreeqc, wrote early version; EP: Advising numerical modelling, provided comments to the manuscript; SG: X-ray diffraction, clay mineral analysis, comments to the manuscript; GD: Shipboard and shore-based porewater analysis, comments to the manuscript; CB: Code writing in C++; BL: Code writing, code testing, advice for mathematical solutions, comments to the manuscript.

FUNDING

This research used samples and data provided by the Ocean Drilling Program (now International Ocean Discovery Program, IODP), sponsored by the participating countries. PM was further supported by the European Union through Marie-Curie Actions MRTN-CT-2006-035868 (project GRASP), and PIEF-GA-2013-626025 (project TRIADOL) and be the Swiss National Science Foundation SNF through project PA00P2-126221. BL acknowledges additional funding from the Helmholtz Association (Alfred Wegener Institute Helmholtz Centre for Polar and Marine Research).

ACKNOWLEDGMENTS

We thank David Parkhurst for providing helpful explanations to the programme Phreeqc by responding to our question on the Phreeqc forum (https://www.phreeqcusers.org). We thank Benjamin Huet, Martin Schöpfer, and Bernhard Grasemann for providing help to solve problems with programming. Rainer Abart and Stephan Krämer provided further advice to the geochemistry. We also thank Steve Schäfer and Mischa Kim of the MathWorks Support Team for help with connecting the Matlab code to Phreeqc in an earlier version of our model. We thank two reviewers for their constructive comments.

SUPPLEMENTARY MATERIAL

The Supplementary Material for this article can be found online at: https://www.frontiersin.org/articles/10.3389/feart.2021.756591/full#supplementary-material

REFERENCES

Aloisi, G., Wallmann, K., Drews, M., and Bohrmann, G. (2004). Evidence for the Submarine Weathering of Silicate Minerals in Black Sea Sediments: Possible Implications for the marine Li and B Cycles. *Geochem. Geophys. Geosyst.* 5, Q04007. doi:10.1029/2003gc000639

Amiotte Suchet, P., Probst, J. L., and Ludwig, W. (2003). Worldwide Distribution of continental Rock Lithology: Implications for the Atmospheric/soil CO_2 Uptake by continental Weathering and Alkalinity River Transport to the Oceans. *Glob. Biogeochem. Cycles* 17, 1038–1051. doi:10.1029/2002gb001891

Archer, D. E., Buffett, B. A., and McGuire, P. C. (2012). A Two-Dimensional Model of the Passive Coastal Margin Deep Sedimentary Carbon and Methane Cycles. *Biogeosciences* 9, 2859–2878. doi:10.5194/bg-9-2859-2012

Arndt, S., Brumsack, H.-J., and Wirtz, K. W. (2006). Cretaceous Black Shales as Active Bioreactors: A Biogeochemical Model for the Deep Biosphere Encountered during ODP Leg 207 (Demerara Rise). *Geochimica et Cosmochimica Acta* 70, 408–425. doi:10.1016/j.gca.2005.09.010

Arndt, S., Hetzel, A., and Brumsack, H.-J. (2009). Evolution of Organic Matter Degradation in Cretaceous Black Shales Inferred from Authigenic Barite: a Reaction-Transport Model. *Geochimica et Cosmochimica Acta* 73, 2000–2022. doi:10.1016/j.gca.2009.01.018

Arndt, S., Jørgensen, B. B., LaRowe, D. E., Middelburg, J. J., Pancost, R. D., and Regnier, P. (2013). Quantifying the Degradation of Organic Matter in marine Sediments: A Review and Synthesis. *Earth-Science Rev.* 123, 53–86. doi:10.1016/j.earscirev.2013.02.008

Arning, E. T., Berk, W., and Schulz, H. M. (2012). Quantitative Geochemical Modeling along a Transect off Peru: Carbon Cycling in Time and Space, and the Triggering Factors for Carbon Loss and Storage. *Glob. Biogeochem. Cycles* 26, GB4012. doi:10.1029/2011GB004156

Baker, P. A., and Burns, S. J. (1985). Occurrence and Formation of Dolomite in Organic-Rich continental Margin Sediments. *AAPG Bull.* 69, 1917–1930. doi:10.1306/94885570-1704-11d7-8645000102c1865d

Bickle, M., Chadwick, A., Huppert, H. E., Hallworth, M., and Lyle, S. (2007). Modelling Carbon Dioxide Accumulation at Sleipner: Implications for Underground Carbon Storage. *Earth Planet. Sci. Lett.* 255, 164–176. doi:10.1016/j.epsl.2006.12.013

Boatman, C. D., and Murray, J. W. (1982). Modeling Exchangeable NH4 + Adsorption in marine Sediments: Process and Controls of Adsorption1,2. *Limnol. Oceanogr.* 27, 99–110. doi:10.4319/lo.1982.27.1.0099

Boudreau, B. P. (1997). *Diagenetic Models and Their Implementation: Modelling Transport and Reactions in Aquatic Sediments*. Berlin, Heidelberg, New York: Springer.

Boudreau, B. P., Meysman, F. J. R., and Middelburg, J. J. (2004). Multicomponent Ionic Diffusion in Porewaters: Coulombic Effects Revisited. *Earth Planet. Sci. Lett.* 222, 653–666. doi:10.1016/j.epsl.2004.02.034

Boudreau, B. P., and Ruddick, B. R. (1991). On a Reactive Continuum Representation of Organic Matter Diagenesis. *Am. J. Sci.* 291, 507–538. doi:10.2475/ajs.291.5.507

Brønsted, J. N. (1921). Studies on Solubility. IV. The Principle of the Specific Interaction of Ions. *J. Am. Chem. Soc.* 44, 877–898.

Burdige, D. J., and Komada, T. (2013). Using Ammonium Pore Water Profiles to Assess Stoichiometry of Deep Remineralization Processes in Methanogenic continental Margin Sediments. *Geochem. Geophys. Geosyst.* 14, 1626–1643. doi:10.1002/ggge.20117

Burns, S. J., and Baker, P. A. (1987). A Geochemical Study of Dolomite in the Monterey Formation, California. *J. Sediment. Petrol.* 57, 128–139. doi:10.1306/212f8ac6-2b24-11d7-8648000102c1865d

Chamley, H. (1989) *Clay Sedimentology*. Springer, Berlin, Heidelberg, 623 pp. ISBN 978-3-540-50889-2.

Chatterjee, S., Dickens, G. R., Bhatnagar, G., Chapman, W. G., Dugan, B., Snyder, G. T., et al. (2011). Pore Water Sulfate, Alkalinity, and Carbon Isotope Profiles in Shallow Sediment Above Marine Gas Hydrate Systems: A Numerical Modeling Perspective. *J. Geophys. Res.* 116, 1–25. doi:10.1029/2011JB008290

Claypool, G. E., and Kaplan, I. R. (1974). "The Origin and Distribution of Methane in marine Sediments," in *" in* Natural Gases In Marine Sediments. Editor I. R. Kaplan (New York: Plenum Press), 99–139. doi:10.1007/978-1-4684-2757-8_8

Colbourn, G., Ridgwell, A., and Lenton, T. M. (2015). The Time Scale of the Silicate Weathering Negative Feedback on Atmospheric CO2. *Glob. Biogeochem. Cycles* 29 (5), 583–596. doi:10.1002/2014GB005054

Conrad, R. (1999). Contribution of Hydrogen to Methane Production and Control of Hydrogen Concentrations in Methanogenic Soils and Sediments. *FEMS Microbiol. Ecol.* 28, 193–202. doi:10.1111/j.1574-6941.1999.tb00575.x

Contreras, S., Meister, P., Liu, B., Prieto-Mollar, X., Hinrichs, K.-U., Khalili, A., et al. (2013). Cyclic 100-ka (Glacial-interglacial) Migration of Subseafloor Redox Zonation on the Peruvian Shelf. *Proc. Natl. Acad. Sci.* 110, 18098–18103. doi:10.1073/pnas.1305981110

Cook, P. J. (1974). Geochemistry and Diagenesis of Interstitial Fluids and Associated Calcareous Oozes, Deep Sea Drilling Project, Leg 27, Timor Trough. *Init. Rep. Deap Sea Drill. Project* 27, 463–480. doi:10.2973/dsdp.proc.27.119.1974

D'Hondt, S., Jørgensen, B. B., Miller, J., Batzke, A., Blake, R., Cragg, B. A., et al. (2004). Distributions of Microbial Activities in Deep Subseafloor Sediments. *Science* 306, 2216–2221.

D'Hondt, S. L., Jørgensen, B. B., and Miller, D. J. (2003). *Proc. ODP, Init. Repts. 201*. College Station TXUSA: Ocean Drilling Program, Texas A&M University. 77845-9547. The shipboard scientific party

Dickens, G. R. (2003). Rethinking the Global Carbon Cycle with a Large, Dynamic and Microbially Mediated Gas Hydrate Capacitor. *Earth Planet. Sci. Lett.* 213, 169–183. doi:10.1016/s0012-821x(03)00325-x

Dickson, A. G. (1981). An Exact Definition of Total Alkalinity and a Procedure for the Estimation of Alkalinity and Total Inorganic Carbon from Titration Data. *Deep Sea Res. A: Oceanographic Res. Pap.* 28, 609–623. doi:10.1016/0198-0149(81)90121-7

Donohue, C. M., Snyder, G. T., and Dickens, G. R. (2006). "Data Report: Major Cation Concentrations of Interstitial Waters Collected from Deep Sediments of Eastern Equatorial Pacific and Peru Margin (ODP Leg 201)," in *Proc. ODP, Sci. Results 201*. Editors B. B. Jørgensen, 1–19, Ocean Drilling Program, College Station, Texas. doi:10.2973/odp.proc.sr.201.104.2006

Duan, Z., Møller, N., and Weare, J. H. (1992). An Equation of State for the CH4-CO2-H2O System: I. Pure Systems from 0 to 1000°C and 0 to 8000 Bar. *Geochimica et Cosmochimica Acta* 56, 2605–2617. doi:10.1016/0016-7037(92)90347-l

Engelhardt, W., Füchtbauer, H., and Müller, G. (1974). *Sedimentary Petrology, Part 1: Methods in Sedimentary Petrology*, Vol. 1. Stuttgart, Germany: Schweizerbart'sche Verlagsbuchhandlung.

Eslinger, E., and Pevear, D. R. (1988). "Clay Minerals and Sandstone Diagenesis," in *Clay Minerals For Petroleum Geologists And Engineers*. Editors E. Eslinger and D. Pevear, 22, 6, 1988 . 1–6.29.*SEPM Short Course*

Froelich, P. N., Klinkhammer, G. P., Bender, M. L., Luedtke, N. A., Heath, G. R., Cullen, D., et al. (1979). Early Oxidation of Organic Matter in Pelagic Sediments of the Eastern Equatorial Atlantic: Suboxic Diagenesis. *Geochimica et Cosmochimica Acta* 43 (7), 1075–1090. doi:10.1016/0016-7037(79)90095-4

Garrison, R. E., Kastner, M., and Zenger, D. H. (1984). *Dolomites of the Monterey Formation and Other Organic-Rich Units*. Los Angeles, California: SEPM, Pacific Section, 215.

Gaucher, E., Robelin, C., Matray, J. M., Négrel, G., Gros, Y., Heitz, J. F., et al. (2004). ANDRA Underground Research Laboratory: Interpretation of the Mineralogical and Geochemical Data Acquired in the Callovian-Oxfordian Formation by Investigative Drilling. *Phys. Chem. Earth, Parts A/B/C* 29, 55–77. doi:10.1016/j.pce.2003.11.006

Goldich, S. S. (1938). A Study in Rock-Weathering. *J. Geology.* 46, 17–58. doi:10.1086/624619

Grenthe, I., and Plyasunov, A. (1997). On the Use of Semiempirical Electrolyte Theories for Modeling of Solution Chemical Data. *Pure Appl. Chem.* 69, 951–958. doi:10.1351/pac199769050951

Guggenheim, E. A., and Turgeon, J. C. (1955). Specific Interaction of Ions. *Trans. Faraday Soc.* 51, 747–761. doi:10.1039/tf9555100747

Ingle, J. C., Jr., Suyehiro, K., and von Breymann, M. T. (1990). "Japan Sea," in *Proc. ODP, Init. Repts.* (College Station, TX, 128. (Ocean Drilling Program).

Jasmund, K., and Lagaly, G. (1993). *Tonminerale und Tone: Struktur, Eigenschaften, Anwendungen und Einsatz in Industrie und Umwelt*. Darmstadt: Steinkopff. 3-7985-0923-9.

Kasina, M., Morozova, D., Michalik, M., Pudlo, D., and Wuerdemann, H. (2014). Impact of Gas Storage on Reservoir Rocks - Long-Term Study to Investigate the

Effects on Mineral Content and Fluid Chemistry. *Energ. Proced.* 59, 418–424. doi:10.1016/j.egypro.2014.10.397

Kastanja, M. M., Diekmann, B., and Henrich, R. (2006). Controls on Carbonate and Terrigenous Deposition in the Incipient Benguela Upwelling System during the Middle to the Late Miocene (ODP Sites 1085 and 1087). *Palaeogeogr. Palaeoclimatol. Palaeoecol.* 241, 515–530. doi:10.1016/j.palaeo.2006.05.004

Kastner, M., Elderfield, H., Martin, J. B., Suess, E., Kvenvolden, K. A., and Garrison, R. E. (1990). "Diagenesis and Interstitial-Water Chemistry at the Peruvian Continental Margin, Major Constituents and Strontium Isotopes," in, *Proc. ODP, Sci. Results*. Editors E. Suess and R. von Huene, 112, 413–440, Ocean Drilling Program, College Station, TX.doi:10.2973/odp.proc.sr.112.144.1990

Katz, A., and Ben-Yaakov, S. (1980). Diffusion of Seawater Ions. Part II. The Role of Activity Coefficients and Ion Pairing. *Mar. Chem.* 8, 263–280. doi:10.1016/0304-4203(80)90016-x

Kelts, K., and McKenzie, J. A. (1984). "A Comparison of Anoxic Dolomite from Deep-Sea Sediments: Quaternary Gulf of California and Messinian Tripoli Formation of Sicily," in *Dolomites Of the Monterey Formation And Other Organic-Rich Units*. Editors R. E. Garrison, M. Kastner, and D. H. Zenger (Los Angeles, CA: Pacific Section SEPM), 41, 19–28.

Knab, N. J., Dale, A. W., Lettmann, K., Fossing, H., and Jørgensen, B. B. (2008). Thermodynamic and Kinetic Control on Anaerobic Oxidation of Methane in marine Sediments. *Geochimica et Cosmochimica Acta* 72, 3746–3757. doi:10.1016/j.gca.2008.05.039

Kowalewski, M., and Rimstidt, J. D. (2003). Average Lifetime and Age Spectra of Detrital Grains: toward a Unifying Theory of Sedimentary Particles. *J. Geology.* 111, 427–439. doi:10.1086/375284

Krumins, V., Gehlen, M., Arndt, S., Van Cappellen, P., and Regnier, P. (2013). Dissolved Inorganic Carbon and Alkalinity Fluxes from Coastal marine Sediments: Model Estimates for Different Shelf Environments and Sensitivity to Global Change. *Biogeosciences* 10, 371–398. doi:10.5194/bg-10-371-2013

Kutvonen, H., Rajala, P., Carpén, L., and Bomberg, M. (2015). Nitrate and Ammonia as Nitrogen Sources for Deep Subsurface Microorganisms. *Front. Microbiol.* 6, 1079. doi:10.3389/fmicb.2015.01079

Lasaga, A. C. (1998). *Kinetic Theory in the Earth Sciences. Princeton Series in Geochemistry*. Princeton, Chichester: Princeton University Press, 811.

Loyd, S. J., Corsetti, F. A., Eiler, J. M., and Tripati, A. K. (2012). Determining the Diagenetic Conditions of Concretion Formation: Assessing Temperatures and Pore Waters Using Clumped Isotopes. *J. Sediment. Res.* 82, 1006–1016. doi:10.2110/jsr.2012.85

Lyle, M., Koizumi, I., and Richter, C. Shipboard Scientific Party (1997). Proceedings of the Ocean Drilling Program. *Initial Rep.* 167, 353–387. doi:10.2973/odp.proc.ir.167.113.1997

Marinoni, L., Setti, M., Salvi, C., and López-Galindo, A. (2008). Clay Minerals in Late Quaternary Sediments from the South Chilean Margin as Indicators of Provenance and Palaeoclimate. *Clay miner.* 43, 235–253. doi:10.1180/claymin.2008.043.2.07

Matmon, D., and Bekins, B. A. (2006). Hydromechanics of a High Taper Angle, Low-Permeability Prism: A Case Study from Peru. *J. Geophys. Res.* 111, B07101. doi:10.1029/2005JB003697

Mavromatis, V., Meister, P., and Oelkers, E. H. (2015). Using Stable Mg Isotopes to Distinguish Dolomite Formation Mechanisms: A Case Study from the Peru Margin. *Chem. Geology.* 385, 84–91.

Meister, P., Brunner, B., Picard, A., Böttcher, M. E., and Jørgensen, B. B. (2019a). Sulphur and Carbon Isotopes as Tracers of Past Sub-seafloor Microbial Activity. *Sci. Rep.* 9 (604), 604–609. doi:10.1038/s41598-018-36943-7

Meister, P., Chapligin, B., Picard, A., Meyer, H., Fischer, C., Rettenwander, D., et al. (2014). Early Diagenetic Quartz Formation at a Deep Iron Oxidation Front in the Eastern Equatorial Pacific - A Modern Analogue for Banded Iron/chert Formations? *Geochimica et Cosmochimica Acta* 137, 188–207. doi:10.1016/j.gca.2014.03.035

Meister, P. (2015). For the Deep Biosphere, the Present Is Not Always the Key to the Past: what We Can Learn from the Geological Record. *Terra Nova* 27, 400–408. doi:10.1111/ter.12174

Meister, P., Gutjahr, M., Frank, M., Bernasconi, S. M., Vasconcelos, C., and McKenzie, J. A. (2011). Dolomite Formation within the Methanogenic Zone Induced by Tectonically Driven Fluids in the Peru Accretionary Prism. *Geology* 39, 563–566. doi:10.1130/g31810.1

Meister, P., Liu, B., Ferdelman, T. G., Jørgensen, B. B., and Khalili, A. (2013). Control of Sulphate and Methane Distributions in marine Sediments by Organic Matter Reactivity. *Geochimica et Cosmochimica Acta* 104, 183–193. doi:10.1016/j.gca.2012.11.011

Meister, P., Liu, B., Khalili, A., Böttcher, M. E., and Jørgensen, B. B. (2019b). Factors Controlling the Carbon Isotope Composition of Dissolved Inorganic Carbon and Methane in marine Porewater: An Evaluation by Reaction-Transport Modelling. *J. Mar. Syst.* 200, 1032271–1032318. doi:10.1016/j.jmarsys.2019.103227

Meister, P., McKenzie, J. A., Vasconcelos, C., Bernasconi, S., Frank, M., Gutjahr, M., et al. (2007). Dolomite Formation in the Dynamic Deep Biosphere: Results from the Peru Margin. *Sedimentology* 54, 1007–1032. doi:10.1111/j.1365-3091.2007.00870.x

Meister, P., McKenzie, J. A., Warthmann, R., and Vasconcelos, C. (2006). "Mineralogy and Petrography of Diagenetic Dolomite, Peru Margin, ODP Leg 201," in *Proc. ODP, Sci. Results*. Editors B. B. Jørgensen, S. L. D'Hondt, and D. J. Miller, 1–34. doi:10.2973/odp.proc.sr.201.102.2006

Meister, P., Prokopenko, M., Skilbeck, C. G., Watson, M., and McKenzie, J. A. (2005). "Data Report: Compilation of Total Organic and Inorganic Carbon Data from Peru Margin and Eastern Equatorial Pacific Drill Sites (ODP Legs 112, 138, and 201)," in *Proc. ODP, Sci. Results*. Editors B. B. Jørgensen, S. L. D'Hondt, and D. J. Miller, 201. doi:10.2973/odp.proc.sr.201.105.2005

Meister, P., and Reyes, C. (2019). "The Carbon-Isotope Record of the Sub-seafloor Biosphere," in *Tracking the Deep Biosphere through Time*. Editors H. Drake, M. Ivarsson, and C. Heim, 9, 1–25. doi:10.3390/geosciences9120507

Meister, P. (2013). Two Opposing Effects of Sulfate Reduction on Carbonate Precipitation in normal marine, Hypersaline, and Alkaline Environments. *Geology* 41, 499–502. doi:10.1130/g34185.1

Meister, P. (2014). Two Opposing Effects of Sulfate Reduction on Carbonate Precipitation in normal marine, Hypersaline, and Alkaline Environments: Reply. *Geology* 42, e315. doi:10.1130/g35240y.1

Michalopoulos, P., and Aller, R. C. (1995). Rapid Clay Mineral Formation in Amazon Delta Sediments: Reverse Weathering and Oceanic Elemental Cycles. *Science* 270, 614–617. doi:10.1126/science.270.5236.614

Middelburg, J. J., Soetaert, K., and Hagens, M. (2020). Ocean Alkalinity, Buffering and Biogeochemical Processes. *Rev. Geophys.* 58, e2019RG000681. doi:10.1029/2019RG000681

Moore, D. M., and Reynolds, R. C. (1997). *X-ray Diffraction and the Identification and Analysis of clay Minerals*. 2nd ed. Oxford, New York: Oxford University Press.

Moore, T. S., Murray, R. W., Kurtz, A. C., and Schrag, D. P. (2004)., 229. Amsterdam: Elsevier B.V., 141–154. doi:10.1016/j.epsl.2004.10.015Anaerobic Methane Oxidation and the Formation of Dolomite*Earth Planet. Sci. Lett.*

Morse, J. W., Arvidson, R. S., and Lüttge, A. (2007). Calcium Carbonate Formation and Dissolution. *Chem. Rev.* 107, 342–381. doi:10.1021/cr050358j

Mozley, P. S., and Burns, S. J. (1993). Oxygen and Carbon Isotopic Composition of marine Carbonate Concretions – an Overview. *J. Sediment. Petrol.* 63, 73–83.

Murata, K. J., Friedman, I., and Madsen, B. H. (1969). Isotopic Composition of Diagenetic Carbonates in Marine Miocene Formations of California and Oregon. *U.S. Geological Survey Professional Paper*. Washington, DC: U.S. Government Printing Office 614-B, 1–24. doi:10.3133/pp614B

Murray, R. W., and Wigley, R. Shipboard Scientific Party (1998). Interstitial Water Chemistry of Deeply Buried Sediments from the Southwest African Margin: A Preliminary Synthesis of Results from Leg 175. *Proc. Ocean Drill. Prog. Initial Rep.* 175, 547–553. doi:10.2973/odp.proc.ir.175.120.1998

Nauhaus, K., Boetius, A., Krüger, M., and Widdel, F. (1995). *In Vitro* demonstration of Anaerobic Oxidation of Methane Coupled to Sulphate Reduction in Sediment from a marine Gas Hydrate Area. *Environ. Microbiol.* 4, 296–305. doi:10.1046/j.1462-2920.2002.00299.x

Ockert, C., Wehrmann, L. M., Kaufhold, S., Ferdelman, T. G., Teichert, B. M. A., and Gussone, N. (2014). Calcium-ammonium Exchange Experiments on clay Minerals Using a45Ca Tracer Technique in marine Pore Water. *Isotopes Environ. Health Stud.* 50, 1–17. doi:10.1080/10256016.2013.806505

Park, Y. K., Lee, J. I., Jung, J., Hillenbrand, C.-D., Yoo, K.-C., and Kim, J. (2019). Elemental Compositions of Smectites Reveal Detailed Sediment Provenance Changes during Glacial and Interglacial Periods: the Southern Drake Passage

and Bellingshausen Sea, Antarctica. *Minerals* 9 (322), 1–14. doi:10.3390/min9050322

Parkes, R. J., Webster, G., Cragg, B. A., Weightman, A. J., Newberry, C. J., Ferdelman, T. G., et al. (2005). Deep Sub-seafloor Prokaryotes Stimulated at Interfaces over Geological Time. *Nature* 436, 390–394. doi:10.1038/nature03796

Parkhurst, D., and Appelo, C. (2013). Description of Input and Examples for PHREEQC Version 3—A Computer Program for Speciation, Batch-Reaction, One-Dimensional Transport, and Inverse Geochemical Calculations. *U.S. Geol. Surv. Tech. Methods* 6-A43, 497.

Parkhurst, D. L., and Wissmeier, L. (2015). PhreeqcRM: A Reaction Module for Transport Simulators Based on the Geochemical Model PHREEQC. *Adv. Water Resour.* 83, 176–189. doi:10.1016/j.advwatres.2015.06.001

Paull, C. K., Matsumoto, R., and Wallace, P. J. Shipboard Scientific Party (1996). *Gas Hydrate Sampling on the Blake Ridge and Carolina Rise Proc. ODP, Init. Repts. 164*. College Station, TX: Ocean Drilling Program. doi:10.2973/odp.proc.ir.164.1996

Pisciotto, K. H., and Mahoney, J. J. (1981). Isotopic Survey of Diagenetic Carbonates, Deep Sea Drilling Project Leg 63. *Drilling Project* 63, 595–609. doi:10.2973/dsdp.proc.63.118.1981

Prokopenko, M. G., Hammond, D. E., Spivack, A. J., and Stott, L. D. (2006). *Sediment and Pore Water C and N Composition of ODP Holes 201-1227A*, 201–1230A. doi:10.1594/PANGAEA.773410

Raiswell, R., and Fisher, Q. J. (2000). Mudrock-hosted Carbonate Concretions: a Review of Growth Mechanisms and Their Influence on Chemical and Isotopic Composition. *J. Geol. Soc.* 157, 239–251. doi:10.1144/jgs.157.1.239

Rodriguez, N. M., Paull, C. K., and Borowski, W. S. (2000). "Zonation of Authigenic Carbonates within Gas Hydrate-Bearing Sedimentary Sections on the Blake ridge: Offshore southeastern North America," in *Proc. ODP, Sci. Results*. Editors C. K. Paull, R. Matsumoto, P. J. Wallace, and W. P. Dillon College Station, TX: Ocean Drilling Program, 164, 301–312. doi:10.2973/odp.proc.sr.164.227.2000

Scholz, F., Hensen, C., Schmidt, M., and Geersen, J. (2013). Submarine Weathering of Silicate Minerals and the Extent of Pore Water Freshening at Active continental Margins. *Geochimica et Cosmochimica Acta* 100, 200–216. doi:10.1016/j.gca.2012.09.043

Schrag, D. P., Higgins, J. A., Macdonald, F. A., and Johnston, D. T. (2013). Authigenic Carbonate and the History of the Global Carbon Cycle. *Science* 339, 540–543. doi:10.1126/science.1229578

Smith, D. C. (2005). "Data Report: Dissolved Organic Carbon in Interstitial Waters, Equatorial Pacific and Peru Margin, ODP Leg 201," in *Proc. ODP, Sci. Results 201*. Editors B. B. Jørgensen, S. L. D'Hondt, and D. J. Miller. doi:10.2973/odp.proc.sr.201.111.2005

Soetaert, K., Hofmann, A. F., Middleburg, J. J., Meysman, F. J. R., and Greenwood, J. (2007). The Effect of Biogeochemical Processes on pH. *Marine Chem.* 105, 30–51. doi:10.1016/j.marchem.2006.12.012

Solomon, E. A., Spivack, A. J., Kastner, M., Torres, M. E., and Robertson, G. (2014). Gas Hydrate Distribution and Carbon Sequestration Through Coupled Microbial Methanogenesis and Silicate Weathering in the Krishna–Godavari Basin, Offshore India. *Marine Petrol. Geol.* 58, 233–253. doi:10.1016/j.marpetgeo.2014.08.020

Spivack, A. J., McNeil, C., Holm, N. G., and Hinrichs, K.-U. (2006). "Determination of *In Situ* Methane Based on Analysis of Void Gas," in *Proc. ODP, Sci. Results*. Editors B. B. Jørgensen, S. L. D'Hondt, and D. J. Miller, 1–11. doi:10.2973/odp.proc.sr.201.119.2006

Suess, E. (1988). *Peru continental Margin. Proc. ODP, Init. Repts*. College Station, TX: Ocean Drilling Program.

Sun, X., and Turchyn, A. V. (2014). Significant Contribution of Authigenic Carbonate to marine Carbon Burial. *Nat. Geosci* 7, 201–204. doi:10.1038/ngeo2070

Tada, R., Murray, R. W., and Alvarez Zarikian, C. A. Expedition 346 Scientists (2015). Site U1426. *Proc. Integr. Ocean Drill. Prog.* 346, 1–113. doi:10.2204/iodp.proc.346.107.2015

Tarpgaard, I. H., Jørgensen, B. B., Kjeldsen, K. U., Kjeldsen, K. U., and Røy, H. (2017). The marine Sulfate Reducer Desulfobacterium Autotrophicum HRM2 Can Switch between Low and High Apparent Half-Saturation Constants for Dissimilatory Sulfate Reduction. *FEMS Microbiol. Ecol.* 93, 12. doi:10.1093/femsec/fix012

Thornburg, T. M., and Suess, E. (1992). "Carbonate Cementation of Granular and Fracture Porosity: Implications for the Cenozoic Hydrologic Development of the Peru Continental Margin," in *Proc. ODP, Sci. Results*. Editor M. Suess, 112, 95–109.

Tishchenko, P., Hensen, C., Wallmann, K., and Wong, C. S. (2005). Calculation of the Stability and Solubility of Methane Hydrate in Seawater. *Chem. Geology.* 219, 37–52. doi:10.1016/j.chemgeo.2005.02.008

Tréhu, A. M., Bohrmann, G., Rack, F. R., and Torres, M. E.Shipboard Scientific Party (2003). "Drilling Gas Hydrates on Hydrate Ridge, Cascadia Continental Margin," in *Proc. ODP, Init. Repts.* (College Station, TX: Ocean Drilling Program), 1–75.

Treude, T., Boetius, A., Knittel, K., Wallmann, K., and Barker Jørgensen, B. (2003). Anaerobic Oxidation of Methane above Gas Hydrates at Hydrate Ridge, NE Pacific Ocean. *Mar. Ecol. Prog. Ser.* 264, 1–14. doi:10.3354/meps264001

Ussler, W., and Paull, C. K. (2008). Rates of Anaerobic Oxidation of Methane and Authigenic Carbonate Mineralization in Methane-Rich Deep-Sea Sediments Inferred from Models and Geochemical Profiles. *Earth Planet. Sci. Lett.* 266, 271–287. doi:10.1016/j.epsl.2007.10.056

Van Cappellen, P. (1996). Reactive Surface Area Control of the Dissolution Kinetics of Biogenic Silica in Deep-Sea Sediments. *Chem. Geology.* 132, 125–130. doi:10.1016/s0009-2541(96)00047-2

Von Breymann, M. T., Collier, R., and Suess, E. (1990). Magnesium Adsorption and Ion Exchange in marine Sediments: a Multi-Component Model. *Geochimica et Cosmochimica Acta* 54, 3295–3313. doi:10.1016/0016-7037(90)90286-t

Wallmann, K., Aloisi, G., Haeckel, M., Tishchenko, P., Pavlova, G., Greinert, J., et al. (2008). Silicate Weathering in Anoxic marine Sediments. *Geochim. Cosmochim. Acta*, 72, 3067–3090. doi:10.1016/j.gca.2008.03.026

Wang, G., Spivack, A. J., Rutherford, S., Manor, U., and D'Hondt, S. (2008). Quantification of Co-occurring Reaction Rates in Deep Subseafloor Sediments. *Geochimica et Cosmochimica Acta* 72, 3479–3488. doi:10.1016/j.gca.2008.04.024

Wefer, G., Berger, W. H., and Richter, C. Shipboard Scientific Party (1998). "Benguela Current," in *Proc. ODP, Init. Repts. 175* (College Station, TX: Ocean Drilling Program). doi:10.2973/odp.proc.ir.175.1998

Wehrmann, L. M., Ockert, C., Mix, A. C., Gussone, N., Teichert, B. M. A., and Meister, P. (2016). Repeated Occurrences of Methanogenic Zones, Diagenetic Dolomite Formation and Linked Silicate Alteration in Southern Bering Sea Sediments (Bowers Ridge, IODP Exp. 323 Site U1341). *Deep Sea Res. Part II* 125–126, 117–132. doi:10.1016/j.dsr2.2013.09.008

Wehrmann, L. M., Knab, N. J., Pirlet, H., Unnithan, V., Wild, C., and Ferdelman, T. G. (2009). Carbon Mineralization and Carbonate Preservation in Modern Cold-Water Coral Reef Sediments on the Norwegian Shelf. *Biogeosciences* 6, 663–680. doi:10.5194/bg-6-663-2009

Wolf-Gladrow, D. A., Zeebe, R. E., Klaas, C., Körtzinger, A., and Dickson, A. G. (2007). Total Alkalinity: the Explicit Conservative Expression and its Application to Biogeochemical Processes. *Mar. Chem.* 106, 287–300. doi:10.1016/j.marchem.2007.01.006

Zeebe, R. E. (2007). Modeling CO2 Chemistry, δ13C, and Oxidation of Organic Carbon and Methane in Sediment Porewater: Implications for Paleo-Proxies in Benthic Foraminifera. *Geochimica et Cosmochimica Acta* 71, 3238–3256. doi:10.1016/j.gca.2007.05.004

Conflict of Interest: The authors declare that the research was conducted in the absence of any commercial or financial relationships that could be construed as a potential conflict of interest.

Publisher's Note: All claims expressed in this article are solely those of the authors and do not necessarily represent those of their affiliated organizations, or those of the publisher, the editors and the reviewers. Any product that may be evaluated in this article, or claim that may be made by its manufacturer, is not guaranteed or endorsed by the publisher.

Advantages of publishing in Frontiers

OPEN ACCESS
Articles are free to read for greatest visibility and readership

FAST PUBLICATION
Around 90 days from submission to decision

HIGH QUALITY PEER-REVIEW
Rigorous, collaborative, and constructive peer-review

TRANSPARENT PEER-REVIEW
Editors and reviewers acknowledged by name on published articles

Frontiers
Avenue du Tribunal-Fédéral 34
1005 Lausanne | Switzerland

Visit us: www.frontiersin.org
Contact us: frontiersin.org/about/contact

REPRODUCIBILITY OF RESEARCH
Support open data and methods to enhance research reproducibility

DIGITAL PUBLISHING
Articles designed for optimal readership across devices

FOLLOW US
@frontiersin

IMPACT METRICS
Advanced article metrics track visibility across digital media

EXTENSIVE PROMOTION
Marketing and promotion of impactful research

LOOP RESEARCH NETWORK
Our network increases your article's readership